PLANNING AND OPERATION OF HYBRID RENEWABLE ENERGY SYSTEMS

EDITED BY: Weihao Hu, Amjad Anvari-Moghaddam, Haoran Zhao, Liansong Xiong and Yuefang Du

PUBLISHED IN: Frontiers in Energy Research

frontiers Research Topics

ISSN 1664-8714
ISBN 978-2-83250-280-8
DOI 10.3389/978-2-83250-280-8

About Frontiers

Frontiers is more than just an open-access publisher of scholarly articles: it is a pioneering approach to the world of academia, radically improving the way scholarly research is managed. The grand vision of Frontiers is a world where all people have an equal opportunity to seek, share and generate knowledge. Frontiers provides immediate and permanent online open access to all its publications, but this alone is not enough to realize our grand goals.

Frontiers Journal Series

The Frontiers Journal Series is a multi-tier and interdisciplinary set of open-access, online journals, promising a paradigm shift from the current review, selection and dissemination processes in academic publishing. All Frontiers journals are driven by researchers for researchers; therefore, they constitute a service to the scholarly community. At the same time, the Frontiers Journal Series operates on a revolutionary invention, the tiered publishing system, initially addressing specific communities of scholars, and gradually climbing up to broader public understanding, thus serving the interests of the lay society, too.

Dedication to Quality

Each Frontiers article is a landmark of the highest quality, thanks to genuinely collaborative interactions between authors and review editors, who include some of the world's best academicians. Research must be certified by peers before entering a stream of knowledge that may eventually reach the public - and shape society; therefore, Frontiers only applies the most rigorous and unbiased reviews.
Frontiers revolutionizes research publishing by freely delivering the most outstanding research, evaluated with no bias from both the academic and social point of view. By applying the most advanced information technologies, Frontiers is catapulting scholarly publishing into a new generation.

What are Frontiers Research Topics?

Frontiers Research Topics are very popular trademarks of the Frontiers Journals Series: they are collections of at least ten articles, all centered on a particular subject. With their unique mix of varied contributions from Original Research to Review Articles, Frontiers Research Topics unify the most influential researchers, the latest key findings and historical advances in a hot research area! Find out more on how to host your own Frontiers Research Topic or contribute to one as an author by contacting the Frontiers Editorial Office: frontiersin.org/about/contact

PLANNING AND OPERATION OF HYBRID RENEWABLE ENERGY SYSTEMS

Topic Editors:
Weihao Hu, University of Electronic Science and Technology of China, China
Amjad Anvari-Moghaddam, Aalborg University, Denmark
Haoran Zhao, Shandong University, China
Liansong Xiong, Xi’an Jiaotong University, China
Yuefang Du, University of Electronic Science and Technology of China, China

Citation: Hu, W., Anvari-Moghaddam, A., Zhao, H., Xiong, L., Du, Y., eds. (2022). Planning and Operation of Hybrid Renewable Energy Systems.
Lausanne: Frontiers Media SA. doi: 10.3389/978-2-83250-280-8

Table of Contents

frontiers | Frontiers in Energy Research

EDITORIAL
published: 08 September 2022
doi: 10.3389/fenrg.2022.945794

Editorial: Planning and Operation of Hybrid Renewable Energy Systems

Hu Weihao[1]*, *Amjad Anvari-Moghaddam*[2], *Haoran Zhao*[3], *Liansong Xiong*[4] and *Yuefang Du*[1]

[1]*School of Mechanical and Electrical Engineering, University of Electronic Science and Technology of China, Chengdu, China,* [2]*Aalborg University, Aalborg, Denmark,* [3]*Shandong University, Jinan, China,* [4]*Nanjing Institute of Technology (NJIT), Nanjing, China*

Keywords: location planning, energy scheduling, voltage control, frequency stability, hybrid renewable energy system

Editorial on the Research Topic

Planning and Operation of Hybrid Renewable Energy Systems

Renewable energy sources such as wind and solar power have attracted worldwide attention as ways of addressing energy shortages and carbon emission issues, meaning they have become largely integrated into power systems. However, the utilization of renewable energy brings great challenges in terms of the planning and operation of the power system due to its uncertainty and intermittency. Hybrid renewable energy systems (HRESs), which combine different kinds of renewable energy sources, make the system more complex to plan and operate. On the other hand, the characteristics of several renewable energy provide an opportunity to take advantage of and achieve better planning and operations.

This Frontiers Research Topic aims to present state-of-the-art studies on the planning and operation of HRESs. A total of 22 papers were accepted to this collection after careful peer-to-peer review, covering the following three categories.

Edited and reviewed by:
Carlo Roselli,
University of Sannio, Italy

****Correspondence:***
Hu Weihao
whu@uestc.edu.cn

Specialty section:
This article was submitted to Process and Energy Systems Engineering, a section of the journal Frontiers in Energy Research

Received: *16 May 2022*
Accepted: *15 June 2022*
Published: *08 September 2022*

Citation:
Weihao H, Anvari-Moghaddam A, Zhao H, Xiong L and Du Y (2022) Editorial: Planning and Operation of Hybrid Renewable Energy Systems. Front. Energy Res. 10:945794. doi: 10.3389/fenrg.2022.945794

PLANNING OF HYBRID RENEWABLE ENERGY SYSTEMS

To minimize the curtailment of renewable energy, power to hydrogen (P2H) plays an important role in improving renewable energy integration. Wang et al. propose a two-stage stochastic mixed-integer nonlinear planning framework to decide on P2H sizing and siting to reduce the total capital and operational costs. In deciding the locations of pumped storage plants, photovoltaic and wind power, Qing et al. introduce a bi-layer planning optimization model to reduce the cable cost and the distribution network operation cost. Wang et al. studied both the energy generation benefits and investment costs of a large-scale photovoltaic plant in undertaking its economic evaluation. Batteries also play an important role in the utilization of renewable energy, and Wang et al. provide reasonable investment suggestions for the stepwise utilization of retired power batteries based on economic boundary value models. To enable optimal crop growth and maintain low operation costs, Tian et al. optimize the capacity of the combined cooling, heating and power supply, energy storage, and air source heat pump.

SCHEDULING OF HYBRID RENEWABLE ENERGY SYSTEMS

To better undertake the energy scheduling of HRESs, the characteristics of renewable energy should be taken into account. One way to do this is to improve the prediction accuracy, as outlined in the work by Li et al., and another is to consider its uncertainty. With the consideration of the uncertainty of renewable energy sources, the energy of the data center microgrid is scheduled in the contribution by Zhu et al. to minimize the operation cost and maintain system stability. Since multiple energy sources make the system more complex and hard to obtain the optimal schedule, Tian et al. and Wang et al. design solving algorithms for scheduling optimization and these algorithms improve the computation efficiency. In addition, the HRESs should be scheduled in the normal condition and Wang et al. and Xiong et al. achieve fault detection based on a neural network.

CONTROL OF HYBRID RENEWABLE ENERGY SYSTEMS

With the increasing penetration of renewable energy generation, the frequency stability of a power grid is significantly threatened, Yang et al. and Xu et al. boost the frequency nadir and guarantee rapid frequency stabilization. Liu et al. contribute to the transient stability of the HRESs. For the voltage challenge, Wang et al. investigate the dual-loop voltage–current control to manage voltage sags and Shang et al. enhance grid voltage dynamics. As new energies are integrated into the grid, the harmonics become more serious, Suo et al. introduce a multi-time-scale harmonic mitigation method based on model predictive control and Li et al. adopt the neutral-point potential control of interleaved parallel three-level inverters. Li et al. improve the converter design method to reduce the current total harmonic distortion of the grid side. In addition, to obtain a stable wind turbine output, a pitch control strategy is proposed in the work by Shao et al. Li et al. control the charging and discharge of batteries to improve the operation stability and economy of a DC microgrid. Zhao et al. designed an active impedance to suppress the resonance of the multi-inverter parallel system to improve power quality.

Overall, recent years have seen great progress in the planning and operation of HRESs. However, there are still many challenges and opportunities related to the further integration of renewable energy sources, and the theory and technology of HRESs need to be further investigated.

AUTHOR CONTRIBUTIONS

WH wrote the draft and other authors gave the suggestions and did the proofreading.

Conflict of Interest: The authors declare that the research was conducted in the absence of any commercial or financial relationships that could be construed as a potential conflict of interest.

frontiers in Energy Research

ORIGINAL RESEARCH
published: 22 November 2021
doi: 10.3389/fenrg.2021.788989

Torque Limit-Based Inertial Control of a DFIG for Rapid Frequency Stabilization

*Yien Xu and Hongmei Wang**

Department of Electrical Engineering, Nantong University, Nantong, China

With the increasing penetration of renewable energy generation, the frequency stability of a power grid can be significantly threatened. A doubly-fed induction generator (DFIG) participates in the frequency support of a power grid by releasing kinetic energy (KE) to boost the frequency nadir (FN). However, during rotor speed restoration, it is difficult to counterbalance the size of a second frequency drop (SFD) and the rotor speed recovery duration. This paper proposes an improved torque limit-based inertial control (TLBIC) to raise the FN by releasing less kinetic energy while guaranteeing rapid frequency stabilization with reduced SFD. To this end, when detecting a disturbance, the DFIG enhances the active reference power to the torque limit, and then the active power reduces smoothly based on an exponential function until the maximum power point tracking (MPPT) curve is met, and the rotor speed reverts to the initialization operating condition along the MPPT curve. A simulation system model with various wind power penetrations is established in EMTP-RV. Results show that the proposed scheme boosts the FN at a high level with less KE and guarantees rapid frequency stabilization.

Keywords: frequency stability, torque limit-based inertial control, frequency nadir, second frequency drop, rotor speed recovery

Edited by:
Liansong Xiong,
Nanjing Institute of Technology (NJIT),
China

Reviewed by:
Jun Cong Ge,
Jeonbuk National University, South Korea
Huimin Wang,
University of Electronic Science and Technology of China, China
Zhaoyang Jin,
Shandong University, China

****Correspondence:***
Hongmei Wang
wanghongmei@ntu.edu.cn

Specialty section:
This article was submitted to Process and Energy Systems Engineering,
a section of the journal
Frontiers in Energy Research

Received: *04 October 2021*
Accepted: *21 October 2021*
Published: *22 November 2021*

Citation:
Xu Y and Wang H (2021) Torque Limit-Based Inertial Control of a DFIG for Rapid Frequency Stabilization.
Front. Energy Res. 9:788989.
doi: 10.3389/fenrg.2021.788989

INTRODUCTION

Recently, wind power generation has developed rapidly due to the shortage of fossil fuel and worsening environmental situations. Doubly-fed induction generators (DFIGs) are widely applied in the field of wind power because of the relatively low price, decoupling control operation of the active power and reactive power, maximum power point tracking (MPPT) control, deloading operation, and other advanced control strategies (Bao et al., 2020; Xiong et al., 2020). In addition, DFIGs are connected to the grid by power electronic converters, which decouple the rotor speed of the wind turbine from the system frequency. Consequently, DFIGs are unable to sustain the system frequency (Yang et al., 2022; Yang et al., 2021; Xiong et al., 2021a). With the increasing penetration level of wind power, the power system will face significant challenges in system frequency stability. Therefore, more and more attention has been paid to DFIG active frequency support (Wang and Tomsovic, 2018; Xiong et al., 2021b).

DFIGs supply inertial control using additional control strategies. In Kheshti et al. (2019), the most characteristic inertial control can be roughly divided into two types: virtual inertial control (PD control) (Morren et al., 2006; Fernandez et al., 2008; Lee et al., 2016; Van de Vyver et al., 2016; Li et al., 2017; Hu and Wu, 2019; Peng et al., 2020) and stepwise inertial control (Ullah et al., 2008; Lao, 2021). PD control emulates the inertia response and primary frequency response of synchronous generations (SGs) to provide a frequency response. Compared with PD control, stepwise inertial control can supply a rapid frequency response due to the operating characteristics of a DFIG (Kheshti et al., 2019). However, after DFIGs participate in frequency regulation by releasing rotor kinetic energy, the rotor speed will deviate from the optimal state corresponding to MPPT operation. Therefore, the rotor speed needs to regain the optimal state considering the economic benefits of the wind farm, but the speed recovery is accompanied by power mutation, which trend to cause a significant SFD (Xiong et al., 2021c).

In Hafiz and Abdennour (2015), the active power is designed as a slope function. Even though this scheme lessens the SFD to a certain extent, but it delays the rotor speed recovery. Furthermore, the parameters of this function in different scenarios need to be reset. In order to recover the rotor speed, a constant power reference is addressed (Kang et al., 2016a; Kang et al., 2016b). However, the tradeoff between the depth of an SFD and the rotor speed restoration is difficult to achieve. The study of Xu and Xu (2017) suggests a constant accelerating power reference based on the mechanical power curve, which realizes the smooth recovery of the rotor speed. Nevertheless, the mechanical power curve is difficult to acquire and SFD still exists due to the sudden power drop. The authors of (Lao, 2021) suggested a frequency regulation strategy based on logistic regression function, which realizes smooth rotor speed recovery. However, the function used in this strategy is too complex, and too many parameters need to be defined, which brings difficulties to engineering applications. To compensate for the energy required for rotor speed recovery, a coordinated frequency control strategy for the wind turbine and SG is addressed (Xu et al., 2018). The rotor speed recovery can be realized with reduced SFD by adjusting the primary frequency modulation parameters of the SG. However, for a large-scale power system with high wind power penetrations, this strategy is not economical to regain the rotor speed. In Wu et al. (2017), a frequency control strategy based on the energy storage system is suggested, which realizes the rapid speed recovery while eliminating the SFD. However, the overall operation and maintenance cost of the power system increases due to the high cost of the energy storage system.

To approach the above issues, this paper addresses an improved torque limit-based inertial control (TLBIC) scheme to raise the FN by releasing less rotational energy while guaranteeing rapid frequency stabilization with reduced SFD. To this end, when detecting a disturbance, the power reference of the DFIG increases to the torque limit. Afterward, the power reference decreases smoothly based on an exponential function until it the maximum power point tracking (MPPT) curve is met, and then the rotor speed reverts to the initialization operating condition along the MPPT curve. In addition, DFIGs are assumed to work in MPPT mode prior to frequency disturbance. The benefits of the proposed TLBIC scheme are verified under various wind power penetrations and wind speed conditions based on an EMTP-RV simulator.

MODELING OF A DOUBLY-FED INDUCTION GENERATOR

This section mainly introduces the typical structure of a DFIG, as illustrated in **Figure 1** which includes a wind turbine model, two-mass shaft model, and DFIG controllers.

Wind Turbine Model

The mechanical input power captured by a wind turbine from moving air is represented as:

$$P_m = \frac{1}{2} c_P(\lambda, \beta)\rho A v_w^3 = \frac{1}{2} c_P(\lambda, \beta)\rho \pi R^2 v_w^3 \tag{1}$$

where c_p represents the power coefficient; λ and β are the tip-speed ratio and pitch angle, respectively; ρ is the air density; A indicates the swept area by blade; R means the blade length and v_w means the wind velocity.

As in (Kang et al., 2016a; Kang et al., 2016b), c_p employed in **Eq. 1** can be represented as:

$$c_P(\lambda, \beta) = 0.645\left\{0.00912\lambda + \frac{-5 - 0.4(2.5+\beta) + 116\lambda_i}{e^{21\lambda_i}}\right\} \tag{2}$$

where

$$\lambda_i = \frac{1}{\lambda + 0.08(2.5+\beta)} - \frac{0.035}{1 + (2.5+\beta)^3} \tag{3}$$

and λ is given as:

$$\lambda = \frac{\omega_r R}{v_w}. \tag{4}$$

where ω_r represents the rotor speed of the generator.

For capturing more wind energy resources, the DFIG usually works in MPPT operation. As in Fernandez et al. (2008), the MPPT operation power reference, P_{MPPT}, is expressed as:

$$P_{MPPT} = \frac{1}{2} c_{P,\ \max} \rho \pi R^2 \left(\frac{\omega_r R}{\lambda_{opt}}\right)^3 = k\omega_r^3 \tag{5}$$

where $c_{p,\ \max}$ is a maximum value of c_p when $\beta = 0°$, $\lambda = \lambda_{opt}$ and set to 0.5 in this paper; λ_{opt} is the optimal λ of the wind turbine to capture the maximum wind energy and set to 9.95 in this paper; k is a calculation of the characteristic parameters of the wind turbine and set to 0.512 in this paper.

Two-Mass Shaft Model

This paper uses a two-mass shaft model to express the mechanical dynamics between the wind turbine and induction generator, the model can be represented as **Eqs 6–9** in (Boukhezzar and Siguerdidjane, 2011).

$$J_t \frac{d\omega_t}{dt} = T_m - T_L \tag{6}$$

$$J_g \frac{d\omega_r}{dt} = T_H - T_{em} \tag{7}$$

$$T_L = K\theta + D(\omega_t - \omega_L) \tag{8}$$

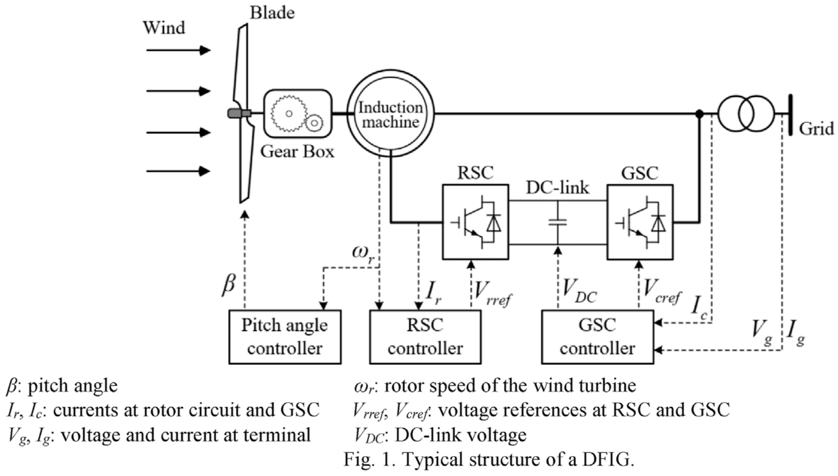

FIGURE 1 | Typical structure of a DFIG.

$$N = \frac{T_L}{T_H} = \frac{\omega_r}{\omega_L} \tag{9}$$

where J_t and J_g are the inertia constants of the wind turbine and generator, respectively; T_m and T_{em} are the mechanical torque, electrical torque of the wind turbine and generator, respectively; ω_t is the rotor speed of the wind turbine; T_L and T_H are the torques of the low-speed and the high-speed shafts, respectively; ω_L is the rotor speed of the low-speed shaft; K is the spring constant; D is the damping constant; θ is the torsional twist; N is the gear ratio.

β: pitch angle ω_r: rotor speed of the wind turbine.

I_r, I_c: currents at rotor circuit and GSC V_{rref}, V_{cref}: voltage references at RSC and GSC.

V_g, I_g: voltage and current at terminal V_{DC}: DC-link voltage.

Control System of a DFIG

The control system consists of a pitch angle controller, a rotor-side controller (RSC) and grid-side controller (GSC). The pitch angle controller adjusts the pitch angle according to the current wind speed to ensure the maximum of DFIG output power on the premise of the stable operation. An RSC realizes active and reactive power decoupling control and MPPT control of the DFIG. The GSC is mainly responsible for maintaining the DC-link voltage.

When the wind turbine output power is abnormally excessive or rapidly increased, the rapid change of the torque is inevitable. Especially in severe cases, severer mechanical torsion may damage the wind turbine. In order to protect the mechanical structure of the wind turbine and ensure the safe operation, the output power should meet Kang et al. (2016a)

$$P_{em} \le P_{T\lim} = T_{\lim}\omega_r \tag{10}$$

where P_{em} is the electromagnetic output power; P_{Tlim} is the maximum reference power based on torque limit; T_{lim} indicates the torque limit of the wind turbine and set to 0.88 p. u. in this paper.

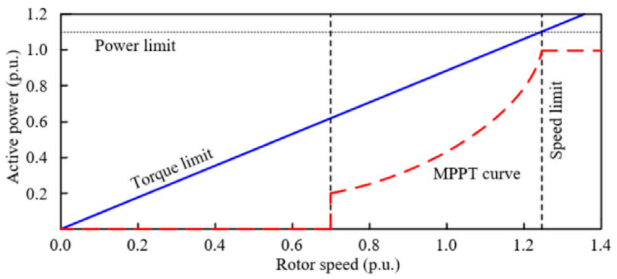

FIGURE 2 | Power characteristic curve of a DFIG.

Furthermore, the maximum power is 1.10 p. u., the minimum rotor speed is 0.70 p. u., and the maximum rotor speed is 1.25 p. u. as in Yang et al. (2018) (**Figure 2**).

ANALYSIS THE INERTIAL CONTROL OF A DFIG ON THE DYNAMIC SYSTEM FREQUENCY

When the DFIG implements the inertial control, the relationship between the active power variation (ΔP_{IC}) and the rotor speed of the DFIG can be represented as:

$$\Delta P_{IC} = J_{DFIG}\omega_r d\omega_r / dt \tag{11}$$

where J_{DFIG} means the moment of inertia of the DFIG.

According to the definition of the inertia constant of the SG, the inertia constant of the DFIG (H_{DFIG}) can be expressed as:

$$H_{DFIG} = J_{DFIG}\omega_n^2 / 2S_{DFIG} \tag{12}$$

where ω_n and S_{DFIG} indicate the rated rotor speed and rated capacity of the DFIG, respectively.

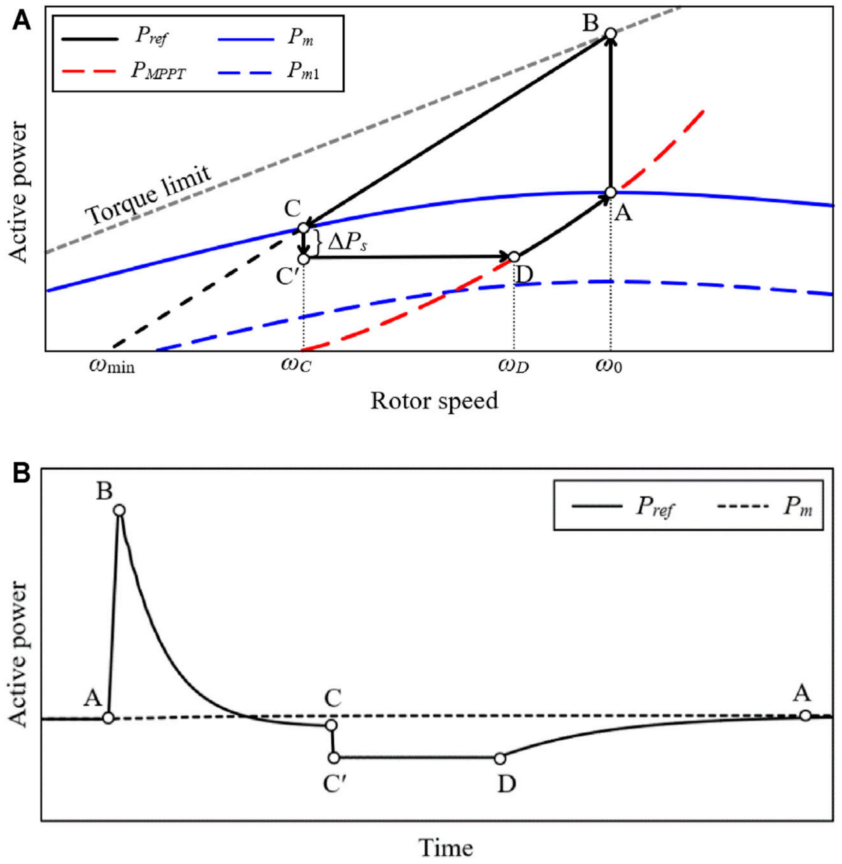

FIGURE 3 | Operational features of the conventional TLBIC scheme: **(A)** Power trajectory in the ω_r domain; **(B)** Active power in the time domain.

Rearranging **Eq. 11** and converting it to a per unit (p.u.) system, the expression of **Eq. 11** can be modified as in **Eq. 13**

$$\Delta P_{IC\_pu} = 2H_{DFIG}\omega_{pu}\frac{d\omega_{pu}}{dt} \tag{13}$$

where ΔP_{IC_pu} and ω_{pu} are ΔP_{IC} and the rotor speed of the DFIG in p. u., respectively.

By integrating both sides of **Eqs 13**, **14** is obtained

$$\Delta E_{pu} = H_{DFIG}\left[\omega_{pu}^2(t_1) - \omega_{pu}^2(t_0)\right] \tag{14}$$

where ΔE_{pu} is the released kinetic energy of the DFIG in p. u. during the inertia response, $\omega_{pu}(t_1)$ and $\omega_{pu}(t_0)$ are the rotor speed of the DFIG at t_1 and t_0 in p. u., respectively.

As in Miao et al. (2015), since the system frequency in p. u. is the same as ω_{pu}, ω_{pu} in **Eq. 14** is replaced by the frequency in p. u., thus, the expression of **Eq. 14** can be modified as:

$$f_{pu}(t_1) = \sqrt{\frac{\Delta E_{pu}}{H_{DFIG}} + f_{pu}^2(t_0)} \tag{15}$$

where $f_{pu}(t_1)$ and $f_{pu}(t_0)$ are the system frequency at t_1 and t_0 in p. u., respectively.

Therefore, the frequency deviation, $\Delta f_{pu} = f_{pu}(t_1)—f_{pu}(t_0)$, is given by **Eq. 16**:

$$\Delta f_{pu} = -f_{pu}(t_0) + \sqrt{\frac{\Delta E_{pu}}{H_{DFIG}} + f_{pu}^2(t_0)} \tag{16}$$

As shown in **Eq. 16**, it is evidenced that the DFIG can support the system frequency by inertia response. The large ΔE_{pu} can reduce the system frequency deviation so as to boost the FN.

TORQUE LIMIT-BASED INERTIAL CONTROL OF A DFIG

After the KE stored in rotor is released to support the system frequency, the rotor speed will deviate from the initial operation state, and even cause the wind turbine stalling. Furthermore, the rotor speed recovery trends to cause a significant SFD due to the reduction on the output power. In order to effectively heighten the FN without a stalling and recover the rotor speed with reduced SFD, the inertial control strategy of the DFIG should be carefully designed.

The following section briefly introduces the characteristics of the conventional TLBIC scheme of (Kang et al., 2016a).

Thereafter, the proposed TLBIC scheme is described in detailed in the second part of this section.

Conventional Torque Limit-based Inertial Control Scheme of a DFIG.

To improve the FN without causing the wind turbine stalling, the process of the TLBIC contains two periods: period of supporting the system frequency (A-B-C trajectory) and period of recovering rotor speed of the wind turbine (C-C'-D-A trajectory) (**Figure 3A**).

Period of Supporting the System Frequency

As shown in A-B-C trajectory of **Figure 3A**, the DFIG operates at MPPT mode prior to a disturbance, which corresponds to Point A. Upon detecting a disturbance, the power reference of a DFIG instantly increases to Point B (which is the torque limit) along Line A-B so as to boost the FN effectively. To avoid the wind turbine stalling, the reference power P_{ref} decreases along Point B to Point C. During the period of supporting the system frequency, the reference power P_{ref}, is given by:

$$P_{ref} = P_{MPPT}(\omega_{\min}) + \frac{P_{T\lim}(\omega_0) - P_{MPPT}(\omega_{\min})}{\omega_0 - \omega_{\min}}(\omega_r - \omega_{\min}) \tag{17}$$

where ω_{min} is the minimum rotor speed; ω_0 is the rotor speed prior to a disturbance; $P_{MPPT}(\omega_{\min})$ and $P_{MPPT}(\omega_0)$ are the value of P_{MPPT} at ω_{min} and ω_0, respectively; $P_{Tlim}(\omega_0)$ is the maximum power corresponding to torque limit at ω_0.

Since P_{ref} is greater than the input mechanical power P_m, ω_r decreases continuously based on the swing equation. Besides, as described in **Eq. 17**, the power reference P_{ref} is a linear function of ω_r, the active power output will decrease along the Line B-C with ω_r (see B-C trajectory in **Figure 3A**). When P_{ref} becomes equal to P_m at Point C, the rotor speed converges to ω_C. Accordingly, ω_C is higher than the minimum speed limit $\omega_{\min}$, so that this strategy effectively avoids the stalling of the wind turbine.

Period of Recovering Rotor Speed of the Wind Turbine

As in (Kang et al., 2016a), if ω_r satisfies the following condition, ω_r converges.

$$|\omega(t+T) - \omega(t)| \leq 3.45 \times 10^{-7}\text{p.u.} \tag{18}$$

where T is the sampling interval of ω_r.

At Point C, the active power $P_{ref}(\omega_C)$ instantly reduces ΔP_s to Point C′ so as to recover ω_r, and keep the value until the MPPT curve is met. At Point D, P_{ref} is switched to P_{MPPT}. Afterwards, ω_r returns from Point D to Point A by the action of the MPPT curve. P_{ref} for C-C′-D stage can be expressed as in **Eq. 19**.

$$P_{ref} = P_{ref}(\omega_C) - \Delta P_s \tag{19}$$

where ΔP_s is a constant.

As displayed in **Figure 3B**, since the condition **Eq. 18** is difficult to achieve. Accordingly, this period of ω_r convergence

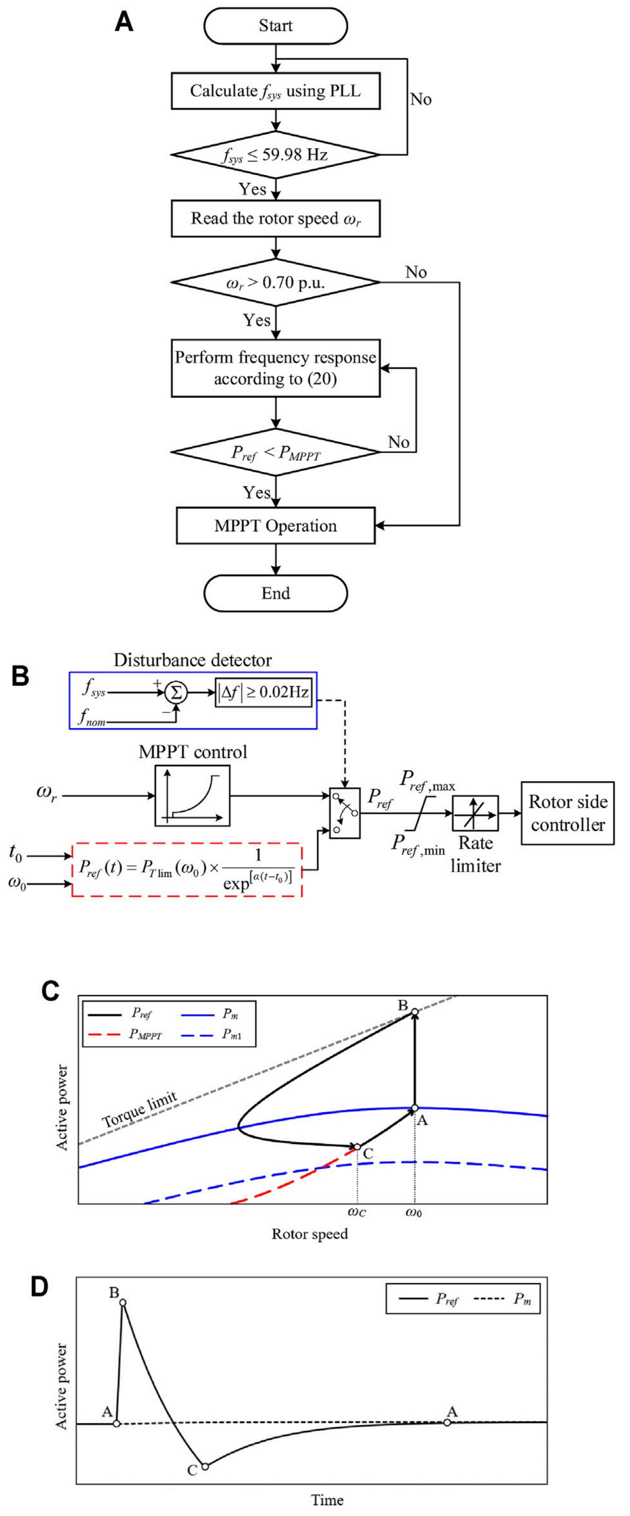

FIGURE 4 | Operational features of the proposed TLBIC scheme: **(A)** Flowchart of the proposed TLBIC scheme; **(B)** Block diagram of the proposed TLBIC scheme; **(C)** Power trajectory in the ω_r domain; **(D)** Active power in the time domain.

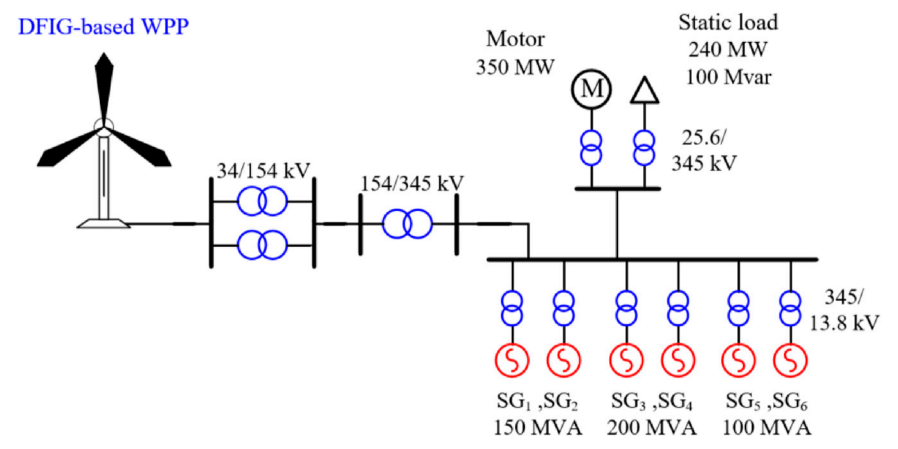

FIGURE 5 | Model system with an aggregated wind farm.

TABLE 1 | Parameters of the DFIG.

	Units	Values
Inertia constant	s	5.0
Apparent power	MVA	5.5
Active power	MW	5.0
Stator voltage	kV	2.3
Stator resistance	p.u	0.023
Stator leakage reactance	p.u.	0.18
Rotor resistance	p.u.	0.016
Rotor leakage reactance	p.u.	0.16

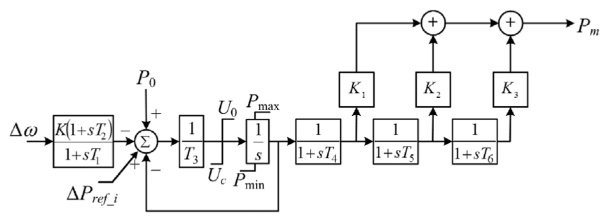

FIGURE 6 | IEEEG1 model (type B).

remains for a long time and leads to a waste of the KE which is unnecessary. In addition, to accelerate ω_r recovery, a large ΔP_s is desirable. However, too large ΔP_s may result in a severe SFD undoubtedly. Therefore, it is difficult to counterbalance the size of an SFD and the rotor speed recovery duration.

Proposed Torque Limit-based Inertial Control Scheme of a DFIG

To approach the above issues of the conventional TLBIC scheme, a proposed TLBIC scheme is carried out in this study.

The proposed TLBIC scheme aims to 1) improve the FN at a high level with less released kinetic energy and 2) ensure the frequency stabilization with reduced SFD. To this end, P_{ref} is represented as in **Eq. 20**, as shown in **Figure 4B**.

$$P_{ref}(t) = P_{T\lim}(\omega_0) \times \frac{1}{\exp^{[\alpha(t-t_0)]}} \quad t \geq t_0 \tag{20}$$

where α is the frequency control parameter; t_0 is the moment of disturbance occurrence.

The flowchart and the power operation features of the proposed TLBIC scheme are presented in **Figures 4A,C**, respectively. As the conventional TLBIC scheme, the proposed reference power increases instantly from $P_{MPPT}(\omega_0)$ to $P_{Tlim}(\omega_0)$ at t_0 (see A-B trajectory in **Figure 4C**), so as to provide short-term frequency response. Different from the conventional reference power (which is a function of ω_r), the proposed reference power is a function of the time. As time goes on, P_{ref} continues to decrease smoothly until the MPPT curve is met (see B-C trajectory in **Figure 4C**). At Point C, P_{ref} equals P_m and ω_r converges to ω_C. Afterwards, P_{ref} of the DFIG switches to P_{MPPT}, and the rotor speed returns to the initial state along the P_{MPPT} curve for optimum power production (see C-A trajectory in **Figure 4C**).

Compared with the conventional TLBIC scheme, the proposed TLBIC scheme is more manageable, which can control the output active power at the initial period of the frequency response by adjusting α. In addition, the proposed TLBIC scheme starts the restoration of ω_r earlier without the period of ω_r convergence and avoids the release of unnecessary KE. As shown in **Figure 4D**; **Eq. 20**, with the assistance of time-varying power function, P_{ref} decreases smoothly with time and switches to MPPT mode without an active power mutation, which effectively ensures frequency stabilization.

It is quite important to remark that the setting of α in **Eq. 20**: a small α is instrumental in rapid ω_r restoration. However, a small α is not benefit to release the rotating KE and boost the FN; On the contrary, a large α could rise the FN effectively, but it delays ω_r recovery and causes a severe SFD. Therefore, the setting of α is critically important. Besides, P_{ref} should be limited by an active power rate limiter and a maximum power limiter.

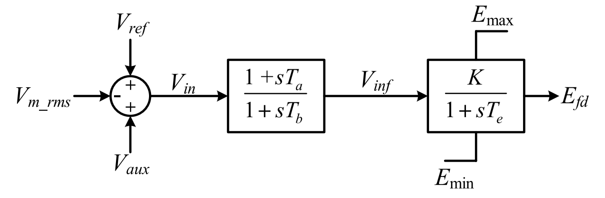

FIGURE 7 | SEXS exciter.

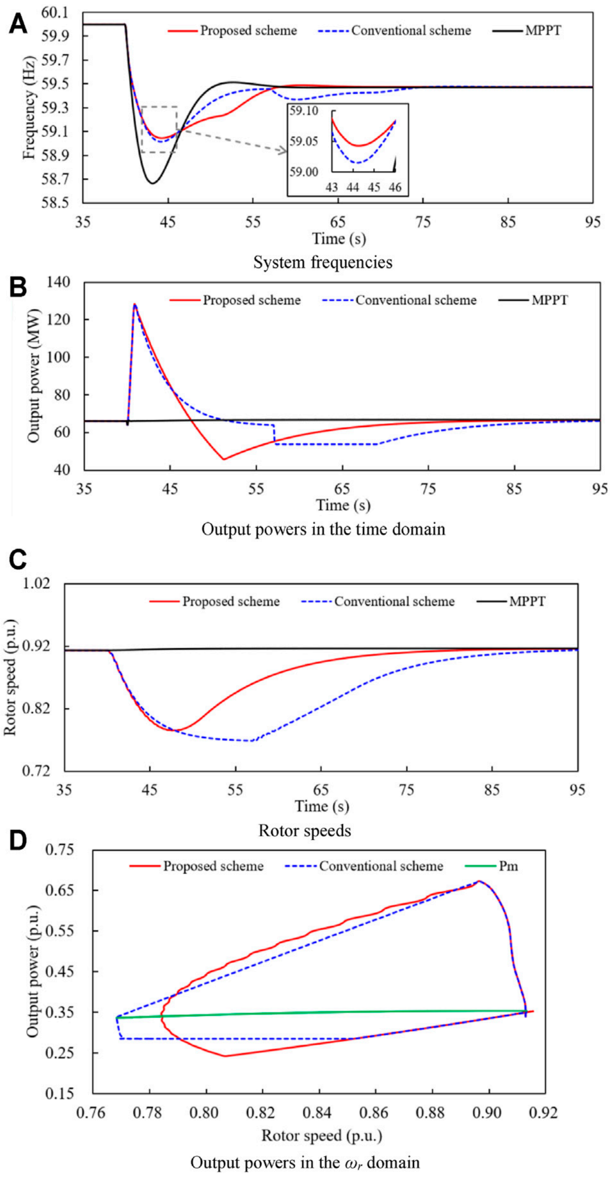

FIGURE 8 | Simulation results for case 1. **(A)** System frequencies. **(B)** Output powers in the time domain. **(C)** Rotor speeds. **(D)** Output powers in the ωr domain.

MODELING OF SIMULATION SYSTEM

Simulations on various wind power penetrations and wind speed conditions are conducted in EMTP-RV simulator to demonstrate the effectiveness of the proposed TLBIC scheme. As displayed in **Figure 5**, the model system consists of one aggregated DFIG-based wind farm, six synchronous generators, a 350-MW asynchronous motor, and a 240-MW static load. The main parameters of the DFIG are shown in **Table 1**.

As in (Byerly et al., 1973), all synchronous generators use the IEEEG1 governor and SEXS exciter. The classical configurations of the IEEEG1 model (type B) and SEXS exciter are displayed in **Figure 6**, **7**, respectively. Note that the secondary frequency response is not implemented in this study, thus the frequency will not eventually return to the acceptable range.

CASE STUDIES

In this section, the performances of the proposed scheme under the scenarios by varying the wind power penetration levels of 30 and 40% are verified. Moreover, the average wind speed is set to 8.0 m/s and a stochastic wind speed model is employed in this study. As a disturbance, SG_4 which generates 150 MW prior to a disturbance is tripped at 40.0 s.

The following several subsections will compare the performances of the proposed scheme with the conventional scheme and MPPT operation in terms of the system frequency nadir, second frequency drop, starting time of rotor speed recovery, and released kinetic energy, respectively.

The released kinetic energy ΔE_{rel} in this paper is defined as:

$$\Delta E_{rel} = H_{DFIG}\left(\omega_0^2 - \omega_C^2\right) \tag{21}$$

Case 1: Wind Power Penetration = 30% and Wind Speed = 8 m/s

Figure 8 shows the simulation results for case 1, in which the wind power penetration level is 30% and wind speed condition is 8.0 m/s. In addition, ΔP_s for the conventional scheme is set to 0.05 p. u., as suggested in (GB/T19963, 2011), and the KE available from the wind turbine is 1.708 s.

Since SG_4 is offline at $t = 40$ s, the system active power is out-off-balanced so that the frequency drops. As shown in **Figure 8A**, the frequency nadirs of the proposed TLBIC scheme, conventional TLBIC scheme, and MPPT control are 59.043, 59.014, and 58.665 Hz, respectively. When the DFIG operates at MPPT mode, it does not participate in system frequency response including inertia response and governor response, thus, its active power output and rotor speed remain unchanged. In addition, compared with the conventional strategy, the FN of the proposed TLBIC strategy is slightly boosted by 0.029 Hz. This is mainly because α is set to 0.1 so that the active power of the proposed TLBIC scheme is larger in the initial period of the inertial response (**Figure 8D**).

Figure 8C displays the rotor speeds of case 1, ω_r in the proposed TLBIC strategy drops faster and decreases to 0.784 p. u. at 47.6 s,

TABLE 2 | Simulation results for all cases.

		Case 1	Case 2	Case 3
Frequency nadir (Hz)	MPPT	58.665	58.501	58.614
	Conventional scheme	59.014	58.953	58.930
	Proposed scheme	59.043	58.977	59.010
Second frequency nadir (Hz)	Conventional scheme	59.368	59.265	59.330
	Proposed scheme	—	—	—
Starting time of rotor speed recovery (s)	Conventional scheme	57.0	57.0	57.4
	Proposed scheme	47.6	47.6	47.1
Released kinetic energy (s)	Conventional scheme	1.209	1.221	1.350
	Proposed scheme	1.085	1.167	1.203

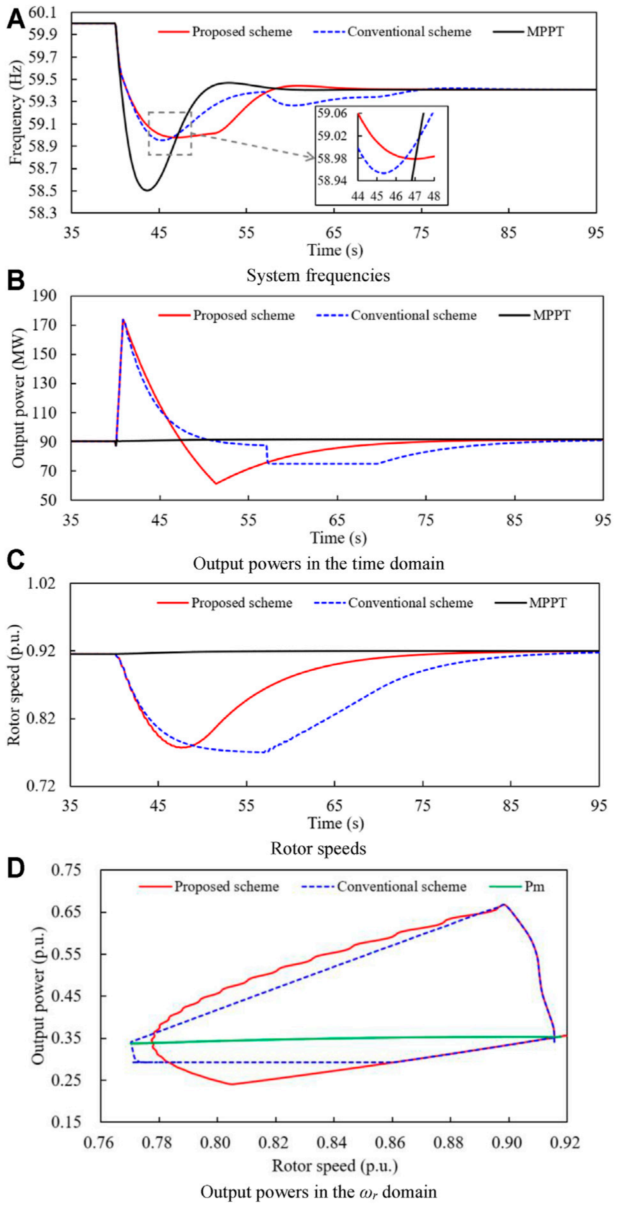

FIGURE 9 | Simulation results for case 2. **(A)** System frequencies. **(B)** Output powers in the time domain. **(C)** Rotor speeds. **(D)** Output powers in the ωr domain.

and then gradually returns to ω_0. Due to the slow rotor speed convergence, ω_r in the conventional TLBIC scheme converges to 0.768 p. u. at 57.0 s. Consequently, the proposed TLBIC scheme begins the restoration of the rotor speed earlier than the conventional TLBIC scheme by 9.4 s. Moreover, the KE released from the wind turbine during the inertial response in the proposed TLBIC scheme is 1.085 s, while the released KE in the conventional TLBIC scheme is 1.209 s (**Table 2**). The reason for this phenomenon is that ω_C is more in the proposed TLBIC scheme.

In order to recover ω_r, the conventional scheme instantly reduces the output power by 10 MW at 57 s to accelerate the recovery of ω_r, which causes a severe SFD of 0.632 Hz (**Figures 8A,B**). In contrast, the proposed reference power P_{ref} decreases smoothly with time by **Eq. 20**, which effectively ensures the rapid rotor recovery and frequency stabilization without a fluctuation, as shown in **Figure 8A**.

Case 2: Wind Power Penetration = 40% and Wind Speed = 8 m/s

Figure 9 shows the simulation results for case 2, in which the wind power penetration level is more than it is in case 1 by 10%.

As illustrated in **Figure 9A**, the FN of the MPPT operation is 58.501 Hz, which is lower than that of case 1 by 0.164 Hz obviously. This mainly suffers from the higher wind power penetration. Furthermore, the frequency nadirs of the proposed and conventional TLBIC strategy are 58.977 Hz, 58.953 Hz, respectively. Compared with the conventional TLBIC scheme, the FN of the proposed TLBIC scheme is improved by 0.024 Hz due to the setting of α in **Eq. 20**. In addition, the system frequencies for the proposed and conventional TLBIC strategy reach the steady state at 68.0 and 85.0 s, respectively.

ω_r in the proposed and conventional TLBIC scheme start the restoration at 47.6 and 57.0 s, respectively. Moreover, a significant SFD occurs at 60.3 s in the conventional TLBIC scheme while there is no frequency fluctuation in the proposed TLBIC scheme during the restoration of ω_r. The size of the SFD for the conventional TLBIC scheme is 0.735 Hz, which is larger than that in case 1 by 0.103 Hz because of a bigger ΔP_s.

Table 2 presents the simulation results for case 2, the released KE in the proposed and conventional TLBIC scheme are 1.167 and 1.221 s, respectively. Obviously, the released KE of the proposed TLBIC scheme is less.

Simulation results of the above two cases clearly illustrate that the proposed TLBIC strategy can heighten the FN at a high level

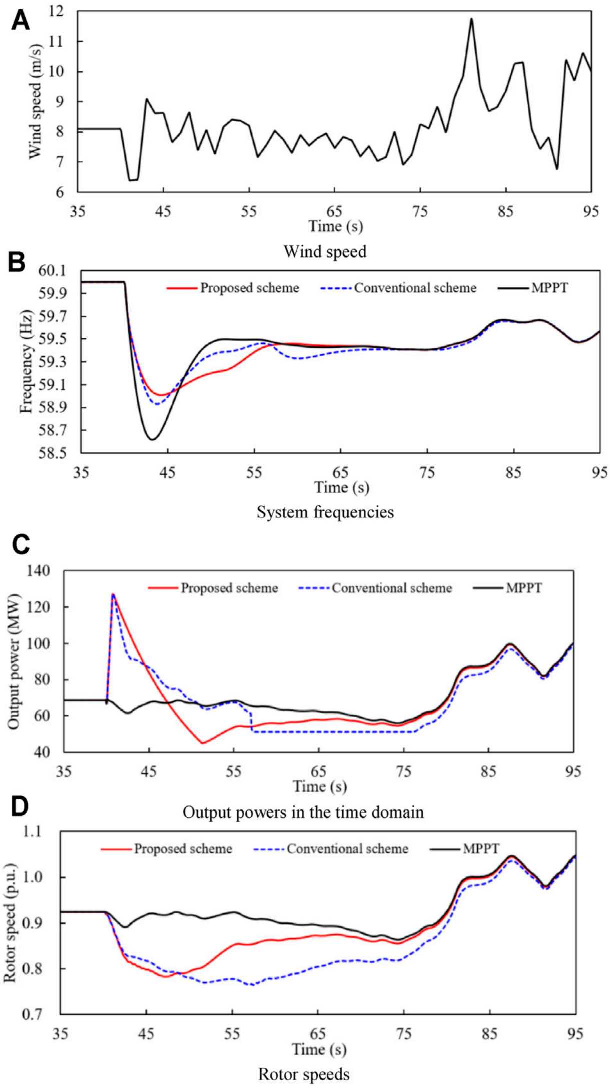

FIGURE 10 | Simulation results for case 3. **(A)** Wind speed. **(B)** System frequencies. **(C)** Output powers in the time domain. **(D)** Rotor speeds.

with less KE while guaranteeing the fast frequency stabilization under high wind power penetrations.

The above two cases have demonstrated the benefits of the proposed TLBIC strategy under constant wind speed. Whereas, considering the wind velocities are variable in a realistic scenario, the availability of the proposed TLBIC strategy will be investigated on a stochastic wind speed model in the following section.

Case 3: Wind Power Penetration = 30% and Random Wind Speed Condition

The stochastic wind speed model is presented in **Figure 10A**. As displayed in **Figure 10B**, the frequency nadirs of the proposed TLBIC scheme, conventional TLBIC scheme, and MPPT control occur at 44.2, 43.7 and 43.2 s and are 59.043, 59.014, and 58.665 Hz, respectively, and the frequency nadirs of three control schemes is all lower than those of case 1 due to the influence of the wind speed drop (**Figure 10A**). Moreover, the system frequencies for the proposed and conventional TLBIC scheme reach the steady state at 62.0 and 72.0 s, respectively.

Since the DFIG output power is closely related to the wind speed, the output power raise at 73 s with the increase of the wind speed (**Figures 10A,C**). As displayed in **Table 2**, ω_r of the proposed TLBIC scheme starts the recovery at 47.1 s which is earlier than that of the conventional TLBIC scheme by 10.3 s. Furthermore, the released KE during the frequency response in the proposed and conventional TLBIC scheme are 1.203 and 1.350 s, respectively.

Simulation results displayed in case 3 also demonstrate that the advantages and effectiveness of the proposed TLBIC scheme. Even though in a stochastic wind speed, the proposed TLBIC scheme still heightens the FN at a high level with less KE while guaranteeing the rapid frequency stabilization with reduced SFD.

CONCLUSION

This study suggests an optimized inertial control of a DFIG for heightening the FN at a high level with less KE and guaranteeing the fast frequency stabilization under high wind power penetrations with reduced SFD. To this end, when detecting a disturbance, the active power of the DFIG increases to the torque limit so that enough rotor kinetic energy is released into the power grid, and then the power reference smoothly reduces until the MPPT curve is met. Afterwards, the rotor speed reverts to the initialization along the MPPT curve without a frequency fluctuation.

Simulation results on various wind penetrations and wind velocities significantly demonstrate that the proposed TLBIC scheme shows better performances during the frequency response over the conventional TLBIC scheme: 1) during the period of supporting the system frequency, the proposed TLBIC strategy heightens the FN at a high level with less released KE; 2) during the period of recovering the rotor speed, the proposed TLBIC scheme guarantees the rapid frequency stabilization with reduced SFD effectively. Consequently, the optimized scheme can provide an effective approach for reducing the waste of the KE and balancing the depth of the SFD and the duration of rotor speed restoration.

DATA AVAILABILITY STATEMENT

The raw data supporting the conclusions of this article will be made available by the authors, without undue reservation, to any qualified researcher. Requests to access the datasets should be directed to HW, wanghongmei@ntu.edu.cn.

AUTHOR CONTRIBUTIONS

YX contributed to the conception and design of the proposed strategy. All authors wrote and edited the manuscript.

FUNDING

This work was supported by the Natural Science Foundation of the Jiangsu Higher Education Institutions of China (20KJB470026).

REFERENCES

Bao, W., Ding, L., and Liu, Z. (2020). Analytically derived fixed termination time for stepwise inertial control of wind turbines—Part I: Analytical derivation. *Inter. J. Elect. Power Energ. Sys* 121, 1–10. doi:10.1016/j.ijepes.2020.106120

Boukhezzar, B., and Siguerdidjane, H. Nonlinear control of a variable speed wind turbine using a two-mass model. *IEEE Trans. Energ. Convers.* 26 (1), 149–161. Mar. 2011.

Byerly, R. T., Aanstad, O., and Berry, D. H. (1973). Dynamic models for steam and hydro turbines in power system studies. *IEEE Trans. Power App. Syst.* 92 (6), 1904–1915.

Fernandez, L. M., Garcia, C. A., and Jurado, F. (2008). Comparative study on the performance of control systems for doubly fed induction generator (DFIG) wind turbines operating with power regulation. *Energy* 33 (9), 1438–1452. doi:10.1016/j.energy.2008.05.006

GB/T19963 (2011). *Technical Rule for Connecting to Power System*. China.

Hafiz, F., and Abdennour, A. (2015). Optimal use of kinetic energy for the inertial support from variable speed wind turbines. *Renew. Energ.* 80, 629–643. doi:10.1016/j.renene.2015.02.051

Hu, Y.-L., and Wu, Y.-K. (2019). Approximation to frequency control capability of a DFIG-based wind farm using a simple linear gain droop control. *IEEE Trans. Ind. Applicat.* 55 (3), 2300–2309. doi:10.1109/tia.2018.2886993

Kang, M., Kim, K., and Muljadi, E. (2016). Frequency control support of a doubly-fed induction generator based on the torque limit. *IEEE Trans. Power Syst.* 31 (6), 4574–4583. doi:10.1109/tpwrs.2015.2514240

Kang, M., Muljadi, E., Hur, K., and Kang, Y. C. (2016). Stable adaptive inertial control of a doubly-fed induction generator. *IEEE Trans. Smart Grid* 7 (6), 2971–2979.

Kheshti, M., Ding, L., Nayeripour, M., Wang, X., and Terzijia, V. (2019). Active power support of wind turbines for grid frequency events using a reliable power reference scheme. *Renew. Energ.* 139, 1421–1454. doi:10.1016/j.renene.2019.03.016

Lao, H. (2021). Innovated inertia control of DFIG with dynamic rotor speed recovery. *CSEE J. Power Energ. Syst.*

Lee, J., Jang, G., Muljadi, E., Blaabjerg, F., Chen, Z., and Cheol Kang, Y. (2016). Stable short-term frequency support using adaptive gains for a DFIG-based wind power plant. *IEEE Trans. Energ. Convers.* 31 (3), 1068–1079. doi:10.1109/tec.2016.2532366

Li, Y., Xu, Z., and Wong, K. P. (2017). Advanced control strategies of PMSG-based wind turbines for system inertia support. *IEEE Trans. Power Syst.* 32 (4), 3027–3037. doi:10.1109/tpwrs.2016.2616171

Miao, L., Wen, J., Xie, H., Yue, C., and Lee, W.-J. (2015). Coordinated Control Strategy of Wind Turbine Generator and Energy Storage Equipment for Frequency Support. *IEEE Trans. Ind. Applicat.* 51 (4), 2732–2742. doi:10.1109/tia.2015.2394435

Morren, J., Pierik, J., and de Haan, S. W. H. (2006). Inertial response of variable speed wind turbines. *Electric Power Syst. Res.* 76 (11), 980–987. doi:10.1016/j.epsr.2005.12.002

Peng, X., Yao, W., Yan, C., Wen, J., and Cheng, S. (2020). Two-Stage Variable Proportion Coefficient Based Frequency Support of Grid-Connected DFIG-WTs. *IEEE Trans. Power Syst.* 35 (2), 962–974. doi:10.1109/tpwrs.2019.2943520

Ullah, N. R., Thiringer, T., and Karlsson, D. (2008). Temporary Primary Frequency Control Support by Variable Speed Wind Turbines- Potential and Applications. *IEEE Trans. Power Syst.* 23 (2), 601–612. doi:10.1109/tpwrs.2008.920076

Van de Vyver, J., De Kooning, J. D. M., Meersman, B., Vandevelde, L., and Vandoorn, T. L. (2016). Droop control as an alternative inertial response strategy for the synthetic inertia on wind turbines. *IEEE Trans. Power Syst.* 31 (2), 1129–1138. doi:10.1109/tpwrs.2015.2417758

Wang, S., and Tomsovic, K. (2018). A novel active power control framework for wind turbine generators to improve frequency response. *IEEE Trans. Power Syst.* 33 (6), 6579–6589. doi:10.1109/tpwrs.2018.2829748

Wu, Y.-K., Yang, W. H., and Hu, Y. L. Frequency regulation at a wind farm using a timing–varying inertia and droop controls. *IEEE Trans. Ind. Appl.* 55 (1), 213–2224. Jan./Feb. 2019.

Wu, Z., Gao, D. W., Zhang, H., Yan, S., and Wang, X. (2017). Coordinated control strategy of battery energy storage system and PMSG-WTG to enhance system frequency regulation capability. *IEEE Trans. Sustain. Energ.* 8 (3), 1330–1343. doi:10.1109/tste.2017.2679716

Xiong, L., Liu, L., Liu, X., and Liu, Y. (2021). Frequency Trajectory Planning Based Strategy for Improving Frequency Stability of Droop-Controlled Inverter Based Standalone Power Systems. *IEEE J. Emerg. Sel. Top. Circuits Syst.* 11 (1), 176–187. doi:10.1109/jetcas.2021.3052006

Xiong, L., Liu, X., Liu, Y., and Zhuo, F. (2020). Modeling and Stability Issues of Voltage-Source Converter Dominated Power Systems: a review. *CSEE J. Power Energ. Syst. (Early Access)*, 1–18.

Xiong, L., Liu, X., Zhang, D., and Liu, Y. (2021). Rapid Power Compensation-Based Frequency Response Strategy for Low-Inertia Power Systems. *IEEE J. Emerg. Sel. Top. Power Electron.* 9 (4), 4500–4513. doi:10.1109/jestpe.2020.3032063

Xiong, Y., Yao, W., and Fen, J. (2021). Two-level combined control scheme of VSC-HVDC integrated off shore wind farms for onshore system frequency support. *IEEE Trans. Power Syst.* 36 (1), 781–792.

Xu, G., Liu, F., Hu, J., and Bi, T. (2018). Coordination of wind turbines and synchronous generators for system frequency control. *Renew. Energ.* 129, 225–236. doi:10.1016/j.renene.2018.05.104

Xu, G., and Xu, L. (2017). Improved use of WT kinetic energy for system frequency support. *IET Renew. Power Generation* 11 (8), 1094–1100. doi:10.1049/iet-rpg.2016.0183

Yang, D., Jin, Z., Zheng, T., Jin, E., Zhang, X., and Hua, L. (2021). Frequency Control Scheme with Dynamic Droop Characteristics of a DFIG for Mitigating the Frequency Fluctuations. *Int. Trans. Ele ctr. Energ. Syst.* 33 (11), 1–11.

Yang, D., Jin, Z., Zheng, T., and Jin, E. (2022). An adaptive droop control strategy with smooth rotor speed recovery capability for type III wind turbine generators. *Int. J. Electr. Power Energ. Syst.* 135, 107532. doi:10.1016/j.ijepes.2021.107532

Yang, D., Kim, J., Kang, Y. C., Muljadi, E., Zhang, N., Hong, J., et al. (2018). Temporary frequency support of a DFIG for high wind power penetration. *IEEE Trans. Power Syst.* 33 (3), 3428–3437. doi:10.1109/tpwrs.2018.2810841

Conflict of Interest: The authors declare that the research was conducted in the absence of any commercial or financial relationships that could be construed as a potential conflict of interest.

frontiers
in Energy Research

ORIGINAL RESEARCH
published: 22 November 2021
doi: 10.3389/fenrg.2021.781989

Two-Phase Short-Term Frequency Response Scheme of a DFIG-Based Wind Farm

Dejian Yang[1], Shun Sang[2,3] and Xinsong Zhang[3]*

[1]Key Laboratory of Modern Power System Simulation and Control and Renewable Energy Technology Ministry of Education (Northeast Electric Power University), Jilin, China, [2]Key Laboratory of Control of Power Transmission and Conversion (Shanghai Jiao Tong University), Ministry of Education, Shanghai, China, [3]Department of Electrical Engineering, Nantong University, Nantong, China

The kinetic energy stored in the doubly-fed induction generators (DFIG)-based wind farm can be utilized to sustain the dynamic system frequency. However, difficulties arise in determining the control gain to effectively improve the frequency nadir and smoothly return to the maximum power point tracking (MPPT) operation. This paper addresses a two-phase short-term frequency response (STFR) scheme to boost the frequency nadir and minimize the second drop in the system frequency based on a piecewise control gain. To achieve the first goal, a constant control coefficient, which is determined according to the initial operating conditions of the DFIG-based wind farm, is employed until the frequency nadir produces. To achieve the second goal, the control coefficient, which changes with time, facilitates to smoothly return to the MPPT operation. The effectiveness of the proposed two-phase STFR scheme is verified under various wind power penetration levels, wind speeds, and disturbances. The results reveal that the frequency nadir is improved, and simultaneously, it smoothly returns to the MPPT operation and minimizes the second drop in the system frequency.

Keywords: generation, power system control, short-term frequency response, two phase, second frequency drop

OPEN ACCESS

Edited by:
Liansong Xiong,
Nanjing Institute of Technology (NJIT), China

Reviewed by:
Taiying Zheng,
Zhejiang University, China
Hongchao Gao,
Tsinghua University, China
Arghya Mitra,
Visvesvaraya National Institute of Technology, India

***Correspondence:**
Xinsong Zhang
zhang.xs@ntu.edu.cn

Specialty section:
This article was submitted to Process and Energy Systems Engineering,
a section of the journal Frontiers in Energy Research

Received: *23 September 2021*
Accepted: *14 October 2021*
Published: *22 November 2021*

Citation:
Yang D, Sang S and Zhang X (2021) Two-Phase Short-Term Frequency Response Scheme of a DFIG-Based Wind Farm.
Front. Energy Res. 9:781989.
doi: 10.3389/fenrg.2021.781989

INTRODUCTION

During the past few years, the power grid with renewable power generations has been experiencing a reduction of the primary frequency response capability and system inertia response capability (Xiong et al., 2020)– (Xiong et al., 2021a; Xiong et al., 2021b). The reason is that conventional synchronous generators (SGs) are replaced by electronic converter-based renewable power generations, which cannot provide the system inertia response and primary response. This tendency continues to increase in renewable power generation-dominated power systems (Yang et al., 2018). Hence, renewable power generations are required to provide frequency response functions to boost the system frequency nadir (National Grid UK, 2010; EirGrid Grid Code Version 6.0, 2015).

Electronic converter interfaced variable-speed wind turbine generators (VSWTGs), e.g., doubly-fed induction generators (DFIGs), which are the most promising replacement for SGs, are able to provide frequency response functions for sustaining the dynamic system frequency by designing the control strategies (Dreidy and Mokhlis, 2017)– (Wu et al., 2019).

The frequency response functions include long-term frequency response (utilizing reserve power of the VSWTGs implemented by over-speed control, pitch angle control, or both of them) (Ye et al., 2019; Cai et al., 2020), and short-term frequency response (utilizing kinetic energy of the VSWTGs).

When performing long-term frequency response, the VSWTGs are forced to operate in deloading mode. Although it ensures a secure reserve power for supporting the system frequency, significant annual wind energy loss is inevitable. Furthermore, the slow response of the pitch angle control and increasing mechanical stress caused by frequent activations of pitch angle are not beneficial to participate in frequency support (Li et al., 2017; Yang et al., 2021a).

Short-term frequency response (STFR) sustains the dynamic system frequency based on two additional control loops: *df/dt* control loop and droop control loop. Vyver (2016) shows that even though the *df/dt* loop can emulate the inertia response of SG to boost the system frequency nadir, it creates a power system instability due to the noise in the system frequency. The droop control can emulate governor response of SGs and is taken into account as an alternative inertial control of VSWTGs (Li et al., 2017). The contribution of droop control is analyzed and with various constant control gains, it illustrates that the droop control with fixed gain is not suitable for various wind speed conditions and may cause stalling of the DFIG (Margaris et al., 2012; Hu and Wu, 2019). The variable control gain is, thus, suggested for boosting the frequency stability while preventing stalling of DFIGs (Lee et al., 2016; Hu and Wu, 2019). However, the control gain of Ref. (Lee et al., 2016) is a quadratic function of the rotor speed, and it is not feasible to be implemented in the DFIG. To avoid this, the linear control gain is suggested to provide approximated performance of the quadratic droop control gain (Hu and Wu, 2019).

After the frequency support phase, returning to the maximum power point tracking (MPPT) operation and rotor speed recovery may potentially create a second drop in the frequency (Garmroodi et al., 2018). To mitigate it, the authors reset the setting of the governor response to provide more output power from SGs (Xu et al., 2018). Another strategy employs energy storage systems to prevent the second drop in the frequency when returning to the MPPT operation (Wu et al., 2017). However, both strategies require additional investments for additional reserve power of SGs and energy storage systems (Bao et al., 2020). Furthermore, (Zhong et al., 2021; Kheshti et al., 2019) mention that the strategy for regaining the rotor speed and mitigating the second frequency drop should be considered during the MPPT operation recovery phase. However, it should be pointed out that the strategy to return to the MPPT operation or quit the frequency support phase has not been paid enough attention (Peng et al., 2020).

This paper presents a two-phase STFR scheme of a DFIG-based wind farm that effectively sustains the system frequency and smoothly returns to the MPPT operation while minimizing the second drop in the system frequency. For these objectives, this paper determines the control gain as a piecewise function, which remains fixed prior to the frequency nadir to boost the frequency nadir; the control gain then linearly decreases with time to smoothly regain the rotor speed after the frequency nadir. The performance of the two-phase STFR is investigated under three scenarios with different wind speed conditions, wind power penetration levels, and sizes of disturbance.

MODEL OF THE DOUBLY-FED INDUCTION GENERATOR

The extracted mechanical power (P_{m}) by the wind turbine from wind can be defined as a nonlinear function of air density (ρ), power coefficient (c_p), wind speed (v_w), and rotor radius (R), as in:

$$P_{\mathrm{mec}} = \frac{1}{2}\rho A v_{wind}^{3} c_P \tag{1}$$

where β and λ, respectively, represent pitch angle and tip-speed ratio.

As in Boukhezzar and Siguerdidjane (2011), $c_p(\lambda, \beta)$ used in this study is a function related to λ and β, which can be represented as:

$$c_P(\lambda, \beta) = 0.645\left\{0.00912\lambda + \frac{-5 - 0.4(2.5+\beta) + 116\lambda_i}{e^{21\lambda_i}}\right\} \tag{2}$$

where

$$\lambda_i = \frac{1}{\lambda + 0.08(2.5+\beta)} - \frac{0.035}{1+(2.5+\beta)^3} \tag{3}$$

$$\lambda = \frac{\omega_r R}{v_w}. \tag{4}$$

To illustrate the dynamics between the induction machine and wind turbine, one two-mass model is implemented, as shown in **Eqs 5–7**. Among them, H_t, ω_t, T_t, and D_t are, respectively, the inertia time constant, angular speed, torque, and damping constant of the turbine of the DFIG; H_g, ω_r, T_g, and D_g are, respectively, the inertia time constant, angular speed, torque, and damping constant of the induction generator; and D_s, K_s, ω, and θ_s are, respectively, the damping constant, shaft stiffness, base value of angular speed, and torsional twist (Ajjarapu et al., 2010).

$$2H_t\frac{d\omega_t}{dt} = T_t - K_s\theta_s - D_s(\omega_t - \omega_r) - D_t\omega_t \tag{5}$$

$$2H_g\frac{d\omega_r}{dt} = K_s\theta_s + D_s(\omega_t - \omega_r) - D_g\omega_r - T_g \tag{6}$$

$$\frac{d\theta_s}{dt} = \omega(\omega_t - \omega_r) \tag{7}$$

As shown in **Figure 1**, the DFIG control system receives the measurements and determines the commands for a rotor-side converter (RSC) and grid-side converter (GSC) controllers. The top loop of the RSC controller focuses on maintaining the voltage of stator. Its bottom loop focuses on controlling the output fed to the power grid (see **Figure 1**). The top loop of the GSC controller controls the DC-link voltage (**Figure 1**). Its bottom loop regulates the requested reactive power (Fernandez et al., 2008).

FUNDAMENTAL FEATURES OF SHORT-TERM FREQUENCY RESPONSE STRATEGIES OF A DOUBLY FED INDUCTION GENERATOR

When performing inertia control of the DFIG, the additional power, ΔP_{in}, can be expressed as:

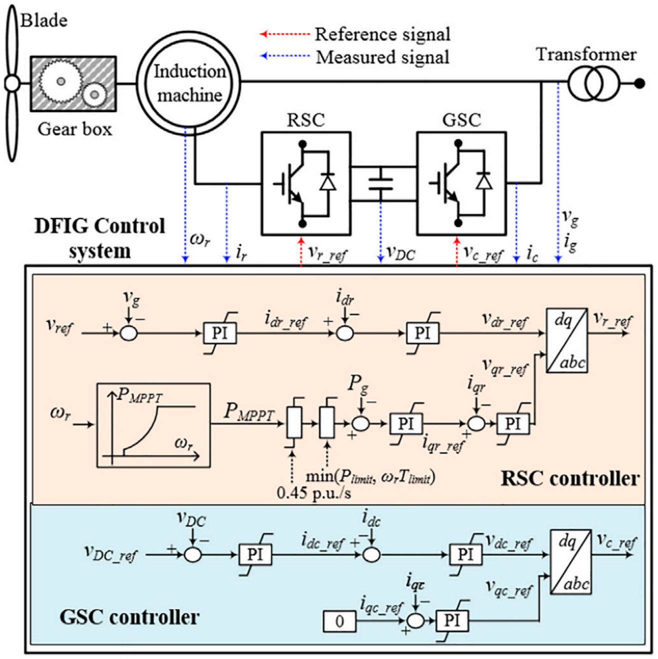

i_r, i_c, i_g: currents at RSC, GSC, and terminal
v_g, v_{DC}: voltages at terminal and DC-link
v_{r_ref}, v_{c_ref}: voltage references for GSC and RSC
i_{dc}, i_{qc}: terminal currents for d-axis and q-axis
i_{dr}, i_{qr}: rotor currents for d-axis and q-axis
P_g: active power at terminal
v_{ref}, v_{DC_ref}: voltage commands for stator and DC-link
v_{dr_ref}, v_{qr_ref}: voltage commands of rotor for *d*- and *q*-axis
v_{dc_ref}, v_{qc_ref}: terminal voltage commands for *d*- and *q*-axis

FIGURE 1 | Simplified doubly fed induction generator (DFIG) control topology.

$$\Delta P_{in} = 2H_{DFIG} f_{sys} \frac{df_{sys}}{dt} \tag{8}$$

where f_{sys} means the system frequency. H_{DFIG} is the inertia constant of the DFIG and includes the inertia constants of induction generator and turbine.

Integrating **Eqs 8**, **9** can be derived as:

$$\Delta P_{in} \times \Delta t = H_{DFIG} \times \left[f_{sys}^2 (t + \Delta t) - f_{sys}^2 (t) \right] \tag{9}$$

where $f_{sys}(t)$ and $f_{sys}(t+\Delta t)$, respectively, are the system frequencies at t and $t + \Delta t$. Δt is the time interval.

Rearranging **Eq. 9**:

$$f_{sys}(t + \Delta t) = \sqrt{\frac{(\Delta P_{in} \times \Delta t)}{H_{DFIG}} + f_{sys}^2 (t)} \tag{10}$$

In **Eq. 10**, it is shown that with the larger additional injected power, the system frequency deviation becomes less.

As in Lee et al. (2016), the available kinetic energy from DFIGs is represented as:

$$E_{avail} = H_{DFIG}\omega_0^2 - H_{DFIG}\omega_{\min}^2 \tag{11}$$

where ω_0 and $\omega_{\min}$, respectively, are the rotor speed before disturbance and minimum rotor speed limit.

In addition, **Eq. 11** can be utilized to calculate the released energy by substituting the minimum rotor speed during STFR for $\omega_{\min}$. STFR of DFIGs mainly relies on ω_0, as shown in **Figure 2**. Furthermore, if the rotor speed decreases to $\omega_{\min}$ during droop control, stalling of the wind turbine is caused by excessive release of the kinetic energy.

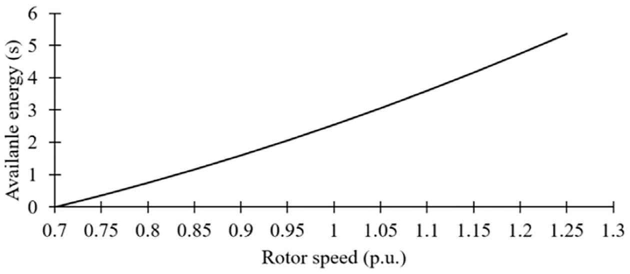

FIGURE 2 | Available kinetic energy of a DFIG.

Conventional Short-Term Frequency Response of a Doubly Fed Induction Generator

The characteristics of the STFR with droop control are similar to that of the primary response of SGs. Unlike in the governor

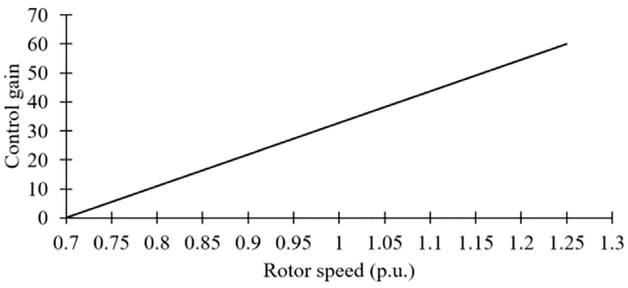

FIGURE 3 | Diagram of conventional control gain when C = 60.

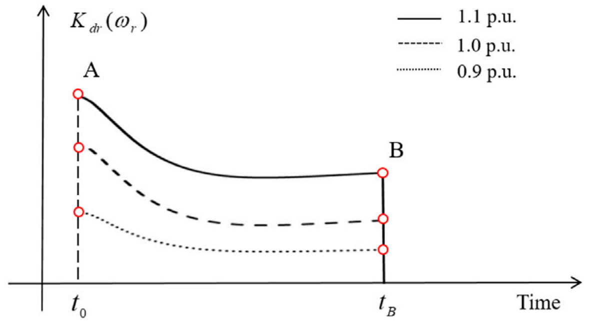

FIGURE 4 | Diagram of the conventional droop control gain in the time domain.

response, the droop control from DFIGs releases the kinetic energy from the rotating masses without reserve power.

When performing droop control, the power reference is expressed as follows:

$$P_{ref} = P_{MPPT} + \Delta P_{droop} = k_g \omega_r^3 + \Delta P_{droop} \tag{12}$$

$$\Delta P_{droop} = -\frac{1}{R}\left(f_{sys} - f_{nom}\right) = K_{dr}\left(f_{sys} - f_{nom}\right) \tag{13}$$

where ΔP_{droop} indicates the output of droop control loop, K_{dr} represents the control gain of the droop control, and f_{nom} denotes the nominal system frequency.

According to **Eq. 13**, the short power injected to the power grid from the droop control loop strongly depends on K_{dr}, which becomes large so as to improve the frequency nadir.

As illustrated in **Figure 2**, the retained kinetic energy of a DFIG for various wind conditions is different, therefore, increasing the difficulties of setting the control gain for various rotor speeds. To mitigate this problem, Ref. (Hu and Wu, 2019) addresses a linear variable droop gain, which is expressed as:

$$K_{\mathrm{dr}} = C\frac{\omega_r - \omega_{\min}}{\omega_{\max} - \omega_{\min}} \tag{14}$$

where C indicates a constant and determines the contribution of the STFR of the DFIG.

As in **Eq. 14** and **Figure 3**, there are two key features of the linear variable control gain. The first is that the linear variable droop gain is a monotonously linear function related to the rotor speed. This implies that the STFR becomes better with the increasing ω_r. The second is that $K_{dr}(\omega_r)$ is zero when $\omega_r = \omega_{\min}$, so that it effectively avoids the stalling of DFIGs. Nevertheless, in the initial stage of a disturbance, $K_{dr}(\omega_r)$ becomes small with the decreasing ω_r until the system frequency passes into the steady state (**Figures 4A,B**) so that the injected power from the DFIG decreases; therefore, the DFIG could not effectively improve the frequency nadir.

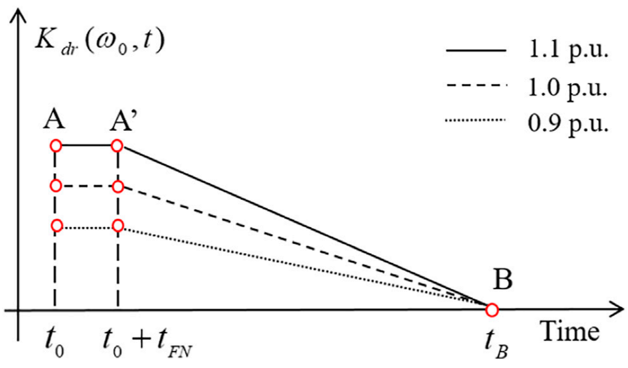

FIGURE 5 | Diagram of the proposed droop control gain in the time domain.

Another point to be considered is that after the frequency support phase, the DFIG should return back to MPPT operation in order to regain the kinetic energy. For the conventional STFR scheme, to quit the frequency support phase and return to the MPPT operation, ΔP_{droop} in **Eq. 12** and $K_{dr}(\omega_r)$ in **Eq. 13** instantly decrease to zero. This indicates that the power reference of the DFIG stepwise switches back to the MPPT operation. According to the swing equation, if ΔP_{droop} decreases to zero, the right hand side of **Eq. 15** becomes negative; as a result, the system frequency decreases and produces a second frequency drop. The decreased shape of ΔP_{droop} judges the size of the second frequency deviation. Furthermore, a large drift in the rotor speed from its initial value consequently causes a significantly deep second frequency drop (Garmroodi et al., 2018). In some cases, the second drop in the system frequency may be lower than the first frequency nadir. This conclusion can be confirmed in the simulation results of this study.

$$\begin{aligned} J_{sys} f_{sys} \frac{df_{sys}}{dt} &= P_{Load} - \left(P_{SG} + P_{\mathrm{MPPT}} + \Delta P_{droop}\right) \\ &= P_{Load} - \left(P_{SG} + P_{\mathrm{MPPT}} + K_{dr} \times \Delta f\right) \end{aligned} \tag{15}$$

where J_{sys} is the moment inertia of the power system. P_{load} and P_{SG}, respectively, mean the system load and total output power SGs.

Two-phase Short-Term Frequency Response of a Doubly Fed Induction Generator

This paper aims to 1) improve the frequency nadir during the frequency support phase, and 2) minimize the size of a second drop in the system frequency during the MPPT operation recovery

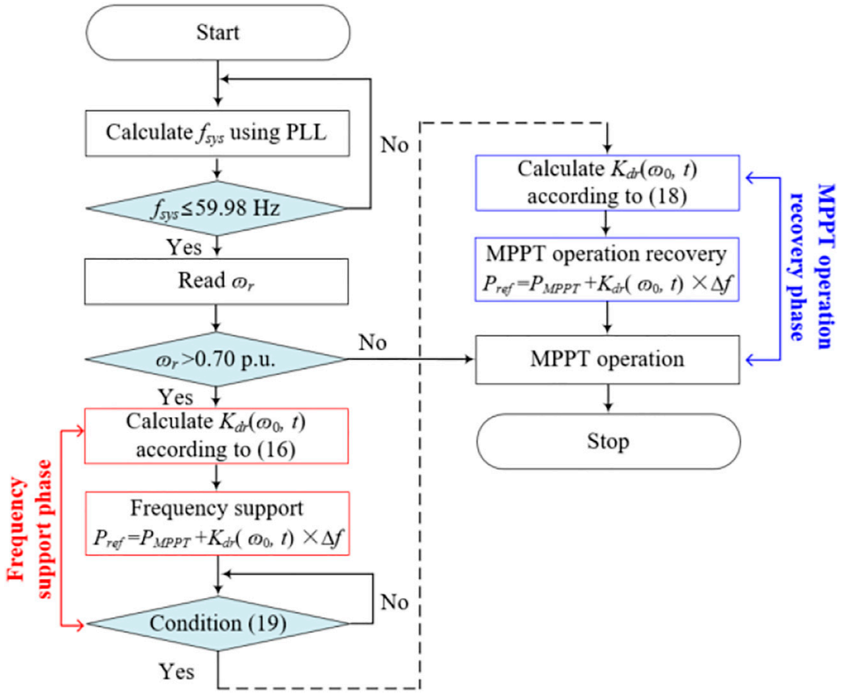

FIGURE 6 | Flowchart of the proposed two-phase short-term frequency response.

phase. For these objectives, this paper determines the control gain as a piecewise function, which remains fixed prior to the frequency nadir and linearly decreases with time after the frequency nadir.

Frequency Support Phase of a Doubly Fed Induction Generator

Compared with the conventional STFR, to inject more output before the frequency nadir appears, the control gain in this study is defined as a constant prior to the frequency nadir, as in:

$$K_{\mathrm{dr}} = C\frac{\omega_0 - \omega_{\min}}{\omega_{\max} - \omega_{\min}}, \quad t_0 < t < t_0 + t_{\mathrm{FN}} \tag{16}$$

where C is a constant the same as in **Eq. 14**; t_0 and t_{FN}, respectively, represent the moment when starting up STFR and moment of the frequency nadir occurrence after a disturbance.

As illustrated in **Figure 5** and **Eq. 16**, the initial value of the proposed control gain is proportional to the initial conditions of DFIGs and maintained fixed until the frequency nadir appearance (from A to A′ in **Figure 5**). For the conventional STFR, at the instant of detecting disturbance, the control gain is the same as in the two-phase STFR; after that, the control gain decreases with reducing rotor speed. Therefore, the proposed two-phase STFR is able to inject more power from DFIGs to support the system frequency compared with the conventional STFR.

Maximum Power Point Tracking Operation Recovery Phase of a Doubly Fed Induction Generator

During the MPPT operation recovery phase, to compromise the second drop in the system frequency and the time of the rotor speed recovery, the ΔP_{droop} in **Eq. 12** should gradually decrease to zero instead of stepwise decreasing to zero. To this end, a weighting factor of time shown in **Eq. 17** is considered based on **Eq. 16** to determine the control gain during the MPPT operation recovery. Thus, the control gain can be represented as in **Eq. 18**.

$$f(t) = \frac{t_0 + t_{\mathrm{FN}} - t}{\Delta t} + 1 \tag{17}$$

$$K_{\mathrm{dr}}(\omega_0, t) = C\frac{\omega_0 - \omega_{\min}}{\omega_{\max} - \omega_{\min}} \times f(t), \quad t_0 + t_{\mathrm{FN}} \le t \tag{18}$$

After the frequency nadir appears, the control gain gradually decreases to zero so that the output power of the DFIG smoothly decreases to the MPPT curve (from A′ to B in **Figure 5**). This is the reason why the proposed two-phase STFR can minimize the secondary frequency drop while smoothly returning to the MPPT operation. Furthermore, the proposed two-phase STFR initiates the MPPT operation recovery significantly earlier compared with the conventional strategy so that it can ensure a similar duration of the restoration of ω_r while minimizing the second drop in the system frequency.

In this paper, the frequency nadir detector is used to switch the control gain from **Eq. 14–16** once the measured *df*/*dt* meets the following condition:

$$\left|\frac{df}{dt}\right| \le 0.01 \text{ Hz/s} \tag{19}$$

For the robust *df*/*dt* measurement, two low-pass filters are used in this study. When calculating the system frequency, a second-order low-pass filter is used for a phase-locked loop (PLL) in a VSWTG controller and its cutoff frequency is 1 Hz. In addition, when

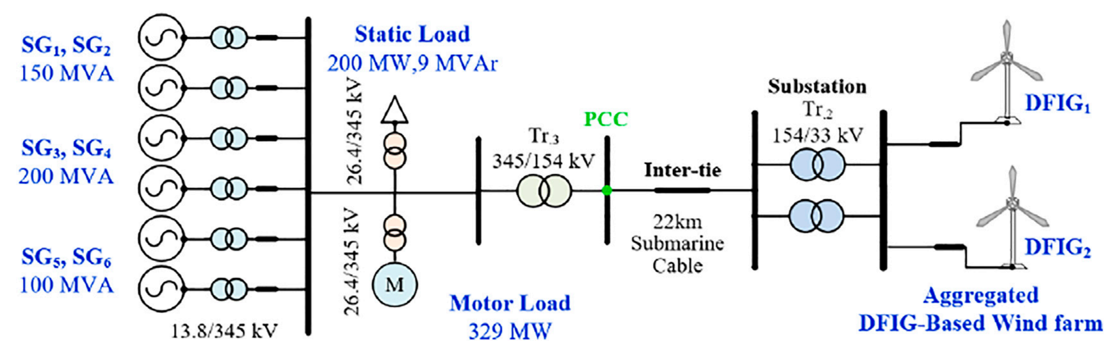

FIGURE 7 | Model system.

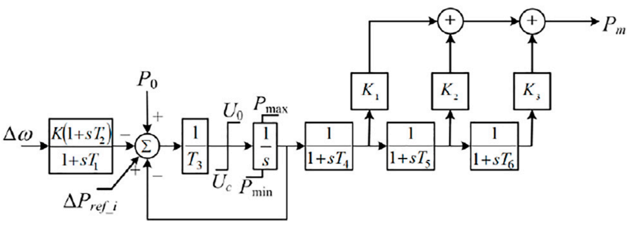

FIGURE 8 | Tandem-compound, single-reheat governor model.

TABLE 1 | Parameters of the governor model.

T_1	T_2	T_3	T_4	T_5	T_6	K
0.1	1.0	0.25	0.3	10	0.4	20
K_1	K_2	K_3	P_{max}	P_{min}	U_o	U_c
0.3	0.4	0.3	1	0.4	0.1	–0.2

calculating *df*/*dt*, a first-order low-pass filter is used. If the calculated meets **Eq. 19**, the waiting counter increases by one; otherwise, it decreases by one. Once the counter equals five, the frequency nadir is detected. This way of detecting the frequency nadir may detect the frequency nadir earlier or later than the actual value. Therefore, special attention should be paid on selecting countermeasures against noise components to avoid the adverse impact on the performance of the proposed scheme caused by earlier or later detection of the frequency nadir.

Figure 6 shows the flowchart of the proposed two-phase STFR strategy, which includes four parts: disturbance detecting part, frequency support part, frequency nadir detecting part, and MPPT operation recovery part.

Limitations of the Active Power Reference of a Doubly Fed Induction Generator

To obtain the realistic results while protecting VSWTGs, the power reference is limited by the limiter of maximum power (P_{limit}) and the limiter of the rate of change in power ($\omega_r T_{limit}$). The former limiter is set to 10% or 20% more than that of the nominal power of a VSWTG (Margaris et al., 2012; Bao et al., 2020). In addition, the setting of the latter limiter is 0.45 p.u./s (Hu and Wu, 2019; Zhong et al., 2021). The upper limit is the minimum value between P_{limit} and $\omega_r T_{limit}$.

MODEL SYSTEM

Figure 7 illustrates the model system to indicate the efficacy of the two-stage STFR scheme in EMTP-RV. It comprises two DFIG-based wind farms, static load, six SGs, and motor load. Total load consumption is 529 MW.

Synchronous Generators

The model system includes two 200-MVA SGs, two 150-MVA SGs, and two 100-MVA SGs, as shown in **Figure 7**. The inertia constants of 100-MVA SG, 150-MVA SG, and 200-MVA SG are, respectively, set to 4, 4.3, and 5 s (Hu and Wu, 2019). In addition, six SGs are assumed as steam turbine generators with the tandem-compound, single-reheat IEEEG1 governor model (Byerly et al., 1973). The configuration of the governor model and its coefficients are, respectively, illustrated in **Figure 8** and **Table 1**. IEEE X1 is used for voltage control.

Doubly Fed Induction Generator

Two aggregated DFIG-based wind farms are modeled in this paper. To deliver the power to the main grid, two 72-MVA transformers and one 22 km 154-kV submarine cable are used (see **Figure 7**).

As illustrated in **Figure 9**, the defined stable ω_r operating range of the DFIG ranges from 0.7 to 1.25 p.u. (Yang et al., 2021b); therefore, once ω_r reaches 0.7 p.u., the STFR schemes are disabled to prevent the DFIG from stalling. The power limit of the DFIG is 1.1 p.u.

CASE STUDIES

The performance of the two-phase STFR strategy is investigated by comparing it with the conventional STFR strategy and MPPT operation under three scenarios with different wind conditions, wind penetration levels, and sizes of disturbance. The input wind speeds of first DFIG-based wind farm and second DFIG-based

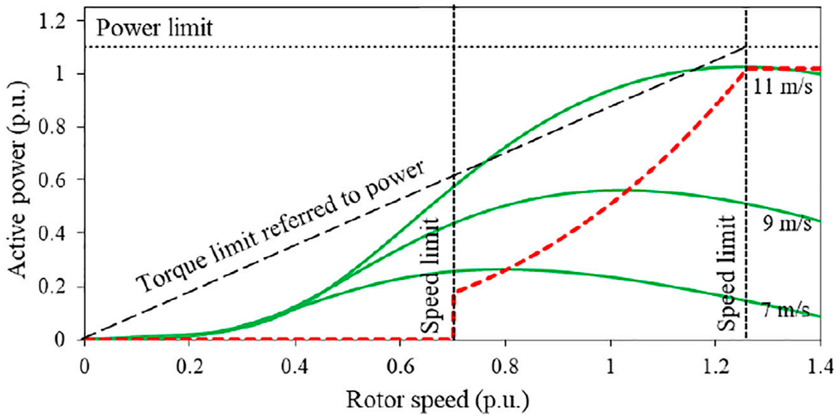

FIGURE 9 | Power characteristics of the doubly-fed induction generator (DFIG) used in this study.

wind farm, which are denoted as $DFIG_1$ and $DFIG_2$, are, respectively, 7.5 and 9.5 m/s. At 40 s, SG_4 supplying 90 MW for Case 1 and Case 2, and 120 MW for Case 3, is tripped as frequency disturbances. For the proposed and conventional STFR scheme, C in **Eqs 14**, **16**, **18** is set to 60. Once the system frequency passes into the steady state, the conventional STFR scheme decreases the output power for returning to the MPPT operation. For the proposed two-phase frequency support scheme, MPPT operation recovery starts up when **Eq. 19** is satisfied. Δt in **Eq. 18** is set to 20 s so as to ensure a similar duration of the rotor speed recovery while minimizing the second drop in the system frequency.

Case 1: Wind Penetration of 19% and 90-MW Generator Trip

Figure 10 illustrates the results for Case 1. The frequency nadir for the proposed two-phase STFR, conventional STFR, and MPPT operation are 59.356, 59.344, and 59.095 Hz, respectively. The two-phase STFR has the highest frequency nadir because of the most power injection, as shown in **Figure 10B**. For the conventional STFR, the severe second drop in the system frequency occurs at 64 s because the MPPT operation recovery begins and the output power instantly decreases to the MPPT curve, as illustrated in **Figures 10A,B**. However, in the proposed two-phase STFR, even if it has a similar rotor speed recovery, no second drop in the system frequency is produced since the output power smoothly decreases to the MPPT operation curve. The nadir-based frequency response of the proposed two-phase STFR is better compared with the conventional STFR because of the less system frequency deviation.

As illustrated in **Figures 10C,F**, in the conventional STFR, the output peak value for the $DFIG_1$ is 24.4 MW, which is less than that of the proposed two-phase STFR by 0.7 MW due to the large control gain of the two-phase STFR. The peak value of the output power for the $DFIG_2$ is the same as in the proposed two-phase STFR since the output power is limited by the torque limit.

During the frequency support phase, the released kinetic energies in the conventional STFR for the $DFIG_1$ and $DFIG_2$ are 0.633 and 1.577 s, respectively; the released kinetic energies in the proposed two-phase STFR for the $DFIG_1$ and $DFIG_2$ are 0.818 and 1.814 s, respectively, which are more than those in the conventional STFR, as illustrated in **Figures 10D,G**.

Figures 10E,I illustrate the locus of output power versus rotor speed for $DFIG_1$ and $DFIG_2$. It can be observed that the output power of the proposed two-phase STFR gradually decreases to the MPPT operation curve, whereas the output power of the conventional STFR instantly decreases to the MPPT operation curve; as a result, the proposed STFR can minimize the second dip in the frequency, but the conventional STFR results in a severe second drop in the system frequency.

Case 2: Wind Penetration of 28% and 90-MW Generator Trip

Figure 11 illustrates the results for Case 2 with a higher wind power penetration level of 28% compared with Case 1. To realize this, SG_6 is out of service, while the capacities of both the $DFIG_1$ and $DFIG_2$ increase from 50 to 75 MW, respectively. Thus, the system inertia constant becomes less, and the primary frequency response capability becomes worse.

The frequency nadir for the MPPT operation is 58.933 Hz, which is less than that of low wind power penetration (Case 1); this is because of the reduced inertia constant and primary frequency response capability. In the conventional STFR, the first frequency nadir is 59.357 Hz caused by the disturbance. However, during the MPPT operation recovery phase, a severe second drop in the system frequency is caused, which leads the system frequency nadir decrease to 59.344 Hz. In the proposed two-phase STFR, the frequency nadir is 59.392 Hz, which is much more compared with that of the conventional STFR, as in Case 1. Furthermore, no second frequency drop is created. The reasons are that more active power is injected to the power grid, and the output power smoothly decreases to the MPPT curve. Moreover, as in Case

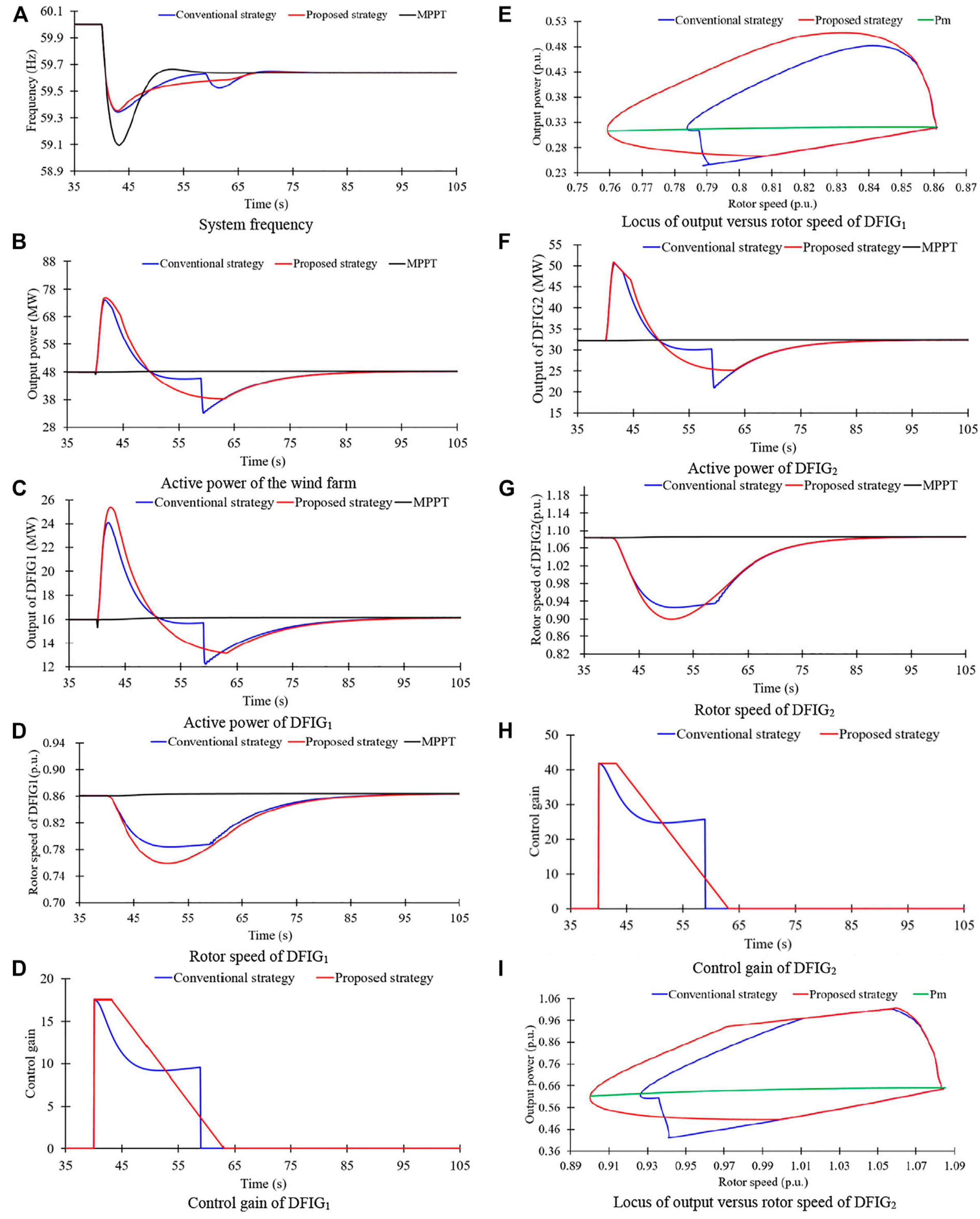

FIGURE 10 | Results for case 1. **(A)** System frequency. **(B)** Active power of the wind farm. **(C)** Active power of DFIG_1. **(D)** Rotor speed of DFIG_1, Control gain of DFIG_1. **(E)** Locus of output versus rotor speed of DFIG_1. **(F)** Active power of DFIG_2. **(G)** Rotor speed of DFIG_2. **(H)** Control gain of DFIG_2. **(I)** Locus of output versus rotor speed of DFIG_2

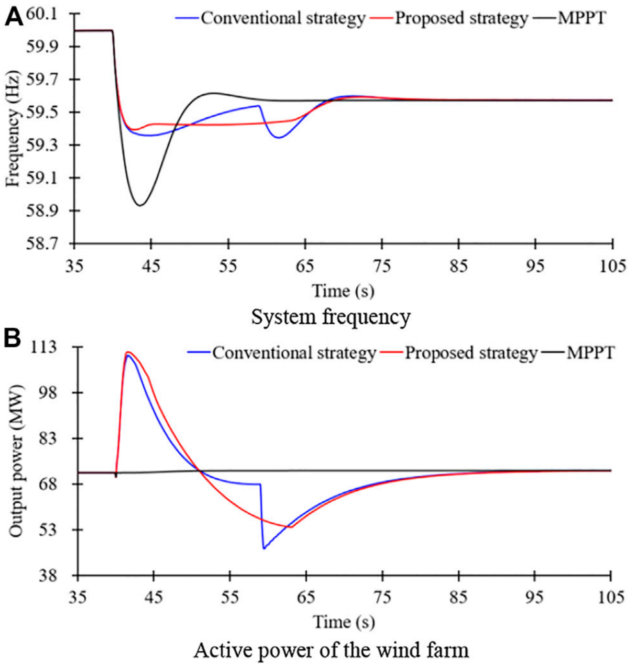

FIGURE 11 | Results for case 2.

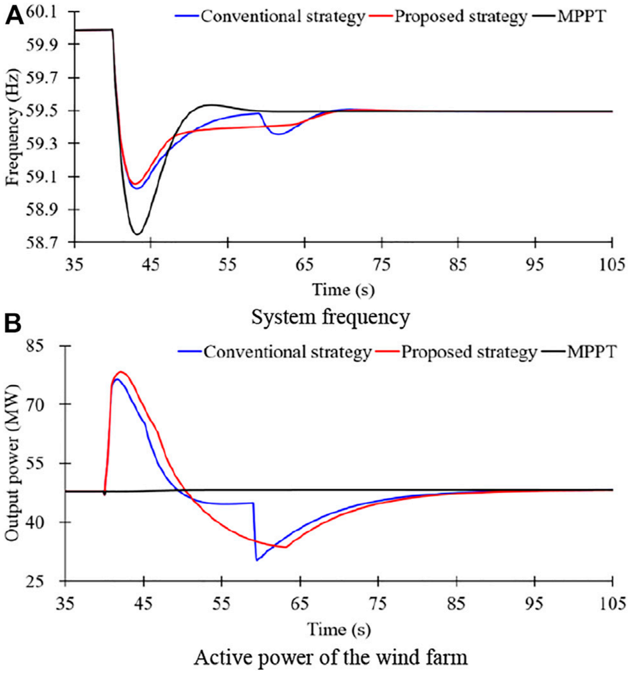

FIGURE 12 | Results for case 3.

1, due to the higher-frequency nadir, the nadir-based frequency response for the two-phase STFR is more than the other schemes.

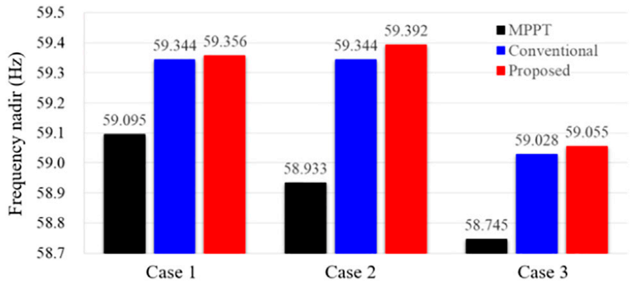

FIGURE 13 | Frequency nadirs for all cases.

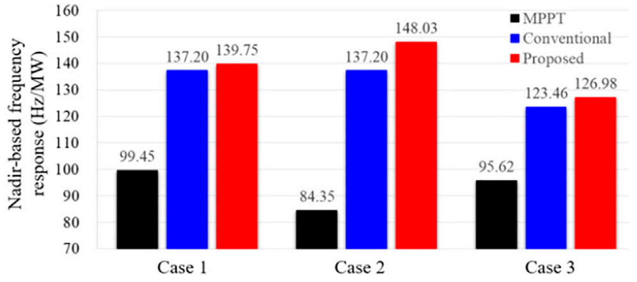

FIGURE 14 | Nadir-based frequency responses for all cases.

Case 3: Wind Penetration of 19% and 120-MW Generator Trip

Figure 12 shows the results for Case 3 with a severe disturbance compared with Case 1. Thus, the system frequency deviation becomes large, and more additional power should be compensated for the larger disturbance.

The frequency nadir for the MPPT operation is 58.745 Hz, which is less than that of small disturbance; this is because of the large power deficiency. In the conventional STFR, the frequency nadir is 59.028 Hz, which is less than that of the proposed two-phase STFR by 0.027 Hz. Furthermore, as in previous two cases, the nadir-based frequency response in the proposed two-phase STFR is large compared with that of the conventional STFR. A significant second frequency drop produces around 64 s; however, the proposed two-phase STFR can minimize the second frequency drop while ensuring the similar rotor speed recovery to the conventional STFR, as in Case 1 and Case 2.

Figures 13, **14** show the comparison results of the proposed two-phase STFR to the conventional STFR for the three cases. Since the control gain is fixed prior to the frequency nadir, the frequency nadir and nadir-based frequency response of the two-phase STFR scheme are higher than those of the conventional scheme under various wind power penetration levels and sizes of disturbance. Furthermore, since the control gain linearly decreases with time, the two-phase STFR scheme minimizes the second drop in the system frequency and smoothly recovers the DFIG to the MPPT operation.

CONCLUSION

This paper proposes a two-phase STFR scheme based on a piecewise droop control gain for the DFIG-based wind farm. During the frequency support phase (prior to the frequency nadir), the droop control gain remains fixed to improve the frequency nadir determined by the initial DFIG operating conditions. During the MPPT operation recovery phase, the droop control gain linearly decreases with time to minimize the second drop in the system frequency and smoothly return to the MPPT operation.

Although the concept is applicable to VSWTGs (DFIG and full-scale VSWTGs), in this paper, we only use the DFIG to illustrate the concept. Results clearly indicate that the two-phase STFR scheme is beneficial in improving the frequency nadir and minimizing the second drop in the system frequency under three scenarios with different wind conditions, wind power penetration levels, and sizes of disturbance. Thus, the proposed two-phase STFR provides benefits to the system frequency stability.

A distributed model of the DFIG-based wind farm would have been more realistic compared with using an aggregated model. In the future, the coordinated control strategy between DFIGs in a wind farm would be designed based on a distributed model.

DATA AVAILABILITY STATEMENT

The original contributions presented in the study are included in the article/Supplementary Materials, further inquiries can be directed to the corresponding author.

AUTHOR CONTRIBUTIONS

DY and SS contributed to the conception and design of the proposed strategy. All authors wrote and edited the manuscript.

FUNDING

This work was supported, in part, by the National Natural Science Foundation of China (51877112), the Natural Science Foundation of the Jiangsu Higher Education Institutions of China (20KJB470026), the Key Project of the Natural Science Foundation of the Jiangsu Higher Education Institutions of China (18KJA470003), and, in part, by the Key Laboratory of Control of Power Transmission and Conversion (SJTU), Ministry of Education (2021AC03).

REFERENCES

Ajjarapu, V., McCalley, J. D., Rover, D., Wang, Z., and Wu, Z. (2010). *Novel Sensorless Generator Control and Grid Fault Ride-Through Strategies for Variable-Speed Wind Turbines and Implementation on a New Real-Time Simulation Platform*. Ames, Iowa: Ph.D. dissertation, Dept. Elect. Eng., Iowa State Univ.

Bao, W., Ding, L., and Liu, Z. (2020). Analytically Derived Fixed Termination Time for Stepwise Inertial Control of Wind Turbines—Part I: Analytical Derivation. *Inter. J. Elect. Power Energ. Sys.* 121, 1–10. doi:10.1016/j.ijepes.2020.106120

Boukhezzar, B., and Siguerdidjane, H. (2011). Nonlinear Control of a Variable Speed Wind Turbine Using a Two Mass Model. *IEEE Trans. Energ. Convers.* 26 (1), 149–161. doi:10.1109/TEC.2010.2090155

Byerly, R. T., Aanstad, O., and Berry, D. H. (1973). Dynamic Models for Steam and Hydro Turbines in Power System Studies. *IEEE Trans. Power App. Syst.* PAS-92 (6), 1904–1915. doi:10.1109/TPAS.1973.293570

Cai, Y., Li, Z., and cai, X. (2020). Optimal Inertia Reserve and Inertia Control Strategy for Wind Farms. *Energies.* 13, 1067–1079. doi:10.3390/en13051067

Dreidy, M., and Mokhlis, H. (2017). Inertia Response and Frequency Control Techniques for Renewable Energy Sources: A Review. *Rene. Sustain. Energ. Rev.* 69, 144–155. doi:10.1016/j.rser.2016.11.170

EirGrid Grid Code Version 6.0 (2015). Available at: http://www.eirgridgroup.com/site.

Fernandez, L. M., Garcia, C. A., and Jurado, F. (2008). Comparative Study on the Performance of Control Systems for Doubly Fed Induction Generator (DFIG) Wind Turbines Operating With Power Regulation. *Energy.* 33 (9), 1438–1452. doi:10.1016/j.energy.2008.05.006

Garmroodi, M., Verbic, G., and Hill, D. J. (2018). Frequency Support From Wind Turbine Generators With a Time-Variable Droop Characteristic. *IEEE Trans. Sustain. Energ.* 9 (2), 676–684. doi:10.1109/tste.2017.2754522

Hu, Y.-L., and Wu, Y.-K. (2019). Approximation to Frequency Control Capability of a DFIG-Based Wind Farm Using a Simple Linear Gain Droop Control. *IEEE Trans. Ind. Applicat.* 55 (3), 2300–2309. doi:10.1109/tia.2018.2886993

Kheshti, M., Ding, L., Nayeripour, M., Wang, X., and Terzijia, V. (2019). Active Power Support of Wind Turbines for Grid Frequency Events Using a Reliable Power Reference Scheme. *Renew. Energ.* 139, 1421–1454. doi:10.1016/j.renene.2019.03.016

Lee, J., Jang, G., Muljadi, E., Blaabjerg, F., Chen, Z., and Cheol Kang, Y. (2016). Stable Short-Term Frequency Support Using Adaptive Gains for a DFIG-Based Wind Power Plant. *IEEE Trans. Energ. Convers.* 31 (3), 1068–1079. doi:10.1109/tec.2016.2532366

Li, Y., Xu, Z., and Wong, K. P. (2017). Advanced Control Strategies of PMSG-Based Wind Turbines for System Inertia Support. *IEEE Trans. Power Syst.* 32 (4), 3027–3037. doi:10.1109/tpwrs.2016.2616171

Margaris, I. D., Papathanassiou, S. A., Hatziargyriou, N. D., Hansen, A. D., and Sorensen, P. (2012). Frequency Control in Autonomous Power Systems With High Wind Power Penetration. *IEEE Trans. Sustain. Energ.* 3 (2), 189–199. doi:10.1109/tste.2011.2174660

National Grid UK (2010). *Grid Code Review Panel Paper, Future Frequency Response Services*.

Peng, X., Yao, W., Yan, C., Wen, J., and Cheng, S. (2020). Two-Stage Variable Proportion Coefficient Based Frequency Support of Grid-Connected DFIG-WTs. *IEEE Trans. Power Syst.* 35 (2), 962–974. doi:10.1109/tpwrs.2019.2943520

Vyver, J. V. d. (2016). Droop Control as an Alternative Inertial Response Strategy for the Synthetic Inertia on Wind Turbines. *IEEE Trans. Power Syst.* 31 (2), 1129–1138. doi:10.1109/TPWRS.2015.2417758

Wu, Y.-K., Yang, W. H., and Hu, Y. L. (2019). Frequency Regulation at a Wind Farm Using a Timing–Varying Inertia and Droop Controls. *IEEE Trans. Ind. Appl.* 55 (1), 213–2224. doi:10.1109/ICPS.2018.8369978

Wu, Z., Gao, D. W., Zhang, H., Yan, S., and Wang, X. (2017). Coordinated Control Strategy of Battery Energy Storage System and PMSG-WTG to Enhance System Frequency Regulation Capability. *IEEE Trans. Sustain. Energ.* 8 (3), 1330–1343. doi:10.1109/tste.2017.2679716

Xiong, L., Liu, L., Liu, X., and Liu, Y. (2021a). Frequency Trajectory Planning Based Strategy for Improving Frequency Stability of Droop-Controlled Inverter Based Standalone Power Systems. *IEEE J. Emerg. Sel. Top. Circuits Syst.* 11 (1), 176–187. doi:10.1109/jetcas.2021.3052006

Xiong, L., Liu, X., Zhang, D., and Liu, Y. (2021b). Rapid Power Compensation-Based Frequency Response Strategy for Low-Inertia Power Systems. *IEEE J. Emerg. Sel. Top. Power Electron.* 9 (4), 4500–4513. doi:10.1109/jestpe.2020.3032063

Xiong, L., Liu, X., Liu, Y., and Zhuo, F. (2020). Modeling and Stability Issues of Voltage-Source Converter Dominated Power Systems: a Review. In CSEE Journal of Power and Energy Systems. Early Access, 1–18.

Xu, G., Liu, F., Hu, J., and Bi, T. (2018). Coordination of Wind Turbines and Synchronous Generators for System Frequency Control. *Renew. Energ.* 129, 225–236. doi:10.1016/j.renene.2018.05.104

Yang, D., Jin, Z., and Zheng, T. (2021a). An Adaptive Droop Control Strategy With Smooth Rotor Speed Recovery Capability for Type III Wind Turbine Generators. *Int. J. Electr. Power Energ. Syst.* 135, 107532. doi:10.1016/j.ijepes.2021.107532

Yang, D., Jin, Z., Zheng, T., Jin, E., Zhang, X., and Hua, L. (2021b). Frequency Control Scheme with Dynamic Droop Characteristics of a DFIG for Mitigating the Frequency Fluctuations. *Int. Trans. Electr. Energ Syst.* 33 (11), 1–11.

Yang, D., Kim, J., Kang, Y. C., Muljadi, E., Zhang, N., Hong, J., et al. (2018). Temporary Frequency Support of a DFIG for High Wind Power Penetration. *IEEE Trans. Power Syst.* 33 (3), 3428–3437. doi:10.1109/tpwrs.2018.2810841

Ye, Y., Qiao, Y., and Lu, Z. (2019). Revolution of Frequency Regulation in the Converter-Dominated Power System. *Renew. Sustainable Energ. Rev.* 111, 145–156. doi:10.1016/j.rser.2019.04.066

Zhong, C., Lv, Y., and Zhou, Y. (2021). An Equivalent Rotor Speed Compensation Control of PMSG-Based Wind Turbines for Frequency Support in Islanded Microgrids. *Front. Energ. Res.* 9, 1–13. doi:10.3389/fenrg.2021.717327

Conflict of Interest: The authors declare that the research was conducted in the absence of any commercial or financial relationships that could be construed as a potential conflict of interest.

frontiers in Energy Research

ORIGINAL RESEARCH
published: 24 December 2021
doi: 10.3389/fenrg.2021.804405

Fault Location with High Precision of Flexible DC Distribution System Using Wavelet Transform and Convolution Neural Network

Dafei Wang, Baohua Wang*, Wenhui Zhang, Chi Zhang and Jiacheng Yu

School of Automation, Nanjing University of Science and Technology, Nanjing, China

Though flexible DC distribution system (FDCDS) is becoming a new hotspot in power systems lately because of the rapid development of power electronic devices and massive use of renewable energy, the failure to realize accurate fault location with high precision restricts its further application. Thus, a novel precise pole-to-ground fault location method of FDCDS based on wavelet transform (WT) and convolution neural network (CNN) is proposed in this paper for the limitation on the number of measuring points and high difficulty in extracting characteristics of FDCDS. The fault voltage signal is decomposed with multi-resolution by discrete wavelet transform (DWT), and then the transient energy function is constructed to select the frequency bands containing rich fault characteristics for signal reconstruction. The reconstructed signal forms two-dimensional time-frequency images through continuous wavelet transform (CWT), which are used as the input of CNN classifier after image enhancement to form the mapping relation between the fault feature and fault position using the powerful generalization ability of CNN, so as to complete fault location with high precision. The sample data on PSCAD/EMTDC verifies the accuracy and reliability of the proposed method, which can achieve fault location with positioning precision of 30 m. The proposed method overcomes the influence of the control strategy of the converter and the number of input capacitors of the bridge arm in the time-domain analysis, and still has strong robustness in the case that FDCDS is connected with many distributed generations (DGs) with output fluctuation. Furthermore, four other methods for fault location as comparisons are given to reflect the validity and anti-interference ability of proposed methods in various noises.

Keywords: fault location with high precision, signal decomposition and reconstruction, transient energy, feature extraction, wt, CNN

Edited by:
Liansong Xiong,
Nanjing Institute of Technology (NJIT), China

Reviewed by:
Zhongxue Chang,
Xi'an Jiaotong University, China
Haitao Zhang,
Xi'an Jiaotong University, China
Baohong Li,
Sichuan University, China

***Correspondence:**
Baohua Wang
wangbaohuaa@163.com

Specialty section:
This article was submitted to Process and Energy Systems Engineering, a section of the journal Frontiers in Energy Research

Received: *29 October 2021*
Accepted: *26 November 2021*
Published: *24 December 2021*

Citation:
Wang D, Wang B, Zhang W, Zhang C and Yu J (2021) Fault Location with High Precision of Flexible DC Distribution System Using Wavelet Transform and Convolution Neural Network. Front. Energy Res. 9:804405. doi: 10.3389/fenrg.2021.804405

INTRODUCTION

Flexible DC distribution system (FDCDS) is becoming a new developing direction of power system due to its advantages of being suitable for DGs multi-point access and asynchronous interconnection (Mohsenian-Rad and Davoudi, 2014). FDCDS based on Modular Multilevel Convertor (MMC) has been widely applied in many demonstration projects. However, the characteristics of FDCDS are different from traditional AC distribution networks in that the complex control strategies and dense branches, which make it difficult to directly apply the protection principle and scheme of AC network to the fault detection and location of FDCDS, thus, its large-scale engineering application is limited (Liu et al., 2020), (Huang et al., 2011). When a short-circuit fault occurs, the voltage drops rapidly and the current rises fast, seriously endangering the safe and stable operation of the power system, so it is necessary to quickly identify, locate the fault, and remove it.

Nowadays, the fault location method for FDCDS can be roughly divided into two approaches, the first is that the fault characteristics are analyzed and the fault distance equation is solved to obtain the fault location. The second approach is to utilize an intelligent algorithm to locate the fault.

Copied from the traditional line protection method of high voltage direct current transmission (HVDC) (Zheng et al., 2021), (Tang et al., 2019), three ways of line protection are introduced to FDCDS, which are the travelling wave method, the active injection method, and the fault analysis method (Dhar et al., 2018). Lin et al. (2017) proposed extracting travelling waves by using wavelet modulus maximum, which only needs to record the first time of travelling waves arriving at each terminal and select the nearest fault occurring time (FOT) to achieve location. Though the method performs better than traditional travelling wave method, it is restricted by the blind zone and the number of the measuring points. Additional signals are injected by the injection device and further detected to obtain additional signals to calculate the fault distance in the active injection method (Christopher et al., 2011), (Mohanty et al., 2016). But this method is strict with the topological structure of the network and is easily affected by noise. Apart from these two, most of the current research on fault location of FDCDS is based on the analysis of its fault characteristics and the corresponding algorithm is introduced to construct the relationship of fault location and transient component (Wang et al., 2019; Li et al., 2020; Yan et al., 2020; Yuan et al., 2020). Except the basic fault feature analysis, the fault's modal parameters and time domain characteristics are also utilized to the fault location. Tawfik and Morcos (2005) use the Prony method to extract modal information of fault current waveform which is strongly relevant to the fault location. But the fundamental frequency component's damping coefficients will cause influence on the accuracy of the location. On this basis, the linear relation between fault location and damping coefficient is established in the Prony method to locate the fault, which eliminates the effect of load fluctuation and fault types. However, the influence of transient resistance is not considered (Gou and Owusu, 2008). References (Jia et al., 2020) and (He et al., 2014) analyze the relationship between the frequency feature of fault voltage or current and fault distance, but it also means that the selection of frequency range will have an impact on the final positioning result.

The development of intelligent algorithm provides a novel solution for fault location, such as expert system (Lee et al., 2000), fuzzy algorithm (Huisheng Wang and Keerthipala, 1998), improved genetic algorithm (Li et al., 2012), and deep learning (Guomin et al., 2018). Both bionic algorithm and deep learning based on neural network have the problems in convergence performance and easily falling into local optimal when facing complex situations, hence, the directions to increase the accuracy of methods are divided into two categories: enhancing the characteristics information of sample data and multiple algorithms fusion. The time delay, characteristic frequency, energy attenuation, and high-frequency energy via the Hilbert-Huang Transform (HHT) are used as the input of support vector regression (SVR) to get fault distance, then the parameters of the model is optimized by the bat algorithm (BA) (Hao et al., 2018). Based on the feature extraction ability of the convolution neural network (CNN), reference (Liang et al., 2020) adopts the improving pooling model and the result shows the method improves the accuracy greatly.

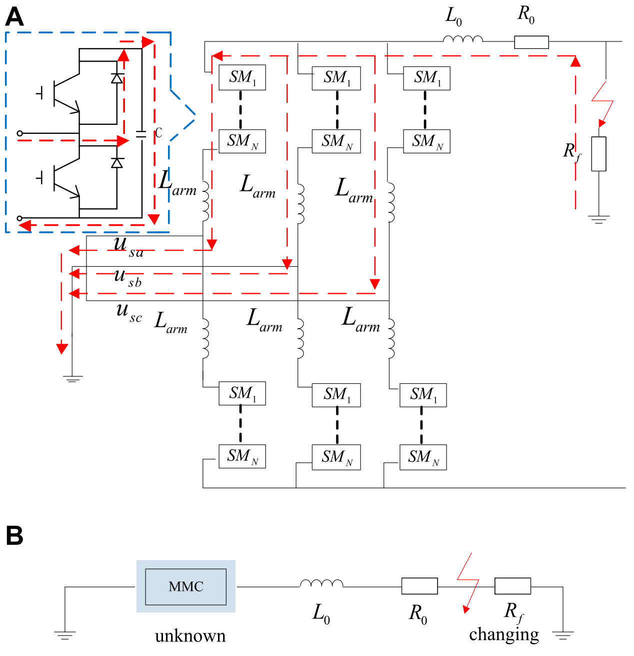

FIGURE 1 | Fault analysis. **(A)** The discharging circuit of SM's capacitor. **(B)** Fault equivalent circuit.

In general, the current fault location problems of FDCDS are mainly reflected in the difficulty to extract fault features. Especially the location accuracy is easily affected by noise and converter, which cause the low location precision. Therefore, the main contribution of this paper is a novel pole-to-ground fault location method of FDCDS, it can identity fault position with high precision, even under the interference of transient resistance, output fluctuation of DGs, and different noises. In addition, the proposed method eliminates the influence of the converter control strategy and the switching of sub-modules (SMs). Compared with the existing methods, this paper adopts wavelet transform to enhance the sample feature, magnify the sample characteristics, and increase the number of the input data, to solve the problem of difficulty in feature extraction and insufficient feature quantity under the limited fault information. Convolutional neural network is used to mine the mapping relationship between fault features and fault positions to solve the problem of insufficient accuracy of existing algorithms.

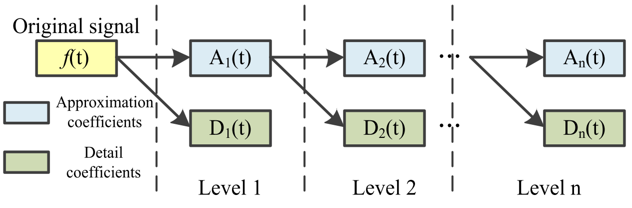

FIGURE 2 | The decomposition tree of DWT-based MRA.

FAULT LOCATION METHOD

Fault Analysis

In FDCDS, pole-to-pole faults do great harm to the system and have obvious fault characteristics, most of the current fault location research is focused on pole-to-pole faults. While single-pole faults do not have obvious fault features due to transition resistance, there are few studies on its fault location. In fact, pole-to-ground fault is the fault with the highest frequency, so the fault location of the distribution line for pole-to-ground is mainly studied in this paper. The transient process after short-circuiting mainly can be divided into two processes: SM's capacitor discharging; the grid side feeds the short-circuit current into the DC system through the bridge-arm reactor and the anti-parallel diode when the DC side's voltage drops to less than the peak voltage of the AC side. Considering that the fault current rises fast when the fault occurs, which will cause a huge impact on expensive converter equipment, so the SM's capacitor discharging stage of the transient process is taken to locate the faults in this paper.

Figure 1A shows the discharging circuit of SMs, in which FDCDS converter transformer valve side is grounded, and the current direction has been marked. To analyze the pole-to-ground fault from the fault equivalent loop in **Figure 1B**, the quantity of the input capacitor and the value of transient resistance need to be considered. But at the fault initial time, the input capacitor of the upper and lower bridge arm is unknown as the SMs are normally switched under the control strategy and transient resistance is also changing, making it difficult to utilize the fault loop to deduce the relationship between voltage (or current) and fault location. But it is clear that the electric data emerged at different fault locations on the line are different, although the relationship between these two cannot be explicitly given by an equation. Therefore, this paper decided to use deep learning and wavelet transform to fit the relationship between fault features and fault locations instead of manual formula derivation.

Signal Analysis Based WT

Wavelet transform is a time-frequency analysis tool, which can show the amplitude of a signal in a different frequency domain over a period of time. WT mainly includes discrete wavelet transform (DWT) and continuous wavelet transform (CWT). DWT is used to decompose the fault voltage signal into multiple frequency bands in this paper, and then the selected frequency band signals are reconstructed to obtain the reconstructed signals with rich fault features. CWT is applied to the processed signals to generate two-dimensional grayscale images that serve as the inputs of CNN to complete fault location.

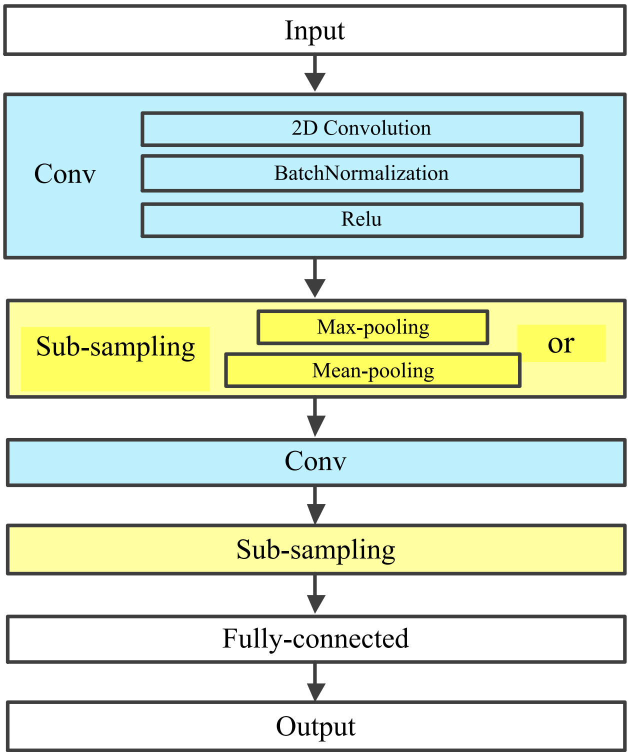

FIGURE 3 | The structure of CNN.

The multi-resolution analysis (MRA) is used to decompose the signal in multiple frequency bands, it is applied to DWT to divide signals to approximate component *A* (t) and detail component *D* (t), which represent the low and high frequency bands, respectively, and the decomposition tree of DWT-based MRA is shown in **Figure 2**.

If the Fourier transform of function φ (t) satisfies the admissibility condition shown in **Equation (1)**, then φ (t) is called a fundamental wavelet, also known as a mother wavelet function.

$$C_{\varphi} = \int \frac{\left|\hat{\varphi}(\omega)\right|^{2}}{|\omega|} d\omega < \infty \tag{1}$$

The integral transforms of the following formulas are defined as the CWT and DWT based on φ(t).

$$CWT_{x}(a,b) = |a|^{\frac{1}{2}} \int f(x)\bar{\varphi}\left(\frac{x-a}{b}\right)dx, f(x) \in L^{2}(R) \tag{2}$$

$$DWT_{x}(u,v) = \left|a_{0}^{u}\right|^{\frac{1}{2}} \sum_{v} f(x)\varphi\left(\frac{x - va_{0}^{u}b_{0}}{a_{0}^{u}}\right) \tag{3}$$

where *a* is a scale parameter, *b* is a translation parameter in CWT. For DWT, $a_0{}^u$is a scale parameter and $va_0{}^u b_0$ is a translation parameter.

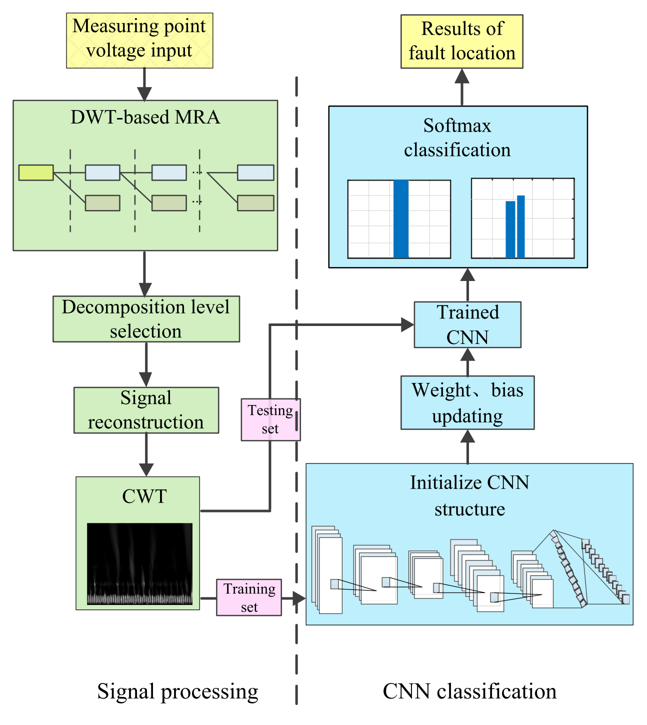

FIGURE 4 | The flowchart of the proposed method.

The Structure and Principle of CNN

The typical structure of CNN is depicted in **Figure 3**. The 2D gray image as input is expanded to the fully connected layer after passing though the convolutional layer (Conv layer) and sub-sampling layer (S layer) and outputs the results via softmax classification. The Conv layer is composed of a 2D image convolution, batch normalization (BN), and Rectified Linear Unit (ReLU) (Gu et al., 2015). The 2D gray value matrix after padding is mapped to the next layer through the convolution kernel. BN is set to prevent gradient explosion. ReLU, as the activation function, effectively solves the problem of gradient dispersion. The two main methods of sub-sampling are maximum pooling (max-pooling) and mean pooling (mean-pooling) (Zhao et al., 2018), and they are mainly used to extract the signal features more finely. Through multi-level non-linear transformation, the neural network would automatically extract and recognize the feature of input set and classify mass data according to the labels.

A fully connected layer is a one-dimensional vector to store an eigenvector after the Conv layers and S layers. The column vectors are mapped to an output layer, and then the classification results are generated via softmax function, which calculation formula is denoted as **Equation (4)**.

$$y_i = \varphi(v_i) = \frac{e^{vi}}{e^{v1} + e^{v2} + e^{v3} + \cdots e^{vM}} = \frac{e^{vi}}{\sum\limits_{i\in M} e^{vk}} \qquad (4)$$

where M is the number of the output nodes. According to **Equation (4)**, the sum of the vectors output after the classifier is 1.

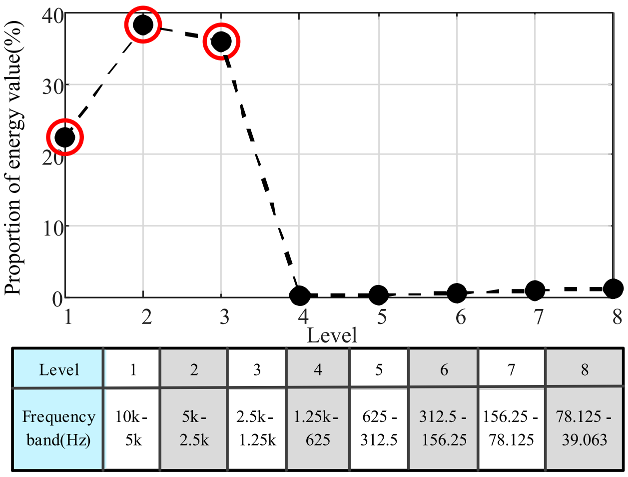

Level	1	2	3	4	5	6	7	8
Frequency band(Hz)	10k-5k	5k-2.5k	2.5k-1.25k	1.25k-625	625-312.5	312.5-156.25	156.25-78.125	78.125-39.063

FIGURE 5 | Transient energy proportion of each level.

CNN neural network training process involves the adjustment of many weights. In order to speed up the training and improve the stability, the concept of "momentum" in physics is introduced (Kim, 2017). In physics, momentum is a concept similar to inertia, which can prevent objects from rapidly changing the motion state. The momentum term is used in weight adjustment to push the weight to adjust to a certain direction to a certain extent, instead of causing immediate changes.

Proposed Method

The proposed method is illustrated in **Figure 4**, and it is mainly divided into two parts: signal processing based WT and classification based CNN. The main problem to be solved in this paper is fault location with high precision, so it is necessary to extract rich and effective fault features in the signal processing stage. First, DWT-based MRA is used to decompose the signal, and then the transient energy of each frequency band is constructed to select the frequency band where the useful signal is and complete the signal reconstruction. Then, CWT is applied to generate a two-dimensional time-frequency image with rich characteristic information. Apart from signal processing, fault location mainly relies on CNN to process a grayscale image with characteristic information. After initialization and a lot of trainings, the fault location task with high precision can be accurately completed. The following part will explain the feature extraction in signal processing in detail, and the steps of CNN classification will be given in the third part combined with experiments.

DWT-Based MRA

In wavelet transform, db4 wavelet with good regularity is used as the wavelet basis function. According to Nyquist sampling theorem, the frequency band of the high-filter of each decomposition level is $[F_S/2^{n+1}, F_S/2^n]$, then $[0, F_S/2^{n+1}]$ is for low-filter of each level. The principle of signal decomposition is to make the reconstructed signal contain the most unique features as far as possible. If the decomposition level is too little, the feature

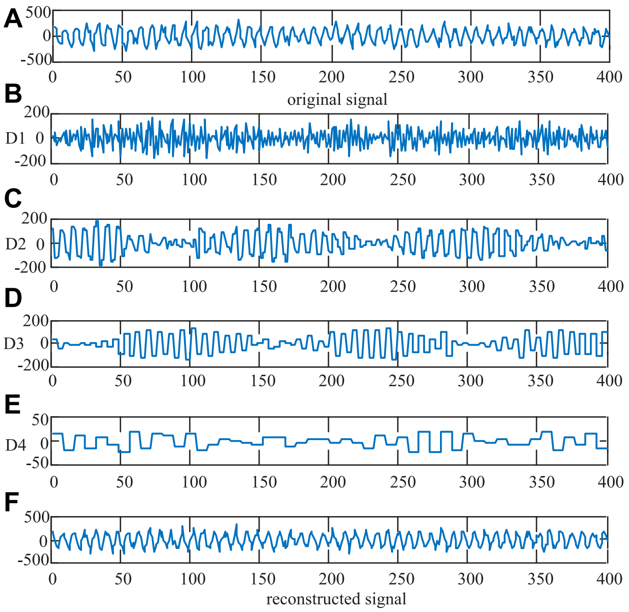

FIGURE 6 | Signal reconstruction. **(A)** original signal **(B)** detail coefficient D1 **(C)** detail coefficient D2 **(D)** detail coefficient D3 **(E)** detail coefficient D4 **(F)** reconstructed signal.

information and irrelevant information will be overlapped together, affecting the final location results. If the decomposition level is too much, according to the MRA principle, the frequency of decomposition has dropped below 39 Hz after level 8, and there is no need to continue decomposition. So, the decomposition level is set to 8. In the preliminary simulation test process, the sampling rate of 20 kHz is found to be sufficient and brings the right balance between accuracy and speed, guaranteeing high precision of fault location and quick and timely response. So, the original signal is decomposed into 8 frequency bands covering frequencies from 39.163 Hz to 10 kHz. Frequency band after multi-resolution decomposition is shown in **Figure 5**.

Decomposition Level Selection

To extract effective fault feature information and select the frequency bands where the useful signal is located, define the voltage transient energy E_h as shown in **Equation (5)**, which can reflect the richness of fault characteristics in each frequency band.

$$E_h = \int_0^T d_n(t)^2 dt \tag{5}$$

where d_n is a high-filter coefficient, T is integral time. **Figure 5** is the ratio of the transient energy of each frequency band to the sum of the energy of the 8 frequency bands when pole-to-ground fault occurs at a distribution line. As can be seen from **Figure 5**, the energy in the transient process is mainly concentrated in Level 1, 2, and 3 (the frequency band covering from 1.25 to 10 kHz), which indicates that this part of the frequency band contains most of the characteristic information. Therefore, it is more accurate to select the fault information within these three levels to complete the fault location in the next step.

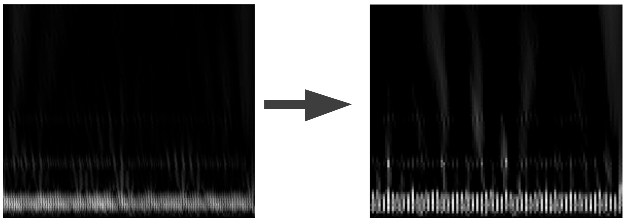

FIGURE 7 | Grayscale image and image preprocessing.

Signal Reconstruction

Signal reconstruction of the frequency band selected in the previous step can effectively eliminate noise interference caused by external factors such as sensors (noise occupies a low proportion of energy). According to Mallat's algorithm (Mallat, 1989), in multi-resolution decomposition, signals are decomposed via high-pass and low-pass filters, and reconstruction is the convolution of decomposed signals, and the mirror filter banks. Suppose that D^{-1} is the reconstructed signal of detail coefficient D, the reconstructed signal is denoted as $S(t)$,

$$S(t) = D_1^{-1}(t) + D_2^{-1}(t) + D_3^{-1}(t) \tag{6}$$

Figure 6 shows the process of signal reconstruction, in which **Figure 6A** is the original signal. **Figures 6B–E** are part of the signal (D1-D4) after decomposition, and it can be clearly seen that the transient energy of signal is mainly concentrated in D1, D2 and D3, D4, and the other bands contain only a small amount of useful information. The decomposition levels D1, D2, and D3 are used to reconstruct a new signal (**Figure 6F**), which not only can extract the effective feature information, but also can eliminate the noise interference.

Grayscale Image and Image Preprocessing

CWT is applied to the reconstructed signal to generate a two-dimensional time-frequency image (grayscale image) for CNN classifier. In order to enhance the effect of image recognition, the image is preprocessed before the CNN training. **Figure 7** is the grayscale image after image enhancement, and the fault features are more obvious. Meanwhile, the noise influence of the reconstructed signal of the selected frequency band is eliminated in this step, and the accuracy of positioning is further improved.

SIMULATION RESULTS

FDCDS Model

A typical FDCDS of 10 kV voltage class (adapted from the demonstration project of flexible DC distribution system in

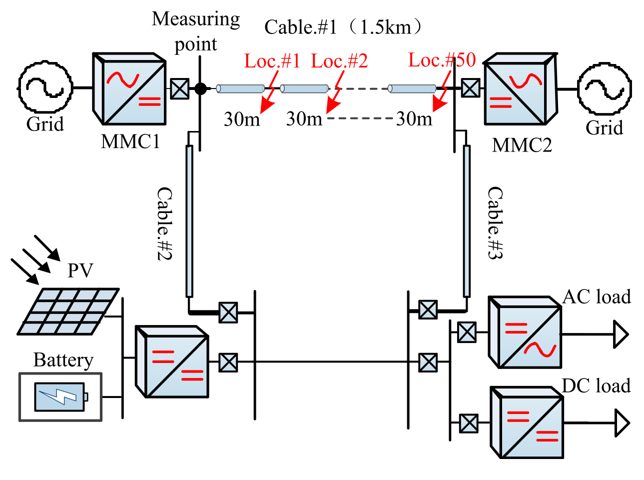

FIGURE 8 | The structure of FDCDS.

Shenzhen) in **Figure 8** is built in PSCAD/EMTDC to verify the reliability and accuracy of the proposed method. The selected topology in this paper is the loop structure, which has the highest power supply reliability and the highest requirements for protection. In addition, the adaptive feature extraction based on transient energy method according to different topologies is adopted in the paper, theoretically applicable to the relatively simple radial structure and other topologies. Cable #1 connects two AC grids (10 kV) through two MMCs (5MVA) that are operated at the constant DC voltage mode and the constant active/reactive power mode to carry out rectifier and inverter. Generally, the length of the distribution line is no more than 2 km, so Cable #1 with 0.71 Ω /km resistance and 8.9 mH/km inductance is set as 1.5 km. In addition, Cable #2 and Cable #3 connect photovoltaic (PV) arrays, energy storge system, DC loads (5 MW), and AC loads, respectively.

Considering the limitations of simulation time-step and resolution for finding the fault location (Li et al., 2018), a frequency dependent π cable model is adopted under small time-step simulation speed ($50\,\mu s$), which is a lumped π model with frequency dependent resistance and inductance.

In **Figure 8**, Cable #1 is divided into 50 sections equally (each section is 30 m), and Loc. #1 to Loc. #50 denote the end point of each section, respectively. Segments between every two Loc. # are marked as Sec. #1 to Sec. #50. Because the minimum distance is 30 m in each section, the resolution for fault location using the proposed method is 30 m.

Sample Data

DC loads fluctuation has a pretty big impact on power flow of FDCDS, so five types of DC loads are set to simulate the fluctuation (the rated power of DC loads is S_N, the actual power is S_{real}, and k represents the proportion of actual power in rated power, i.e., $k = S_{real}/S_N$): k is 80, 90, 100, 105, 110%, respectively. In order to make the fault location more accurate and give full play to learning and generalization ability of CNN, it is necessary to traverse the faults in various cases. In the training process of CNN, the following factors that may affect the location results need to be traversed: fault distance, fault pole, transient resistance, DC loads fluctuation, and distributed capacitance are considered during the training process of CNN. The traversal table of sample parameters is shown in **Table 1**, it can be worked out that the total sample number is 9000.The sampling frequency is 20 kHz, and the fault data is the fundamental frequency period after the fault is taken, therefore, the number of sampling points is 400. To sum up, the sample set from the measured voltage is 9000 × 400, and the output set is a matrix with dimension of 9000 × 50 after CNN to produce the results of the fault location.

Verification of the Proposed Method

Verification of Signal Analysis

The signal processing and CNN classification are all carried out on MATLAB 2020b. The PC used in the test platform with RAM of 12 GB has a CPU model of Inter (R) Core (TM) i7-10510U and a GPU model of NVIDIA GeForce MX250.

The correctness of the signal analysis is verified first. According to the signal processing procedure mentioned above, the voltage signals at 50 positions of Cable #1 in **Figure 8** were extracted, respectively. After signal decomposition and transient energy calculation, the transient energy values of each signal decomposition frequency band as shown in **Figure 9** were obtained. Most of the energy in the fault is concentrated in Level 1, 2, and 3, which is consistent with the previous analysis. Moreover, from the perspective of the transient energy of each frequency band from Loc. #1 to Loc. #50, the transient energy trend of Level 1, 2, and 3 are obvious and regular. Compared with other frequency bands, it is easier to form a mapping relationship between fault features and fault positions to complete high precision fault location.

Verification of CNN Classification

The structure, convolution kernel, and way of sub-sampling of CNN will have a big impact on the learning effect. In order to get the best parameters of CNN, many CNNs with different structure, convolution kernel, way of sub-sampling, and batch size are tested in this paper, and the most appropriate CNN structure was selected by comparing the training speed and accuracy. Finally, a typical structure of CNN is picked out after numerous experiments, in which its topology structure is 8C-2S-16C-2 S. The sub-sampling layer adopts mean-pooling, and the kernel size of convolution is 7 and 9, respectively. The gradient calculation method is stochastic gradient descent with momentum.

Figure 10 shows the changing trend of training accuracy and learning rate with epochs. In the early stage of training, the learning rate is relatively high, which ensures the training speed and accuracy. In the middle and late part of learning, when the training model tends to be stable, the learning rate is also significantly reduced, which ensures the effectiveness of the training model. The training process tends to be stable roughly at 2000 epochs, which is consistent with the change of learning rate. Finally, the accuracy of the fault location model obtained by training can reach more than 99%, almost close to 100%.

TABLE 1 | The traversal table of sample parameters

Parameter type	Variables	Number
Fault location	Loc.#1 to Loc.#50	50
Fault pole	Positive, negative	2
Transient resistance (Ω)	0.001, 0.01, 0.05 0.1, 0.2, 0.5	6
DC loads fluctuation (%)	80, 90, 100, 105, 110	5
Distributed capacitance (nF/km) (Jia et al., 2020)	0, 8.34, 20.34	3

Level	1	2	3	4	5	6	7	8
Frequency band(Hz)	10k-5k	5k-2.5k	2.5k-1.25k	1.25k-625	625-312.5	312.5-156.25	156.25-78.125	78.125-39.063

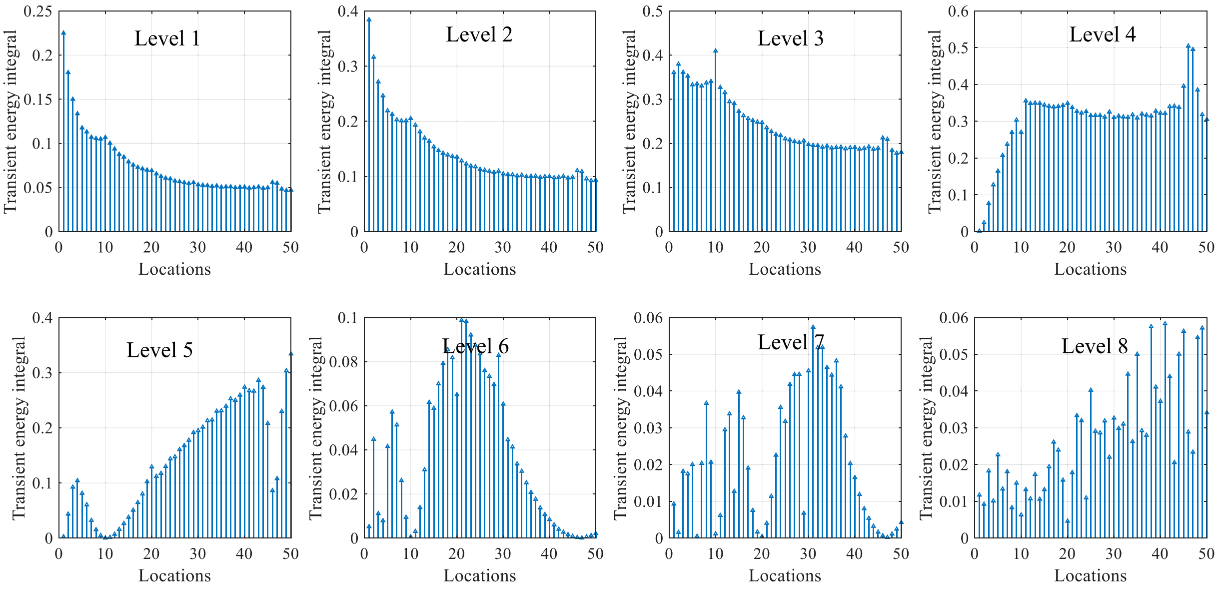

FIGURE 9 | The transient energy of each signal decomposition level from Loc.#1 to Loc.#50.

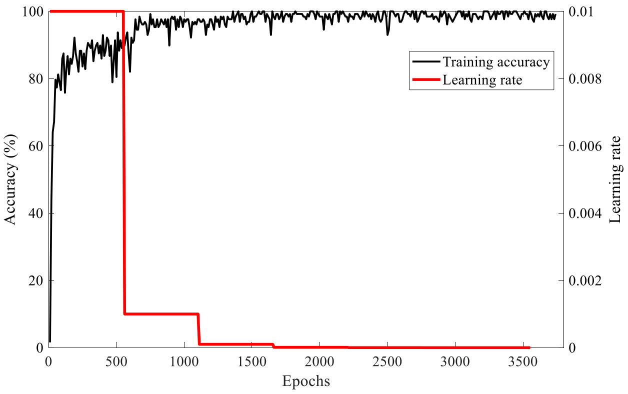

FIGURE 10 | The curve changing of training accuracy and learning rate.

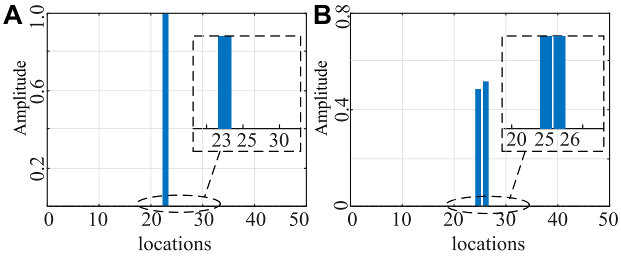

FIGURE 11 | The location results. **(A)** Loc.# fault. **(B)** Sec.# fault.

The output of softmax function is 50 values with a sum of one according to (1), and the category of the largest value is selected as the output result. Hence, when the fault occurs at the Loc. #1 to Loc. #50, the classification directly output the specific number of Loc. #, which is shown in **Figure 11A**. In addition, when there is a Sec. # fault, the output of the softmax function is two bigger values, which signifies that the fault is between these two locations, also known as Sec. # fault, just as shown in **Figure 11B**. Therefore, no matter which point on the line occurs the fault, the classifier will output the corresponding results (Loc. # fault or Sec. # fault).

TABLE 2 | The performance of the trained CNN

Fault type	Sample number	Location accuracy (%)
Loc. # fault	50	100
Sec. # fault	115	96.5217
Total	165	97.5758

D. verification of influence of control strategy.

TABLE 3 | Control strategy interference test results

MMC1	MMC2	Number	Accuracy (%)
Constant voltage mode	Constant power mode	120	100.00
Constant power mode	Constant voltage mode	120	100.00

To test the performance of trained CNN network in location accuracy, two fault types, Loc. # fault and Sec. # fault, with different transient resistances are tested, and the result is illustrated in **Table 2**. The fault positions on the line are random and do not always fall on the set fault points. Therefore, most of the fault points in the test fall randomly on the positions between the set fault points, i.e., Sec. # fault. Although the training data required in the process of model building is obtained by setting Loc. # fault, the test results show that the CNN model trained has a very high accuracy for Sec. # fault, which demonstrates the feasibility of softmax classifier in solving the fault location. When the location precision reaches 30 m, the final positioning can be carried out through manual inspection or UAV. Compared with the traditional line inspection method, the proposed method greatly reduces the time of fault location and improves the accuracy.

In the literature (Jia et al., 2020), the control strategy of MMC converter has an impact on the location accuracy, so the reliability of the proposed algorithm is tested by changing the control strategy of the MMC converter at both ends of Cable #1, when MMC1 is constant DC voltage control mode, MMC2 is constant power control mode and vice versa, and the test results are shown in **Table 3**.

As MMC adopts the modulation mode of step wave approaching the sinusoidal wave, the switching frequency of MMC is low, usually around 150 Hz. In the procedure of signal reconstruction, the frequency band range selected is from 1.25 to 10 kHz, which exceeds the switching frequency of the MMC converter. Therefore, the control strategy will not affect the location results. The input capacitor of the upper and lower bridge arm is unknown during the fault in the aforementioned analysis, which may cause the difficulty of the time-domain analysis. The frequency band range selected in this paper is 1.5–2 kHz, which belongs to the high frequency range. The SM's capacitor impedance is $-j/\omega C_0$, in which C_0 is the SM's capacitor and $\omega = 2\pi f$. In a high frequency domain, it is known that $\omega L_{arm} >> j/\omega C_0$. Therefore, the effect of the number of SM's capacitor can be ignored at this stage.

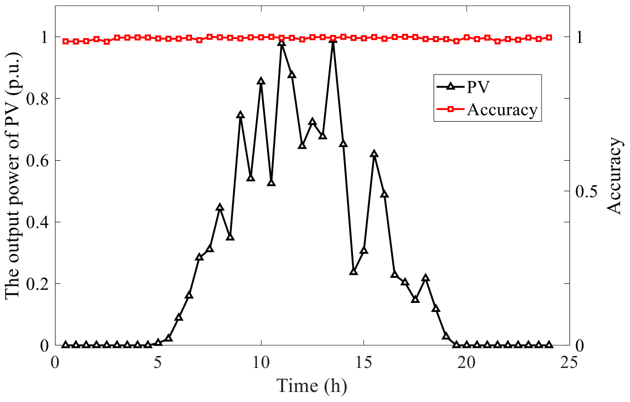

FIGURE 12 | The influence of PV's output power fluctuation on location accuracy.

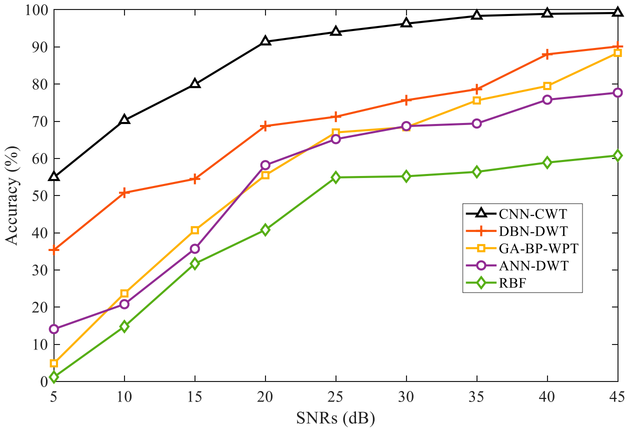

FIGURE 13 | The classification accuracy of different methods under different SNRs.

Verification of the Fluctuation of PV's Output Power

Most of the existing fault location methods in the flexible DC distribution network have poor application effects in practical projects, the main reason is that the location results are easily influenced by fluctuation of PV's output power. In addition, the robustness of the proposed method is tested with the actual PV output power in a day. The output power of PV is mainly affected by illumination intensity. According to **Equation (7)**, the per-unit value of PV's output power in a day (assuming the maximum output power as the rated value) is calculated on the basis of the change of illumination intensity in a day. The accuracy of locating results is shown in **Figure 12**.

$$P_{PV} = \begin{cases} P_{pv}^{r}\dfrac{I}{I_r} & I \le I_r \\ P_{PV}^{r} & I > I_r \end{cases} \tag{7}$$

where I is illumination intensity and Ir is rated intensity; and $P_{PV}{}^{r}$ represents the rated value of PV's output power and P_{PV} is the true output power of PV.

TABLE 4 | Comparisons result of different methods when the SNR is 45 DB

Methods	Calculation time (s)	Iterations (s)	MAE	RMSE	Accuracy (100%)
CNN-WT	773.21	1450	0.0599[a]	0.250[a]	99.130[a]
DBN-DWT (Ye et al., 2020)	685.66	2000	0.233	0.907	90.120
GA-BP-WPT (Chen et al., 2017)	1037	9013	0.304	1.103	88.400
ANN-DWT (Li et al., 2018)	9983	26[a]	0.417	1.682	77.700
RBF (Guifeng et al., 2014)	276.14[a]	50	0.759	2.324	60.800

[a]*Note: indicates that this criterion is significantly better than other algorithms.*

The major influence of PV's output fluctuation on the FDCDS is the change of power flow distribution in the system, so the changes of transient quantity in the fault are mainly concentrated in the low frequency band. In this paper, the frequency bands are selected by comparing the transient energy of each decomposition level, and the low frequency bands are filtered out because they contain only a small amount of feature information, already analyzed in the section on *Fault Location Method*. Therefore, PV's output fluctuation has almost no effect on the accuracy of location, as shown in **Figure 12**. Furthermore, FDCDS has many branches connected to various types of loads and DGs, affecting the magnitude and distribution of the fault component. The boundary conditions of FDCDS at the line exit, composed of DC reactor and parallel filter, absorb and block the high frequency components of voltage and current, resulting in high frequency component of branches entered into the studied line being greatly reduced (Karmacharya and Gokaraju, 2018). Because the data used in the paper is the high frequency band of voltage, the influence of branches on positioning can be ignored. So, the fault location method proposed has a high robustness in the situation of massive branches access and is more valuable to the engineering application.

COMPARISONS WITH EXISTING METHOD

There are a lot of intelligent algorithms being applied to fault location of FDCDS, but few methods have solved the problems of long distribution lines and short resolution for located distance. In this paper, the resolution is set at 30 m, and the accurate location of 50 faults distances is realized. To verify the superiority of method in this paper, methods in literatures (Ye et al., 2020), (Chen et al., 2017), (Li et al., 2018), (Guifeng et al., 2014) are introduced to tested in FDCDS presented in article. **Table 4**. illustrates the comparing result of different methods when the noise's SNR is 45dB. The evaluation criterions involve calculation time and iterations in the training phase, mean absolute error (MAE), root mean squared error (RMSE), and accuracy in the testing phase. The equation of MAE, RMSE, and accuracy is in (**Equations 8–10**):

$$MAE = \frac{1}{N}\sum_{i}^{N}\left|y_i - \hat{y}_i\right| \tag{8}$$

$$RMSE = \sqrt{\frac{1}{N}\sum_{i}^{N}\left(y_i - \hat{y}_i\right)^2} \tag{9}$$

$$accuracy = \frac{n}{N} \times 100\% \tag{10}$$

here, N is the number of testing samples, y_i is the output value, $\hat{y}_i$ is the true value, and n represents the number of samples whose output value is consistent with the true value in the testing process.

The literature (Ye et al., 2020) develops a single pole-to-ground fault location method using wavelet decomposition and deep belief network (DBN), in which the low-frequency components and high-frequency components after three levels wavelet decomposition are used to characterize the fault's overall trend. Although DBN with a stack of multiple RBMs is a strong classification, the feature extraction in frequency-domain is not sufficient to form a strong mapping relationship between fault distance and signal, so its performance is inferior to the proposed method in this paper.

Back-propagation (BP) optimized by genetic algorithm (GA) presented in the literature (Chen et al., 2017) utilizes wavelet packet decomposition to gather the signal energy of each frequency band and construct an energy feature vector. The test results show that the more detailed fault feature extracted, the more accurate the fault location. Aimed at ungrounded photovoltaic system, the literature (Li et al., 2018) proposes a location method that the high-frequency signal of fault information is extracted by DWT, and then the norm of different frequency bands' detail coefficients is used as the input data vector for artificial neural network (ANN). Though this method ranging accuracy is accurate enough, the required sample frequency is quite high, which is up to 340 kHz. Therefore, at the sample frequency of 20 kHz, the method is difficult to identify 50 fault locations. To reflect the availability of signal analysis, the literature (Guifeng et al., 2014), which directly applies the radial basis function (RBF) neural network to use fault information to find fault distance, is regarded as a comparison to other smart algorithms with signal processing. The results in **Table 4** show that the location method via RBF has the worst performance compared to the others though the training time is the shortest, so the signal analysis is necessary to extract fault characteristics when the location resolution is short, and the distribution line is quite long in FDCDS. It should be noted that the structures in the four classification methods are all optimized models based on the methods in the original literature under the environment created in this paper after vast tests, to guarantee the fairness and reliability of comparisons. From the comparison results, the MAE, RMSE, and accuracy criterions of the proposed method are significantly better than those of other methods under the same conditions.

In signal analysis and fault location, noise will affect the result, and Gaussian white noise following normal distribution is an important factor affecting fault location in the power system because of its strong randomness. In order to test the anti-interference ability of different methods aforementioned to noise, 9 groups of different signal-to-noise ratios (SNRs) from 5 dB to 45 dB are set for testing, and the SNRs reflect the ratio between normal signal and noise, which means that the higher the SNR, the closer the signal is to the normal signal.

Figure 13 gives the classification accuracy of different methods under different SNRs. When the signal interference is not large (more than 25dB), CNN with WT can have a better performance than other methods. Furthermore, when the SNRs are less than 20dB, the signal collected at this time contains a lot of interference, the proposed method still be much more accurate. But when the SNR comes to 5dB, the signal is already so distorted that any algorithms will lose accuracy. Due to the effective feature extracted in the signal processing and the elimination of noise interference, the proposed algorithm can achieve high precision fault location under noise interference comparing to four other methods.

CONCLUSION

In this paper, a fault location method with high precision is presented. DWT-based MRA is applied to decompose the voltage signal into 8 levels, and the signal bands with a large proportion of transient energy are selected for reconstruction. Then CWT is used to produce the grayscale images, which serve as the input of the CNN with the optimal structure and parameters under various tests after image enhancement.

A large number of simulation data show that the proposed method based on WT and CNN has a remarkable effect in the fault location of FDCDS, and eliminates the influence of the converter control strategy and the switching of SMs. Due to the effectiveness of the signal feature extraction, the method proposed in this paper still has high accuracy in the case of large-scale access of DGs with output fluctuation. Verification results of comparisons show that the proposed method has better performance and is more accurate and efficient than four other methods under various noises, thus it can be extended to complex FDCDS with little measuring points, which is of great significance to development of the DC system.

DATA AVAILABILITY STATEMENT

The raw data supporting the conclusions of this article will be made available by the authors, without undue reservation.

AUTHOR CONTRIBUTIONS

Idea and innovation of the paper: DW and BW; data collection: DW, WZ, and CZ; article writing: DW; revision of the paper: DW and JY.

FUNDING

This work was supported by the National Natural Science Foundation of China under Grant 51807092.

REFERENCES

Chen, Y., Zhang, C., Zhang, Q., and Hu, X. (2017). "UAV Fault Detection Based on GA-BP Neural Network," in Proceedings of 32nd Youth Academic Annual Conference of Chinese Association of Automation (YAC) (Hefei, China, 806–811. doi:10.1109/yac.2017.7967520

Christopher, E., Sumner, M., Thomas, D., and de Wildt, F. (2011). "Fault Location for a DC Zonal Electrical Distribution Systems Using Active Impedance Estimation," in Proceedings of 2011 IEEE Electric Ship Technologies Symposium (Alexandria, VA, USA, 310–314. doi:10.1109/ests.2011.5770888

Dhar, S., Patnaik, R. K., and Dash, P. K. (2018). Fault Detection and Location of Photovoltaic Based DC Microgrid Using Differential Protection Strategy. *IEEE Trans. Smart Grid* 9 (5), 4303–4312. doi:10.1109/tsg.2017.2654267

Gou, B., and Owusu, K. O. (2008). Linear Relation between Fault Location and the Damping Coefficient in Faulted Signals. *IEEE Trans. Power Deliv.* 23 (4), 2626–2627. doi:10.1109/tpwrd.2008.2002992

Gu, J., Wang, Z., Ma, L., Kuen, J., Shahroudy, A., Shuai, B., et al. (2015). Recent Advances in Convolutional Neural Networks, *Pattern Recognition*, 77, 354–377. doi:10.1016/j.patcog.2017.10.013

Guifeng, W., Hong, C., and Xuan, W. (2014). "Research of Small Current Grounding Fault Location Algorithm in Distribution Grid Based on RBF," in Proceedings of 2014 International Conference on Information Science, Electronics and Electrical Engineering, 154–158. doi:10.1109/infoseee.2014.6948087*Sapporo, Jpn. Nov.*

Guomin, L., Yingjie, T., Changyuan, Y., Yinglin, L., and Jinghan, H. (2018). Deep Learning-based Fault Location of DC Distribution Networks. *J. Eng.* 2019, 3301–3305. doi:10.1049/joe.2018.8902

Hao, Y., Wang, Q., Li, Y., and Song, W. (2018). An Intelligent Algorithm for Fault Location on VSC-HVDC System. *Int. J. Electr. Power Energ. Syst.* 94, 116–123. doi:10.1016/j.ijepes.2017.06.030

He, Z.-y., Liao, K., Li, X.-p., Lin, S., Yang, J.-w., and Mai, R.-k. (2014). Natural Frequency-Based Line Fault Location in HVDC Lines. *IEEE Trans. Power Deliv.* 29 (2), 851–859. doi:10.1109/tpwrd.2013.2269769

Huang, A. Q., Crow, M. L., Heydt, G. T., Zheng, J. P., and Dale, S. J. (2011). The Future Renewable Electric Energy Delivery and Management (FREEDM) System: The Energy Internet. *Proc. IEEE* 99 (1), 133–148. doi:10.1109/jproc.2010.2081330

Huisheng Wang, Huisheng., and Keerthipala, W. W. L. (1998). Fuzzy-neuro Approach to Fault Classification for Transmission Line protection. *IEEE Trans. Power Deliv.* 13 (4), 1093–1104. doi:10.1109/61.714467

Jia, K., Feng, T., Zhao, Q., Wang, C., and Bi, T. (2020). High Frequency Transient Sparse Measurement-Based Fault Location for Complex DC Distribution Networks. *IEEE Trans. Smart Grid* 11 (1), 312–322. doi:10.1109/tsg.2019.2921301

Karmacharya, I. M., and Gokaraju, R. (2018). Fault Location in Ungrounded Photovoltaic System Using Wavelets and ANN. *IEEE Trans. Power Deliv.* 33 (2), 549–559. doi:10.1109/tpwrd.2017.2721903

Kim, P. (2017). Training of Multi-Layer Neural Network, *MATLAB Deep Learning : With Machine Learning, Neural Network and Artificial Intelligence*. New York: Apress Media, 48–53. doi:10.1007/978-1-4842-2845-6_3

Lee, H-J., Park, D-Y., Ahn, B-S., Deung-Yong Park, Y-M., Park, J-K., Bok-Shin Ahn, S. S., et al. (2000). A Fuzzy Expert System for the Integrated Fault Diagnosis. *IEEE Trans. Power Deliv.* 15 (2), 833–838. doi:10.1109/61.853027

Li, J., Yang, Q., Mu, H., Le Blond, S., and He, H. (2018). A New Fault Detection and Fault Location Method for Multi-Terminal High Voltage Direct Current of Offshore Wind Farm. *Appl. Energ.* 220, 13–20. doi:10.1016/j.apenergy.2018.03.044

Li, J., Li, Y., Xiong, L., Jia, K., and Song, G. (2020). DC Fault Analysis and Transient Average Current Based Fault Detection for Radial MTDC System. *IEEE Trans. Power Deliv.* 35 (3), 1310–1320. doi:10.1109/tpwrd.2019.2941054

Li, Y., Zhang, S., Li, H., Zhai, Y., Zhang, W., and Nie, Y. (2012). A Fault Location Method Based on Genetic Algorithm for High-Voltage Direct Current Transmission Line. *Euro. Trans. Electr. Power* 22 (6), 866–878. doi:10.1002/etep.1659

Liang, J., Jing, T., Niu, H., and Wang, J. (2020). Two-Terminal Fault Location Method of Distribution Network Based on Adaptive Convolution Neural Network. *IEEE Access* 8, 54035–54043. doi:10.1109/access.2020.2980573

Lin, Q., Luo, G., and He, J. (20172017). Travelling-wave-based Method for Fault Location in Multi-terminal DC Networks. *J. Eng.* 2017 (13), 2314–2318. doi:10.1049/joe.2017.0744

Liu, H., Deng, Z., Li, X., Guo, L., Huang, D., Fu, S., et al. (2020). Oct.) the Averaged-Value Model of Flexible Power Electronics Substation in Hybrid AC/DC Distribution Systems. [Online]. Available: https://ieeexplore.ieee.org/document/9215150.

Mallat, S. G. (1989). A Theory for Multiresolution Signal Decomposition: the Wavelet Representation. *IEEE Trans. Pattern Anal. Machine Intelligence* 11 (7), 674–693. doi:10.1109/34.192463

Mohanty, R., Balaji, U. S. M., and Pradhan, A. K. (2016). "An Accurate Non-iterative Fault Location Technique for Low Voltage DC Microgrid," " in Proceedings of 2016 IEEE Power and Energy Society General Meeting (PESGM) (Boston, MA, USA, 1. doi:10.1109/pesgm.2016.7741136

Mohsenian-Rad, H., and Davoudi, A. (2014). Towards Building an Optimal Demand Response Framework for DC Distribution Networks. *IEEE Trans. Smart Grid* 5 (5), 2626–2634. doi:10.1109/tsg.2014.2308514

Tang, L., Dong, X., Shi, S., and Qiu, Y. (2019). A High-Speed protection Scheme for the DC Transmission Line of a MMC-HVDC Grid. *Electric Power Syst. Res.* 168, 81–91. doi:10.1016/j.epsr.2018.11.008

Tawfik, M. M., and Morcos, M. M. (2005). On the Use of Prony Method to Locate Faults in Loop Systems by Utilizing Modal Parameters of Fault Current. *IEEE Trans. Power Deliv.* 20 (1), 532–534. doi:10.1109/tpwrd.2004.839739

Wang, C., Jia, K., Bi, T., Xuan, Z., and Zhu, R. (2019). Transient Current Curvature Based protection for Multi-terminal Flexible DC Distribution Systems. *IET Generation, Transm. Distribution* 13 (15), 3484–3492. doi:10.1049/iet-gtd.2018.5152

Yan, X., CShu, C., and Yanjing, X. (2020). "Fault Location Method for DC Distribution Network Based on Impedance Parameters Identification," in Proceedings of 2020 IEEE 3rd International Conference on Electronics Technology (ICET) (Chengdu, China, 378–381. doi:10.1109/icet49382.2020.9119551

Ye, X., Lan, S., Xiao, S-J., and Yuan, Y. (2020). Single Pole-to-Ground Fault Location Method for MMC-HVDC System Using Wavelet Decomposition and DBN. *IEEJ Trans. Electr. Electron. Eng.* 16 (2), 238–247. doi:10.1002/tee.23290

Yuan, Y., Kang, X., and Li, X. (2020). "A Fault Location Algorithm for DC Distribution Network Based on Transient Fault Components," in Proceedings of 2020 5th Asia Conference on Power and Electrical Engineering (ACPEE) (Chengdu, China, 1316–1320. doi:10.1109/acpee48638.2020.9136507

Zhao, S., Liu, Y., Han, Y., Hong, R., Hu, Q., and Tian, Q. (2018). Pooling the Convolutional Layers in Deep ConvNets for Video Action Recognition. *IEEE Trans. Circuits Syst. Video Tech.* 28 (8), 1839–1849. doi:10.1109/tcsvt.2017.2682196

Zheng, X., Nadeem, M. H., Tai, N., Habib, S., Wang, B., Yu, M., et al. (2021). A Transient Current protection and Fault Location Scheme for MMC-HVDC Transmission Network. *Int. J. Electr. Power Energ. Syst.* 124, 1–9. doi:10.1016/j.ijepes.2020.106348

Conflict of Interest: The authors declare that the research was conducted in the absence of any commercial or financial relationships that could be construed as a potential conflict of interest.

frontiers
in Energy Research

METHODS
published: 05 January 2022
doi: 10.3389/fenrg.2021.811845

Harmonic Analysis and Neutral-Point Potential Control of Interleaved Parallel Three-Level Inverters for Flywheel Energy Storage System

*Zhongrui Li, Ziling Nie, Jie Xu, Huayu Li and Sheng Ai**

National Key Laboratory of Science and Technology on Vessel Integrated Power System, Naval University of Engineering, Wuhan, China

Flywheel energy storage system is a popular energy storage technology, in which inverters are the center of electrical energy conversion, directly affecting the power capacity. Parallel operation of three-level inverters is an effective approach to achieve larger motor drive power and the interleaved operation can improve the harmonic characteristics. However, harmonic analysis models of the interleaved parallel three-level inverters are rare in the literature and how the neutral-point potential imbalance affects the harmonics characteristics has not been discussed. This article establishes the harmonic calculation for balanced and unbalanced neutral-point potential through the five-level voltage capability of the interleaved parallel three-level inverters. Moreover, a neutral-point potential control method based on zero-sequence voltage injection is proposed. The implement process of the method is proposed, and how the operating frequency affect the ability of the neutral-point potential balance is studied. Finally, the simulation and experiment results verify the feasibility and practicability of the established harmonic analysis models and the neutral-point potential control method.

Keywords: flywheel energy storage system, parallel operation, three-level inverter, interleaved, harmonic analysis, neutral-point potential control, zero-sequence voltage injection

Edited by:
Liansong Xiong,
Nanjing Institute of Technology (NJIT),
China

Reviewed by:
Ze Li,
Hebei University, China
Ning Li,
Xi'an University of Technology, China

****Correspondence:***
Sheng Ai
ai__sheng@163.com

Specialty section:
This article was submitted to
Process and Energy Systems
Engineering,
a section of the journal
Frontiers in Energy Research

Received: *09 November 2021*
Accepted: *06 December 2021*
Published: *05 January 2022*

Citation:
Li Z, Nie Z, Xu J, Li H and Ai S (2022)
Harmonic Analysis and Neutral-Point
Potential Control of Interleaved Parallel
Three-Level Inverters for Flywheel
Energy Storage System.
Front. Energy Res. 9:811845.
doi: 10.3389/fenrg.2021.811845

INTRODUCTION

Flywheel energy storage system (FESS) is a sustainable and environmentally friendly energy storage system for the efficient and safe utilization of intermittent renewable energy (Mir and Senroy, 2018; Rafi and Bauman, 2021). FESS completes the mutual conversion of electrical energy into mechanical energy, stores energy as kinetic energy and generates no pollution, which mainly has the advantages of high power density, short charging and discharging time, high energy conversion efficiency, low maintenance cost, long service life (Zhang and Yang, 2017; Zhang and Yang, 2018; Ghanaatian and Lotfifard, 2019; Ho et al., 2019). Benefiting from these advantages, FESS is currently an indispensable energy storage method in modern power systems.

In the flywheel energy storage system, the power converters are the center of electrical energy conversion. The electrical machine used in the system has large rotational mass, high speed, and low loss (Gengji and Ping, 2016). However, traditional two-level inverters cannot meet the requirement of voltage level and harmonic content. Compared with two-level inverters, three-level inverters (TLIs) have the merits of low voltage stress, low harmonic content and high power rating (Nabae et al., 1981; Gao et al., 2021; Zhang et al., 2021). Moreover, parallel operation of TLIs can achieve larger current capacity (Jiang et al., 2021). The parallel operation can be classified into synchronous operation and interleaved operation. The two inverters receive synchronous switching signals in the synchronous operation while asynchronous switching signals in the interleaved operation.

Pulse width modulation (PWM) inevitably produces undesired harmonics. Industrial applications such as motor drive require total harmonic distortion (THD) within the specified range (generally less than 5%). When the synchronous operation is used, the current capacity of parallel TLIs can increase but the harmonic characteristics cannot be improved. The interleaved operation can improve the current distortion and increase the waveform quality. Identification of harmonics for parallel TLIs in the interleaved operation is essential to improve the harmonic characteristics of the motor speed regulation system. Double Fourier integral can establish an accurate analytical model of harmonics through strict mathematical derivation, which is an intuitive and effective method for harmonic analysis. The harmonics of TLIs for carrier-based PWM have been calculated (Mazzucchelli et al., 1981; Holmes and Lipo, 2003; Dolguntseva et al., 2015). Besides, the harmonic analysis model of TLIs with popular space vector-based PWM is discussed (Chen et al., 2020). For interleaved parallel two-level inverters, the analysis of harmonics is illustrated (Zhang et al., 2011). However, little literature is found on the interleaved parallel three-level inverter harmonic analysis model.

In addition, the interleaved parallel three-level inverters have both inherent problems of neutral-point potential control and circulating current suppression. Undesirable characteristics of capacitors and loads, as well as inherent defects of the control algorithm, result in unbalanced capacitor voltages (Stala, 2013; Liu et al., 2021; Dargahi et al., 2022). The imbalance increases the harmonic contents, reduces the device life and affects the system operation. Based on space vector PWM, the control of neutral-point potential is realized by adjusting the vector action time, but complex sector division and duty ratio calculation are inevitable (Yamanaka et al., 2002; Jiang et al., 2020). Zero-sequence voltage injection (ZSVI) is a commonly used neutral-point potential control method for TLIs with carrier-based PWM, which maintains the balance by injecting specific zero sequence components into three-phase modulation waves and has the merits of simplicity, utility and easy implement (Tallam et al., 2005; Song et al., 2013; Xing et al., 2020). The neutral-point potential control algorithms based on ZSVI for TLIs have been proposed (Wang and Li, 2010; Chaturvedi et al., 2014; Chen et al., 2018; Wan et al., 2021), but the interleaved operation of inverters is not considered.

Moreover, the interleaved operation can improve current distortion, but high-frequency circulating current unavoidably occurs due to inconsistencies of two parallel inverters. Therefore, different circulating current suppression methods for parallel three-level inverters have been proposed in literature. From the perspective of control (Liu et al., 2021; Xing and Chen, 2021) and modulation (Zhang et al., 2019; Tcai et al., 2021), the circulating current is suppressed. In the flywheel energy storage system, the parallel circuit series filter inductors, which can effectively suppress circulating current but also decrease the system power factor, especially when the system operates at a higher frequency. The way of the ZSVI for high operating frequency and low operating frequency is different.

This article is organized as follows. *Parallel Three-Level Inverters Model* develops the basic model of parallel TLIs and the mechanism of neutral-point potential imbalance. A novel perspective of harmonic analysis for interleaved parallel TLIs under balanced and unbalanced neutral-point potential is discussed in *Harmonic Analysis of the Interleaved Operation*, which considers the five-level capability of the output voltage. A neutral-point potential control algorithm is analyzed in *Neutral-Point Potential Control*. The model of average neutral current is derived by using the equivalent duty ratio calculation thus the calculation method of zero sequence voltage is introduced. The implementation of the ZSVI method at low operating frequency is analyzed, while the problem and improvement for high operating frequency is proposed. *Simulation and Experimentation* shows and compares the simulation and experimental results, verified the validity of theoretical analysis. Finally, the conclusion is summarized in *Conclusion*.

PARALLEL THREE-LEVEL INVERTERS MODEL

Topology and Modulation Strategy

The topology of the parallel TLI system is shown in **Figure 1A**. Two TLIs called TLI-1 and TLI-2, share the common neutral point (O) of the capacitors (C_1 and C_2) and the DC bus ($U_{\mathrm{dc}} = 2E$). Each phase leg of two parallel TLIs is connected through a filter inductance L_{xk} ($x = a$, b, c; $k = 1, 2$), while the output is connected to a flywheel motor. The principle of interleaved parallel PWM is shown in **Figure 1B**. Both TLI-1 and TLI-2 are modulated by carrier phase disposition PWM. The modulation waves of two TLIs are the same while the carriers are interleaved, and phase shifted by π. The carriers of TLI-1 are $v_{\mathrm{c1\text{-}1}}$ and $v_{\mathrm{c1\text{-}2}}$, while the carriers of TLI-2 are $v_{\mathrm{c2\text{-}1}}$ and $v_{\mathrm{c2\text{-}2}}$. The modulation wave v_{r} is compared with the four carriers to generate the switching signal of the parallel TLI system.

Considering O as the reference point, x phase voltage of TLI-k can be expressed as

$$\boldsymbol{U_{xkO} = S_{xk} \cdot E} \tag{1}$$

where S_{xk} ($x = a$,b,c; $k = 1$,2) is x phase switching signal of TIL-k inverter, and E is the voltage level. While S_{xk} has three possible values (S_{xk} = -1, 0, 1), $U_{xk\mathrm{O}}$ can have three voltage levels from **(2)**, and it is possible for $U_{x\mathrm{O}}$, the x phase voltage of the system, to obtain five voltage levels. The waveforms of $U_{xk\mathrm{O}}$ and $U_{x\mathrm{O}}$ is shown in **Figure 1B**.

Although parallel legs of the system use the same modulation wave, the switching pulses is asynchronous because of the different carriers, leading to unequal instantaneous values of leg output voltages. Then, according to Kirchhoff's law, the voltage equation of the parallel circuit can be expressed as

$$\boldsymbol{U_{xkO} = L\frac{di_{xk}}{dt} + U_{xO}} \tag{2}$$

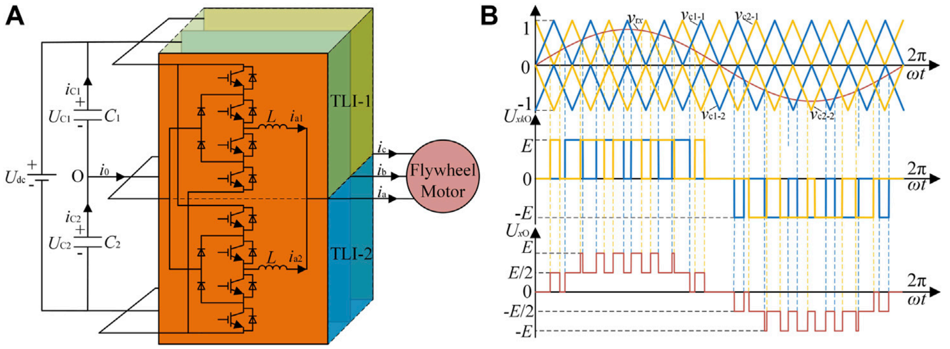

FIGURE 1 | Topology and modulation of the parallel system: **(A)** topology, **(B)** interleaved parallel PWM.

where L is the inductance value of L_{xk}, and i_{xk} is the x phase current of TIL-k.

From **(1) (2)**, owing to the asynchronous switching pulses, the circulating current $i_{\mathrm{h}x}$ of x phase inevitably emerges, which can be expressed as

$$\frac{di_{hx}}{dt} = \frac{(S_{x1} - S_{x2})E}{2L} \tag{3}$$

In order to suppress circulating current, improving the stability of the parallel TLI system, the parallel circuit series filter inductors. Ignoring the magnetic saturation of the filter inductors, the inductive resistance in the AC circuit is proportional to the angular frequency of the current passing through the inductors. Therefore, although filter inductors can effectively suppress circulating current, the system inductive resistance increases, reducing the power factor when operating at high frequency.

Mechanism of Neutral-Point Potential Imbalance

The essential reason for the neutral-point potential imbalance is that the flow of the neutral current causes the neutral voltage to fluctuate. Assume that the reference direction of the neutral current is positive when it flows out of the neutral point, as shown in **Figure 1A**. According to Kirchhoff's law, the relationship between neutral current and capacitor currents and the relationship between neutral voltage and capacitor voltages can be expressed as

$$i_0(t) = i_{C1}(t) - i_{C2}(t) \tag{4}$$

$$u_0(t) = \frac{u_{C2}(t) - u_{C1}(t)}{2} \tag{5}$$

From **(4) (5)**, the relationship between the neutral voltage and the neutral current can be expressed as

$$u_0(t) = -\frac{1}{2C}\int_0^t i_0(t)d\tau + U_0 \tag{6}$$

where C is the capacitor value and U_0 is the steady-state error of the neutral-point potential.

Then, during a switching period T_s, (6) can be expressed as

$$u_{0\_\mathrm{average}} = -\frac{1}{2C} i_{0\_\mathrm{average}} T_s + U_0 \tag{7}$$

where $u_{0\_\ \mathrm{average}}$ and $i_{0\_\ \mathrm{average}}$ are the averages of $u_0(t)$ and $i_0(t)$ during a switching period, respectively.

From **(7)**, the neutral-point potential can be balanced by eliminating the DC offset of the capacitor voltages and controlling the average neutral current $i_{0\_\ \mathrm{average}}$ to 0.

HARMONIC ANALYSIS OF THE INTERLEAVED OPERATION

Harmonic Characteristic

In the flywheel energy storage system, the output harmonics of the inverter generate the motor stator harmonics, which directly affect the motor harmonic losses, and then affect the stable operation of the system. Therefore, this paper regards the parallel TLIs as an integrated system to analyze its harmonic characteristic.

From Double Fourier Transform theory, the spectrum of the system switched phase output voltage can be expressed as (Holmes and Lipo, 2003)

$$\begin{aligned} f(t) = \frac{A_{00}}{2} + \sum\nolimits_{n=1}^{\infty} A_{0n}\cos(ny) + \sum\nolimits_{m=1}^{\infty} A_{m0}\cos(mx) \\ + \sum\nolimits_{m=1}^{\infty} \sum\nolimits_{\substack{n=-\infty \\ (n \neq 0)}}^{\infty} A_{mn}\cos(mx + ny) \end{aligned} \tag{8}$$

$$A_{mn} = \frac{1}{2\pi^2}\int_{-\pi}^{\pi}\int_{-\pi}^{\pi} f(x,y)\cos(mx+ny)dxdy, x = \omega_c t, y = \omega_o t \tag{9}$$

where m and n are the index variables of carrier and baseband, ω_r and ω_o are the carrier angular frequency and the fundamental angular frequency, respectively.

The harmonic characteristic of the parallel TLI system in the synchronous operation is the same as a single TLI, so it is unnecessary to repeat it. Moreover, for harmonic analysis of the interleaved operation, the per unit of the carrier frequency is used to simplify the analysis. The carrier waves of TLI-1 and TLI-2 in a switching period are shown in **Figure 2A**, while the

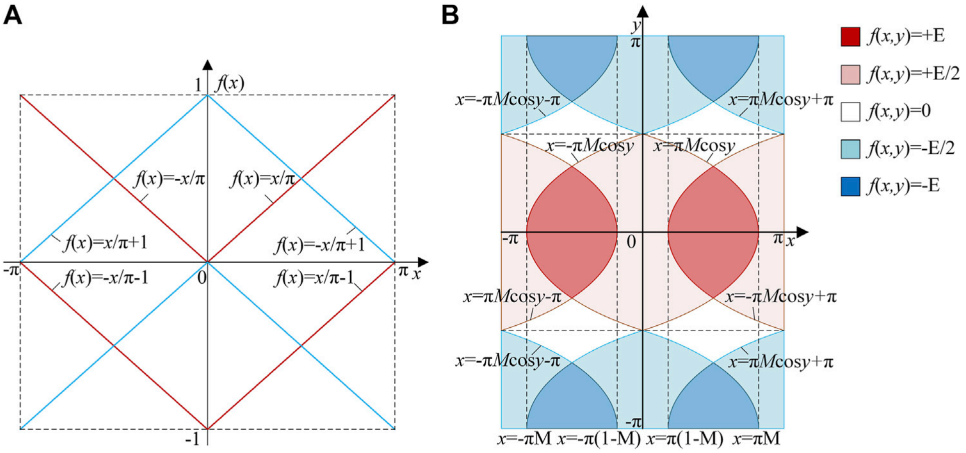

FIGURE 2 | Harmonic analysis of interleaved parallel PWM: **(A)** carrier waves, **(B)** the unit cell.

modulation wave expression in the switching period is *f*(*y*) = *M*cos*y*, where *M* is the modulation ratio. A direct comparison between the amplitudes of the carrier waves and the modulation wave is used to determine the distribution region of the switching function *f*(*t*), which is shown in the unit cell **Figure 2B**.

The distribution of the switching function is related to the modulation ratio *M*, for instance, the value of *M* determines that the regions of voltage level + *E* and -*E* exist or not in the unit cell. In fact, the output voltage is able to obtain five levels when $M > 0.5$, and the harmonic content is less because the non-zero levels of TLI-1 and TLI-2 tend to be synchronous. In the switching period, the moments when the leg output non-zero voltages of TLI-1 and TLI-2 is the same increase with *M*, as well as the number of synchronous switching pulses. However, when $M \le 0.5$, the output voltage can only obtain three levels and the non-zero levels of TLI-1 and TLI-2 are asynchronous, hence, the harmonic content is larger. Actually, the number of synchronous switching pulses is zero in the switching period, thus there is no moments when the leg output non-zero voltages of TLI-1 and TLI-2 is the same.

When the integral limits are determined, the harmonic characteristic of different modulation ratios in the interleaved operation is calculated as follows

$$\begin{aligned} U_o = {} & EM\cos\omega_o t \\ & + \frac{2E}{\pi}\sum_{m=1}^{\infty}\frac{1}{2m}\sum_{n=-\infty}^{\infty}J_{2n+1}(2m\pi M)\cos(n\pi)\cos[2m\omega_c t \\ & + (2n+1)\omega_o t] \end{aligned} \tag{10}$$

where *Jn* (.) is the n-order Bessel function. A significant feature of the phase voltage U_o in the interleaved operation is only composed of the fundamental component and even carrier frequency with odd fundamental frequency sideband harmonic components. The fundamental component is identical to the synchronous operation, while the harmonic components is different. Also, the amplitude of the fundamental waveform is related to the modulation ratio *M* and DC voltage, while the amplitudes of harmonics are determined by Bessel functions when certain modulation ratio *M* and DC voltage are chosen. Further, the harmonics of the phase voltage U_o in interleaved operation have following characteristics:

1) When *m* is an odd number, partial harmonic components of TLI-1 and TLI-2 are offset, and there is no odd carrier harmonic components or odd carrier frequency with even fundamental frequency sideband harmonic components in the parallel system output voltage, compared with the synchronous operation.
2) When *m* is 0, the fundamental component of the parallel system output voltage is the same as the synchronous operation, and there is no DC component or baseband harmonic components.
3) When *m* is a non-zero even number, the harmonic components of the parallel system output voltage are in common with synchronous operation, containing even carrier frequency with odd fundamental frequency sideband harmonics.

The interleaved operation does not affect the fundamental waveform of the parallel system but can eliminate odd carrier harmonics and odd carrier frequency with even fundamental frequency sideband harmonics, compared with the synchronous operation, therefore, the system output voltage harmonic content is lower.

Harmonic Characteristic Under Unbalanced Neutral-Point Potential.

For harmonic analysis of the interleaved parallel TLI system when DC offset inevitably emerges in neutral-point potential, the distribution regions of the switching function are unchanged, but the values in the regions, also called the leg output levels are different in the unit cell.

In the interleaved operation, the possible values of the parallel TLI system output levels are + $E + E_0$ $(+E + E_0)/2$, 0, $(-E + E_0)/2$, $-E + E_0$, where E_0 is the DC offset. Hence, the Fourier series

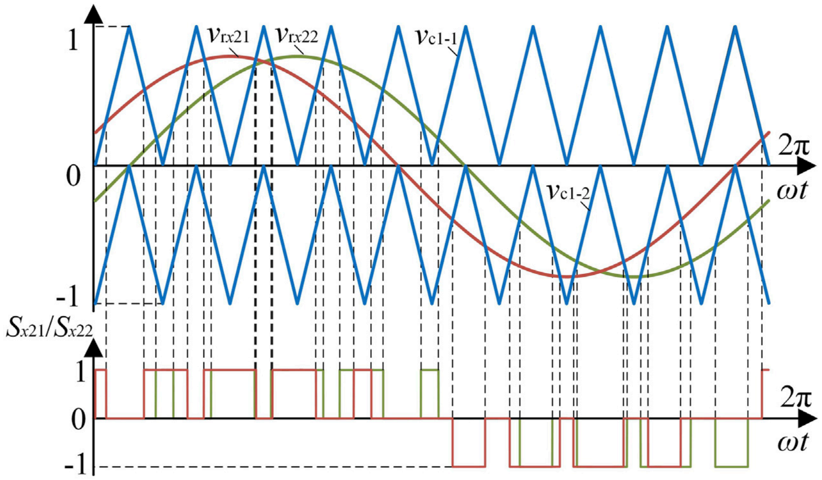

FIGURE 3 | Diagram of the equivalent duty ratio calculation.

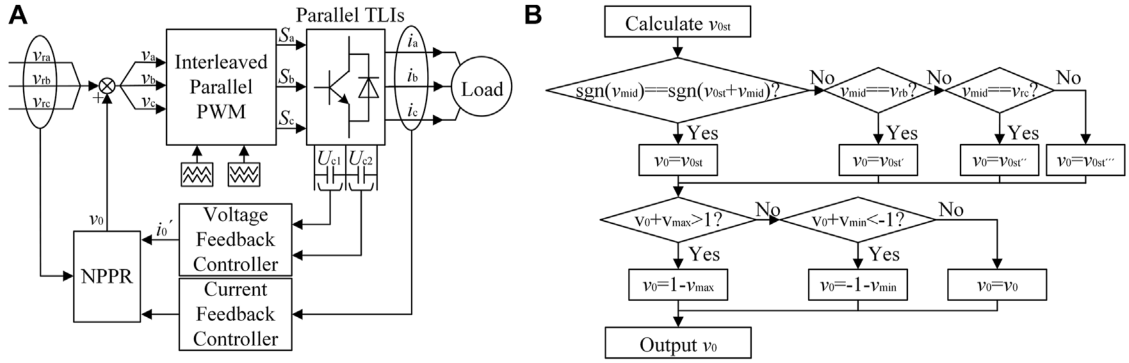

FIGURE 4 | Implementation of ZSVI: **(A)** block diagram, **(B)** flowchart of NPPR.

expression of the output voltage for the parallel TLI system is calculated as follows

$$\begin{aligned}U_o = {} & \frac{2ME_0}{\pi} + EM\cos(\omega_o t) \\ & + \frac{4ME_0}{\pi}\sum_{n=1}^{\infty}\frac{\cos(n\pi)}{(1-2n)(1+2n)}\cos[2n(\omega_0 t)] \\ & + \frac{2E}{\pi}\sum_{m=1}^{\infty}\frac{1}{2m}\sum_{n=-\infty}^{\infty}J_{2n+1}(2m\pi M)\cos(n\pi)\cos[2m\omega_c t \\ & + (2n+1)\omega_o t] \\ & + \frac{8E_0}{\pi^2}\sum_{m=1}^{\infty}\frac{1}{2m}\sum_{n=-\infty}^{\infty}\sum_{k=1}^{\infty}\frac{J_{2k-1}[2m\pi M](2k-1)\cos(n\pi)}{(2k-1+2n)(2k-1-2n)} \\ & \cos[2m\omega_c t + 2n\omega_0 t]\end{aligned} \tag{11}$$

In the interleaved operation, the imbalance of neutral-point potential leads to DC bias and harmonics of even baseband component and even carrier frequency with even fundamental frequency sideband component. Furthermore, the amplitude of the DC bias is related to M and E_0, as well as the amplitudes of additional harmonics which is also related to Bessel functions. An obvious merit of the interleaved operation is odd carrier harmonics and odd carrier frequency sideband harmonics are eliminated whether the neutral-point potential is balanced or not.

NEUTRAL-POINT POTENTIAL CONTROL

Zero-Sequence Voltage Injection Method

Zero-sequence voltage injection method is an effective approach to achieve the neutral-point potential balance of multilevel inverters using carrier-based PWM. The method has been widely used in TLIs, achieving excellent results. However, applications on parallel TLIs, especially interleaving, have not been discussed in the literature.

The steady-state expression of the three-phase positive sequence modulation signal v_{rx} in the parallel TLI system can be written as

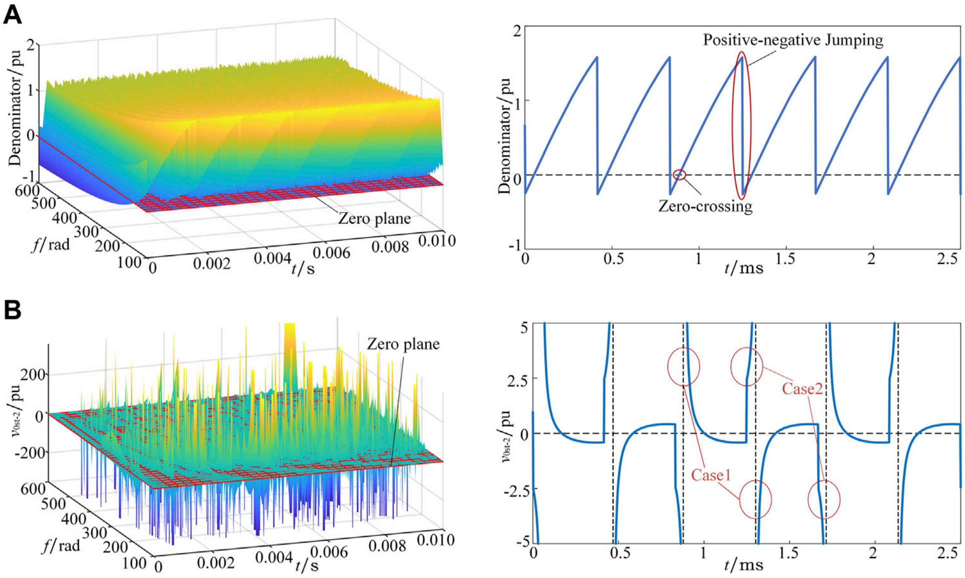

FIGURE 5 | Function surfaces and curves: **(A)** denominator, **(B)** $v_{0st\text{-}2}$.

$$\begin{bmatrix} v_{ra} \\ v_{rb} \\ v_{rc} \end{bmatrix} = \begin{bmatrix} M\cdot\cos\omega_o t \\ M\cdot\cos(\omega_o t - 2\pi/3) \\ M\cdot\cos(\omega_o t + 2\pi/3) \end{bmatrix} \tag{12}$$

Define the x phase duty ratio of TIL-k inverter as d_{xk}. Based on the model analysis in Section 2.1, it can be seen that carriers of the parallel legs for TLI-1 and TLI-2 in the interleaved operation are different, therefore, the duty ratios d_{x1} and d_{x2} are not equal, which causes the three-phase positive sequence modulation signal v_{rx} cannot be directly equivalent to the duty ratio d_{x1} and d_{x2} using the impulse equivalent principle. To this end, this paper proposes an equivalent duty ratio calculation method. Based on the carrier and modulation wave of TLI-1, TLI-2 is equivalent to be modulated by carriers the same as the TLI-1 carriers and two modulation waves phase shift by a certain angle, as shown in **Figure 3**. The modulation wave v_{rx21} phase shifts forward $\omega_0 T_s/2$ while the modulation wave v_{rx22} phase shifts backward $\omega_0 T_s/2$, compared with v_{rx}. Consequently, the impulse equivalent principle can be applied to calculate d_{x1} and d_{x2}.

Hence, the duty ratio d_{x1} of TLI-1 is equivalent to v_{rx}, while the duty ratio d_{x2} of TLI-2 can be approximately calculated in the following way

$$d_{x2} = \frac{v_{rx21} + v_{rx22}}{2} = \cos\left(\frac{\omega_o T_s}{2}\right)\cdot v_{rx} \tag{13}$$

When a certain phase leg is clamped at the neutral point, this phase current flows through its corresponding clamp diode into the neutral point. Considering the existence of circulating current, the instantaneous neutral current $i_0(t)$ can be expressed as

$$i_0(t) = -\sum_{x=a,b,c}\left(\text{abs}(S_{x1}) + \text{abs}(S_{x2})\right)\frac{i_x}{2} - \sum_{x=a,b,c}\left(\text{abs}(S_{x1}) - \text{abs}(S_{x2})\right)i_{hx} \tag{14}$$

where abs (.) is the absolute value function, and i_x is x-phase load current of the parallel TLI system.

From **(13) (14)**, the mathematical model of the average neutral current during a switching period is given by

$$i_{0\_average} = -\sum_{x=a,b,c}\text{abs}(v_x)\left(\frac{i_x}{2}\left(1+\cos\left(\frac{\omega_o T_s}{2}\right)\right) + i_{hx}\left(1 - \cos\left(\frac{\omega_o T_s}{2}\right)\right)\right) \tag{15}$$

where v_x is the actual three-phase modulation signal. From section 1.2, the balance control of the neutral-point potential is to keep the average neutral current at 0 while eliminate the DC offset of capacitor voltages. Based on the mathematical model of the average neutral current, a control degree of freedom must be introduced to ensure the average neutral current is 0. The control degree of freedom is the zero-sequence voltage v_0.

From **(15)**, the mathematical expression of the zero-sequence voltage v_0 is calculated as

$$v_0 = -\frac{\sum_{x=a,b,c}\text{sign}(v_x)v_{rx}\left(\frac{i_x}{2}\left(1+\cos\left(\frac{\omega_o T_s}{2}\right)\right) + i_{hx}\left(1-\cos\left(\frac{\omega_o T_s}{2}\right)\right)\right)}{\sum_{x=a,b,c}\text{sign}(v_x)\left(\frac{i_x}{2}\left(1+\cos\left(\frac{\omega_o T_s}{2}\right)\right) + i_{hx}\left(1-\cos\left(\frac{\omega_o T_s}{2}\right)\right)\right)} \tag{16}$$

where sign (.) is the symbol function.

Since it is not possible to determine the symbol of the three-phase modulation signal v_x, the three-phase positive sequence modulation

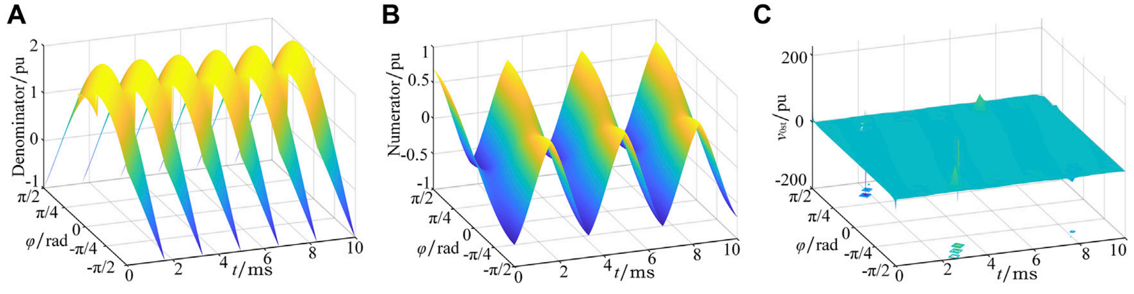

FIGURE 6 | Function surfaces at different power factors: (A) denominator, (B) numerator, (C) $v_{0st\text{-}2}$.

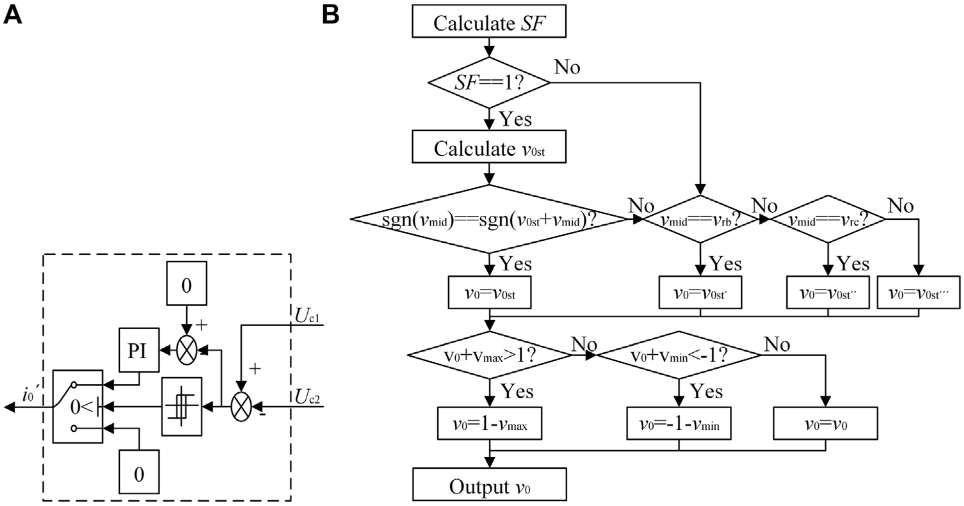

FIGURE 7 | Improved ZSVI: (A) improved voltage feedback controller, (B) improved NPPR algorithm.

signal v_{rx} is generally used to estimate zero sequence voltage. The estimated value of zero sequence voltage is calculated as (17), which is used to control the neutral-point potential. (17) indicates that v_{0st} can be decoupled into two control objectives: voltage feedback control $v_{0st\text{-}1}$ and current feedback control $v_{0st\text{-}2}$. Firstly, the elimination of the DC offset between capacitor voltages is realized by voltage feedback control $v_{0st\text{-}1}$. Then, the variation of the average neutral current is controlled to 0 by current feedback control $v_{0st\text{-}2}$, maintaining the neutral-point potential balanced.

$$\begin{aligned} v_{0st} = {} & \frac{-i'_0}{\sum_{x=a,b,c} sgn(v_{rx})\left(\frac{i_x}{2}\left(1+\cos\left(\frac{\omega_o T_s}{2}\right)\right)+i_{hx}\left(1-\cos\left(\frac{\omega_o T_s}{2}\right)\right)\right)\Big/ v_{0st-1}} \\ & - \frac{\sum_{x=a,b,c} sgn(v_{rx}) v_{rx}\left(\frac{i_x}{2}\left(1+\cos\left(\frac{\omega_o T_s}{2}\right)\right)+i_{hx}\left(1-\cos\left(\frac{\omega_o T_s}{2}\right)\right)\right)}{\sum_{x=a,b,c} sgn(v_{rx}) v_{rx}\left(\frac{i_x}{2}\left(1+\cos\left(\frac{\omega_o T_s}{2}\right)\right)+i_{hx}\left(1-\cos\left(\frac{\omega_o T_s}{2}\right)\right)\right)\Big/ v_{0st-2}} \end{aligned} \tag{17}$$

where i_0' is the capacitor voltage feedback controller output value.

Implementation and Problem

Figure 4A is the block diagram of the interleaved parallel TLI system, the center of which is the Neutral Point Potential Regulator (NPPR) based on the zero-sequence voltage injection method. The flowchart of the NPPR algorithm is shown in **Figure 4B** v_{max}, v_{mid} and v_{min} are the maximum value, the middle value and the minimum value of the three-phase positive sequence modulation signal v_{rx}, respectively.

The voltage feedback controller is a PI controller. Obviously, $v_{0st\text{-}1}$ is obtained by the voltage feedback controller, while $v_{0st\text{-}2}$ is obtained by the current feedback controller.

In fact, v_{0st} is not necessarily the final injected zero sequence voltage and needs to be verified. The v_{0st} that cannot satisfy the verification condition should be revised. There are three possible correction values for v_{0st}, calculated as follows:

1) $v_{mid} = v_{ra}$

$$v_{0st'} = -\frac{i_0^* - sgn(v_{ra}) \cdot v_{ra} \cdot i_a + sgn(v_{rb}) \cdot v_{rb} \cdot i_b + sgn(v_{rc}) \cdot v_{rc} \cdot i_c}{-sgn(v_{ra}) \cdot i_a + sgn(v_{rb}) \cdot i_b + sgn(v_{rc}) \cdot i_c} \tag{18}$$

2) $v_{mid} = v_{rb}$

$$v_{0st''} = -\frac{i_0^* + sgn(v_{ra}) \cdot v_{ra} \cdot i_a - sgn(v_{rb}) \cdot v_{rb} \cdot i_b + sgn(v_{rc}) \cdot v_{rc} \cdot i_c}{sgn(v_{ra}) \cdot i_a - sgn(v_{rb}) \cdot i_b + sgn(v_{rc}) \cdot i_c} \tag{19}$$

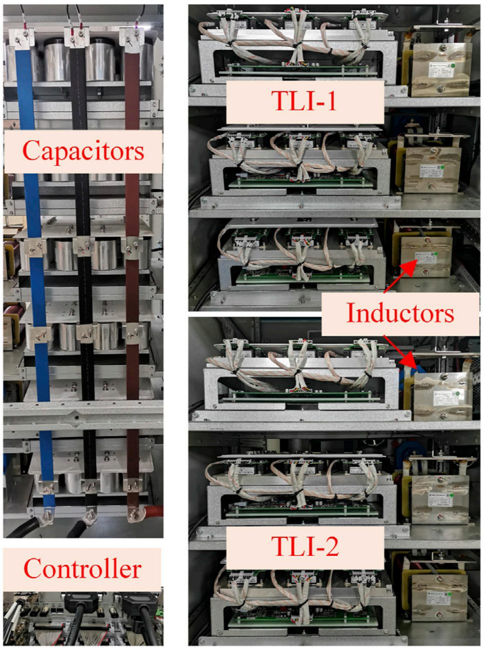

FIGURE 8 | Experiment platform.

3) $v_{\text{mid}} = v_{\text{rc}}$

$$\mathrm{v}_{0\text{st}'''} = -\frac{\boldsymbol{i}_0^* + \boldsymbol{sgn}(\boldsymbol{v}_{\text{ra}}) \cdot \boldsymbol{v}_{ra} \cdot \boldsymbol{i}_a + \boldsymbol{sgn}(\boldsymbol{v}_{\text{rb}}) \cdot \boldsymbol{v}_{\text{rb}} \cdot \boldsymbol{i}_b - \boldsymbol{sgn}(\boldsymbol{v}_{\text{rc}}) \cdot \boldsymbol{v}_{\text{rc}} \cdot \boldsymbol{i}_c}{\boldsymbol{sgn}(\boldsymbol{v}_{\text{ra}}) \cdot \boldsymbol{i}_a + \boldsymbol{sgn}(\boldsymbol{v}_{\text{rb}}) \cdot \boldsymbol{i}_b - \boldsymbol{sgn}(\boldsymbol{v}_{\text{rc}}) \cdot \boldsymbol{i}_c} \tag{20}$$

However, in order to suppress circulating current, parallel circuit series filter inductors which causes the emergence of zero-crossing and positive-negative jumping of $v_{0\text{st}}$ denominator. **Figure 5A** shows the function surface of the variables *f* and *t*, and the function curve when *f* is 400 Hz for $v_{0\text{st}}$ denominator. As the operating frequency increases, the $v_{0\text{st}}$ denominator is going to be 0 or even negative, and the function curves gradually change from flat curves to sawtooth curves. Hence, the phenomenon of zero-crossing and positive-negative jumping is further analyzed by taking the function curve when *f* is 400 Hz as an example.

For voltage feedback control, $i_0^{'}$ is only related to the capacitor voltage difference and the controller internal parameters. The polarity of $i_0^{'}$ is constant while zero-crossing and positive-negative jumping of $v_{0\text{st}}$ denominator inevitably emerge, leading to a sudden change of the $v_{0\text{st-1}}$ polarity. Consequently, the charging and discharging ability of the parallel TLI system to the neutral-point is unbalanced, and the neutral-point potential can be completely out of control. For current feedback control, theoretically, the polarity of $v_{0\text{st-2}}$ is determined by its numerator. However, zero-crossing and positive-negative jumping of the denominator cause the polarity of $v_{0\text{st-2}}$ to be uncontrolled by its numerator, resulting in two extreme cases of $v_{0\text{st-2}}$, as shown in **Figure 5B**. It can be seen from the function surface of $v_{0\text{st-2}}$ that when the operating frequency is high, $v_{0\text{st-2}}$ reaches extreme values. Furthermore, the function curve of $v_{0\text{st-2}}$ when *f* is 400 Hz shows that extreme case 1 occurs when the denominator has a zero-crossing, thus the value of $v_{0\text{st-2}}$ is uncertain. Extreme case 2 occurs when the denominator has a positive-negative jumping, the numerator polarity remains unchanged while the $v_{0\text{st-2}}$ polarity mutates.

For the existence of filter inductors, the inductance of the parallel TLI system increases with the operating frequency, while the power factor decreases. Hence, the phase difference between the phase current and the modulation signal changes to ±π/2, which causes zero-crossing and positive-negative jumping of $v_{0\text{st-2}}$ denominator. The function surfaces of $v_{0\text{st-2}}$ denominator, $v_{0\text{st-2}}$ numerator, and $v_{0\text{st-2}}$ at different power factors are shown as **Figure 6**.

Although the aforementioned method can verify and revise $v_{0\text{st}}$, it is not possible to correct case 1 and case 2 because of the existence of filter inductors. In order to effectively control the neutral-point potential balance of the interleaved parallel TLI system, the aforementioned method must be improved.

Improvement

Figure 7A shows the voltage feedback controller of the improved method, consisting of hysteresis controller, PI controller, etc. Based on the DC offset between capacitor voltages caused by interference or other factors, hysteresis controller chooses whether to use the PI controller or not.

In order to solve the problem mentioned above, a variable called Symbol Factor (*SF*) is introduced to the NPPR. *SF* is calculated as

$$\boldsymbol{SF} = \begin{cases} \mathbf{1} & \sum_{x=\text{a,b,c}} \boldsymbol{sgn}(\boldsymbol{v}_x)\boldsymbol{i}_x > 0 \\ \mathbf{0} & \sum_{x=\text{a,b,c}} \boldsymbol{sgn}(\boldsymbol{v}_x)\boldsymbol{i}_x \le 0 \end{cases} \tag{21}$$

According to *SF*, $\mathrm{v}_{0\text{st}}$ is verified and revised, or just revised. The improved NPPR algorithm is shown as **Figure 7B**.

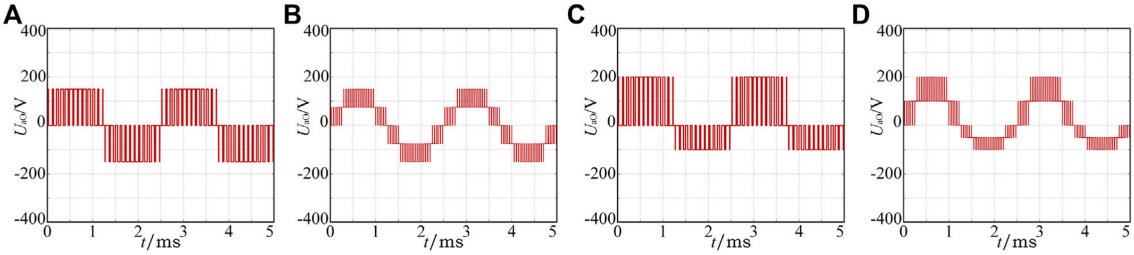

FIGURE 9 | Simulation results of phase voltage for various operation modes and conditions: **(A)** parallel, **(B)** interleaved, **(C)** unbalanced parallel, **(D)** unbalanced interleaved.

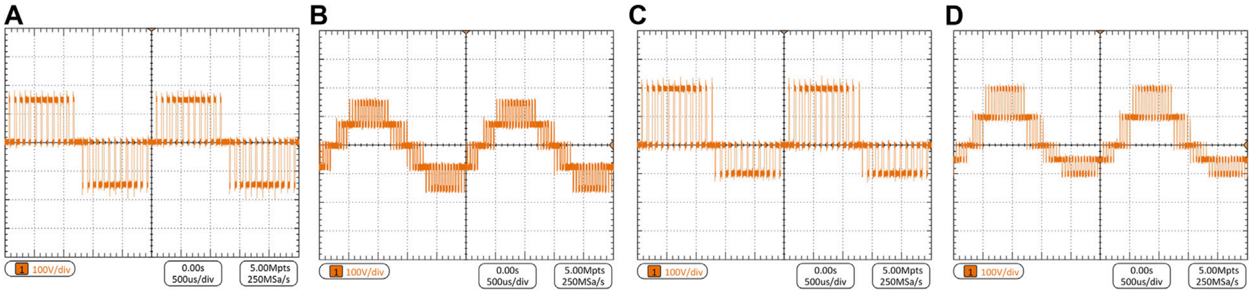

FIGURE 10 | Experiment results of phase voltage for various operation modes and conditions: **(A)** parallel, **(B)** interleaved, **(C)** unbalanced parallel, **(D)** unbalanced interleaved.

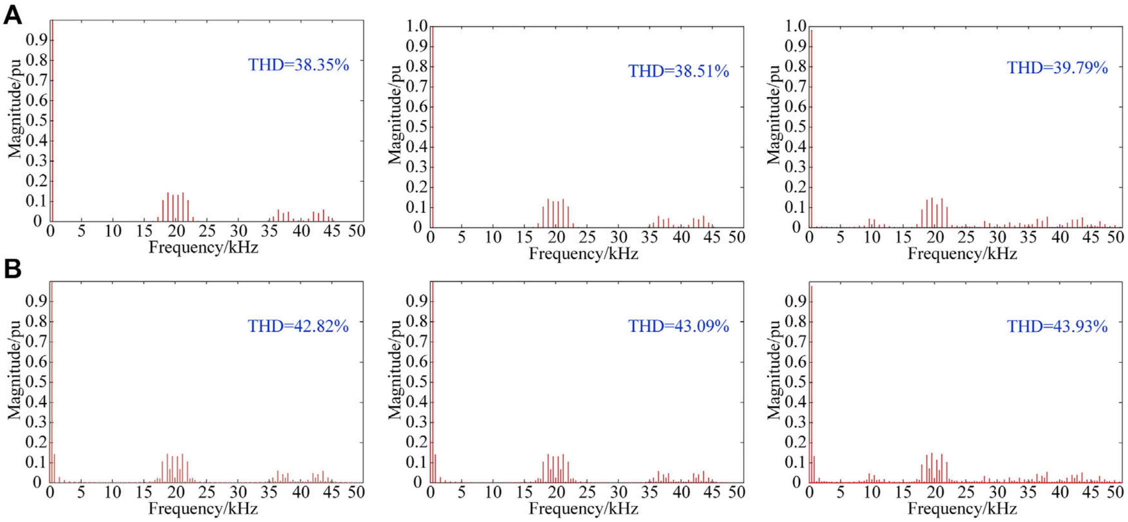

FIGURE 11 | Harmonic spectrums of phase voltage for calculation, simulation and experimentation: **(A)** balanced, **(B)** unbalanced.

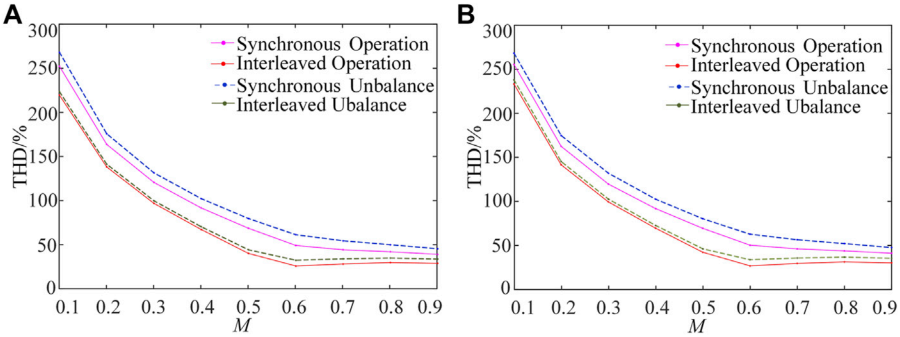

FIGURE 12 | Results of line-to-line voltage THD for different modulation ratios: **(A)** simulation, **(B)** experiment.

SIMULATION AND EXPERIMENTATION

In order to verify the feasibility of the developed harmonic models and the proposed neutral-point potential control method, a MATLAB/Simulink model of 200kW parallel TLI system is constructed. **Figure 8** shows the experimental platform. The consistent parameters are used for the simulation and the experiment, as listed in **Table 1**. In

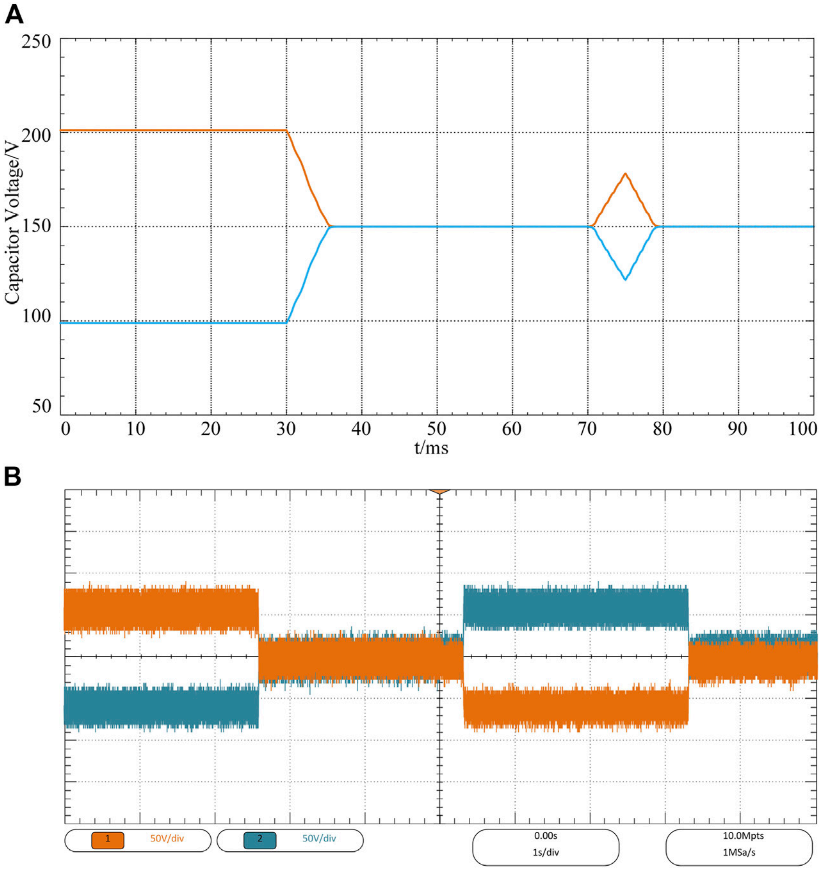

FIGURE 13 | Waveforms of capacitor voltages: **(A)** simulation, **(B)** experimentation.

addition, TMS320F28346 (DSP) and EP3C80F484I7 (FPGA) are used to implement the experiment.

Harmonic Characteristic Comparison

Figure 9 and **Figure 10** show the simulation and experimental waveforms of phase voltage for synchronous and interleaved operation under balanced and unbalanced neutral-point potential when the modulation ratio is 0.8 and the operating frequency is 400 Hz. The phase voltage waveforms for various operation modes and conditions have three and five clearly separated levels, respectively. But, there is an obvious asymmetry for the positive half wave and the negative half wave of the phase voltage when the neutral-point potential is unbalanced.

Figure 11 shows the calculated harmonic spectrum, the simulated harmonic spectrum and the experimental harmonic spectrum of phase voltage with the developed model. The main components among calculation, simulation and experimentation are compared clearly. Obviously, the simulated and experimental results match well with the calculated result. In fact, dead time will impact the harmonics amplitude, but the dead time of the developed system is small (3.5% of the switching period), thus its impact on harmonics is very small and can be neglected.

Figure 12 shows the line-to-line voltage THD with modulation ratios from 0.1 to 0.9 stepped by 0.1, when various parallel operations and neutral-point conditions are applied. It can be seen from the results that the harmonic contents of different operations and conditions are smaller when the modulation ratio is larger. The interleaved operation has remarkably reduced THD compared with the synchronous operation at every modulation ratio, regardless of whether the neutral-point potential is balanced. However, when the neutral-point potential is unbalanced, the line-to-line voltage quality is decreased while the harmonic content is increased at modulation ratios in the range of 0.1–0.9. Therefore, it is necessary to control the neutral-point potential to improve the harmonic characteristics. The experimental results are consistent with the simulation analysis.

Neutral Point Balancing Process

The neutral-point potential balancing algorithm is developed to the experiment platform to verify its feasibility and practicability. **Figures 13A,B** show the simulation and experimental waveforms of the capacitor voltage dynamic control, respectively. At the beginning, the voltage offset of the upper capacitor and the lower capacitor is 100V, and the neutral-point potential is uncontrolled thus unbalanced. The initial operating frequency of the system is 100 Hz. **Figure 13A** shows that at $t = 30$ ms, the proposed ZSVI method is enabled, the capacitor voltages are balanced quickly

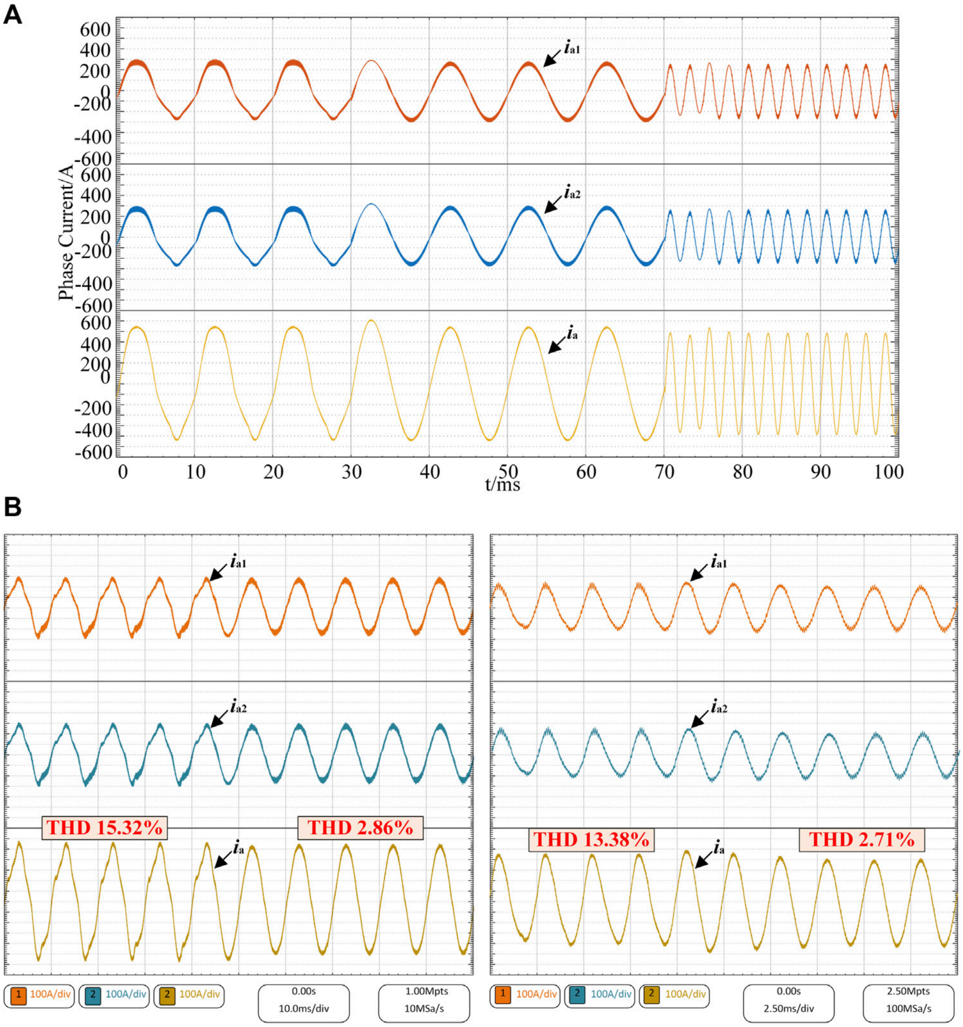

FIGURE 14 | Waveforms of phase currents: **(A)** simulation, **(B)** experimentation.

TABLE 1 | Simulation and Experiments Parameters.

Symbol	Quantity	Value
U_{dc}	DC link voltage	300
C	DC link capacitor	9.12mF
L	Inverter inductor	90 μH
f_c	Switching frequency	10 kHz
f	Fundamental frequency	400 Hz

and remain at 150 V. However, at $t = 70$ ms, the operating frequency is suddenly changed to 400 Hz, the balance is disrupted, and the voltage offset increases rapidly. To remain the balance when the operating frequency is high, the improved ZSVI method is used shortly after the frequency change, thus the capacitor voltages are controlled effectively.

Figure 13B shows the same control process, and the dynamic performance of capacitor voltages is consistent with the simulation result. The slightly different is that at about 5.4s, the capacitor voltages are out of control and the lower capacitor is 100 V higher than the upper for approximately 3s, while the frequency changes from 100 to 400 Hz. But the capacitor voltages can quickly eliminate the offset and maintain the balance because of the enablement of the improved ZSVI. The results prove the ZVI method has outstanding dynamic performance when the operating frequency is low while the improved ZVI method works more evidently when the operating frequency is high.

The simulation and experimental waveforms for a phase currents of TLI-1 (i_{a1}), TLI-2 (i_{a2}), and the output current (i_a) before and after the balancing algorithm is enabled with the corresponding process of **Figure 13** are shown in **Figure 14**. When the neutral-point potential is unbalanced, the phase currents are distorted severely. The ZVI method can restore balanced capacitor voltages and subsequently reduce the phase current distortion when the frequency is 100 Hz, while the improved ZVI method can achieve the same effect when the frequency is 400 Hz.

CONCLUSION

This article proposes the harmonic analytical model and neutral-point potential control method for interleaved parallel TLIs. First, the harmonic characteristic and calculation of interleaved parallel TLIs under balanced and unbalanced neutral-point potential are developed. The harmonic characteristics of interleaved operation is significantly better than the synchronous operation. Besides, the unbalance of the neutral-point potential can increase the harmonic content.

Second, the ZSVI method is proposed, which can be directly applied to balance the neutral-point potential at a lower operating frequency. However, when the system operates at a higher operating frequency, the ZSVI method is useless. The problem that the ZSVI method cannot be directly applied when the operating frequency is high is studied, and an improved neutral-point potential control algorithm is proposed. Simulation and experimental results demonstrate the validity of proposed models and algorithms.

DATA AVAILABILITY STATEMENT

The original contributions presented in the study are included in the article/Supplementary Material, further inquiries can be directed to the corresponding author.

AUTHOR CONTRIBUTIONS

ZL contributed for analysis of the work and wrote the first draft of the manuscript. SA is the corresponding author and takes primary responsibility. All authors contributed to manuscript revision, read and approved the submitted version.

FUNDING

This work was supported by National Natural Science Foundation of China (NSFC) under Project Numbers 52077219, 51807199.

REFERENCES

Chaturvedi, P., Jain, S., and Agarwal, P. (2014). Carrier-based Neutral point Potential Regulator with Reduced Switching Losses for Three-Level Diode-Clamped Inverter. *IEEE Trans. Ind. Electron.* 61, 613–624. doi:10.1109/TIE.2013.2254092

Chen, H.-C., Tsai, M.-J., Wang, Y.-B., and Cheng, P.-T. (2018). A Modulation Technique for Neutral point Voltage Control of the Three-Level neutral-point-clamped Converter. *IEEE Trans. Ind. Applicat.* 54, 2517–2524. doi:10.1109/TIA.2018.2799906

Chen, R., Niu, J., Gui, H., Zhang, Z., Wang, F., Tolbert, L. M., et al. (2020). Modeling, Analysis, and Reduction of Harmonics in Paralleled and Interleaved Three-Level Neutral point Clamped Inverters with Space Vector Modulation. *IEEE Trans. Power Electron.* 35, 4411–4425. doi:10.1109/TPEL.2019.2939727

Chenchen Wang, C., and Yongdong Li, Y. (2010). Analysis and Calculation of Zero-Sequence Voltage Considering Neutral-point Potential Balancing in Three-Level NPC Converters. *IEEE Trans. Ind. Electron.* 57, 2262–2271. doi:10.1109/TIE.2009.2024093

Dargahi, V., Sadigh, A. K., Khorasani, R. R., and Rodriguez, J. (2022). Active Voltage Balancing Control of a Seven-Level Hybrid Multilevel Converter Topology. *IEEE Trans. Ind. Electron.* 69, 74–89. doi:10.1109/TIE.2020.3048288

Di Zhang, D., Wang, F., Burgos, R., Rixin Lai, R., and Boroyevich, D. (2010). Impact of Interleaving on AC Passive Components of Paralleled Three-phase Voltage-Source Converters. *IEEE Trans. Ind. Applicat.* 46, 1042–1054. doi:10.1109/TIA.2010.2045336

Dolguntseva, I., Krishna, R., Soman, D. E., and Leijon, M. (2015). Contour-based Dead-Time Harmonic Analysis in a Three-Level neutral-point-clamped Inverter. *IEEE Trans. Ind. Electron.* 62, 203–210. doi:10.1109/TIE.2014.2327579

Gao, Z., Ge, Q., Li, Y., Zhao, L., Zhang, B., and Wang, K. (2021). Hybrid Improved Carrier-Based PWM Strategy for Three-Level neutral-point-clamped Inverter with Wide Frequency Range. *IEEE Trans. Power Electron.* 36, 8517–8538. doi:10.1109/TPEL.2020.3047952

Gengji, W., and Ping, W. (2016). Rotor Loss Analysis of PMSM in Flywheel Energy Storage System as Uninterruptable Power Supply. *IEEE Trans. Appl. Supercond.* 26, 1–5. doi:10.1109/TASC.2016.2594826

Ghanaatian, M., and Lotfifard, S. (2019). Control of Flywheel Energy Storage Systems in the Presence of Uncertainties. *IEEE Trans. Sustain. Energ.* 10, 36–45. doi:10.1109/TSTE.2018.2822281

Ho, C.-Y., Wang, J.-C., Hu, K.-W., and Liaw, C.-M. (2019). Development and Operation Control of a Switched-Reluctance Motor Driven Flywheel. *IEEE Trans. Power Electron.* 34, 526–537. doi:10.1109/TPEL.2018.2814790

Holmes, D. G., and Lipo, T. A. (2003). *Pulse Width Modulation for Power Converters: Principles and Practice*. Piscataway: Wiley-IEEE Press.

Jiang, C., Quan, Z., Zhou, D., and Li, Y. (2021). A Centralized CB-MPC to Suppress Low-Frequency ZSCC in Modular Parallel Converters. *IEEE Trans. Ind. Electron.* 68, 2760–2771. doi:10.1109/TIE.2020.2982111

Jiang, W., Wang, P., Ma, M., Wang, J., Li, J., Li, L., et al. (2020). A Novel Virtual Space Vector Modulation with Reduced Common-Mode Voltage and Eliminated Neutral point Voltage Oscillation for Neutral point Clamped Three-Level Inverter. *IEEE Trans. Ind. Electron.* 67, 884–894. doi:10.1109/TIE.2019.2899564

Liu, X., Liu, T., Chen, A., Xing, X., and Zhang, C. (2021). Circulating Current Suppression for Paralleled Three-Level T-type Inverters with Online Inductance Identification. *IEEE Trans. Ind. Applicat.* 57, 5052–5062. doi:10.1109/TIA.2021.3089115

Liu, Y., Mao, X., Ning, G., Dan, H., Wang, H., and Su, M. (2021). Model Predictive-Based Voltage Balancing Control for Single-phase Three-Level Inverters. *IEEE Trans. Power Electron.* 36, 12177–12182. doi:10.1109/TPEL.2021.3077011

Mazzucchelli, M., Puglisi, L., and Sciutto, G. (1981). PWM Systems in Power Converters: An Extension of the ``Subharmonic" Method. *IEEE Trans. Ind. Electron. Control. Instrum.* IECI-28, 315–322. doi:10.1109/TIECI.1981.351056

Mir, A. S., and Senroy, N. (2019). Intelligently Controlled Flywheel Storage for Enhanced Dynamic Performance. *IEEE Trans. Sustain. Energ.* 10, 2163–2173. doi:10.1109/TSTE.2018.2881317

Nabae, A., Takahashi, I., and Akagi, H. (1981). A New Neutral-Point-Clamped PWM Inverter. *IEEE Trans. Ind. Applicat.* IA-17, 518–523. doi:10.1109/TIA.1981.4503992

Rafi, M. A. H., and Bauman, J. (2021). A Comprehensive Review of DC Fast-Charging Stations with Energy Storage: Architectures, Power Converters, and Analysis. *IEEE Trans. Transp. Electrific.* 7, 345–368. doi:10.1109/TTE.2020.3015743

Song, W., Feng, X., and Smedley, K. M. (2013). A Carrier-Based PWM Strategy with the Offset Voltage Injection for Single-phase Three-Level neutral-point-clamped Converters. *IEEE Trans. Power Electron.* 28, 1083–1095. doi:10.1109/TPEL.2012.2210248

Stala, R. (2013). A Natural DC-link Voltage Balancing of Diode-Clamped Inverters in Parallel Systems. *IEEE Trans. Ind. Electron.* 60, 5008–5018. doi:10.1109/TIE.2012.2219839

Tallam, R. M., Naik, R., and Nondahl, T. A. (2005). A Carrier-Based PWM Scheme for Neutral-point Voltage Balancing in Three-Level Inverters. *IEEE Trans. Ind. Applicat.* 41, 1734–1743. doi:10.1109/TIA.2005.858283

Tcai, A., Kwon, Y., Pugliese, S., and Liserre, M. (2021). Reduction of the Circulating Current Among Parallel NPC Inverters. *IEEE Trans. Power Electron.* 36, 12504–12514. doi:10.1109/TPEL.2021.3075562

Wan, W., Duan, S., Chen, C., and Yu, T. (2021). A Hybrid Control Method for Neutral-point Voltage Balancing in Three-Level Inverters. *IEEE Trans. Power Electron.* 36, 8575–8582. doi:10.1109/TPEL.2021.3051044

Xing, X., and Chen, H. (2021). A Fast-Processing Predictive Control Strategy for Common-Mode Voltage Reduction in Parallel Three-Level Inverters. *IEEE J. Emerg. Sel. Top. Power Electron.* 9, 316–326. doi:10.1109/JESTPE.2019.2956315

Xing, X., Li, X., Qin, C., Chen, J., and Zhang, C. (2020). An Optimized Zero-Sequence Voltage Injection Method for Eliminating Circulating Current and Reducing Common Mode Voltage of Parallel-Connected Three-Level Converters. *IEEE Trans. Ind. Electron.* 67, 6583–6596. doi:10.1109/TIE.2019.2939962

Yamanaka, K., Hava, A. M., Kirino, H., Tanaka, Y., Koga, N., and Kume, T. (2002). A Novel Neutral point Potential Stabilization Technique Using the Information of Output Current Polarities and Voltage Vector. *IEEE Trans. Ind. Applicat.* 38, 1572–1580. doi:10.1109/TIA.2002.804761

Zhang, G., Zhou, Z., Shi, T., and Xia, C. (2021). An Improved Multimode Synchronized Space Vector Modulation Strategy for High-Power Medium-Voltage Three-Level Inverter. *IEEE Trans. Power Electron.* 36, 4686–4696. doi:10.1109/TPEL.2020.3023622

Zhang, Q., Xing, X., and Sun, K. (2019). Space Vector Modulation Method for Simultaneous Common Mode Voltage and Circulating Current Reduction in Parallel Three-Level Inverters. *IEEE Trans. Power Electron.* 34, 3053–3066. doi:10.1109/TPEL.2018.2848928

Zhang, X., and Yang, J. (2018). A DC-link Voltage Fast Control Strategy for High-Speed PMSM/G in Flywheel Energy Storage System. *IEEE Trans. Ind. Applicat.* 54, 1671–1679. doi:10.1109/TIA.2017.2783330

Zhang, X., and Yang, J. (2017). A Robust Flywheel Energy Storage System Discharge Strategy for Wide Speed Range Operation. *IEEE Trans. Ind. Electron.* 64, 7862–7873. doi:10.1109/TIE.2017.2694348

Conflict of Interest: The authors declare that the research was conducted in the absence of any commercial or financial relationships that could be construed as a potential conflict of interest.

frontiers in Energy Research

ORIGINAL RESEARCH
published: 20 January 2022
doi: 10.3389/fenrg.2021.823746

Research on the Resonance Suppression Method for Parallel Grid-Connected Inverters Based on Active Impedance

Tao Zhao, Yunkai Cao, Mingzhou Zhang, Chunlin Wang and Quan Sun*

Nanjing Institute of Technology, Nanjing, China

Under the condition of weak grid, the coupling between parallel inverters and grid impedance is easy to cause harmonic resonance, which seriously affects the grid-connected power quality. First, the equivalent circuit model of the multi-inverter parallel system is established, and the mechanism of harmonic resonance is analyzed from the perspective of impedance; through the resonance detection method based on a self-tuning filter, the voltage resonance component of the parallel node is extracted; on that basis, an active impedance is designed to suppress the resonance of the multi-inverter parallel system, which can equivalently construct a virtual impedance branch to improve the grid impedance characteristics at the resonance frequency, and its effectiveness is verified using the impedance stability criterion. Finally, simulation experiments are carried out. The results show that this method can effectively suppress the resonance of the multi-inverter parallel system and can significantly improve the adaptability of inverters to weak grid.

Keywords: resonance, parallel inverters, LCL filter, weak grid, active impedance

Edited by:
Weihao Hu,
University of Electronic Science and Technology of China, China

Reviewed by:
Xiaokang Liu,
Politecnico di Milano, Italy
Youyuan Ni,
Hefei University of Technology, China

***Correspondence:**
Tao Zhao
zdhxzt@njit.net.cn

Specialty section:
This article was submitted to Process and Energy Systems Engineering, a section of the journal Frontiers in Energy Research

Received: *28 November 2021*
Accepted: *20 December 2021*
Published: *20 January 2022*

Citation:
Zhao T, Cao Y, Zhang M, Wang C and Sun Q (2022) Research on the Resonance Suppression Method for Parallel Grid-Connected Inverters Based on Active Impedance.
Front. Energy Res. 9:823746.
doi: 10.3389/fenrg.2021.823746

1 INTRODUCTION

With the continuous advancement of the global energy structure transformation process, the proportion of renewable energy such as wind energy and solar energy connected to the utility grid is gradually increasing. The research on the grid-connected inverter has attracted people's attention (Hong et al., 2019; Xiong et al., 2020; Akhavan et al., 2021). In the actual system, considering the factors such as long-distance transmission lines and transformer leakage reactance, the connection between the new energy power generation link and the utility grid becomes weaker, which makes the utility grid to show the characteristics of weak grid. In the environment of weak grid, there is interaction coupling between inverters and utility grid, which increases the risk of harmonic resonance of the system, and may lead to global resonance instability of the system in serious cases (Zhang et al., 2016; Lu et al., 2019; Fang et al., 2021; Xiong et al., 2021).

At present, the research on the resonance mechanism and resonance suppression method of the multi-inverter parallel system is a research hot spot of new energy grid connection technology (Yu et al., 2019). Different from the single inverter, the resonance mechanism of the multi-inverter parallel system is more complex. Through calculation and analysis, it has been shown in Zhen-Ao et al. (2014) that there are two resonance frequency points in the multi-inverter parallel system under weak grid: one is the inherent resonance of the LCL-type inverter, and the other is the external coupling resonance between grid impedance and parallel inverters. The equivalent circuit model of the multi-inverter parallel system is established in Agorreta et al. (2011), when n inverters operate in parallel, the equivalent grid impedance of the single grid-connected inverter can be equivalent to n times of the actual grid impedance. Furthermore, it is proposed that with the increase of the number of parallel inverters, the natural resonance of LCL remains unchanged, while the external coupling resonance shifts to low frequency in Hu et al. (2015). In fact, the reason for resonance instability of the multi-inverter parallel system under weak grid lies in the existence of grid inductance, and grid resistance is conducive for improving the stability of the grid-connected system (Pan et al., 2014). Therefore, in the research process, the resistance can be ignored and only the grid inductance is considered.

The resonance suppression methods of the multi-inverter parallel system are mainly divided into single type and centralized type. The former is to reshape the inverter output impedance by adding the state variable feedback link to each inverter control circuit (Yang et al., 2014; Gao et al., 2020; Natori et al., 2020). However, when the number of inverters is large, the single impedance remodeling method needs to modify the control algorithm of each inverter, which is difficult to realize in practical application. From the global point of view, the centralized resonance suppression method can effectively suppress the occurrence of harmonic resonance by reasonably designing the damping circuit at the point of common coupling (PCC). To suppress the resonance of the multi-inverter system, a method of parallel RC branches at PCC is implemented in Wan et al. (2018). That passive suppression circuit is simple in design, but the problem of power loss is serious. Furthermore, Wang et al. (2015) proposed to install an active damper at PCC to effectively construct the resistance at the resonant frequency, so as to improve the damping characteristics of the system at the resonant frequency. This method effectively reduces the power loss but has high requirements for resonant frequency extraction. In view of the idea of the active damper, a global active inductor is designed in Kang (2020), which can realize the approximate parallel virtual inductance at PCC. However, adding virtual inductance will cause the phase angle lag of 90° in the whole frequency band of the system, so it is necessary to add an additional phase angle compensation link. Most of the above resonance suppression methods only deal with the harmonic resonance of specific frequency. However, in the actual system, the grid impedance will fluctuate due to environmental changes and the working condition of inverter switching. The resonance frequency in the system is often time-varying, and the resonance problem in the grid-connected system is more complex.

Considering the complex grid-connected operation conditions of weak grid, active impedance designed to suppress the resonance of the multi-inverter parallel system is discussed in this article. In **Section 2**, the equivalent model of the multi-inverter parallel system under weak grid is established, and its stability is analyzed by the impedance analysis method. **Section 3** presents the main development of this article, which includes the design method of active impedance and its extraction method based on a self-tuning filter. Meanwhile, the influence of active impedance on system stability is analyzed by the Nyquist stability criterion. Finally, the effectiveness and accuracy of the proposed resonance suppression method is verified by simulation in **Section 4**.

2 RESONANCE MECHANISM ANALYSIS OF THE MULTI-INVERTER PARALLEL SYSTEM

2.1 Model of the Multi-Inverter Parallel System

The system structure of the T-type three-level inverter based on an LCL filter shown in **Figure 1** consists of neutral-point (NP) switches and vertical half-bridge switches, followed by an LCL filter, where U_{dc} is the DC voltage, C_1 and C_2 are the DC support capacitors with equal capacitance, L_{line} represents the line impedance from the inverter to PCC, L_{g} is the equivalent impedance of the grid, i_{g} is the grid-connected current and u_{g} is the grid voltage, and θ is the voltage phase angle. The voltage outer loop adopts PI control, and the voltage outer loop provides the current reference value to the current inner loop. The current inner loop is controlled by QPR to generate the SVPWM modulation signal to drive the inverter.

Figure 2 depicts the current feedback control block diagram of the LCL-type grid-connected inverter. $G_{\mathrm{C}}(s)$ is the QPR controller, and $H(s)$ is the feedback used to weaken the inherent resonant peak of LCL and is taken as the combination of quadratic differential link, primary differential link, proportional link, and integral link. Specific design methods are shown in reference (Chen et al., 2013; Xu 2019).

The expression of the grid-connected current can be obtained as:

$$i_{\mathrm{g1}}(s) = \frac{G_1(s)}{1 + sL_{\mathrm{line}}Y_1(s)} i_{g1}^{*}(s) - \frac{Y_1(s)}{1 + sL_{\mathrm{line}}Y_1(s)} u_{\mathrm{pcc}}(s), \tag{1}$$

where

$$G_1(s) = \frac{K_{\mathrm{pwm}}G_c(s)}{s^3L_1L_2C + s(L_1 + L_2) + K_{\mathrm{pwm}}(G_{\mathrm{c}}(s) + H(s))}; \tag{2}$$

$$Y_1(s) = \frac{s^2L_1C + 1}{s^3L_1L_2C + s(L_1 + L_2) + K_{\mathrm{pwm}}(G_{\mathrm{c}}(s) + H(s))}, \tag{3}$$

According to the expression of the grid-connected current, the Norton equivalent circuit can be established which includes the controlled current source $G_1 i_{\mathrm{g1}}*$ and admittance Y_1. When multiple inverters operate in parallel in the system, it can be equivalent to the Norton equivalent model of multiple inverters in parallel as shown in **Figure 3**.

2.2 Resonance Mechanism Analysis

According to the superposition theorem, the expression of the total grid-connected current i_{g} can be deduced:

$$\begin{aligned} i_{\mathrm{g}}(s) &= \frac{Z_{\mathrm{op}}(s)}{Z_{\mathrm{op}}(s) + Z_{\mathrm{g}}(s)} \cdot \sum_{\mathrm{i}=1}^{n} \Big(G_{\mathrm{i}}(s) i_{\mathrm{i}}^{*}(s) - \frac{u_{\mathrm{g}}(s)}{Z_{\mathrm{outi}}}\Big) \\ &= \frac{1}{1 + Z_g(s)\big/Z_{op}(s)} \cdot \sum_{i=1}^{n} \Big(G_i(s) i_i^{*}(s) - \frac{u_g(s)}{Z_{\mathrm{outi}}}\Big), \end{aligned} \tag{4}$$

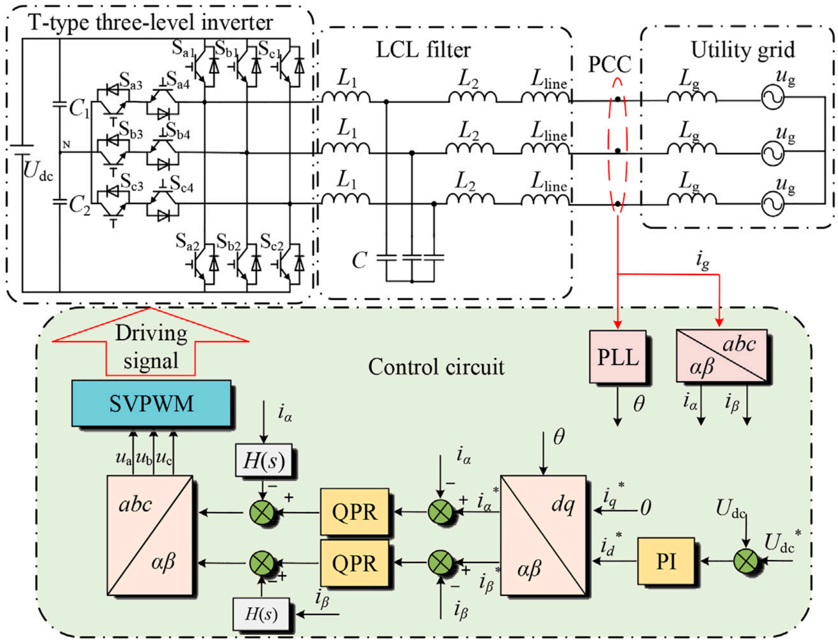

FIGURE 1 | Typical structure of the grid-connected inverter.

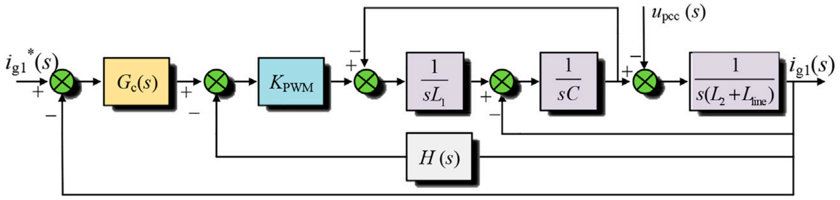

FIGURE 2 | Grid-connected current feedback control block diagram.

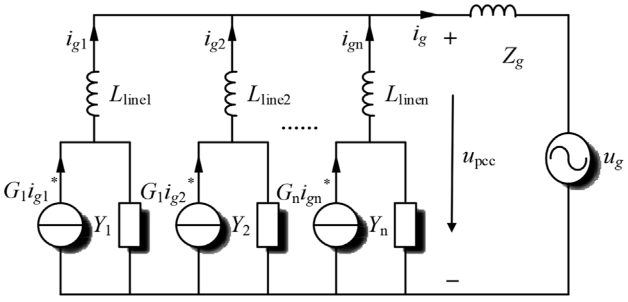

FIGURE 3 | Norton equivalent model.

where Z_{outi} represents the output impedance of the ith inverter, $Z_{outi} = sL_{linei}+1/Y_i$, and Z_{op} represents the total output impedance of inverters in parallel. When the ratio T_m of grid impedance Z_g to output impedance Z_{op} satisfies the Nyquist stability criterion, the grid-connected system can be considered stable (Sun 2011).

TABLE 1 | Parameters of the grid-connected inverter.

Parameter		Value
DC voltage	U_{dc}	750 V
Capacitance on the DC side	C_1, C_2	4700 μF
Grid voltage	u_g	220V/50 Hz
Grid impedance	L_g	1 mH
Filter inductance	L_1	1.8 mH
Inductance on the grid side	L_2	0.2 mH
Filter capacitor	C	15 μF
Line impedance	L_{line}	0.1 mH

When the parameters of parallel inverters are the same, $Z_{out} = n*Z_{op}$, and the impedance ratio T_m can be written as **Eq. 5**.

$$T_m(s) = \frac{Z_g(s)}{Z_{op}(s)} = \frac{nZ_g(s)}{Z_{out}(s)}, \tag{5}$$

Utility grid impedance $Z_g = sL_g$ draws the impedance ratio Nyquist curve of single inverter and two inverters in parallel

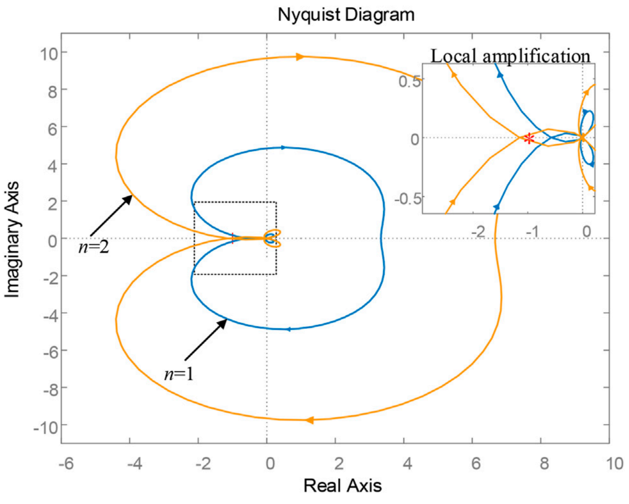

FIGURE 4 | Nyquist curve of impedance ratio.

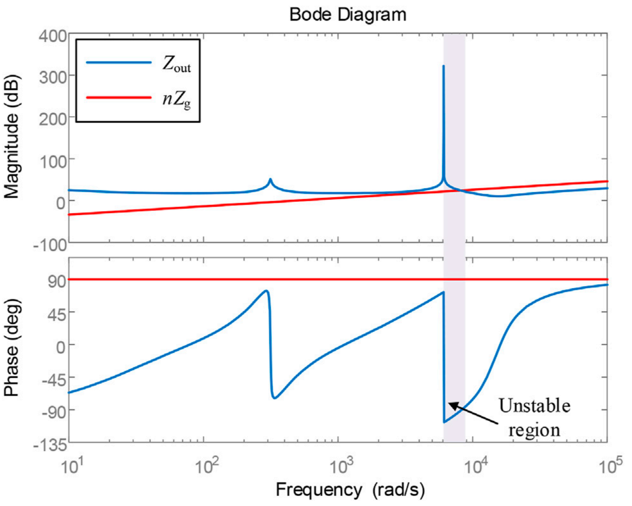

FIGURE 5 | Bode diagram of inverter output impedance.

according to **Eq. 5**, as shown in **Figure 4**. The parameters of the grid-connected inverter are shown in **Table 1**.

It can be seen from **Figure 4** that when there is only one inverter, the Nyquist curve of $T_m(s)$ does not surround $(-1, j0)$ point and satisfies the impedance stability criterion. However, it should be noted that the curve of the single inverter is close to $(-1, j0)$ point, indicating that the stability margin of the system is relatively low at this time. When the number of inverters in the system increases, the range of the Nyquist envelope becomes larger. When n takes 2, the Nyquist curve of $T_m(s)$ obviously surrounds $(-1, j0)$ point. It can be determined that resonance instability occurs in the multi-inverter parallel system at this time. Therefore, although the single inverter can operate stably, when multiple inverters operate in parallel, the system still has a resonance-hidden danger.

The frequency characteristic curves of inverter output impedance Z_{out} and grid equivalent impedance nZ_g are drawn, as shown in **Figure 5**. It can be seen from the figure that there will be an unstable region with a phase difference greater than or equal to 180° between the inverter output impedance and grid impedance in a certain frequency band under the weak grid. When the intersection frequency of the two impedance is in this frequency band, the system is easy to resonate with the harmonics, which is consistent with the results of Nyquist plot analysis.

3 RESEARCH ON THE RESONANCE SUPPRESSION METHOD

In order to solve the resonance instability problem of the multi-inverter parallel system, from the perspective of system global resonance suppression, it is necessary to extract the resonance signal in the system first and then use the resonance suppression unit installed at PCC for centralized treatment.

3.1 Resonance Detection Method Based on Self-Tuning Filter

The resonance information in the actual grid-connected system is often uncertain and will change with the change of the system. Although the traditional wavelet packet and discrete Fourier transform methods can detect the resonant signal, the extracted information is not accurate enough, the amount of calculation is large, and the detection time is long (Zeng et al., 2014). Therefore, this article adopts the resonance detection method of the grid-connected inverter based on a self-tuning filter (STF). The transfer function $G_{STF}(s)$ of STF can be expressed as:

$$G_{STF}(s) = \frac{V_{xy}(s)}{U_{xy}(s)} = K \cdot \frac{s + K + j\omega_c}{(s + K)^2 + \omega_c^2}, \tag{6}$$

where U_{xy} is the input signal of STF, V_{xy} is the output signal, and ω_c is the fundamental angular frequency. As long as K takes a positive value, STF can remain stable (Biricik et al., 2014). Based on **Eq. 6**, the frequency response curve of STF can be obtained as shown in **Figure 6**.

It can be seen from **Figure 6** that STF has band-pass filtering characteristics for the input signal, and the output signal is unattenuated only at the angular frequency ω_c. Hence, this characteristic of STF can be used to extract the resonant signal. The principle is shown in **Figure 7**, where the subscript f represents the voltage fundamental component, and the subscript r represents the voltage resonant component.

First, by self-tuning filtering the voltage sampled at PCC, the fundamental frequency component can be tracked without a static difference, and then the resonance voltage can be obtained by subtracting the fundamental frequency voltage from the sampled voltage. Therefore, the resonant detection method based on the self-tuning filter can quickly and accurately filter the fundamental frequency component in the

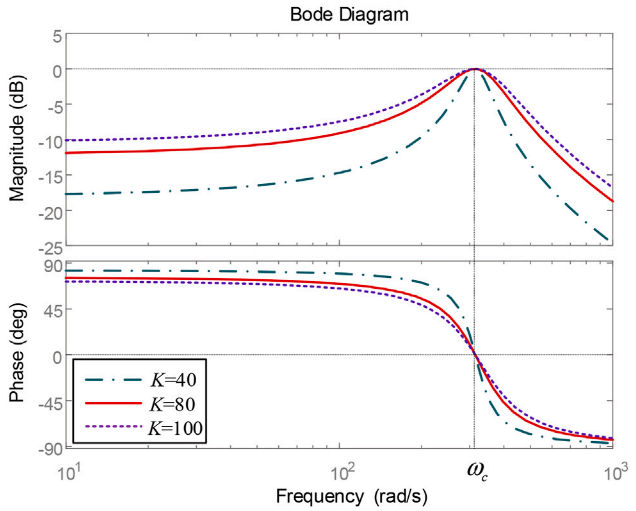

FIGURE 6 | Amplitude frequency characteristic curve of STF.

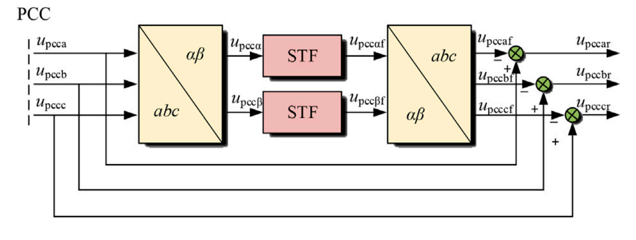

FIGURE 7 | Schematic diagram of resonance detection based on STF.

voltage signal and extract the voltage resonant component as the input signal for active impedance.

3.2 Resonance Suppression Strategy Based on Active Impedance

The active impedance is usually installed at PCC, and its topology is similar to APF, as shown in **Figure 8**. The active impedance designed in this article adopts a T-type three-level DC/AC converter, L_{1a}, C_a, and L_{2a} constitute LCL filter, R_a is damping resistance, and subscript a represents the active impedance. I^* is the command current, and the resonance detection module adopts the resonance detection method based on STF. The extracted voltage resonance signal u_{pccr} passes through the virtual impedance $R_v + sL_v$ to generate the reference value of the current resonance signal $i_{ga}{}^*$, and the sampled output current i_{ga} is added to the QPR controller to simulate the parallel passive impedance element at PCC, which increases the damping of the system at the resonance frequency.

Figure 9 is the current loop feedback control block diagram of the active impedance, and $G_r(s)$ represents the STF resonance extraction link. According to the method of deriving the inverter equivalent circuit model in the previous section and combined with **Figure 9**, the expression of the output current i_{ga} can be derived, as shown in **Eq. 7**.

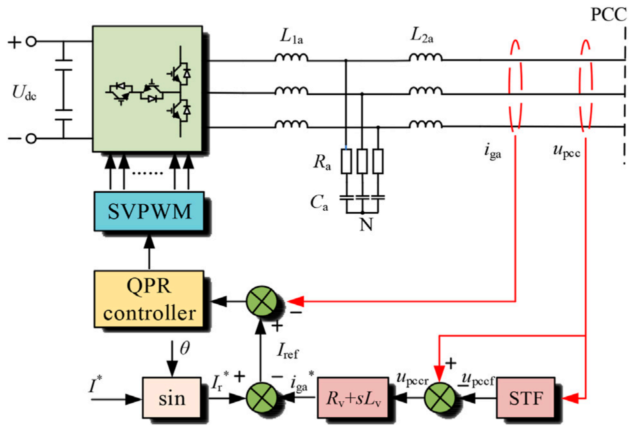

FIGURE 8 | System circuit model with active impedance.

$$i_{ga}(s) = G_a(s)I_{ref} - Y_a(s)u_{pcc}(s) - Y_v(s)u_{pcc}(s), \tag{7}$$

The Norton equivalent model of active impedance can be obtained, as shown in **Figure 10**. Y_a and Y_v represent the output admittance and virtual admittance of the active impedance, respectively.

In which,

$$\begin{cases} G_a(s) = \dfrac{K_{pwma}G_{ca}(s)H_1(s)}{1 + K_{pwma}G_{ca}(s)H_1(s)} \\ Y_a(s) = \dfrac{H_2(s)}{1 + K_{pwma}G_{ca}(s)H_1(s)}, \\ Y_v(s) = G_a(s)G_r(s) \cdot \dfrac{1}{R_v + sL_v} \end{cases} \tag{8}$$

where $H_1(s)$ and $H_2(s)$ represent the admittance characteristics at both ends of the LCL filter, and $G_{ca}(s)$ represent the transfer function of the QPR current controller.

$$H_1(s) = \frac{sC_aR_a + 1}{s^3L_{1a}L_{2a}C_a + s^2(L_{1a} + L_{2a})C_aR_a + s(L_{1a} + L_{2a})}; \tag{9}$$

$$H_2(s) = \frac{s^2L_{1a}C_a + sC_aR_a + 1}{s^3L_{1a}L_{2a}C_a + s^2(L_{1a} + L_{2a})C_aR_a + s(L_{1a} + L_{2a})}; \tag{10}$$

$$G_{ca}(s) = K_p + \frac{2K_r\omega_i s}{s^2 + 2\omega_i s + \omega_0^2}. \tag{11}$$

Since the active impedance only works at the resonant frequency, the transfer function of the current controller can be approximated to include only the proportional link K_p. When the system resonates, the transfer function $G_a(s)$ of the controlled source of the active impedance approaches 1, and the equivalent output admittance $Y_a(s)$ approaches 0. If the influence of the resonance detection link is ignored, the virtual admittance $Y_v(s)$ can be approximately written as:

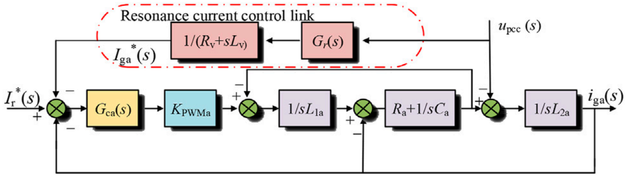

FIGURE 9 | Control block diagram of active impedance.

$$Y_v = \frac{1}{R_v + sL_v}. \tag{12}$$

Hence, adding an active impedance can be approximately equivalent to parallel passive impedance at PCC, and the virtual impedance of resonance control is consistent with the size of passive impedance. The stability analysis of passive impedance can be approximately used to judge the influence of the active device on system stability and select the appropriate impedance. The circuit model of the multi-inverter parallel system with active impedance is drawn, as shown in **Figure 11**.

3.3 Stability Analysis

From the PCC point to the utility grid side, it is not difficult to find that the virtual impedance branch and the grid impedance nL_g are in parallel. The total parallel impedance is defined as the equivalent power grid impedance $Z_g{}^*$. By reasonably designing the parameters of R_v and L_v, so that $Z_g{}^*$ and Z_{out} meet the Nyquist stability criterion, the stable operation of the system can be ensured.

$$Z_g^*(s) = \frac{(R_v + sL_v) \cdot n \cdot sL_g}{(R_v + sL_v) + n \cdot sL_g}, \tag{13}$$

Taking Laplace transform for **Eq. 13**, the phase frequency characteristic expression of $Z_g{}^*$ is calculated as follows:

$$\psi(\omega) = 90^\circ + \arctan\left(\frac{L_v}{R_v}\omega\right) - \arctan\left(\frac{L_v + nL_g}{R_v}\omega\right), \tag{14}$$

Through calculation and analysis of **Eq. 14**, it is found that the phase of $Z_g{}^*$ reaches the lowest value in the frequency band near the angular frequency ω_v. When it is higher or lower than this frequency band, the phase approaches 90°. It is consistent with the actual grid impedance. According to this characteristic, the parameters of virtual impedance are designed to make ω_v in or close to the resonance instability region of **Figure 5** which can reduce the phase difference between the grid impedance and the inverter output impedance, so as to reduce the system resonance risk. The expression of ω_v is as follows:

$$\omega_v = \frac{R_v}{\sqrt{L_v\left(L_v + nL_g\right)}}, \tag{15}$$

The grid impedance L_g is 1 mH, R_v is 10 Ω, and L_v is 0.5 mH. Bode diagrams of inverter output impedance Z_{out} and grid equivalent impedance $Z_g{}^*$ are drawn, as shown in **Figure 12**.

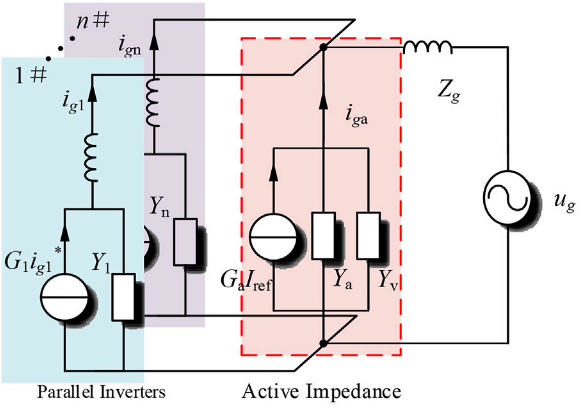

FIGURE 10 | Norton equivalent model of active impedance.

TABLE 2 | Parameters of active impedance.

Parameter		Value
Angular frequency of STF	ω_c	100 rad/s
Constant of STF	K	80
Virtual resistance	R_v	10 Ω
Virtual inductance	L_v	0.5 mH
Filter inductance	L_{1a}	1 mH
Filter inductance	L_{2a}	0.6 mH
Filter capacitor	C_a	20 μF
Damping resistance	R_a	1 Ω

It can be seen from **Figure 12** that the parallel active impedance at PCC only changes the grid impedance characteristics in the resonance unstable region, while the grid impedance curves in the low-frequency band and high-frequency band are almost unchanged. The phase angle difference between the inverter output impedance Z_{out} and the grid impedance $Z_g{}^*$ at the intersection frequency is obviously less than 180°, meeting the Nyquist stability criterion. Therefore, the input of active impedance improves the system stability and effectively suppresses the resonance caused by the impedance coupling between the multi-inverter parallel system and weak grid.

In the actual system, the grid impedance is not fixed but will fluctuate under the influence of various factors. The impedance ratio of the system containing active impedance is shown in **Eq. 16**. The Nyquist plot of $T_m{}'$ at different grid impedances is drawn, as shown in **Figure 13**.

$$T'_m(s) = \frac{Z_g^*(s)}{Z_{out}(s)}, \tag{16}$$

It can be seen from **Figure 13** that after the resonance suppression strategy based on active impedance is applied to the grid-connected system, the Nyquist curve of $T_m{}'$ does not surround (−1, j0) with the grid impedance increases from 1 mH to 4 mH. Hence, it can be determined that the system is stable. Therefore, the resonance suppression method proposed in this

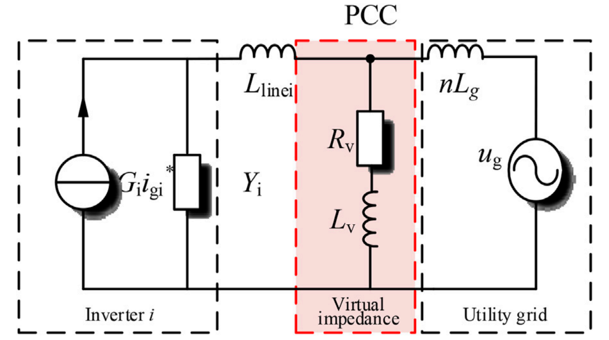

FIGURE 11 | System circuit model with active impedance.

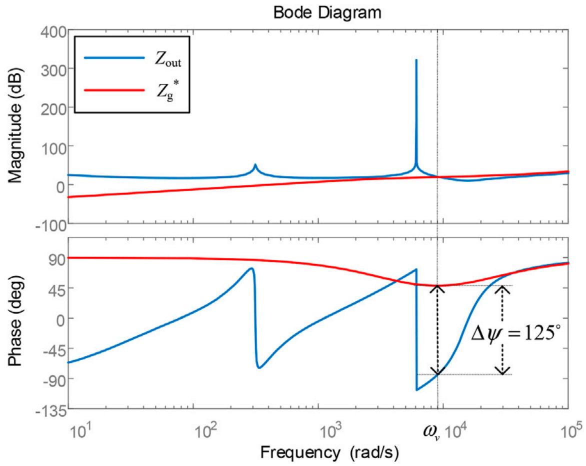

FIGURE 12 | Bode diagram of system impedance with active impedance.

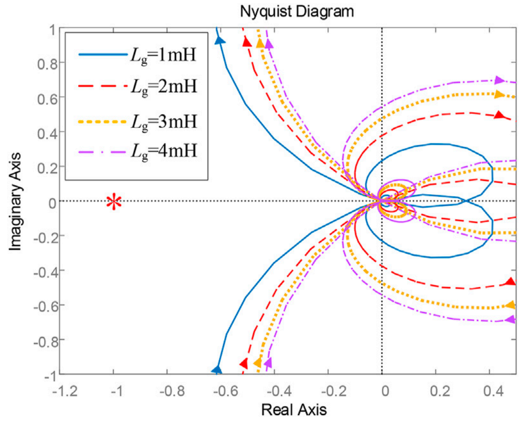

FIGURE 13 | Nyquist plot of impedance ratio under different Lg.

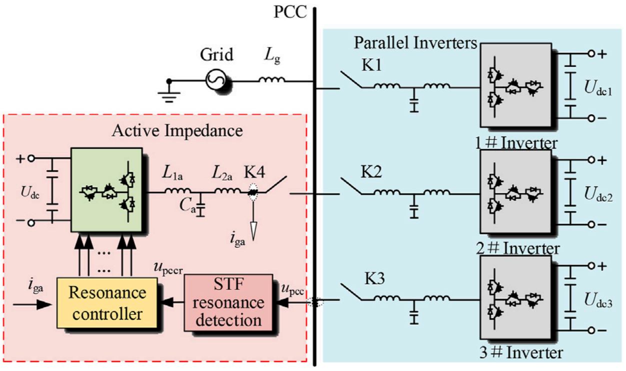

FIGURE 14 | Overall system block diagram.

article can effectively improve the adaptability of inverters to weak grid and enhance the stability of the multi-inverter parallel system.

4 SIMULATION RESULTS

In order to verify the effectiveness of the resonance suppression strategy proposed in this article, the parallel system simulation model of active impedance based on the STF resonance extraction method and T-type three-level inverter are carried out in Simulink. The parameters of grid-connected inverter and active impedance are shown in **Table 1** and **Table 2**, respectively. The overall block diagram of the system is shown in **Figure 14**.

Considering the environment of weak grid, the simulated grid impedance L_g is 1mH, and the voltage at PCC of the multi-inverter parallel system is shown in **Figure 15**. Due to the coupling with weak grid, the system has harmonic resonance, and PCC voltage distortion is serious. In the figure, u_{pccf} and u_{pccr} are the fundamental voltage and resonance voltage waveforms separated by the resonance detection method based on STF, respectively. It can be seen from the figure that the separated fundamental voltage waveform is good and changes sinusoidally with an equal amplitude over time; the envelope of the resonant voltage component is clear and presents the divergent sinusoidal law. The simulation results show that by applying the resonance detection method proposed in this article to the sampled voltage, the fundamental frequency component of the voltage can be tracked without the static error, and the resonance component can be completely extracted.

Figure 16 shows the waveform of the total grid-connected current and PCC voltage. It can be seen from the figure that before 0.1 s the resonance of the grid-connected system was unstable, the voltage and current were harmonic resonance amplified, and the grid-connected power quality decreased. Put into the active impedance at 0.1 s. After about one-cycle transition, the resonance in the system is eliminated, the sinusoidal degree of the voltage and current waveform becomes better, the grid-connected power quality is improved, and the system is gradually stable. When the active impedance is

TABLE 3 | THD value of voltage and current.

L_g/mH	1	2	3	4	5
THD of i_g (%)	1.66	1.20	0.73	0.55	1.03
THD of u_{pcc} (%)	2.03	2.61	2.77	2.55	2.70

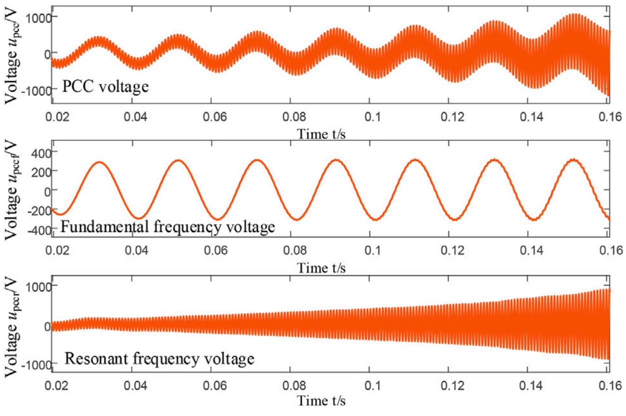

FIGURE 15 | Voltage signal detection waveform under resonance.

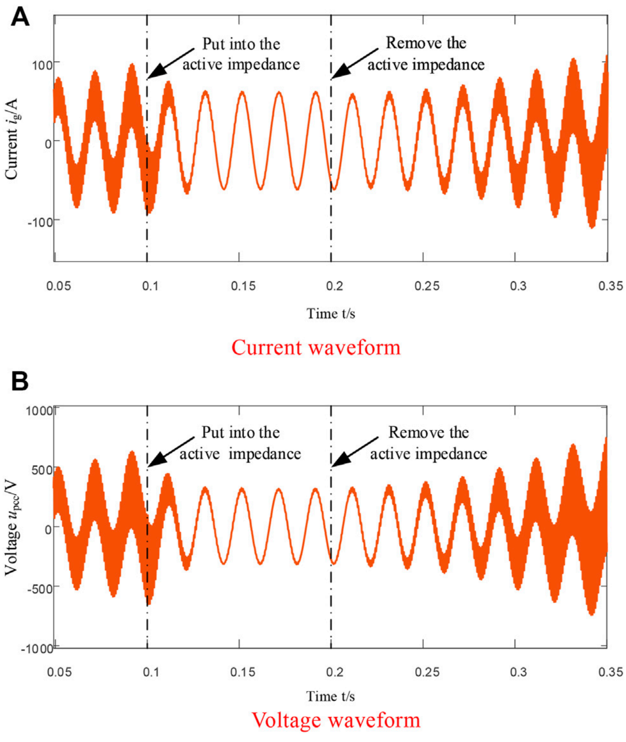

FIGURE 16 | Waveform of grid-connected current and PCC voltage.

cut off again at 0.2 s, the system has harmonic resonance, the voltage and current waveform gradually oscillates and diverges, and the power quality gradually deteriorates.

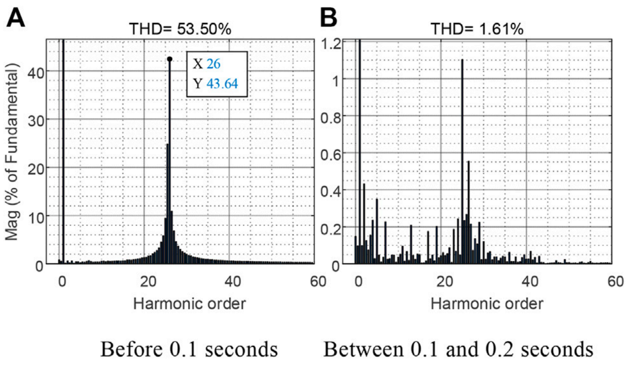

FIGURE 17 | Harmonic analysis of grid-connected current.

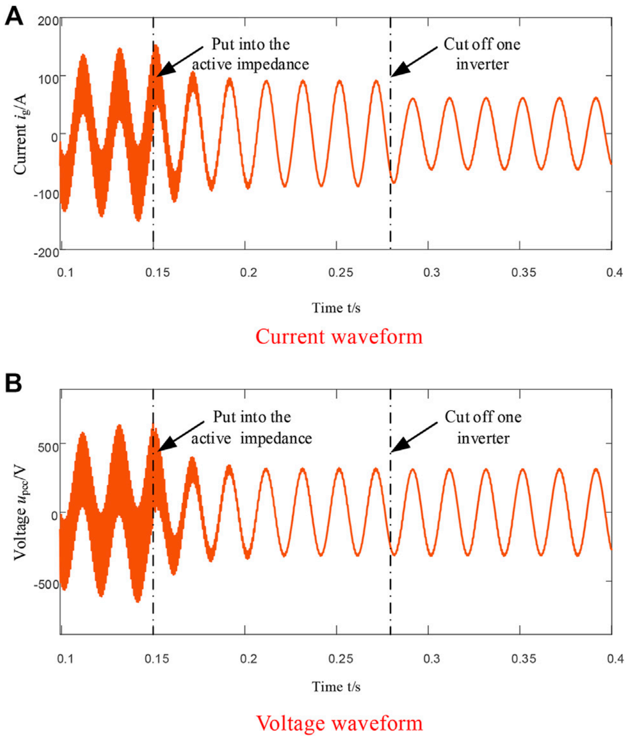

FIGURE 18 | Simulation waveform of voltage and current.

FFT harmonic analysis of the grid-connected current shall be carried out before 0.1 s, as shown in **Figure 17A**. At this time, the total harmonic distortion (THD) of the current reaches 53.50%, of which the 26th harmonic reaches 43.64%, indicating that the system has resonance at this frequency, which is the resonance peak generated by coupling with the weak grid. **Figure 17B** shows the harmonic analysis after the active impedance is put into operation. It can be seen from the figure that the harmonic of each order has been reduced below 1.2%, and the resonance has been suppressed. At this time, the distortion rate of the grid-connected current is 1.61%, which meets the grid-connected requirements.

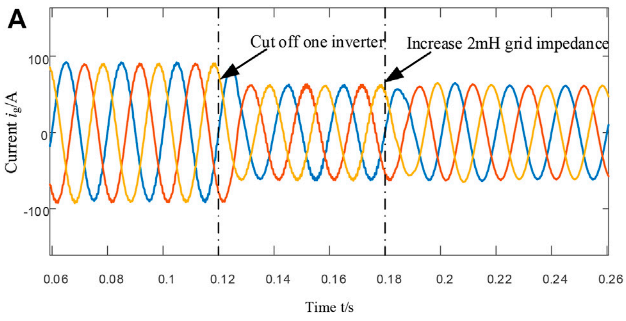

Current waveform

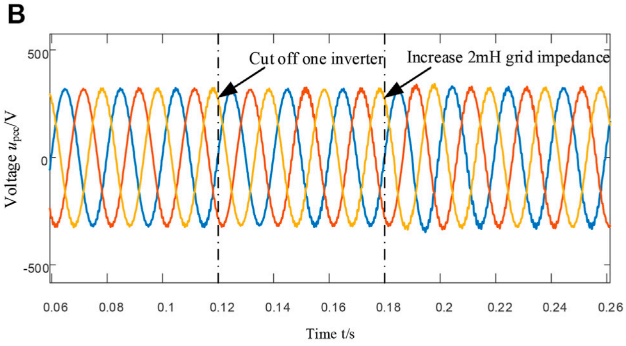

Voltage waveform

FIGURE 19 | Voltage and current waveform in dynamic process.

As shown in **Figure 18**, before 0.15 s, the grid-connected system resonated due to the coupling effect of grid impedance, and the voltage and current waveform was seriously distorted. When the active impedance is put at 0.15 s, the system gradually recovers to a stable state. When one inverter is cut off at 0.28 s, only the amplitude of the total grid-connected current in the system decreases, the PCC voltage waveform remains normal, the inverter can still maintain stable operation, and the system has good robustness.

Conduct harmonic analysis on the voltage and current of the multi-inverter parallel system under different grid impedance, and calculate the THD of the grid-connected current and PCC voltage after putting into the active impedance, as shown in **Table 3**. After adopting the resonance suppression method proposed in this article, the voltage and current distortion rate is not more than 5%, which meets the requirements of grid connection. The adaptability of inverters to weak grid is enhanced, and the simulation results are consistent with the theoretical analysis.

The voltage and current waveform of the grid-connected system with active impedance in the dynamic process is shown in **Figure 19**. One inverter is cut off at 0.12 s, and the grid impedance is increased form 1 mH–3 mH at 0.18 s. As shown, the total grid-connected current fluctuates only slightly during switching, and the current amplitude decreases rapidly to two-thirds of the original, and the system can still realize stable operation, and the grid-connected current will quickly return to a stable state after 0.18 s. PCC voltage can remain stable in the dynamic process of inverter switching and grid impedance fluctuation.

5 CONCLUSION

Aiming at the issue that resonance instability is easy to occur in parallel operation of multi-inverters under weak grid, active impedance and its resonance detection method are designed. The simulation results show that the resonance detection method based on STF proposed in this article can accurately extract the resonance voltage signal at PCC, and the design of the resonance detection module is simple and convenient for digital realization. The input of active impedance can improve the impedance characteristics of utility grid at resonance frequency, so as to reduce the resonance instability risk of the multi-inverter parallel system. Meanwhile, the resonance suppression method proposed in this article increases the safe and stable operation margin of the system, enhances the adaptability of the multi-inverter parallel system to the actual working conditions such as utility grid impedance fluctuation and inverter switching, and improves the system stability.

DATA AVAILABILITY STATEMENT

The raw data supporting the conclusions of this article will be made available by the authors, without undue reservation, to any qualified researcher. Requests to access the datasets should be directed to TZ, zdhxzt@njit.net.cn.

AUTHOR CONTRIBUTIONS

TZ contributed to the conception and design of the proposed strategy. All authors wrote and edited the manuscript.

FUNDING

This work was supported by the National Natural Science Foundation of China (61901212).

REFERENCES

Agorreta, J. L., Borrega, M., López, J., and Marroyo, L. (2011). Modeling and Control of N -Paralleled Grid-Connected Inverters with LCL Filter Coupled Due to Grid Impedance in PV Plants. *IEEE Trans. Power Electron.* 26 (3), 770–785. March 2011. doi:10.1109/TPEL.2010.2095429

Akhavan, A., Vasquez, J. C., and Guerrero, J. M. (2021). A Robust Method for Controlling Grid-Connected Inverters in Weak Grids. *IEEE Trans. Circuits Syst.*68 (4), 1333–1337. doi:10.1109/TCSII.2020.3033427

Biricik, S., Redif, S., Özerdem, Ö. C., Khadem, S. K., and Basu, M. (2014). Real-time Control of Shunt Active Power Filter under Distorted Grid Voltage and Unbalanced Load Condition Using Self-tuning Filter. *Iet Power Electron.* 7 (7), 1895–1905. doi:10.1049/iet-pel.2013.0924

Chen, D., Zhang, J., and Qian, l. (2013). Single Current Feedback Control Strategy of Grid-Connected Inverters with LCL Filters. *Proc. CSEE* 33 (9), 10–16.

Fang, T., Shen, S., Jin, Y., and Ruan, X. (2021). Robustness Investigation of Multi-Inverter Paralleled Grid-Connected System with LCL-Filter Based on the Grid-Impedance Allocation Mechanism. *IEEE Trans. Power Electron.* 36 (12), 14508–14524. Dec. 2021. doi:10.1109/TPEL.2021.3088992

Gao, J., Tu, C., Guo, Q., Xiao, F., Jiang, F., and Lu, B. (2020). "Impedance Reshaping Control Method to Improve Weak Grid Stability of Grid-Connected Inverters, in" ECON 2020 The 46th Annual Conference of the IEEE Industrial Electronics Society, Singapore, October 18–21, 2020, 1342–1346. doi:10.1109/IECON43393.2020.9254917

Hong, L., Shu, W., Wang, J., and Mian, R. (2019). Harmonic Resonance Investigation of a Multi-Inverter Grid-Connected System Using Resonance Modal Analysis. *IEEE Trans. Power Deliv.* 34 (1), 63–72. Feb. 2019. doi:10.1109/TPWRD.2018.2877966

Hu, W., Zhou, H., Sun, J., Jiang, Y., and Zha, X. (2015). Resonance Analysis and Suppression of System with Multiple Grid-Connected Inverters, in" 2015 IEEE 2nd International Future Energy Electronics Conference (IFEEC), Taipei, Taiwan, November 1–4, 2015. doi:10.1109/IFEEC.2015.7361517

Kang, H. (2020). *Research on Resonance Instability Suppression Strategy for Multi-Inverter Grid-Connected System Based on Reshaping of Global Admittance at PCC.* Nanjing, China: Southeast University.

Natori, K., Ishikawa, A., and Sato, Y. (2020). A Study on Resonance Suppression Control Based on Virtual Resistance Concept for Parallel Inverters in Islanded Microgrid, in" 2020 IEEE 9th International Power Electronics and Motion Control Conference (IPEMC2020-ECCE Asia), Nanjing, China, November 29–December 2, 2020. doi:10.1109/IPEMC-ECCEAsia48364.2020.9367851

Lu, M., Yang, Y., Johnson, B., and Blaabjerg, F. (2019). An Interaction-Admittance Model for Multi-Inverter Grid-Connected Systems. *IEEE Trans. Power Electron.* 34 (8), 7542–7557. Aug. 2019. doi:10.1109/TPEL.2018.2881139

Pan, D., Ruan, X., Bao, C., Li, W., and Wang, X. (2014). Capacitor-Current-Feedback Active Damping with Reduced Computation Delay for Improving Robustness of LCL-type Grid-Connected Inverter. *IEEE Trans. Power Electron.* 29 (7), 3414–3427. doi:10.1109/TPEL.2013.2279206

Sun, J. (2011). Impedance-Based Stability Criterion for Grid-Connected Inverters. *IEEE Trans. Power Electron.* 26 (11), 3075–3078. Nov. 2011. doi:10.1109/TPEL.2011.2136439

Zhen-Ao, S., Zi-Long, Y., Yi-Bo, W., and Hong-Hua, X.. (2014). Analysis of Harmonic Resonances Among Parallel Grid-Connected Inverters, in" 2014 International Conference on Power System Technology, Chengdu, China, October 20–22, 2014. doi:10.1109/POWERCON.2014.6993560

Wan, Q., Zhang, H., Zhang, X., and Sun, J. (2018). Research on Resonance Mechanism and Suppression Technology of Photovoltaic Cluster Inverter. *Power Syst. Tech.* 42 (10), 3377–3384. doi:10.3390/en11040938

Wang, X., Pang, Y., Loh, P. C., and Blaabjerg, F. (2015). A Series-LC-Filtered Active Damper with Grid Disturbance Rejection for AC Power-Electronics-Based Power Systems. *IEEE Trans. Power Electron.* 30 (8), 4037–4041. doi:10.1109/TPEL.2014.2382477

Xiong, L., Liu, X., and Liu, Y. (2021). Decaying DC and Harmonic Components Detection for Absorbing Impact Load Currents in Weak Grids. *IEEE Trans. Power Deliv.* 36 (3), 1907–1910. June 2021. doi:10.1109/TPWRD.2020.3038077

Xiong, L., Liu, X., Liu, Y., and Zhuo, F. (2020). Modeling and Stability Issues of Voltage-Source Converter Dominated Power Systems: A Review. *Csee Jpes.* doi:10.17775/CSEEJPES.2020.03590

Xu, C. (2019). *Research on Control System for Single-phase Grid-Connected Inverter with LCL Filter*. Zhenjiang, China: Jiangsu University.

Yang, D., Ruan, X., and Wu, H. (2014). Impedance Shaping of the Grid-Connected Inverter with LCL Filter to Improve its Adaptability to the Weak Grid Condition. *IEEE Trans. Power Electron.* 29 (11), 5795–5805. Nov. 2014. doi:10.1109/TPEL.2014.2300235

Yu, C., Xu, H., Liu, C., Wang, Q., and Zhang, X. (2019). Modeling and Analysis of Common-Mode Resonance in Multi-Parallel PV String Inverters. *IEEE Trans. Energ. Convers.* 34 (1), 446–454. March 2019. doi:10.1109/TEC.2018.2877911

Zeng, J., Zhang, Z., and Qiao, W. (2014). An Interconnection and Damping Assignment Passivity-Based Controller for a DC-DC Boost Converter with a Constant Power Load. *IEEE Trans. Ind. Applicat.* 50 (4), 2314–2322. July-Aug. 2014. doi:10.1109/TIA.2013.2290872

Zhang, X., Yu, C., Liu, F., Li, F., and Xu, H. (2016). Overview on Resonance Characteristics and Resonance Suppression Strategy of Multi-Parallel Photovoltaic Inverters. *Chin. J. Electr. Eng.* 2 (1), 40–51. doi:10.23919/CJEE.2016.7933114

Conflict of Interest: The authors declare that the research was conducted in the absence of any commercial or financial relationships that could be construed as a potential conflict of interest.

frontiers in Energy Research

ORIGINAL RESEARCH
published: 24 January 2022
doi: 10.3389/fenrg.2021.795513

A Dynamic and Cooperative Control Strategy for Multi-Hybrid Energy Storage System of DC Microgrid Based on SOC

Hao Li*, Lijun Fu, Yan Zhang and Yiyong Xiong

National Key Laboratory of Science and Technology on Vessel Integrated Power System, Naval University of Engineering, Wuhan, China

With the increasingly serious crisis of fossil energy and environmental pollution, clean renewable energy becomes the inevitable choice of energy structure adjustment. The instability of output power of distributed renewable energy system greatly affects the operation of DC microgrid. The hybrid energy storage system (HESS) composed of High-Energy Battery (HEB) and High-Power Battery (HPB) can solve the above problems. Thus, this paper proposes a dynamic and cooperative control strategy for multi-HESS based on state of charge (SOC). Based on the traditional LPF method and droop control, this paper proposes a control strategy that requires no communication among multiple hybrid energy storage (HES) modules. This method can realize the stable control of HEB current, reduce the change times of HEB charging-discharging mode, prevent HEB from overcharging and overdischarging, prolong the service life of HEB and balance different energy storage SOC, so as to improve the operation stability and economy of DC microgrid. In addition, the method has certain robustness against sudden failures. Simulation and experiment results show the effectiveness of the proposed method.

Keywords: DC microgrid, distributed access, multi-hybrid energy storage system (multi-HESS), dynamic balance of SOC, renewable energy

Edited by:
Haoran Zhao,
Shandong University, China

Reviewed by:
Yuji Zeng,
Dalian Maritime University, China
Bo Wang,
University of New South Wales, Australia
Salman Hajiaghasi,
Shahid Beheshti University, Iran

****Correspondence:***
Hao Li
18351930189@163.com

Specialty section:
This article was submitted to Process and Energy Systems Engineering,
a section of the journal Frontiers in Energy Research

Received: *15 October 2021*
Accepted: *20 December 2021*
Published: *24 January 2022*

Citation:
Li H, Fu L, Zhang Y and Xiong Y (2022) A Dynamic and Cooperative Control Strategy for Multi-Hybrid Energy Storage System of DC Microgrid Based on SOC.
Front. Energy Res. 9:795513.
doi: 10.3389/fenrg.2021.795513

INTRODUCTION

The increasing penetration rate of renewable energy such as photovoltaic and wind power promotes the development of DC microgrid (Kathiresan et al., 2020; Zhou et al., 2020). Compared with AC microgrid, DC microgrid has no problems such as synchronization, reactive power transmission, harmonic current and converter loss, so it has attracted more and more attention (Rahimi and Ghadiriyan, 2019; Song et al., 2019).

However, due to the intermittent impact of renewable energy distributed generation and the short-term impact of some large loads, the stability of DC microgrid is severely challenged. Therefore, the corresponding energy storage system should be equipped to enhance the anti-interference ability of DC microgrid (Singh and Lather, 2021). On the one hand, combining High-Energy Battery (Such as lithium battery, lead-acid battery, sodium sulfur battery) with High-Power Battery (Such as supercapacitor, flywheel energy storage, super-magnetic energy storage) to form HESS is an important way of energy storage configuration based on the existing energy storage technology and satisfying the demand for DC microgrid (Kotra and Mishra, 2019; Mathews and Rajeev, 2020). On the other hand, in order to improve the access flexibility of energy storage system, and avoid the cost increase of using large-capacity converters in centralized energy storage system and the problems of operational reliability, distributed multi-HESS should be used (Su et al., 2018).

In terms of applying HESS to suppress grid-connected power fluctuations of distributed power generation, many scholars have studied various control strategies according to the characteristics of different types of energy storage, such as LPF method (Manandhar et al., 2015), fuzzy logic control (FLC) (Musilek et al., 2017; Mathews and Rajeev, 2020), wavelet decomposition method (Chiang et al., 2017), layered drooping control (Li et al., 2016; Zhang et al., 2018), virtual inertial control (Ming et al., 2017; Wang et al., 2017), machine learning (Chen et al., 2020) and so on. The above method mainly focuses on centralized HESS, when extended to distributed multi-HESS, they have some inapplicability. With the increase of using time, the differences among HES modules become larger and larger. If not restrained and controlled, the performance of HES modules will be seriously affected.

The concept of a virtual power rating was introduced in Literature (Hoang and Lee, 2019) to achieve accurate power sharing between batteries. However, this control method requires communication, and the scope of its application has certain limitations. In literature (Zhou et al., 2018), multi-HEB SOC is divided into five regions, and the whole system is divided into six working modes. However, this method may switch modes frequently under the circumstance of high-frequency fluctuation, leading to system instability. Most importantly, the above literatures mainly focus on the cooperative control of multiple energy storage units with the same medium and the same property.

In view of the collaborative control problem of distributed multi-HESS in DC microgrid, a power control strategy for multi-HESS was proposed based on the consensus protocol in literature (Chen et al., 2019). The communication was established among different energy storage units, and the SOC of different energy storage units was balanced by the consensus protocol, thus effectively solving the problem of balanced power distribution among multi-HESS. In literature (Wu et al., 2020), the control system automatically switches the operating mode based on the DC bus voltage, the supercapacitor voltage and the accumulator state. However, these methods still depend on external communication and are not suitable for situations requiring high reliability. To solve this problem, literature (Chen et al., 2016) proposed voltage-current droop control for HEB and voltage-change rate-current droop control for HPB. When the system only relies on the local information of the energy storage, it realizes the automatic power distribution between the components of different types of energy storage. However, this method is controlled by difference, and the deviation of bus voltage is large.

In order to solve the problem of high dependence on external communication in power distribution, this paper takes the island operation of DC microgrid as the research object, based on the traditional LPF method and droop control, proposes a SOC based power secondary distribution method without communication among HES modules. The control system automatically redistributes power according to SOC of different energy storage to achieve SOC balance. The smooth control of HEB current can be realized by using the characteristic that HPB voltage cannot change suddenly, so as to reduce the number of charging-discharging mode changes of HEB and extend the service life of HEB. The effectiveness of the proposed control strategy for distributed multi-hybrid energy storage module parallel system is verified by simulation and experiment.

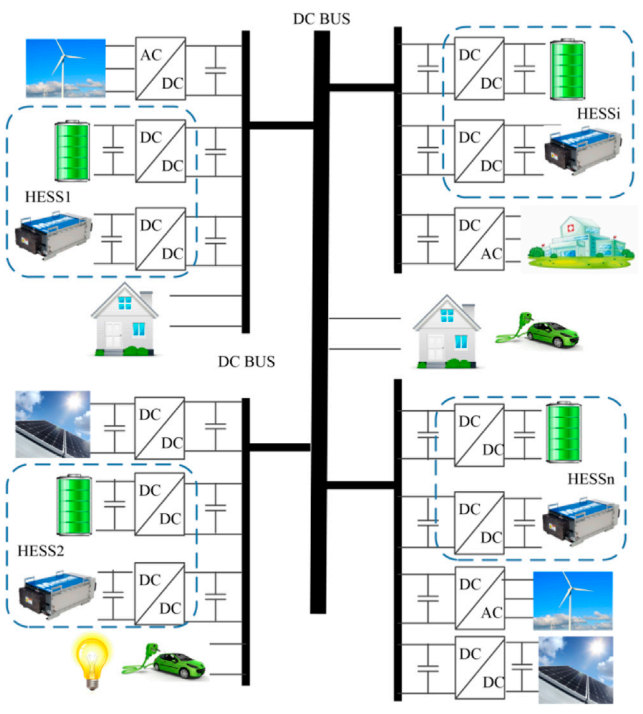

FIGURE 1 | Schematic diagram of DC microgrid with multi-HESS.

SYSTEM MODEL

The schematic diagram of DC microgrid with multi-HESS is shown in **Figure 1**, which mainly includes renewable energy power generation unit, AC/DC load and energy storage unit. Each part is a distributed structure, and each unit is connected to the DC bus through the corresponding converter. The power relationship of each part is as follows:

$$P_{\mathrm{Gen}} + P_{\mathrm{HESS}} = P_{\mathrm{Load}} \tag{1}$$

P_{Gen} is the power generated by renewable energy, P_{HESS} is the total power of multi-HESS, and P_{Load} is the total load power, including AC load and DC load.

In system analysis and calculation, the load of renewable energy power generation and power electronic equipment access can be equivalent to a controllable current source, which can be positive or negative. When it is positive, the renewable energy power generation is greater than the load; when negative, the load is greater than the renewable energy power generation.

HESS in **Figure 1** consists of High-Energy Battery and High-Power Battery. High-Energy Battery has high energy density and

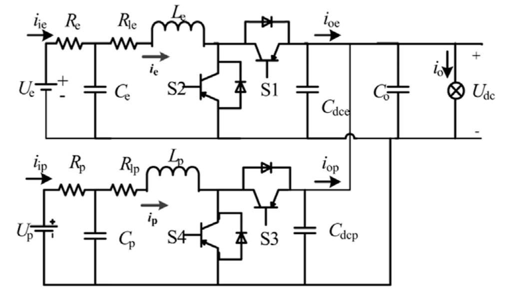

FIGURE 2 | Single HES module topology.

long storage time, but low power density and low cycle times. High-Power Battery has high power density and high cycle times, but low energy density and short energy storage time.

The single HES module topology adopted in this paper is shown in **Figure 2**. U_e and U_p, R_e and R_p are the voltage and resistance of High-Energy Battery and High-Power Battery respectively. U_{dc} is the DC bus voltage. The converter in the **Figure 2** is a bidirectional Buck-Boost converter. C_e and C_p, L_e and L_p are respectively the filter capacitance and inductance of the converters. R_{le} and R_{lp} are the internal resistance of respective inductors. S1-S4 are power tubes. C_{dce} and C_{dcp} are filter capacitors of converters respectively. C_o is the bus voltage regulator capacitor. (Subscript "e" means High-Energy Battery, and subscript "p" means High-Power Battery.)

COOPERATIVE CONTROL STRATEGY FOR MULTI-HESS

The overall architecture of multi-HESS collaborative control strategy is shown in **Figure 3**. The improved LPF control structure is adopted to regulate the power distribution within the single HES module. Based on the HPB SOC, the output power of HEB and HPB inside the module is adjusted to maintain the HPB SOC in a healthy range as far as possible. Among the multiple HES modules, the output of the whole module is regulated through the reference bus voltage adaptive regulator based on HEB SOC, so as to maintain the overall available capacity of each HES module relatively consistent. Since each HES module adopts V-I droop control, the coordinated control among HES modules does not require communication, which has high reliability and scalability, plug and play, and is convenient for installation and deployment.

Basic Control Structure

In microgrid, there are many control methods for converters, among which droop control is a widely used decentralized control method. It does not need communication, and only uses local information to realize the coordination control between distributed power supplies. It is suitable for DC microgrid with high reliability requirements, such as islands, reefs and ships, etc. Therefore, in order to maximize the autonomous control of each HES module, and enhance the system reliability and "plug and play" capability, the converter of HESS adopts droop control to stabilize the DC bus voltage.

V-I droop control (Li et al., 2016; Zhang et al., 2018) can be expressed as:

$$U_{o*} = U_{\mathrm{ref}} - R_V i_o \tag{2}$$

U_{ref} is the value of DC bus voltage under no load, U_{o*} is the specified value of converter output voltage after correction, and R_V is the droop coefficient.

The value of R_V is determined by **Eq. 3**:

$$R_V = (U_{\mathrm{ref}} - U_{\mathrm{omin}})/I_{\mathrm{omax}} \tag{3}$$

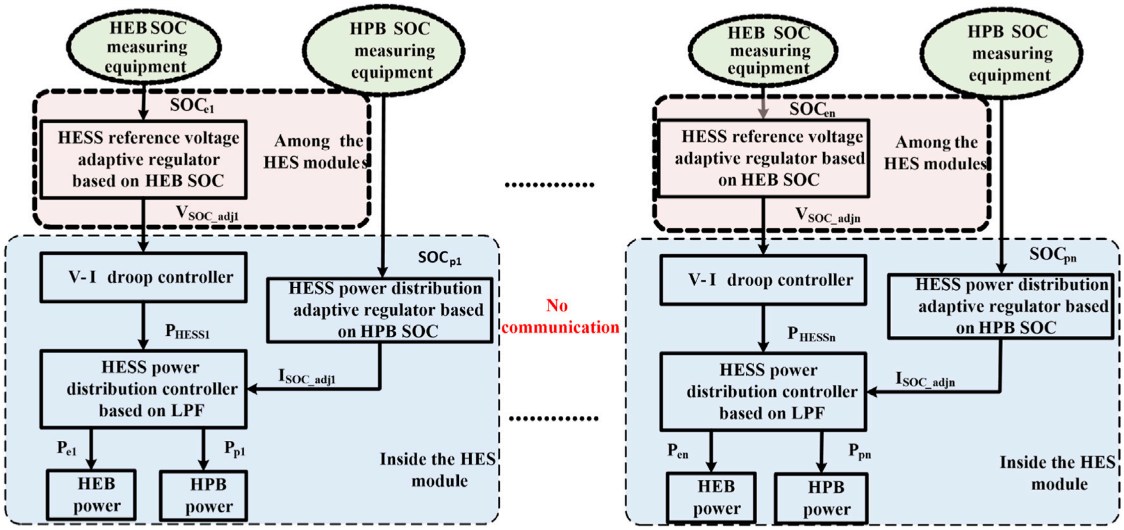

FIGURE 3 | The overall architecture of multi-HESS collaborative control strategy.

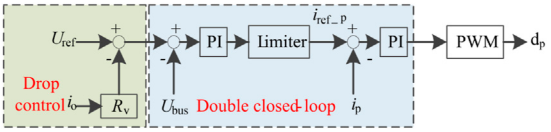

FIGURE 4 | The control structure diagram of High-Power Battery.

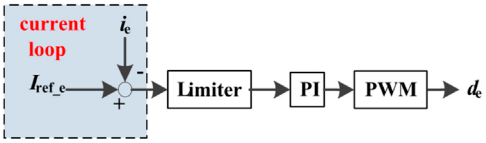

FIGURE 5 | The control structure diagram of High-Energy Battery.

U_{omin} is the allowable minimum steady state value of DC bus voltage, and I_{omax} is the maximum current value that DC/DC converter can output/input.

Ignoring the line impedance, the output current relationship of several DC/DC converters with V-I droop control is shown as follows.

$$R_{V1}i_{o1} = \ldots = R_{Vk}i_{ok} = \ldots = R_{Vn}i_{on} \tag{4}$$

The control structure of High-Power Battery consists of a droop control outer loop and a voltage and current double closed-loop, as shown in **Figure 4**. U_{ref}, U_{bus} and I_{ref_p} respectively represent the reference voltage of the bus, the actual voltage of the bus and the reference current of the High-Power Battery.

HEB is mainly used to follow the current instructions given by the power distribution controller, as shown in **Figure 5**. I_{ref_e} and i_e respectively represent the reference current and the actual current of the High-Energy Battery.

HES Module Control Based on LPF

Figure 6 is the control structure diagram of LPF-based. Reasonable power distribution method is the key to the stability and reliability of HESS. The traditional LPF method has less computation and parameters, and the control is simple. It can realize the power distribution based on frequency without any communication. Thus, this paper adopts LPF method for power distribution. On the basis of the traditional LPF control, the adaptive power redistribution module is added to regulate the output of different energy storage units in real time and balance the remaining electric quantity. The adaptive power redistribution modules represented by the two blue squares are described in detail in the next section.

iDC_{HESSi} is the sum of the current at the bus end of the DC/DC converter in the ith HES module, as shown in **Eq. 5**. i_{ei} and i_{pi} are the current of High-Energy Battery and High-Power Battery in the ith HES module, while d_{ei} and d_{pi} are the control signals of DC/DC converter. The limiter prevents the reference current from exceeding the converter maximum current.

$$iDC_{HESSi} = iDC_{ei} + iDC_{pi} \tag{5}$$

iDC_{ei} and iDC_{pi} are the current at the bus end of the DC/DC converter connected with High-Energy Battery and the High-Power Battery in the ith HES module.

Overall Idea of Adaptive SOC Layered Control

During the use of the HESS, there are different initial SOC and rated capacity of each energy storage unit connected by the converter in a certain working condition. If SOC are not considered, some energy storage units may overcharge or overdischarge, affecting the stable operation of the whole system. Therefore, the balanced control of energy storage SOC is the key to the stable and economical operation of HESS.

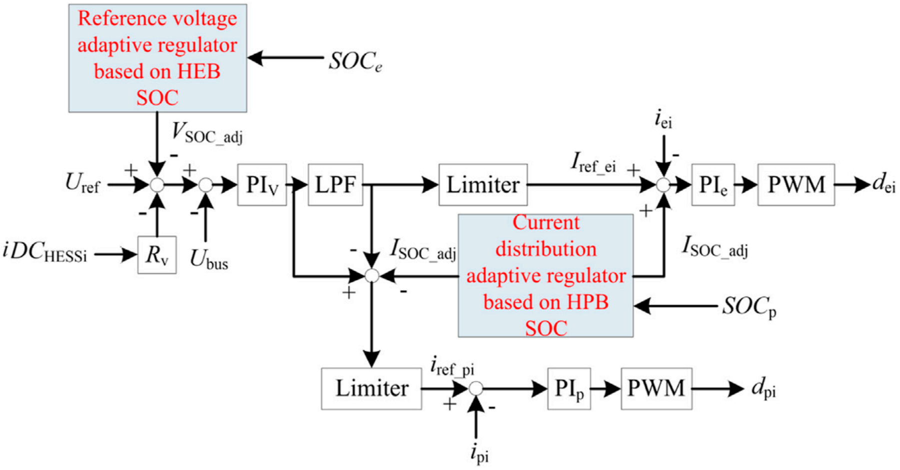

FIGURE 6 | The control structure diagram of LPF-based.

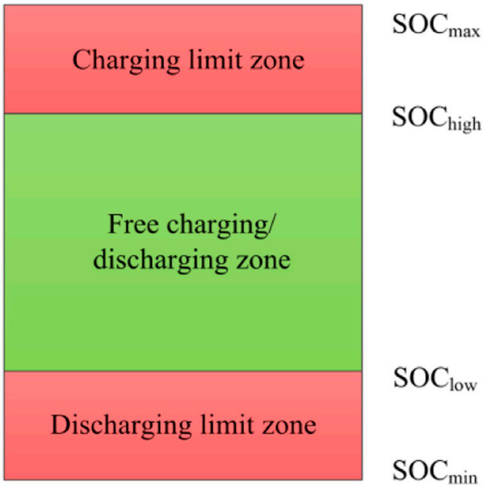

FIGURE 7 | SOC restriction classification of energy storage unit.

In order to prevent energy storage units from overcharging/overdischarging and frequent charging/discharging change, this paper adopts adaptive SOC layered control strategy. According to the SOC level of each energy storage unit, it is divided into different operating range as shown in **Figure 7**.

(1) Free charging/discharging zone. When $SOC_{low} \le SOC \le SOC_{high}$, the energy storage unit can conduct normal charge/discharge in accordance with the droop relationship, without imposing other control operations based on SOC.
(2) Charging limit zone. When $SOC_{high} \le SOC \le SOC_{max}$, the energy storage charging will be limited, and as SOC gets closer and closer to SOC_{max}, the charging limit becomes more and more serious until no more charging is allowed.
(3) Discharging limit one. When $SOC_{min} \le SOC \le SOC_{low}$, the energy storage discharging will be limited, and as SOC gets closer and closer to SOC_{min}, the discharging limit becomes more and more serious until no more discharging is allowed.

Adaptive SOC Control Method Inside the HES Module

In HESS, power fluctuation is usually divided into low frequency and high frequency, which are borne by High-Energy Battery and High-Power Battery respectively. The response speed of High-Power Battery is obviously faster than that of High-Energy Battery. DC microgrid is operating in island mode, the High-Power Battery will quickly compensate the power shortage in case of sudden change of load. When the High-Power Battery responds quickly, its SOC fluctuates. Then, the High-Energy Battery responds slowly to maintain the stability of the High-Power Battery SOC, achieving a dynamic adaptive balance. Through such a master-slave double structured with adaptive control, the system will gradually transfer the power deficiency firstly borne by the High-Power Battery to the High-Energy Battery, which can make the High-Energy Battery charge/discharge change relatively smooth, reduce the depth of the charge/discharge, prolong the life of High-Energy Battery, and avoid overcharge/overdischarge of High-Power Battery.

The ampere-hour integral method is used to calculate the SOC of High-Power Battery (Manandhar et al., 2015).

$$SOC_p = SOC_{p0} - \frac{1}{C_{Np}} \int_0^T \mu_p i_p \partial t \tag{6}$$

SOC_p is the real-time SOC of High-Power Battery, SOC_{p0} is the initial SOC, T is the running time, μ_p is the charging/discharging efficiency, i_p is the charging/discharging current, C_{Np} is the rated capacity of the HPB.

According to the layered control principle introduced in **Figure 5**, partial charging/discharging current of High-Power Battery is transferred to the High-Energy Battery. This paper designs I_{SOC_adj} that is the current of the High-Power Battery transferred to the High-Energy Battery based on the concept of partition operation as shown in **Figure 7**. The specific expression is shown in **Eq. 7**:

$$I_{SOC\_adj} = \begin{cases} \frac{SOC_p - SOC_{plow}}{SOC_{p\,min} - SOC_{plow}} I_{ref\_p} \left(SOC_{p\,min} \le SOC_p \le SOC_{plow}, V_{diff} > 0\right) \\ \frac{SOC_p - SOC_{phigh}}{SOC_{p\,max} - SOC_{phigh}} I_{ref\_p} \left(SOC_{phigh} \le SOC_p \le SOC_{p\,max}, V_{diff} < 0\right) \\ \qquad 0 \qquad (\text{othor}) \end{cases} \tag{7}$$

I_{ref_p} refers to the initial reference current of the High-Power Battery, and V_{diff} refers to the difference between the reference voltage and the actual voltage of the bus, which is used to characterize the charging and discharging state of energy storage unit at this time.

$$V_{diff} = U_{ref} - U_{bus} \tag{8}$$

$V_{diff} > 0$ means the energy storage unit is in charge, and $V_{diff} < 0$ means it is in discharge.

$$I_{ref\_p*} = I_{ref\_p} - I_{SOC\_adj} \tag{9}$$

$$I_{ref\_e*} = I_{ref\_e} + I_{SOC\_adj} \tag{10}$$

$I_{ref\_p^*}$ and $I_{ref\_e^*}$ represent the regulated High-Power Battery and High-Energy Battery reference current.

According to **Eqs 7–10**, when the High-Power Battery is in the charging limit zone, a certain proportion of the charging current is transferred to the High-Energy Battery according to the current SOC_p. The higher the SOC_p is, the larger the proportion of the transferred current will be. On the contrary, when the High-Power Battery is in the discharging limit zone, situation is the opposite. Finally, the High-Power Battery SOC is always in a reasonable operating range.

Among the HES Modules

High-Power Battery has low energy density. The adaptive regulating frequency of power among HES modules is much lower than that in a single HES module, so the High-Energy

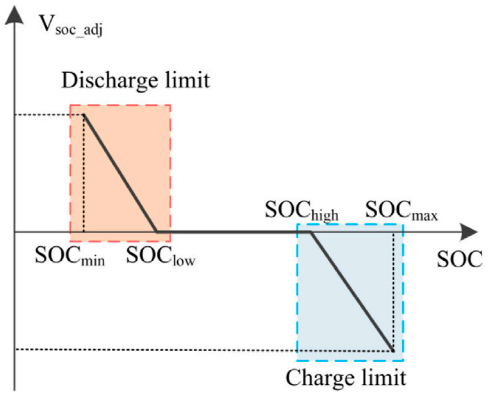

FIGURE 8 | Piecewise linearization regulation model based on SOC.

Battery SOC can be used as an indicator of the whole HES module available capacity.

The ampere-hour integral method is used to calculate the SOC of High-Energy Battery (Manandhar et al., 2015).

$$SOC_{\mathrm{e}} = SOC_{\mathrm{e0}} - \frac{1}{C_{\mathrm{Ne}}} \int_0^T \mu_{\mathrm{e}} i_{\mathrm{e}} \partial t \tag{11}$$

SOC_{e} is the real-time SOC of High-Energy Battery, SOC_{e0} is the initial SOC, T is the running time, μ_{e} is the charging/discharging efficiency, i_{e} is the charging/discharging current, C_{Ne} is the rated capacity of the HEB.

The proposed adaptive regulation strategy of reference voltage based on SOC is used to regulate the reference voltage of droop control model.

$$U_{\mathrm{bus}} = U_{\mathrm{ref}} - V_{\mathrm{SOC\_adj}} - R_{\mathrm{V}} i_{\mathrm{o}} \tag{12}$$

$V_{\mathrm{SOC\_adj}}$ is the reference voltage regulation. In order to improve the regulation performance of the strategy and avoid system oscillation caused by re-regulation of critical SOC, the layered regulation framework shown in **Figure 7** is adopted. The specific algorithm is as follows:

$$V_{\mathrm{SOC\_adj}} = \begin{cases} k\dfrac{SOC_{\mathrm{e}} - SOC_{\mathrm{elow}}}{SOC_{\mathrm{e\,min}} - SOC_{\mathrm{elow}}} & (SOC_{\mathrm{e\,min}} \le SOC_{\mathrm{e}} \le SOC_{\mathrm{elow}}, V_{\mathrm{diff}} > 0) \\ k\dfrac{SOC_{\mathrm{ehigh}} - SOC_{\mathrm{e}}}{SOC_{\mathrm{e\,max}} - SOC_{\mathrm{ehigh}}} & \left(SOC_{\mathrm{ehigh}} \le SOC_{\mathrm{e}} \le SOC_{\mathrm{e\,max}}, V_{\mathrm{diff}} < 0\right) \\ 0 & (\text{othor}) \end{cases} \tag{13}$$

k is the proportional amplification gain, which is determined by the maximum power of the converter and the requirement of the system on the regulation ability.

According to **Eqs 12, 13** when the SOC of an energy storage unit is in the charging limit zone, the reference voltage value of the DC/DC convert output should be increased to reduce the charging current of the energy storage unit. On the contrary, when the SOC is in the discharging limit zone, the situation is the opposite. Finally, SOC of different energy storage units tends to be relatively consistent. The specific process is shown in **Figure 8**, where the X-axis is the SOC of energy storage unit and the Y-axis is the regulator of the reference voltage value of the DC/DC convert output. The model is simple and easy to implement, and the switching between modes is relatively smooth.

STABILITY ANALYSIS AND CONTROL PARAMETER SELECTION

Stability Analysis Model

Because the control strategy proposed in this paper presents a coupling state inside a single HES module, it is difficult to adopt impedance analysis method. Thus, this paper intends to adopt small-signal analysis method to establish a mathematical analysis model for a single HES module as a whole.

Since resistive load increases system damping, constant power load (CPL) decreases system damping. So in the worst case, assume that the load on the system contains only CPL. Once the system is stable in the worst case, it is stable in all cases. Thus, in the study, the load will select the CPL, which can be expressed as:

$$i_{\mathrm{Load}} = \frac{P_{\mathrm{CPL}}}{u_{\mathrm{dc}}} \tag{14}$$

i_{Load} is load current, P_{CPL} is load power, u_{dc} is bus voltage transient value.

The small signal model can be obtained as follows:

$$\Delta i_{\mathrm{Load}} = \frac{P_{\mathrm{CPL}}}{U_{\mathrm{dc}}^2} \Delta u_{\mathrm{dc}} \tag{15}$$

U_{dc} is steady-state value of bus voltage at equilibrium point.

The state equation of the main circuit is shown in **Eq. 16**:

$$\begin{cases} L_{\mathrm{p}} \dfrac{di_{\mathrm{p}}}{dt} = u_{\mathrm{p}} - R_{\mathrm{p}} i_{\mathrm{p}} - (1 - d_{\mathrm{p}}) u_{\mathrm{dc}} \\ L_{\mathrm{e}} \dfrac{di_{\mathrm{e}}}{dt} = u_{\mathrm{e}} - R_{\mathrm{e}} i_{\mathrm{e}} - (1 - d_{\mathrm{e}}) u_{\mathrm{dc}} \\ C_{\mathrm{dc}} \dfrac{du_{\mathrm{dc}}}{dt} = (1 - d_{\mathrm{p}}) i_{\mathrm{p}} + (1 - d_{\mathrm{e}}) i_{\mathrm{e}} - \dfrac{P_{\mathrm{CPL}}}{u_{\mathrm{dc}}} \end{cases} \tag{16}$$

d_{e} and d_{p} are the duty cycle instantaneous value of HEB and HPB control signal.

The small signal model can be obtained as follows:

$$\begin{cases} L_{\mathrm{p}} \Delta \widehat{i_{\mathrm{p}}} = -R_{\mathrm{p}} \Delta i_{\mathrm{p}} - (1 - D_{\mathrm{p}}) \Delta u_{\mathrm{dc}} + U_{\mathrm{dc}} \Delta d_{\mathrm{p}} \\ L_{\mathrm{e}} \Delta \widehat{i_e} = -R_{\mathrm{e}} \Delta i_{\mathrm{e}} - (1 - D_{\mathrm{e}}) \Delta u_{\mathrm{dc}} + U_{\mathrm{dc}} \Delta d_{\mathrm{e}} \\ C_{\mathrm{dc}} \Delta \widehat{u_{dc}} = (1 - D_{\mathrm{p}}) \Delta i_{\mathrm{p}} - I_{\mathrm{p}} \Delta d_{\mathrm{p}} + (1 - D_{\mathrm{e}}) \Delta i_{\mathrm{e}} - I_{\mathrm{e}} \Delta d_{\mathrm{e}} - \dfrac{P_{\mathrm{CPL}}}{U_{\mathrm{dc}}^2} \Delta u_{\mathrm{dc}} \end{cases} \tag{17}$$

Eq. 17 is written in matrix form:

$$\Delta \widehat{x_1} = \mathbf{A}_1 \Delta x_1 + \mathbf{B}_1 \Delta u_1 \tag{18}$$
$$\Delta x_1 = \begin{bmatrix} \Delta i_{\mathrm{p}} & \Delta i_{\mathrm{e}} & \Delta u_{\mathrm{dc}} \end{bmatrix}^T \quad \Delta u_1 = \begin{bmatrix} \Delta d_{\mathrm{e}} & \Delta d_{\mathrm{p}} \end{bmatrix}^T$$

$$\mathbf{A}_1 = \begin{bmatrix} -\dfrac{R_\mathrm{p}}{L_\mathrm{p}} & 0 & \dfrac{D_\mathrm{p}-1}{L_\mathrm{p}} \\ 0 & -\dfrac{R_\mathrm{e}}{L_\mathrm{e}} & \dfrac{D_\mathrm{e}-1}{L_\mathrm{e}} \\ \dfrac{1-D_\mathrm{p}}{C_\mathrm{dc}} & \dfrac{1-D_\mathrm{e}}{C_\mathrm{dc}} & \dfrac{P_\mathrm{CPL}}{C_\mathrm{dc}U_\mathrm{dc}^2} \end{bmatrix} \quad \mathbf{B}_1 = \begin{bmatrix} 0 & \dfrac{U_\mathrm{dc}}{L_\mathrm{p}} \\ \dfrac{U_\mathrm{dc}}{L_\mathrm{e}} & 0 \\ \dfrac{-I_\mathrm{e}}{C_\mathrm{dc}} & \dfrac{-I_\mathrm{p}}{C_\mathrm{dc}} \end{bmatrix}$$

The small-signal model of the HEB control loop in **Figure 6**:

$$\hat{X}_\mathrm{v} = U_\mathrm{ref} - R_\mathrm{v}\left[(1-d_\mathrm{e})i_\mathrm{e} + (1-d_\mathrm{p})i_\mathrm{p}\right] - u_\mathrm{dc} - V_\mathrm{SOC\_adj} \tag{19}$$

$$I_\mathrm{DCref} = k_\mathrm{vi}X_\mathrm{v} + k_\mathrm{vp}\hat{X}_\mathrm{v} \tag{20}$$

$$I_\mathrm{ref\_e} = \frac{1}{1+T_\mathrm{f}s}I_\mathrm{DCref} \tag{21}$$

$$\hat{X}_\mathrm{ie} = \left(I_\mathrm{ref\_e} + \frac{U_\mathrm{p}}{U_\mathrm{dc}}I_\mathrm{SOC\_adj}\right)\frac{U_\mathrm{dc}}{U_\mathrm{e}} - i_\mathrm{e} \tag{22}$$

X_v and X_ie are the steady-state values of the input of the voltage loop and the current loop in the control loop of HEB. I_DCref is the total current reference value, $I_\mathrm{ref\_e}$ is the current reference value of HEB, T_f is the filtering time constant of the low-pass filter, k_vp and k_vi, k_ep and k_ei are the PI parameters of the voltage loop and the current loop in the control loop of HEB.

The deformation of **Eq. 21** can be obtained as follows:

$$\hat{I}_\mathrm{ref\_e} = \frac{1}{T_\mathrm{f}}I_\mathrm{DCref} - \frac{1}{T_\mathrm{f}}I_\mathrm{ref\_e} \tag{23}$$

The duty cycle of HEB converter can be expressed as:

$$d_\mathrm{e} = k_\mathrm{ei}X_\mathrm{ie} + k_\mathrm{ep}\hat{X}_\mathrm{ie} \tag{24}$$

The control loop of HPB can be expressed as:

$$I_\mathrm{ref\_p} = I_\mathrm{DCref} - I_\mathrm{ref\_e} \tag{25}$$

$$\hat{X}_\mathrm{ip} = \frac{U_\mathrm{dc}}{U_\mathrm{p}}I_\mathrm{ref\_p} - i_\mathrm{p} - \mathrm{I}_\mathrm{SOC\_adj} \tag{26}$$

X_ip is the steady-state input value of the current loop in the HPB control loop, $I_\mathrm{ref\_p}$ is the current reference value of the HPB, and k_pp and k_pi are the PI parameters of the current loop in the HPB control loop.

$$d_\mathrm{p} = k_\mathrm{pi}X_\mathrm{ip} + k_\mathrm{pp}\hat{X}_\mathrm{ip} \tag{27}$$

In combination with **Eqs 24**, **27**, the small-signal model can be written as:

$$\Delta u_1 = \mathbf{B}_{11}\Delta x_1 + \mathbf{B}_{12}\Delta x_2 + \mathbf{B}_{13}\Delta x_3 + \mathbf{B}_2\Delta u_1 \tag{28}$$

$$\Delta x_2 = \begin{bmatrix} \Delta X_\mathrm{v} & \Delta X_\mathrm{ie} & \Delta X_\mathrm{ip} & \Delta I_\mathrm{ref\_e} \end{bmatrix}^T$$

$$\Delta x_3 = \begin{bmatrix} \Delta V_\mathrm{SOC\_adj} & \Delta I_\mathrm{SOC\_adj} \end{bmatrix}^T$$

$$\mathbf{B}_{11} = \begin{bmatrix} 0 & -k_\mathrm{ep} & 0 \\ -k_\mathrm{pp}k_\mathrm{vp}R_\mathrm{v}\dfrac{U_\mathrm{dc}}{U_\mathrm{p}}(1-D_\mathrm{p}) - k_\mathrm{pp} & -k_\mathrm{pp}k_\mathrm{vp}R_\mathrm{v}\dfrac{U_\mathrm{dc}}{U_\mathrm{p}}(1-D_\mathrm{e}) & -k_\mathrm{pp}k_\mathrm{vp}\dfrac{U_\mathrm{dc}}{U_\mathrm{p}} \end{bmatrix}$$

$$\mathbf{B}_{12} = \begin{bmatrix} 0 & k_\mathrm{ei} & 0 & k_\mathrm{ep}\dfrac{\mathrm{U}_{dc}}{\mathrm{U}_e} \\ k_{pp}k_\mathrm{vi}\dfrac{U_\mathrm{dc}}{U_\mathrm{p}} & 0 & k_\mathrm{pi} & -k_\mathrm{pp}\dfrac{U_\mathrm{dc}}{U_\mathrm{p}} \end{bmatrix}$$

$$\mathbf{B}_{13} = \begin{bmatrix} 0 & k_\mathrm{ep}\dfrac{U_\mathrm{dc}}{U_\mathrm{e}} \\ -k_\mathrm{pp}k_\mathrm{vp}\dfrac{U_\mathrm{dc}}{U_\mathrm{p}} & -k_\mathrm{pp} \end{bmatrix}$$

$$\mathbf{B}_2 = \begin{bmatrix} 0 & 0 \\ k_\mathrm{pp}k_\mathrm{vp}R_\mathrm{v}I_\mathrm{e}\dfrac{U_\mathrm{dc}}{U_\mathrm{p}} & k_\mathrm{pp}k_\mathrm{vp}R_\mathrm{v}I_\mathrm{p}\dfrac{U_\mathrm{dc}}{U_\mathrm{p}} \end{bmatrix}$$

The state vector Δx_2 of the controller variable can be expressed as:

$$\Delta\widehat{x_2} = \mathbf{A}_{21}\Delta x_1 + \mathbf{A}_{22}\Delta x_2 + \mathbf{A}_{23}\Delta x_3 + \mathbf{B}_3\Delta u_1 \tag{29}$$

According to **Eqs 12–22** and **25**, **26**, we can get:

$$\mathbf{A}_{21} = \begin{bmatrix} -R_\mathrm{v}(1-D_\mathrm{p}) & -R_\mathrm{v}(1-D_\mathrm{e}) & -1 \\ 0 & -1 & 0 \\ -k_\mathrm{vp}R_\mathrm{v}(1-D_\mathrm{p})\dfrac{U_\mathrm{dc}}{U_\mathrm{p}} - 1 & -k_\mathrm{vp}R_\mathrm{v}(1-D_\mathrm{e})\dfrac{U_\mathrm{dc}}{U_\mathrm{p}} & -k_\mathrm{vp}\dfrac{U_\mathrm{dc}}{U_\mathrm{p}} \\ \dfrac{-k_\mathrm{vp}R_\mathrm{v}(1-D_\mathrm{p})}{T_\mathrm{f}} & \dfrac{-k_\mathrm{vp}R_\mathrm{v}(1-D_\mathrm{e})}{T_\mathrm{f}} & \dfrac{-k_\mathrm{vp}}{T_\mathrm{f}} \end{bmatrix}$$

$$\mathbf{A}_{22} = \begin{bmatrix} 0 & 0 & 0 & 0 \\ 0 & 0 & 0 & \dfrac{U_\mathrm{dc}}{U_\mathrm{e}} \\ k_\mathrm{vi}\dfrac{U_\mathrm{dc}}{U_\mathrm{p}} & 0 & 0 & -\dfrac{U_\mathrm{dc}}{U_\mathrm{p}} \\ \dfrac{k_\mathrm{vi}}{T_\mathrm{f}} & 0 & 0 & \dfrac{-1}{T_\mathrm{f}} \end{bmatrix} \mathbf{A}_{23} = \begin{bmatrix} -1 & 0 \\ 0 & \dfrac{U_\mathrm{p}}{U_\mathrm{e}} \\ -k_\mathrm{vp}\dfrac{U_\mathrm{dc}}{U_\mathrm{p}} & -1 \\ -\dfrac{k_\mathrm{vp}}{T_\mathrm{f}} & 0 \end{bmatrix}$$

$$\mathbf{B}_3 = \begin{bmatrix} R_\mathrm{v}I_\mathrm{e} & R_\mathrm{v}I_\mathrm{p} \\ 0 & 0 \\ k_\mathrm{vp}R_\mathrm{v}I_\mathrm{e}\dfrac{U_\mathrm{dc}}{U_\mathrm{p}} & k_\mathrm{vp}R_\mathrm{v}I_\mathrm{p}\dfrac{U_\mathrm{dc}}{U_\mathrm{p}} \\ \dfrac{k_\mathrm{vp}R_\mathrm{v}I_\mathrm{e}}{T_\mathrm{f}} & \dfrac{k_\mathrm{vp}R_\mathrm{v}I_\mathrm{p}}{T_\mathrm{f}} \end{bmatrix}$$

The upper control input vector Δx_3 can be expressed as:

$$\Delta\hat{x}_3 = \mathbf{A}_{31}\Delta x_1 + \mathbf{A}_{32}\Delta x_2 + \mathbf{A}_{33}\Delta x_3 + \mathbf{B}_4\Delta u_1 \tag{30}$$

The energy storage unit has an integral relation between SOC and time. Despite the existence of such an integral relationship, the present state value of the SOC is calculated and output by sampling, so the changes of the output current and voltage are difficult to reflect the changes of the SOC in very short time. Therefore, the SOC is only treated as an input signal in small signal modeling. At the same time, considering that the change of SOC is not as rapid

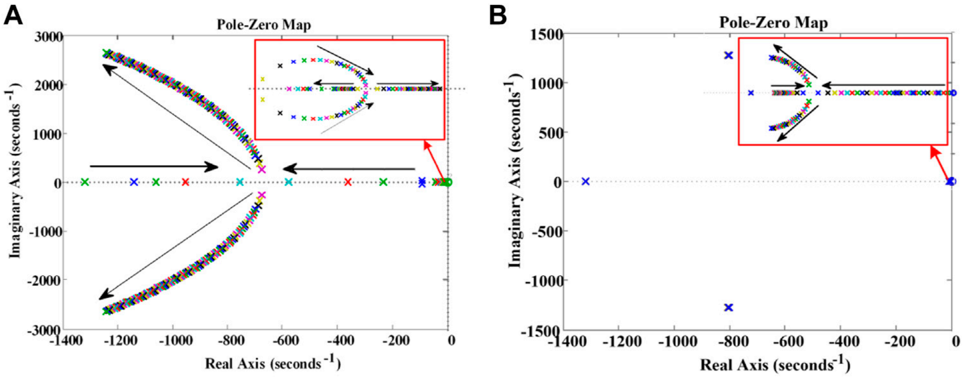

FIGURE 9 | Closed-loop pole distribution of voltage outer loop PI parameters: **(A)** The scale parameter k_{vp} increases from 0.1 to 20; **(B)** The integral parameter k_{vi} increases from 0.1 to 50).

TABLE 1 | The simulation parameters.

Parameters	Value
Bus voltage rating/V	400
Energy storage terminal filter capacitance C_e, C_p/μF	20
Bus terminal filter capacitance C_{dce}, C_{dcp}, C_o/μF	940
Filter inductance L_e, L_p/H	0.001
Filter inductance internal resistance R_e, R_p, R_{le}, R_{lp}/Ω	0.01
Bus voltage regulator capacity C_e, C_p/μF	4000
Filtering time constant/T_f	1
NO.1,2,3 High-Energy Battery rated capacity/Ah	15, 13, 12
NO.1,2,3 High-Power Battery rated capacity/Ah	5, 5, 4

TABLE 2 | PI parameter.

Parameter name	Value	Parameter name	Value
k_{vp}	5	k_{vi}	35
k_{ep}	0.003	k_{ei}	0.4
k_{pp}	0.003	k_{pi}	1

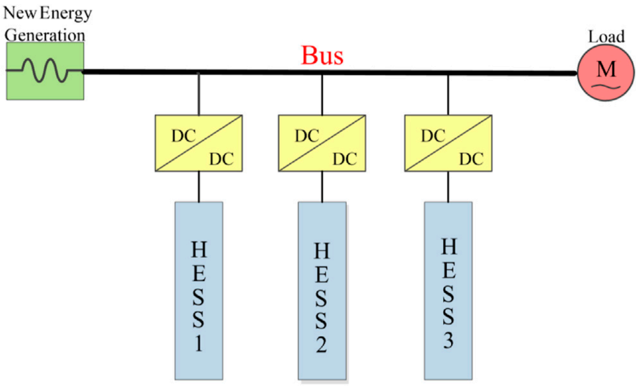

FIGURE 10 | The overall simulation model.

as the change of voltage and current, delay sampling strategy is generally adopted, and LPF can be used to replace short delay.

As V_{SOC_adj} and I_{SOC_adj} are both piecewise functions in the optimization of upper power allocation considering SOC. In the stability analysis, only the case with the worst stability is considered, that is, they are all in the discharge limit region:

$$V_{SOC\_adj} = \frac{w}{w+s} k \frac{SOC_e - SOC_{elow}}{SOC_{e\min} - SOC_{elow}} \left(SOC_{e\min} \le SOC_e \le SOC_{elow}, V_{diff} > 0\right) \tag{31}$$

$$I_{SOC\_adj} = \frac{w}{w+s} \frac{SOC_p - SOC_{plow}}{SOC_{p\min} - SOC_{plow}} I_{pref} \left(SOC_{p\min} \le SOC_p \le SOC_{plow}, V_{diff} > 0\right) \tag{32}$$

Small signal transformation is performed for **Eqs 31, 32**:

$$\Delta \hat{V}_{SOC\_adj} = -w \Delta V_{SOC\_adj} \left(SOC_{e\min} \le SOC_e \le SOC_{elow}, V_{diff} > 0\right) \tag{33}$$

$$\Delta \hat{I}_{SOC\_adj} = \begin{cases} w \dfrac{SOC_p - SOC_{plow}}{SOC_{p\min} - SOC_{plow}} \Delta I_{pref} - w \Delta I_{SOC\_adj} \\ \left(SOC_{p\min} \le SOC_p \le SOC_{plow}, V_{diff} > 0\right) \end{cases} \tag{34}$$

w is the cutoff frequency of LPF.

In summary, the following formula can be obtained by combining **Eqs 19, 20** and **25**:

$$\mathbf{A}_{31} = \begin{bmatrix} 0 & 0 & 0 \\ -wMk_{vp}R_v(1-D_p) & -wMk_{vp}R_v(1-D_e) & -wMk_{vp} \end{bmatrix}$$

$$\mathbf{A}_{32} = \begin{bmatrix} 0 & 0 & 0 & 0 \\ wMk_{vi} & 0 & 0 & -wM \end{bmatrix} \quad \mathbf{A}_{33} = \begin{bmatrix} -w & 0 \\ -wMk_{vp} & -w \end{bmatrix}$$

$$\mathbf{B}_4 = \begin{bmatrix} 0 & 0 \\ wMk_{\mathrm{vp}}R_{\mathrm{v}}I_{\mathrm{e}} & wMk_{\mathrm{vp}}R_{\mathrm{v}}I_{\mathrm{p}} \end{bmatrix} \quad M = \frac{SOC_{\mathrm{p}} - SOC_{\mathrm{plow}}}{SOC_{\mathrm{p\,min}} - SOC_{\mathrm{plow}}}$$

By comprehensively considering **Eqs 18**, **29**, **30**, it can be obtained:

$$\begin{bmatrix} \Delta\dot{x}_1 \;. \\ \Delta\dot{x}_2 \;. \\ \Delta\dot{x}_3 \;. \end{bmatrix} = \begin{bmatrix} \mathbf{X}_{11} & \mathbf{X}_{12} & \mathbf{X}_{13} \\ \mathbf{X}_{21} & \mathbf{X}_{22} & \mathbf{X}_{23} \\ \mathbf{X}_{31} & \mathbf{X}_{32} & \mathbf{X}_{33} \end{bmatrix} \times \begin{bmatrix} \Delta x_1 \\ \Delta x_2 \\ \Delta x_3 \end{bmatrix} \quad \begin{cases} \mathbf{X}_{11} = \mathbf{A}_1 + \mathbf{B}_1(1-\mathbf{B}_2)^{-1}\mathbf{B}_{11} \\ \mathbf{X}_{12} = \mathbf{B}_1(1-\mathbf{B}_2)^{-1}\mathbf{B}_{12} \\ \mathbf{X}_{13} = \mathbf{B}_1(1-\mathbf{B}_2)^{-1}\mathbf{B}_{13} \\ \mathbf{X}_{21} = \mathbf{A}_{21} + \mathbf{B}_3(1-\mathbf{B}_2)^{-1}\mathbf{B}_{11} \\ \mathbf{X}_{22} = \mathbf{A}_{22} + \mathbf{B}_3(1-\mathbf{B}_2)^{-1}\mathbf{B}_{12} \\ \mathbf{X}_{23} = \mathbf{A}_{23} + \mathbf{B}_3(1-\mathbf{B}_2)^{-1}\mathbf{B}_{13} \\ \mathbf{X}_{31} = \mathbf{A}_{31} + \mathbf{B}_4(1-\mathbf{B}_2)^{-1}\mathbf{B}_{11} \\ \mathbf{X}_{32} = \mathbf{A}_{32} + \mathbf{B}_4(1-\mathbf{B}_2)^{-1}\mathbf{B}_{12} \\ \mathbf{X}_{33} = \mathbf{A}_{33} + \mathbf{B}_4(1-\mathbf{B}_2)^{-1}\mathbf{B}_{13} \end{cases} \tag{35}$$

Stability Analysis and Control Parameter Selection

Figure 9 is the closed-loop pole distribution diagram of **Eq. 35** when different PI parameters are selected (the black arrow indicates the increasing direction of the parameters taken). SOC limited boundaries of High-Energy Batteries and High-Power Batteries $\mathrm{SOC}_{\mathrm{min}}$, $\mathrm{SOC}_{\mathrm{max}}$, $\mathrm{SOC}_{\mathrm{low}}$, $\mathrm{SOC}_{\mathrm{high}}$ respectively are 50, 70, 56, 63, and 40, 80, 55, 65%. Other specific simulation parameters are shown in **Table 1**.

It can be seen from **Figure 9** that when k_{vi} and k_{vp} change in the specified range, the system pole is always on the left of the Y-axis, so the system is always stable. As shown in **Figure 9A**, the poles close to the imaginary axis are conjugate poles when the voltage outer loop proportionality parameter k_{vp} is less than 6, and it is an underdamped system. At the same time, with the increase of k_{vp}, the damping ratio of the system gradually increases, and the overshoot decreases. Therefore, when $k_{\mathrm{vp}} = 5$, the overshoot of the system is small and the response speed is fast. As shown in **Figure 9B**, when k_{vi} is greater than 30, the closed loop dominates the pole conjugate. At this time, the system has good dynamic response characteristics. As k_{vi} continues to increase, the peak value of the system decreases, but the response time increases. Therefore, the trade-off is $k_{\mathrm{vi}} = 35$.

The same method is adopted for other control parameters and their stability analysis. The PI parameters of the proposed method are obtained and summarized as shown in **Table 2**.

SIMULATION AND EXPERIMENT

In this paper, PSCAD/EMTDC software will be used for simulation. In order to fully verify the performance of the proposed HESS control strategy, three groups of HESS will be set up. HESS1 is overdischarged, HESS2 is in the free charging/discharging zone, and HESS3 is overcharged. The structure of each group is shown in **Figure 2**. The overall simulation model is shown in **Figure 10**. In this simulation, lithium battery is used for HEB and supercapacitor is used for HPB. Simulation parameters are shown in **Tables 1**, **2**.

Step Load Change

In this case, the response of the system to consecutive step load changes is simulated to observe the net power decomposition between High-Energy Battery and High-Power Battery. The specific waveform is shown in **Figure 11A**. At 10 s, the load current increases from 50 to 125 A, then drops back to 50 A at 25 s, and finally jumps to 150 A at 50 s. The initial SOC of three High-Energy Batteries and High-Power Batteries are 55, 62, 67, 60, 70%. To verify the effectiveness of the proposed strategy, it will be compared with the LPF-based HESS control method without SOC regulation, that is, the control method shown in **Figure 5** removes the SOC regulation module represented by the blue square. The results are shown in **Figures 11B–K**.

It can be seen from **Figures 11B,C** that both methods can effectively cope with the step change of load and make the deviation of bus voltage stable within 2.5%. However, the voltage deviation rate of the proposed method is reduced by about 50%.

Figures 11D–G shows that SOC of each energy storage unit cannot be balanced without SOC regulation. Considering the practical differences of energy storage units, SOC difference will become larger and larger, eventually leading to the overcharge or overdischarge of some energy storage units. However, under the SOC coordinated control method proposed in this paper, SOC can tend to be consistent which can effectively prevent some energy storage units from overcharging/overdischarging, and improve the stability and reliability of the system.

According to the comparison among **Figures 11H–K**, it can be seen that under the SOC regulation, the energy storage unit with SOC higher than the limit increases its output power when discharging. The energy storage unit with SOC lower than the limit decreases output power when discharging. Under this regulation, SOC of each energy storage unit will gradually tend to be consistent. At the same time, High-Power Battery quickly responds to sudden load change, then gradually falls back, and gradually transfers the power shortage to the High-Energy Battery. In other words, frequency distribution is realized in the HESS, and the output/input current of the High-Energy Battery is smoothed, which effectively extends the service life of the High-Energy Battery and improves the economy and reliability of the energy storage system.

Random Fluctuations in Renewable Energy Generation

Considering the random fluctuation of renewable energy, the response characteristics of High-Energy Battery and High-Power Battery in the control strategy proposed in this paper are studied. The initial state of each energy storage unit is consistent with the previous section. **Figure 12** shows the output curve of renewable energy adopted in simulation, the power response and SOC changing of High-Energy Batteries and High-Power Batteries.

From **Figures 12B,C**, it can be seen that multi-HESS can effectively make real-time power compensation in the case of

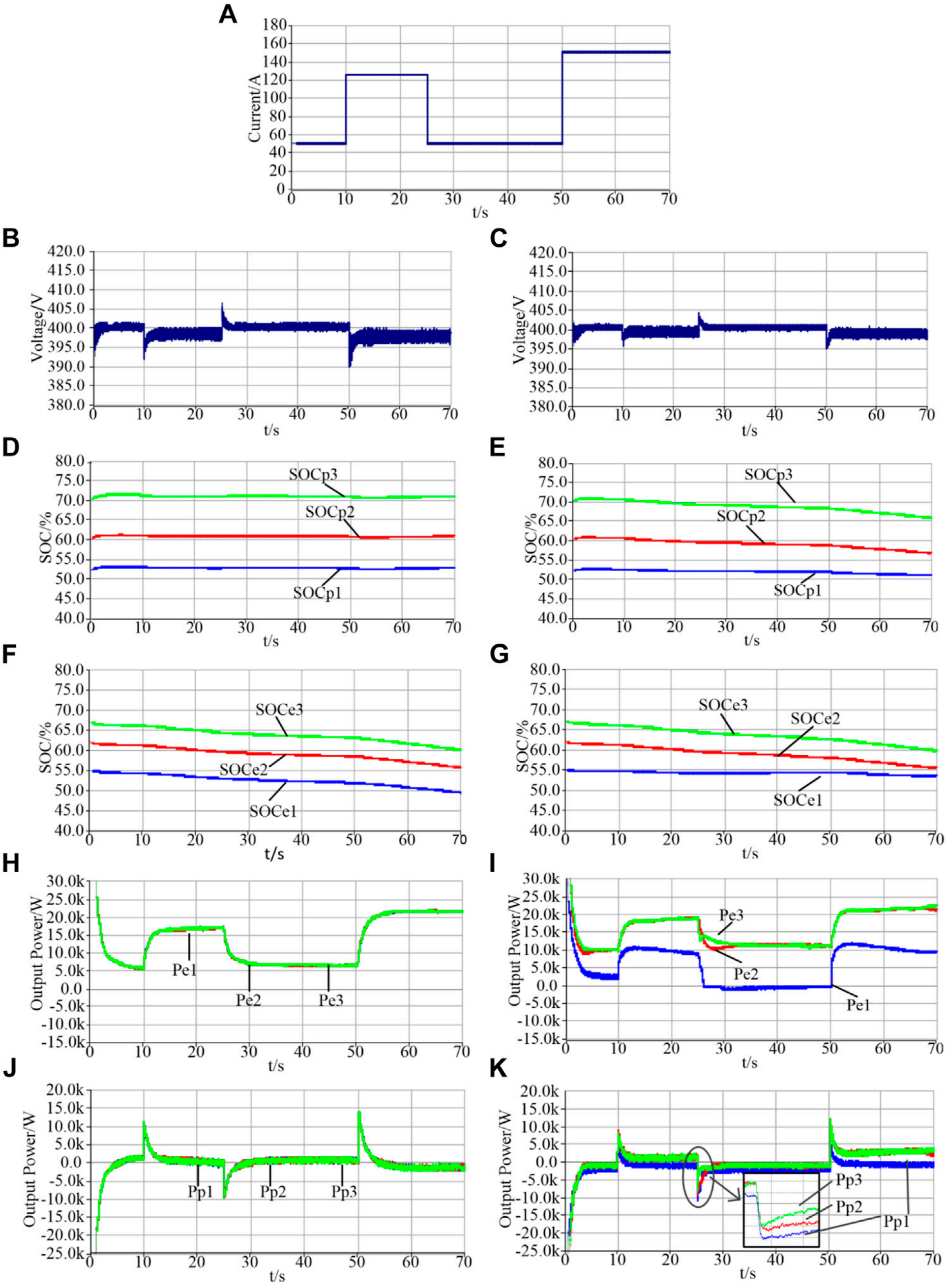

FIGURE 11 | Simulation results under step load condition: **(A)** Load current; **(B)** Bus voltage-No SOC regulation; **(C)** Bus voltage-SOC regulation; **(D)** High-Power Battery SOC-No SOC regulation; **(E)** High-Power Battery SOC-SOC regulation; **(F)** High-Energy Battery SOC-No SOC regulation; **(G)** High-Energy Battery SOC-SOC regulation; **(H)** The output power of High-Energy Battery-No SOC regulation; **(I)** The output power of High-Energy Battery-SOC regulation; **(J)** The output power of High-Power Battery-No SOC regulation; **(K)** The output power of High-Power Battery-SOC regulation).

random fluctuation of renewable energy. The partial power compensated by the High-Energy Batteries is more gradual than that of the High-Power Batteries and achieves the expected frequency distribution effect.

At the same time, from **Figures 12D,E**, the output of different High-Energy Battery and High-Power Battery varies due to SOC differences and the energy storage output power with high SOC is larger, so that SOC tends to be consistent. Moreover, due to the setting of free charging/discharging zone, the regulation of energy storage unit is smoother, reducing the number of charging/discharging mode changes, and effectively extending the service life of energy storage unit. Simulation results show that the proposed control strategy can ensure the

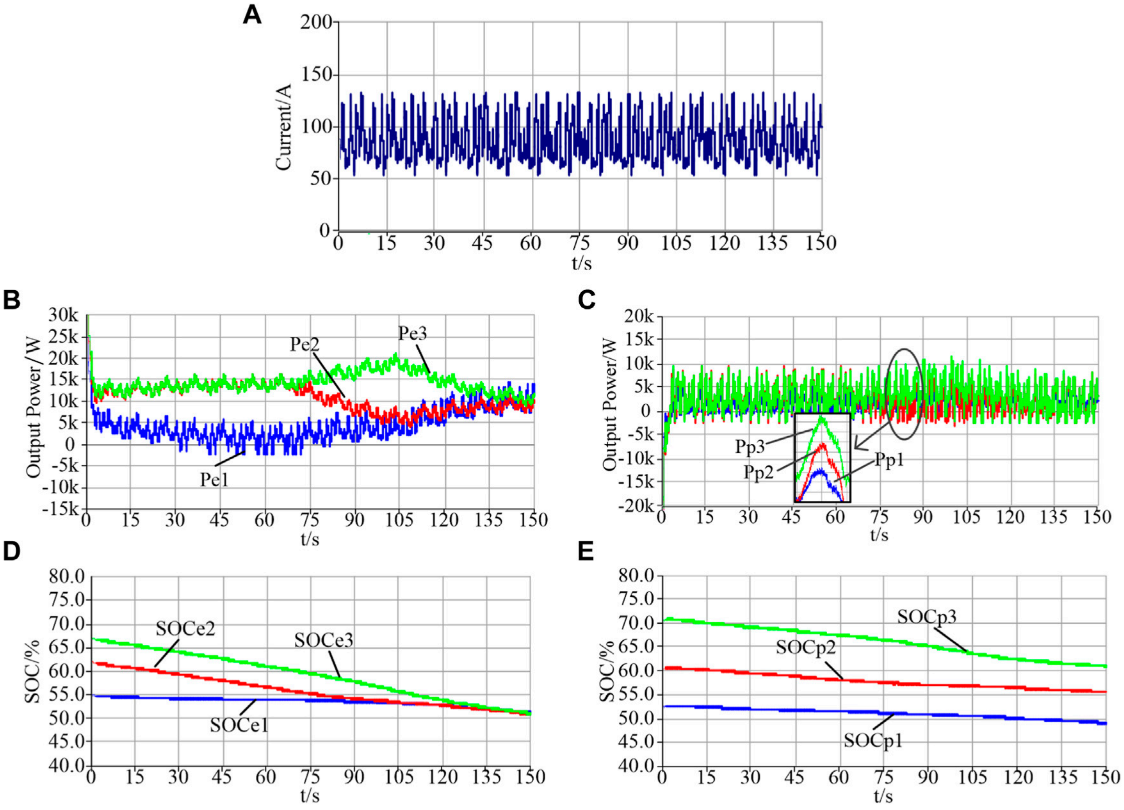

FIGURE 12 | Simulation results under random load condition: **(A)** Random power of renewable energy-Random output of renewable energy; **(B)** Output power of High-Energy Battery; **(C)** Output power of High-Power Battery; **(D)** High-Energy Battery SOC; **(E)** High-Power Battery SOC).

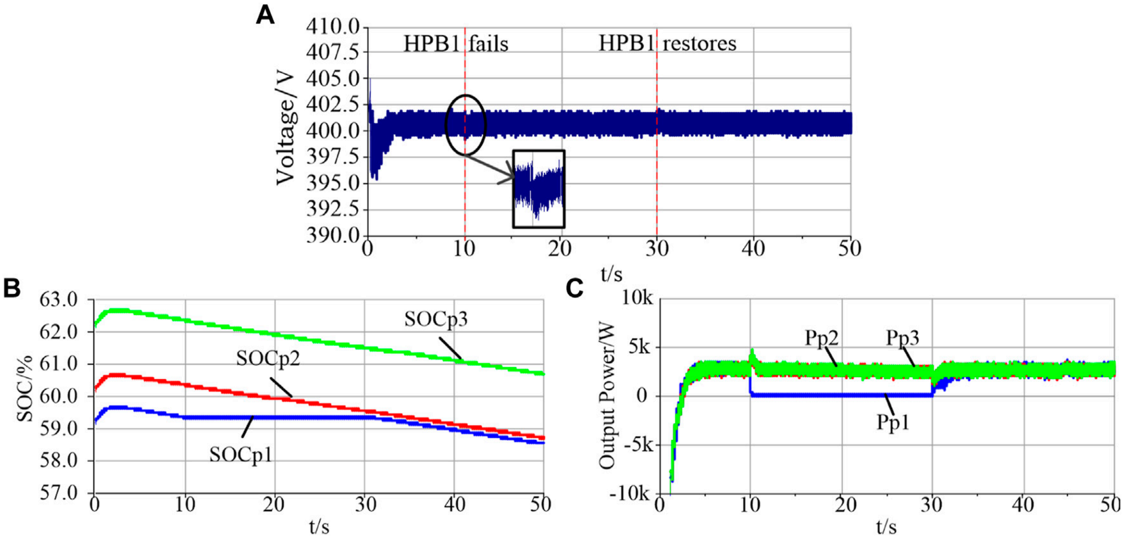

FIGURE 13 | Simulation results when No. 1 High-Power Battery fault: **(A)** Bus voltage; **(B)** High-Power Battery SOC; **(C)** Output power of High-Power Battery).

reasonable operation of the multi-HESS when the random fluctuations of renewable energy are taken into account.

Failure of a High-Power Battery

It is assumed that a High-Power Battery breaks down and runs out, and all energy storage units are in free charging/discharging

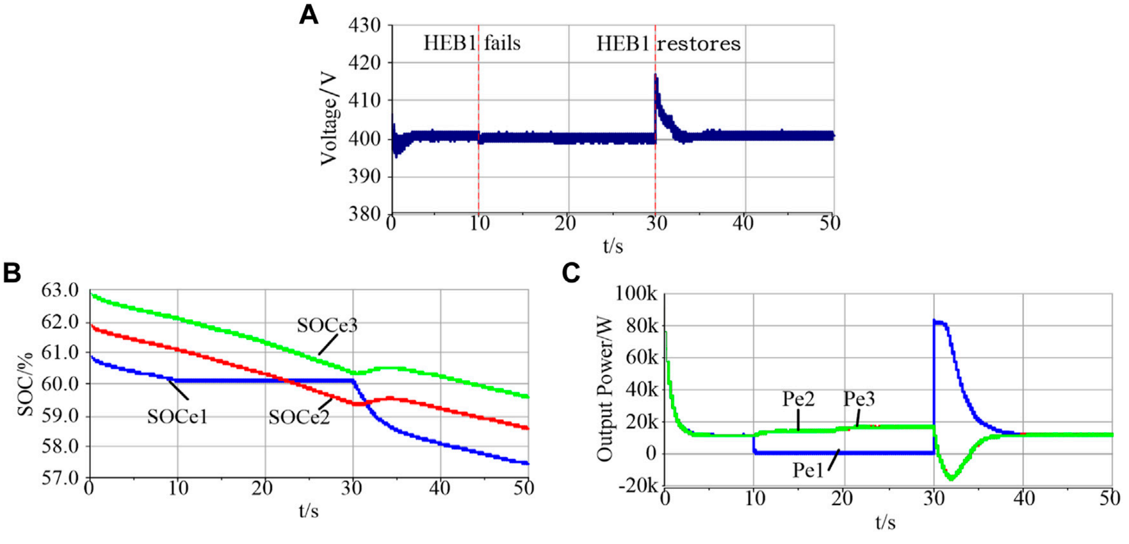

FIGURE 14 | Simulation results when No. 1 High-Energy Battery fault: **(A)** Bus voltage; **(B)** High-Energy Battery SOC; **(C)** Output power of High-Energy Battery).

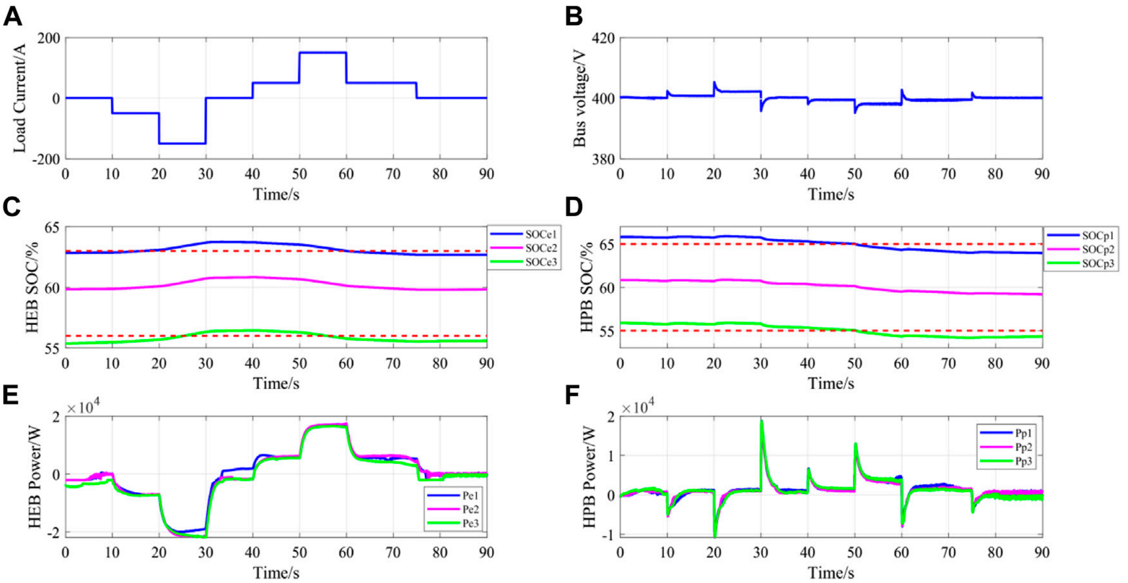

FIGURE 15 | Experimental results of DC microgrid in step load change: **(A)** Load current; **(B)** Bus voltage; **(C)** High-Energy Battery SOC; **(D)** High-Power Battery SOC; **(E)** Output power of High-Energy Battery; **(F)** Output power of High-Power Battery).

zone, so as to verify the stability of the proposed control strategy. Under normal operating conditions, the system is connected to 100 A load. At 10 s, No. 1 High-Power Battery fails, exits operation, and cuts off relevant communication. At 30 s, No. 1 High-Power Battery resumes and puts into operation. The simulation results are shown in **Figure 13**.

Figure 13A shows that when it comes to 10 and 30 s, the cut and input of No. 1 High-Power Battery only causes a small impact on the bus voltage. **Figure 13B** shows that SOC of No. 1 High-Power Battery remains unchanged after failure, while the decline rate of other High-Power Battery increases. After the No. 1 High-Power Battery is repaired and put into operation in 30 s, the SOC of the three groups of High-Power Battery is still in the free charging/discharging zone, so it quickly keeps in sync. It can be seen from **Figure 13C** that the other two groups of High-Power Battery respond quickly at the moment of the cut and input of No. 1 High-Power Battery. Simulation results show that the remaining energy storage under the proposed control strategy can still work normally and respond to the expected power when some High-Power Batteries fail.

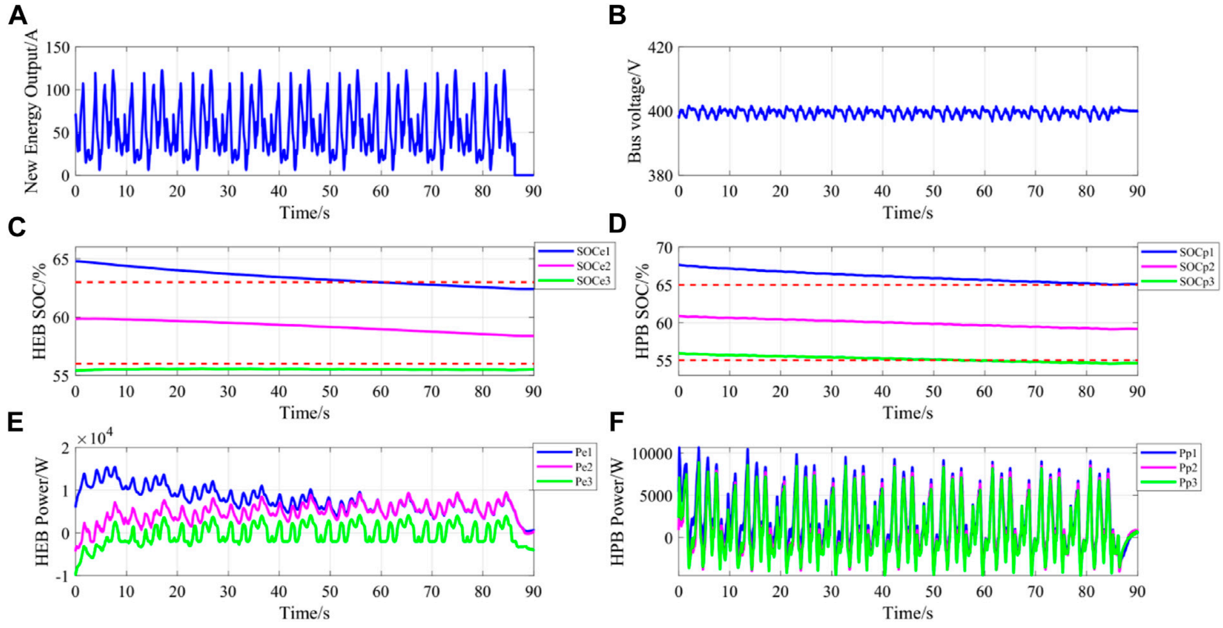

FIGURE 16 | Experimental results of DC microgrid in renewable energy generation: **(A)** Renewable energy output; **(B)** Bus voltage; **(C)** High-Energy Battery SOC; **(D)** High-Power Battery SOC; **(E)** Output power of High-Energy Battery; **(F)** Output power of High-Power Battery).

Failure of a High-Energy Battery

Under the same condition of **section 4.2**, replace the fault unit with No. 1 High-Energy Battery. The simulation results are shown in **Figure 14**.

The results in **Figure 14** are similar to **Figure 13**, but more volatile. The main reason is that the High-Energy Battery has to bear more power in normal operation, and the impact on the system during cutting and input is also greater. But bus voltage deviation is still within a reasonable range, it's not more than 5% and soon returns to the normal reference voltage. The proposed method is robust to partial energy storage element faults.

Experimental Verification and Result Analysis

A microgrid model was established in the laboratory for verification. The analog diesel generator cabinet and analog wind generator cabinet are used as the power supply, the switching frequency of the energy storage bidirectional DC/DC converter is 10 kHz, the load is a programmable DC load, HEB is lithium iron phosphate battery, HPB is supercapacitor and other control parameters are the same as the simulation model. The experimental results are shown in **Figures 15**, **16**.

It can be seen from **Figures 15**, **16A** and **Figures 15**, **16B** that after power fluctuation, the bus voltage can be quickly restored to stability with small voltage fluctuation. **Figures 15**, **16E** and **Figures 15**, **16F** show the output power changes of HEB and HPB. As can be seen from the figure, the change of HEB is relatively slow, while the response of HPB to power fluctuation is fast, which is in line with the design goal of the control strategy. Combined with the SOC change curves in **Figures 15**, **16C** and **Figures 15**, **16D**, it can be seen that the power curve of energy storage when SOC is higher than the limited range moves upward, that is, the discharge power is higher while the charge power is lower. When SOC is below the limit range, the power curve of energy storage moves downward, that is, the discharge power is lower while the charge power is higher. This shows that the proposed control strategy can effectively carry out SOC balancing.

CONCLUSION

Aiming at the problem that the traditional distributed multi-HESS cooperative control method of DC microgrid relies heavily on external communication, a communication free dynamic cooperative control strategy based on SOC is proposed. The simulation and experiment results show that the proposed control strategy has the following advantages: *1*) being able to adjust the power distribution within HES module and among HES modules meet the needs of large-scale distributed new energy generating sets and loads; *2*) using HPB to respond to the high frequency component of the bus voltage fluctuation, and using HEB to compensate the insufficient power of HPB to realize the optimization of HEB charge-discharge current, so as to effectively reduce the number of HEB charge-discharge mode change and prolong its service life; *3*) reducing the dependency on communication among HES modules, thus improving the reliability of DC microgrid in island mode. However, this method does not take into account the impact of energy storage element aging, such as SOC estimation errors and reduced maximum output power due to declining energy storage life. How to consider these aspects under the condition of minimal communication requirements will be the focus of future research.

DATA AVAILABILITY STATEMENT

The raw data supporting the conclusions of this article will be made available by the authors, without undue reservation.

AUTHOR CONTRIBUTIONS

HL completed the theoretical derivation, modeling and simulation, data analysis and full text drafting of the project. YZ and YX provided research direction, theoretical guidance and paper revision. LF provided theoretical guidance, financial and site support.

FUNDING

This work was supported by the National Natural Science Foundation of China under Grant 51877211.

REFERENCES

Chen, H., Zhang, Z., Guan, C., and Gao, H. (2020). Optimization of Sizing and Frequency Control in Battery/supercapacitor Hybrid Energy Storage System for Fuel Cell Ship. *Energy* 197, 117285. doi:10.1016/j.energy.2020.117285

Chen, M., Zhao, X., Jin, X., Liu, J., and Wu, X. (2016). Research on Parallel Technology of Compound Energy Storage Device in DC Microgrid [J]. *Trans. China Electrotechnical Soc.* 31 (a02), 142–149. doi:10.19595/j.cnki.1000-6753.tces.2016.s2.016

Chen, X., Shi, M., Zhou, J., Chen, Y., Zuo, W., and Wen, J. (2019). Distributed Cooperative Control of Multiple Hybrid Energy Storage Systems in a DC Microgrid Using Consensus Protocol[J]. *IEEE Trans. Ind. Electro.*, 1968–1979. doi:10.1109/TIE.2019.2898606

Chiang, P. H., Chiluvuri, S. P. V., Dey, S., and Nguyen, T. Q. (2017). "Forecasting of Solar Photovoltaic System Power Generation Using Wavelet Decomposition and Bias-Compensated Random Forest[C]," in 2017 Ninth Annual IEEE Green Technologies Conference (GreenTech), Denver, CO, USA, 29–31 March 2017.

Hoang, K. D., and Lee, H.-H. (2019). Accurate Power Sharing with Balanced Battery State of Charge in Distributed DC Microgrid. *IEEE Trans. Ind. Electron.* 66 (3), 1883–1893. doi:10.1109/tie.2018.2838107

Kathiresan, J., Natarajan, S. K., and Jothimani, G. (2020). Energy Management of Distributed Renewable Energy Sources for Residential DC Microgrid Applications [J]. *Int. Trans. Electr. Energ. Syst.* 30 (3), e12258. doi:10.1002/2050-7038.12258

Kotra, S., and Mishra, M. K. (2019). "Design and Stability Analysis of DC Microgrid with Hybrid Energy Storage System[J]. *IEEE Trans. Sustain. Energy* PP (3), 1-1.1603-1612. doi:10.1109/TSTE.2019.2891255

Li, J., Rui, X., Yang, Q., Liang, F., and Zhang, M. (2016). Design/test of a Hybrid Energy Storage System for Primary Frequency Control Using a Dynamic Droop Method in an Isolated Microgrid Power System[J]. *Appl. Energ.* 201, 257. doi:10.1016/j.apenergy.2016.10.066

Manandhar, U., Ukil, A., Kollimalla, S. K., and Gooi, H. B. (2015). "Application of HESS for PV System with Modified Control Strategy[C]," in 2015 7th IEEE Innovative Smart Grid Technologies Conference-ISGT Asia, Bangkok, Thailand, 3–6 Nov. 2015.

Mathews, M. A., and Rajeev, T. (2020). "Fuzzy Based Management of Hybrid Energy Storage System for Improved Dynamic Response of DC Microgrid[C]," in 2020 IEEE International Conference on Power Electronics, Smart Grid and Renewable Energy (PESGRE), Cochin, India, 2–4 Jan. 2020.

Ming, Y. U., Wang, Y., and Li, Y. G. (2017). Virtual Inertia Control of Hybrid Energy Storage in DC Microgrid Based on Predictive Method[J]. *Power Syst. Tech.* 41 (5), 7. doi:10.13335/j.1000-3673.pst.2016.1947

Musilek, P., Krömer, P., Martins, R., and Hesse, H. C. (2017). "Optimal Energy Management of Residential PV/HESS Using Evolutionary Fuzzy Control[C]," in 2017 IEEE Congress on Evolutionary Computation (CEC), Donostia, Spain, 5–8 June 2017.

Rahimi, M., and Ghadiriyan, S. (2019). A Generalized Droop-Based Compensator for Addressing the Issues Raised in a DC Microgrid Comprising Hybrid Wind-Battery-Back up Generation Sources[J]. *Int. Trans. Electr. Energ. Syst.* 29 (9), e12052. doi:10.1002/2050-7038.12052

Singh, P., and Lather, J. S. (2021). Power Management and Control of a Grid-independent DC Microgrid with Hybrid Energy Storage System. *Sustainable Energ. Tech. Assessments* 43, 100924. doi:10.1016/j.seta.2020.100924

Song, W., Chen, Y., Zhang, Y., Wen, A., and Wei, C. (2019). Bidirectional Boost Converter for High-power Transmission Between Energy Storage Battery and DC Microgrid. *Electron. Lett.* 55 (7), 402–404. doi:10.1049/el.2018.7561

Su, H., Zhang, J., Wang, N., and Guo, W. (2018). Energy Management Strategy of High Capacity Hybrid Energy Storage System Based on Hierarchical Optimization[J]. *High-Voltage Tech.* 44 (4), 1177–1186. doi:10.7500/AEPS20160729015

Wang, Y., Hei, Y., Fu, Y., Wu, Z. K., and Yang, P. H. (2017). Adaptive Virtual Inertia Control of Dc Distribution Network Based on Variable Droop Coefficient[J]. *Automation Electric Power Syst.* 41 (8), 116–124. doi:10.19595/j.cnki.1000-6753.tces.171119

Wu, T., Ye, F., Su, Y., Wang, Y., and Riffat, S. (2020). Coordinated Control Strategy of DC Microgrid with Hybrid Energy Storage System to Smooth Power Output Fluctuation. *Int. J. Low-Carbon Tech.* 15 (1), 46–54. doi:10.1093/ijlct/ctz056

Zhang, J. H., Wang, H. M., Wei, Y. L., et al. (2018). The Layered Control Strategy of Dc Micro-grid Bus Voltage Fluctuation Including Composite Energy Storage and Gas Turbine Generator[J]. *Trans. China Electrotechnical Soc.* 33 (6), 1238–1246.

Zhou, G., Tian, Q., Leng, M., Fan, X., and Bi, Q. (2020). Energy Management and Control Strategy for DC Microgrid Based on DMPPT Technique. *IET Power Electro.* 13 (4), 658–668. doi:10.1049/iet-pel.2019.0383

Zhou, J. P., Zhang, W. Z., Wang, T., Li, X. Y., Li, X. Q., and Mao, D. J. (2018). Multi-cell Control Strategy Based on Power Interaction and Dynamic Distribution[J]. *High-Voltage Tech.* 44 (4), 1149–1156. doi:10.13336/j.1003-6520.hve.20180329014

frontiers
in Energy Research

ORIGINAL RESEARCH
published: 25 January 2022
doi: 10.3389/fenrg.2021.822252

Study of Voltage Sag Detection and Dual-Loop Control of Dynamic Voltage Restorer

Shuzheng Wang*, Shaowen Zhang and Xianyun Li

School of Electric Power Engineering, Nanjing Institute of Technology, Nanjing, China

Voltages sags have become the major issue that prevents the customers from getting high-quality power supply, and the dynamic voltage restorer (DVR) is considered an effective way to solve this issue. In this work, a method for voltage sag detection implemented in the time-domain is firstly addressed, which features highly accurate and fast response. Then, the dual-loop voltage–current control for the DVR is intensively investigated. Specifically, the optimal tuning of the inner current loop to achieve the maximum active damping is approached, and the voltage controller implemented in the discrete-time is developed. Tuning of the voltage loop based on critical damping is also approached, which features reduced settling time and avoidance of overshoot. The simulation and experimental results have verified the effectiveness of the proposed method for detection and management of voltage sags.

Keywords: voltage sags, dual-loop control strategy, active damping, critical damping, discrete-time domain

Edited by:
Amjad Anvari-Moghaddam,
Aalborg University, Denmark

Reviewed by:
Zhao Zhihong,
Nanjing University of Science and Technology, China
Ning Li,
Xi'an University of Technology, China
Ansal V.,
National Institute of Technology Goa, India

****Correspondence:***
Shuzheng Wang
wsz310@126.com

Specialty section:
This article was submitted to Process and Energy Systems Engineering,
a section of the journal Frontiers in Energy Research

Received: *25 November 2021*
Accepted: *31 December 2021*
Published: *25 January 2022*

Citation:
Wang S, Zhang S and Li X (2022) Study of Voltage Sag Detection and Dual-Loop Control of Dynamic Voltage Restorer.
Front. Energy Res. 9:822252.
doi: 10.3389/fenrg.2021.822252

1 INTRODUCTION

It has been reported that according to the statistics, voltage sags, which can cause enormous economic loss every year, account for over 70% of the cases that give rise to the power-supply deterioration, resulting in severe complaints from the customers (Nagata et al., 2017; Parreño Torres et al., 2019; Han et al., 2020). In other words, voltage sags have become the major issue that prevents consumers from getting the uninterrupted and high-quality power supply.

Many literature studies have been devoted to the control and management of voltage sags for a long period of time (Jowder, 2009; Nagata et al., 2017; Parreño Torres et al., 2019; Gontijo et al., 2020; Han et al., 2020). Presently, among the proposed methods, the dynamic voltage restorer (DVR), which is connected between the grid and the load, has been commonly considered an effective and economical way to solve the issue of voltage sags, and a high-quality power supply can be expected. The basic idea of DVR is to generate the compensation voltage through the power-electronics–based converter, so as to keep the load-side voltage unaffected when sags occur on the grid-side voltage. Consequently, the fast and accurate voltage sag detection and the effective voltage regulation strategy are of almost importance to the DVR to achieve a high level of performance.

With regard to sag detection, many methods have been developed from either the time- or frequency-domain, such as the Kalman filter (Cisneros-Magaña et al., 2018), fast Fourier transform (Wang Y et al., 2019), wavelet transform (Hu et al., 2020), and approaches based on instantaneous reactive power theory (Pradhan and Mishra, 2019; Tu et al., 2020; He et al., 2021). Specifically, it has been proved that both the output speed and the accuracy of the Kalman filter are related to the system model, and there is also convergence issue which can result in an unstable response. Alternatively, methods based on the Fourier or wavelet transforms require historical data, resulting in heavy computation burden which is, therefore, unacceptable for real-time signal implementation with a commercial digital signal processor (DSP) or microcontroller unit (MCU). Although this issue can be avoided with the employment of a sliding window as addressed by Wang J et al. (2019), it has, however, been proved that there are also stability and high-frequency noise amplification issues, which need careful considerations for the practical implementation with a DSP or MCU. The method based on instantaneous reactive power theory is suitable for a three-phase system and has, in fact, been studied and implemented in a lot of literature studies, such as He et al. (2021) and Pradhan and Mishra (2019). This kind of method, however, has a blind zone for the detection of unbalanced voltage drops.

On the contrary, for the DVR, the LC filter is commonly employed at the output terminal of the converter. This can put a great challenge to the system's overall control since the LC filter has resonance phenomenon and causes stability problem (Wang J et al., 2019; Naidu et al., 2019; Bajaj, 2020; Xiong et al., 2020). Although various passive methods, for instance, connecting resisters in parallel or series with the capacitor, have been developed and can be employed to increase the system's physical damping, this kind of method is however not preferred, since it can further cause other issues, such as increase in power loss and deteriorated filter effectiveness for high-frequency voltage harmonics (Pal and Gupta, 2020; Vo Tien et al., 2018). On the contrary, the counterpart, i.e., active damping methods, is realized by modifying the control structure, which can avoid the aforementioned issues faced by the passive methods, and has therefore been intensively investigated in recent years (Suppioni et al., 2017; Liu et al., 2018; Roldán-Pérez et al., 2019; Liu et al., 2021; Xiong et al., 2021). Specifically, the following two types of control strategies: 1) single-loop voltage and 2) dual-loop voltage–current control, can be employed to achieve enhanced active damping. Nevertheless, it has been addressed that the single-loop voltage control method suffers from the issues of poor stability and constrained loop-bandwidth, which can result in an oscillatory and slow transient response of the output voltage. Hence, this approach is not preferred for high-performance applications, although it has the merits of simple structure and easy implementation.

Alternatively, the dual-loop control method, in which additional active damping can be achieved by incorporating the current loop, has been proved to have improved performance compared to that of the single-loop control method. Hence, numerous studies have been dedicated to the analysis and tuning of the current loop. Commonly, the frequency response analysis is employed in these studies, where the bandwidth of the voltage loop is tuned to be one-fifth to one-tenth of that of the current loop, which is a rule of thumb for a common dual- or multi-loop control structure for grid-following converters. This rule is however not applicable for the dual-loop regulated DVR, since the objective of the current loop is to improve damping, instead of signal tracking where bandwidth is concerned. Hence, the explicit guidance for tuning of the current loop needs to be clarified, which is approached in this work. Also, based on the equivalent plant which is damped with the current loop, a voltage controller implemented in the discrete-time domain is developed, which features fast response and avoidance of overshoot.

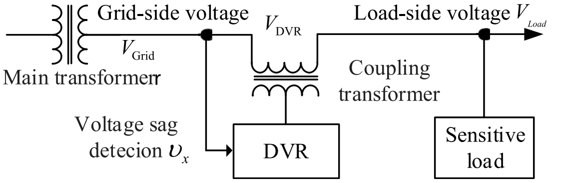

FIGURE 1 | Voltage sag compensation of the DVR.

To do that systematically, the rest of this work is organized as follows: **Section 2** begins with the description of the basic principle of DVR succinctly, and then based on signal reconstruction, a method for voltage sag detection in the time-domain is developed, which features low settling time, high accuracy, and frequency adaptive characteristic. The inner current loop is addressed in **Section 3**, with the objective of obtaining the maximum active damping. The developed discrete voltage controller is addressed in **Section 4**, in which the tuning of the voltage loop based on optimization of settling time and overshoot is also addressed. The simulation and experimental verifications are presented in **Section 5**, before concluding the findings in **Section 6**.

2 PRINCIPLE OF DVR AND VOLTAGE DROP DETECTION

As shown in **Figure 1**, the load-side voltage V_{Load} can be expressed as the superposition of the grid-side voltage V_{Grid} and the compensation voltage V_{DVR}, which can be expressed as follows:

$$V_{\text{Load}} = V_{\text{Grid}} + V_{\text{DVR}}. \tag{1}$$

In this manner, when a fault occurs in the main grid or adjacent transmission line, the voltage drop can occur on the grid-side voltage V_{Grid}. The DVR detects the voltage sag and injects the compensation voltage V_{DVR} to the grid through the coupling transformer. In this manner, the load-side voltage V_{Load} remains stable and the voltage supply for the sensitive load is unaffected.

According to the Fourier theory, the periodic grid voltage can be expressed as the sum of different frequency signals, which can be expressed as follows:

$$\begin{aligned} v_x &= \sum_{h=1}^{\infty} v_x^h \\ &= \underbrace{A_1 \sin(\omega_1 t + \theta_{l1})}_{v_x^1} + \underbrace{A_2 \sin(2\omega_1 t + \theta_{l2})}_{v_x^2} + \cdots, \end{aligned} \tag{2}$$

where ω_1 is the grid frequency and A_h, θ_{lh} are the amplitude and initial phase of v_x^h, respectively. Also, the fundamental voltage v_x^1

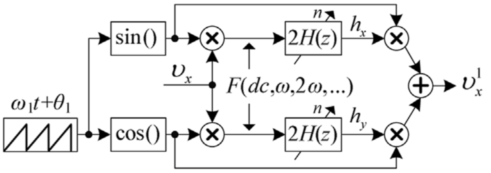

FIGURE 2 | Detection of the fundamental voltage.

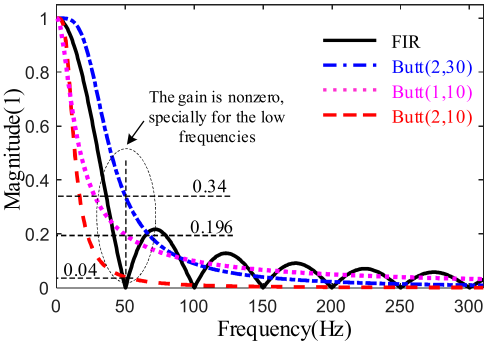

FIGURE 3 | Frequency response of the LPFs.

can be expressed as the sum of two orthogonal signals, which is shown as follows:

$$v_x^1 = h_x \sin(\omega_1 t + \theta_1) + h_y \cos(\omega_1 t + \theta_1), \tag{3}$$

where θ_1 is the initial value of the phase for implementation, which has no impact on the output value of v_x^1, while the expressions of h_x and h_y are expressed as follows:

$$\begin{aligned} h_x &= A_1 \cos(\theta_{l1} - \theta_1), \\ h_y &= A_1 \sin(\theta_{l1} - \theta_1). \end{aligned} \tag{4}$$

It can be noted that θ_{l1}, θ_1, and A_h are constant; hence, h_x and h_y are dc signals. In order to obtain their values, the following derivations are performed:

$$v_x \times \sin(\omega_1 t + \theta_1) = \frac{1}{2}\left[\underbrace{A_1 \cos(\theta_{l1} - \theta_1)}_{h_x} + F(\omega_1, 2\omega_1, 3\omega_1, \cdots)\right], \tag{5}$$

$$v_x \times \cos(\omega_1 t + \theta_1) = \frac{1}{2}\left[\underbrace{A_1 \sin(\theta_{l1} - \theta_1)}_{h_y} + F(\omega_1, 2\omega_1, 3\omega_1, \cdots)\right]. \tag{6}$$

Combining **Eqs 2–5**, the structure for the detection of the fundamental voltage v_x^1 can be obtained, which is shown in **Figure 2**, where H(z) is the low-pass filter.

From **Eqs 4, 5**, it can be observed that the frequency of the alternating signals is multiple of the fundamental frequency. Therefore, in this work, a finite impulse response (FIR) filter is employed, whose expression is shown as follows:

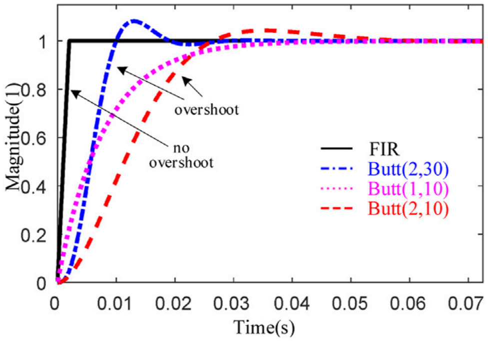

FIGURE 4 | Step response of the LPFs.

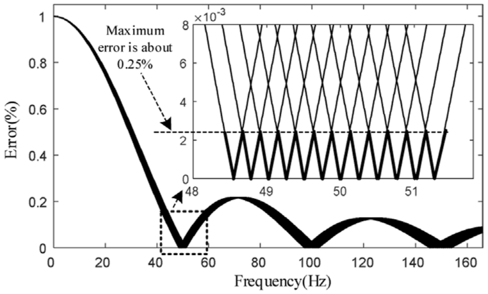

FIGURE 5 | Frequency adaption for the FIR filter.

$$H(z) = \frac{1}{n}\cdot\frac{1 - z^{-n}}{1 - z^{-1}}, \tag{7}$$

where n is the number of sampling points within a period of the grid voltage. For comparison, the magnitude responses of the FIR filter and Butterworth filter Butt(a, b) are illustrated in **Figure 3**, noting that a is the order and b is the cutoff frequency of the filter. It can be noted that the amplitude of the FIR filter at the fundamental frequency ω_1 as well as the high frequencies $h\omega_1$ is zero. Hence, the alternating signal in **Eqs 4, 5** can be canceled completely with the FIR filter of **Eq. 7**. On the contrary, the magnitude response of Butt(a, b) presents a monotonic characteristic. However, it can be observed that the gains at the lower frequencies are non-zero, which can further result in poor accuracy of dc signal detection in **Eqs 4, 5**.

It should be mentioned that the output accuracy of Butt(a, b) can be improved by reducing the cutoff frequency b. This is, however, at the cost of the reduction of the bandwidth for the filter, leading to a slow transient response. As shown in **Figure 4** where the step response of different filters is illustrated, comparing Butt(2,30), the settling time is much extended for the case of Butt(1,10) and Butt(2,10). Alternatively, the fastest response can be obtained with the employment of FIR filter, and no overshoot can be observed.

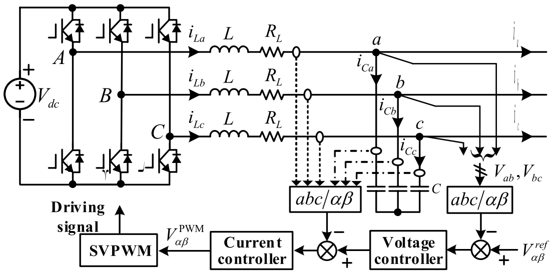

FIGURE 6 | Main circuit of the DVR and the related dual-loop control method.

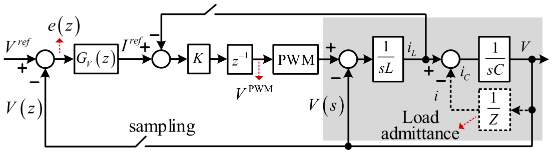

FIGURE 7 | Block diagram of the dual-loop control method.

From the above analysis, it can be concluded that, from the viewpoint of accuracy and speed of detection of h_x and h_y in **Eqs 4, 5**, the performance of FIR filter is superior to that of Butt(a, b). The main shortcoming of employing the FIR filter (7) is the storage requirement, which is, commonly, RAM for microprocessors. The next step is to achieve frequency adaption for the FIR filter, since the grid voltage ω_1 can vary within a certain range. In this work, the order n of FIR is dynamically adjusted according to the real value of ω_1 which is obtained with a frequency locked loop. As shown in **Figure 5**, the maximum error is 0.25% approximately.

In this manner, with the developed method illustrated in **Figure 2**, the fundamental grid voltage can finally be obtained, whose amplitude and phase are employed for voltage sag identification. It should be noted that the developed method can be employed for either three- or single-phase configuration, although only the three-phase one is taken as an example for analysis in this work.

3 OPTIMAL ACTIVE DAMPING TUNING OF THE INNER CURRENT LOOP

In **Figure 6**, the main circuit and the corresponding dual-loop control method of the three-phase DVR are both illustrated. The dc bus voltage can be supplied by either a rectifier or an energy storage system. Hence, a dc source Vdc can be assumed for simplicity here. The output of the converter is connected to the LC filter, where L is the inductor, C is the capacitor, and R_L is the equivalent resistor which is employed for emulating the power loss of the converter. After the filter, the voltage is fed to the coupling transformer shown in **Figure 1**. The reference voltage $V_{\alpha\beta}^{ref}$ is the detected voltage sag, which is compared with the measured capacitor voltage. The error signal is fed to the voltage controller, whose output is the reference of the inner current loop. It should be noted that either the capacitor current i_C or the inductor current i_L can be measured and fed back for regulation. The difference of feeding back of i_C and i_L lies in that i_L can be employed for the overcurrent protection of the converter. In this work, the inductor current is employed since it can be adopted for overcurrent protection of the converter.

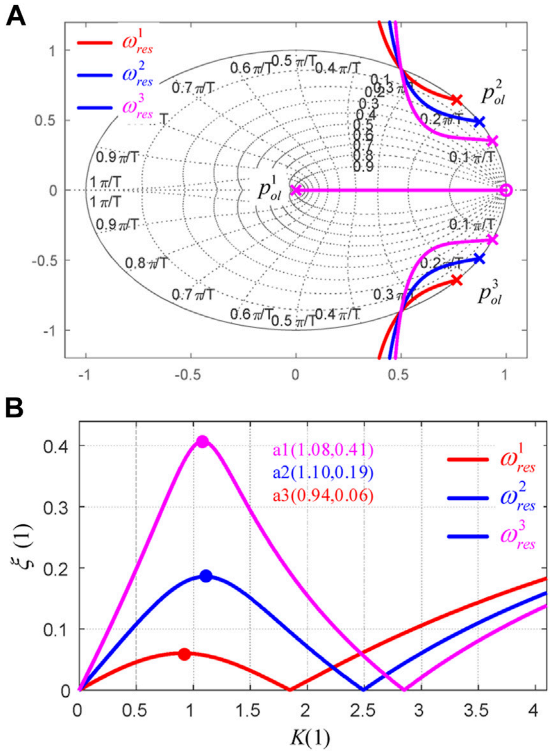

FIGURE 8 | Root locus and active damping of the plant when K varies, where **(A)** shows the root locus and **(B)** shows the plot of K vs ξ.

For better illustration, the dual-loop control method is further depicted in **Figure 7**, where V^{ref} represents the reference voltage (either V_α^{ref} or V_β^{ref}), $G_V(z)$ is the voltage controller, K is the current loop proportional gain, z^{-1} is the one-sampling delay, and V^{PWM} is the modulation signal. It should be noted that the case of $R_L = 0$ is employed here, in order to emulate the worst case without any physical damping.

The modulation signal V^{PWM} is updated at each sampling point and kept constant during the sampling period. Hence, the zero-order holding method is employed for discretization here. Combining **Figure 7**, the transfer function of the output voltage V related to the current reference I^{ref} can be derived as follows:

$$\begin{aligned} G_{\mathrm{PL}}^{V}(z) &= \frac{V(z)}{I^{rerf}(z)} \\ &= \frac{K\cdot[1-\cos(\omega_{res}\cdot T_s)]\cdot(z+1)}{z^3-2z^2\cos(\omega_{res}T_s)+b_1\cdot z-\dfrac{K}{\omega_{res}L}\sin(\omega_{res}T_s)}, \end{aligned} \tag{8}$$

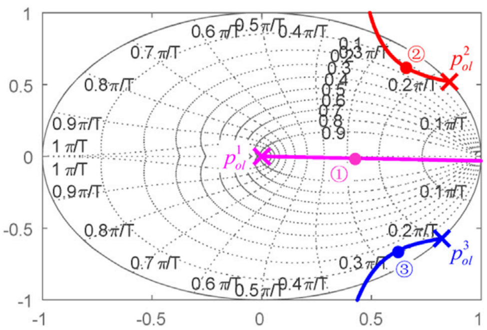

FIGURE 9 | Pole distribution of the equivalent plant in the SRF for K=K_{opt}.

where $b_1 = 1 + K/(\omega_{res}L)\cdot \sin(\omega_{res}T_s)$, T_s is the sampling period, and $\omega_{res} = \sqrt{1/(LC)}$ is the LC resonance frequency.

Recalling **Figure 7**, it can be observed that **Eq. 8** is actually the equivalent plant of the voltage controller. Since the inclusion of the current loop is for active damping, the damping characteristic of **Eq. 8** is investigated. As shown in **Figure 8A**, with the increase of K, the conjugate poles $p_{ol}^{2,3}$ which are located on the unit circle and related to the filter resonance move inside of the unit circle, and the damping ξ increases gradually, as shown in **Figure 8B**. For the case of K=K_{opt} = 1.1 of ω_{res}^2, the active damping ξ reaches the maximum value of 0.19. With the further increase of K, the pole moves to the unit circle, and the active damping ξ decreases instead. When K=K_{max} = 2.5, the poles cross the unit circle, resulting in a non-minimum phase system. This certainly should be avoided. From the above analysis, it can be concluded that, for the optimal gain of K=K_{opt} = 1.1, the maximum active damping can be achieved for the equivalent plant.

4 THE DEVELOPMENT OF VOLTAGE CONTROLLER IN THE DISCRETE-TIME DOMAIN

In order to have zero steady-state error signal tracking of the sinusoidal waveform, the following analysis is performed in the synchronous reference frame (SRF). Hence, with the replacement of z with $z = ze^{j\omega_1 T_s}$ in **Eq. 8**, the equivalence of the voltage controller in the SRF can be obtained. With the substitute of the optimal gain K_{opt} for (8), the distribution of poles of the equivalent plant for the case of ω_{res}^2 is depicted in **Figure 9**, as illustrated with the solid circle "●."

Observing **Figure 9**, it can be noted that, with the optimal damping of K_{opt}, the damping ξ of the poles on branch ① is unity; however, the damping of the other poles $p_{ol}^{2,3}$ located on branches ② and ③ is only 0.19, which can be observed from **Figure 8B**. Therefore, the equivalent plant actually features a weak damping characteristic, even with the optimal active damping gain K_{opt} employed.

With the objective of canceling the above weak damping poles, in this work, a voltage controller is developed, whose transfer function is shown as follows:

$$G_V^{SRF}(z) = K_V \cdot \frac{z^3 e^{-j3\omega_1 T_s} - 2z^2 e^{-j2\omega_1 T_s}\cdot c + (1+a)ze^{-j\omega_1 T_s} - a}{z^2\cdot(z-1)}, \qquad (9)$$

where $c = 2e^{-j2\omega_1 T_s}\cos(\omega_{res}T_s)$, $a = K\sin(\omega_{res}T_s)/(\omega_{res}T_s)$, and K_V is the controller gain. It can be noted that **Eq. 9** achieves the pole zero cancellation with the equivalent plant (8), and the denominator of **Eq. 9** provides infinite open-loop gain for the dc signal in the SRF, which equivalently achieves infinite gain for the ac signal alternating at ω_1 in the stationary reference frame, resulting in zero steady-state tracking error for the sinusoidal signal.

5 TUNING OF THE VOLTAGE LOOP WITH THE EMPLOYMENT OF THE DEVELOPED CONTROLLER BASED ON CRITICAL DAMPING

Combining (8), (9), and **Figure 7**, the open-loop transfer function of the voltage loop can be derived. Then, by varying the controller gain K_V from zero to infinity, the root locus of the voltage loop can be obtained, as shown in **Figure 10**. It can be noted that, for lower values of K_V, the closed-loop poles on branches ① and ② are initially on the real axis and move toward the unit circle with the further increase of K_V, while for higher values of K_V, the poles on both ① and ② can move outside of the circle, resulting in an unstable response of the voltage loop.

Nevertheless, the damping and magnitude of the poles obtained from the discrete root locus analysis are not straightforward as those derived in the continuous-time domain. Hence, the damping and magnitude of the equivalence of the poles in the continuous-time domain are employed for analysis, which can be expressed as follows:

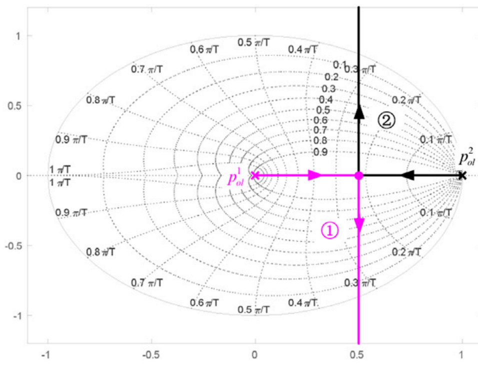

FIGURE 10 | Root locus diagram of the voltage loop with the employment of the developed controller.

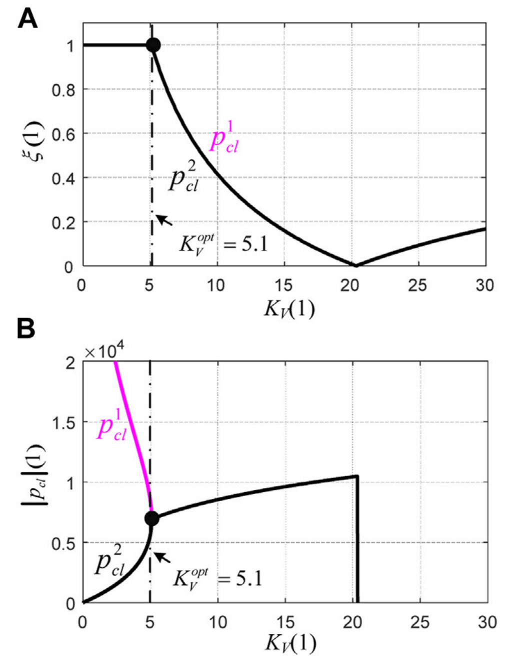

FIGURE 11 | Curve of **(A)** Kv vs ξ and **(B)** Kv vs $|p|$.

$$\xi = \sqrt{\frac{1}{\left\{\arctan\left(\frac{\mathrm{Im}\left(p_{cl}^z\right)}{\mathrm{Re}\left(p_{cl}^z\right)}\right)\cdot\frac{1}{\ln\left|p_{cl}^z\right|}\right\}^2+1}} \tag{10}$$

and

$$\left|p_{cl}\right| = \frac{\ln\left|p_{cl}^z\right|}{T_s}, \tag{11}$$

where p_{cl}^z is the pole in the z-domain, ξ is the damping, and $|p_{cl}|$ is the equivalent magnitude in the s-domain.

For better illustration, the damping ξ and magnitude $|p_{cl}|$ of the poles in **Figure 10** are further calculated, and the plots of Kv vs ξ and Kv vs $|p_{cl}|$ are depicted in **Figures 11A,B**, respectively. To begin with, as shown in **Figure 11A**, for $K_V<Kopt\ V$, unity damping is achieved for both poles $p_{cl}^{1,2}$, and the magnitude of p_{cl}^2 is much lower than that of $|p_{cl}^1|$. As a result, p_{cl}^2 is the dominant pole, and the voltage loop is overdamped in this case. As a result, a monotonically rising step response can be expected. In particular, for $K_V = Kopt\ V$, it can be noted that $|p_{cl}^1| = |p_{cl}^2|$ from **Figure 11B**, and unity damping is valid for both poles. With the further increase of K_V, the damping of $p_{cl}^{1,2}$ decreases sharply, resulting in overshoot in the step response. Therefore, the voltage loop is critically damped for the case of $K_V = Kopt\ V$.

However, for $K_V>Kopt\ V$, the magnitude of $|p_{cl}^{1,2}|$ increases overall, while the added value is relatively limited. However, in this case, the damping ξ of both poles $p_{cl}^{1,2}$ decreases sharply, resulting in deteriorated performance, which is certainly undesired.

Form the above analysis, it can be concluded that, for $K_V = Kopt\ V$, the possible maximum magnitude of both $p_{cl}^{1,2}$ can be achieved. Besides, in this case, the unity damping for $p_{cl}^{1,2}$ is valid. Consequently, the voltage loop is critically damped, which means minimum settling time with the avoidance of overshoot for the step response can be expected.

6 SIMULATION AND EXPERIMENTAL RESULTS

To verify the effectiveness of the developed method for voltage sag detection and the controller for voltage regulation of DVR, the simulation is performed in Matlab/Simulink. In particular, the parameters are shown as follows: the filter inductance of 0.4 mH, the filter capacitor of 180 uF, the switching frequency of i5 kHz, the sampling frequency of 10 kHz, and the grid line voltage of 380 V.

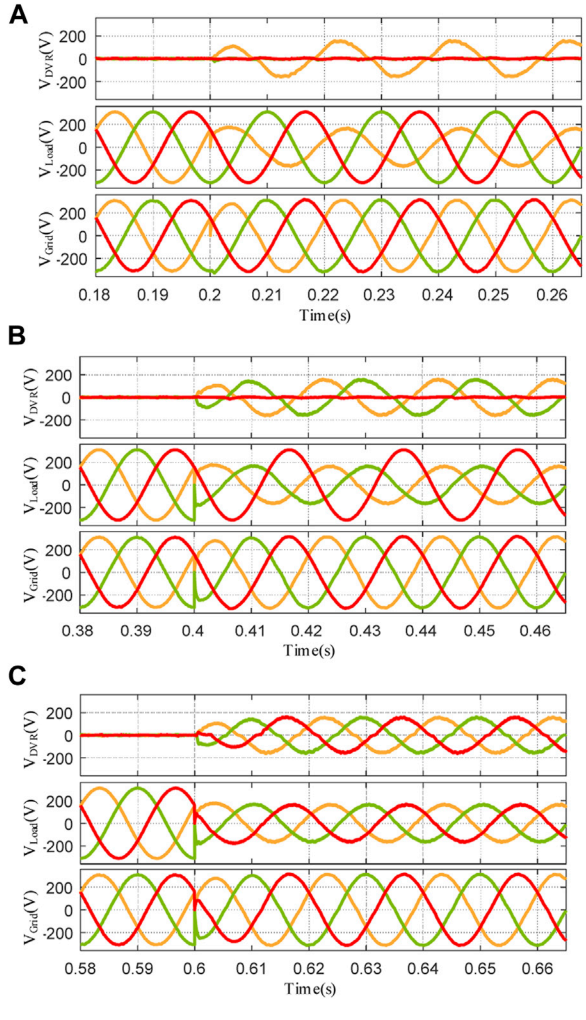

FIGURE 12 | Simulation results of **(A)** single-phase, **(B)** dual-phase, and **(C)** three-phase voltage sag compensation for the DVR.

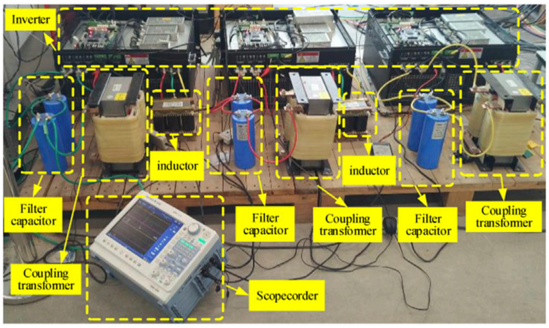

FIGURE 13 | Experimental setup for voltage sag compensation.

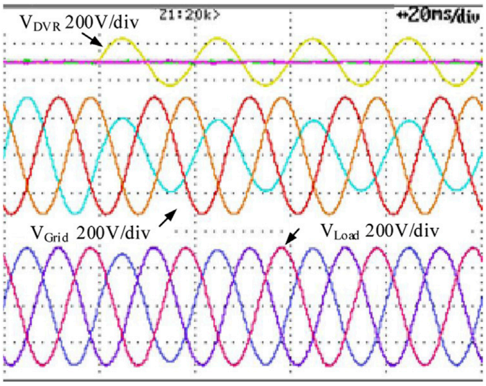

FIGURE 14 | Experimental results of single-phase voltage sag compensation.

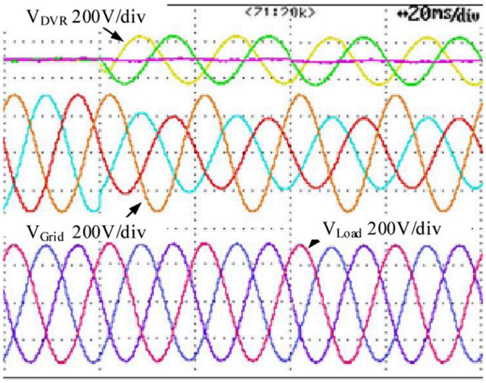

FIGURE 15 | Experimental results of dual-phase voltage sag compensation.

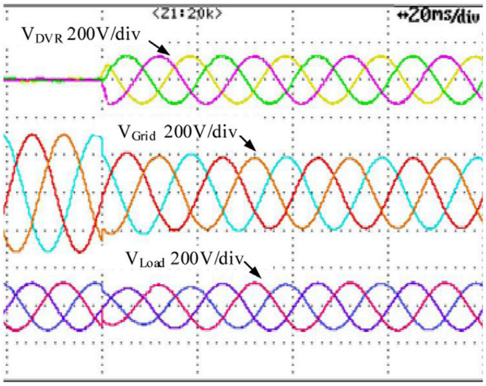

FIGURE 16 | Experimental results of three-phase voltage sag compensation.

In **Figure 12**, the simulation results for the single-phase, dual-phase, and three-phase voltage sags of 40% are illustrated, where the grid-side voltage, the load-side voltage, and the DVR voltage are represented as V_{Grid}, V_{Load}, and V_{DVR}, respectively. It can be noted that, for the three evaluated cases, the DVR can generate the required voltage within 2 ms approximately, and no overshoot can be observed. In this manner, the load-side voltage remains unaffected and a high-quality power supply can be guaranteed.

The experimental setup is shown in **Figure 13**, whose parameters are the same as those addressed for simulation. The rated capacity of the setup is 100 kVA. The digital controller is a TMS320F28346 DSP and a EP3C25 FPGA, and the DSP is responsible for the calculation and data process, while the FPGA is employed for logic management and protection. Also, the measuring equipment includes a DL850 ScopeCorder and several P5200 differential probes.

The experiment is performed for different voltage sag sceneries. To begin with, the single-phase voltage sag of 40% is investigated. As shown in **Figure 14**, it can be noted that the DVR compensation voltage has a fast response with no overshoot, which is in good agreement with the theoretical findings addressed before. In this manner, the load-side voltage is stable regardless of the sag on the grid-side voltage.

Also, the case of dual-phase voltage sag of 40% is addressed. The experimental result is shown in **Figure 15**, where it can be observed the settling time is about 2 ms with no overshoot, which agrees with the analytical findings addressed before.

Finally, the case of voltage sag for the three-phase voltage is investigated. As shown in **Figure 16**, the amplitude of the three-phase voltage sag is 40% simultaneously, and the compensation voltage is fast and accurate, and a similar conclusion to that of the single- and dual-phase voltage drops can be drawn, i.e., reduced settling time and avoidance of overshoot. It should be emphasized that if non-linear loads are considered, the load-side voltage can be distorted by the high-frequency harmonic currents, since the voltage controller developed in this work is employed for handling the fundamental frequency voltage.

7 CONCLUSION

In this work, the DVR for voltage sag compensation is intensively addressed. A method implemented in the time-domain for voltage sag identification is developed, which features fast response, high accuracy, and frequency adaptive characteristic. Then, the dual-loop voltage–current regulation for the DVR is approached, where the optimal tuning of the current loop to achieve the maximum active damping is addressed. Also, a discrete voltage controller is developed, and tuning of the voltage loop based on critical damping is lastly addressed, which can be employed to achieve a fast response and avoidance of overshoot for output voltage regulation.

DATA AVAILABILITY STATEMENT

The original contributions presented in the study are included in the article/supplementary material, and further inquiries can be directed to the corresponding author.

AUTHOR CONTRIBUTIONS

All authors listed have made a substantial, direct, and intellectual contribution to the work and approved it for publication.

FUNDING

This work was supported by the National Natural Science Foundation of China (No. 51807092), Open Fund of Jiangsu Distribution Network Intelligent Technology and Equipment Collaborative Innovation Center (XTCX202004, XTCX201905), and Hubei Provincial Key Laboratory for Operation and Control of Cascaded Hydropower Station (2019KJX04).

REFERENCES

Bajaj, M. (2020). Design and Simulation of Hybrid DG System Fed Single-phase Dynamic Voltage Restorer for Smart Grid Application. *Smart Sci.* 8 (1), 24–38. doi:10.1080/23080477.2020.1748928

Cisneros-Magaña, R., Medina, A., and Anaya-Lara, O. (2018). Time-Domain Voltage Sag State Estimation Based on the Unscented Kalman Filter for Power Systems with Nonlinear Components. *Energies* 11 (6), 1411. doi:10.3390/en11061411

Gontijo, G. F., Tricarico, T. C., da Silva, L. F., Krejci, D., França, B. W., Aredes, M., et al. (2020). Modeling, Control, and Experimental Verification of a DFIG with a Series-Grid-Side Converter with Voltage Sag, Unbalance, and Distortion Compensation Capabilities. *IEEE Trans. Industry Appl.* 56 (1), 584–600. doi:10.1109/TIA.2019.2946950

Han, Y., Feng, Y., Yang, P., Xu, L., Xu, Y., and Blaabjerg, F. (2020). Cause, Classification of Voltage Sag, and Voltage Sag Emulators and Applications: A Comprehensive Overview. *IEEE Access* 8, 1922–1934. doi:10.1109/access.2019.2958965

He, H.-Y., Zhang, W.-H., Wang, Y., and Xiao, X.-Y. (2021). A Sensitive Industrial Process Model for Financial Losses Assessment Due to Voltage Sag and Short Interruptions. *IEEE Trans. Power Deliv.* 36 (3), 1293–1301. doi:10.1109/tpwrd.2020.3006017

Hu, W. X., Xiao, X. Y., and Zheng, Z. X. (2020). Voltage Sag/swell Waveform Analysis Method Based on Multi-dimension Characterisation. *IET Generation, Transm. Distribution* 14 (3), 486–493. doi:10.1049/iet-gtd.2019.1038

Jowder, F. A. L. (2009). Design and Analysis of Dynamic Voltage Restorer for Deep Voltage Sag and Harmonic Compensation. *IET generation, Transm. distribution* 3 (6), 547–560. doi:10.1049/iet-gtd.2008.0531

Liu, B., Li, Z., Chen, X., Huang, Y., and Liu, X. (2018). Recognition and Vulnerability Analysis of Key Nodes in Power Grid Based on Complex Network Centrality. *IEEE Trans. Circuits Syst.* 65 (3), 346–350. doi:10.1109/tcsii.2017.2705482

Liu, B., Li, Z., Dong, X., Yu, S. S., Chen, X., Oo, A. M. T., et al. (2021). Impedance Modeling and Controllers Shaping Effect Analysis of PMSG Wind Turbines. *IEEE J. Emerg. Sel. Top. Power Electron.* 9 (2), 1465–1478. doi:10.1109/jestpe.2020.3014412

Nagata, E. A., Ferreira, D. D., Duque, C. A., and Cequeirab, A. S. (2017). Voltage Sag and Swell Detection and Segmentation Based on Independent Component Analysis. *Electric Power Syst. Res.* 155, 274–280. doi:10.1016/j.epsr.2017.10.029

Naidu, T. A., Arya, S. R., and Maurya, R. (2019). Multiobjective Dynamic Voltage Restorer with Modified EPLL Control and Optimized PI-Controller Gains. *IEEE Trans. Power Electron.* 34 (3), 2181–2192. doi:10.1109/tpel.2018.2837009

Pal, R., and Gupta, S. (2020). Topologies and Control Strategies Implicated in Dynamic Voltage Restorer (DVR) for Power Quality Improvement. *Iran J. Sci. Technol. Trans. Electr. Eng.* 44 (2), 581–603. doi:10.1007/s40998-019-00287-3

Parreño Torres, A., Roncero-Sánchez, P., Vázquez, J., López-Alcolea, F. J., and Molina-Martínez, E. J. (2019). A Discrete-Time Control Method for Fast Transient Voltage-Sag Compensation in DVR. *IEEE Access* 7, 170564–170577. doi:10.1109/access.2019.2955177

Pradhan, M., and Mishra, M. K. (2019). Dual \$P\$ - \$Q\$ Theory Based Energy-Optimized Dynamic Voltage Restorer for Power Quality Improvement in a Distribution System. *IEEE Trans. Ind. Electron.* 66 (4), 2946–2955. doi:10.1109/tie.2018.2850009

Roldán-Pérez, J., García-Cerrada, A., Ochoa-Giménez, M., and Zamora-Macho, J. L. (2019). Delayed-Signal-Cancellation-Based Sag Detector for a Dynamic Voltage Restorer in Distorted Grids. *IEEE Trans. Sust. Energ.* 10 (4), 2015–2027. doi:10.1109/tste.2018.2877505

Suppioni, V. P., Grilo, A. P., and Teixeira, J. C. (2017). Improving Network Voltage Unbalance Levels by Controlling DFIG Wind Turbine Using a Dynamic Voltage Restorer. *Int. J. Electr. Power Energ. Syst.* 96, 185–193. doi:10.1016/j.ijepes.2017.10.002

Tu, C., Guo, Q., Jiang, F., Wang, H., and Shuai, Z. (2020). A Comprehensive Study to Mitigate Voltage Sags and Phase Jumps Using a Dynamic Voltage Restorer. *IEEE J. Emerg. Sel. Top. Power Electron.* 8 (2), 1490–1502. doi:10.1109/jestpe.2019.2914308

Vo Tien, D., Gono, R., Leonowicz, Z., Tran Duy, T., and Martirano, L. (2018). Advanced Control of the Dynamic Voltage Restorer for Mitigating Voltage Sags in Power Systems. *Adv. Electr. Electron. Eng.* 16 (1), 36–45. doi:10.15598/aeee.v16i1.2350

Wang J, J., Xing, Y., Wu, H., and Yang, T. (2019). A Novel Dual-DC-Port Dynamic Voltage Restorer with Reduced-Rating Integrated DC-DC Converter for Wide-Range Voltage Sag Compensation. *IEEE Trans. Power Electron.* 34 (8), 7437–7449. doi:10.1109/tpel.2018.2882534

Wang, Y., Luo, H., and Xiao, X.-Y. (2019). Voltage Sag Frequency Kernel Density Estimation Method Considering protection Characteristics and Fault Distribution. *Electric Power Syst. Res.* 170, 128–137. doi:10.1016/j.epsr.2019.01.009

Xiong, L., Liu, X., Zhang, D., and Liu, Y. (2021). Rapid Power Compensation-Based Frequency Response Strategy for Low-Inertia Power Systems. *IEEE J. Emerg. Sel. Top. Power Electron.* 9 (4), 4500–4513. doi:10.1109/jestpe.2020.3032063

Xiong, L., Liu, X., Zhao, C., and Zhuo, F. (2020). A Fast and Robust Real-Time Detection Algorithm of Decaying DC Transient and Harmonic Components in Three-phase Systems. *IEEE Trans. Power Electron.* 35 (4), 3332–3336. doi:10.1109/tpel.2019.2940891

Conflict of Interest: The authors declare that the research was conducted in the absence of any commercial or financial relationships that could be construed as a potential conflict of interest.

frontiers
in Energy Research

METHODS
published: 27 January 2022
doi: 10.3389/fenrg.2021.801197

Multi-Time Scale Harmonic Mitigation for High Proportion Electronic Grid

Lian Suo[1], *LiJuan Lin*[2], *Licheng Xing*[2]* *and Qingquan Jia*[2]

[1]Key Laboratory of Power Conversion, Transmission and Control of Inner Mongolia Normal University, Jinchuan Industrial Park, Economic and Technological Development Zone, Hohhot, China, [2]School of Electrical Engineering, Yanshan University, Qinhuangdao, China

As new energies integrated into grid, the harmonics in the grid are more serious, and the Voltage Detection Active Power Filter (VDAPF) has been used as the mitigation equipment to solve the harmonic problems in power electronic distribution network. The global optimization method generally utilizes 15 min to mitigate harmonic which is named long-time-scale, and it is impossible to mitigate harmonic timely. This paper studies a multi-time-scale harmonic mitigation method which adds 5 min prediction to the global optimization method which is named multi-time-scale. The objective is to correct the deviation of harmonic caused by the long-time-scale harmonic prediction error. This paper utilizes MPC to predict the amplitude and phase variation of the harmonics in short time scale, and utilizes distributed VDAPF to optimize harmonic in long time scale. The IEEE 33 nodes system was used as an example to conduct a comparative analysis of mitigation effects in two different harmonic injection scenarios which injected separately 10 and 20%. The results shows that the mitigating effect of the global optimization method is limited under two different harmonic injection scenarios, and it needs to combine with short time scale harmonic prediction information to ensure the effectiveness and rationality of the mitigation results. When the harmonic current fluctuates, there are unqualified voltage distortion nodes in each region, and the voltage distortion rate is larger. But the MPC can change harmonic prediction in a short time, so every harmonic of each VDAPF conductance values is set bigger, and harmonic conductance of the higher harmonics is relatively lower.

Keywords: multi-time scale predictive, VDAPF, harmonic mitigation, MPC, high proportion clean energy

Edited by:
Yuefang Du,
University of Electronic Science and Technology of China, China

Reviewed by:
Li Jin,
China University of Geosciences, China
Qi Zhu,
Xi'an Shiyou University, China

****Correspondence:***
Licheng Xing
lichengzhongbei@163.com

Specialty section:
This article was submitted to Process and Energy Systems Engineering, a section of the journal Frontiers in Energy Research

Received: *25 October 2021*
Accepted: *07 December 2021*
Published: *27 January 2022*

Citation:
Suo L, Lin L, Xing L and Jia Q (2022) Multi-Time Scale Harmonic Mitigation for High Proportion Electronic Grid. Front. Energy Res. 9:801197. doi: 10.3389/fenrg.2021.801197

1 INTRODUCTION

The harmonics on the power grid reduce the life of power supply equipment; and nowadays a new situation has emerged from the power grid, that is a large number of new energies such as photovoltaics and wind power are used to distribution network (Yang et al., 2017; Xie et al., 2021), and new elements such as controllable load, distributed power generation, distributed energy storage, and electric vehicles were used (Munir et al., 2020). This forms a power electronic distribution network. Literature (Munir et al., 2019) proposes to improve the performance of harmonic control through the cooperation of multiple APFs. Literature (Chen et al., 2017) proposed a parallel APF with selective closed-loop control to achieve compensation for the harmonic voltage at the common connection point. Literature (Lee et al., 2008) proposed a droop control strategy for multiple distributed APFs operating in parallel. Literature (Tian et al., 2020) studies the optimal configuration method of distributed VDAPF for the decentralized harmonic problem of distribution network. However, a trend of harmonic dispersion and network-wide diffusion has been formed due

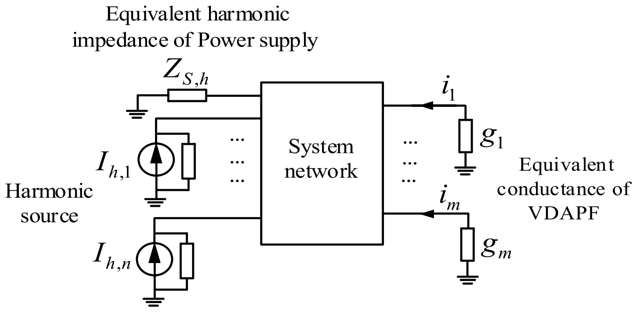

FIGURE 1 | System harmonic equivalent circuit.

to the diversification of equipment types and characteristics, and the complexity of disturbance distribution (Ebrahimzadeh et al., 2019; Wang et al., 2019; Artale et al., 2021).

In response to this situation, a distributed global optimization for harmonics on the grid side was proposed, which used the strategy of combining global optimization and local control to achieve distributed harmonic mitigation. This method aims at the overall optimization of the voltage distortion of all nodes of the distribution network, and solves the global optimization model by establishing the objective function and constraint conditions of the power electronic distribution network, so as to obtain the optimized parameters of VDAPF at operating point in the long-term scale. However, long-term global optimization is based on short-term harmonic prediction, and prediction errors are inevitably present, which may lead to deviation from long-term global optimization solutions. In order to correct the deviation from harmonic caused by the long-time-scale harmonic prediction error. This paper used the prediction in short-time-scale based on the model predictive control (MPC) to make up for the shortcomings of the long-time-scale global optimization. The long-time scale global optimization method which combined with the short-time scale optimization is called the multi-time scale harmonic optimization method.

2 MODEL AND PARAMETERS SETTING

2.1 Harmonic Equivalent Circuit of Power Electronic Distribution Network

The harmonic Norton equivalent model is used to characterize the model of the distributed harmonic source of the distribution network. The equivalent parameters of each model are received by experiment. The power electronic distribution network can be represented by the system network shown in **Figure 1**. The equivalent harmonic injection and linear load of each node can be represented by Norton circuit, and it is approximately considered that the scattered harmonic sources distributed among each node are not affected by the node voltage.

In **Figure 1**, the conductance to ground for each VDAPF which connected to parallel on the node is expressed by the harmonic conductance. The power branch of the large power grid side is equivalent to the harmonic impedance to ground. Taking the *h*th harmonic circuit as an example, $Z_{S,h}$ is the equivalent harmonic impedance of the power supply on the large grid side, and $I_{h,n}$ is the *h*th harmonic current of the harmonic source *n*, and g_m is the equivalent harmonic conductance of *m*th VDAPF, and i_m is the harmonic compensation current injected by *m*th VDAPF.

2.2 Harmonic Optimization Method on Long Time Scale

2.2.1 Global Optimization Objective Function

The data monitoring and collection system of distribution network generally collects data every 15 min, and the active and reactive power dispatching of the distribution network usually takes 15 min as the dispatching period (Xia et al., 2019; Zhao et al., 2019). Therefore, the long-time scale optimization takes 15 min as the time granularity. It considers the overall optimization of power quality at the nodes in the entire network, and it takes harmonic conductance values of VDAPF at distributed and parallel connected nodes as the optimization variables. The weight coefficient c_n corresponding to different nodes is set to characterize the degree of requirements for the power quality.

This paper introduces the node sensitivity factor α, whose value reflects the sensitivity about voltage distortion of the load equipment which is connected to nodes. The larger the value of α, the higher requirement for distortion of the node. As shown in **Eq. 1**, the weight coefficient of the node is defined by the proportion of the sensitivity factor of the known nodes in all the nodes.

$$c_j = \frac{\alpha_j}{\sum\limits_{j=1}^{N} \alpha_j} \tag{1}$$

In the formula, α_j is the load sensitivity factor of node *j*, and its value can be set and adjusted according to actual situation, and *N* is the total number of system nodes.

Considering the difference in the weight coefficients of different nodes, the objective function of long-term global optimization are set as the weighted summation of the harmonic voltage distortion rate of the nodes. The calculation formula is shown in **Eq. 2**.

$$f_{THD} = \min \sum_{j=1}^{N} c_j \cdot \mathrm{THD}_j \tag{2}$$

In the formula, f_{THD} is the objective function of global optimization; c_j is the weight coefficient of node *j*, whose magnitude can be obtained by **Eq. 1**; THD_j represents the total voltage distortion rate of node *j*, which is calculated by **Eq. 3**.

$$\mathrm{THD}_j = \frac{\sqrt{\sum\limits_{h=2}^{\infty} U_{h,j}^2}}{U_{1,j}} \times 100\% \tag{3}$$

In the formula, $U_{1,j}$ is the effective value of the fundamental wave's voltage at node *j*; $U_{h,j}$ is the effective value of the voltage *of* *h*-order harmonic at node j, which can be calculated by the *h*-order harmonic power flows.

2.2.2 Global Optimization Constraints

During the harmonic compensation process of VDAPF, the maximum compensation amount cannot exceed the rated capacity limit. That expressed as **Eq. 4**.

$$S_{\mathrm{APF},ci} \le S^{0}_{\mathrm{APF},ci} \tag{4}$$

In the formula, $S_{\mathrm{APF},ci}$ are the actual total harmonic compensation capacity of the c_i VDAPF; $S^{0}_{APF,ci}$ are the rated capacity of the c_i VDAPF.

The compensation capacity $S_{\mathrm{APF},ci}$ can be calculated by **Eq. 5**.

$$S_{\mathrm{APF},ci} = \sqrt{\sum_{h=2}^{\infty} \left(G_{h,ci} \times U_{h,ci}\right)^2} \tag{5}$$

In the formula, $G_{h,ci}$ are the values of *h*th harmonic conductance of VDAPF, and $U_{h,ci}$ are the *h*th harmonic voltages of the VDAPF node. The particle swarm optimization (PSO) has fast solution speed and few parameters. The particle updates its speed and position according to **Eq. 6**.

$$\begin{aligned} \boldsymbol{V}_i^{k+1} &= \omega \boldsymbol{V}_i^{k} + c_1 r_1\left(\boldsymbol{P}_{besti}^{k} - \boldsymbol{X}_i^{k}\right) + c_2 r_2\left(\boldsymbol{g}_{best}^{k} - \boldsymbol{X}_i^{k}\right) \\ \boldsymbol{X}_i^{k+1} &= \boldsymbol{X}_i^{k} + \boldsymbol{V}_i^{k+1} \end{aligned} \tag{6}$$

In the formula, $\boldsymbol{V_i^{k+1}}$ represents the particle velocity of particle *i* in the *k*+1 iteration; X_i^{k+1} *i* represents the position of particle *i* in the *k*+1 iteration; $\boldsymbol{P}_{besti}^{k}$ and $\boldsymbol{g}_{besti}^{k}$ respectively represent the particle *i* at individual optimal position and global optimal position at the *k* iteration; ω is the inertia weight; c_1 and c_2 are respectively the individual learning factor and the group learning factor; r_1 and r_2 are random values between [0, 1].

The inertia weight when the particle update velocity needs to be increased successively with the number of iterations, the inertia weight shown in **Eq. 7** changes from the maximum to the minimum.

$$\omega = \omega_{\max} - \frac{t * (\omega_{\max} - \omega_{\min})}{t_{\max}} \tag{7}$$

The steps to improve the PSO algorithm are:

1) Initializing the conductance value and the change rate of each harmonic conductance of VDAPF;
2) Comparing the objective function's values of all conductance under different harmonics and getting the corresponding optimal conductance value;
3) Updating the conductance value and the change rate according to current inertia weight value;
4) Performing the next iteration calculation;
5) Setting the error threshold or the number of iterations as the iteration termination condition. If one of them is met, the iteration will be terminated and the final global optimal conductance value will be obtained; otherwise, return to step (4).

2.3 Multi-Time Scale Rolling Optimization

According literature (Zhang et al., 2017; Huang et al., 2019; Yan et al., 2019), the time granularity of the daily active and reactive power dispatching of the distribution network is generally maintained at the minute level, such as 1–5 min. Therefore, the short-time-scale prediction choose 5 min. The rolling optimization method is an optimization method which combined 5 min prediction and the long-time scale optimization. Its feature is to perform the rolling optimization of the local control operating characteristic parameters based on the short-term prediction of the harmonic current.

The model predictive control (MPC) method was used in short-time scale current prediction. Its characteristic is to solve the optimization model in a finite time domain according to the objective function and the constraints. In the vector of the obtained optimal solution, the first decision variable is taken as the optimal decision for on the current period. The optimization task of each sampling time is performed according to this cycle, and a new objective function is obtained according to the updated measurement information, and the solution is updated. Combining the control method and optimization objective of the VDAPF local controller of the zone, the difference between the actual voltage and the reference voltage of each node in the zone is controlled firstly. That is to make the difference between actual harmonic voltage and reference value of the harmonic voltage smallest in time domain. For the *h*th harmonic, the objective function *J* is shown as **Eq. 8**:

$$J = \min \sum_{j=1}^{N} \left| U_j^h - U_j^{h*} \right| \tag{8}$$

In the formula, U_j^h is the actual *h*th harmonic voltage of node *j*, and $U_j^{h^*}$ is the reference voltage of *h*th harmonic of node *j*.

The constraints during the solution process are shown in **Eq. 9**.

$$U_j^h \le U_{j\max}^h \tag{9}$$

In the formula, U_j^h *max* is the limit voltage of each harmonic.

Based on current state and system model, the rolling method cycle of a limited time domain, and updates the forecast information and operating status in the future scheduling cycle. Then it re-optimizes in the current rolling window, and executes results of scheduling decisions.

2.4 Parameters Setting

In order to verify the effectiveness of the harmonic distributed optimization method based on the combination of VDAPF global optimization and local control, IEEE 33-nodes distribution network system is taken as the example.

According literature (Zhou et al., 2015), the electrical load connected to each node contains a variety of sensitive loads, and different equipment is divided into four levels by the sensitivity of equipment voltage sags. The weight coefficient c_j of each observation node is set to represent the degree of voltage distortion, and is reflected in the proportion of voltage distortion in the total objective function in the optimization process. For the nodes which connected to electric sensitive load, the sensitivity factors of nodes 4, 23, and 28 is setting to 10, 9, and 7, and the sensitivity factors of other nodes is setting to 1. The weight coefficient of each node is shown in **Table 1**.

Long-term scale PSO parameters: the maximum inertia weight $\omega_{\max}$ is 1.4; the minimum inertia weight $\omega_{\min}$ is 0.4; the initial value of the learning factor is 2; the particle swarm size is 400, and the maximum number of iterations is 150.

TABLE 1 | Weight coefficient of each node.

Node number	Weight coefficient
4	0.179
23	0.156
28	0.125
Else	0.018

3 RESULTS AND DISCUSSION

3.1 Results of Two Scenario

Since the affection of harmonic are different, this paper considers two different harmonic injection scenarios which injected 10 and 20%. The global optimization results of the equivalent conductance of each harmonic of the VDAPF at each control node in Scenario 1 and Scenario 2 were shown in **Tables 2**, **3**.

In scenario 1, the harmonic conductance values of VDAPF can be seen from **Table 2**. The conductance value of higher-order harmonic is smaller than the lower-order. For example, the 13th and 11th harmonic conductance values of the control nodes 13 and 24 are smaller than the 5th and 7th harmonic conductance values; the 13th harmonic conductance value of the control node 29 is smaller than the harmonic conductance values of other control nodes; and the conductance value of the 13th harmonic of node 5 is small. Because the low-order harmonics injected into the network by the harmonic source such as the 5th and 7th harmonics have larger amplitudes, while the content of higher-order harmonics is less. Since the equivalent harmonic conductance of VDAPF characterizes the intensity of harmonic control, the content of low-order harmonics in the network is relatively high, and the corresponding harmonic conductance value is relatively large, so greater control intensity is required for low-order harmonics.

In **Table 3**, the harmonic conductance value of VDAPF also follows the same law, that is the conductance value of higher-order harmonic is smaller than the lower-order. Because the overall harmonic current injection of scenario 2 is larger than that in scenario 1, and the resulting harmonic pollution is also more serious. At the same time, it also satisfies that the injection amplitude of high-order harmonic current is smaller than that of low-order harmonic current injection. Similarly, the equivalent harmonic conductance of VDAPF characterizes its treatment strength. Therefore, under the same network parameters, more serious harmonic pollution requires more treatment to smooth the harmonic current injection.

Comparing the harmonic conductance optimization results of scenario 1 and scenario 2, it can be concluded that the harmonic conductance value of the VDAPF in scenario 1 is generally smaller than the value of scenario 2. Because the harmonic pollution of scenario 2 are more serious than scenario 1, and stronger treatment is required, and the harmonic conductance value represents the intensity of VDAPF's treatment of harmonics. The greater the harmonic conductance, the greater the required intensity of harmonic control. Therefore, under the requirements of the same harmonic voltage limit, the VDAPF needs to output more control amounts under the scenario of more serious harmonic pollution.

3.2 Comparison of Multi-Time Scale Rolling Optimization and Global Optimization Results

Option 1: Distributed global optimization method used in this paper based on the voltage detection type APF grid-side.

Option 2: Decentralized local harmonic control method based on current detection type APF.

The results of voltage distortion rate of each node before and after mitigation in two scenarios are shown as **Figures 2**, **3**.

The voltage distortion of each node is compared, and the comparison results under scenario 1 and scenario 2 are shown in **Figures 4**, **5**, respectively.

For Scenario 1, when a 10% fluctuation occurs to the harmonic current injection, the harmonic voltage distortion

TABLE 2 | Global optimization results of VDAPF harmonic equivalent conductance under scenario 1.

Node	5th harmonic conductance reference value/S	7th harmonic conductance reference value/S	11th harmonic conductance reference value/S	13th harmonic conductance reference value/S
5	0.51	0.32	0.42	0.34
13	0.62	0.42	0.34	0.24
24	0.53	0.31	0.22	0.13
29	0.44	0.61	0.52	0.34

TABLE 3 | Global optimization results of VDAPF harmonic equivalent conductance under scenario 2.

Node	5th harmonic conductance reference value/S	7th harmonic conductance reference value/S	11th harmonic conductance reference value/S	13th harmonic conductance reference value/S
5	0.81	0.63	0.63	0.22
13	0.80	0.61	0.51	0.50
24	0.71	0.44	0.34	0.23
29	0.82	0.82	0.76	0.45

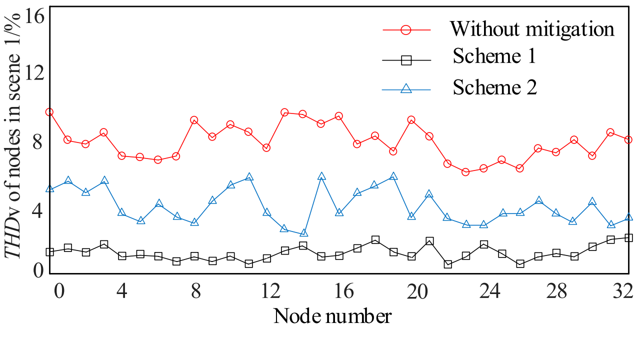

FIGURE 2 | Total voltage distortion rate of each node before and after mitigation under scenario 1.

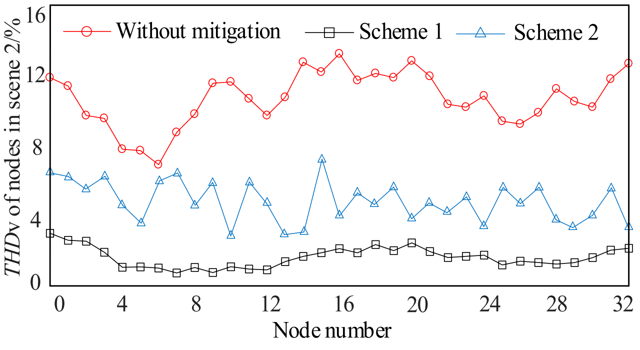

FIGURE 3 | Total voltage distortion rate of each node before and after mitigation under scenario 2.

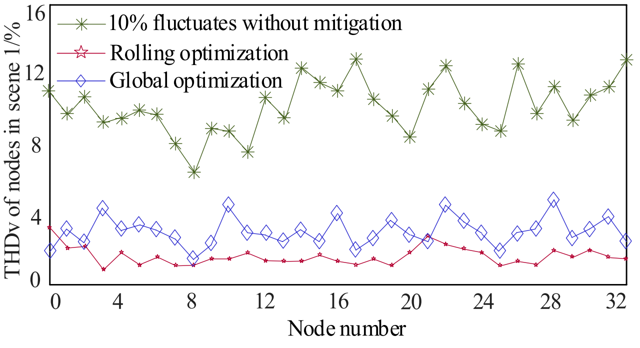

FIGURE 4 | Comparison results of operating point mitigation between rolling optimization and global optimization under scenario 1.

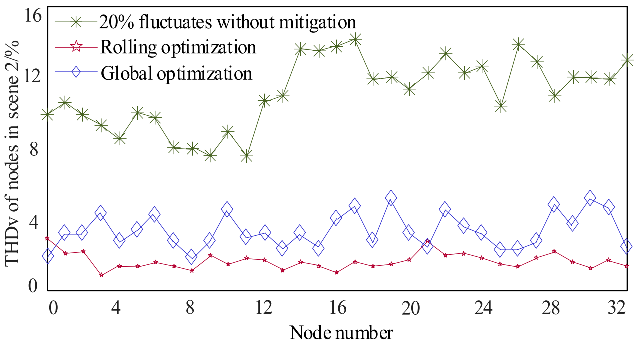

FIGURE 5 | Comparison results of operating point mitigation between rolling optimization and global optimization under scenario 2.

of each node is aggravated. If the solution to the global optimization result is still used to manage, it can be seen in **Figure 4** that there are nodes with unqualified voltage distortion in each partition, such as node 3, node 10, node 22, and node 28. This verifies that the global optimization results are only feasible for long-term but the actual harmonic current injection fluctuates in real time. The fluctuation range after multi-time scale rolling optimization are smaller than global optimization method. The multi-time scale optimization method is more efficient than Global optimization method.

It can be seen from **Figures 3–5** that for scenario 2, the harmonic current injected by the harmonic source load has a 20% fluctuation, and the harmonic voltage distortion of each node is aggravated also, and global optimization is adopted. As a result of the solution, the number of nodes with unqualified voltage distortions in each partition is significantly increased compared with scenario 1, such as node 10, node 19, and node 30, which are more serious. It is also verified that the global optimization results are only for the long-term, and the actual harmonic current is injected into real-time fluctuations. The global optimization results need to be combined with the short-time-scale rolling optimization to ensure the harmonics of all nodes in each region. The multi-time scale optimization method is more efficient than Global optimization method.

4 CONCLUSION

This paper proposes a multi-time-scale harmonic optimization method based on the long-term scale global optimization of the distributed VDAPF and the short-time scale rolling optimization of local control. The long-term scale global optimization aims at the overall optimization of the voltage distortion at all nodes of the distribution network. It constructs a global optimization objective function and constraint conditions, and using intelligent optimization algorithms to solve the global optimization model. The operating characteristic parameters of VDAPF are optimized on a short time scale base on MPC, and the feedback correction is brought in to correct the predict deviation caused by mitigation error to make the harmonic voltage of every node always maintained at a qualified level. Through the multi-time scale optimization, the harmonic control is continuously revised, and optimized entire nodes of the distribution network. It provides a grid-side solution for the power electronic distribution network to optimize the harmonic voltage of the entire network nodes.

The multi-time-scale optimize method can solve the large fluctuation problem of harmonic voltage in global optimization method, but the short-time-scale prediction need more memory and calculation. It needs communication on time with control computer. In addition, this method can efficiently mitigate the 13th and lower harmonic, but the effects about higher harmonic are not verified in this paper, and that would be studied in after work.

DATA AVAILABILITY STATEMENT

The original contributions presented in the study are included in the article/Supplementary Material, further inquiries can be directed to the corresponding author.

REFERENCES

Artale, G., Caravello, G., Cataliotti, A., Cosentino, V., Cara, D. D., Guaiana, S., et al. (2021). Measurement of Simplified Single- and Three-phase Parameters for Harmonic Emission Assessment Based on IEEE 1459-2010. *IEEE Trans. Instrum. Meas.* 70 (99), 1–10. doi:10.1109/tim.2020.3037949

Chen, X., Dai, K., Xu, C., Peng, L., and Zhang, Y. (2017). Harmonic Compensation and Resonance Damping for SAPF with Selective Closed-loop Regulation of Terminal Voltage. *IET Power Elect.* 10 (6), 619–629. doi:10.1049/iet-pel.2016.0344

Ebrahimzadeh, E., Blaabjerg, F., Wang, X., and Bak, C. L. (2019). Optimum Design of Power Converter Current Controllers in Large-Scale Power Electronics Based Power Systems. *IEEE Trans. Ind. Applicat.* 55 (3), 2792–2799. doi:10.1109/tia.2018.2886190

Huang, W., Liu, S., and Yi, Y. (2019). Multi-Time-Scale Slack Optimal Control in Distribution Network Based on Voltage Optimization for point of Common Coupling of PV[J]. *Automation Electric Power Syst.* 43 (3), 92–100. doi:10.7500/AEPS20180328003

Lee, T.-L., Cheng, P.-T., Akagi, H., and Fujita, H. (2008). A Dynamic Tuning Method for Distributed Active Filter Systems. *IEEE Trans. Ind. Applicat.* 44 (2), 612–623. doi:10.1109/tia.2008.916596

Munir, H. M., Zou, J., Xie, C., and Li, K. (2019). Direct Harmonic Voltage Control Strategy of Shunt Active Power Filters Suitable for Microgrid Applications [J]. *J. Power Elect.* 19 (1), 265–277. doi:10.6113/JPE.2019.19.1.265

Munir, M. S., Tian, H., and Li, Y. W. (2020). Residential Distribution System Harmonic Compensation Using Priority Driven Droop Controller. *Cpss Tpea* 5, 213–223. doi:10.24295/CPSSTPEA.2020.00018

Tian, S., Jia, Q., Xue, S., Yu, H., Qu, Z., and Gu, T. (2020). Collaborative Optimization Allocation of VDAPFs and SVGs for Simultaneous Mitigation of Voltage Harmonic and Deviation in Distribution Networks. *Int. J. Electr. Power Energ. Syst.* 120, 106034. doi:10.1016/j.ijepes.2020.106034

Wang, X., Blaabjerg, F., and Blaabjerg, F. (2019). Harmonic Stability in Power Electronic-Based Power Systems: Concept, Modeling, and Analysis. *IEEE Trans. Smart Grid* 10 (3), 2858–2870. doi:10.1109/tsg.2018.2812712

Xia, P., Liu, W., and Zhu, D. (2019). Multi-Time Scale Optimal Control Method of Reactive Power and Voltage Based on Model Predictive Control[J]. *Electric Power Automation Equipment* 39 (3), 64–70. doi:10.16081/j.issn.1006-6047.2019.03.010

Xie, X., Sun, Y., Wang, Q., Li, Y., Zhang, Y., and Zhang, L. (2021). A Piecewise Probabilistic Harmonic Model of Aggregate Residential Loads. *IEEE Trans. Power Deliv.* 36 (2), 841–852. doi:10.1109/TPWRD.2020.2995081

Yan, X., Xu, Y., Li, R., and Jin, Y. (2019). Multi-Time Scale Reactive Power Optimization of Distribution Grid Based on Model Predictive Control and Including RDG Regulation[J]. *Trans. China Electrotechnical Soc.* 34 (10), 2022–2037. doi:10.19595/j.cnki.1000-6753.tces.181605

Yang, W., Jing, Y., Sun, Y., and Xu, W. (2017). Characteristics of Harmonic Distortions in Residential Distribution Systems[J]. *IEEE Trans. Power Deliv.* 32 (3), 1495–1504. doi:10.1109/TPWRD.2016.2606431

Zhang, B., Tang, W., and Cong, P. (2017). Multi-Time Scale Optimal Control in Hybrid AC/DC Distribution Networks Based on SOP and VSC[J]. *Adv. Tech. Electr. Eng. Energ.* 36 (9), 11–19.

Zhao, B., Ni, C., and Li, Z. (2019). Multi-Time Scale Optimal Scheduling of Electricity-Gas Hybrid System Based on Adaptive Step Size ADMM[J]. *Electric Power Automation Equipment* 39 (8), 294–299.

Zhou, X., Fenghua, W., and Ronghui, H. (2015). Assessment of Voltage Sags in Substations Based on Power System and Equipment Sensitivity Analysis [J]. *Proc. CSEE* 35 (08), 1940–1946. doi:10.13334/j.0258-8013.pcsee.2015.08.013

AUTHOR CONTRIBUTIONS

LS, Work concept or data collection; LX, Draft the paper and make revisions to the paper; LL, Model design and simulation; QJ, make revisions to the paper.

FUNDING

This work was supported in part by Open Fund Project of Key Laboratory of Power Conversion, Transmission and Control in Inner Mongolia Autonomous Region (No. IMEECTC2020002).

Conflict of Interest: The authors declare that the research was conducted in the absence of any commercial or financial relationships that could be construed as a potential conflict of interest.

frontiers
in Energy Research

ORIGINAL RESEARCH
published: 02 February 2022
doi: 10.3389/fenrg.2022.835066

Voltage Source Converter–Based Voltage Stiffness Compensator to Improve Grid Voltage Dynamics

Lei Shang[1]*, *Chunyi Han*[1], *Xuzhu Dong*[1], *Ye Tian*[2] *and Jianing Liu*[3]

[1]School of Electrical Engineering and Automation, Wuhan University, Wuhan, China, [2]State Grid Liaoning Electric Power Supply Company, Liaoning, China, [3]State Grid Jilin Electric Power Supply Company, Chuanying Power Supply Center, Jilin, China

This study proposes a novel voltage source converter (VSC)-based voltage dynamic regulatory device based on energy storage and virtual synchronous control, called as a rotating inertia and voltage stiffness compensator (RIVSC), to enhance grid voltage dynamics. In the proposed RIVSC, there is no inner cascaded current control, and the output voltage of the VSC, i.e., inner potential, is directly connected to the grid *via* a filter. Stiffness characteristic is featured in the inner potential of the RIVSC by the virtual synchronous control. On the basis of the stiffness characteristic, the RIVSC can naturally provide dynamic support for grid voltage. Compared to the traditional synchronous condenser, the proposed RIVSC is more flexible and contributes less short-circuit current. Compared to the existing power electronic-interfaced voltage regulatory device, dynamic support is natural without any time delay, and the proposed RIVSC can improve the dynamic performance of the grid voltage, which is helpful to alleviate the temporary overvoltage at the sending terminal. The basic principle, control methods, and application analysis are presented. Meanwhile, a 10 kW prototype is set up, and the experiment results validate the feasibility and effectiveness of the proposed RIVSC on improving grid voltage dynamics.

Keywords: voltage stiffness, rotating inertia and voltage stiffness compensator (RIVSC), voltage dynamic, voltage regulation, overvoltage

Edited by:
Liansong Xiong,
Nanjing Institute of Technology (NJIT),
China

Reviewed by:
Yuanzhu Chang,
Polytechnique Montréal, Canada
Xinshou Tian,
North China Electric Power University,
China
Ning Li,
Xi'an University of Technology, China

Correspondence:
Lei Shang
shanglei@whu.edu.cn

Specialty section:
This article was submitted to
Process and Energy Systems
Engineering,
a section of the journal
Frontiers in Energy Research

Received: *14 December 2021*
Accepted: *03 January 2022*
Published: *02 February 2022*

Citation:
Shang L, Han C, Dong X, Tian Y and Liu J (2022) Voltage Source Converter–Based Voltage Stiffness Compensator to Improve Grid Voltage Dynamics.
Front. Energy Res. 10:835066.
doi: 10.3389/fenrg.2022.835066

1 INTRODUCTION

With more and more renewable energy generations (RES) integrated into the grid, the equivalent inertia of the power system declines and the voltage regulation capability is weakened, which deteriorates the dynamic behavior of grid voltage (Du et al., 2019). Some issues and potential risks are appearing. The temporary overvoltage risk may raise some cascading failure in the sending terminal of HVDC with large-scale integration of RESs during lockdown or commutation failure, such as Qinghai and Gansu in China, and has been published in the study by (Zhao et al., 2016). The large-scale reactive power compensation is installed at the sending terminal to compensate the reactive power. However, the local voltage control is not fast enough to reduce the reactive power and leads to temporary reactive power excess, which is the immediate cause of the overvoltage. In other words, the temporary overvoltage is reactive power surplus raised by the dynamic mismatch of reactive power in the regional power grid of the sending terminal (Xue and Zhang, 2017; Liu et al., 2018; Lee et al., 2020; Varma and Mohan, 2020; Liu et al., 2021).

The shunt capacitor, SVC, and STATCOM are the main reactive power compensations at the sending terminal. The shunt capacitor is switched on or off with a mechanical switch to compensate the inductive reactive power consumed in the power system (Ramos and Tyll, 1989), which can provide large capacity and low cost-reactive power compensation, but the reactive power adjustment is not continuous, and the dynamic response is limited by the behavior of the mechanical switch. In recent years, the SVC (Zhang, 2010) and STATCOM (Hou et al., 2018) are developed as rapid reactive power compensators with power electronic technology, which has become the main stream of reactive power compensation due to the excellent dynamic performance. The local voltage control bandwidth and gain are attempted an increase for alleviating the temporary overvoltage, but the control bandwidth and gain of the voltage control are limited by stability constraint, and too high gain voltage control may cause some instability (Xiong et al., 2020), (Huang et al., 2012). A traditional synchronous condenser (SC) is installed at the sending terminal to alleviate the temporary overvoltage by its natural dynamic voltage support capability (Teleke et al., 2008), (Mendis et al., 2014), which is a reluctant solution. However, the traditional SC is very expensive, inflexible, and bull. More importantly, large-scale integrations of SC lead to the short-circuit current exceeding standard.

In recent years, the virtual synchronous control has been developed for the VSC to emulate the synchronous generator to cope with the issue of a low-inertia system. In the study by (Zhong et al., 2014), the synchronverter is proposed and controlled entirely according to the mechanical and electrical equations of synchronous generators (SGs) without any assumptions. It is able to provide the inertial response as SGs but seriously confine the controllability of VSCs. The virtual synchronous control based on the second-order motion equation is applied in DFIG-based WTs to enhance the operation of WTs in a weak grid and to provide inertial support (Wang et al., 2015), which is with a simple control structure and clear physical significance, but it may confront with severe difficulty on fault current limitation because it is without any current controls. Ref (Cao et al., 2018) develops a virtual synchronous control with the cascaded AC current and voltage controls, which is effective to reduce fault current, but its dynamic support capability by natural response is weakened. In summary, the virtual synchronous control has been developed for the improvement of grid frequency dynamics, but the impact on grid voltage dynamics is still not discussed, and the specialized reactive power dynamic compensator is still not reported.

In the study by (Shang et al., 2021a), the impact of the ac current-controlled VSC is discussed, and the negative effect of the ac current control on grid voltage is analyzed. In the study by (Shang et al., 2021b)- (Shang, 2019), a novel idea of compensation control was proposed to improve the grid frequency and voltage based on the inertia and stiffness compensation, but the rounded analysis and fault protection under the grid fault are not discussed. This study develops the theory analysis of the stiffness compensation and studies a virtual synchronous condenser (RIVSC) simultaneously for stiffness compensation to improve the grid frequency and voltage dynamics like the traditional SC by experiment validation. The RIVSC is consisted by the VSC and energy storage based on virtual synchronous control, more flexible than the traditional SC. On one hand, different from existing dynamic compensation, the RIVSC can naturally provide dynamic reactive power support prior to the functioning of the local voltage control based on stiffness compensation, which is effective to improve grid voltage dynamics. On the other hand, the existing virtual synchronous generator (VSG) is mainly focused on inertia and frequency regulation, whereas the proposed RIVSC focuses on grid voltage stiffness compensation and dynamic voltage regulation. The grid voltage stiffness introduced in this study means the resistant capability of grid voltage under the imbalance between injected and consumed reactive powers, which reflects the grid voltage dynamic characteristic and impacts on the rate of change of the grid voltage. The grid voltage resilience is different from the normal grid voltage control. The grid voltage control is to recover the balance between injected and consumed reactive powers after disturbed.

The rest of this study is organized as follows. The principles and control system of the static synchronous condenser are presented in **Sections 2**, **3**. Then, the dynamic response characteristics and potential applications of the RIVSC are analyzed and discussed in **Section 4**. Experimental results are presented to validate the effectiveness and feasibility of the RIVSC in **Section V**. Finally, some conclusions are drawn in **Section VI**.

2 PRINCIPLES OF THE STATIC SYNCHRONOUS CONDENSER

The study proposes a novel voltage source converter (VSC)-based voltage regulatory device based on energy storage and virtual synchronous control, called as the static synchronous condenser (RIVSC). The proposed RIVSC is composed by a VSC, an ES, and a control system, as depicted in **Figure 1**.

2.1 The VSC Model

Considering both terminal voltage and inner potential, i.e., the output voltage of a three-phase voltage source converter (VSC), the topology of the grid-connected VSC is depicted in **Figure 1**. The inner potential vector $\boldsymbol{U}_c$ of the VSC and terminal voltage vector $\boldsymbol{U}_t$ can be written as

$$U_c = U_c e^{j\theta_c}, U_t = U_t e^{j\theta_t}, \tag{1}$$

where U_c and U_t are the magnitudes of the inner potential and terminal voltage. θ_c and θ_t are the corresponding phase angles.

In this study, the filter is an inductance. Ignoring the filter's electromagnetic dynamic, the output current is expressed as

$$I_s = \frac{U_c - U_t}{jX_c}, \tag{2}$$

where $\boldsymbol{I}_s$ is the VSC's current. X_c is the filter's impedance.

The instantaneous active and reactive power (P_e and Q_e) of the VSC is calculated by

$$\begin{cases} P_e = u_{t\alpha} i_{s\alpha} + u_{t\beta} i_{s\beta} \\ Q_e = -u_{t\alpha} i_{s\beta} + u_{t\beta} i_{s\alpha} \end{cases}, \tag{3}$$

where $u_{t\alpha}$, $u_{t\beta}$, $i_{s\alpha}$, and $i_{s\beta}$ are the components of instantaneous voltage and current in the $\alpha\beta$ reference frame, respectively.

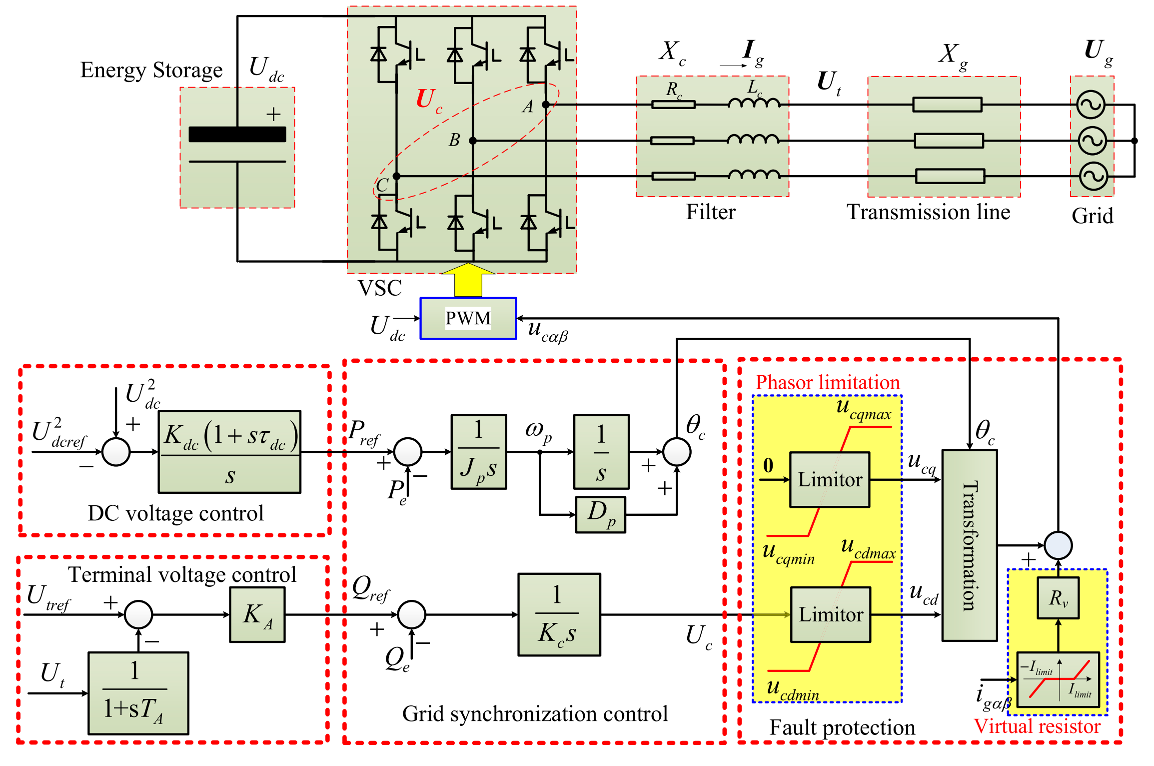

FIGURE 1 | Circuit and control system of the proposed RIVSC.

2.2 Grid Integration Control

In the proposed RIVSC, the inner potential is generated by the VSC, which is synchronized with the grid by the active and reactive power controls.

The active power control is responsible for regulating the inner potential's frequency and phase. The inertial response is featured in the inner potential by a well-known swing equation of SGs, as shown in **Figure 1**. The energy source comes from the energy storage equipped in the DC-link.

$$\begin{cases} \frac{d\theta_c}{dt} = \omega_c \\ \frac{d\omega_c}{dt} = \frac{P_{ref} - P_e}{J_p} - \frac{D_p \Delta\omega_c}{J_p}, \\ \Delta\omega_c = \omega_c - \omega_g \end{cases} \tag{4}$$

where ω_c and θ_c are the frequency and phase of the inner potential of VSCs, respectively. ω_g is the grid frequency. P_{ref} and P_e are reference and instantaneous power of VSCs, respectively. J_p is the virtual inertia coefficient, and D_c is the damping coefficient to enlarge the phase margin of the second-order control loop.

The reactive power control is responsible for regulating the inner potential's magnitude, as shown in **Figure 1**. The controller is an integral.

$$\frac{dU_c}{dt} = \frac{1}{K_c}\left(Q_{ref} - Q_e\right), \tag{5}$$

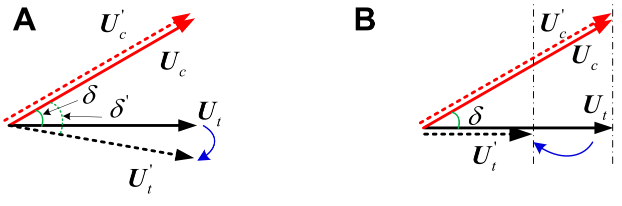

FIGURE 2 | Phasor diagram of the RIVSC's inner potential. **(A)** phase dynamic. **(B)** voltage dynamic.

where U_c is the inner potential's magnitude. Q_{ref} and Q_e are the reference and instantaneous reactive power of VSCs. K_c is the control coefficient of the reactive power control. With the increase in K_c, the change rate of the inner potential's magnitude is decreasing under a certain reactive power disturbance.

Under a steady state, the active and reactive power controls regulate the output powers with no error. Under dynamic state, the intrinsic inertial response in active power control is able to provide dynamic support for the grid frequency as **Figure 2A**. Similarly, due to the integral link in the reactive power control, the magnitude of inner potential maintains the original movement, which can be called as stiffness. Therefore, the voltage difference is spontaneously generated with an additional reactive power output as **Figure 2B**. The dynamic support of the voltage is spontaneously and passively provided

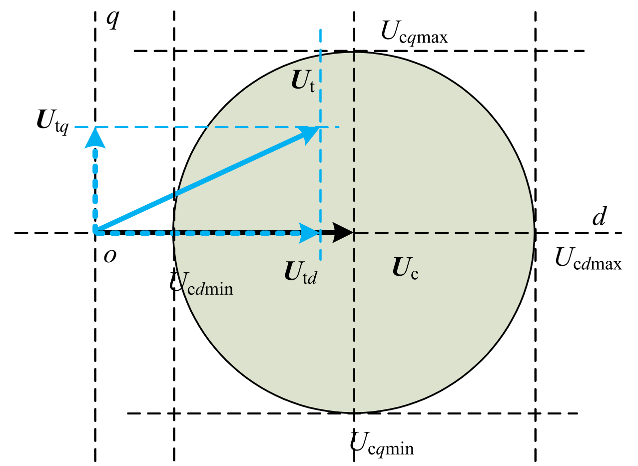

FIGURE 3 | Constraint of the proposed RIVSC's inner potential.

nearly without any time delay and grid condition estimation, which is helpful to improve the dynamics of the grid voltage.

2.3 Energy Storage Configuration and Control

The ES is connected into the DC-link of the VSC, and the VSC is integrated into the grid *via* a filter.

The stored energy in the DC-link is

$$E_s = \int_0^{\infty} [P_{in}(t) - P_e(t)]dt = \frac{1}{2}C_{dc}U_{dc}^2, \tag{6}$$

where E_s is the stored energy, and U_{dc} is the voltage of the DC-link. In this study, the supercapacitor is selected as the energy storage; C_{dc} is the capacitor of the DC-link. P_{in} is the input active power. In the RIVSC, the input active power is zero, i.e., $P_{\mathrm{in}} = 0$, and the energy storage is just required to provide energy support during the inertial response. Under steady state, the RIVSC exchanges with the grid with no active power; thus, the DC-side energy state and voltage is stable.

During the inertial response, the energy state of the RIVSC changes.

$$E_{inertia} = \int_0^{T_J} P_{rate}dt = P_{rate}T_J, \tag{7}$$

where E_{inertia} is the energy change during the inertial response. P_{rate} is the rate active power, and T_{J} is the equivalent time constant.

The energy state change behaves the DC voltage change. More energy storage will raise less DC voltage deviation. Ideally, more energy storage is better, but the cost should be considered.

The dynamic variant of the DC voltage of the RIVSC should be kept in appropriate scope, i.e.,

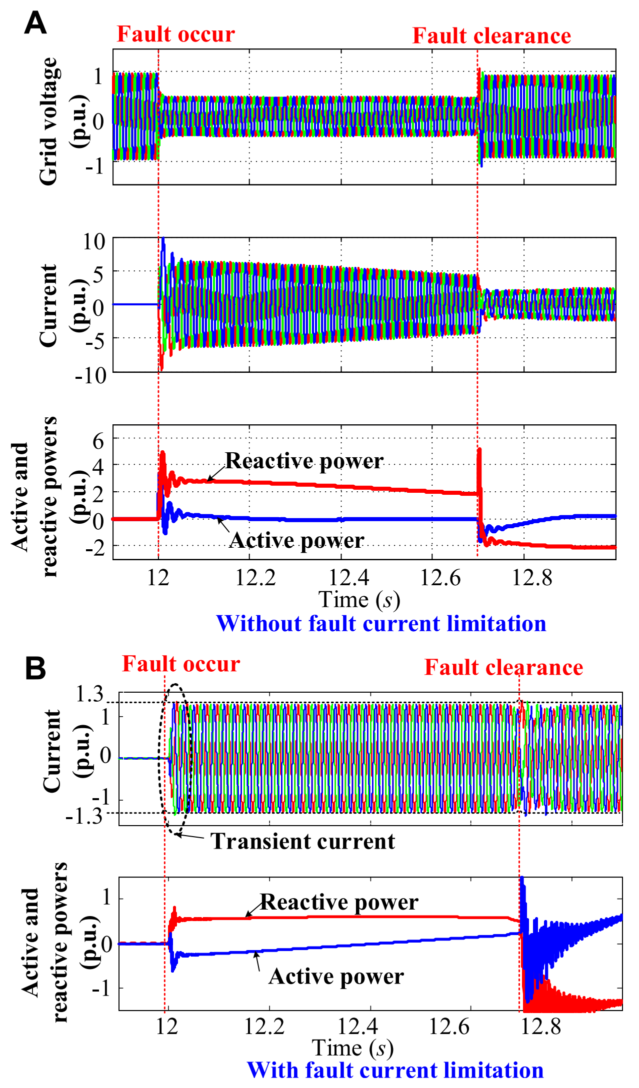

FIGURE 4 | Performance of the RIVSC under grid fault condition. **(A)** Without fault current limitation. **(B)** With fault current limitation

$$\frac{1}{2}CU^2_{dc\min} \le E_{inertia} + \frac{1}{2}CU^2_{dcN} \le \frac{1}{2}CU^2_{dc\max}, \tag{8}$$

where

$$C \ge \max\left(\frac{2P_{rate}}{U^2_{dcN} - U^2_{dc\min}}T_J, \frac{2P_{rate}}{U^2_{dc\max} - U^2_{dcN}}T_J\right). \tag{9}$$

The maximum DC voltage should consider the tolerance of the Chopper. The DC voltage min should consider the limitation of the PWM.

$$U_{c\max} = U_g + X_c I_{g\max}. \tag{10}$$

The Minimum DC voltage U_{dcmin} is

$$U_{dc\min} \ge \frac{\sqrt{3}U_{c\max}}{S_m} \ge \frac{\sqrt{3}}{S_m}\left(U_g + X_c I_{g\max}\right). \tag{11}$$

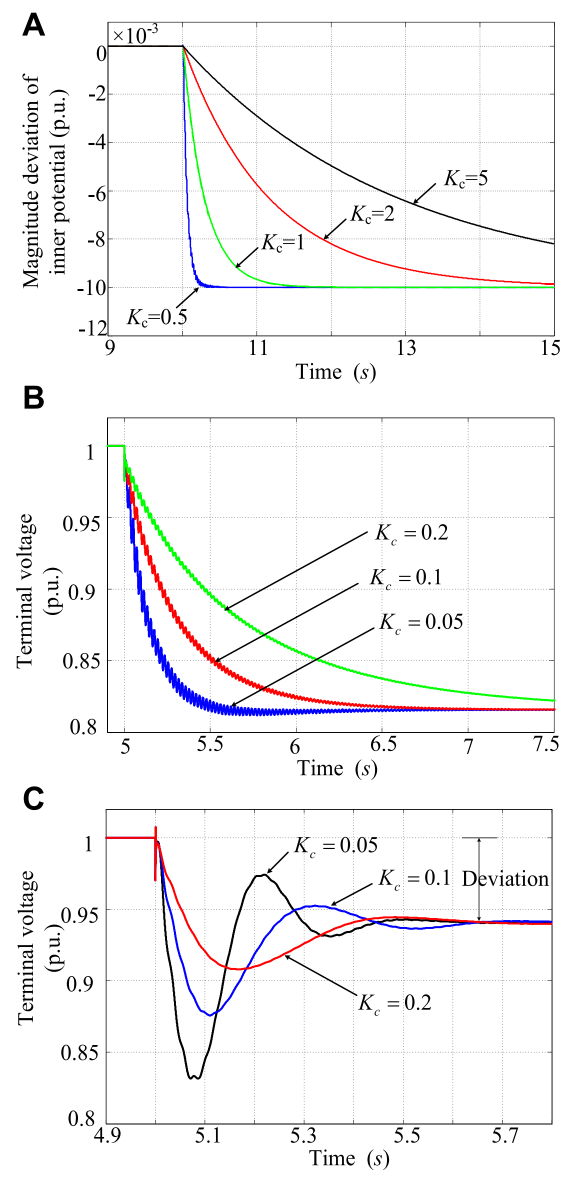

FIGURE 5 | Dynamics of the inner potential and the AC voltage at the PCC bus. **(A)** Magnitude deviation of inner potential **(B)** without voltage control **(C)** with voltage control.

The phase dynamic is related to the active power flow and energy. The DC voltage control is designed as shown in **Figure 1** to regulate the active power reference according to the DC-side voltage deviation for maintaining the state of charge (SOC) of the supercapacitor and DC voltage stable.

$$P_{ref} = \frac{K_{dc}(1 + s\tau_{dc})}{s}\left(U_{dc}^2 - U_{dcref}^2\right), \quad (12)$$

where K_{dc} and τ_{dc} are the control gain and time constant.

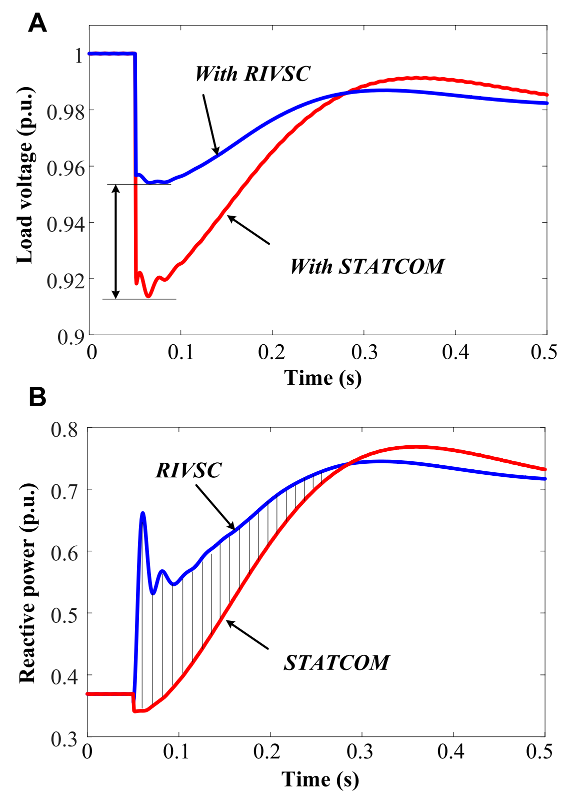

FIGURE 6 | Potential application scenario for improving voltage dynamics. **(A)** Load voltage **(B)** reactive power.

2.4 AC Voltage Controls

The terminal voltage control aims to maintain the terminal voltage in a certain scope, which is designed as shown in **Figure 1** by a proportional control. The terminal voltage control is designed to regulate the reactive power of the proposed RIVSC according to the terminal voltage deviation.

$$Q_{ref} = K_{AT}\left(U_t - U_t^*\right), \quad (13)$$

where K_{AT} is the control gain. U_t and U_t^* fnlowast are the terminal voltage and its reference, respectively.

2.5 Fault Protection Control Procedure

The inertia and stiffness of the RIVSC are beneficial for dynamic active and reactive power support, but the electromagnetic force increases due to the regulation rate of the inner potential decrease under the effect of the inertia and stiffness. With traditional current control, how to limit the fault current of the RIVSC is a very severe problem.

A current limitation method is presented as **Figure 1**. There are two parts in the current limitation method. This study combines the virtual resistance with a phasor limitation, which are used to reduce the rapid-transient and steady-state fault currents, respectively.

First, a virtual resistor is activated to limit the fault current during transient state when the output current of the RIVSC exceeds the current limit (Qoria et al., 2020).

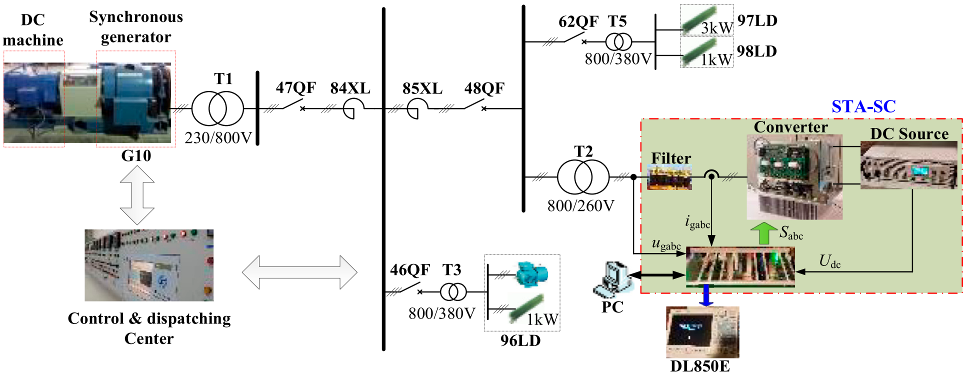

FIGURE 7 | Experimental system in the laboratory.

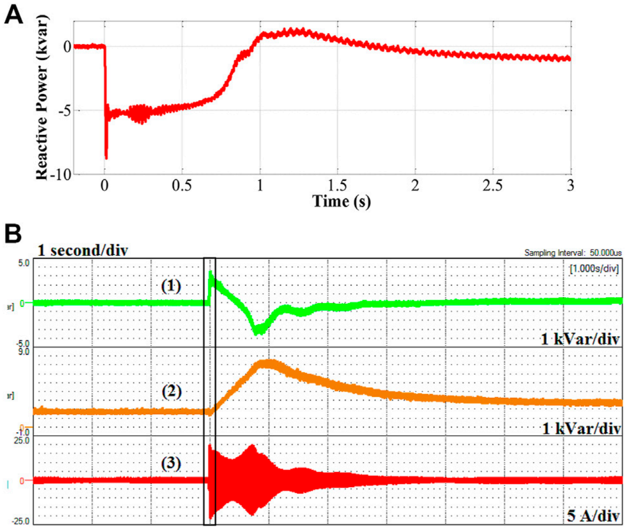

FIGURE 8 | Experimental results of the dynamic reactive power response and currents during the reactive power disturbance raised by the launching of the induction motor in 96LD (1s/div). **(A)** Reactive power characteristics of the induction motor when launched and **(B)** Dynamic response of the RIVSC and voltage control. (1) Reactive power from the RIVSC (1 kvar/div), (2) Reactive power from the voltage control unit (1 kvar/div), and (3) Phase-a current of the RIVSC (5 A/div).

$$\begin{cases} R_v = R_{set} & |I_s| > I_{limit} \\ R_v = 0 & |I_s| \le I_{limit} \end{cases}, \tag{14}$$

where R_v and I_{limit} are virtual resistor and current limitation. R_{set} is the value of the virtual resistor. Under normal conditions, the virtual resistor does not work.

Second, a phasor limitation method is used to restrict the difference between the inner potential of the RIVSC and fault point, as shown in **Figure 3**.

The fault current of the RIVSC is projected into the inner potential reference coordinate frame as **Figure 3**.

$$\begin{cases} -I_{d\max} \le i_{sd} \le I_{d\max} \\ -I_{q\max} \le i_{sq} \le I_{q\max} \\ \sqrt{I_{d\max}^2 + I_{q\max}^2} \le I_{\max} \end{cases}, \tag{15}$$

where I_{dmax} and I_{qmax} are the *dq*-axis max current limits.

During the fault operation, the inner potential is limited in the safe zone as in **Figure 3**.

$$\begin{cases} u_{cd\max} = u_{td} + \omega L_f I_{sq\max} \\ u_{cd\min} = u_{td} - \omega L_f I_{sq\max} \\ u_{cq\max} = u_{tq} + \omega L_f I_{sd\max} \\ u_{cq\min} = u_{tq} - \omega L_f I_{sd\max} \end{cases}. \tag{16}$$

The dynamic performances of the RIVSC under the grid fault condition are presented in **Figure 4**.

As shown in **Figure 4A**, the fault current of the RIVSC rushes to about 10 times rated current without fault current limitation under grid fault, which is unbearable and damages the device. When the fault protection control proposed in this study is enabled, the fault current is less than 1.2 p.u. inside a safe operation range of the power electronic devices, as shown in **Figure 4B**. Based on the fault protection control, the RIVSC can provide the dynamic reactive power support for grid in a safe operation range, as shown in **Figure 4B**.

3 VOLTAGE STIFFNESS CHARACTERISTIC AND ITS INFLUENCE

3.1 Stiffness Characteristic

The stiffness characteristic means the inner potential's capability of tolerating the reactive power difference between the actual reactive power and its reference over a time window. The stiffness coefficient K_c determines the stiffness value. With larger stiffness, the changing rate of the inner potential can be reduced under a certain reactive power imbalance condition. As shown in **Figure 5A**, the deviation rate of the inner potential is reduced with the increase of K_c under a certain reactive power disturbance, but the static deviation still keeps the same.

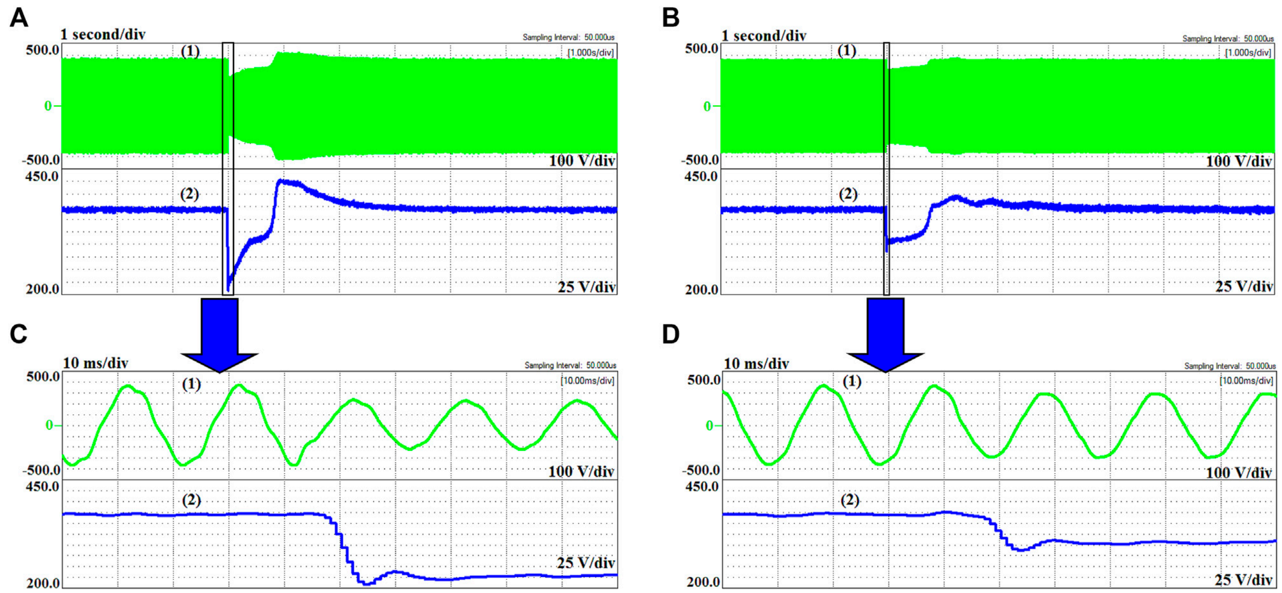

FIGURE 9 | Experimental results of the PCC's voltage during reactive power disturbance raised by the launching of the inductive motor in 96LD (1s/div). **(A)** Without the RIVSC. **(B)** With the RIVSC. **(C)** and **(D)** are the enlarged windows. (1) PCC's ac voltage (line-to-line) (100V/div) and (2) PCC's voltage magnitude (25V/div).

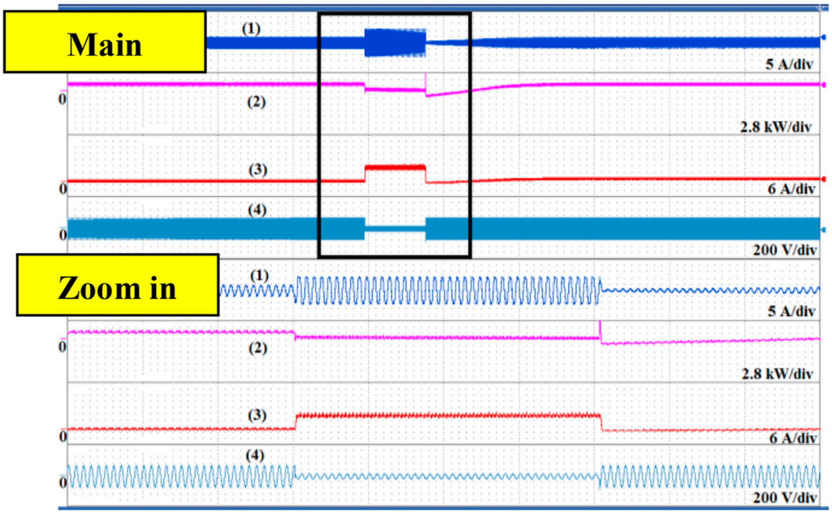

FIGURE 10 | Experimental results of the dynamic performance of the RIVSC under grid fault. (1) is the fault current (2) and (3) are active and reactive powers of the RIVSC, (4) is the grid voltage.

With the stiffness increase, the natural reactive power response of the RIVSC is helpful to reduce the change rate of the PCC voltage, as shown in **Figure 5B**. When the natural reactive power response of the RIVSC stiffness is combined with the normal voltage control, the static deviation of the PCC voltage is not improved, but the nadir is pulled up and enhanced, as shown in **Figure 5C**. As a result, the stiffness characteristic of the RIVSC and its natural reactive power response are beneficial to improve the voltage dynamics.

3.2 Influence on Grid Voltage Dynamics

This comparison is to highlight the grid voltage stiffness compensation which is quite different from the grid voltage control. The STATCOM is the well-known rapid control device of grid voltage *via* reactive power compensation and widely used in the bulk power system. Thus, the comparison is made by the STATCOM in this study.

As shown in **Figure 6A**, the voltage nadir is 0.917 p.u. and 0.957 p.u. with the STATCOM and RIVSC under the same

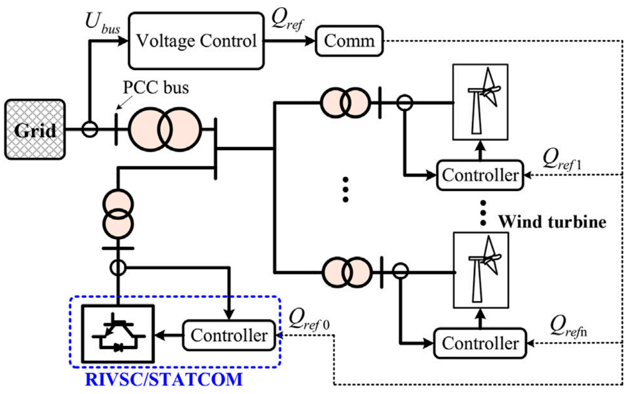

FIGURE 11 | Potential application scenario for improving voltage dynamics.

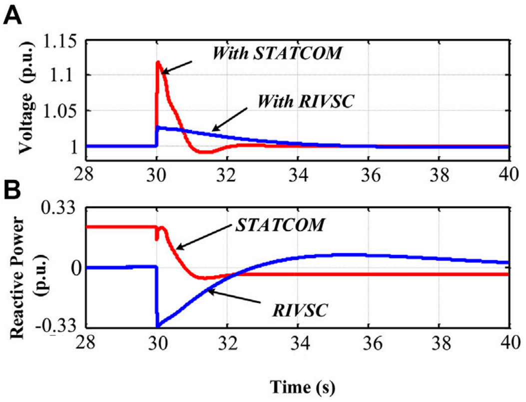

FIGURE 12 | Simulated results of PCC's voltage with and without the RIVSC. **(A)** PCC's voltage. **(B)** Reactive power.

voltage control gain and disturbance, respectively. But the voltage recovery is faster with the STATCOM than with the RIVSC. **Figure 6B** illustrates the reason of different voltage responses with the STATCOM and RIVSC. First, the STATCOM is equivalent to a controllable current source, and its reactive power slightly declines under disturbance, which will deteriorate the initial voltage deviation. However, the RIVSC provides more and faster reactive power responses under the effect of stiffness after disturbance, which is in favor of reducing the voltage deviation.

4 PROTOTYPING TESTING

4.1 Experimental System in the Laboratory

Experimental tests were performed in an experiment power system, as shown in **Figure 7**. The experiment system is established by a synchronous generator (G10) and a RIVSC. The distributed inductances and capacitors are used to emulate the parameters of the transmission lines (84XL and 85XL), and the resistance and induction motors are regarded as the loads (96LD, 97LD, and 98LD). The primary frequency regulation and auto voltage regulation are equipped in the synchronous generator (G10). In the experiment system, the voltage of the main network is 800V, and T1, T2, T3, T4, and T5 are the variances to couple the facilities into the main network. In addition, the dynamic characteristic of the transmission lines (84XL and 85XL) is equivalent to a 70-km high voltage transmission line with an impedance $12\angle 85^\circ\Omega$. The breakers (46QF, 47QF, 48 QF, and 62 QF) are employed to switch on and off transmission lines and loads. The experiment system in physics can reflect more realistic dynamics to obtain more credible results. A power wave recorder is set in the control and dispatching center to collect and record the experimental data of the synchronous generator (G10), transmission network, and loads. The signals of the RIVSC are recorded by *YOKOGAWA® ScopeCorders* (DL850E). The main parameters are presented in **Table A1** in **Appendix A1**.

4.2 Effects on Grid Voltage Dynamics

In this test, an induction motor in 96LD is launched directly coupled with the grid to emulate the reactive power disturbance. The reactive power characteristic of the inductive motor is presented according to the data of the power wave recorder, as shown in **Figure 8A**. The consumed reactive power sharply increases to about 6 kvar (inductive) when the induction motor is switched on (0 s). In 0–0.7 s, the consumed reactive power slowly declines and then rapidly decreases at the 0.7 s thereafter. In 0.7–1.0 s, the consumed reactive power rapidly climbs from 4 kvar (inductive) to 1 kvar (capacitive) under this characteristic of reactive power disturbance.

The dynamic behaviors of the RIVSC and the voltage control are presented in **Figure 8B**. With the sharp increase of the reactive power consumption when launched, about 4.2 kvar (capacitive) reactive power is provided by the dynamic reactive power response of the RIVSC without any time delays, while the reactive power of the voltage control unit climbs up much more slowly due to the limited control bandwidth and inevitable time delays, as shown in **Figure 8B**. Moreover, with the rapid decline of the consumed reactive power after launch, the voltage control cannot decline its output reactive power with enough dynamic response and leads to the reactive power surplus due to the limited control bandwidth and time delay, while the natural reactive power response of the RIVSC raised by its stiffness characteristic sharply declines and absorbs more.

Furthermore, **Figures 9A,B** show the dynamic behavior of the voltage with and without the RIVSC during disturbance of reactive power, respectively. At switching on of the induction motor, the voltage nadir is much higher (280 V) with the RIVSC than the one without the RIVSC (205 V), while the voltage climbs to 425 V without the RIVSC much higher than that with the RIVSC (405 V). Thus, the dynamic reactive power support of the RIVSC is effective to resist the rapid deviation of the voltage.

4.3 Fault Ride Through Operation

Figure 10A presents the performance of the RIVSC under grid fault, and **Figure 10B** is the corresponding zooming window. Grid voltage rapidly declines, and then, the fault current climbs rapidly but is still in the safe zone based on the fault protection control presented in this study. Experimental results illustrate that the fault protection control is effective to reduce the fault current. The case without the fault protection control cannot be implemented because the fault current may damage the facilities.

5 APPLICATION IN THE POWER SYSTEM

A potential application scenario is established. The RIVSC is combined with the voltage control of the wind farm, as in **Figure 11** (Tapia et al., 2007). The voltage control regulates the reactive powers of the RIVSC and wind turbines (Hughes et al., 2005). With a switch off of a reactive load, simulation results of PCC's voltage are depicted in **Figure 12** to illustrate the influence of the RIVSC on the temporary overvoltage. Under the effect of the voltage control without the RIVSC, the PCC's voltage without the RIVSC jumps over 1.12 p.u. and then gradually falls back. The temporary overvoltage may be raised by the sudden large change of the load flow, which harms the operation security of grid-connected devices. The traditional voltage control cannot immediately reduce the reactive power after disturbance; thus, the overvoltage lasts about 1 s, as shown in **Figure 12A**, which may trip off some sensitive devices, whereas with the RIVSC, the abundant reactive power is immediately absorbed under the effect of the RIVSC's stiffness as shown in **Figure 12B**, which is able to alleviate the temporary overvoltage.

6 CONCLUSION

This paper presented a novel dynamic compensator called as the static synchronous condenser (RIVSC). The inertia and stiffness characteristics are featured in the RIVSC by the virtual synchronous control for dynamic active and reactive power support for the grid frequency and voltage. Simulation and experiment results validate the feasibility and effectiveness on improving the grid frequency and voltage of the proposed RIVSC. The main contributions of this study can be summarized as follows.

1) The basic principle and control system of the RIVSC is presented by the limited energy storage capacity. The virtual synchronous control is used based on the second-order equation and without the AC current control for better dynamic support capability, and the comprehensive fault current limitation method is proposed to reduce the fault current and keep the RIVSC operating in a safe zone.
2) The inertia and stiffness characteristics are featured in the proposed RIVSC by the virtual synchronous control, and the RIVSC can naturally provide the dynamic active and reactive powers to support the grid frequency and voltage with a better dynamic response than traditional inertia control based on the *df/dt*-method and voltage control.
3) The stiffness compensation of the RIVSC is first proposed and can be used as the supplement to the traditional voltage control to improve grid voltage dynamics, which is a potential application to alleviate the temporary overvoltage. It is validated that the RIVSC is effective to alleviate the temporary overvoltage.
4) The prototype of the RIVSC is set up, and the improving frequency and voltage dynamics are validated by the physical experiment systems with the more realistic dynamics.

In the future research, the topology for large capacity, control, and application of the proposed RIVSC requires deep study. The RIVSC is potential to replace the conventional STATCOM and synchronous condenser. There are some application scenarios, e.g., located at the sending terminal of the HVDC to alleviate the transient overvoltage, located at the distributed to reduce the voltage flicker to improve the power quality.

DATA AVAILABILITY STATEMENT

The original contributions presented in the study are included in the article/supplementary material; further inquiries can be directed to the corresponding author.

AUTHOR CONTRIBUTIONS

XD proposed the idea of the experiment. LS proposed the idea of voltage resilience and experimental devices.

FUNDING

The work is supported by the National Natural Science Funds of China (Grant No. 52007135).

REFERENCES

Cao, Y., Wang, W., Li, Y., Tan, Y., Chen, C., He, L., et al. (2018). A Virtual Synchronous Generator Control Strategy for VSC-MTDC Systems. *IEEE Trans. Energ. Convers.* 33 (2), 750–761. doi:10.1109/tec.2017.2780920

Du, E., Zhang, N., Hodge, B.-M., Wang, Q., Lu, Z., Kang, C., et al. (2019). Operation of a High Renewable Penetrated Power System with CSP Plants: A Look-Ahead Stochastic Unit Commitment Model. *IEEE Trans. Power Syst.* 34 (1), 140–151. doi:10.1109/tpwrs.2018.2866486

Hou, X., Sun, Y., Han, H., Liu, Z., Su, M., Wang, B., et al. (2018). A General Decentralized Control Scheme for Medium-/High-Voltage Cascaded STATCOM. *IEEE Trans. Power Syst.* 33 (6), 7296–7300. doi:10.1109/tpwrs.2018.2865127

Huang, S-H., Schmall, J., Conto, J., Adams, J., Chang, Y., and Carter, C. (2012). "Voltage Control Challenges on Weak Grids with High Penetration of Wind Generation: ERCOT Experience," in Proc. IEEE Power Energy Soc. General Meeting, San Diego, CA, USA, 22-26 July 2012 (IEEE), 1–7.

Hughes, F. M., Anaya-Lara, O., Jenkins, N., and Strbac, G. (2005). Control of DFIG-Based Wind Generation for Power Network Support. *IEEE Trans. Power Syst.* 20 (4), 1958–1966. doi:10.1109/tpwrs.2005.857275

Lee, G.-S., Kwon, D.-H., Moon, S.-I., and Hwang, P.-I. (2020). Reactive Power Control Method for the LCC Rectifier Side of a Hybrid HVDC System Exploiting DC Voltage Adjustment and Switched Shunt Device Control. *IEEE Trans. Power Deliv.* 35 (3), 1575–1587. doi:10.1109/tpwrd.2019.2949906

Liu, B., Li, Z., Chen, X., Huang, Y., and Liu, X. (2018). Recognition and Vulnerability Analysis of Key Nodes in Power Grid Based on Complex Network Centrality. *IEEE Trans. Circuits Syst.* 65 (3), 346–350. doi:10.1109/tcsii.2017.2705482

Liu, B., Li, Z., Dong, X., Yu, S. S., Chen, X., Oo, A. M. T., et al. (2021). Impedance Modeling and Controllers Shaping Effect Analysis of PMSG Wind Turbines. *IEEE J. Emerg. Sel. Top. Power Electron.* 9 (2), 1465–1478. doi:10.1109/jestpe.2020.3014412

Mendis, N., Muttaqi, K. M., and Perera, S. (2014). Management of Battery-Supercapacitor Hybrid Energy Storage and Synchronous Condenser for Isolated Operation of PMSG Based Variable-Speed Wind Turbine Generating Systems. *IEEE Trans. Smart Grid* 5 (2), 944–953. doi:10.1109/tsg.2013.2287874

Qoria, T., Gruson, F., Colas, F., Denis, G., Prevost, T., and Guillaud, X. (2020). Critical Clearing Time Determination and Enhancement of Grid-Forming Converters Embedding Virtual Impedance as Current Limitation Algorithm. *IEEE J. Emerg. Sel. Top. Power Electron.* 8 (2), 1050–1061. doi:10.1109/jestpe.2019.2959085

Ramos, A. J. P., and Tyll, H. (1989). Dynamic Performance of a Radial Weak Power System with Multiple Static VAR Compensators. *IEEE Trans. Power Syst.* 4 (4), 1316–1325. doi:10.1109/59.41681

Shang, L., Dong, X., Liu, C., and Gong, Z. (2021). Fast Regulation Control for Grid Frequency and Voltage Based on the Amplitude-Phase-Locked-Loop. *IEEE Trans. Smart Grid, Early Access*, 1. doi:10.1109/TSG.2021.3133580

Shang, L., Dong, X., Liu, C., and He, W. (2021). Modelling and Analysis of Electromagnetic Time Scale Voltage Variation Affected by Power Electronic Interfaced Voltage Regulatory Devices. *IEEE Trans. Power Syst.*, 1. doi:10.1109/TPWRS.2021.3100606

Shang, L. (2019). "Rotational-inertia-and-voltage-stiffness Compensator to Improve Grid Voltage Dynamic," in Proceedings of IEEE Sustainable Power and Energy Conference, Beijing, China, 21-23 Nov. 2019 (iSPEC).

Tapia, G., Tapia, A., and Ostolaza, J. X. (2007). Proportional-Integral Regulator-Based Approach to Wind Farm Reactive Power Management for Secondary Voltage Control. *IEEE Trans. Energ. Convers.* 22 (2), 488–498. doi:10.1109/tec.2005.858058

Teleke, S., Abdulahovic, T., Thiringer, T., and Svensson, J. (2008). Dynamic Performance Comparison of Synchronous Condenser and SVC. *IEEE Trans. Power Deliv.* 23 (3), 1606–1612. doi:10.1109/tpwrd.2007.916109

Varma, R. K., and Mohan, S. (2020). Mitigation of Fault Induced Delayed Voltage Recovery (FIDVR) by PV-STATCOM. *IEEE Trans. Power Syst.* 35 (6), 4251–4262. doi:10.1109/tpwrs.2020.2991447

Wang, S., Hu, J., and Yuan, X. (2015). Virtual Synchronous Control for Grid-Connected DFIG-Based Wind Turbines. *IEEE J. Emerg. Sel. Top. Power Electron.* 3 (4), 932–944. doi:10.1109/jestpe.2015.2418200

Xiong, L., Liu, X., Liu, Y., and Zhuo, F. (2020). Modeling and Stability Issues of Voltage-Source Converter Dominated Power Systems: a Review. *Csee Jpes*. early access. doi:10.17775/CSEEJPES.2020.03590

Xue, Y., and Zhang, X.-P. (2017). Reactive Power and AC Voltage Control of LCC HVDC System with Controllable Capacitors. *IEEE Trans. Power Syst.* 32 (1), 753–764. doi:10.1109/tpwrs.2016.2557342

Zhang, L. (2010).Modeling and Control of VSC-HVDC Links Connected to Weak Ac Systems. Ph.D. dissertation, *School of Electrical Engineering*. Stockholm, Sweden: KTH University.

Zhao, M., Yuan, X., Hu, J., and Yan, Y. (2016). Voltage Dynamics of Current Control Time-Scale in a VSC-Connected Weak Grid. *IEEE Trans. Power Syst.* 31 (4), 2925–2937. doi:10.1109/tpwrs.2015.2482605

Zhong, Q., Nguyen, P., Ma, Z., and Sheng, W. (2014). Self-synchronized Synchronverters: Converters without a Dedicated Synchronization Unit. *IEEE Trans. Power Electron.* 29 (2). doi:10.1109/tpel.2013.2258684

Conflict of Interest: Author YT was employed by the company State Grid Liaoning Electric Power Supply Company. Author JL was employed by the company State Grid Jilin Electric Power Supply Company.

The remaining authors declare that the research was conducted in the absence of any commercial or financial relationships that could be construed as a potential conflict of interest.

APPENDIX

TABLE A1 | Parameters of the experiment system.

Parameters of the RIVSC

Parameters	Symbols	Value
Nominal power	S_N	10 kW
Nominal voltage	U_N	260 V
Filter	L	3 mH
DC voltage	V_{dc}	650 V
Switch frequency	f_{c}	5 kHz

Parameters of SG (G10)

Parameters	Symbols	Value
Nominal power	S_N	15 kVA
Nominal voltage	U_N	230 V
Nominal frequency	f_N	50 Hz
d-axis synchronous reactance	x_{d}	0.56
d-axis transient reactance	x_{d}'	0.132
d-axis subtransient reactance	x_{d}''	0.113
q-axis subtransient and transient reactance	$x_{\mathrm{q}}''\ddot{x}_{\mathrm{q}}$	0.135
Damping coefficient for active power	T_{d0}	0.9 s
Inertia time constant	T_j	3.51 s

frontiers in Energy Research

ORIGINAL RESEARCH
published: 10 February 2022
doi: 10.3389/fenrg.2022.825994

Modeling and Energy Generation Evaluations of Large-Scale Photovoltaic Plants Equipped With Panel-Level DC Optimizers

Qin Wang[1], Lingling Le[1], Dahu Li[2], Xiaomeng Ai[1], Jiakun Fang[1]*, Wei Yao[1] and Jinyu Wen[1]

[1]State Key Laboratory of Advanced Electromagnetic Engineering and Technology, School of Electrical and Electronic Engineering, Huazhong University of Science and Technology, Wuhan, China, [2]State Grid Hubei Electric Power Company Limited, Wuhan, China

Edited by:
Weihao Hu,
University of Electronic Science and Technology of China, China

Reviewed by:
Di Cao,
University of Electronic Science and Technology of China, China
Bin Zhang,
Aalborg University, Denmark

***Correspondence:**
Jiakun Fang
jfa@hust.edu.cn

Specialty section:
This article was submitted to Process and Energy Systems Engineering,
a section of the journal Frontiers in Energy Research

Received: 30 November 2021
Accepted: 10 January 2022
Published: 10 February 2022

Citation:
Wang Q, Le L, Li D, Ai X, Fang J, Yao W and Wen J (2022) Modeling and Energy Generation Evaluations of Large-Scale Photovoltaic Plants Equipped With Panel-Level DC Optimizers.
Front. Energy Res. 10:825994.
doi: 10.3389/fenrg.2022.825994

The distributed maximum power point tracking (DMPPT) technology, based on a DC optimizer (DCO, a DC/DC micro-converter) for each single photovoltaic (PV) panel, is one of the most popular solutions to mitigating the waste of solar energy when suffering mismatch conditions. However, the trade-off between the additional costs of deploying the panel-level power electronic equipment and the improved generation benefits of a large-scale PV plant (LPP) remains to be further studied. This study presents a static modeling method for the DCO-based distributed LPPs to study the long-term energy generation characteristics based on historical hourly weather data and then evaluate the economic benefits. The operational characteristics of the PV strings equipped with series-connected DCOs for three different topologies (Boost, Buck, and Buck-boost) are investigated, and then the control strategies for the PV-DCO generation units are proposed to maximize the energy generation of LPPs under frequent mismatch conditions. Different mismatch scenarios caused by the panel aging, geographical location settings, and the partial shading in PV arrays are simulated in the model. Six typical centralized or distributed PV plant configurations are carried out for comparison in case studies, to explore the generation characteristics and the advantages of energy production for the DCO-based distributed LPPs. Besides, the Levelized cost of energy (LCOE) which considers both the energy generation benefits and investment costs is introduced to the economic evaluation of different structures of LPPs.

Keywords: large-scale photovoltaic, DC optimizer, mismatch condition, modeling, generation characteristics, levelized cost of energy

---

Abbreviations: DCO, DC optimizer; DMPPT, distributed maximum power point tracking; GMPPT, global maximum power point tracking; LCOE, Levelized cost of energy; LPP, large-scale PV plant; MERRA, Modern-era retrospective analysis for research and applications; PV, photovoltaic.

INTRODUCTION

Solar photovoltaic (PV) technology plays an increasingly important role in energy supply as it is freely available, environmentally friendly, and economically efficient (Ma et al., 2019; Li et al., 2020; Chen et al., 2021). The PV cumulative installed capacity has experienced significant growth from 138 GW in 2013 to 760 GW in 2020 worldwide, which shows the great potential for low-carbon energy system transition (World Energy Outlook, 2020).

Conventionally, PV panels are series-connected into a string to achieve a high DC voltage and then the strings are connected in parallel to create an array of the large-scale PV plant (LPP). Central inverters are employed to implement the global maximum power point tracking (GMPPT) technology on each PV array and connect the plant to the power grid, which is called centralized configuration. However, modules in a PV plant may show different operational characteristics when suffering from partial shading or other mismatch problems (Bana and Saini, 2017; Wang et al., 2020). The shaded panels of the PV string would limit the current of the unshaded panels since they are connected in series, thus resulting in a great solar energy loss. Besides, the mismatch conditions may cause the "hotspot" problem in the PV array; for this reason, the bypass diode is introduced to each PV panel. The seriously shaded modules in a string are usually shorted out by diodes to maintain the total power generation. However, the utilization of bypass diodes may trigger an additional problem of multiple maxima in the power-voltage curve of the PV array, resulting in difficulties in the optimization process of GMPPT implementation (Batzelis et al., 2014; Cao et al., 2020a).

Various approaches have been proposed to solve the local optimal problems under multiple extremum points. Studies (Ram et al., 2017; Alik and Jusoh, 2018; Cao et al., 2020b) have presented the improved searching methods of GMPPT techniques under mismatch conditions based on fuzzy logic control, artificial neural network, and particle swarm optimization methods. Although GMPPT shows the advantages of implementation simplicity, reduced cost, and immediate adoption, the severe power loss caused by frequent mismatch conditions remains unresolved. To address this problem, the distributed maximum power point tracking (DMPPT) technology, based on a DC optimizer (DCO, a DC/DC micro-converter) for each single PV panel, is increasingly developed for LPPs due to its superior generation efficiency, unified configuration, and modular layout (Khan et al., 2016; Vavilapalli et al., 2018; Zhang et al., 2021). **Figure 1** shows the overall structure of the DCO-based distributed LPP with the series-connected structure. The PV-DCO array contains *P* parallel PV strings, each of which includes *S* cascaded PV-DCO units. A grid-connected inverter is deployed for the PV array to integrate solar energy into the power system through a short DC transmission line. The individual power optimization process (MPPT) can be realized for each PV panel with the controllers of DCOs, which eliminates the adverse effects of mismatch conditions for PV arrays compared with the global searching algorithms.

With the DCO-based distributed configuration, the waste of solar energy when suffering partial shading is greatly mitigated, leading to an improvement in the economic benefits of LPPs. However, the trade-off between the additional costs of deploying the panel-level power electronic equipment and the improved generation benefits for an LPP remains to be further considered. The modeling and analysis of long-term energy generation characteristics of LPPs equipped with panel-level DCOs are critical to studying the feasibility and economics of this type of structural design compared with conventional centralized configurations.

The existing modeling research studies on the DCO-based LPPs mainly focus on the dynamic models covering the high-efficiency topologies (Wang et al., 2013; Amir et al., 2019), distributed control strategies (Biswas et al., 2017; Lópezdel Moral et al., 2018), or the stability analysis (Mahdavyfakhr et al., 2017; Wang et al., 2020) for the PV system, which cannot be used for the long-term energy production calculation of PV plants. In the studies by Petrone and

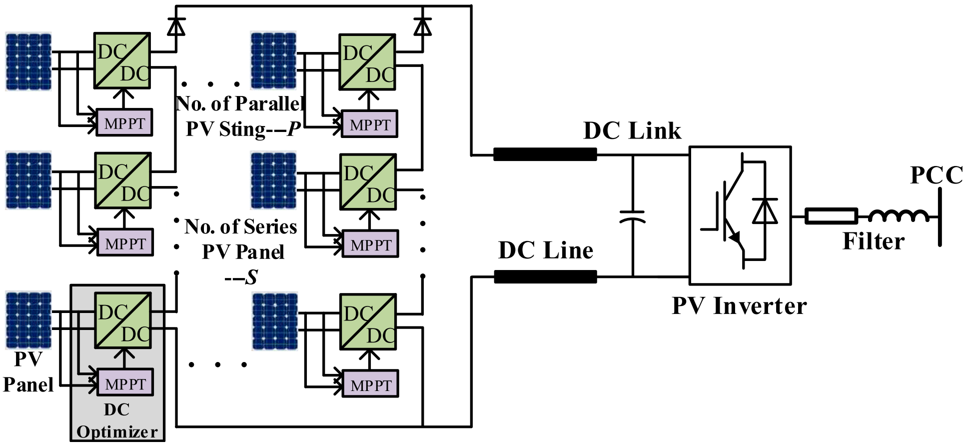

FIGURE 1 | Overall structure of DCO-based distributed LPPs.

Ramos-Paja (2011) and Cook et al. (2018), the static models were developed for the calculation and assessment of long-term energy production of LPPs. However, none of them considered the operational characteristics of the panel-level DCOs assembled in the array. In the study by Castro et al. (2020), a steady-state model is also proposed for a multi-array PV system constructed in parallel to study the power flows and power generation issues; nevertheless, the modeling method is not applicable to analyze the mismatch problems involved in series-connected PV-DCO generation units, and only the Boost topology is considered in the micro-converters.

On the other hand, with the increased availability of DCOs, quantifying the energy generation characteristics and benefits of DMPPT solutions becomes necessary for the design of LPPs (Khan and Xiao, 2017; Wijeratne et al., 2019). Existing studies on this point can be divided into two categories. The former focuses on short-term performance under some specific mismatching conditions. Olalla et al. (2013) demonstrated that a portion of energy loss due to partial shading and panel aging can be recovered by distributed power electronics, and the corresponding economic evaluation method is carried out. Simulation results in the study by MacAlpine et al. (2012) proved that panel-level power optimization can recover 34–42% of the short-term energy lost to partial shading caused by clouds. However, the medium- or long-term analysis is more valuable and persuasive for the design of an LPP. Therefore, some researchers turn their attention to the long-term energy production of LPPs based on the experienced data. The literature (De Prada-Gil et al., 2016) has utilized the reliability multi-state models which assume that each PV module has several states of service to the annual output calculation and evaluation of PV plants. However, the micro-converter is designed for a PV string or array rather than the panel level. The literature (Hanson et al., 2014) has shown an annual generation performance increase of 5.8% after installation of the module-level DCO, which is verified experimentally against a system that has site survey images. Nevertheless, the energy loss due to panel-level mismatch that occurs in series-connected PV-DCO units is underestimated, since it is assumed to be an ideal situation that all the PV panels can operate in their independent MPPT modes under severe partial shading conditions, which is impossible in practice. Moreover, since only one topology of the DCOs is taken into consideration in the studies by De Prada-Gil et al. (2016) and Hanson et al. (2014), the comparative analysis of the operational characteristics and economic benefits with different DCO topologies is lacking, which involves the structural optimization design of DCO-based distributed LPPs.

Within the context alluded to above, this article presents a modeling and analysis method for the long-term energy generation evaluation (on the year level) of the LPPs equipped with panel-level DC optimizers, which considers three different topologies for DCOs and multiple types of mismatch conditions that occur in PV strings and arrays. Besides, the improved DMPPT control strategies designed for cascaded PV-DCO generation units are proposed, and then the solar energy loss caused by array mismatch problems can be greatly compensated for the LPPs compared with the traditional GMPPT control strategy. The main contributions of this study are listed as follows:

- A static modeling method is presented for the DCO-based distributed LPPs to study the long-term energy generation performances during 1 year with hourly simulation accuracy, combining historical hourly weather data and various mismatching factors.
- For various DCO topologies including Boost, Buck, and Buck-boost, different control strategies for the PV strings equipped with series-connected DCOs are proposed to maximize the energy production of LPPs when suffering severe mismatch conditions.
- An energy generation evaluation method is proposed to analyze the economic benefits of LPPs, based on the Levelized cost of energy (LCOE) which considers the trade-off between energy production yields and plant investment costs during the life cycle of LPPs.
- Contrastive analysis with six typical centralized or distributed PV plant configurations is carried out to explore the optimal structure and layout for LPPs during the long-term energy generation, and then the suggestions for design improvement can be given.

The rest of this article is organized as follows. *Fundamental Models* introduces the fundamental model of the PV-DCO generation unit. *Control Strategies for Series-Connected PV-DCO Units* proposes the control strategies for series-connected PV units based on the operational characteristics of the PV-DCO strings with different topologies. *Framework for Static Modeling of Energy Generation Evaluation* presents the framework of the static modeling method for the evaluation of the long-term energy generation performance in LPPs. *Case Study* gives the case studies involving six typical PV plant configurations. Finally, the conclusions are drawn in *Conclusion*.

FUNDAMENTAL MODELS

Model of PV Panels

PV panels are the main components of a PV plant, which generate power based on the photoelectric effect on semiconductor materials. Usually, a simplified engineering model for describing the current-voltage characteristic of a PV panel is employed in the design of the PV system (Ma et al., 2019), as shown in **Eqs 1**, **2**:

$$\begin{cases} I = \mathrm{I}_{sc}\left(1 - C_1\left(\exp\left(\frac{U}{C_2 U_{oc}}\right) - 1\right)\right) \\ C_1 = \left(1 - \frac{I_m}{I_{sc}}\right)\exp\left(-\frac{U_m}{C_2 U_{oc}}\right), C_2 = \left(\frac{U_m}{U_{oc}} - 1\right)\left(\ln\left(1 - \frac{I_m}{I_{sc}}\right)\right)^{-1} \end{cases} \tag{1}$$

$$\begin{cases} I_{sc} = \frac{I_{scref} S}{S_{ref}}\left(1 + \alpha\left(T - T_{ref}\right)\right), I_m = \frac{I_{mref} S}{S_{ref}}\left(1 + \alpha\left(T - T_{ref}\right)\right) \\ U_{oc} = U_{ocref}\left(1 - \gamma\left(T - T_{ref}\right)\right) ln\left(e + \varepsilon\left(S - S_{ref}\right)\right) \\ U_m = U_{mref}\left(1 - \gamma\left(T - T_{ref}\right)\right) ln\left(e + \varepsilon\left(S - S_{ref}\right)\right) \end{cases} \tag{2}$$

where U and I represent the operating voltage and current for PV panels, C_1 and C_2 are intermediate variables that are determined

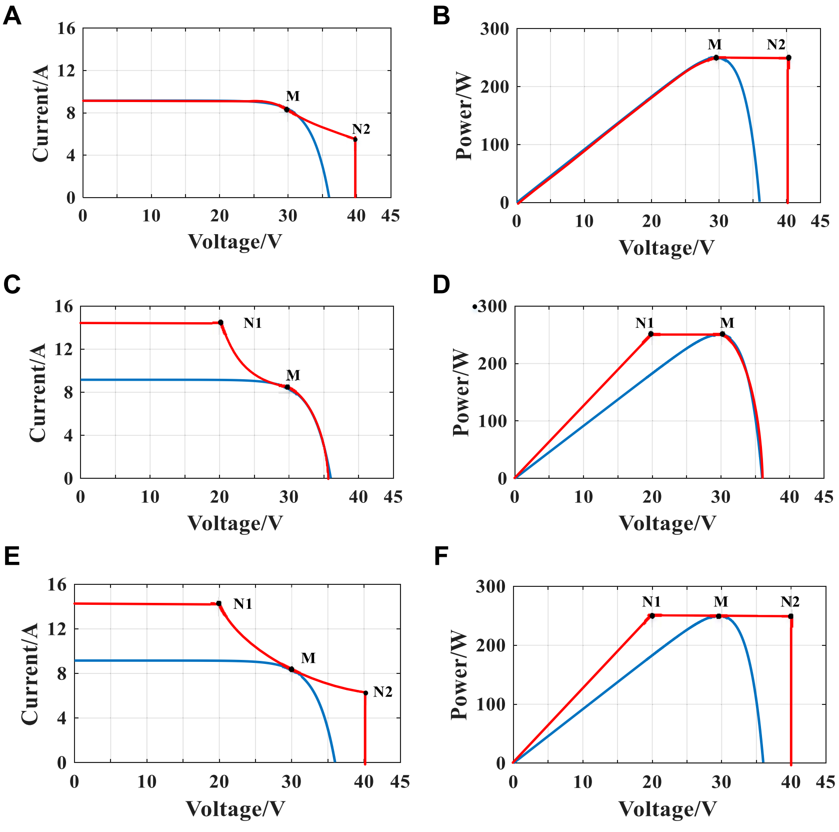

FIGURE 2 | Operational capability of Boost DCO **(A,B)**, Buck DCO **(C,D)**, and Buck-boost DCO **(E,F)**.

by four electrical parameters: short-circuit current I_{sc}, open-circuit voltage U_{oc}, the voltage U_m, and the current I_m at the maximum power point. Solar radiation S and temperature T are the environmental factors around the PV panels, which affect the above four parameters with a certain rule as indicated in **Eq. 2**, resulting in the differences in current-voltage characteristics. α and γ are the temperature compensation coefficients on the PV current and voltage, respectively, and ε is the light intensity compensation coefficient on the PV voltage. "ref" means the values of each parameter under standard operating conditions.

Model of DCOs

In DMPPT configurations, DCOs are introduced and equipped on the output port of PV panels to track the MPP and adjust the output voltage of PV-DCO generation units by changing the conversion ratio. The inherent voltage limit characteristic for DCOs is shown in **Eq. 3**:

$$U_{out} = k_{dco} U_{in}, k_{dcomin} \le k_{dco} \le k_{dcomax} \tag{3}$$

where the U_{in} and U_{out} represent the input and output voltages of the DCO, the k_{dco} indicates the conversion ratio of the DCO, and the k_{dcomin} and k_{dcomax} are the lower and upper limits of k_{dco}, which bound the operating range according to the electrical topology of the DCO. Three topologies including Boost, Buck, and Buck-boost are discussed in this article. Boost topology owns the characteristic of converting the input voltage to a higher output voltage while Buck topology is the opposite. Buck-boost topology combines the features of both Buck and Boost topologies. The upper and lower bands of the conversion ratio k_{dco} for different topologies are given as follows (Wang et al., 2013):

$$Boost: k_{\mathrm{dcomin}} = 1, k_{\mathrm{dcomax}} = U_{N2}/U_M \tag{4}$$

$$Buck: k_{\mathrm{dcomin}} = U_{N1}/U_M, k_{\mathrm{dcomax}} = 1 \tag{5}$$

$$Buck-boost: k_{\mathrm{dcomin}} = U_{N1}/U_M\ , k_{\mathrm{dcomax}} = U_{N2}/U_M \tag{6}$$

With the above operational constraints, the operational capability of the three DCO topologies when connected to the PV panel can be presented in **Figure 2**. The output characteristic curves of DCOs are in red and the tracked PV panels are in blue: (A), (C), and (E) represent current-voltage curves while (B), (D), and (F) represent power-voltage curves. M indicates the maximum power point of the PV panel while N1 and N2 stand for the point with minimum and maximum operating voltages for each DCO, respectively. These characteristic curves will be used as constraints for the optimization program involving the energy generation evaluation of LPPs described in *Framework for Static Modeling of Energy Generation Evaluation.*

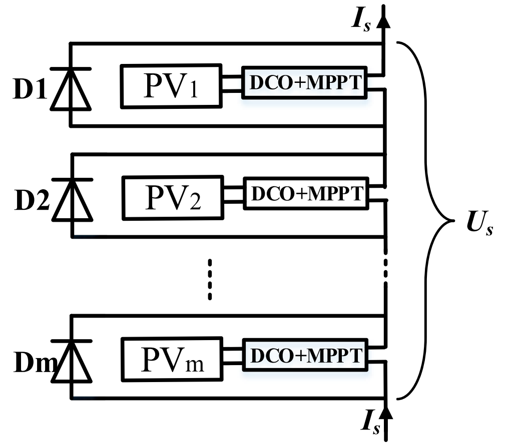

FIGURE 3 | PV string with panel-level DCOs.

CONTROL STRATEGIES FOR SERIES-CONNECTED PV-DCO UNITS

For DCO-based PV systems, each DCO is connected with a PV panel from the input side to implement the MPPT algorithm on the controller of the DCO. At the output side, DCOs connect either in parallel or in series according to the voltage limit characteristic of PV inverters. The series or parallel connections are all applicable for the Buck-boost topology since the range of the PV operating voltage in this topology is flexible. However, the disadvantages of low efficiency and complex control technology limit its application and popularization. For Buck topology, the series connection is the only choice due to its lower voltage output; in this way, the output voltage of the whole PV arrays can be raised to match the rated voltage of grid-connected inverters through the sum of DCO voltages in series. On the contrary, the Boost topology is suitable for both series and parallel connections due to its higher voltage output feature.

The parallel connection structure is easier to control and achieve the maximum power output. However, the higher voltage conversion ratio between a single PV panel and DC link may limit the efficiency of the DCO. For the series connection structure, a lower voltage conversion ratio means higher efficiency. However, either the Boost or the Buck topology, the DCOs connected in series will inevitably influence each other for their unilateral operation capability (the features that can only increase/decrease the voltage), which led to the maximum available power sometimes being unachievable when suffering mismatch. This is the reason why the series-connected DCOs cannot control each PV panel in its own individual MPPT mode under severe partial shading conditions. Therefore, analyzing the interactions between the PV-DCO generation units in a PV string is critical, and the corresponding control strategies for the PV-DCOs should be studied to maximize energy generation when the PV panels deployed in the arrays cannot work in the MPP mode simultaneously. The rest of this section presents the control strategies for series-connected Boost DCO and Buck DCO based on that.

Figure 3 shows a PV string consisting of PV panels connected in series by corresponding DCOs and bypass diodes. The output voltage and current of each DCO in a PV string should satisfy Kirchhoff's law:

$$\begin{cases} \sum_{i=1}^{m} U_{DCO,i} = U_s = U_{DC} \\ I_s = I_{DCO,i}, i = 1, \ldots, m \end{cases} \tag{7}$$

where m represents the number of DCOs in a PV string and i indicates the index. U_s and I_s represent the string voltage and current, respectively. $U_{DCO,i}$ and $I_{DCO,i}$ are the output voltage and current of the ith DCO. As several PV strings in parallel share a common DC link in a PV array (as shown in **Figure 1**), the output voltages of all the strings equal the DC link voltage U_{DC}. When suffering serious mismatch conditions, series-connected Boost or Buck DCOs are unable to make all PV panels work in the MPP mode while satisfying the rated operating range of the DC link voltage because the operating range of the panels (the current-voltage characteristic curves) under severe partial shading could be narrowed and the conversion ratios k_{dco} may exceed the threshold values.

Control Strategy for Boost Topology

Assuming that each panel in the PV string can operate at the maximum power point ($P_{MPP,i}$, $U_{MPP,i}$, and $I_{MPP,i}$), the ideal maximum output power $P_{\max}$ and current $I_{\max}$ of the string could be obtained by using **Eq. 8**:

$$\begin{cases} P_{\max} = \sum_{i=1}^{m} P_{MPP,i} = \sum_{i=1}^{m} U_{m,i} I_{m,i} \\ I_{\max} = P_{\max} / U_{DC} \end{cases} \tag{8}$$

where $P_{MPP,i}$, $U_{MPP,i}$, and $I_{MPP,i}$ indicate the power, voltage, and current of the ith PV panel at the MPP working mode, and U_{DC} is the rated DC link voltage. Combining (4) and (7), the constraint between the string output current and individual panel operating current can be given in **Eq. 9** due to the topological feature where the input current must be greater than the output current for the Boost DCO ($k_{dco} \geq 1$).

$$I_{\max} < I_{MPP,i}, i = 1, \cdots m \tag{9}$$

If Eq. 9 is satisfied for all PV-DCO units, the PV string could obtain the ideal maximum output power $P_{\max}$ and all of the PV panels could reach the MPP. This usually happens when there are no mismatch problems in the PV array. However, when suffering the mismatch conditions such as the partial shading, the MPP currents $I_{MPP,i}$ of the panels shaded by the cloud will be reduced. In severe cases, the $I_{MPP,i}$ of the shaded panels could be less than the $I_{\max}$; then Eq. 9 will not be satisfied and this part of PV panels cannot operate in the MPPT mode. There are two choices to be compared:

a. Bypassing the shaded PV panels and the remaining normal PV panels are controlled in the MPPT mode.

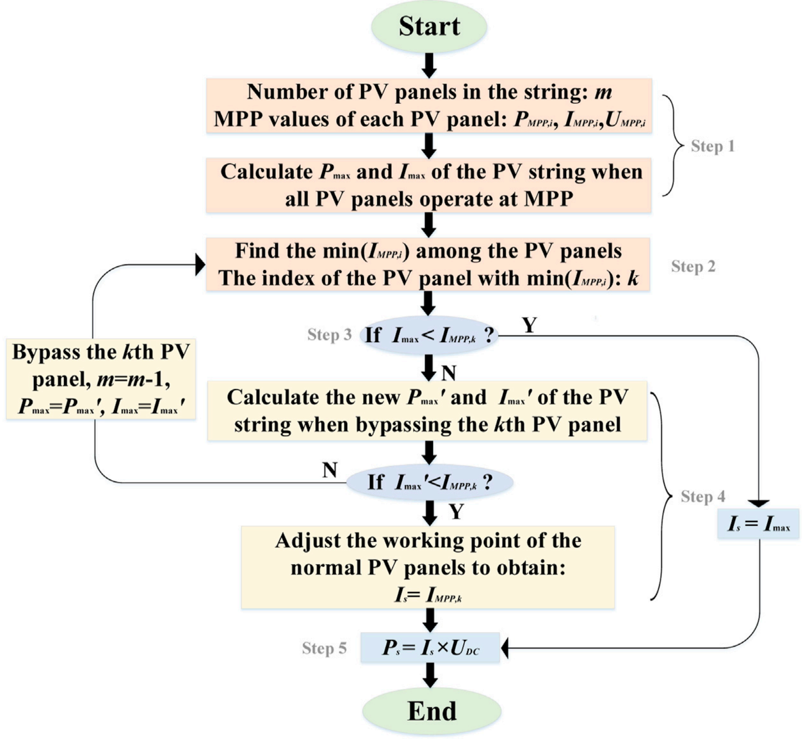

FIGURE 4 | Control strategy of DCOs with Boost topology.

b. Adjusting the working points of normal PV panels slightly below their MPP points and the shaded PV panels are controlled in the MPPT mode.

Based on the above two treatments, the flowchart of the control strategy for obtaining the maximum power output of the PV string can be presented as shown in **Figure 4**. Briefly, the first step involves calculating the output power $P_{\max}$ and current $I_{\max}$ of the PV-DCO string when all series-connected PV panels operate in the MPPT mode, based on the simplified PV engineering model as indicated in **Eqs 1**, **2**, **8**. Step 2 then finds the minimum MPP current $I_{MPP,k}$ of the PV panels. Step 3 compares the quantitative relationship between the $I_{MPP,k}$ and $I_{\max}$ and determines whether all PV panels can operate in the MPPT mode. If the boolean output is "Y," perform the string power calculation in final Step 5. Otherwise, Step 4 determines whether the panels under partial shading should be bypassed to maximize the power generation. Finally, Step 5 calculates the total power output of the PV string after the optimization process.

Control Strategy for Buck Topology

Similarly to the Boost topology, the ideal string power and current should be first calculated using **Eq. 8**. Considering (5) and (7), the value of the string current should be bigger than the operating current of all PV panels ($k_{dco} \le 1$), which can be expressed as follows:

$$I_{\max} > I_{MPP,i}, i = 1, m \tag{10}$$

If constraint **Eq. 10** is satisfied for all PV-DCOs, the PV string could obtain the $P_{\max}$ and all of the PV panels could work at the MPP. Otherwise, the normal PV panels with the higher MPP current $I_{MPP,i}$ cannot operate in the MPPT mode and should be transferred to a new working point ($P_{new,j}$, $U_{new,j}$, $I_{new,j}$) below the MPP, to obtain the maximum power output of the PV string in case of maintaining a current balance. The corresponding control method can be expressed in **Eq. 11**:

$$\begin{cases} P_s = \sum_{j=1}^{n} P_{new,j} + \sum_{i=n+1}^{m} P_{MPP,u} = I_s U_{DC} \\ P_{new,j} = U_{new,j} I_{new,j} \\ I_{new,j} = I_{sc}\left(1 - C_1\left(\exp\left(\frac{U_{new,j}}{C_2 U_{oc}}\right) - 1\right)\right) \\ P_{MPP,u} = U_{MPP,u} I_{MPP,u} \\ I_{new,j} = I_s, I_{MPP,i} \le I_s \\ j = 1, Ln, u = n+1, Lm \end{cases} \tag{11}$$

where n represents the number of normal PV panels and j indicates the index, u represents the index of the shaded PV panels from n+1 to m, and P_s stands for the maximum power output by the PV string after the adjustment.

Control Strategy for Buck-Boost Topology

Different from the Buck or Boost topology, the conversion ratio k_{dco} of DCOs in the Buck-boost topology is more flexible with a

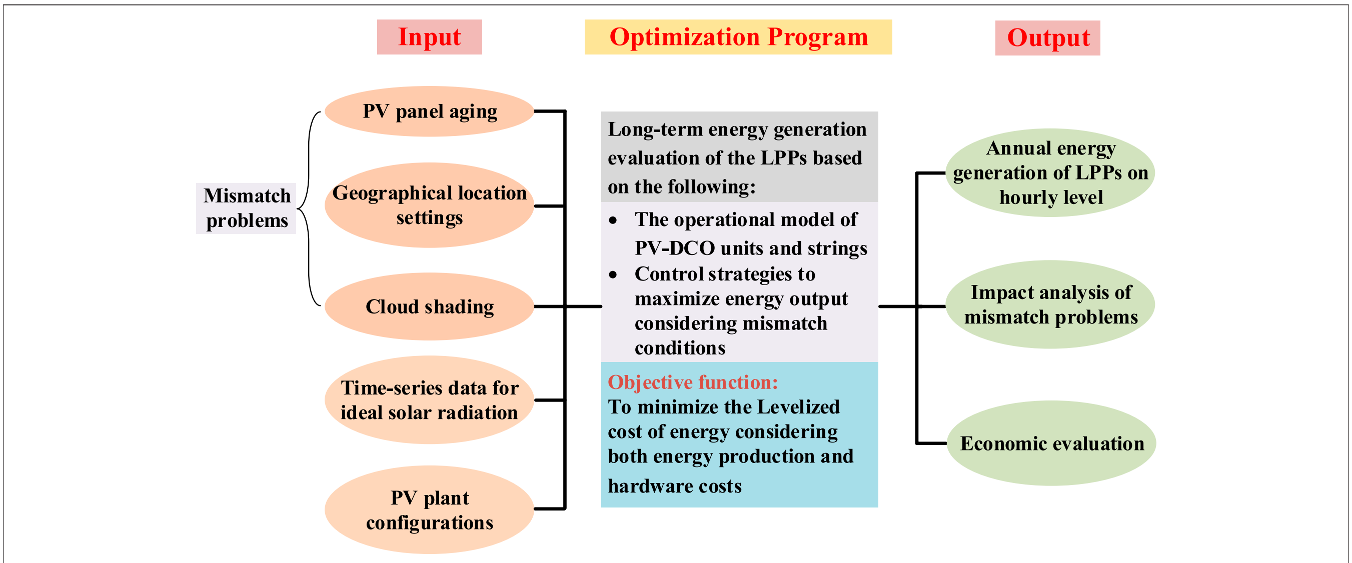

FIGURE 5 | Framework for static modeling of long-term energy generation evaluation in LPPs.

larger value range as indicated in **Eq. 6**. Thus, there is no fixed quantitative relationship between the output current of the PV string I_s and the operating current of PV panels $I_{MPP,i}$. All of the series-connected PV panels can output their own individual MPP power whether there is a mismatch condition in the PV array or not. The control strategy, in this case, remains the same as the original DMPPT control.

FRAMEWORK FOR STATIC MODELING OF ENERGY GENERATION EVALUATION

This section gives a static modeling method for the evaluation of long-term energy generation performances of LPPs. The model framework is shown in **Figure 5**. First, the input information of the optimization program in the model should be clarified. PV panel aging, geographical location settings, and partial shading by clouds, which may cause mismatch conditions on PV energy harvest, are modeled and analyzed as the input information. Besides, the other two input variables are the time-series data for the ideal solar radiation and plant configurations, which are the basic parameters for a certain PV plant. With these five input information, the optimization process of the long-term energy generation evaluation of LPPs can be carried out based on the operational model of PV-DCO units/strings and the control strategies of DCOs described in *Fundamental Models and Control Strategies for Series-Connected PV-DCO Units*. The objective function of the optimization model is to minimize the LCOE of LPPs during the life cycle. Finally, the output information including the annual hourly energy generation data, the impact analysis of mismatch problems on energy production, and the economic evaluation for LPPs of different structures under various scenarios can be obtained to explore the energy generation performances and economic benefits for the DCO-based distributed LPPs.

Impact Factors for Mismatch Conditions

PV Panel Aging:

The aging is inevitable and shows the individual difference in a PV array. For a PV panel, the main reason for the loss in energy production when aging occurs is the degradation in short-circuit current (Chandel et al., 2015), as shown in **Eq. 12**:

$$I_{sc,k} = I_{sc,k-1}\left(1-\sigma_k\right) \tag{12}$$

where σ_k indicates the aging coefficient on the energy production of a PV panel in the kth year, which is randomly distributed among the range of [0.5%, 0.8%] per year for PV panels in a plant. $I_{sc,k\text{-}1}$ and $I_{sc,k}$ represent the short-circuit current of PV panels in the (k-1)th and kth year.

Considering that the aging coefficient is reflected in the variation of short-circuit current, the modified current-voltage characteristic considering PV panel aging can be deduced by substituting the **Eq. 12** to **Eq. 1** as follows:

$$I = \prod_{\mathrm{i}=1}^{\mathrm{k}}\left(1-\sigma_{\mathrm{i}}\right).I_{sc}.\left(1-C_1\left(\exp\left(\frac{U}{C_2 U_{oc}}\right)-1\right)\right) \tag{13}$$

Geographical Location Settings:

The mismatch condition caused by geographical location settings can be reflected in the different solar radiation received by individual PV panels in the PV plant (Seme et al., 2019). The actual solar radiation $S(t)$ received by the PV panel placed at an inclined angle of β with the horizon at moment t can be expressed as follows:

$$S(t) = S_s(t)\,sin\left(\beta+\varphi-\delta\right)cos\left(\varphi-\varphi_0\right) \tag{14}$$

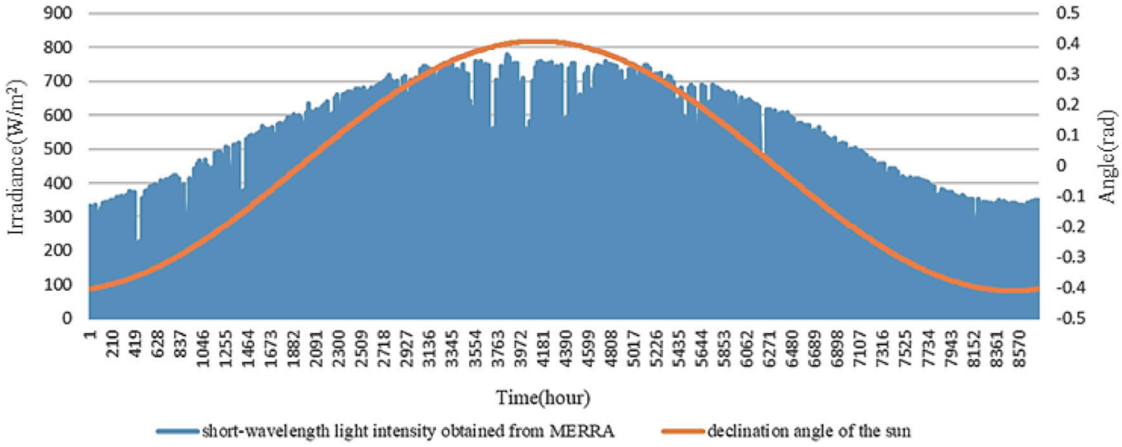

FIGURE 6 | Hourly data for the ideal solar radiation $S_s(t)$ received by the PV panel and the declination angle of the Sun δ during a year.

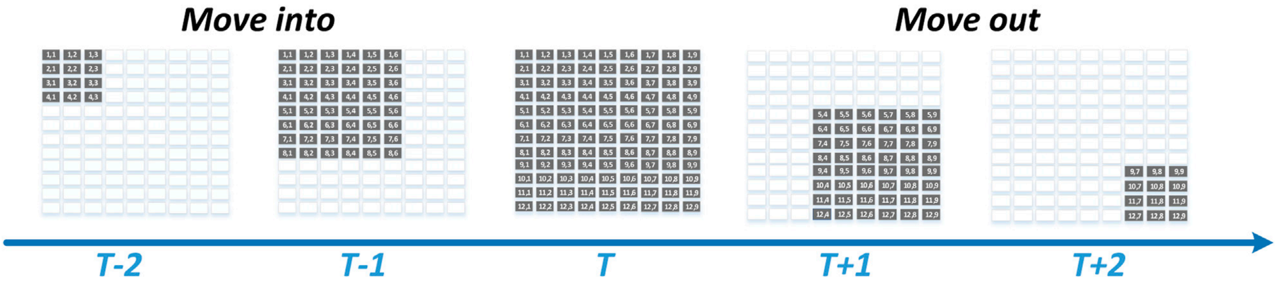

FIGURE 7 | Simplified simulation of the cloud movement for a PV plant.

where $S_s(t)$ is the vertical incident short-wavelength light intensity in the horizontal plane, and ϕ indicates the latitude of the PV plant location. φ and φ_0 represent the azimuth of PV panels and the Sun, respectively. δ is the declination angle of the Sun and changes with time. For the nth day in a year, δ can be calculated as follows:

$$\delta = 23.45^o \cos\left(\frac{2\pi}{365}(n-173)\right) \tag{15}$$

After the site of the PV plant is determined, the time-series data for ideal solar radiation $S_s(t)$ can be obtained from the MERRA as shown in **Figure 6** (take Jiuquan of Gansu Province as an example). The variation trend of the maximal solar radiation received by PV panels is consistent with the declination angle of the Sun δ from the first hour to the 8760th hour during a year. When given the known $S_s(t)$, the actual solar radiation received by the PV panel is mainly influenced by the inclined angle β and the azimuth φ. PV panels are usually set at the best-inclined angle for the maximum absorbed solar radiation (Le et al., 2018), which can be calculated for a certain plant location in advance based on the $S_s(t)$. However, the azimuth for panels in PV plants may differ in terms of the terrain.

Partial Shading by Clouds:

Irradiance fluctuations due to cloud shading are the main cause of mismatch problems in LPPs. Power losses can be up to 25% during a partial shading event caused by the slow-moving clouds. Therefore, the impact of moving clouds on the solar radiation received by PV panels is supposed to be investigated.

Figure 7 gives a simplified simulation of the cloud movement for a 12 × 9 PV array consisting of 108 PV panels. The moving direction is from the upper left to the bottom right (Sánchez Reinoso et al., 2013). The effective radiation received by each PV panel is reduced in proportion to the coverage of the cloud (the gray area) at a given time, as expressed in **Eq. 16**:

$$S_c(x,y,t) = S(x,y,t)\tau(x,y,t) \tag{16}$$

where coordinate (x,y) indicates the position of the PV panel in a PV array, S and S_c represent the solar radiations received by the PV panel before and after partial shading occurs, respectively, and τ represents the cloud cover coefficient.

Available PV Plant Configurations

Six typical centralized (PV1~PV2) or distributed (PV3~PV6) configurations of LPPs are carried out for comparison in this

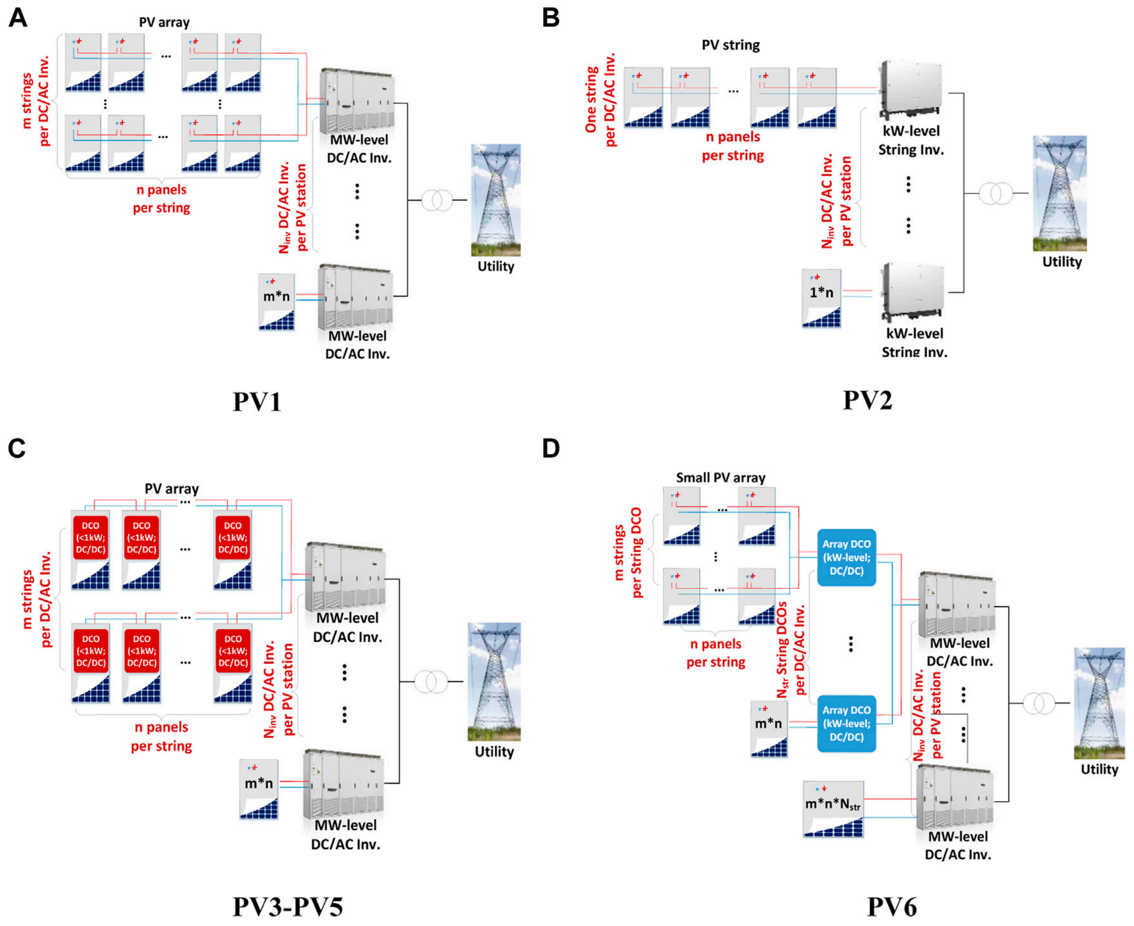

FIGURE 8 | Six typical configurations for LPPs. **(A)** PV1. **(B)** PV2. **(C)** PV3–PV5. **(D)** PV6.

study, as shown in **Figure 8**: PV1---PV plant with conventional array-level central inverters; PV2---PV plant with string-level inverters; PV3---PV plant with series-connected panel-level Boost DCOs and central inverters; PV4---PV plant with series-connected panel-level Buck DCOs and central inverters; PV5---PV plant with series-connected panel-level Boost-Buck DCOs and central inverters; and PV6---PV plant with small array-level Boost DCOs in parallel and central inverters.

PV1 represents the conventional array-level GMPPT configurations and can be viewed as the baseline scenario. In this configuration, several PV panels are series-connected to form a PV string by corresponding bypass diodes, and then several PV strings are parallel connected into a PV array by corresponding blocking diodes. Each PV array is connected with a central converter. The numbers of series-connected PV panels N_{panel} and parallel-connected PV strings N_{string} in a PV array are constrained by the parameters of central inverters, given in **Eqs 17–19**:

$$N_{panel} \le \frac{U_{DC\max}}{U_{oc}\left[1+\left(T_{\min}-T_{ref}\right)\gamma\right]} \tag{17}$$

$$\frac{U_{mppt\min}}{U_m\left[1+\left(T_{max}-T_{ref}\right)\gamma\right]} \le N_{panel} \le \frac{U_{mppt\max}}{U_m\left[1+\left(T_{\min}-T_{ref}\right)\gamma\right]} \tag{18}$$

$$N_{string} \le \frac{I_{DC\max}}{I_{sc}\left[1+\left(T_{\max}-T_{ref}\right)\alpha\right]} \tag{19}$$

where $U_{DC\max}$ and $I_{DC\max}$ represent the maximum input DC voltage and current of the central inverter, respectively. $U_{mppt\min}$ and $U_{mppt\max}$ show the lower and upper operation voltage limits for the MPP tracker. $T_{\min}$ and $T_{\max}$ indicate the minimum and maximum ambient temperature for PV panels.

PV2 employs string-level inverters equipped with multiple MPP trackers in place of central inverters compared to PV1. An improvement of power generation by implementing string-level MPPT can be achieved in this configuration, but still belonging to the GMPPT architecture. Similar constraints should be satisfied for string inverters as indicated for central inverters.

PV3–PV5 are series-connected DMPPT architectures with three different topologies of DCOs. PV-DCO units are connected in series to form a PV-DCO string with panel-level decentralized MPPT implementation. Several PV-DCO strings share a common DC link in a PV system and are connected to the central inverter. The series-connected PV-DCO units for PV3–PV5 are constrained by **Eqs 4–6**, respectively, and the proposed control strategies are adopted.

PV6 shows the parallel-connected DMPPT architectures. Buck topology can only convert the voltage to lower and Buck-boost topology may suffer lower conversion efficiency than boost topology under the same conversion ratio. Thus, the Boost topology is chosen for the DCOs in this configuration to match the high-level DC link voltage for central inverters. Besides, a small PV array instead of a single panel is connected to the input side of the Boost DCO since the difference between the panel-level voltage and the DC-link voltage is so high that it results in lower energy generation efficiency of LPPs.

The total number of PV panels employed for each type of plant configuration should be identical in the following comparative analysis in *Case Study*.

LCOE Calculation

The LCOE is used for the economic evaluation for the long-term energy generation performances of LPPs in this study, which equals to the hardware cost C divided by the total energy production P_{life} during the life cycle, given by **Eq. 20**:

$$LCOE = C/P_{life} \tag{20}$$

The hardware cost considering the capital and installation costs of PV components C_i, as well as the operation and maintenance costs C_{om} over the lifetime of PV plants, is expressed in **Eq. 21**:

$$C = \underbrace{C_W W}_{C_i} + \underbrace{n_{life} R_{om} C_i}_{C_{om}} \tag{21}$$

where C_W is the installation cost per unit capacity of the PV components, including PV panels, inverters, DCOs, cables, etc., and W represents the installed capacity. R_{om} and n_{life} indicate the annual O&M rate and life cycle of a PV plant, respectively.

The life-cycle energy production P_{life} is calculated based on the energy yield for the first year P_1 and the annual energy loss coefficient A_p, given by **Eq. 22**:

$$P_{life} = \sum_{i=1}^{n_{life}} P_1\left(1 - (i-1)A_p\right) \tag{22}$$

Assuming that the power loss of PV plants caused by PV panel aging grows linearly year by year, the A_p could be calculated by dividing the reduced energy production for the 25th year compared with the 1st year by the n_{life} (the life cycle is 25 years in this study). The energy reduction (P_{25}—P_1) during the life cycle can be obtained after the optimization process of annual energy production (as presented in **Figure 5**) for the 1st year and 25th year, respectively.

CASE STUDY

In this section, different case studies are carried out to verify the correctness and validity of the proposed static model and energy generation evaluation methods. First, the hourly energy generation performances without mismatch problems are studied. Second, the impact analysis of the various mismatching factors on long-term energy generation of LPPs is presented, and the simulation scenarios only considering one mismatching factor are built, including the PV panel aging, the geographical location settings of plants, and the partial shading condition caused by clouds. Finally, the comparative analysis of the six typical PV plant configurations for the operational economy of LPPs is simulated combining three different mismatching factors, to explore the optimal structure and layout.

TABLE 1 | Parameter values of a PV panel.

Parameter name	Value
Number of series cells	60
Nominal DC power (W)	250
Voltage at nominal power (V)	30
Current at nominal power (A)	8.33
Open circuit voltage (V)	36
Short circuit current (A)	9.16
Temperature compensation coefficient on PV current (°C^{-1})	0.045%
Temperature compensation coefficient on PV voltage (°C^{-1})	-0.34%
Irradiance compensation coefficient on PV voltage (m^2/W)	-0.47%
Light intensity in the standard operating conditions (W/m^2)	1,000
Temperature in the standard operating conditions (°C)	25

Data Preparation

The investigated PV plant is assumed to be located in the city of Jiuquan, Gansu province (98.5E, 40N), in which all the PV panels are placed at the best-inclined angle. The total capacity of the PV plant is 10 MVA. Solar radiation and temperature profile are obtained from Modern-Era Retrospective Analysis for Research and Applications (MERRA) (Project Science Office (2016). **Table 1** gives the parameter values of the employed PV panels. The parameters of central inverters, string inverters, and three types of DCOs are collected from three manufactures (ABB; Sungrowpower; Solaredge, 2021), as well as the relationship curves between conversion efficiency and input power of the electrical topologies. According to the rated capacity of the PV plant and the nominal DC output power of PV panels, the layouts of the six typical PV plants are listed in **Table 2** to be compared. **Table 3** investigates the investment costs per unit of capacity for the components of PV plants (Annual Energy Outlook, 2019). The life cycle of the LPP is set as 25 years as stated in the latest global PV report (World Energy Outlook, 2020). The annual O&M rate for a PV plant is usually 3% (U.S. Energy Information Administration, 2019).

Hourly Energy Generation Performances Without Mismatch Problems

Assuming that all the PV panels in the PV plant are placed at the azimuth of zero, and there is no PV panel aging and cloud shading events in the PV array. In other words, the mismatch conditions are not considered in this scenario. The total energy

TABLE 2 | Layouts of the six PV plants.

Configuration	Layout
PV1	5 central inverters × 256 PV strings × 36 PV panels
PV2	160 string inverters × 8 PV strings × 36 PV panels
PV3	5 central inverters × 256 PV strings × 36 PV panels with Boost DCOs
PV4	5 central inverters × 128 PV strings × 72 PV panels with Buck DCOs
PV5	5 central inverters × 192 PV strings × 48 PV panels with Buck-boost DCOs
PV6	5 central inverters × 384 PV arrays with Boost DCOs × 3 PV strings ×8 PV panels

TABLE 3 | Investment costs per unit of capacity for the components of PV plants.

Device	Cost (yuan/W)
Central inverter	0.135
String inverter	0.215
Boost DCO	0.138
Buck DCO	0.126
Boost-buck DCO	0.162
Parallel DCO	0.159
The others	6.22

production of the PV plant for six typical configurations during a year is calculated on the hour level as displayed in **Figure 9**.

As shown in **Figure 9**, the shape of the energy envelope curve mainly depends on the solar radiation received by the PV plant when there are no mismatch problems. The generation performances among these six configurations are similar since there are no energy loss events caused by mismatch conditions and the advantages of DMPPT structures cannot be highlighted. Since the solar radiation around noon is better than that in other times, the energy generation will also peak at about 12:00 and drop to almost zero before 8:00 and after 19:00 in a day. Besides, the daily peak values of energy production throughout the year show a similar variation trend to that of the ideal solar radiation distribution as shown in **Figure 6**. More specifically, PV1 and PV2 can yield more power than the other four configurations during the periods with stronger solar radiation in a day for the reason of not considering the transmission loss of DCOs. However, during the periods (08:00, 09:00) and (18:00, 19:00) in a few days, the energy production for PV1 and PV2 is nearly zero since the received radiation is too poor to produce sufficient input voltage for the GMPPT operation of centralized inverters. Therefore, total annual energy production for DMPPT configurations may exceed PV1 and PV2 if the conversion efficiency of DCOs is high enough.

Impact Analysis of Mismatch Problems

The impacts of the three factors for mismatch conditions on solar energy yields of LPPs are analyzed one by one in this section.

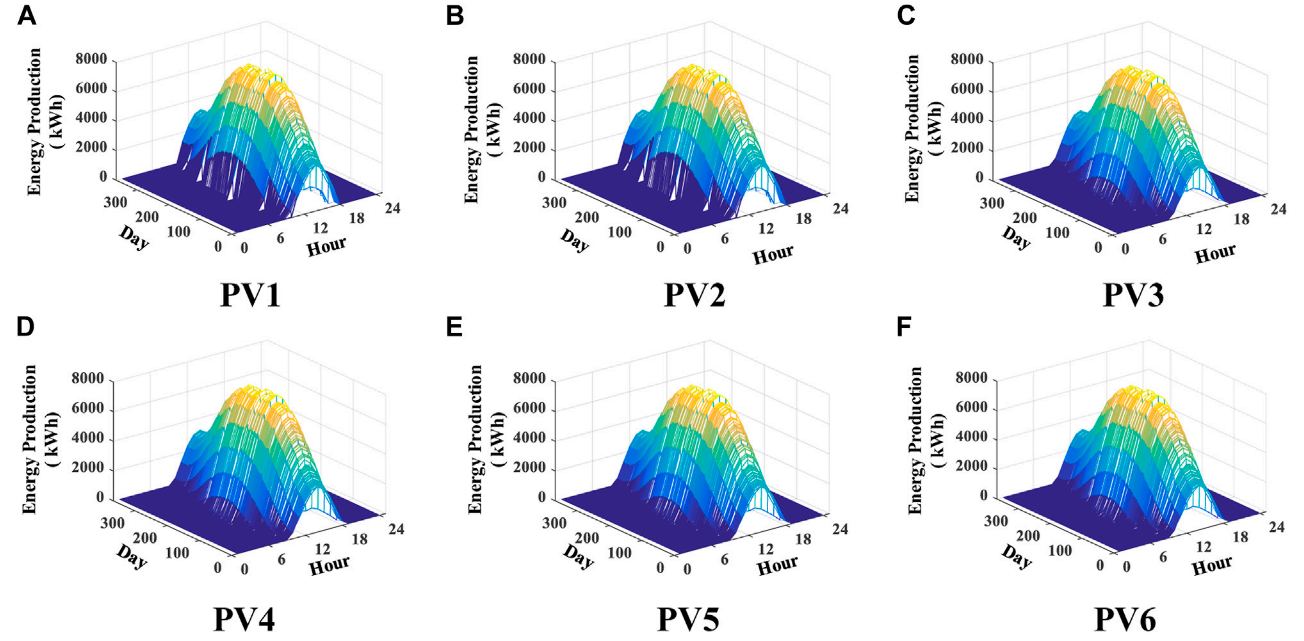

FIGURE 9 | Energy production for each hour during a year of the six configurations. **(A)** PV1. **(B)** PV2. **(C)** PV3. **(D)** PV4. **(E)** PV5. **(F)** PV6.

TABLE 4 | Case settings for the PV panel aging.

Number	Aging years
Case 1.1	No PV panel aging
Case 1.2	5 years
Case 1.3	10 years
Case 1.4	15 years
Case 1.5	20 years
Case 1.6	25 years

TABLE 5 | Case settings for geographical location settings.

Number	Azimuth for PV panels
Case 2.1	Zero for all panels
Case 2.2	Evenly distributed from −10° to 10° for the panels of each PV string
Case 2.3	Evenly distributed from −20° to 20° for the panels of each PV string
Case 2.4	Evenly distributed from −30° to 30° for the panels of each PV string
Case 2.5	Evenly distributed from −40° to 40° for the panels of each PV string

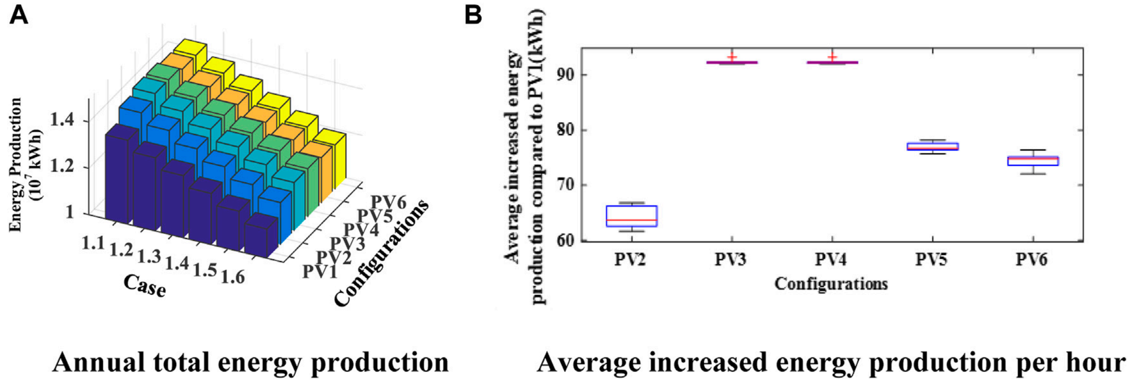

Annual total energy production

Average increased energy production per hour

FIGURE 10 | Comparison of six cases for the PV panel aging. **(A)** Annual total energy production. **(B)** Average increased energy production per hour.

PV Panel Aging: Assuming that all the PV panels in the PV plant are placed at the same azimuth of zero and there is no cloud shading. Six cases are set as listed in **Table 4** to analyze the impact of PV panel aging on the long-term energy production of LPPs. Considering that the difference of aging degrees between PV panels in an array will increase as the aging year increases because of the multiplicative effects of the random variable σ_k as indicated in **Eq. 13**, the effect of the mismatch problems is also becoming more significant.

Figure 10 compares the energy production performances for six typical PV configurations under the given cases: (A) annual total energy production of LPPs and (B) the average increased energy production per hour (marked in the red lines) for PV2~PV6 compared to PV1 in case 1.6. In **Figure 10A**, the energy productions of the PV plant for all configurations decrease from case 1.1 to case 1.6 since the energy loss caused by the PV panel aging becomes more serious with the increase in the aging coefficient. Comparing Case 1.1 to Case 1.6, the energy loss in PV1 and PV2 is greater than that in PV3~PV6 due to the lower generation efficiency of the GMPPT structure compared to the DMPPT deployment when suffering mismatch conditions. Besides, the overall energy generation level in PV1 is lower than that in PV2 due to the array-level GMPPT control. On the other hand, it can be found in **Figure 10B** that PV2 owns the minimum average energy production level (63.64 kWh) while PV3 and PV4 enjoy the maximum (about 92.35 kWh). It indicates that the mismatch problems caused by the difference in the aging coefficients of PV panels could be greatly mitigated by the proposed control strategies of Boost and Buck DCOs. Since the energy transmission efficiency is lower for Buck-boost DCOs, the generation level in PV5 (77.71 kWh) is between that of PV1 and PV3/PV4. PV6 shows a smaller production increase (74.11 kWh) than PV5 because of the greater effect of mismatch problems in small array-level DCO deployment compared with the panel-level DMPPT structure. Moreover, the box areas in PV3 and PV4 are almost zero, which shows the smaller variance of the hourly energy generation performances throughout a year compared with other configurations, resulting in better stability for energy capture with the proposed control strategies for DCOs.

Geographical Location Settings: Assuming that there is no PV panel aging and cloud shading events. Five cases are set as listed in **Table 5** to analyze the impact of the azimuth setting of PV panels on the energy production of LPPs (Case 2.1 is the baseline scenario). Considering the terrains of PV plant sites could be gentle or steep, the PV panels should be placed at various azimuths to maximize the received solar radiation.

The comparison of the energy production performances for six typical PV configurations in the five given cases is displayed in **Figure 11**: (A) annual total energy production of LPPs and (B) the average increased energy production per hour (marked in the red lines) for PV2~PV6 compared to PV1 in case 2.5. Similar to the conclusions drawn in the cases for PV panel aging, the energy productions of LPPs decrease from case 2.1 to case 2.5 gradually as shown in **Figure 11A** since the azimuth settings for PV panels are more uneven and the solar radiations accepted by PV panels become less. The DMPPT configurations including PV3~PV6 show a better mitigation effect for the energy loss under mismatch

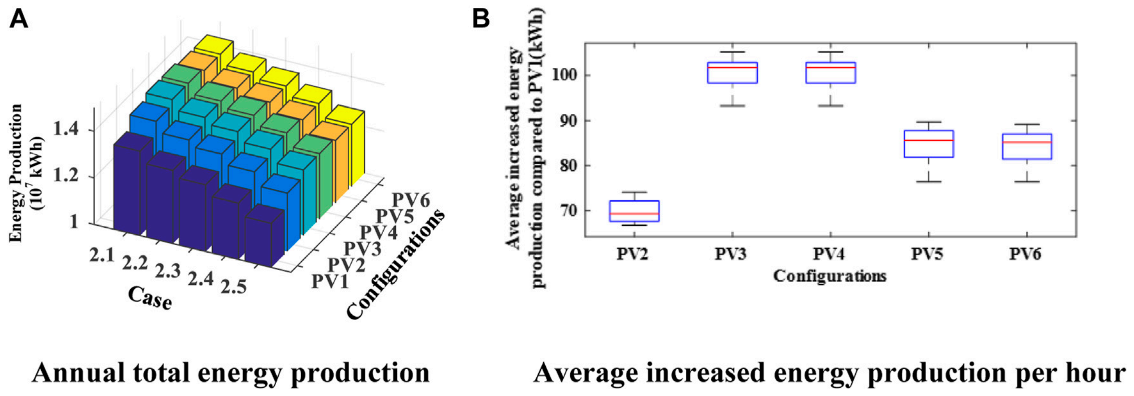

FIGURE 11 | Comparison of five cases for the geographical location settings. **(A)** Annual total energy production. **(B)** Average increased energy production per hour.

TABLE 6 | Case settings for the partial shading by clouds.

Number	Times of cloud shading during a year
Case 3.1	No cloud shading
Case 3.2	343 times
Case 3.3	681 times
Case 3.4	965 times
Case 3.5	1,251 times

conditions. In **Figure 11B**, the average increased energy production per hour for PV2~PV6 are 69.29 kWh, 101.71 kWh, 102.06 kWh, 85.61 kWh, and 85.16 kWh, respectively, whose variation trend is similar to the analysis of case 1.6 (as shown in **Figure 10B**). However, the box areas of PV3 and PV4 become manifest, which indicates that the mismatch problems caused by geographical location settings impose a bigger influence on long-term energy production than that for the PV panel aging, and the DMPPT technology could not completely make up for the energy loss sometimes.

Partial Shading by Clouds: Assuming that all the PV panels in the PV plant are placed at the same azimuth of zero and there is no PV panel aging. Five cases are set as listed in **Table 6** to analyze the impact of cloud shading on the energy production of LPPs (Case 3.1 is the baseline scenario). The duration of the partial shading caused by clouds is assumed as 1 h per time, and the cloud cover coefficient τ is generated in a random way.

Figure 12 shows the energy production comparison for six configurations in the five given cases: (A) annual total energy production of LPPs and (B) the average increased energy production per hour (marked in the red lines) for PV2~PV6 compared to PV1 in case 3.5, a severe mismatch scenario. As shown in **Figure 12A**, the annual energy productions of the PV plant for all configurations also decrease from case 3.1 to case 3.5 since the more times the cloud shading occurs, the less radiation the panels receive, and the more energy is lost. However, it should be noted that the rank of the six PV configurations for the energy production level in cases 3.1–3.5 shows some differences

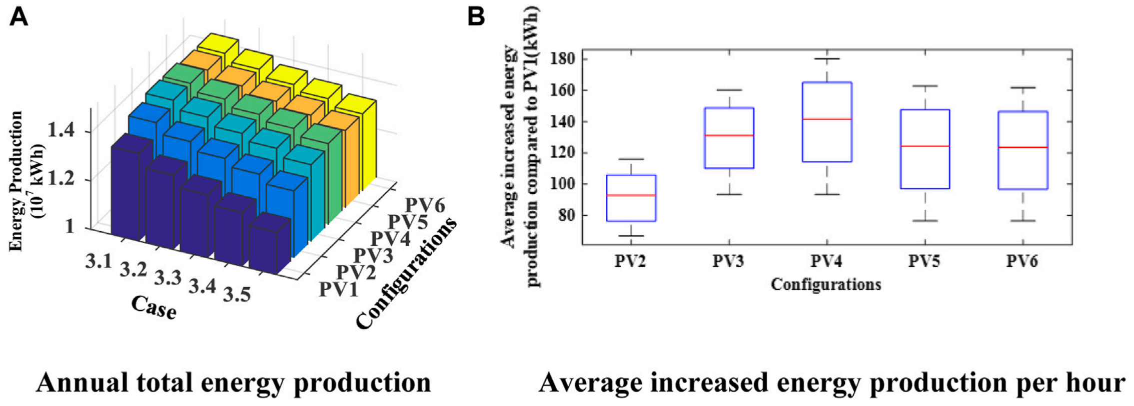

FIGURE 12 | Comparison of five cases for the partial shading by clouds. **(A)** Annual total energy production. **(B)** Average increased energy production per hour.

TABLE 7 | Case settings for the synthetic analysis.

Number	Azimuth for PV panels	Times of cloud shading during a year
Case 4.1	All are placed at zero	No cloud shading
Case 4.2	All are placed at zero	343 times
Case 4.3	All are placed at zero	1,251 times
Case 4.4	Evenly distributed from −10° to 10°	No cloud shading
Case 4.5	Evenly distributed from −10° to 10°	343 times
Case 4.6	Evenly distributed from −10° to 10°	1,251 times
Case 4.7	Evenly distributed from −40° to 40°	No cloud shading
Case 4.8	Evenly distributed from −40° to 40°	343 times
Case 4.9	Evenly distributed from −40° to 40°	1,251 times

compared to the first two case sets (cases 1.1–1.6 and 2.1–2.5). More specifically, PV4 enjoys better energy generation performances than PV3. It indicates that a better effect can be obtained with the control strategy of series-connected Buck DCOs to deal with the mismatch problems than that of series-connected Boost DCOs. The main reason is that the severely shaded PV panels may be shorted by the bypass-diodes according to the control strategy of Boost DCOs to avoid affecting the solar energy utilization of normal panels in PV-DCO strings; nevertheless, all of the PV panels within the strings can output the power in Buck-DCO–based LPPs.

Similarly, the average increased energy production per hour for PV2~PV6 is 92.69 kWh, 131.05 kWh, 141.55 kWh, 124.31 kWh, and 123.51 kWh, respectively, which is consistent with the changing trend of the annual total energy production levels in **Figure 12A**. Besides, the significant increases in the box areas of all configurations can be found in **Figure 12B**, which proves that the mismatch problems caused by cloud shading impose the biggest influence on the long-term energy production performances compared to the other two factors including the PV panel aging and geographical location settings. Although the DCO-based DMPPT technology could not entirely mitigate the power loss when suffering serious partial shading, the improvement of energy production is still considerable compared to the GMPPT-based LPPs (PV1 and PV2).

Synthetic Analysis and Economic Evaluation

To combine all the impact factors, three types of mismatch conditions are coordinated in this section for the synthetic analysis and economic evaluation of the long-term energy generation performances of LPPs. Nine cases are carried out as listed in **Table 7** to compare the life-cycle energy production characteristics and the LCOEs for six PV plant configurations based on (20–22). Since the effect of the panel aging on power loss is less than the other two factors, the annual aging coefficients for all the cases are set as the same. Different combinations for the placed azimuth for PV panels and times of partial shading by clouds in a year are reflected in these nine cases.

Figure 13 simulates the trend of life-cycle energy production in two dimensions (azimuth and partial shading) to include all possible mismatch conditions bounded by the settings in **Table 7** from PV1 to PV6. Energy production decreases with either the increased placed azimuth for PV panels or times of cloud shading. For PV1 and PV2, the energy yields are smaller than those in the other four DMPPT configurations during the life cycle. Besides, the mean curvatures of the surface that represents the decline rates of energy production when suffering a mismatch are larger in PV1 and PV2, showing that the DMPPT is superior to the GMPPT in dealing with mismatch conditions. Similarly, it can be seen that PV4 enjoys the most energy generation level and the least decline rate when suffering mismatch, which indicates that the Buck topology is a superior choice for the long-term energy generation over the entire life cycle for LPPs.

On the other hand, the total investment costs of LPPs for six configurations can be calculated as given in **Table 8**. PV1 enjoys the least hardware cost due to its simple structure. PV2 owns the most investment cost due to the expensive string inverters. The costs for PV3 and PV4 are different since the hardware cost of Buck DCOs is less than that of Boost DCOs. Besides, deploying panel-level power electronic devices requires additional costs compared to PV1. PV5 and PV6 share almost the same cost, which is more expensive than that in PV3 and PV4 since the higher voltage ratios between DCOs and inverters in PV5 and PV6 require the higher cost for DCOs.

Based on the life-cycle energy production and total investment costs, the LCOE of the six PV configurations in cases 4.1–4.9 can be calculated using **Eq. 20** as shown in **Figure 14**. For each PV configuration, the LCOE shows the same changing trend from case 4.1 to case 4.9 since more energy production corresponds to a smaller LCOE when the investment costs are the same. In addition, it can be seen that PV3~PV6 show more cost-effective LCOE for all the cases than PV1 and PV2. The main reason is that the additional benefit from increased energy generation with DMPPT control methods is more than the additional costs for the deployment of the panel-level DCOs; in other words, net earnings are achieved by the DCO-based distributed structures for LPPs compared to the GMPPT configurations. More importantly, when the mismatch problems become more serious, the PV4 configuration equipped with the Buck DCOs shows more competitive LCOE performances for all the nine cases due to the more efficient control strategy for energy generation and the lower hardware costs for DCOs, compared with the PV3 configuration involving Boost DCOs.

In conclusion, the PV4 configuration deploying panel-level Buck DCOs and the corresponding DMPPT control strategy is the optimal choice for LPPs in terms of the optimization objective for minimizing the LCOE. PV3, PV5, and PV6 own a relatively lower LCOE than PV1 and PV2, which can be regarded as the sub-optimal solution depending on the actual operational situation of PV plants.

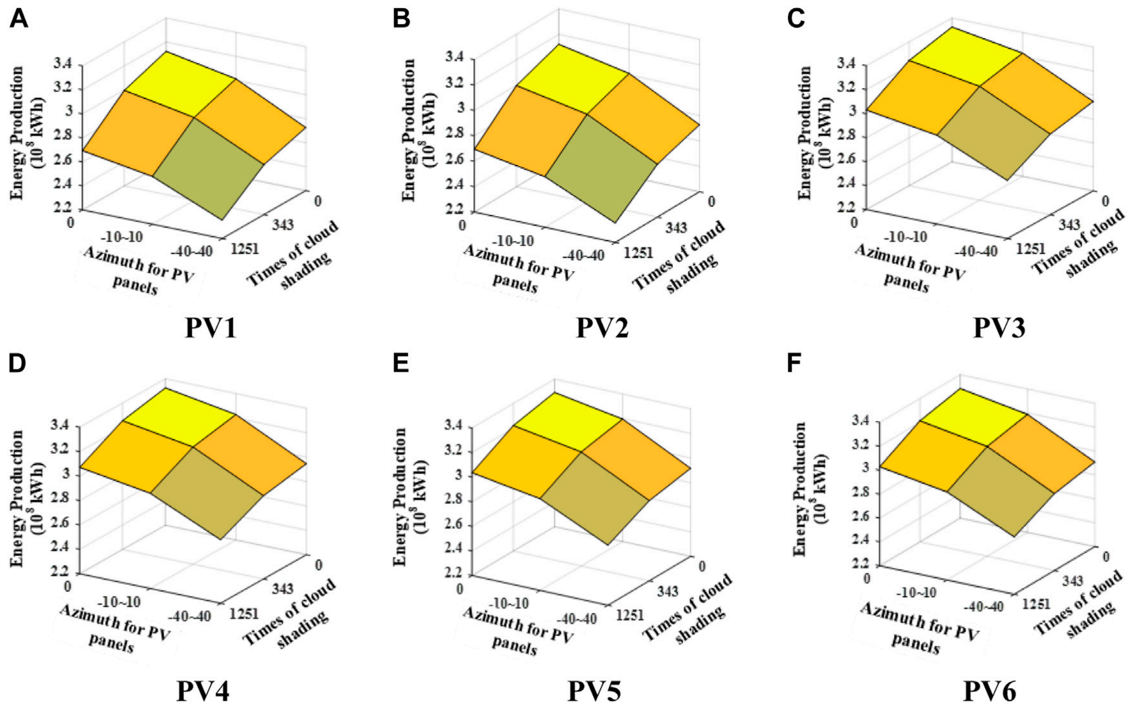

FIGURE 13 | Life-cycle energy production of PV plants for six configurations. **(A)** PV1. **(B)** PV2. **(C)** PV3. **(D)** PV4. **(E)** PV5. **(F)** PV6.

TABLE 8 | Total investment cost of the PV plant of six configurations.

Configurations	PV1	PV2	PV3	PV4	PV5	PV6
Investment cost (10^8 yuan)	1.1594	1.2014	1.1783	1.1695	1.1877	1.1863

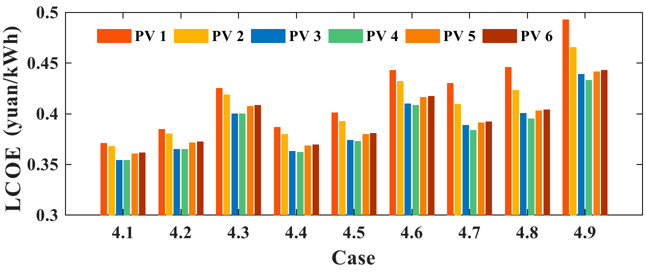

FIGURE 14 | LCOE of the PV plants for six configurations.

CONCLUSION

This article presents a modeling and energy generation evaluation method for large-scale PV plants equipped with panel-level DCOs. Based on the operational characteristics and the proposed control strategies for PV-DCO strings with three different topologies (including Boost, Buck, and Buck-boost), the design-oriented analysis method is proposed for the economic evaluation of the long-term energy generation performances in LPPs, considering frequent mismatch conditions. The modeling for various factors affecting mismatch problems, including panel aging, geographical location settings, and partial shading by clouds, are structured in this study. After that, six typical centralized or distributed PV plant configurations are carried out for comparison analysis, and finally, the optimal designing scheme with the least LCOE is obtained for LPPs. The main conclusions can be listed as follows:

a. The influence of the partial shading by clouds on the mismatch problems is more serious than that of the PV panel aging and geographical location settings.
b. The DCO-based DMPPT configurations, especially the Buck topology, have higher energy utilization efficiency than the GMPPT operation structure in terms of the long-term energy generation performances for LPPs when considering frequent mismatch.
c. The PV plant configuration, which deploys panel-level Buck DCOs and the proposed control strategy for maximizing solar energy captures, is the economically optimal choice for LPPs with the least LCOE.

It is worth pointing out that the interaction for the power flow between PV power plants and the thermal power generators of AC systems is not considered in the proposed static models. Since the unit commitment could affect the power output of PVs, the power flow calculation methods for the power system incorporating the DCO-based large-scale distributed PV plants can be further studied in our future works for the steady-state power flow studies of practical electrical networks.

DATA AVAILABILITY STATEMENT

The original contributions presented in the study are included in the article/Supplementary Material; further inquiries can be directed to the corresponding author.

AUTHOR CONTRIBUTIONS

QW and JF contributed to the conception and design of the study. QW, LL, DL, XA, and JF organized case studies. QW wrote the first draft of the manuscript. All authors contributed to manuscript revision and read and approved the submitted version.

FUNDING

This study received funding from the Science and Technology Project of State Grid Hubei Electric Power Company Limited (Number: SGHB0000DKJS2104209). The funder had the following involvement with the study: the organization of case studies, the manuscript revision of this article and the decision to submit it for publication.

REFERENCES

Abb (2020). Main Parameters and the Relation Curve between Efficiency and Output of central Inverter. Available at: https://search.abb.com/library/Download.aspx?DocumentID=3AXD50000026013&LanguageCode=en&DocumentPartId=1&Action=Launch. (Accessed February 11, 2020).

Alik, R., and Jusoh, A. (2018). An Enhanced P&O Checking Algorithm MPPT for High Tracking Efficiency of Partially Shaded PV Module. *Solar Energy* 163, 570–580. doi:10.1016/j.solener.2017.12.050

Amir, A., Amir, A., Che, H. S., Elkhateb, A., and Rahim, N. A. (2019). Comparative Analysis of High Voltage Gain DC-DC Converter Topologies for Photovoltaic Systems. *Renew. Energ.* 136, 1147–1163. doi:10.1016/j.renene.2018.09.089

Bana, S., and Saini, R. P. (2017). Experimental Investigation on Power Output of Different Photovoltaic Array Configurations under Uniform and Partial Shading Scenarios. *Energy* 127, 438–453. doi:10.1016/j.energy.2017.03.139

Batzelis, E. I., Georgilakis, P. S., and Papathanassiou, S. A. (2014). Energy Models for Photovoltaic Systems under Partial Shading Conditions: A Comprehensive Review. *IET Renew. Power Gener.* 9 (4), 340–349. doi:10.1049/iet-rpg.2014.0207

Biswas, J., Kamath, A. M., Gopi, A. K., and Barai, M. (2017). Design, Architecture, and Real-Time Distributed Coordination DMPPT Algorithm for PV Systems. *IEEE J. Emerg. Sel. Top. Power Electron.* 6 (3), 1418–1433. doi:10.1109/jestpe.2017.2756698

Cao, D., Hu, W., Zhao, J., Huang, Q., Chen, Z., and Blaabjerg, F. (2020a). A Multi-Agent Deep Reinforcement Learning Based Voltage Regulation Using Coordinated PV Inverters. *IEEE Trans. Power Syst.* 35 (5), 4120–4123. doi:10.1109/tpwrs.2020.3000652

Cao, D., Hu, W., Zhao, J., Zhang, G., Zhang, B., Liu, Z., et al. (2020b). Reinforcement Learning and its Applications in Modern Power and Energy Systems: A Review. *J. Mod. Power Syst. Clean. Energ.* 8 (6), 1029–1042. doi:10.35833/mpce.2020.000552

Castro, L. M., Rodríguez-Rodríguez, J. R., and Martin-del-Campo, C. (2020). Modelling of PV Systems as Distributed Energy Resources for Steady-State Power Flow Studies. *Int. J. Electr. Power Energ. Syst.* 115, 105505. doi:10.1016/j.ijepes.2019.105505

Chandel, S. S., Nagaraju Naik, M., Sharma, V., and Chandel, R. (2015). Degradation Analysis of 28 Year Field Exposed Mono-C-Si Photovoltaic Modules of a Direct Coupled Solar Water Pumping System in Western Himalayan Region of India. *Renew. Energ.* 78, 193–202. doi:10.1016/j.renene.2015.01.015

Chen, H., Wang, Y., Ding, Y., Cai, B., and Yang, J. (2021). Numerical Analysis on the Performance of High Concentration Photovoltaic Systems under the Nonuniform Energy Flow Density. *Front. Energ. Res.* 9, 705801. doi:10.3389/fenrg.2021.705801

Cook, T., Shaver, L., and Arbaje, P. (2018). Modeling Constraints to Distributed Generation Solar Photovoltaic Capacity Installation in the US Midwest. *Appl. Energ.* 210, 1037–1050. doi:10.1016/j.apenergy.2017.08.108

De Prada-Gil, M., Domínguez-García, J. L., Trilla, L., and Gomis-Bellmunt, O. (2016). Technical and Economic Comparison of Various Electrical Collection Grid Configurations for Large Photovoltaic Power Plants. *IET Renew. Power Gener.* 11 (3), 226–236. doi:10.1049/iet-rpg.2016.0304

Hanson, A. J., Deline, C. A., MacAlpine, S. M., Stauth, J. T., and Sullivan, C. R. (2014). Partial-shading Assessment of Photovoltaic Installations via Module-Level Monitoring. *IEEE J. Photovoltaics* 4 (6), 1618–1624. doi:10.1109/jphotov.2014.2351623

Khan, O., and Xiao, W. (2017). Review and Qualitative Analysis of Submodule-Level Distributed Power Electronic Solutions in PV Power Systems. *Renew. Sustain. Energ. Rev.* 76, 516–528. doi:10.1016/j.rser.2017.03.073

Khan, O., Xiao, W., and Zeineldin, H. H. (2016). Gallium-Nitride-Based Submodule Integrated Converters for High-Efficiency Distributed Maximum Power Point Tracking PV Applications. *IEEE Trans. Ind. Electron.* 63 (2), 966–975. doi:10.1109/tie.2015.2491888

Le, L., Zhang, M., Ai, X., and Yang, X. (2018). "Evaluation of Energy Production for Large-Scale Photovoltaic Plant with Different Configurations," in International Conference on Power System Technology (POWERCON), Guang Zhou, November 6–8, 2018, 1453–1458. doi:10.1109/powercon.2018.8602327

Li, H., Li, H., Lu, W., Wang, Z., and Bian, J. (2020). Optimal Power Flow Calculation Considering Large-Scale Photovoltaic Generation Correlation. *Front. Energ. Res.* 8, 590418. doi:10.3389/fenrg.2020.590418

López del Moral, D., Barrado, A., Sanz, M., Lázaro, A., and Zumel, P. (2018). Analysis and Implementation of the Buck-Boost Modified Series Forward Converter Applied to Photovoltaic Systems. *Solar Energy* 176, 771–787. doi:10.1016/j.solener.2018.10.053

Ma, T., Gu, W., Shen, L., and Li, M. (2019). An Improved and Comprehensive Mathematical Model for Solar Photovoltaic Modules under Real Operating Conditions. *Solar Energy* 184, 292–304. doi:10.1016/j.solener.2019.03.089

MacAlpine, S. M., Erickson, R. W., and Brandemuehl, M. J. (2012). Characterization of Power Optimizer Potential to Increase Energy Capture in Photovoltaic Systems Operating under Non-uniform Conditions. *IEEE Trans. Power Electron.* 28 (6), 2936–2945. doi:10.1109/tpel.2012.2226476

Mahdavyfakhr, M., Rashidirad, N., Hamzeh, M., Sheshyekani, K., and Afjei, E. (2017). Stability Improvement of DC Grids Involving a Large Number of Parallel Solar Power Optimizers: An Active Damping Approach. *Appl. Energ.* 203, 364–372. doi:10.1016/j.apenergy.2017.06.044

Olalla, C., Deline, C., and Maksimovic, D. (2013). Performance of Mismatched PV Systems with Submodule Integrated Converters. *IEEE J. Photovolt.* 4 (1), 396–404. doi:10.1109/jphotov.2013.2281878

Petrone, G., and Ramos-Paja, C. A. (2011). Modeling of Photovoltaic fields in Mismatched Conditions for Energy Yield Evaluations. *Electric Power Syst. Res.* 81, 1003–1013. doi:10.1016/j.epsr.2010.12.008

Project Science Office (2016). *NASA's Earth Observing System*. Available at: https://eospso.nasa.gov/. (Accessed December 20, 2016).

Ram, J. P., Babu, T. S., and Rajasekar, N. (2017). A Comprehensive Review on Solar PV Maximum Power point Tracking Techniques. *Renew. Sustain. Energ. Rev.* 67, 826–847. doi:10.1016/j.rser.2016.09.076

Sánchez Reinoso, C. R., Milone, D. H., and Buitrago, R. H. (2013). Simulation of Photovoltaic Centrals with Dynamic Shading. *Appl. Energ.* 103, 278–289. doi:10.1016/j.apenergy.2012.09.040

Seme, S., Sredenšek, K., Štumberger, B., and Hadžiselimović, M. (2019). Analysis of the Performance of Photovoltaic Systems in Slovenia. *Solar Energy* 180, 550–558. doi:10.1016/j.solener.2019.01.062

Solaredge (2021). Relation Curve between Efficiency and Output of the DCOs of Different Electrical Topologies. Available at: https://www.solaredge.com/sites/default/files/application_note_solaredge_optimizers_efficiency.pdf. (November 5, 2021).

Sungrowpower (2021). Main Parameters and the Relation Curve between Efficiency and Output of String Inverter. Available at: http://www.sungrowpower.com/index.php?s=/Home/business/product_detail/id/136.html. (September 25, 2021).

Annual Energy Outlook (2019). Levelized Cost and Levelized Avoided Cost of New Generation Resources in the Annual Energy Outlook 2019. Washington, DC:Energy Information Administration. Tech. Rep.

Vavilapalli, S., Umashankar, S., Sanjeevikumar, P., Ramachandaramurthy, V. K., Mihet-Popa, L., and Fedák, V. (2018). Three-stage Control Architecture for Cascaded H-Bridge Inverters in Large-Scale PV Systems - Real Time Simulation Validation. *Appl. Energ.* 229, 1111–1127. doi:10.1016/j.apenergy.2018.08.059

Wang, F., Wu, X., Lee, F. C., Wang, Z., Kong, P., and Zhuo, F. (2013). Analysis of Unified Output MPPT Control in Subpanel PV Converter System. *IEEE Trans. Power Electron.* 29 (3), 1275–1284. doi:10.1109/epe.2013.6631752

Wang, Q., Yao, W., Fang, J., Ai, X., Wen, J., Yang, X., et al. (2020). Dynamic Modeling and Small Signal Stability Analysis of Distributed Photovoltaic Grid-Connected System with Large Scale of Panel Level DC Optimizers. *Appl. Energ.* 259, 114132. doi:10.1016/j.apenergy.2019.114132

Wijeratne, W. M. P. U., Yang, R. J., Too, E., and Wakefield, R. (2019). Design and Development of Distributed Solar PV Systems: Do the Current Tools Work? *Sustain. Cities Soc.* 45, 553–578. doi:10.1016/j.scs.2018.11.035

World Energy Outlook (2020). *World Energy Outlook 2020*. Paris, France: International Energy Agency, Tech. Rep.

Zhang, X., Hu, Y., Mao, W., Zhao, T., Wang, M., Liu, F., et al. (2021). A Grid-Supporting Strategy for Cascaded H-Bridge PV Converter Using VSG Algorithm with Modular Active Power reserve. *IEEE Trans. Ind. Electron.* 68 (1), 186–197. doi:10.1109/tie.2019.2962492

Conflict of Interest: DL was employed by State Grid Hubei Electric Power Company Limited.

The remaining authors declare that the research was conducted in the absence of any commercial or financial relationships that could be construed as a potential conflict of interest.

The reviewer DC and the handling editor declared their shared affiliation at the time of the review.

frontiers
in Energy Research

ORIGINAL RESEARCH
published: 15 February 2022
doi: 10.3389/fenrg.2022.844111

A Wind Power Prediction Method Based on DE-BP Neural Network

Ning Li, Yelin Wang, Wentao Ma, Zihan Xiao and Zhuoer An*

School of Electrical Engineering, Xi'an University of Technology, Xi'an, China

With the continuous increase of installed capacity of wind power, the influence of large-scale wind power integration on the power grid is becoming increasingly apparent. Ultra-short-term wind power prediction is conducive to the dispatching management of the power grid and improves the operating efficiency and economy of the power system. In order to overcome the intermittency and uncertainty of wind power generation, this article proposes the differential evolution–back propagation (DE-BP) algorithm to predict wind power and addresses such shortcomings of the BP neural network as its falling into local optimality and slow training speed when predicting. In this article, the DE algorithm is used to find the optimal value of the initial weight and threshold of the BP neural network, and the DE-BP neural network prediction model is obtained. According to the data of a wind farm in Northwest China, the short-term wind power is predicted. Compared with the application of the BP model in wind power prediction, the results show that the accuracy of the DE-BP algorithm is improved by about 5%; compared with the genetic algorithm–BP model, the prediction time is shortened by 23.1%.

Keywords: differential evolution algorithm, wind power prediction, BP neural network, prediction time, accuracy

1 INTRODUCTION

Wind energy is one of the renewable energy resources and the most available resource with the lowest power generation cost. It can substantially reduce greenhouse gases and air pollution caused by the use of traditional power generation systems (Xiong et al., 2020). Wind power technology is now making a significant contribution to the growing global clean power market. However, the intermittency and uncertainty of wind power generation pose challenges to power supply and operation. The large-scale integration of wind power will affect the safety, stability, and power quality of the power system. Therefore, the ultra-short-term power prediction of wind power generation helps the dispatching department to make dispatch plans and avoid the risks in advance, so as to improve the safety of the power system and the competitiveness of wind power generation. The ultra-short-term wind power prediction will help the power system dispatching department to further understand the wind power that will be connected to the grid and provide a basis for hourly power generation operation dispatch (Wan et al., 2014).

At present, there are three types of the commonly used wind power prediction methods: the physical (Agarwal et al., 2018), statistical (Sideratos and Hatziargyriou, 2007), and learning (Catalao et al., 2009) methods. The physical method obtains the predicted power of the wind turbine by refining the numerical weather forecast data into the wind speed and wind direction at the hub height of the wind turbine under the actual terrain and landform conditions of the wind farm, considering the influence of wake, and applying the predicted wind speed to the power curve of the wind turbine (Chang et al., 2014). The disadvantage of this method is that it relies too much on the mastery of meteorological knowledge and physical characteristics of the model itself. If the meteorological

OPEN ACCESS

Edited by:
Liansong Xiong,
Nanjing Institute of Technology (NJIT), China

Reviewed by:
He Li,
Xidian University, China
Yingjie Wang,
University of Liverpool, United Kingdom
Jianquan Shi,
Nanjing Institute of Technology (NJIT), China

****Correspondence:***
Ning Li
lining83@xaut.edu.cn

Specialty section:
This article was submitted to Process and Energy Systems Engineering, a section of the journal Frontiers in Energy Research

Received: *27 December 2021*
Accepted: *18 January 2022*
Published: *15 February 2022*

Citation:
Li N, Wang Y, Ma W, Xiao Z and An Z (2022) A Wind Power Prediction Method Based on DE-BP Neural Network. Front. Energy Res. 10:844111. doi: 10.3389/fenrg.2022.844111

knowledge reserve is less or the physical characteristics are not mastered enough, the model will be relatively rough, and the prediction accuracy will be relatively poor (Chandra et al., 2013).

The statistical method establishes a predictive model by finding the relationship between the historical wind farm data (including power, wind speed, wind direction, etc.) and wind speed or power of the wind farm (Foley et al., 2012), such as regression analysis (Yuqin et al., 2014), exponential smoothing method, time series method (Tasnim et al., 2014), Kalman filter method (Babazadeh et al., 2012), etc., which are all based on statistical models. These models make predictions by capturing information related to time and space in the data. The application of the statistical method is simple, and the original data are not complicated, so its prediction accuracy will be limited, and the prediction time will not be too long.

When using the physical or statistical method to predict wind power generation, the prediction results will also be affected by data quality and collection methods. Wind power prediction requires a large amount of data, such as historical wind farm data, numerical weather prediction data, and the Supervisory Control And Data Acquisition system real-time data, etc. However, these data are often abnormal and incomplete. If statistical methods are used for prediction, the prediction accuracy and reliability will be affected due to insufficient data (Wu et al., 2016). Automatic communication equipment plays an important role in the power system (Yan et al., 2017). Automatic communication failures cause errors in data collection, transmission, and conversion, which will bring about data distortion or loss, and have adverse effects on the accuracy of wind power prediction (Zhang et al., 2020).

The learning method addresses some of the shortcomings of physical and statistical methods in predicting wind power. It uses artificial intelligence methods to learn and train large amounts of data to obtain the nonlinear relationship between input and output. The learning method can adaptively predict the output power of different wind farms, independent of the geographic location of the wind farm. The learning methods for wind power prediction include the neural network method (Bhaskar and Singh, 2012), support vector machine (Liu et al., 2016), and wavelet analysis method (Zhao, 2016). Different from statistical prediction, the learning method predicts that there is no definite functional relationship between the input and output in the model, that is, there is no specific functional expression. Haque et al. (2013) proposed a new hybrid intelligent algorithm based on the wavelet transform and fuzzy ARTMAP network, which predicts the power output of wind farms using meteorological information, for instance, wind speed, wind direction, temperature, etc. Compared with the physical method, the amount of calculation is reduced in this method, but it is greatly affected by the weather and other factors. Tan et al. (2020) proposed an ultra-short-term wind power prediction model based on the Salp Swarm algorithm–extreme learning machine, but this method is complicated to determine network parameters. Paula et al. (2020) applied different machine learning strategies, such as the random forest, the neural network, and the gradient boosting, to predict long-term wind data. Zhang et al. (2019) designed fractional gray models of different orders for prediction and established a combined prediction model based on the neural networks. Considering the limitations of the single convolution model when predicting wind power, Ju et al. (2019) proposed an innovative integration of the LightGBM classification algorithm in the model to improve the prediction accuracy and robustness. Li et al. (2020) proposed a kernel extreme learning machine using differential evolution (DE) and cross-validation optimization methods to predict short-term wind power generation. The DE algorithm was applied to optimize the regularization coefficient and kernel width of the kernel extreme learning machine to improve the prediction accuracy.

Liu et al. (2021) bettered the beetle antennae search algorithm in the iterative process by improving a single beetle into a population. The improved beetle antennae search–BP model not only effectively avoids the possibility of the local minimum but also achieves higher prediction accuracy and stronger robustness. Yang et al. (2019) applied the Levenberg–Marquard (LM)–BP neural network model to the intrusion detection systems and optimized the weight threshold of the traditional BP neural network by using the characteristics of fast optimization and strong robustness of the LM algorithm. Compared with the traditional models, this model has a higher detection rate and a lower false alarm rate. Shen et al. (2020) proposed a particle swarm evolution (PSE)–BP algorithm to predict microchannel resistance factors. Compared with the BP algorithm, the PSE-BP algorithm can dramatically improve ANN training efficiency. The microchannel resistance coefficient predicted by the ANN model and trained by the PSE-BP algorithm is in accordance with the simulation samples.

In the learning method, some basic algorithms are easy to fall into the problem of local optimum, and some complex algorithms take a long time to train. Therefore, this article presents a short-term prediction method of wind power based on the DE–back propagation (BP) neural network. First, the BP neural network is initialized and the gradient descent and BP are used to adjust the weights and thresholds of the network to build a BP neural network model; second, the global search capability of the DE algorithm is introduced to optimize the initial connection weights and neuron thresholds of the BP neural network. The DE algorithm performs accurate local gradient search in the region, converges continuously in the search space to obtain the global optimal solution and establishes a BP neural network short-term prediction model of wind power based on the DE algorithm.

The innovation of this article lies in the following:

1. This model reduces the BP neural network's sensitivity to the initial connection weights and neuron thresholds, improves the speed and accuracy of the network, and shortens the training time by 23.1% when compared with the genetic algorithm (GA)–BP model;
2. The DE algorithm is introduced to optimize the initial connection weights and neuron thresholds of the BP neural network. Compared to the application of the BP model in wind power prediction, the results show that the accuracy of the DE-BP algorithm is improved by about 5%.

The structure of this article is organized as follows: **Section 1** is the introduction; **Section 2** describes the BP neural network, GA,

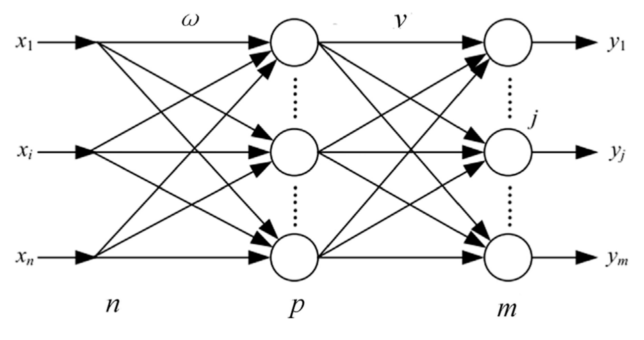

FIGURE 1 | Back propagation neural network structure.

and DE algorithm models; and then **Section 3** proposes an improved DE-BP hybrid intelligent algorithm prediction program. **Section 4** includes the analysis results and the conclusion of this article.

2 BASIC MODEL

2.1 BP Neural Network Model

The back propagation (BP) neural network is a multilayer feedforward neural network. The training process of the BP neural network is the process of continuously adjusting the weights and thresholds of the network to make its prediction results meet the requirements. It can be divided into two elements: the forward propagation and the BP. The forward propagation refers to the transfer of information from the input layer to the output layer of the neural network, and the output result is obtained (Wu et al., 2005).The BP refers to the neural network adjusting and modifying the weights and thresholds layer by layer by means of the backward transmission of errors (Liu, 2019). This article chooses to construct a single hidden layer neural network, and its structure is shown in **Figure 1**.

Here, n and m are the dimensions of the input layer and output layer data sets, corresponding to the number of independent variables and dependent variables in the actual research problem, p is the number of neurons in the hidden layer, and the number of neurons in each layer can also be called the number of nodes. ω_{ij} ($i = 1, 2, \dots, n$) and v_{jk} ($j = 1, 2, \dots, p$; $k = 1, 2, \dots, m$)are the connection weights between the layers, respectively. The steps of the classic BP algorithm are as follows:

Step 1. Forward calculation for unit j on the lth layer

$$v_j^{(l)}(n) = \sum_{i=0}^{P} \omega_{ji}^{(l)}(n) y_j^{(l-1)}(n), \tag{1}$$

where $y_j^{(l-1)}(n)$ is the signal transmitted by unit i of the previous layer *(l-1)*. If the function of unit j is the Sigmoid function, then

$$y_j^{(l)}(n) = \frac{1}{1 + \exp\left[-v_j^{(l)}(n)\right]} \tag{2}$$

and

$$\varphi_j\left[v_j(n)\right] = \frac{\partial y_j^{(l)}(n)}{\partial v_j(n)} = \frac{exp\left[-v_j^{(l)}(n)\right]}{1 + exp\left[-v_j^{(l)}(n)\right]} = y_j^{(l)}(n)\left[1 - y_j^{(l)}(n)\right]. \tag{3}$$

If neuron j belongs to the first hidden layer *($l = 1$)*,then

$$y_j^{(0)}(n) = x_j(n). \tag{4}$$

If the neuron belongs to the output layer *($l = L$)*, then

$$y_j^{(L)}(n) = O_j(n) \tag{5}$$

and

$$e_j(n) = d_j(n) - O_j(n). \tag{6}$$

Step 2. Reverse calculation δ. For output units

$$\delta_j^{(L)}(n) = e_j^{(L)} O_j(n)\left[1 - O_j(n)\right]. \tag{7}$$

For Hidden Units

$$\delta_j^{(L)}(n) = y_j^{(l)}(n)\left[1 - y_j^{(l)}(n)\right] \sum_k \delta_k^{(l+1)}(n) \omega_{kj}^{(l+1)}(n). \tag{8}$$

Step 3. Correct the weights.

$$\omega_{ji}^{(l)}(n+1) = \omega_{ji}^{(l)}(n) + \eta \delta_j^{(l)}(n) y_i^{(l)}(n). \tag{9}$$

In actual situations, the degree of weight change will become more and more intense as the value of η increases, resulting in oscillations. On the contrary, if the value of η is smaller, the corresponding learning process will become more convergent, and the learning speed will also slow down.

Step 4. $n = n + 1$, enter a new sample until the expected requirements are met.

Although the BP neural network is the most widely used algorithm in artificial neural network, there exist the following defects (Huang et al., 2020; Yang et al., 2019).

1. The problem of local minimization. The traditional BP neural network is a local search optimization method. The weights of the network are adjusted gradually along the direction of local improvement. This makes the algorithm trap into a local extremum, and the weights converge to the local minimum.
2. The convergence speed is slow. Since the BP neural network algorithm is essentially a gradient descent method, the objective function to be optimized is very complex, so the "sawtooth phenomenon" will appear, and when the neuron output is approaching 0 or 1, some flat areas appear, in which the weight error changes little, making the training process almost come to a halt. The traditional one-dimensional search method cannot be used in the BP neural network model to find the step length of each iteration, but the updated rule of the step length must be preassigned to the network.
3. The overfitting phenomenon of predictive ability. In general, the predictive ability increases with the improvement of training ability. But this trend is not fixed. When reaching the limit, with the improvement of training ability, the predictive ability will decrease instead, hence appearing the "overfitting" phenomenon. This phenomenon is attributed to

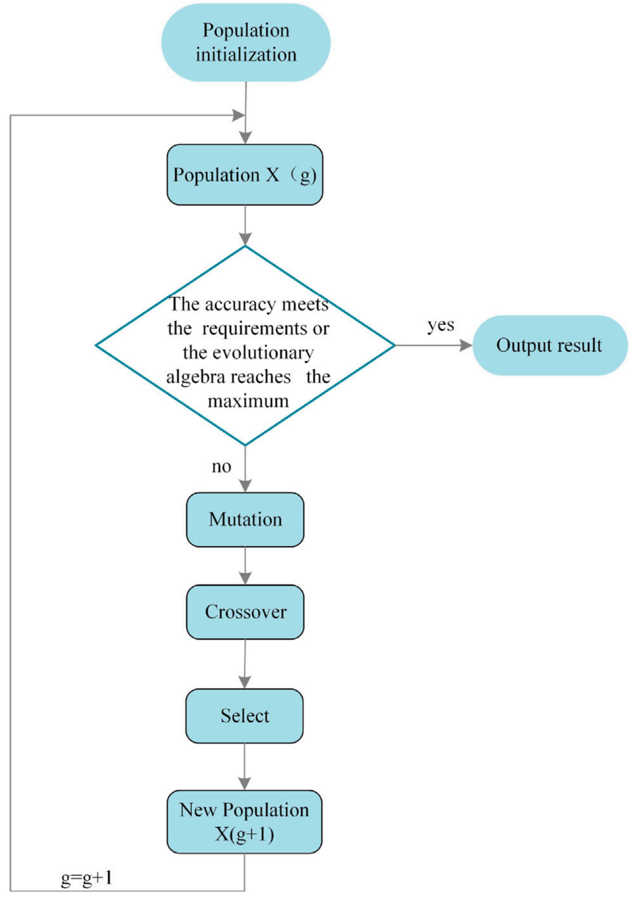

FIGURE 2 | Flowchart of differential evolution algorithm.

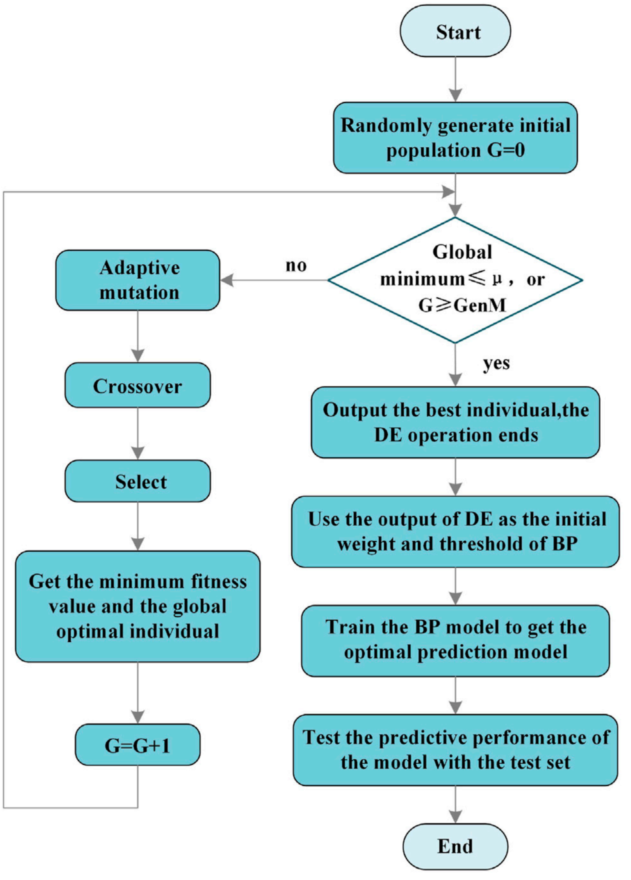

FIGURE 3 | Flowchart of differential evolution–back propagation algorithm.

the fact that the network has grasped too many sample details, and the learned model cannot reflect the laws contained in the samples any more.

4. Sample dependency problem. The approximation and generalization ability of the network model is strongly linked to the typicality of the learning samples, and there exist difficulties to select typical samples from the problems to form the training set.

2.2 Genetic Algorithm Prediction Model

The GA is a parallel random search optimization method put forward by Professor Holland in 1962 to simulate natural genetic mechanisms and biological evolution theory (Bodenhofer, 2003). It introduces the biological evolution principle of "natural selection and survival of the fittest" in nature into the coded tandem population formed by optimized parameters. Individuals are screened according to the selected fitness function and through selection, crossover, and mutation in heredity, such that individuals with good fitness value are retained, while those with poor fitness value are eliminated. The new population inherits the previous generation's information and also performs better than the previous generation. This cycle is repeated until the conditions are met.

GA optimizes the ownership and threshold of the BP neural network using GAs. Each individual in the population contains a network ownership value and threshold. The individual calculates the individual fitness value through the fitness function. The GA finds the corresponding individual of the optimal fitness value through selection, crossover, and mutation. The BP neural network prediction obtains the optimal individual through the GA to assign initial weights and thresholds to the network, and the network is trained to predict the output of the function. The formula of the mean square error fitness function is:

$$f = \frac{1}{N}\sum_{i=1}^{N}(t_i - o_i)^2, \tag{10}$$

where N represents the number of data items in the training data set, and t_i and o_i are the expected target and training output, respectively.

3 WIND POWER PREDICTION MODEL BASED ON DIFFERENTIAL EVOLUTION–BACK PROPAGATION

In order to overcome the BP local minimum problem caused by the initial random weight parameters of the network, this article

TABLE 1 | Wind power changes on 10 October 2016.

Time	Power (MW)	Time	Power (MW)	Time	Power (MW)	Time	Power (MW)
00:00:00	2.22	06:00:00	1.25	12:00:00	0.15	18:00:00	2.2
00:15:00	2.23	06:15:00	1.23	12:15:00	0.15	18:15:00	2.1
00:30:00	2.25	06:30:00	1.21	12:30:00	0.15	18:30:00	1.91
00:45:00	2.28	06:45:00	1.19	12:45:00	0.15	18:45:00	1.73
01:00:00	2.3	07:00:00	1.17	13:00:00	0.15	19:00:00	1.54
01:15:00	2.29	07:15:00	1.1	13:15:00	0.16	19:15:00	1.38
01:30:00	2.25	07:30:00	0.98	13:30:00	0.18	19:30:00	1.24
01:45:00	2.22	07:45:00	0.85	13:45:00	0.19	19:45:00	1.09
02:00:00	2.18	08:00:00	0.73	14:00:00	0.21	20:00:00	0.95
02:15:00	2.15	08:15:00	0.62	14:15:00	0.27	20:15:00	0.87
02:30:00	2.13	08:30:00	0.5	14:30:00	0.38	20:30:00	0.87
02:45:00	2.12	08:45:00	0.39	14:45:00	0.49	20:45:00	0.87
03:00:00	2.1	09:00:00	0.28	15:00:00	0.61	21:00:00	0.86
03:15:00	2.04	09:15:00	0.21	15:15:00	0.81	21:15:00	0.91
03:30:00	1.94	09:30:00	0.19	15:30:00	1.11	21:30:00	1
03:45:00	1.83	09:45:00	0.16	15:45:00	1.41	21:45:00	1.09
04:00:00	1.72	10:00:00	0.13	16:00:00	1.71	22:00:00	1.19
04:15:00	1.66	10:15:00	0.12	16:15:00	1.92	22:15:00	1.25
04:30:00	1.66	10:30:00	0.13	16:30:00	2.03	22:30:00	1.28
04:45:00	1.65	10:45:00	0.14	16:45:00	2.14	22:45:00	1.31
05:00:00	1.64	11:00:00	0.15	17:00:00	2.3	23:00:00	1.34
05:15:00	1.63	11:15:00	0.15	17:15:00	2.27	23:15:00	1.32
05:30:00	1.62	11:30:00	0.15	17:30:00	2.25	23:30:00	1.23
05:45:00	1.61	11:45:00	0.15	17:45:00	2.23	23:45:00	1.15

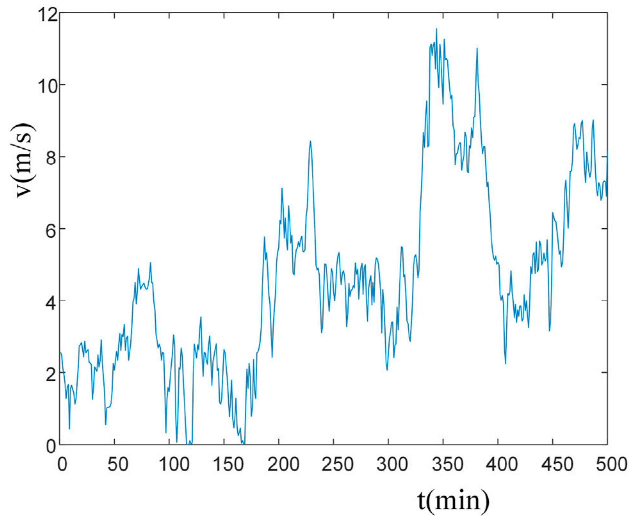

FIGURE 4 | Wind speed distribution.

introduces the DE algorithm, combined with the global search evolution algorithm and the local search gradient algorithm, to overcome the local minimum problem with high generalization and fast convergence speed.

3.1 The Optimization Characteristics of Differential Evolution Algorithm

The DE algorithm is an efficient global optimization algorithm which is a heuristic search algorithm based on population, and each individual in the population corresponds to a solution vector (Das and Suganthan, 2010).

The DE algorithm generates population individuals by using floating-point vectors for encoding (Fan, 2009). In the process of DE algorithm optimization, first, two individuals are selected from the parent individuals to generate a difference vector; second, another individual is selected to sum with the difference vector to generate the experimental individual; the parent individual and the corresponding experimental individual are cross-operated to generate new offspring individuals; finally, the selection is made between the parent individuals and the qualified individuals are saved for the next generation population (Chidambaram et al., 2017; Ramos and Susteras, 2006).

The standard DE algorithm consists of four steps: initialization, mutation, crossover, and selection. As shown in **Figure 2**, this article adopts the DE/rand/1/bin mechanism. The details of each step are as follows:

Step 1. Initialization operation: The DE algorithm in this article adopts the real number coding method. In this step, the parameters are first initialized, including the population size N, gene dimension D, mutation factor F, crossover factor CR, and the value range of each gene *[Umin, Umax]*, and then, the population is initialized randomly, as shown in the formula:

$$x_{ij} = U_{min} + rand \times (U_{max} - U_{min}), \tag{11}$$

where $i = 1, 2, \ldots, N$; $j = 1, 2, \ldots, D$; *rand* is a random number that obeys a uniform distribution.

Step 2. Mutation operation: For each target vector $x_i^G, i = 1, 2, \ldots, N$, the standard DE algorithm generates a corresponding mutation vector by the formula:

TABLE 2 | Differential evolution–back propagation algorithm parameter selection.

Parameter	F = 0.1	F = 0.2	F = 0.3	F = 0.4	F = 0.5	F = 0.6	F = 0.7	F = 0.8	F = 0.9
CR = 0.1	17.232 2	17.387 5	17.231 1	17.262 7	17.258 7	17.263 5	20.370 3	17.215 8	17.231 4
CR = 0.2	17.226 5	17.196 4	17.224 1	17.241 8	17.243 1	17.227 7	17.419 9	17.235 9	17.545 6
CR = 0.3	17.237 3	17.260 8	17.254 7	20.693 1	17.236 4	17.127 5	17.212 9	17.239 1	17.236 2
CR = 0.4	17.244 2	17.218 3	17.214 8	17.285 4	17.229 1	17.261 0	32.244 2	17.309 1	17.320 2
CR = 0.5	17.253 1	17.235 1	17.438 0	17.258 4	17.276 4	17.248 9	20.178 9	17.251 0	17.217 5
CR = 0.6	17.766 5	17.253 0	17.217 3	21.020 1	17.034 4	17.075 9	17.252 0	17.272 5	19.391 4
CR = 0.7	17.447 4	17.188 6	17.243 8	23.924 6	17.219 8	17.271 5	19.214 2	17.336 9	17.182 1
CR = 0.8	17.238 1	18.055 1	17.273 7	17.166 1	17.241 5	17.207 0	17.726 6	17.307 5	17.220 3
CR = 0.9	17.234 6	17.255 7	17.252 0	17.238 6	18.752 7	17.217 1	17.403 5	17.339 7	17.228 3

TABLE 3 | Comparison of wind power prediction error results between back propagation (BP) and differential evolution (DE)–BP algorithms.

Predictive Models	MAE	MSE	RMSE
BP	10.172 4	39.765 1	44.983 4
GA-BP	11.274 4	37.982 0	45.736 3
DE-BP	8.328 9	36.023 4	41.334 1

MAE, mean absolute error; MSE, mean squared error; RMSE, root mean square error; GA, genetic algorithm.

$$V_i^{(G+1)} = x_{r_1}^G + F \times \left(x_{r_2}^G - x_{r_3}^G\right). \tag{12}$$

Step 3.Crossover operation: Crossover operation generates an experimental individual by the formula:

$$u_{ij}^{G+1} = \begin{cases} v_{ij}^{G+1}, & r(j) \leqslant rn(i) \\ x_{ij}^{G} \end{cases}, \tag{13}$$

where *r(j)* is a random number uniformly distributed among [0,1]; *j* represents the *j*th gene; the range of *CR* is [0,1]. In order to ensure the obtaining of at least one-dimensional variable of the experimental individual from the mutated individual, set $rn(i) \in [1, 2, \ldots, D]$ as a randomly selected gene dimension index. The smaller the *CR*, the better the global search effect.

Step 4. Selection operation: DE uses a greedy search strategy. Each target individual x_i^G competes with its corresponding experimental individual u_i^{G+1}, and their fitness values are compared. Only when the fitness value of the experimental individual is better than that of the target individual can it be selected as the offspring. If not, the target individual is directly taken as the offspring. Taking minimization optimization as an example, the selection is demonstrated in **Eq. 14**, where *f(.)* is a fitness function:

$$x_i^{G+1} = \begin{cases} u_i^{G+1}, & f\left(u_i^{G+1}\right) < f\left(x_i^G\right) \\ x_i^G, & otherwise \end{cases}. \tag{14}$$

As a new and efficient heuristic parallel search technology, the DE algorithm possesses such advantages as fast convergence, few control parameters, simple setting, and robust optimization results (Neri and Tirronen, 2010). It has important academic significance for the theory and application of evolutionary algorithms. However, the standard DE algorithm also has the phenomenon of high pressure of control parameter selection and the contradiction between search ability and development ability, which tends to cause such problems as premature convergence of individuals of the population and search stagnation.

3.2 Wind Power Prediction Method Based on Differential Evolution–Back Propagation Neural Network

Considering the shortcomings of the BP algorithm tending to fall into local optima, and the shortcomings of individual premature convergence and search stagnation of DE algorithm population, this article proposes a DE-BP algorithm for wind power prediction. First, the number of nodes of input, output, and hidden layer of the BP neural network are initialized, and traditional gradient descent and BP to adjust the weights and thresholds of the network to construct the BP neural network model are used. Secondly, the DE algorithm is introduced to optimize the initial connection weights and neuron thresholds of the BP neural network, which can avoid its falling into the local optimum. This article establishes a DE-BP neural network model based on the DE algorithm, which reduces the sensitivity of the BP neural network to the initial connection weights and neuron thresholds. The DE-BP model improves the speed and accuracy of network training. Since the BP algorithm is easy to fall into the local optimal value when predicting, the DE algorithm is introduced to optimize this shortcoming. The DE algorithm is used to optimize the initial weights and thresholds of the BP neural network, such that the optimized BP neural network can better predict samples. After the DE algorithm is optimized, the best initial weight and threshold matrix are obtained, and the initial weight and threshold are substituted into the network to obtain the training error value, predicted value, prediction error, and training error. The process of optimizing the BP neural network with the DE algorithm is shown in **Figure 3**.

The initialization step of the DE algorithm first initializes the population size *N*, the individual gene dimension *D*, the maximum number of iterations *G*, the mutation factor *F*, the value range of each gene *[Umin, Umax]*, and the crossover factor *CR*:

$$x_{ij} = U_{min} + rand \times (U_{max} - U_{min}), \tag{15}$$

where $i = 1, 2, \ldots, N$; $j = 1, 2, \ldots, D$; *rand* is a random number that obeys the uniform distribution. It is determined whether the

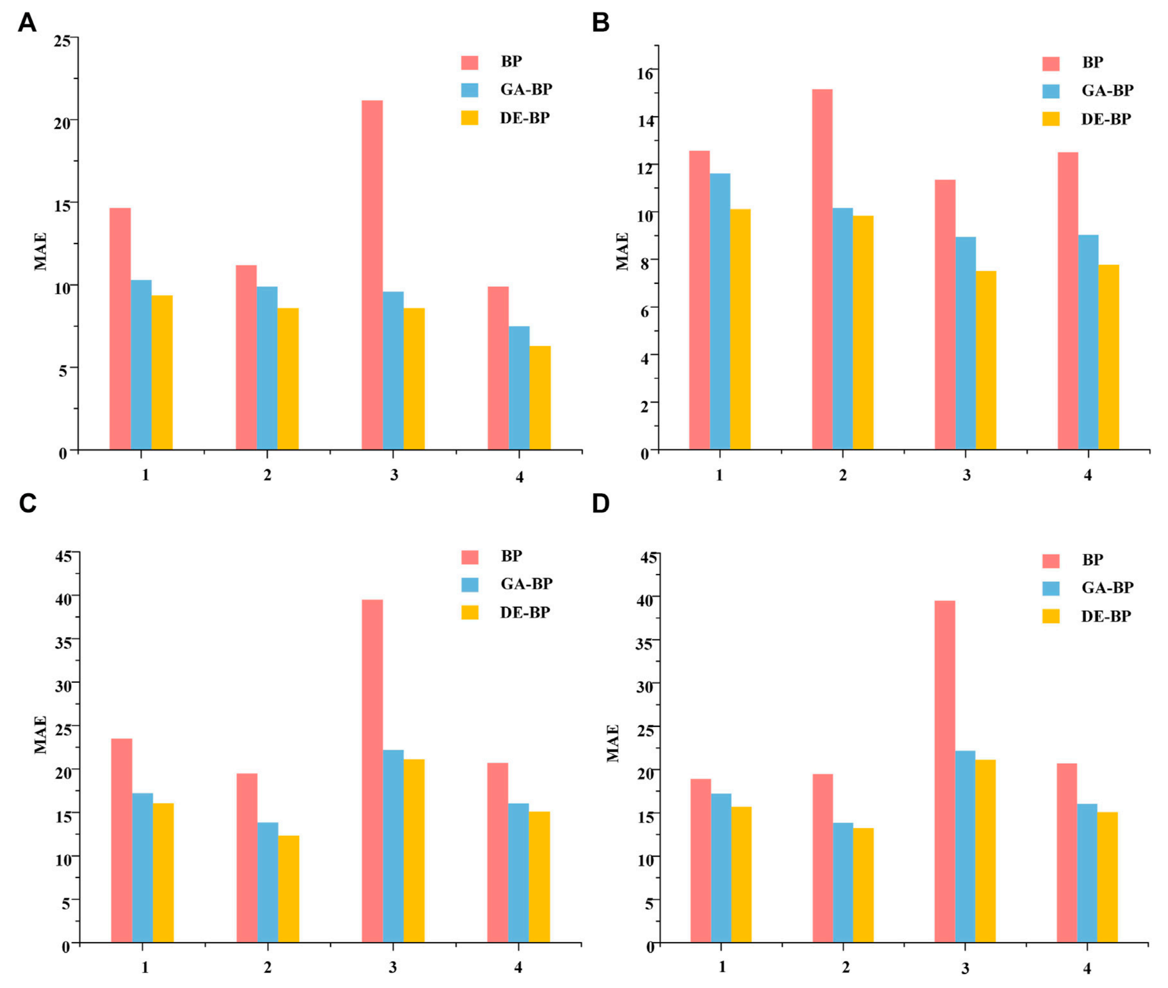

FIGURE 5 | Comparison of prediction errors between differential evolution algorithm and other algorithms in each season: **(A)** spring, **(B)** summer, **(C)** fall, **(D)** winter.

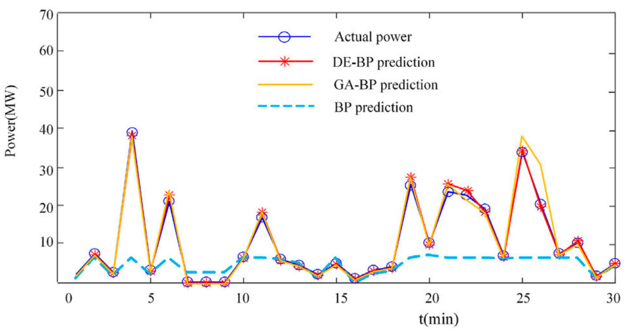

FIGURE 6 | Comparison of the predicted value of differential evolution algorithm with other algorithms.

TABLE 4 | Comparison of wind power prediction error results between back propagation (BP) and differential evolution (DE)–BP algorithms.

Times	BP	GA-BP	DE-BP
1	18.2854	9.2166	8.6913
2	10.8452	8.1528	7.6428
3	12.1274	8.8923	8.3755
4	13.5729	10.7153	8.1888
5	11.7758	12.2039	7.5807
6	18.3066	9.2366	7.5714
7	38.2054	9.9448	8.7113
8	7.4430	16.6829	8.1561
9	23.0241	15.4833	9.4211
10	10.0242	12.2268	7.8967

GA, genetic algorithm.

DE algorithm reaches the termination condition of the iteration. If it does, the DE process is stopped and the best individual is outputted; otherwise, the following operations are continued;

According to the adaptive mutation, crossover, and selection operation methods of the DE algorithm, the next generation of individuals x_i^{G+1} is obtained; for each target vector $x_i^G, i = 1, 2, \ldots, N$, the DE algorithm generates a corresponding mutation:

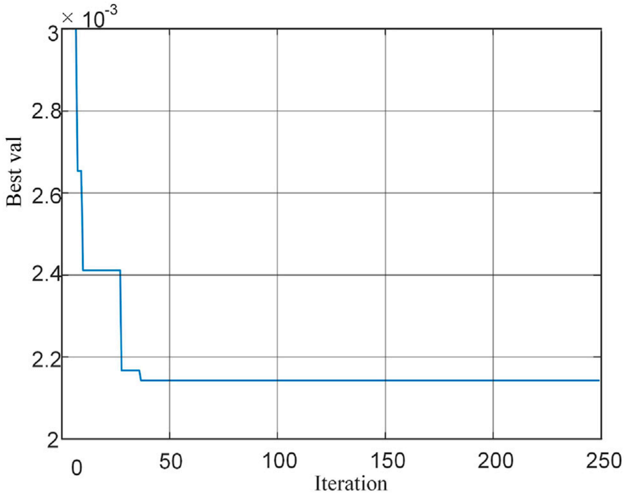

FIGURE 7 | Differential evolution–back propagation algorithm fitness function changes.

TABLE 5 | Training time of wind power prediction model.

Times	GA-BP	DE-BP
1	88.453 1	65.906 3
2	85.390 6	63.781 3
3	87.812 5	64.765 6
4	86.203 1	65.359 4
5	83.437 5	67.843 8
6	84.296 9	69.250 0
7	88.140 6	64.828 1
8	81.015 6	68.640 6
9	86.203 1	68.453 1
10	91.500 0	64.468 8
Average	86.245 3	66.329 7

GA-BP, genetic algorithm–back propagation; DE-BP, differential evolution–back propagation.

$$v_i^{G+1} = x_{r_1}^G + F \times \left(x_{r_2}^G - x_{r_3}^G\right), \tag{16}$$

$$CR(g+1) = CR(g) - \frac{CR(0) - CR_{min}}{GenM}, \tag{17}$$

where $x_{r_1}^G, x_{r_2}^G, x_{r_3}^G$ are the three individuals with different serial numbers. Among them, the individual serial numbers r_1, r_2, and r_3 are randomly selected, and they are different from each other and also different from the target individual's serial number i, so the population size $N \geq 4$, among them:

$$F = F_{min} + (F_{max} - F_{min}) \times e^{1-\frac{GenM}{GenM-G+1}}, \tag{18}$$

where $CR(g)$ represents the mutation probability of generation g; $CR\ (g+1)$, the mutation probability of generation $g+1$; $F_{\min}$ is the smallest mutation factor; $F_{\max}$ is the largest mutation factor; $GenM$ is the maximum number of iterations; G the current number of iterations; $CR\ (0)$ is the initial value of the mutation factor; and $CR_{\min}$ is the minimum value of the mutation factor in the evolution process.

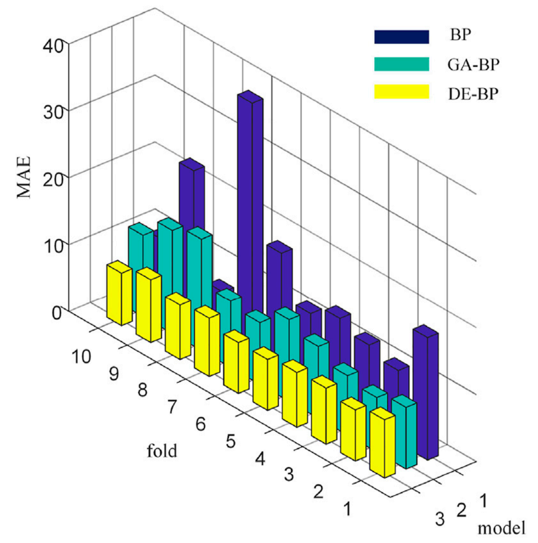

FIGURE 8 | Error of wind power prediction model.

After the next generation of individuals is obtained, the fitness value of their population is evaluated. The minimum fitness value is the current global minimum value, and the corresponding individual is the current global optimal individual; then, let $G = G + 1$, returning to the judgment operation, the judgments are made based on the conditions. The optimal individual output optimized by the DE algorithm is used as the initial weight and threshold of BP, and the network is trained with a training set to obtain the optimal DE-BP prediction model. As shown in **Figure 3**, when the global minimum is $\leq \mu$ or $G \geq GenM$, the optimal individual is outputted and the DE operation ends. The termination condition in judging whether the DE algorithm reaches the termination condition of the iteration is: the minimum fitness value reaches the set error precision requirement μ or the algorithm has reached the maximum iteration number $GenM$.

4 EXPERIMENT RESULTS

This article selects the historical data from a wind farm in Northwest China from October 2016 to April 2018, and samples wind speed, wind direction, temperature, and air pressure at the height of the turbine every 15 min. The 24-h wind power changes on 10 October 2016 are shown in **Table1**.

A total of 5,000 samples and 4,000 sets of model parameter training samples were tested, and 1,000 samples were used as new data to verify the model. All algorithms were programmed by MATLAB, and 4,000 sets of data were randomly trained and 1,000 sets of data were tested. The corresponding wind speed fluctuations with time during wind power output are shown in **Figure 4**.

The error is shown in **Table 2**, when selecting a different mutation factor F and crossover factor CR for prediction. From **Table 2**, when F = 0.5 and CR = 0.6, the prediction error is the smallest, so this parameter is selected as the DE-BP prediction model parameter.

The following three error assessment criteria analyze the feasibility and effectiveness of each model, that is, the mean absolute error (MAE), mean squared error (MSE), and root mean square error (RMSE). The formulas are as follows:

$$MAE = \frac{1}{N}\sum_{t=1}^{N}|y(t) - \hat{y}(t)| \tag{19}$$

$$MSE = \frac{1}{N}\sum_{t=1}^{N}(\hat{y}(t) - y(t))^2, \tag{20}$$

$$RMSE = \sqrt{\frac{1}{N}\sum_{t=1}^{N}(\hat{y}(t) - y(t))^2}. \tag{21}$$

Table 3 lists the errors of using the BP neural network, GA-BP neural network, and DE-BP neural network to predict short-term wind power. The results show that, compared with other models, the DE-BP model has a higher prediction accuracy and stronger ability to track actual wind power. It can realize real-time wind power dispatching, reduce the damage to the wind power grid caused by random changes in wind power, and strengthen the emergency measures of dispatching organization for sudden wind power instability during the process of grid connection.

This article extracts 70 pieces of historical data as training samples and uses the trained network to predict the ultra-short-term wind power within 2 h after the prediction point. The prediction samples of each model are 30 prediction samples on a certain day. Taking into account the influence of the different climates and other factors throughout the year on wind power fluctuation, the wind power of each season is predicted, as shown in **Figures 5A–D**, representing spring, summer, autumn and winter, respectively.

Figure 6 shows the comparison of the prediction curves of short-term wind power prediction using each model. When the power fluctuation range is large, the DE-BP model has better tracking ability than the GA-BP and BP models. Combined with the error indicators in **Table 4**, the prediction error of the DE-BP model is relatively small.

After the training of the BP neural network, the minimum fitness is found by the DE algorithm. The population size of the DE algorithm is 50, the number of iterations is 300, $F = 0.5$, and $CR = 0.6$, and the optimal individual fitness curve in the optimization process is shown in **Figure 7**. The optimal individual fitness value obtained by the DE-BP algorithm is less than 2.2×10^{-3} and close to 0, indicating the effectiveness of the method.

The training time used by the two optimization models is shown in **Table 5**. The average training time of the GA-BP model is 86.245 3 s and that of the DE-BP model is 66.329 7 s. The parameters of the BP neural network can be optimized by the DE algorithm, which effectively improves the training time by 23.1%.

The corresponding errors of the three models in predicting short-term wind power are shown in **Figure 8**. It can be seen that the DE-BP wind power prediction model has the smallest error, which effectively improves the accuracy of the prediction.

5 CONCLUSION

In recent years, as the proportion of wind power generation continues to increase, the research on the accuracy of wind power prediction has become extremely important. This article proposes a hybrid method for wind power prediction, which is based on a feedforward neural network trained through a combination of the DE and BP algorithms.

This article mainly studies the objective function and parameter optimization. The DE algorithm is used to optimize the weight threshold of the BP neural network, and its average MSE is used as the objective function to improve the stability and generalization performance of the model, and the prediction accuracy is more than 95%. The average MAE during model testing was 7.48, highlighting the effectiveness of the proposed method. Compared with the traditional BP and GA-BP algorithms, the accuracy is improved. Finally, the above optimization algorithm is applied to wind power prediction to improve the prediction accuracy and stability, improve the wind power absorption capacity, and provide a reference for power grid dispatching. By preprocessing the historical data of a wind farm in Northwest China, the classic BP prediction, GA-BP prediction, and DE-BP prediction models are established and compared through simulation. It is verified that the DE-BP model is superior to the other models in terms of prediction, fills the gap of DE-BP in the field of wind power prediction, and has good prospect of engineering research value.

DATA AVAILABILITY STATEMENT

The raw data supporting the conclusion of this article will be made available by the authors, without undue reservation.

AUTHOR CONTRIBUTIONS

NL is the corresponding author and takes primary responsibility. YW contributed for analysis of the work and wrote the first draft of the manuscript. All authors contributed to manuscript revision, and read and approved the submitted version.

FUNDING

This work was supported in part by the National Natural Science Foundation of China (52177193); China Scholarship Council (CSC) State Scholarship Fund International Clean Energy Talent Project (Grant No (2018)5046,(2019)157); and Open Research Fund of Jiangsu Collaborative Innovation Center for Smart Distribution Network, Nanjing Institute of Technology (XTCX202107).

REFERENCES

Agarwal, P., Shukla, P., and Sahay, K. B. (2018). "A Review on Different Methods of Wind Power Forecasting," in Proceeding of the 2018 International Electrical Engineering Congress (iEECON), Krabi, Thailand, 7-9 March 2018 (IEEE), 1–4. doi:10.1109/IEECON.2018.8712262

Babazadeh, H., Gao, W., Cheng, L., and Lin, J. (2012). "An Hour Ahead Wind Speed Prediction by Kalman Filter," in Proceeding of the 2012 IEEE Power Electronics and Machines in Wind Applications, Denver, CO, USA, 16-18 July 2012 (IEEE), 1–6.

Bhaskar, K., and Singh, S. N. (2012). Awnn-assisted Wind Power Forecasting Using Feed-Forward Neural Network. *IEEE Trans. Sustain. Energ.* 3, 306–315. doi:10.1109/tste.2011.2182215

Bodenhofer, U. (2003). "Genetic Algorithms: Theory and Applications," in *Lecture Notes, Fuzzy Logic Laboratorium Linz-Hagenberg,* Winter *2004.*

Catalao, J. P. S., Pousinho, H. M. I., and Mendes, V. M. F. (2009). "An Artificial Neural Network Approach for Short-Term Wind Power Forecasting in portugal," in Proceeding of the 2009 15th International Conference on Intelligent System Applications to Power Systems, Curitiba, Brazil, 8-12 Nov. 2009 (IEEE), 1–5. doi:10.1109/ISAP.2009.5352853

Chandra, D. R., Kumari, M. S., and Sydulu, M. (2013). "A Detailed Literature Review on Wind Forecasting," in Proceeding of the 2013 International Conference on Power, Energy and Control (ICPEC), Dindigul, India, 6-8 Feb. 2013 (IEEE), 630–634.doi:10.1109/ICPEC.2013.6527734

Chang, W.-Y. (2014). A Literature Review of Wind Forecasting Methods. *Jpee* 02, 161–168. doi:10.4236/jpee.2014.24023

Chidambaram, B., Ravichandran, M., Seshadri, A., and Muniyandi, V. (2017). Computational Heat Transfer Analysis and Genetic Algorithm–Artificial Neural Network–Genetic Algorithm-Based Multiobjective Optimization of Rectangular Perforated Plate Fins. *IEEE Trans. Components, Packaging Manufacturing Technology* 7, 208–216. doi:10.1109/TCPMT.2016.2646718

Das, S., and Suganthan, P. N. (2010). Differential Evolution: A Survey of the State-Of-The-Art. *IEEE Trans. Evol. Comput.* 15, 4–31. doi:10.1109/TEVC.2010.2059031

Foley, A. M., Leahy, P. G., Marvuglia, A., and McKeogh, E. J. (2012). Current Methods and Advances in Forecasting of Wind Power Generation. *Renew. Energ.* 37, 1–8. doi:10.1016/j.renene.2011.05.033

Haque, A. U., Mandal, P., Meng, J., Srivastava, A. K., Tseng, T.-L., and Senjyu, T. (2013). A Novel Hybrid Approach Based on Wavelet Transform and Fuzzy Artmap Networks for Predicting Wind Farm Power Production. *IEEE Trans. Ind. Applicat.* 49, 2253–2261. doi:10.1109/tia.2013.2262452

Hongmei Fan, H. (2009). Using Radiating Near Field Region to Sample Radiation of Microstrip Traces for Far Field Prediction by Genetic Algorithms. *IEEE Microw. Wireless Compon. Lett.* 19, 272–274. doi:10.1109/lmwc.2009.2017586

Huang, Y., Xiang, Y., Zhao, R., and Cheng, Z. (2020). Air Quality Prediction Using Improved Pso-Bp Neural Network. *Ieee Access* 8, 99346–99353. doi:10.1109/access.2020.2998145

Ju, Y., Sun, G., Chen, Q., Zhang, M., Zhu, H., and Rehman, M. U. (2019). A Model Combining Convolutional Neural Network and Lightgbm Algorithm for Ultra-short-term Wind Power Forecasting. *Ieee Access* 7, 28309–28318. doi:10.1109/access.2019.2901920

Li, N., He, F., Ma, W., Wang, R., and Zhang, X. (2020). Wind Power Prediction of Kernel Extreme Learning Machine Based on Differential Evolution Algorithm and Cross Validation Algorithm. *IEEE Access* 8, 68874–68882. doi:10.1109/access.2020.2985381

Liu, L. (2019). Recognition and Analysis of Motor Imagery Eeg Signal Based on Improved Bp Neural Network. *IEEE Access* 7, 47794–47803. doi:10.1109/access.2019.2910191

Liu, Y., Sun, Y., Infield, D., Zhao, Y., Han, S., and Yan, J. (2016). A Hybrid Forecasting Method for Wind Power Ramp Based on Orthogonal Test and Support Vector Machine (Ot-svm). *IEEE Trans. Sustainable Energ.* 8, 451–457. doi:10.1063/1.4950972

Liu, Z., Tan, Q., Zhou, Y., and Xu, H. (2021). Syncretic Application of Ibas-Bp Algorithm for Monitoring Equipment Online in Power System. *IEEE Access* 9, 21769–21776. doi:10.1109/access.2021.3055247

Neri, F., and Tirronen, V. (2010). Recent Advances in Differential Evolution: a Survey and Experimental Analysis. *Artif. Intell. Rev.* 33, 61–106. doi:10.1007/s10462-009-9137-2

Paula, M., Marilaine, C., Jose Nuno, F., and Wallace, C. (2020). Predicting Long-Term Wind Speed in Wind Farms of Northeast brazil: A Comparative Analysis through Machine Learning Models. *IEEE Latin Am. Trans.* 18, 2011–2018. doi:10.1109/tla.2020.9398643

Ramos, D. S., and Susteras, G. L. (2006). Applying Genetic Algorithms for Predicting Distribution Companies Power Contracting. *IEEE Latin Am. Trans.* 4, 268–278. doi:10.1109/tla.2006.4472123

Shen, T., Chang, J., and Liang, Z. (2020). Swarm Optimization Improved Bp Algorithm for Microchannel Resistance Factor. *IEEE Access* 8, 52749–52758. doi:10.1109/access.2020.2969526

Sideratos, G., and Hatziargyriou, N. D. (2007). An Advanced Statistical Method for Wind Power Forecasting. *IEEE Trans. Power Syst.* 22, 258–265. doi:10.1109/TPWRS.2006.889078

Tan, L., Han, J., and Zhang, H. (2020). Ultra-short-term Wind Power Prediction by Salp Swarm Algorithm-Based Optimizing Extreme Learning Machine. *IEEE Access* 8, 44470–44484. doi:10.1109/access.2020.2978098

Tasnim, S., Rahman, A., Shafiullah, G., Oo, A. M. T., and Stojcevski, A. (2014). "A Time Series Ensemble Method to Predict Wind Power," in Proceeding of the 2014 IEEE symposium on computational intelligence applications in smart grid (CIASG), Orlando, FL, USA, 9-12 Dec. 2014 (IEEE), 1–5. doi:10.1109/CIASG.2014.7011544

Wan, C., Xu, Z., Pinson, P., Dong, Z. Y., and Wong, K. P. (2014). Probabilistic Forecasting of Wind Power Generation Using Extreme Learning Machine. *IEEE Trans. Power Syst.* 29, 1033–1044. doi:10.1109/TPWRS.2013.2287871

Wu, W., Feng, G., Li, Z., and Xu, Y. (2005). Deterministic Convergence of an Online Gradient Method for Bp Neural Networks. *IEEE Trans. Neural Netw.* 16, 533–540. doi:10.1109/tnn.2005.844903

Wu, Y.-K., Su, P.-E., and Hong, J.-S. (2016). "An Overview of Wind Power Probabilistic Forecasts," in Proceeding of the 2016 IEEE PES Asia-Pacific Power and Energy Engineering Conference (APPEEC), Xi'an, China, 25-28 Oct. 2016 (IEEE), 429–433. doi:10.1109/APPEEC.2016.7779540

Xiong, L., Liu, X., Liu, Y., and Zhuo, F. (2020). Modeling and Stability Issues of Voltage-Source Converter Dominated Power Systems: A Review. *CSEE J. Power Energ. Syst.* doi:10.17775/CSEEJPES.2020.03590

Yan, J., Zhang, H., Liu, Y., Han, S., Li, L., and Lu, Z. (2017). Forecasting the High Penetration of Wind Power on Multiple Scales Using Multi-To-Multi Mapping. *IEEE Trans. Power Syst.* 33, 3276–3284. doi:10.1109/TPWRS.2017.2787667

Yang, A., Zhuansun, Y., Liu, C., Li, J., and Zhang, C. (2019). Design of Intrusion Detection System for Internet of Things Based on Improved Bp Neural Network. *IEEE Access* 7, 106043–106052. doi:10.1109/access.2019.2929919

Yuqin, X., Yang, N., and Wenxia, L. (2014). "Predicting Available Transfer Capability for Power System with Large Wind Farms Based on Multivariable Linear Regression Models," in Proceeding of the 2014 IEEE PES Asia-Pacific Power and Energy Engineering Conference (APPEEC), Hong Kong, China, 7-10 Dec. 2014 (IEEE), 1–6. doi:10.1109/APPEEC.2014.7066008

Zhang, H., Liu, Y., Yan, J., Han, S., Li, L., and Long, Q. (2020). Improved Deep Mixture Density Network for Regional Wind Power Probabilistic Forecasting. *IEEE Trans. Power Syst.* 35, 2549–2560. doi:10.1109/tpwrs.2020.2971607

Zhang, Y., Sun, H., and Guo, Y. (2019). Wind Power Prediction Based on Pso-Svr and Grey Combination Model. *IEEE Access* 7, 136254–136267. doi:10.1109/access.2019.2942012

Zhao, R. (2016). "The Study of Wind Power Predict Model Based on Wavelet Transform and Elman Neural Network," in Proceeding of the 2016 Chinese Control and Decision Conference (CCDC), Yinchuan, China, 28-30 May 2016 (IEEE), 6026–6030.doi:10.1109/CCDC.2016.7532077

Conflict of Interest: The authors declare that the research was conducted in the absence of any commercial or financial relationships that could be construed as a potential conflict of interest.

frontiers in Energy Research

METHODS
published: 23 February 2022
doi: 10.3389/fenrg.2022.819420

Optimal Design of Integrated Energy Supply System for Continuous Greenhouse Effect: A Study on Carbon Emission and Operational Cost

Chongyi Tian[1], Zhuliang Shao[1], Ruiqi Wang[2], Yi Yan[1]*, Xuerui Wang[1] and Ang Ren[3]

[1]Shandong Key Laboratory of Intelligent Buildings Technology, School of Information and Electrical Engineering, Shandong Jianzhu University, Jinan, China, [2]State Grid Shandong Integrated Energy Services CO., LTD, Jinan, China, [3]Jinan Power Supply Company, State Grid Shandong Electric Power Company, Jinan, China

The cultivation of crops in greenhouses is well established in China. However, the greenhouse climate is complex, rendering it difficult to analyze the greenhouse load and control the energy supply system. It is important to ensure the optimal design of greenhouse operation to enable optimal crop growth and maintain low operation costs for improving the greenhouse crop production efficiency and economic benefits. To reduce the energy consumption , we propose a new integrated energy supply system. This system uses a combined cooling, heating and power system, and an air source heat pump. A two-stage integrated optimization model of the integrated energy supply system was built, with “minimum average daily economic cost” and “maximum CO_2 emission reduction rate (ERR)” as the objectives in the first stage. The characteristics of the countryside were taken into consideration for optimizing the capacity of the combined cooling, heating and power supply, energy storage and air source heat pump. In the second stage, the objectives were “maximum annual operating saving rate (OSR)”, “maximum CO_2 emission reduction rate”, and “maximum primary energy saving rate (PESR)”. The capacity of the equipment designed in the first stage is used as the constraint to optimize the operating output of the combined cooling, heating and power supply, air source heat pump. Finally, a greenhouse is used as a prototype to carry out simulation calculations for two typical days in summer and winter to verify the effectiveness of this method. The simulation results showed that after the first stage of optimization, the average daily operating cost was significantly lower and the CO_2 emission rate was reduced by 49.53%. After the second stage, annual operating saving rate, CO_2 emission reduction rate, and primary energy saving rate were 39.51, 48.88, and 27.57% for a typical summer day and 52.96, 50.18, and 50.13% for a typical winter day, respectively. Therefore, compared to the existing energy supply systems, the integrated energy supply system and the integrated optimization design of the system could effectively avoid energy wastage, significantly improve the degree of match between the system design and operation, reduce operating cost, and reduce CO_2 emission.

Keywords: greenhouse, combined cooling heating and power (CCHP), energyplus, two-stage optimization design, C-NSGA-II, integrated energy supply system (IESS)

Edited by:
Amjad Anvari-Moghaddam,
Aalborg University, Denmark

Reviewed by:
Fubin Yang,
Beijing University of Technology, China
Rosaria Volpe,
University of Catania, Italy

***Correspondence:**
Yi Yan
yanyi19@sdjzu.edu.cn

Specialty section:
This article was submitted to Process and Energy Systems Engineering,
a section of the journal Frontiers in Energy Research

Received: *02 December 2021*
Accepted: *24 January 2022*
Published: *23 February 2022*

Citation:
Tian C, Shao Z, Wang R, Yan Y, Wang X and Ren A (2022) Optimal Design of Integrated Energy Supply System for Continuous Greenhouse Effect: A Study on Carbon Emission and Operational Cost.
Front. Energy Res. 10:819420.
doi: 10.3389/fenrg.2022.819420

1 INTRODUCTION

Energy shortages and environmental pollution are serious global concerns. Energy saving, emission reduction, development of renewable energy, and distribution of energy supply systems are the need of modern economies. In a modern agronomic facility with high efficiency and high energy consumption, efficient regulation of greenhouses is an inevitable requirement for high crop yield and quality. However, greenhouse regulation is energy-dependent, for which energy consumption is generally high (Vadiee and Martin, 2013). In addition to the characteristics of greenhouses, such as strong coupling, nonlinearity, and strong perturbation (Lin et al., 2019), excessive energy consumption in greenhouses is a major factor that hinders their development (Ahmad et al., 2021). Unlike that in ordinary buildings, each parameter in the greenhouse environment has a significant influence on the entire greenhouse. The greenhouse climate is a nonlinear dynamic system whose temperature depends on several factors such as solar radiation, outdoor temperature, wind speed, and the type of plants cultivated (Jung et al., 2020). In addition, the greenhouse structure and the operation of internal energy supply equipment influences the greenhouse climate significantly (Lin et al., 2020). Therefore, it is extremely difficult to perform load analysis for greenhouses. To reduce the energy consumption in greenhouse operations, optimal design of greenhouse energy consumption and equipment operation is necessary. This could effectively improve the energy efficiency of agricultural greenhouses, while reducing the cost of greenhouse operation and shortening the energy recovery cycle.

To address the difficulties in greenhouse load analysis, we propose a load analysis method for greenhouse energy supply, using an integrated energy supply system (IESS). The IESS consists of a combined cooling, heating, and power (CCHP) system and an ASHP. Combining a CCHP system with an ASHP enables building a highly efficient energy system that provides greater flexibility in meeting the load requirement (Wegener et al., 2021). The IESS contains different types of energy conversion units, which can provide three forms of energy simultaneously: cooling, heating, and electricity. In addition, it regulates its own operation with a high degree of flexibility to mitigate external disturbances in the face of multiple external factors.

The CCHP system can improve energy efficiency significantly. The system structure is flexible and diverse; therefore, it can simultaneously reduce the emission of pollutants effectively. The CCHP system has wide applications; it improves the overall performance of the system and simultaneously increases the complexity of the relationship between the system structure and energy. Therefore, optimized design of the system and the accurate matching of energy supply and demand are important prerequisites for the efficient operation of CCHP system. This has to account for the changes in the cooling, heating, and electric loads and the actual demand of users. To match the energy demand and improve the performance of CCHP systems, Wegener et al. (2018) and Gao et al. (2019) proposed a system design and optimization method for a CCHP system. For the optimal design of a CCHP system, Ren et al. (2021) proposed a hybrid CCHP system, which consisted of a gas turbine, absorption chiller, photovoltaic (PV) panel, and Battery. Song et al. (2020a) investigated the optimal configuration for a hybrid CCHP system and studied the corresponding optimal economic and energy performance, using a multi-objective optimization model. Wang et al. (2020) determined the capacity configuration of a CCHP system that provided the best integrated performance and quantitatively evaluated the sustainability index of the system. Yan et al. (2021) proposed a multi-objective optimization method for optimizing the capacity configuration of a CCHP system. Tian et al. (2018) proposed a decoupling method to decompose the energy, and a matrix optimization model to optimize the capacity of the CCHP system. Liu et al. (2013) optimized the capacity configuration of power generator unit (PGU) to achieve the optimal performance of the CCHP system. Ghersi et al. (2021) proposed a new operation strategy for the CCHP system and optimized its capacity configuration using a multi-objective optimization algorithm. Wang et al. (2014) added biomass gas to the CCHP system and used a genetic algorithm to optimize the capacity of the system. Kang et al. (2021) constructed a multi-objective optimization model and optimized capacity configurations for four types of building CCHP systems.

However, in the process of capacity configuration, the accessibility to renewable energy deepens the complexity of the CCHP system multi-energy flow and introduces several random factors into the operation strategy. This overturns the traditional operation mode of the CCHP system and creates difficulty in source-load matching. This further deepens the coupling between the capacity configuration and operation strategy of the system. For the operational design of the CCHP system, Li et al. (2018) adopted the traditional operation modes of the following electrical load (FEL) and following thermal load (FTL). The system was considered economical for developing an optimal and cooperative strategy for an integrated energy system comprising multiple energy stations and energy storage devices. Kang et al. (2017) and Das et al. (2018) investigated the system performance under FEL and FTL; these two operation strategies could not fully utilize the system advantages for meeting the various demands. Therefore, there is a need for an optimal operation model that is based on specific parameters such as time-of-day tariffs and energy prices, which are combined with load forecasting to achieve work mode switching. Ren et al. (2021) and Ghersi et al. (2021) used multi-objective optimization algorithms to optimize the design of the CCHP system operation strategy. They developed the Pareto Frontier solution applied in the multi-objective optimization model, considering the economic, energy, and environmental performances of the model. Li et al. (2020) proposed a CCHP system operation strategy that followed the thermoelectric load balance. Considering the interaction between the capacity configuration and operation strategy, Ma et al. (2017) took seasonality into account in the equipment operation strategy. They analyzed the capacity configuration and operation strategy of the equipment in the system using a multi-objective optimization method. Song et al. (2020b) modeled the CCHP system and the sub-supply system separately, and optimized them for an optimal capacity configuration and operation strategy. This results in further deepening of the coupling between the capacity configuration and operation strategy of the core equipment of the CCHP system. Therefore, the traditional CCHP system optimization design method can no longer cope with the requirements of renewable energy characteristics and variable operating conditions. Further studies on the two-stage optimization design of the equipment capacity and operation strategy of the renewable energy IESS, are required.

To address these issues, we proposed a two-stage optimal design method for the IESS capacity configuration and operation strategy based on C-NSGA-II. In the first stage, we optimized the capacity configuration of the core equipment of the designed IESS. In the second stage, we used the optimized design results as constraints, to further optimize the operation strategy of the designed core equipment. Therefore, a two-stage interaction mechanism is established between the system capacity configuration and operation strategy, while improving the efficiency and comprehensive performance of the IESS.

This method establishes an interactive feedback between the two stages and builds a two-stage optimization design architecture that can optimize the systems' capacity and operation. EnergyPlus can calculate the building's cooling and heating loads, by analyzing the physical composition of the building and the mechanical system. This can be used to maintain the indoor room temperature through the heating, ventilation, and air conditioning (HVAC) system. We first simulated the energy consumption of the greenhouse's cooling, heating, and electric loads using EnergyPlus. We used the simulated load data as the input for the CCHP system. Based on this, we constructed a two-stage optimization model of the IESS; in the first stage, the optimization objectives of "minimum average daily economic cost" and "maximum CO_2 emission reduction rate" were established based on the results of the second stage optimization design. The C-NSGA-II algorithm was used to optimize the capacity configuration of the core equipment in the IESS. In the second stage, the optimization objectives of "maximum annual operation saving rate," "maximum CO_2 emission reduction rate," and "maximum primary energy saving rate" were established. The C-NSGA-II algorithm was used to further optimize the operation strategy of the core equipment, using the capacity of the equipment optimized in the first stage as the constraint. Finally, a prototype greenhouse was used as a case study to evaluate the advantages of the method. The simulation results indicated that our two-stage method for the optimization of IESS effectively avoided the wastage of resources, reduced the cost, and lowered the CO_2 emissions.

This study uses an innovative approach to improve the functioning of greenhouses. High energy consumption and difficulty in load analysis in the greenhouses is attributed to the challenges in controlling the energy supply system. Therefore, we constructed an integrated energy supply system consisting of CCHP, and ASHP to overcome these challenges.

The introduction of indirect renewable energy in the CCHP system has deepened the coupling between the capacity configuration and operation strategy of the integrated energy supply system. Therefore, we proposed a two-stage optimization for the integrated energy supply system. In the first stage, the optimal capacity of the integrated energy supply system was designed considering the optimization results of the second stage. In the second stage, the optimal capacity of the equipment in the first stage was used as the constraint, for optimizing the design of the optimal operation strategy of the integrated energy supply system. The synergistic optimization in the two stages results in a higher degree of coherence between the system design and operation, greater economy, and energy efficiency.

The remainder of this paper is structured as follows. **Section 2** presents the structure of the constructed integrated energy supply system and the models of each device in the system. **Section 3** presents the specific principles and methods for the two-stage optimization design of the integrated energy supply system, including the optimization objectives, optimization variables, constraints, and optimization algorithms for each stage. In **Section 4**, a simulation case study is conducted with a greenhouse as a prototype to verify the effectiveness of the proposed integrated energy supply system and its optimization design method. Finally, in **Section 5**, the research methods and results of this paper are summarized.

2 SYSTEM STRUCTURE AND ENERGY SUPPLY EQUIPMENT MODEL

The CCHP system is an energy system with low environmental impact and high efficiency. Compared to the conventional energy systems, CCHP systems can achieve sustainable energy savings, typically 10–30%. Therefore, using these systems can significantly reduce CO_2 emissions (Song et al., 2020), which is an ideal way for energy conservation and emission reduction. They also ensure the efficient use of new energy sources, and is therefore, highly promising. This study has considered the aspects of rural resource endowment and has built an integrated energy supply system based on CCHP, distributed new energy generation, and ASHP devices.

2.1 Analysis of Integrated Energy Supply System for Agriculture

The CCHP system makes full use of the "energy-ladder" principle by recovering waste heat for power generation, cooling, and heating, simultaneously. A high-quality CCHP system can achieve a global efficiency of 42% ensuring an efficient integrated supply of heating and cooling electric energy (Lombardo et al., 2021). The structure diagram of the IESS system built based on CCHP is shown in **Figure 1**.

The system consists of three parts: power supply, cooling, and heating, which are explained below:

The power supply consists of an internal combustion engine (ICE), wind turbine (WT), and PV. The electric energy produced by the system supplies electricity to the users and the system itself, and the system was "grid-connected"; therefore, it could purchase electricity from the grid when the produced electricity was

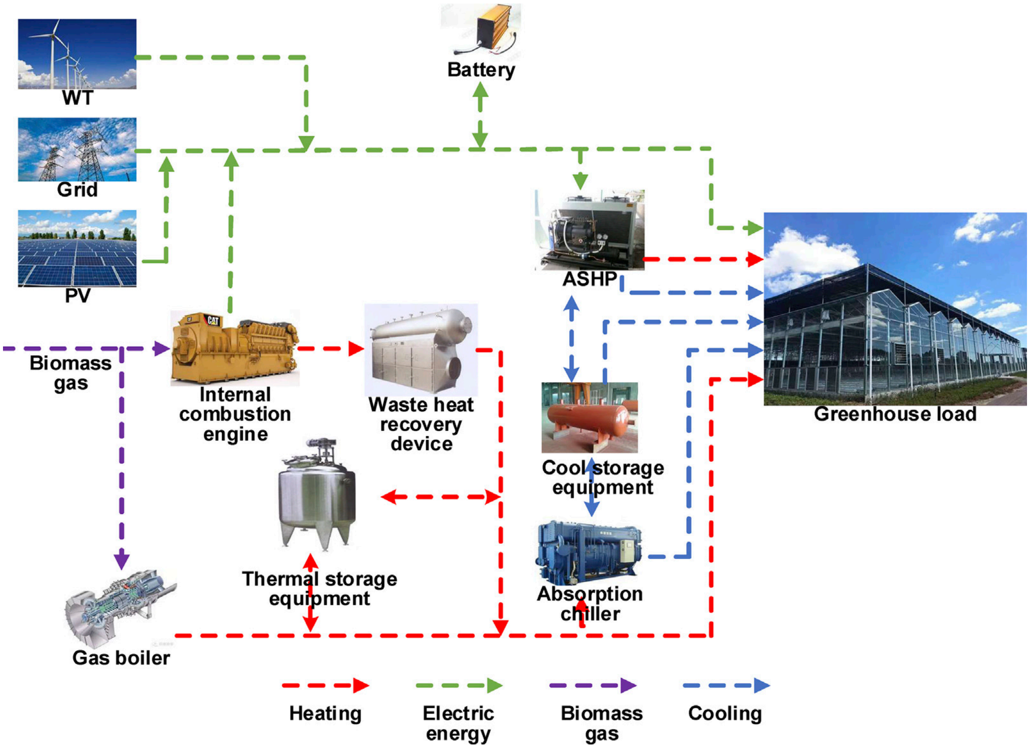

FIGURE 1 | Structure of a combined cooling, heating, and power (CCHP) system.

insufficient; the energy was fed back into the grid when there was an excess of electricity generated (Li et al., 2021).

The heating system includes the waste heat generated by the ICE-consuming biomass gas, gas boiler, and ASHP. The ICE generated cylinder liner water waste heat and flue gas waste heat during operation These were recovered using a cylinder liner water heat exchanger and flue gas heat exchanger, respectively. The recovered waste heat was partly used to operate the absorption chiller for cooling and partly to supply heating to the customers. The ASHP was used for heating during winter. When the waste heat generated by the ICE and the heating provided by the ASHP were insufficient to meet the demand of the customers, the gas boiler was used for auxiliary heating. In cases when excessive heat was available, the thermal storage equipment stored the excess heat from the gas boiler and the waste heat recovery equipment.

The cooling system consists of two parts: an absorption chiller and an ASHP. The cooling load of users is mainly provided by the absorption chillers. When the cooling load is insufficient, the auxiliary cooling of ASHP fulfills the cooling load.

2.1.1 Core Equipment Model of Agricultural Energy Supply System

2.1.2 Wind Turbine (WT)

The relationship between wind power characteristics, mainly output power and wind speed, can be expressed as follows (Zhang et al., 2020):

$$P_{\mathrm{WT}}(t)=\begin{cases}0, & v(t)\le v_{\mathrm{in}}\ \mathit{or}\ v(t)\ge v_{\mathrm{out}}\\ \dfrac{v(t)^3-v_{\mathrm{in}}^3}{v_{\mathrm{r}}^3-v_{\mathrm{in}}^3}P_r, & v_{\mathrm{in}}\le v(t)\le v_{\mathrm{r}}\\ P_{\mathrm{r}}, & v_{\mathrm{r}}\le v(t)\le v_{\mathrm{out}}\end{cases} \tag{1}$$

where $P_{\mathrm{WT}}(t)$ is the output power of WT at time t, P_{r} is the rated power of WT, $v(t)$ is the actual outdoor wind speed at time t, v_{r} is the rated wind speed of WT, v_{in} is the cut-in wind speed of WT, and v_{out} is the cut-out wind speed of WT.

2.1.2.1 Photovoltaic (PV) Output Power

The variation in the PV output power, with respect to the solar radiation and temperature, can be expressed as follows:

$$P_{\mathrm{PV}}(t)=\frac{P_{\mathrm{STC}}I(t)\left[1+k\left(T_{\mathrm{PV}}(t)-T_{\mathrm{r}}\right)\right]}{I_{\mathrm{STC}}} \tag{2}$$

where $P_{\mathrm{PV}}(t)$ is the output power of PV at time t, $I(t)$ is the solar radiation at time t, P_{STC} is the maximum test power under standard test conditions (I_{STC} is $1000\mathrm{W/m}^2$, T_{r} is $25^{\circ}\mathrm{C}$), k is the power temperature coefficient, and $T_{\mathrm{PV}}(t)$ is the temperature of PV at time t, which was estimated using the test ambient temperature. $T_{\mathrm{PV}}(t)$ was calculated using the following equation:

$$T_{\mathrm{PV}}(t)=T_0(t)+0.03I(t) \tag{3}$$

where, $T_0(t)$ is the outdoor temperature at time t.

2.1.2.2 Internal Combustion Engine (ICE)

The operating conditions of the internal combustion generator set are complex and changeable.

The mathematical model of the ICE can be expressed as follows (Yan et al., 2018):

$$\begin{cases} G_{\mathrm{ICE}}(t) = \dfrac{E_{\mathrm{ICE}}(t)}{\eta_{\mathrm{pe}}(t)\eta_{\mathrm{te}}(t)} \\ G_{\mathrm{ICE}}(t)\left(1-\eta_{\mathrm{te}}(t)\right) = Q_{\mathrm{jw}}(t) + Q_{\mathrm{exh}}(t) + Q_{\mathrm{loss}}(t) \\ Q_{\mathrm{re}}(t) = Q_{\mathrm{jw}}(t)\eta_{jw}(t) + Q_{\mathrm{exh}}(t)\eta_{\mathrm{exh}}(t) \end{cases} \tag{4}$$

where, $G_{\mathrm{ICE}}(t)$ is the amount of biomass gas consumed by the ICE at time t, $E_{\mathrm{ICE}}(t)$ is the amount of electricity generated by ICE at time t; $\eta_{\mathrm{pe}}(t)$ is the efficiency of electricity generation at time (t) affected by PLR; $\eta_{\mathrm{te}}(t)$ is the efficiency of heat generation at time (t) affected by PLR; $Q_{\mathrm{re}}(t)$ is the recoverable heating of ICE at time t, $Q_{\mathrm{jw}}(t)$ is the waste heating of the cylinder sleeve water at time t; $\eta_{\mathrm{jw}}(t)$ is the efficiency of the cylinder sleeve water heating exchanger at time t, $Q_{\mathrm{exh}}(t)$ is the waste heating of the flue gas heating exchanger at time t, and $\eta_{\mathrm{exh}}(t)$ is the efficiency of the flue gas heating exchanger at time t, Q_{loss}(t) is the lost heating at time t.

2.1.2.3 Biomass Gas Boiler

The mathematical model of the gas boiler can be expressed as follows (Jia et al., 2021):

$$Q_{\mathrm{b}}(t) = F_{\mathrm{b}}(t)L_{\mathrm{NG}}\eta_{\mathrm{b}} \tag{5}$$

where $Q_{\mathrm{b}}(t)$ is the heat capacity of the gas boiler at time t, $F_{\mathrm{b}}(t)$ is the biomass gas volume of the gas boiler at time t, L_{NG} is the biogas gas calorific value, and η_{b} is the heating efficiency of the gas boiler.

2.1.2.4 Absorption Chiller

The mathematical model of absorption chiller can be expressed as follows (Zhao et al., 2021):

$$Q_{\mathrm{ac}}(t) = Q_{\mathrm{ac\_in}}(t)COP_{\mathrm{ac}} \tag{6}$$

where $Q_{\mathrm{ac}}(t)$ is the cooling capacity of the absorption chiller at time t, $Q_{\mathrm{ac\_in}}(t)$ is the input heating of the absorption chiller at time t, and COP_{ac} is the energy efficiency rate of the absorption chiller.

2.1.2.5 ASHP

$$Q_{\mathrm{hp,h}}(t) = E_{\mathrm{hp,h}}(t)COP_{\mathrm{hp,h}} \tag{7}$$

$$Q_{\mathrm{hp,c}}(t) = E_{\mathrm{hp,c}}(t)COP_{\mathrm{hp,c}} \tag{8}$$

where $Q_{\mathrm{hp,h}}(t)$ is the heat capacity of the ASHP at time t, $Q_{\mathrm{hp,c}}(t)$ is the cooling capacity of the ASHP at time t, $E_{\mathrm{hp,h}}(t)$ is the power consumption of the ASHP (when heating) at time t, $E_{\mathrm{hp,c}}(t)$ is the power consumption of the ASHP (when cooling) at time t, $COP_{\mathrm{hp,h}}$ is the heating energy efficiency rate, and $COP_{\mathrm{hp,h}}$ is the cooling energy efficiency rate.

2.1.2.6 Battery

Notably, in the process of charging and discharging, the state of energy storage at each moment is related to the state of energy storage at the previous moment, amount of charging and discharging at the moment, and amount of power decay of the energy storage capacity of the system, which can be expressed as follows:

$$E_{\mathrm{BT}}(t) = E_{\mathrm{BT}}(t-1) + \left[\mu_{\mathrm{c}}\eta_{\mathrm{charge}}P_{\mathrm{BT,charge}}(t) - \frac{\mu_{\mathrm{d}}}{\eta_{\mathrm{discharge}}}P_{\mathrm{BT,discharge}}(t)\right]\Delta t \tag{9}$$

where $E_{\mathrm{BT}}(t)$ is the remaining capacity of the battery at time t, E_{BT} (t-1) is the remaining capacity of the Battery at time t-1, and $P_{\mathrm{BT,charge}}(t)$ and $P_{\mathrm{BT,discharge}}(t)$ are the average power of the battery charging and discharging, respectively, at time t. H_{charge} and $\eta_{\mathrm{discharge}}$ are the charging and discharging efficiencies of the battery, respectively; μ_{c} is 1 in the storage charging state and 0 in the non-charging state, and μ_{d} is 1 in the storage discharging state and 0 in the non-discharging state.

2.1.3 Energy Flow Analysis of Agricultural Greenhouse Energy Supply System

The electric balance of the agricultural greenhouse energy supply system at moment t can be expressed as follows:

$$\begin{aligned} &E_{\mathrm{ICE}}(t) + E_{\mathrm{PV}}(t) + E_{\mathrm{WT}}(t) + E_{\mathrm{grid}}(t) + E_{\mathrm{BT,discharge}}(t) \\ &\quad = E_{\mathrm{L}}(t) + E_{\mathrm{BT,charge}}(t) + E_{\mathrm{hp}}(t) \end{aligned} \tag{10}$$

where $E_{\mathrm{PV}}(t)$ is the power generation of the PV panel at time t, $E_{\mathrm{WT}}(t)$ is the power generation of the WT at time t, $E_{\mathrm{grid}}(t)$ is the system-grid interaction at time t, $E_{\mathrm{L}}(t)$ is the electric load required by the user at time t, and $E_{\mathrm{BT,charge}}(t)$ and $E_{\mathrm{BT,discharge}}(t)$ are the production and energy storage of the battery at time t, respectively.

The heating balance of the agricultural greenhouse energy supply system at moment t can be expressed as follows:

$$Q_{\mathrm{re}}(t) + Q_{\mathrm{b}}(t) + Q_{\mathrm{hp,h}}(t) = Q_{\mathrm{h,L}}(t) + \frac{Q_{\mathrm{ac}}(t)}{COP_{\mathrm{ac}}} \tag{11}$$

where $Q_{\mathrm{h,L}}(t)$ is the heating load required by the user at time t, and the other components are the same as that expressed in the earlier equation.

The cooling balance of the agricultural greenhouse energy supply system at time t can be expressed as follows:

$$Q_{\mathrm{ac}}(t) + Q_{\mathrm{hp,c}}(t) = Q_{\mathrm{c,L}}(t) \tag{12}$$

where $Q_{\mathrm{c,L}}(t)$ is the cooling load required by the user at time t.

3 TWO-STAGE OPTIMIZATION OF AGRICULTURAL GREENHOUSE ENERGY SUPPLY SYSTEM

The introduction of renewable energy renders the structure of the IESS more complex; the coupling relationship between the capacity configuration and operation strategy of the core equipment is further deepened. In this study, we analyzed the

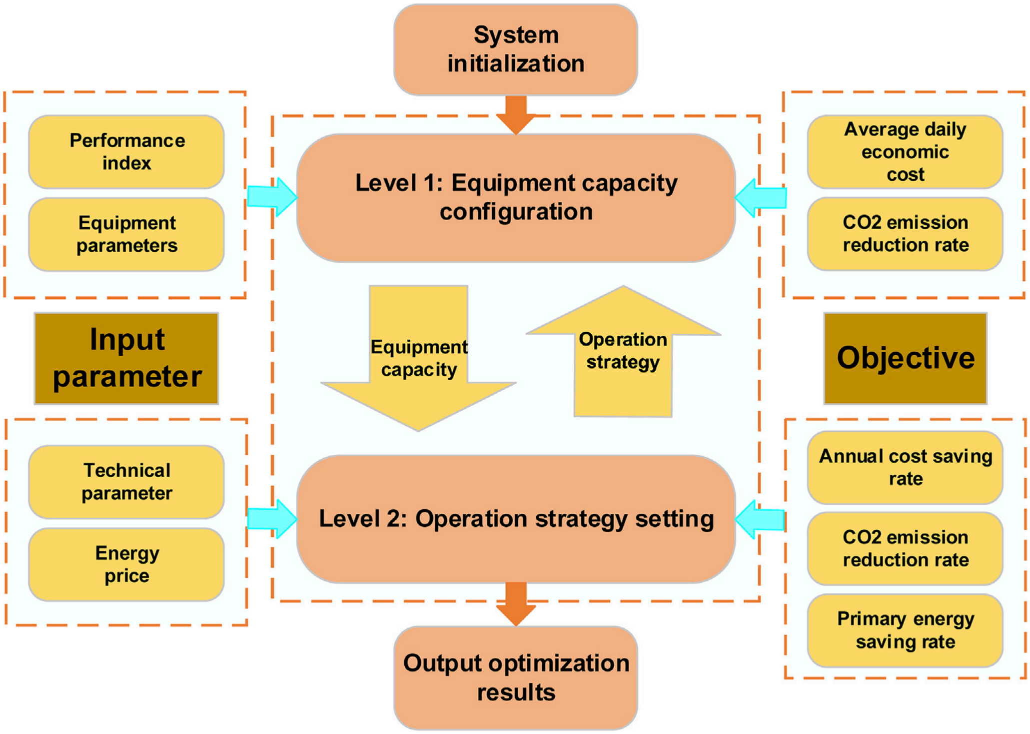

FIGURE 2 | Logic relationship for the two-stage optimization design proposed in this study.

relationship logic between capacity configuration and operation strategy. We adopted a two-stage method for optimizing the capacity configuration and operation strategy of the system. In the second stage, the capacity configuration obtained from the first-stage was used as the constraint for the operation and strategy optimization design; the interaction between the two-stage design was realized, economic and environmental indicators were selected as the optimization targets, and a two-stage optimization model was established. The logical relationship between the two stages is shown in **Figure 2**.

3.1 System Capacity Configuration Optimization Model

3.1.1 Optimization Objectives

3.1.1.1 Economic Indicators

Economy is a prerequisite for the large-scale application of renewable energy IESS; reducing the costs and improving the economy are critical for promoting the new system. Therefore, in the first-stage of the optimization model, we considered the minimum average daily economic cost of the system as one of the optimization objectives, which can be expressed as follows:

$$\min C_{\mathrm{r}} = C_{\mathrm{cap}} + \frac{1}{N_{\mathrm{d}}} \sum_{i}^{N_{\mathrm{d}}} C_{i,\mathrm{var}} \tag{13}$$

where C_{r} is the average daily economic cost of the system; $C_{\mathrm{i,var}}$ is the daily operating cost of each equipment of the system, such as the cost of biomass gas consumption, cost of purchased electricity, and operation and maintenance cost of each equipment. Their calculation is expressed in the second stage; N_{d} is the number of typical days, and C_{cap} is the daily acquisition cost of each piece of equipment of the system converted by the conversion factor, which can be expressed as follows:

$$C_{\mathrm{cap}} = \frac{1}{365} \sum_{i=1}^{N} N_{i,\mathrm{r}} C_{i,\mathrm{v}} \frac{r(1+r)^{T_i}}{(1+r)^{T_i} - 1} \tag{14}$$

where $N_{\mathrm{i,r}}$ is the capacity of the ith equipment, $C_{\mathrm{i,v}}$ is the unit acquisition cost of the ith equipment, r is the conversion factor (8%), and T_i is the lifespan of the ith equipment.

3.1.1.2 Environmental Indicators

CO_2 is the main cause of the greenhouse effect; therefore, the maximum CO_2 emissions reduction rate was considered as another optimization objective. The CO_2 emissions during the operation cycle of the IESS were calculated, using the equation given below:

$$CO_2E_{\mathrm{IESS}} = \mu_{\mathrm{g}} G_{\mathrm{gas}} + \mu_{\mathrm{e}} E_{\mathrm{grid}} \tag{15}$$

where CO_2E_{IESS} is the total CO_2 emission of the IESS, μ_g and μ_e are the CO_2 emission factors of biomass gas and grid generation, respectively, and G_{gas} is the amount of biomass gas consumed by the IESS, which is numerically equal to the sum of biomass gas consumed by the ICE and gas boiler.

The energy supply of the existing greenhouse setup is mainly purchased from the grid; therefore, its CO_2 emissions can be expressed as follows:

$$CO_2E = E_L\mu_e \tag{16}$$

where, $C\ O\ _2E$ is the CO_2 emissions of existing energy supply system.

The emission reduction potential of the IESS relative to that of the existing energy supply system can be further evaluated by defining the ERR of the IESS, which can be expressed as follows (Wen et al., 2022):

$$\max F_{\text{ERR}} = \frac{CO_2E - CO_2E_{\text{IESS}}}{CO_2E} \tag{17}$$

where, F_{ERR} is the maximum CO_2 emission reduction rate.

3.1.1.3 Constraints

WT and PV are important renewable energy generation systems. Their capacity has a great impact on the overall performance of the integrated energy supply system. ICE is the core power equipment of the integrated energy supply system. The capacity of biomass gas boiler, absorption chiller and other equipment is determined by the ICE. ASHP is an important link between cooling and heating, the capacity size affects the degree of matching system operation. Battery is the main energy storage equipment of the integrated energy supply system; it can play the role of peak load shifting. Therefore, the capacity of WT, PV, ICE, ASHP, and battery are selected as the optimization variables in the first stage. The system operation needs to meet certain capacity limits; therefore, there was a range of constraints on the capacity configuration of the system equipment. Notably, the optimization objectives were required to meet the following constraints, as shown below:

$$0 < N_{\text{WT}} < N_{\text{WT,max}} \tag{18}$$

$$0 < N_{\text{PV}} < N_{\text{PV,max}} \tag{19}$$

$$0 < N_{\text{ICE}} < N_{\text{ICE,max}} \tag{20}$$

$$0 < N_{\text{hp,h}} < N_{\text{hp,h, max}} \tag{21}$$

$$0 < N_{\text{hp,c}} < N_{\text{hp,c, max}} \tag{22}$$

$$N_{\text{BT, min}} \le N_{\text{BT}} \le N_{\text{BT, max}} \tag{23}$$

where N_{WT}, N_{PV}, N_{ICE}, and N_{BT} are the configured capacities of WT, PV, ICE, and battery, respectively. $N_{\text{hp,h}}$ and $N_{\text{hp,c}}$ are the configured capacities of the ASHP for heating and cooling, respectively. $N_{\text{PV,max}}$, $N_{\text{ICE,max}}$, and $N_{\text{BT,max}}$ are the maximum capacities of the PV, ICE, and battery, respectively. $N_{\text{hp,h,max}}$ and $N_{\text{hp,c,max}}$ are the maximum capacities of the ASHP for heating and cooling, respectively. and $N_{\text{BT,min}}$ is the minimum capacity of battery.

3.2 System Operation Strategy Optimization Model

3.2.1 Optimization Objectives

3.2.1.1 Economic Indicators

For the second stage of optimization, we first considered the economy of the system. The maximum annual operation saving rate of the system was one of the optimization objectives. It mainly includes the cost of electricity purchased from the grid, cost of biomass gas consumption, and maintenance cost of each equipment. The total annual operation saving rate of the IESS, compared to that of the existing energy supply system of the greenhouse, was calculated using the equations given below:

$$\max C_{\text{OSR}} = \frac{\sum_{t=1}^{8760} C(t) - \sum_{t=1}^{8760} C_{\text{IESS}}(t)}{\sum_{t=1}^{8760} C(t)} \tag{24}$$

where $C(t)$ is the cost of the existing greenhouse energy supply system at time t, and $C_{\text{IESS}}(t)$ is the cost of the IESS at time t.

$$C_{\text{IESS}} = \sum_{t=1}^{8760} \left(C_{\text{grid}}(t) + C_{\text{gas}}(t) + C_{\text{com}}(t) \right) \tag{25}$$

where $C_{\text{grid}}(t)$ is the cost of electricity purchased from the grid at time t, $C_{\text{gas}}(t)$ is the cost of biomass gas consumed by the system at time t, and $C_{\text{com}}(t)$ is the operation and maintenance cost of the system equipment at time t. The costs were calculated using the equations given below:

$$C_{\text{grid}}(t) = c_{\text{gird}}(t) P_{\text{grid}}(t) \tag{26}$$

$$C_{\text{gas}}(t) = c_{\text{gas}}\left(G_{\text{ICE}}(t) + F_{\text{b}}(t)\right) \tag{27}$$

$$C_{\text{com}}(t) = \sum_{i=1}^{N} c_i P_i(t) \tag{28}$$

where $c_{\text{grid}}(t)$ and $c_{\text{gas}}(t)$ are the grid electric price and biomass gas unit price purchased from the grid at time t, respectively. C_i is the operation and maintenance cost of the ith equipment, $P_i(t)$ is the ith equipment in the system operating power at moment t, and $P_{\text{grid}}(t)$ is the power purchased from the grid at moment t.

3.2.1.2 Environmental Indicators

Similar to that in the first stage of optimization, during the second stage of optimization, we considered the emissions of the pollutant gases during system operation. In this study, the maximum ERR of the system was the optimization objective, and its expression was consistent with that in the first stage.

3.2.1.3 Energy-Saving Indicators

The primary energy consumed by the system was estimated using the following equations:

$$G_{\text{IESS}}(t) = G_{\text{e,IESS}}(t) + G_{\text{b}}(t) + G_{\text{ICE}}(t) \tag{29}$$

$$\begin{cases} G_{\text{e,IESS}}(t) = \dfrac{E_{\text{grid}}(t)}{\eta_{\text{e,grid}}\eta_{\text{tr}}} \\ G_{\text{b}}(t) = F_{\text{b}}(t) \\ G_{\text{ICE}}(t) = F_{\text{ICE}}(t) \end{cases} \tag{30}$$

where $G_{\text{IESS}}(t)$ is the primary energy consumed by the system at time t; $G_{\text{e,IESS}}(t)$ is the converted energy consumption of the IESS interacting with the grid at time t; $G_{\text{b}}(t)$ is the amount of biomass gas consumed by the gas boiler of the IESS at time t; $G_{\text{ICE}}(t)$ is the amount of biomass gas consumed by the gas generator at time t, and $\eta_{\text{e,grid}}$ is the power plant generation efficiency, and η_{tr} is the grid transmission efficiency.

TABLE 1 | Continuous greenhouse construction data.

Items	Greenhouse area (m)	Span (m)	Number of spans	Width of gutter (m)	Greenhouse east-west length (m)	Greenhouse north-south length (m)	Sinking (m)	Exterior wall (m)	Shoulder height (m)	Ridge height (m)
Size	80,000^2	12	23	1.6	313.1	252	0.8	1	6	9.5

Energy-saving indicators are important indicators for evaluating the primary energy use of a system. The primary energy saving rate is given below:

$$F_{\mathrm{PESR}} = \sum_{t=1}^{8760} \frac{E_{\mathrm{L}}(t) + Q_{\mathrm{c,L}}(t) + Q_{\mathrm{h,L}}(t)}{G_{\mathrm{IESS}}(t)} \tag{31}$$

3.2.2 Constraints

The ICE is the source of power generation and heat production in the integrated energy supply system. Therefore, it is the key to determining whether the whole system operates efficiently and is an important link between cooling and heating. A reasonable hour-by-hour operation strategy of the ASHP can match the cooling and heating loads more reasonably and improve the efficiency of the integrated energy supply system. The battery is the main energy storage device; it can be designed to further improve the effect of peak load shifting. Therefore, for the second stage, the hour-by-hour operation of the ICE, ASHP, and battery were selected as the optimization variables. The constraints of the optimization variables are shown as follows.

$$0 < E_{\mathrm{ICE}} < N_{\mathrm{ICE}} \tag{32}$$

$$0 < Q_{\mathrm{hp,h}} < N_{\mathrm{hp,h}} \tag{33}$$

$$0 < Q_{\mathrm{hp,c}} < N_{\mathrm{hp,c}} \tag{34}$$

$$E_{\mathrm{BT,min}} \le E_{\mathrm{BT}} \le E_{\mathrm{BT,max}} \tag{35}$$

$$P_{\mathrm{BT,charge,min}} \le P_{\mathrm{BT,charge}} \le P_{\mathrm{BT,charge,max}} \tag{36}$$

$$P_{\mathrm{BT,discharge,\,min}} \le P_{\mathrm{BT,discharge}} \le P_{\mathrm{BT,discharge,\,max}} \tag{37}$$

where $E_{\mathrm{BT,min}}$ and $E_{\mathrm{BT,max}}$ are the upper and lower limits of the energy storage state of the battery, respectively; $P_{\mathrm{BT,charge,min}}$ and $P_{\mathrm{BT,charge,max,}}$ are the upper and lower limits of the battery charging, $P_{\mathrm{BT,discharge,min}}$ and $P_{\mathrm{BT,discharge,max}}$ are the upper and lower limits of the battery discharging.

3.3 Optimization Algorithm

In case of the system multi-objective optimization problem, pure mathematical analysis is limited by the objective function; therefore, it has limited use. In case of the IESS operation strategy problem, the objective function and the system model have nonlinear and discrete characteristics. In this study, we observed a strong coupling between the two stages, which was difficult to solve using traditional analytical methods. In addition, the optimization model had some limitations. Therefore, a hybrid algorithm of non-dominated ranking genetic algorithm and multi-objective particle swarm optimization

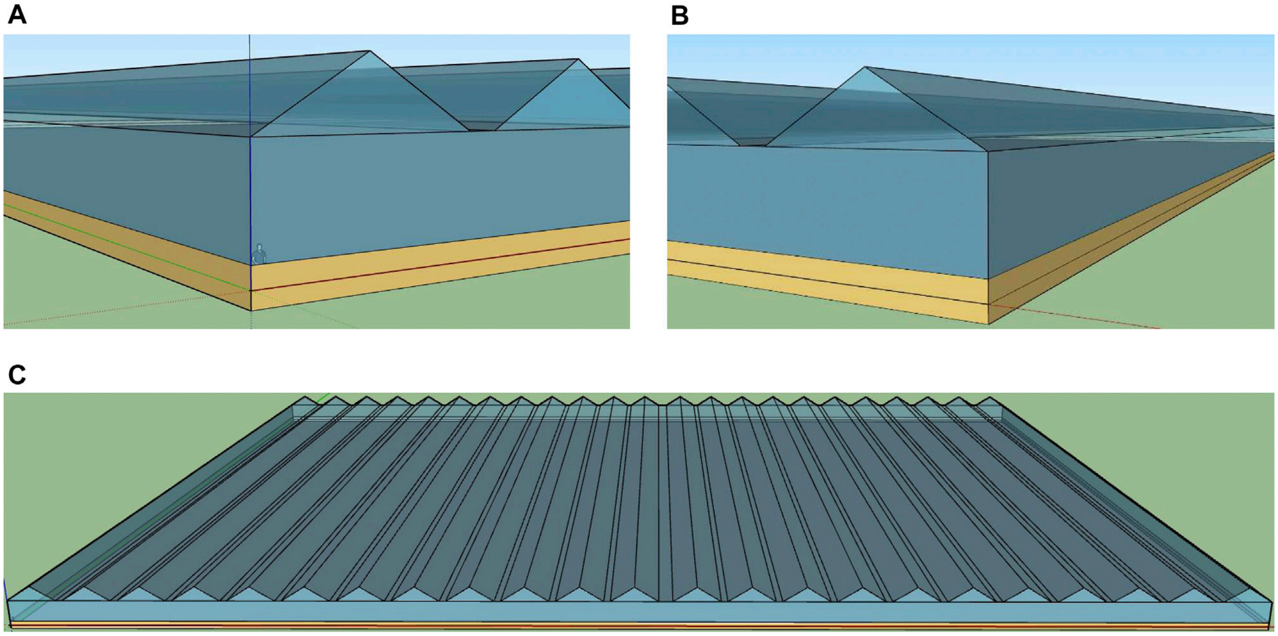

FIGURE 3 | Greenhouse three-dimensional (3D) physical model. **(A)** and **(B)** shows a partial view of the left and right sides of the greenhouse, respectively, and **(C)** shows the overall view of the greenhouse.

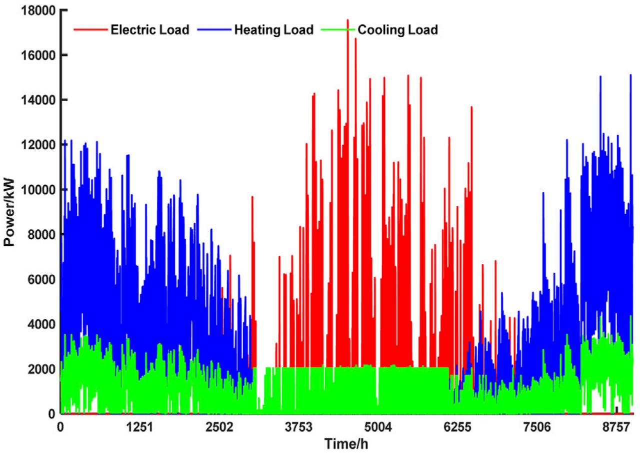

FIGURE 4 | Greenhouse annual load data measured using EnergyPlus.

(C-NSGA-II) was used to solve the multi-objective optimization model. It combines chaotic mapping, multi-objective genetic algorithm (NSGA-II), and multi-objective particle swarm algorithm (MOPSO), with NSGA-II algorithm as the main body, It uses the traversal feature of chaotic mapping to initialize the population, and the speed and position update mode of MOPSO to reconstruct the variation operator, for improving the convergence speed of the algorithm. This could have a significant impact on the field of multi-objective optimization (Zhang et al., 2013).

4 CASE STUDY

In this study, the characteristics of a greenhouse were analyzed using a prototype of a continuous greenhouse with actual crops. The energy supply system was a wet curtain fan and a heat pump system. This often results in energy waste because it is difficult to control the wet curtain fan and heat pump. Therefore, we adopted the IESS for the energy supply and used a two-stage optimization design method for optimizing the energy consumption of the greenhouse.

4.1 Energy Simulation Software

In this study, energy consumption simulations for continuous greenhouses were performed using EnergyPlus, developed by the United States Department of Energy as a whole building energy simulation program based on a modular structure (Mazzeo et al., 2020). EnergyPlus has several modules that are integrated and solved simultaneously. It is a complete energy simulation software that requires a large amount of data input; and, it is time consuming to manually enter all the data. Therefore, to achieve a complete energy simulation, a 3D model of the greenhouse was created using SketchUp and OpenStudio, which allows designers to create intuitive ideas directly and is an excellent tool for creating 3D architectural design solutions. OpenStudio is a plug-in for SketchUp; together, they were used to build a geometric model of the building simulated by EnergyPlus. OpenStudio uses EnergyPlus to simulate the energy consumption of a building and provides it as a visual user interface for EnergyPlus.

4.2 Energy Simulation Data

The construction data of this continuous greenhouse are shown in **Table 1**. A 3D physical model of the continuous greenhouse, drawn using SketchUp and OpenStudio, is shown in **Figure 3**. After importing the physical model into EnergyPlus, the thermal properties, as well as the structural data, were assigned to its various parts.

The greenhouse cooling, heating, and electric load data were simulated using EnergyPlus, and the annual load data are shown in **Figure 4**. The solar radiation and temperature variation curves for the typical summer and typical winter days are shown in **Figure 5A** and **Figure 5B**, respectively. The greenhouse loads on typical summer and typical winter days are shown in **Figure 6** and **Figure 7**, respectively.

Tomato was used as the crop; it requires a temperature range of 10–30°C for optimal growth. Temperatures higher than 35°C or lower than 10°C (Ro et al., 2021) affect the growth of tomatoes.

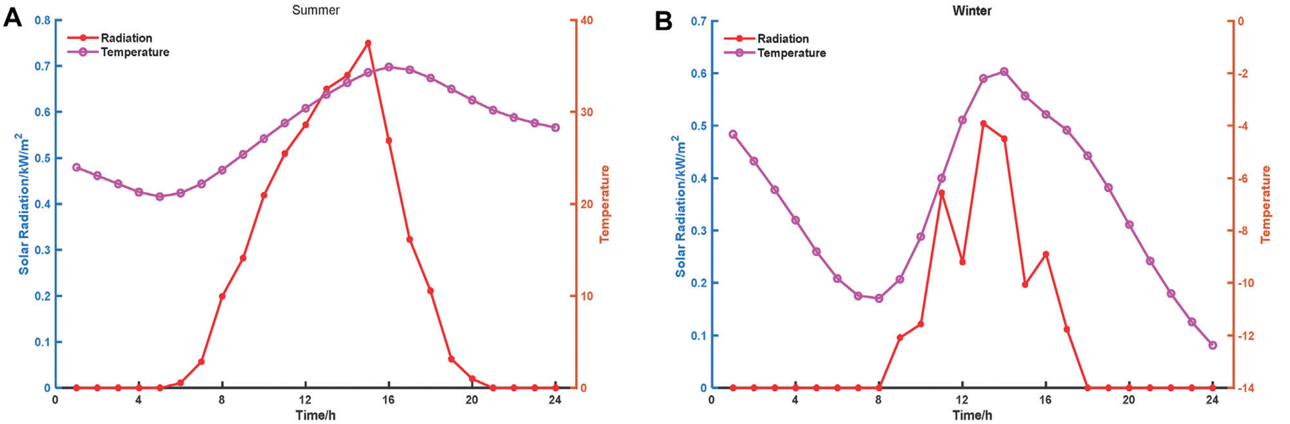

FIGURE 5 | Solar radiation and temperature change curve on a typical day. The solar radiation and temperature variation curves for the typical summer day is shown in **(A)**. The solar radiation and temperature variation curves for the typical winter day is shown in **(B)**.

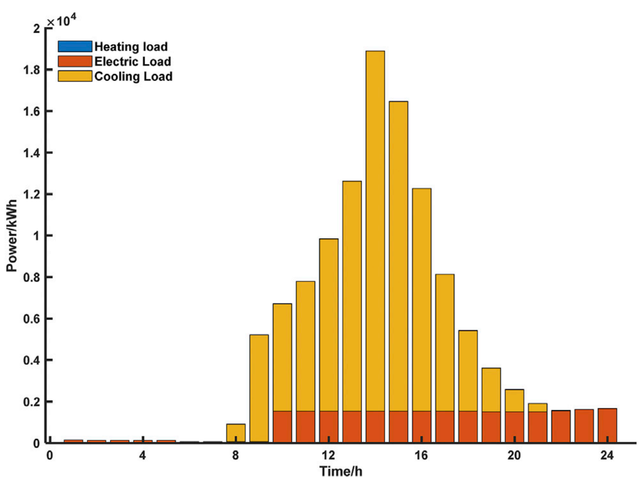

FIGURE 6 | Greenhouse load on a typical summer day.

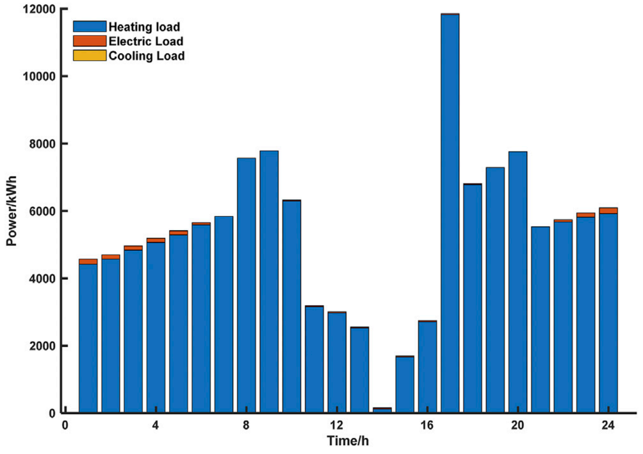

FIGURE 7 | Greenhouse load on a typical winter day.

Therefore, the cooling temperature was set to 30°C and heating temperature was set to 15°C in EnergyPlus. Agricultural greenhouses can reach a maximum heating load of approximately 12,000 kW and maximum cooling load of approximately 17,500 kW, which is much higher than the heating and cooling loads of ordinary buildings (**Figure 4**). The radiation and temperature on a typical summer day were significantly higher than that on a typical winter day (**Figure 5A** and **Figure 5B**). Additionally, the load on a typical summer day was dominated by the cooling load, and the load on the typical winter day was dominated by the heating load (**Figure 6**, **Figure 7**).

4.3 System Optimization Parameters

The basic parameters of the agricultural greenhouse energy supply system are listed in **Table 2** (Yan et al., 2018; Wegener et al., 2020). The cost and lifespan of each equipment in the agricultural greenhouse energy supply system are listed in **Table 3** (Yan et al., 2018; Wegener et al., 2020).

5 ANALYSIS OF SIMULATION RESULTS

To demonstrate the improvements in the optimization method proposed in this study, we compared our method to the existing energy supply model of the greenhouse; we analyzed the advantages of our method in several aspects.

The IESS was used to supply energy to the greenhouse. The annual load simulation data were simulated using EnergyPlus, and then, used as the parameter input for the two-stage optimization. The set of Pareto feasible solutions optimized in the first-stage capacity configuration is shown in **Figure 8**. The optimized Pareto feasible solution sets for a typical summer day and typical winter day obtained in the second stage of the operation strategy are shown in **Figure 9A** and **Figure 9B**, respectively. The greenhouse load in summer is mostly generated at noon, which is the same time as the high power

TABLE 2 | Basic parameters of an agricultural greenhouse energy supply system equipment.

Parameters	Symbol	Value	Unit
Cut-in wind speed of WT	v_{in}	3	m/s
Rated wind speed of WT	v_r	12	m/s
Cut-out wind speed of WT	v_{out}	25	m/s
Temperature coefficient of PV	k	−0.0045	
Heating efficiency of gas boiler	η_b	0.8	-
Calorific value of biogas gas	L_{NG}	9.7	(kW h)/m^3
COP of absorption chiller	COP_{ac}	0.9	-
Charging efficiency of Battery	η_{charge}	0.95	-
Discharging efficiency of Battery	$\eta_{discharge}$	0.95	-
CO$_2$ emission factor of biomass gas	μ_g	220	g/(kW h)
CO$_2$ emission factor of grid	μ_e	968	g/(kW h)
Price of electric			
(11:00-14:00,18:00-23:00)	c_{grid}	0.168	$/(kW h)
(7:00-11:00,14:00-18:00)		0.108	
(23:00-7:00)		0.057	
Unit price of biomass gas	c_{gas}	0.34	$/m^3
Conversion factor	r	0.08	
the heating energy efficiency rate	$COP_{hp,h}$	3.2	-
the cooling energy efficiency rate	$COP_{hp,c}$	3.2	-

TABLE 3 | Cost and lifespan of each equipment in an agricultural greenhouse energy supply system.

Equipment	Acquisition cost /($/kW)	Operation and maintenance costs /($/h)	Lifespan /year
WT	770	0.0028	20
PV	1,230	0.0028	22
ICE	812	0.16	10
Battery	300	0.32	5
Biomass gas boiler	46	0.18	10
ASHP	508	Neglected	20

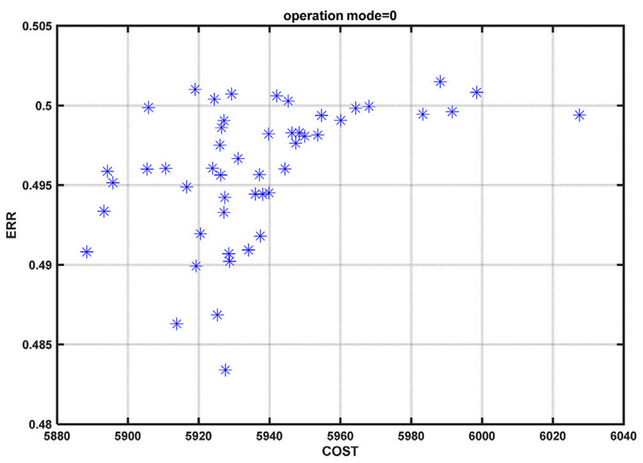

FIGURE 8 | Set of Pareto solutions optimized during the first-stage.

generation of PV generating units. The opposite is true in winter, and there is a clear difference between summer and winter based on the optimization results. When the C-NSGA-II algorithm is used to solve the non-dominated solution of the second-stage optimization objective, the constraints contain a large number of non-linear models and the state of charge (SOC) constraints on the energy storage. This results in a more scattered Pareto feasible solution for the summer optimization compared to that for the winter optimization. The results of the load distribution by equipment on a typical summer day are shown in **Figure 10**.

On a typical summer day (**Figure 10A**), the electric load and price of electricity were low, and the battery was used to store the electricity generated by the ICE, which could achieve peak load shifting. The cooling load demand was highest around 12:00 h on a typical summer day (**Figure 10B**). Owing to the lower cost of the gas boiler, absorption chillers mostly absorb heat from the gas boiler to provide the cooling load. The results of the load distribution by equipment on a typical winter day are shown in **Figure 11**.

On a typical winter day (**Figure 11A**, the required electric load was less, and the power generated by the ICE and PV was mainly stored in the storage equipment, to achieve the peak load shifting. On a typical winter day (as seen in **Figure 11B**), the heating load was low, and the heating load generated by the ICE and electric heating equipment was mainly stored in the storage equipment, to meet the high heating load during the rest of the day. The system optimization results are listed in **Table 4**.

Compared with the existing energy supply system of the greenhouse, the average daily economic cost of the CCHP was USD 5937.89 and the ERR was 49.53% after the first stage optimization design. After the second stage of optimization design, the total annual OSR, ERR, and PESR for a typical summer day was 39.51, 48.88, and 27.57%, respectively, and the OSR, ERR, and PESR for a typical winter day was 52.96, 50.18, and 50.13%, respectively. These data emphasize the unique

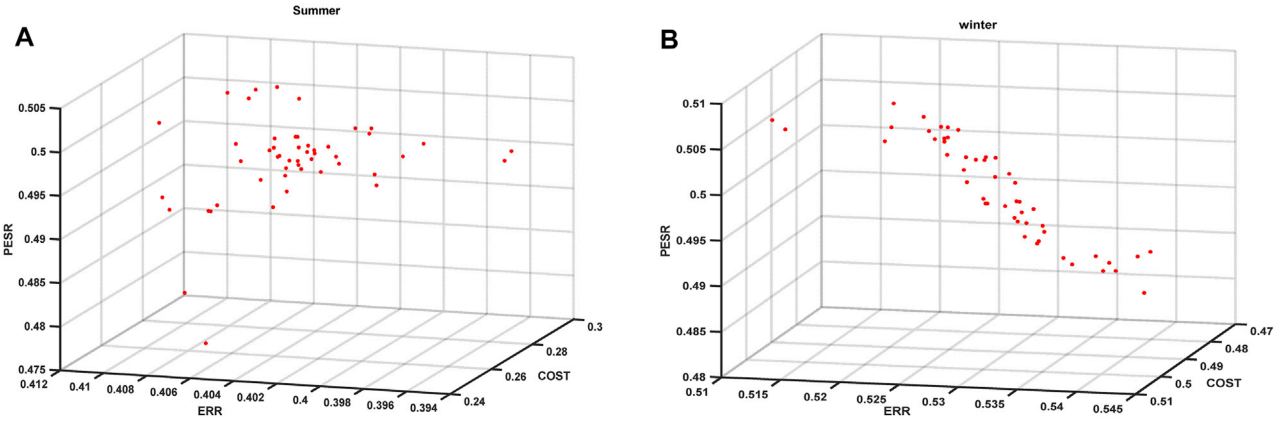

FIGURE 9 | Set of Pareto solutions optimized during the second-stage. The optimized Pareto feasible solution sets for a typical summer day obtained in the second stage of the operation strategy are shown in **(A)**. The optimized Pareto feasible solution sets for a typical winter day obtained in the second stage of the operation strategy are shown in **(B)**.

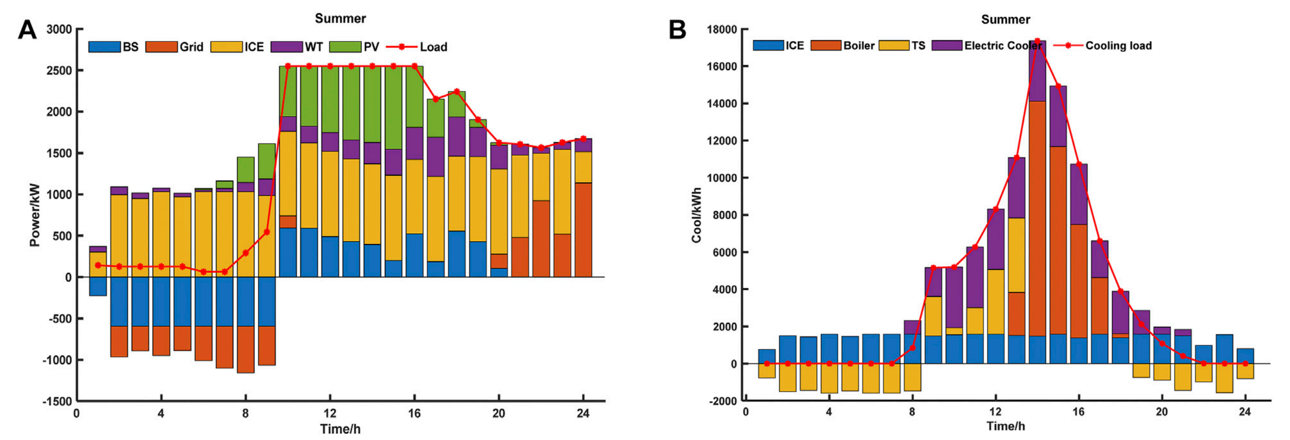

FIGURE 10 | Results of load distribution by equipment on a typical summer day. The results of the load distribution by equipment on a typical summer day are shown in Figure. Figure **(A)** shows the distribution of electrical load in typical summer day; **(B)** shows the distribution of cooling load in typical summer day.

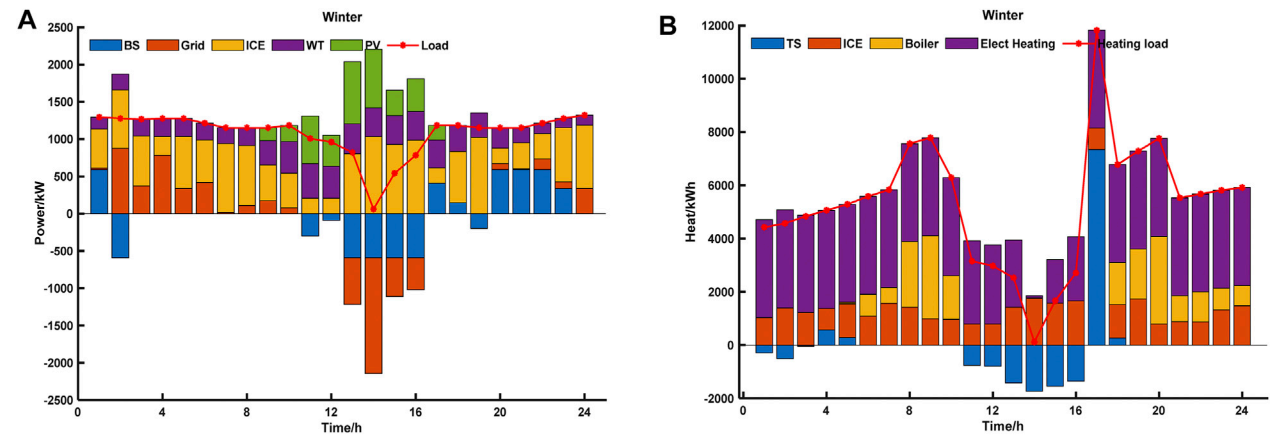

FIGURE 11 | Results of load distribution by equipment on a typical winter day. The results of the load distribution by equipment on a typical winter day are shown in Figure. **(A)** shows the distribution of electrical load in typical winter day; **(B)** shows the distribution of heating load in typical winter day.

TABLE 4 | System optimization results.

	Indicators	Two-stage optimization results	
		summer typical day	**winter typical day (%)**
The first stage	Average daily economic cost	5,937.89 $	
	CO_2 emission reduction rate	49.53%	
The second stage	Annual operation saving rate	39.51%	52.96
	CO_2 emission reduction rate	48.88%	50.18
	Primary energy saving rate	27.57%	50.13

advantages of the two-stage method applied to the IESS for the optimization of energy consumption of the greenhouse. It can further reduce the comprehensive cost of the enterprise and improve the economic and environmental protection index of the system; therefore, the proposed method has practical applicability and advantages.

6 CONCLUSION

In this study, we propose a two-stage collaborative optimization design method for the integrated energy supply system of agricultural greenhouses. We have combined Energy Plus and MATLAB simulation software to enhance the matching of this complex nonlinear system in different stages of design and operation. This improves the overall economy, saves energy, and offers environmental protection. We use a combination of the key equipment output optimization and dynamic adjustment of operating parameters, to make the system operation more suitable for the load characteristics of agricultural greenhouses and the use of a higher percentage of renewable energy.

Greenhouse energy supply systems are difficult to control, resulting in high greenhouse energy consumption and difficult load analysis. Therefore, we constructed an integrated energy supply system consisting of a CCHP and an ASHP. We used this system to supply energy to the greenhouse.

The use of a higher proportion of renewable energy deepens the coupling relationship between capacity configuration and operation strategy of the core equipment of the system. In addition, it becomes difficult to find the optimal operation strategy. Therefore, we proposed a two-stage synergistic optimization design method of integrated energy supply system, based on C-NSGA-II algorithm. This would optimize the design of capacity configuration and the operation strategy of the integrated energy supply system. In the first stage, the optimization objectives are “minimum average daily economic cost” and “maximum CO_2 emission reduction rate”. The optimal capacity of each equipment of the integrated energy supply system is optimized using the optimized design results in the second stage. In the second stage, the optimization objectives are “maximum annual operating saving rate”, “maximum CO_2 emission reduction rate”, and “maximum primary energy saving rate”. The capacity of the equipment designed in the first stage is used as the constraint to further optimize the design of the optimal operation strategy of the integrated energy supply system.

A greenhouse was used as a prototype. We carried out an arithmetic study on two typical days, summer and winter, respectively, considering the actual crop characteristics. We used the IESS, for the energy supply, and the two-stage optimization design. After the first stage of optimized design, compared to the existing greenhouse energy supply systems, the average daily operating cost was significantly lower and the CO_2 emission reduction rate was 49.53%. After the second stage, compared to the existing greenhouse energy supply systems, the annual operating saving rate, the CO_2 emission reduction rate, and the primary energy saving rate were 39.51, 48.88, and 27.57% for the typical summer day and 52.96, 50.18, and 50.13% for the typical winter day, respectively. Therefore, the proposed method can effectively alleviate the high energy consumption, improve the energy utilization efficiency, reduce the cost of enterprises, and lower CO_2 emissions. In addition, it enables the system to feed the energy back into the grid to help peak load shifting through peak electricity consumption. This further emphasizes the advancement of the proposed method.

DATA AVAILABILITY STATEMENT

The original contributions presented in the study are included in the article/Supplementary Material, further inquiries can be directed to the corresponding author.

AUTHOR CONTRIBUTIONS

CT: Funding acquisition, Conceptualization, ZS: Software, Conceptualization, Writing- Original draft preparation, Data Curation, RW: Software, Data Curation, YY: Conceptualization, Methodology, Writing- Original draft preparation, Software, XW: Software, Writing- Original draft preparation, AR: Writing- Original draft preparation.

FUNDING

This work was supported by the Natural Science Foundation of Shandong Province (No. ZR2019MF053).

REFERENCES

Ahmad, B., Mehdi, M., Barat, G., Hadi, P., and Fatemeh, K. (2021). Energy Analysis and Assessing Heating and Cooling Demands of Closed Greenhouse in Iran. *Therm. Sci. Eng. Prog.* 25, 101042. doi:10.1016/j.tsep.2021.101042

Das, B. K., Al-Abdeli, Y. M., and Kothapalli, G. (2018). Effect of Load Following Strategies, Hardware, and thermal Load Distribution on Stand-Alone Hybrid CCHP Systems. *Appl. Energ.* 220, 735–753. doi:10.1016/j.apenergy.2018.03.068

Gao, L., Hwang, Y., and Cao, T. (2019). An Overview of Optimization Technologies Applied in Combined Cooling, Heating and Power Systems. *Renew. Sust. Energ. Rev.* 114, 109344. doi:10.1016/j.rser.2019.109344

Ghersi, D. E., Amoura, M., Loubar, K., Desideri, U., and Tazerout, M. (2021). Multi-objective Optimization of CCHP System with Hybrid Chiller under New Electric Load Following Operation Strategy. *Energy* 219, 119574. doi:10.1016/j.energy.2020.119574

Jia, J., Chen, H., Liu, H., Ai, T., and Li, H. (2021). Thermodynamic Performance Analyses for CCHP System Coupled with Organic Rankine Cycle and Solar thermal Utilization under a Novel Operation Strategy. *Energ. Convers. Manage.* 239, 114212. doi:10.1016/j.enconman.2021.114212

Jung, D.-H., Kim, H. S., Jhin, C., Kim, H.-J., and Park, S. H. (2020). Time-serial Analysis of Deep Neural Network Models for Prediction of Climatic Conditions inside a Greenhouse. *Comput. Electron. Agric.* 173, 105402. doi:10.1016/j.compag.2020.105402

Kang, L., Wu, X., Yuan, X., Ma, K., Wang, Y., Zhao, J., et al. (2021). Influence Analysis of Energy Policies on Comprehensive Performance of CCHP System in Different Buildings. *Energy* 233, 121159. doi:10.1016/j.energy.2021.121159

Kang, L., Yang, J., An, Q., Deng, S., Zhao, J., Li, Z., et al. (2017). Complementary Configuration and Performance Comparison of CCHP-ORC System with a Ground Source Heat Pump under Three Energy Management Modes. *Energ. Convers. Manage.* 135, 244–255. doi:10.1016/j.enconman.2016.12.055

Li, L., Yu, S., Mu, H., and Li, H. (2018). Optimization and Evaluation of CCHP Systems Considering Incentive Policies under Different Operation Strategies. *Energy* 162, 825–840. doi:10.1016/j.energy.2018.08.083

Li, N., Zhao, X., Shi, X., Pei, Z., Mu, H., and Taghizadeh-Hesary, F. (2021). Integrated Energy Systems with CCHP and Hydrogen Supply: A New Outlet for Curtailed Wind Power. *Appl. Energ.* 303, 117619. doi:10.1016/j.apenergy.2021.117619

Li, Y., Tian, R., Wei, M., Xu, F., Zheng, S., Song, P., et al. (2020). An Improved Operation Strategy for CCHP System Based on High-Speed Railways Station Case Study. *Energ. Convers. Manage.* 216, 112936. doi:10.1016/j.enconman.2020.112936

Lin, D., Wei, R., and Xu, L. (2019). An Integrated Yield Prediction Model for Greenhouse Tomato. *Agronomy* 9, 873. doi:10.3390/agronomy9120873

Lin, D., Zhang, L., and Xia, X. (2020). Hierarchical Model Predictive Control of Venlo-type Greenhouse Climate for Improving Energy Efficiency and Reducing Operating Cost. *J. Clean. Prod.* 264, 121513. doi:10.1016/j.jclepro.2020.121513

Liu, M., Shi, Y., and Fang, F. (2013). Optimal Power Flow and PGU Capacity of CCHP Systems Using a Matrix Modeling Approach. *Appl. Energ.* 102, 794–802. doi:10.1016/j.apenergy.2012.08.041

Lombardo, W., Sapienza, A., Ottaviano, S., Branchini, L., De Pascale, A., and Vasta, S. (2021). A CCHP System Based on ORC Cogenerator and Adsorption Chiller Experimental Prototypes: Energy and Economic Analysis for NZEB Applications. *Appl. Therm. Eng.* 183, 116119. doi:10.1016/j.applthermaleng.2020.116119

Ma, W., Fang, S., and Liu, G. (2017). Hybrid Optimization Method and Seasonal Operation Strategy for Distributed Energy System Integrating CCHP, Photovoltaic and Ground Source Heat Pump. *Energy* 141, 1439–1455. doi:10.1016/j.energy.2017.11.081

Mazzeo, D., Matera, N., Cornaro, C., Oliveti, G., Romagnoni, P., and De Santoli, L. (2020). EnergyPlus, IDA ICE and TRNSYS Predictive Simulation Accuracy for Building thermal Behaviour Evaluation by Using an Experimental Campaign in Solar Test Boxes with and without a PCM Module. *Energy and Buildings* 212, 109812. doi:10.1016/j.enbuild.2020.109812

Ren, F., Wei, Z., and Zhai, X. (2021). Multi-objective Optimization and Evaluation of Hybrid CCHP Systems for Different Building Types. *Energy* 215, 119096. doi:10.1016/j.energy.2020.119096

Ro, S., Chea, L., Ngoun, S., Stewart, Z. P., Roeurn, S., Theam, P., et al. (2021). Response of Tomato Genotypes under Different High Temperatures in Field and Greenhouse Conditions. *Plants (Basel)* 10, 10. doi:10.3390/plants10030449

Song, Z., Liu, T., and Lin, Q. (2020a). Multi-objective Optimization of a Solar Hybrid CCHP System Based on Different Operation Modes. *Energy* 206, 118125. doi:10.1016/j.energy.2020.118125

Song, Z., Liu, T., Liu, Y., Jiang, X., and Lin, Q. (2020b). Study on the Optimization and Sensitivity Analysis of CCHP Systems for Industrial Park Facilities. *Int. J. Electr. Power Energ. Syst.* 120, 105984. doi:10.1016/j.ijepes.2020.105984

Tian, X., Deng, S., Kang, L., Zhao, J., and An, Q. (2018). Study on Heat and Power Decoupling for CCHP System: Methodology and Case Study. *Appl. Therm. Eng.* 142, 597–609. doi:10.1016/j.applthermaleng.2018.07.040

Vadiee, A., and Martin, V. (2013). Energy Analysis and Thermoeconomic Assessment of the Closed Greenhouse - the Largest Commercial Solar Building. *Appl. Energ.* 102, 1256–1266. doi:10.1016/j.apenergy.2012.06.051

Wang, J.-J., Xu, Z.-L., Jin, H.-G., Shi, G.-h., Fu, C., and Yang, K. (2014). Design Optimization and Analysis of a Biomass Gasification Based BCHP System: A Case Study in Harbin, China. *Renew. Energ.* 71, 572–583. doi:10.1016/j.renene.2014.06.016

Wang, J., Liu, Y., Ren, F., and Lu, S. (2020). Multi-objective Optimization and Selection of Hybrid Combined Cooling, Heating and Power Systems Considering Operational Flexibility. *Energy* 197, 117313. doi:10.1016/j.energy.2020.117313

Wegener, M., Isalgue, A., Malmquist, A., Martin, A., Santarelli, M., Arranz, P., et al. (2021). Exergetic Model of a Small-Scale, Biomass-Based CCHP/HP System for Historic Building Structures. *Energy Convers. Manag. X* 12, 100148. doi:10.1016/j.ecmx.2021.100148

Wegener, M., Malmquist, A., Isalgue, A., Martin, A., Arranz, P., Camara, O., et al. (2020). A Techno-Economic Optimization Model of a Biomass-Based CCHP/heat Pump System under Evolving Climate Conditions. *Energ. Convers. Manage.* 223, 113256. doi:10.1016/j.enconman.2020.113256

Wegener, M., Malmquist, A., Isalgué, A., and Martin, A. (2018). Biomass-fired Combined Cooling, Heating and Power for Small Scale Applications - A Review. *Renew. Sust. Energ. Rev.* 96, 392–410. doi:10.1016/j.rser.2018.07.044

Wen, Q., Liu, G., Wu, W., and Liao, S. (2022). Performance Evaluation of Distributed Energy System Integrating Photovoltaic, Ground Source Heat Pump, and Natural Gas-Based CCHP. *Energ. Convers. Manage.* 252, 115039. doi:10.1016/j.enconman.2021.115039

Yan, R., Lu, Z., Wang, J., Chen, H., Wang, J., Yang, Y., et al. (2021). Stochastic Multi-Scenario Optimization for a Hybrid Combined Cooling, Heating and Power System Considering Multi-Criteria. *Energ. Convers. Manage.* 233, 113911. doi:10.1016/j.enconman.2021.113911

Yan, Y., Zhang, C., Li, K., and Wang, Z. (2018). An Integrated Design for Hybrid Combined Cooling, Heating and Power System with Compressed Air Energy Storage. *Appl. Energ.* 210, 1151–1166. doi:10.1016/j.apenergy.2017.07.005

Zhang, L., Zhang, L., Sun, B., Zhang, C., and Li, F. (2020). Nested Optimization Design for Combined Cooling, Heating, and Power System Coupled with Solar and Biomass Energy. *Int. J. Electr. Power Energ. Syst.* 123, 106236. doi:10.1016/j.ijepes.2020.106236

Zhang, Y., Yang, K., Li, X., and Xu, J. (2013). The Thermodynamic Effect of thermal Energy Storage on Compressed Air Energy Storage System. *Renew. Energ.* 50, 227–235. doi:10.1016/j.renene.2012.06.052

Zhao, H., Wang, X., Wang, Y., Li, B., and Lu, H. (2021). A Dynamic Decision-Making Method for Energy Transaction price of CCHP Microgrids Considering Multiple Uncertainties. *Int. J. Electr. Power Energ. Syst.* 127, 106592. doi:10.1016/j.ijepes.2020.106592

Conflict of Interest: RW was employed by the State Grid Shandong Integrated Energy Services CO., LTD. AR was employed by the Jinan Power Supply Company.

The remaining authors declare that the research was conducted in the absence of any commercial or financial relationships that could be construed as a potential conflict of interest.

GLOSSARY

IESS integrated energy supply system
CCHP combined cooling, heating, and power
PGU power generator unit
PV photovoltaic
ORC organic Rankine cycle
FEL following electrical load
FTL following thermal load
WT wind turbine
ICE internal combustion engine
P_{WT} output power of WT
P_r rated power of WT
v actual outdoor wind speed
v_r rated wind speed of WT
v_{in} cut-in wind speed of WT
v_{out} cut-out wind speed of WT
P_{PV} output power of PV
I illumination intensity
P_{STC} maximum test power of PV
k power temperature coefficient of PV
T_{PV} temperature of PV
T_0 outdoor temperature
PLR part load rate
G_{ICE} amount of biomass gas consumed by the ICE
E_{ICE} amount of electricity generated by the ICE
η_{pe} efficiency of electricity generation
η_{te} efficiency of heat generation
Q_{re} recoverable heating of ICE
Q_{jw} waste heating of the cylinder sleeve water
η_{jw} efficiency of cylinder sleeve water heating exchanger
Q_{exh} waste heating of the flue gas heating exchanger
η_{exh} efficiency of flue gas heating exchanger
Q_{loss} lost heating
Q_b heat capacity of gas boiler
F_b biomass gas volume of gas boiler
L_{NG} biogas gas calorific value
η_b heating efficiency of gas boiler
Q_{ac} supplied cool capacity of absorption refrigerator
Q_{ac_in} input heat of absorption refrigerator
COP_{ac} energy efficiency rate of absorption chiller
E_{BT} remaining capacity of the battery
$P_{BT,charge}$ average power of the battery charging
$P_{BT,discharge}$ average power of the battery discharging
η_{charge} charging efficiency of the battery
E_{PV} power generation of PV
E_{WT} power generation of WT
E_{grid} system-grid interaction
E_L electric load required
$E_{BT,charge}$ production of battery
$Q_{h,L}$ heating load required
$Q_{c,L}$ cooling load required
C_r average daily economic cost
$C_{i,var}$ daily operating cost
C_{cap} daily acquisition cost
N capacity of equipment
C_i unit acquisition cost
r conversion factor
T_i lifespan of equipment
$C\ O\ _2E_{CCHP}$ total CO_2 emission of the CCHP system
μ_g CO_2 emissions factors of biomass gas
μ_e CO_2 emission factors for grid generation
G_{gas} amount of biomass gas consumed
$C\ O\ _2E$ CO_2 emissions of the existing greenhouse energy supply system
C_{OSR} total annual operation saving rate
C cost of the existing greenhouse energy supply system
C_{CCHP} cost of the CCHP system
C_{grid} cost of electric purchased from the grid
C_{gas} cost of biomass gas
C_{com} operation and maintenance cost
c_{grid} grid electric price
c_{gas} biomass gas unit price
P_{grid} power purchased from the grid
G_{CCHP} primary energy consumed by the system
$G_{e,CCHP}$ converted energy consumption of the CCHP
G_b amount of biomass gas consumed by the gas boiler
G_{ICE} amount of biomass gas consumed by the gas generator
$\eta_{e,grid}$ power plant generation efficiency.
η_{tr} Grid Transmission Efficiency
F_{ERR} maximum CO_2 emissions reduction rate
N_{WT} configured capacity of WT
N_{PV} configured capacity of PV
N_{ICE} configured capacity of ICE
$N_{hp,h}$ heating capacity of ASHP
$N_{hp,c}$ cooling capacity of ASHP
N_{BT} configured capacity of battery
$N_{PV,max}$ maximum capacity of PV
$N_{ICE,max}$ maximum capacity of ICE

$\boldsymbol{N_{\mathrm{hp,h,max}}}$ maximum heating capacity of ASHP

$\boldsymbol{N_{\mathrm{hp,c,max}}}$ maximum cooling capacity of ASHP

$\boldsymbol{N_{\mathrm{BT,max}}}$ maximum capacity of battery

$\boldsymbol{N_{\mathrm{BT,min}}}$ minimum capacity of battery

HVAC heating, ventilation, and air conditioning

ERR emissions reduction rate

PESR primary energy saving rate

OSR cost saving rate

frontiers
in Energy Research

ORIGINAL RESEARCH
published: 15 March 2022
doi: 10.3389/fenrg.2022.852046

Bypass Inductor Type LCL Filter Parameter Optimization for Three-Level Grid-Connected Converter

Ning Li [1], Shiqian Zhang [1], Zihan Xiao [1], Zhuoer An [1], Yan Zhang [2] and Lin Jiang [3]*

[1]School of Electrical Engineering, Xi'an University of Technology, Xi'an, China, [2]School of Electrical Engineering, Xi'an Jiaotong University, Xi'an, China, [3]Department of Electrical Engineering and Electronics, University of Liverpool, Liverpool, United Kingdom

Edited by:
Liansong Xiong,
Nanjing Institute of Technology (NJIT),
China

Reviewed by:
Shuzheng Wang,
Nanjing Institute of Technology (NJIT),
China
Dongbo Guo,
Northeast Electric Power University,
China
Peng Fang,
University of Minnesota Duluth,
United States

***Correspondence:**
Lin Jiang
L.Jiang@liverpool.ac.uk

Specialty section:
This article was submitted to
Process and Energy Systems
Engineering,
a section of the journal
Frontiers in Energy Research

Received: 10 January 2022
Accepted: 09 February 2022
Published: 15 March 2022

Citation:
Li N, Zhang S, Xiao Z, An Z, Zhang Y
and Jiang L (2022) Bypass Inductor
Type LCL Filter Parameter
Optimization for Three-Level Grid-
Connected Converter.
Front. Energy Res. 10:852046.
doi: 10.3389/fenrg.2022.852046

In the application of the three-level grid-connected system, passive damping is the most common method to keep the LCL filter working stably. However, in the case of high power density, the low switching frequency of the grid-connected converter results in the complexity of filter parameter design, and the increase in passive components leads to lower equipment utilization efficiency. To solve the above problems, based on the optimization of resonant frequency and system loss, this study proposes a set of LCL filter parameter design processes of a three-level neutral point clamped (NPC) converter, which can switch components freely and is easy to achieve. This study explores the theoretical evidence and application value of the proposed design, considering the influence of the current ripple and the reactive power limit. The design adopts the improved passive damping method to select the appropriate inductance ratio and impedance ratio to make the resonance frequency of the whole system and the extra loss of the system smaller. The simulation and experiments show that compared with the conventional method, the improved design method reduces the current THD of the grid side by 1.5% and the damping resistance loss by 0.17%.

Keywords: LCL filter, passive damping, stability, voltage-source converters, bypass inductor

1 INTRODUCTION

The three-level NPC grid-connected converter is a kind of multi-level grid-connected converter extensively used in a distributed generation dominated by solar energy and wind energy (Yao et al., 2017). In order to meet the network access standards, a grid-connected filter is introduced between the three-level NPC converter and power grid. Usually, the first-order L-type filter is too bulky and vulnerable to harmonic resonance, which attenuates the system's dynamic performance, and the voltage drop is relatively high (Kouchaki and Nymand, 2018). The third-order LCL filter meets the harmonic attenuation requirements even at a lower switching frequency, and the total inductor is smaller (Xiong et al., 2020). However, it has two zero-impedance resonance points, which amplify the current harmonics at the resonance frequency and affect the system stability, causing resonance. There are two methods for reducing resonance of LCL filter: active damping (Liu et al., 2021) and passive damping (Albatran et al., 2018). Compared with the passive damping method, the active damping method avoids the use of passive components and reduces the loss of passive components, but at the cost of the increasing control complexity (Beres et al., 2016a).

Active damping is the preferred control method when the power supply system is "weak" and the impedance change is not large. The dual-loop grid current control technology based on capacitor-current feedback is extensively used for the LCL filter system (Liu et al., 2018). In addition, Zeng et al. (2016) presented an active damping method that reshapes the harmonic impedance of the grid to suppress resonance. Simultaneously, it is necessary to detect the harmonic components in the grid voltage and current and has high real-time requirements (Xia and Kang, 2017). When the system's damping coefficient exceeds the critical value or reaches a certain resonance frequency, active damping can suppress resonant peaks (Guzman et al., 2018). In fact, the active damping strategy transfers the real damping resistance to the controller through the transformation of the transfer function (Liserre et al., 2005), and the effect is equivalent to a virtual resistor in series or parallel connected with the capacitor. It does not cause extra power loss and has a concise physical meaning, but the conventional active damping scheme requires additional current or voltage sensors (Falkowski and Sikorski, 2018), increasing system cost. In addition, active damping excessively relies on accurate parameter matching and is more sensitive to grid impedance and control parameters (He et al., 2017). Therefore, it needs a complex calculation to select the active damping coefficient and enhance the system's robustness (He et al., 2017).

Passive damping realizes the damping effect by adding actual passive components to the filter circuit, which is simple to operate at a low cost (Su et al., 2019). Young et al. (2020) proposed a new type of passive damping LCL filter based on coupled inductance, which obtains better high-frequency harmonic attenuation ability. Guo et al. (2010) compared the two passive control strategies of series and parallel resistance in the LCL filter system and concluded that series resistance reduces the extra loss. A hybrid control strategy combining active and passive damping is adopted to improve the adaptability of grid inductance and control delay (Wei and Gao, 2017). Although the above studies have improved the passive damping control strategy to some extent, they have not solved the difficulty of filter parameter design at a high power level and low switching frequency. After introducing passive components, some issues are still unsolved, such as large reactive power loss, low power factor, and decreased equipment utilization.

This study proposes an engineering design method of LCL filter based on passive control strategy (Zhang et al., 2021). The proposed method first analyzes the significance of resonance frequency in reactive power compensation and harmonic reduction (Xiong et al., 2021a). Then, the best damping topology is determined based on the attenuation curve of the LCL filter (Ben Saïd-Romdhane et al., 2017). Finally, a simple and effective design is made to obtain the appropriate component parameters by deducing the relationship between the filter parameters. The function of switching components is freely achieved according to different requirements similar to digital filters (Xiong et al., 2021b).

The main contributions of this study are as follows: 1) a passive damping strategy is used to reduce the resonant peak of the LCL filter, and the improved strategy is used to design the impedance ratio so that the equipment power factor and utilization efficiency of the entire filtration system are better improved. 2) Based on inductor optimization, a convenient parameter design method of the current-controlled bypass inductor type LCL grid-connected converter is made. The design steps are simple, and the components are switched freely according to different needs.

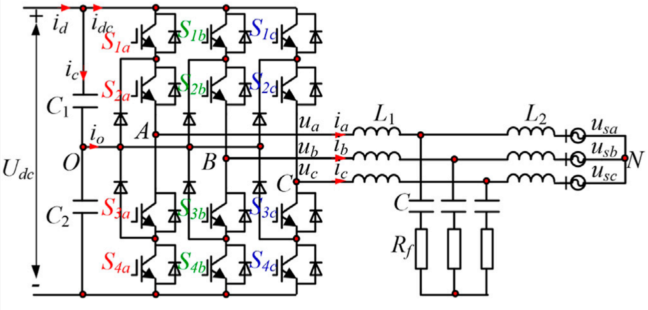

FIGURE 1 | Structure diagram of three-level grid-connected NPC converter with LCL filter.

The rest of this study is arranged as follows: **Section 2** introduces a three-level grid-connected NPC converter with an LCL filter, **Section 3** analyzes the relationship between the filter parameters, **Section 4** discusses the proposed method with design examples, and **Section 5** lists the experimental results to verify the effectiveness of the method.

2 SYSTEM DESCRIPTION OF THREE-LEVEL GIRD-CONNECTED NPC CONVERTER

2.1 System Description and Modeling

Figure 1 shows the structure of the three-level grid-connected NPC converter with the LCL filter (Bosch et al., 2018). u_{sx} ($x = a$, b, c) represents the grid-side phase voltage; u_{dc} is the DC capacitor voltage (Huang et al., 2019); C_1, C_2 are the upper and lower DC capacitors, respectively; $S_{1x} \sim S_{4x}$ represent the four switching devices of the x-phase, respectively; L_1 is the converter side inductor; L_2 is the grid-side inductor, C is the filter capacitor, Rf is the damping resistor, and L_1, C_2, C, and R_f constitute a typical passive damping LCL filter (Zheng et al., 2019).

A single-phase model is taken for analysis as shown in **Figure 2A**, where i_i is the inverter-side current, i_g is the grid-side current, and i_c is the current flowing through the filter capacitor C. The converter's output voltage is equivalent to the sum of the fundamental voltage and the harmonic voltage; u_x and u_H represent the fundamental and harmonic components, respectively; and u_{ON} represents the voltage difference between point N and midpoint O, whose value is obtained by **Eq. 1**. Here, S_x represents the switching function of phase x:

$$\begin{cases} U_{ON} = -\frac{1}{3}\sum u_x \\ u_x = S_x \cdot U_{dc}/2 \end{cases} \quad (x = a, b, c, S_x = 1 or 0 or - 1). \tag{1}$$

The high-frequency equivalent model of the LCL filter is obtained by ignoring the harmonic component in i_g, as shown

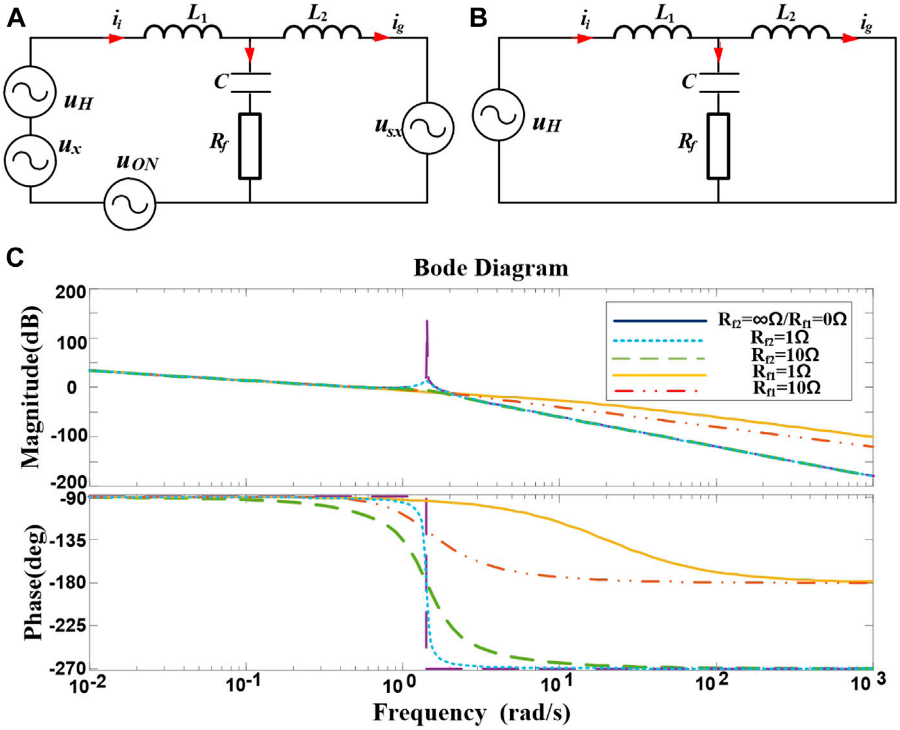

FIGURE 2 | Equivalent model and Bode diagram of the LCL filter. **(A)** Basic equivalent model of series resistance. **(B)** High-frequency equivalent model of series resistance. **(C)** Bode diagram of LCL filter with series (R_{f1}) or parallel resistor (R_{f2}) on the capacitor.

in **Figure 2B**. In this linear system, the relationship between the grid-side current and the inverter-side voltage and between the grid-side current and inverter-side current is obtained according to the superposition theorem as follows:

$$\begin{cases} \dfrac{I_g(s)}{U_H(s)} = \dfrac{R_f Cs + 1}{L_1 L_2 Cs^3 + (L_1 + L_2) R_f Cs^2 + (L_1 + L_2)s} \\ \dfrac{I_g(s)}{I_i(s)} = \dfrac{R_f Cs + 1}{L_2 Cs^2 + R_f Cs + 1} \end{cases} . \tag{2}$$

The relationship between i_g and U_H can be seen in the above equations, including an integral term, a zero point, and a quadratic term. Thus, the conventional LCL transfer function has a resonant peak at zero point, causing a stability problem, but the high-frequency attenuation rate reaches −60 dB/dec. Then, the angular frequency of the system undamped oscillation $\omega_{res}$and the damping ratio ζ can be determined as follows:

$$\omega_{res} = \sqrt{\frac{L_1 + L_2}{L_1 L_2 C}}, \tag{3}$$

$$\xi = \frac{\omega_{res} R_f C}{2}. \tag{4}$$

The zero point of the LCL filter system is calculated as $\omega_z = 1/(RC)$, and the relationship between the undamped oscillation angular frequency and the zero point can be determined as

$$2\xi = \frac{\omega_{res}}{\omega_z}. \tag{5}$$

Based on **Eqs. 2**, **5**, relist the functional relationship between i_g and U_H as follows:

$$\frac{I_g(s)}{U_H(s)} = \frac{\frac{2\xi}{\omega_{res}} s + 1}{(L_1 + L_2)s\left(\frac{1}{\omega_{res}{}^2} s^2 + \frac{2\xi}{\omega_{res}} s + 1\right)}. \tag{6}$$

In summary, the external characteristics of the passive damping LCL filter are determined by $L_1 + L_2$, the damping coefficient, and the undamped oscillation angular frequency (Zheng et al., 2019).

2.2 Topology Contrast

The direct measure of passive damping to eliminate LCL resonance peaks is to connect inductor and capacitor elements in series or in parallel. Then, six methods are classified based on the position of the added devices (Kim and Kim, 2019). Adding a resistor directly at the position of the inductor element obviously affects the harmonics' attenuation ability. Therefore, it is better to connect the resistor in series (**Figure 1** and **Eq. 2**) or in parallel to the capacitor. The transfer function of the parallel resistor at the capacitor position is listed as follows:

$$G_{parallel}s = \frac{i_g s}{U_H s} = \frac{1}{s^3 L_1 L_2 C + s^2 L_1 L_2 \big/ R_f + sL_1 + L_2}. \tag{7}$$

Figure 2C shows the Bode diagram of the LCL filter with a series or parallel resistor on the capacitor. Comparing the Bode diagram and the transfer functions between **Eq. 2** and **Eq. 7**, it can be found that the series resistor causes the branch circuit to

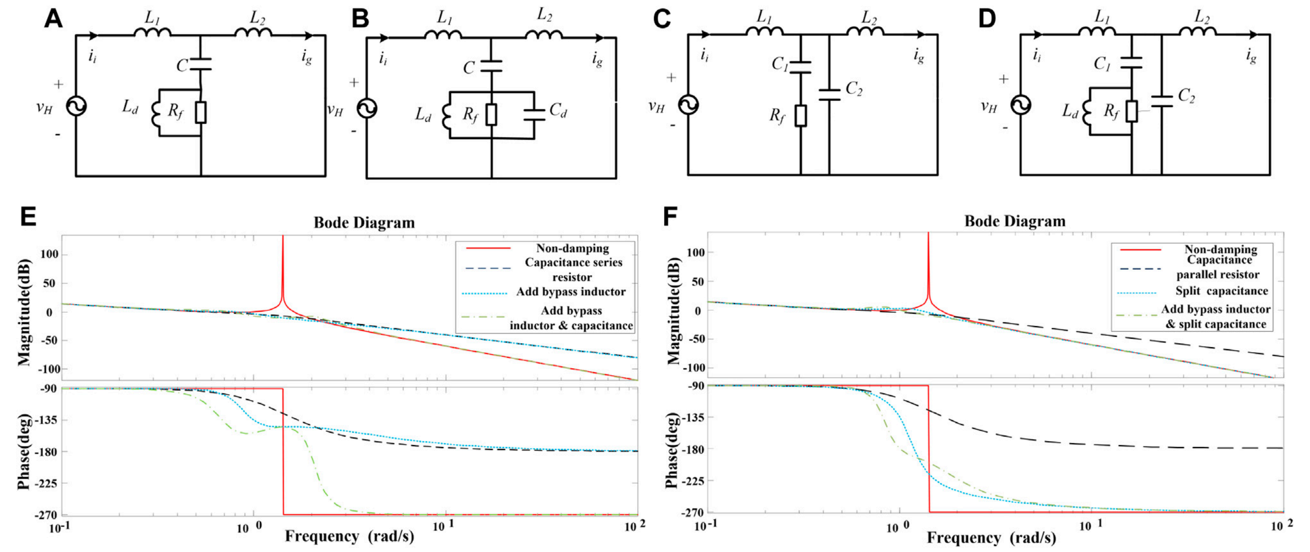

FIGURE 3 | Equivalent model and Bode diagrams of four improved topologies. **(A)** Bypass inductor. **(B)** Bypass inductor plus capacitors. **(C)** Split capacitors. **(D)** Split capacitor plus bypass inductor. **(E)** Bypass elements. **(F)** Split capacitor.

TABLE 1 | The characteristics of four improved topologies.

Improved topologies	Characteristics
Fig. 4a	1. The series resistor maintains the LCL attenuation ability of high-frequency harmonics 2. The inductor reduces damping loss
Fig. 4b	1. The split capacitor improves the LCL attenuation ability of high-frequency harmonics 2. The inductor reduces damping loss 3. More components lead to increased costs and the complex design\enleadertwodots
Fig. 4c	1. The split capacitor improves the LCL attenuation ability of high-frequency harmonics
Fig. 4d	1. The split capacitor improves the LCL attenuation ability of high-frequency harmonics 2. The inductor reduces damping loss 3. More components lead to increased costs and the complex design

reduce the attenuation ability of high-frequency harmonics, whereas the parallel resistor does not affect the attenuation ability of high-frequency or low-frequency harmonics, but it bears the equivalent voltage on the capacitor causing greater system loss. Comparing two passive damping strategies, this study chooses the capacitor series resistor method due to its lower extra loss of the system.

Four improvement methods and their frequency characteristics (Xiao et al., 2018) are compared to solve the problem that the passive damping method selected in this study increases the loss of the filter system, as shown in **Figure 3**. From the comparison between the Bode diagram and **Table 1**, it can be seen that the improved topology shown in **Figure 3A** has improved both in terms of system loss and design simplicity. By connecting a small L_f in parallel with R_f (Wang et al., 2018), the impedance of L_f connected in parallel at the fundamental frequency is much less than R_f. The low impedance becomes the main current flow path so that the fundamental wave loss on R_f is reduced, and the parallel relationship between the small inductor and the resistor at a high frequency reduces the total impedance of the branch and the extra loss of the system.

2.3 The Mathematical Model of the System

According to the passive damping improved topology, is defined as the impedance ratio of L_f to R_f at the switching frequency, as shown in **Eq. 8**, and the transfer function of the system is shown in **Eq. 9**:

$$\alpha = \omega_s L_f \big/ R_f \,, \tag{8}$$

$$\left\{\begin{aligned} \frac{I_g(s)}{U_H(s)} &= \frac{R_f L_f C s^2 + L_f s + R_f}{\left(\begin{gathered} L_1 L_2 L_f C s^4 + \left[L_1 L_2 + (L_1 + L_2) L_f\right] R_f C s^3 \\ + (L_1 + L_2) L_f s^2 + (L_1 + L_2) R_f s \end{gathered}\right)} \\ \frac{I_g(s)}{I_i(s)} &= \frac{R_f L_f C s^2 + L_f s + R_f}{L_2 L_f C s^3 + \left(L_2 + L_f\right) R_f C s^2 + L_f s + R_f} \end{aligned}\right. . \tag{9}$$

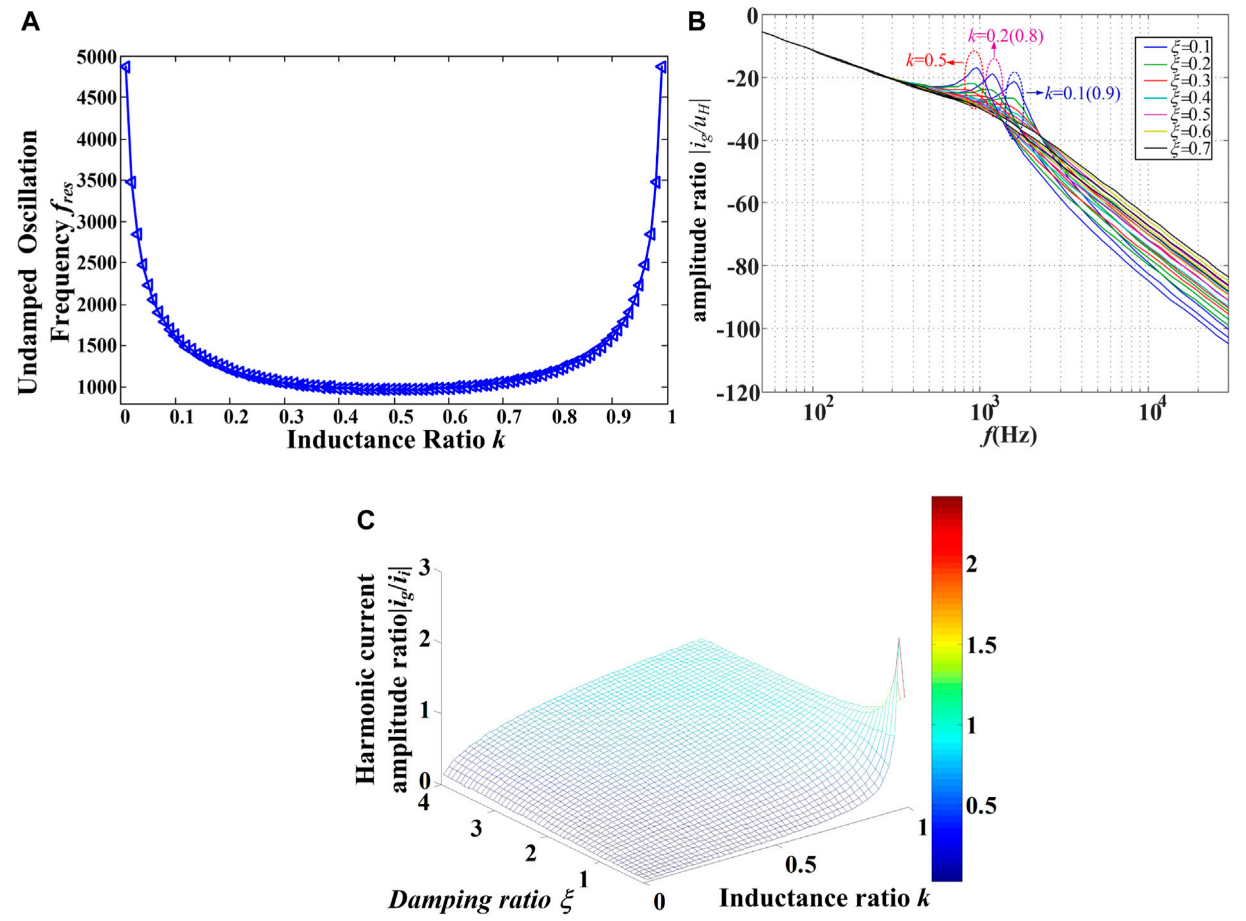

FIGURE 4 | Diagram of the relationship among different parameters. **(A)** undamped oscillation frequency f_{res} and inductor ratio k. **(B)** Amplitude ratio $|i_g/u_H|$ capacitors. **(C)** Amplitude ratio $|i_g/i_i|$.

3 INTERRELATIONSHIP BETWEEN PARAMETERS OF LCL FILTER

3.1 Constraints on Capacitor *C* and Total Inductor L_T

In the design process of the LCL filter, first, determine the size of capacitor C and inductor L_T. When the filter system is working normally, C has a high impedance characteristic in the low-frequency band and a low impedance characteristic in the high-frequency band. Under the same filtering effect, using a larger C reduces the used total inductor value (Beres et al., 2016b). However, an excessive C value increases the reactive current flowing into the capacitor and reduces the power factor and the system efficiency. The upper limit of C should be calculated based on the fundamental capacitive reactive power allowed by the system (Kumar et al., 2020).

When designing the inductor, C and R_f branches are usually considered open circuits so that the effect of the LCL filter is equivalent to that of an L-type filter with a total inductor of L_T, which is convenient for parameter design. The design criteria of L_T should minimize the current harmonics and meet the requirements of fast current tracking, the ripple requirements of the grid-connected current determine the lower limit of L_T, and its dynamic requirements determine the upper limit of the inductor value.

3.2 Ratio *k* (L_1/L_T)

One of the goals of the LCL filter design is to reduce the size of passive components as much as possible, while ensuring that sufficient harmonic attenuation and reactive power are compensated by the filter. According to the analysis of **Eqs. 3**, **4**, under the premise of determining parameters L_T and C, the proportional relationship between two inductor values also affects the angular frequency of the undamped oscillation of the system ω_{res}. Hence, it is necessary to carry out research on the proportional relationship between the inductors:

$$L_1 = kL_T \, , \tag{10}$$

where k is the proportion of the inductor on the inverter side.

Then, the undamped oscillation frequency f_{res} of the LCL filter is expressed as

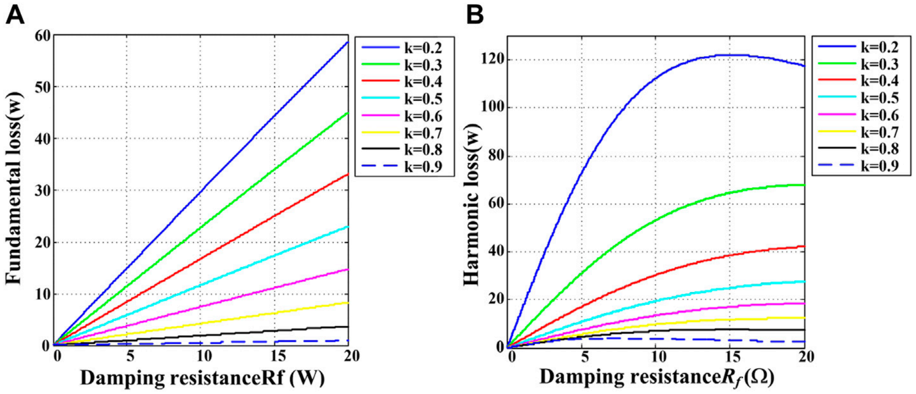

FIGURE 5 | Relation between power loss of R_f, inductor ratio k, and resistor of R_f. **(A)** Fundamental wave loss. **(B)** Harmonic loss.

$$f_{res} = \frac{1}{2\pi} \cdot \sqrt{\frac{1}{k(1-k)L_T C}}. \tag{11}$$

Figure 4A is a diagram of the relationship between f_{res} and k at undamped oscillation frequency, which shows that the resonance frequency is the lowest when k is 0.5.

According to the relationship of **Eqs. 3**, **4**, **10**, **11** is transformed into the expression of ω_{res}, ξ, and k:

$$\frac{I_g(s)}{U_H(s)} = \frac{1}{L_T s} \frac{\left(2\xi\omega_{res}s + \omega_{res}{}^2\right)}{s^2 + 2\xi\omega_{res}s + \omega_{res}{}^2}. \tag{12}$$

The equivalent switching frequency f_s is set to 3 kHz as shown in **Figure 4B**, Assuming that the equivalent switching frequency fs is 3 kHz, the value of ξ changes from 0.1 to 0.7, and k is 0.1 (0.9), 0.2 (0.8) and 0.5, respectively, the amplitudes of i_g and U_h are shown in **Figure 4B**. The closer k is to 0.5, the lower the resonance frequency of the LCL filter is and the better the filtering effect on the higher harmonics generated by the modulation strategy is. The larger ξ is, the better the suppression effect of the resonance peak is. However, the increase in ξ makes the LCL filter's attenuation effect on high-frequency ripple worse. **Figure 4C** shows the relationship between the ratio of i_g to the absolute value of i_i and k or ξ. From **Figure 4C**, it can be found that when k and ξ are small, the value of $|i_g/i_i|$ is also small. When k or ξ is large, the value of $|i_g/i_i|$ is also large, especially when k is close to 1 and ξ is close to 0, and $|i_g/i_i|$ may even be greater than 1. At this time, the harmonics injected by the LCL filter into the grid are greater than those of the converter side. The function of the LCL filter changes from filtering out the harmonic voltage and current, in a general sense, to amplifying harmonic currents.

3.3 Relation Between Ratio *k* and Other Key Parameters

Based on **Eqs. 3**, **4**, it can be seen that k and R_f also affect each other.

Figure 5 shows the relationship between the power loss of the LCL filter, the inductor proportional coefficient k, and R_f. **Figure 5** assumes that the harmonic energy is concentrated at the switching frequency. The larger the value of k, the smaller the loss. When the value of k is the same, the fundamental loss and switching subharmonic loss first increase and then decrease with R_f. Through the above analysis, the relationship among the ratio of correlation coefficient of the system, k, and ξ is obtained. The values of k and ξ that optimize all system performance cannot be found. Thus, a compromise should be made in the practical design, according to the operation situation.

1) When $k = 0.5$, f_{res} is minimal. When k approaches 0(1), f_{res} gets larger.
2) As ξ increases, the smaller the resonance peak is, the larger the high-frequency attenuation is and vice versa.
3) As k or ξ increases, $|i_g/i_i|$ gets larger; k is the main influencing factor of $|i_g/i_i|$.
4) As k increases, damping resistor power loss (P_{loss}) gets smaller. As ξ increases, P_{loss} increases firstly and then decreases*.

*ξ is proportional to R_f when k is determined.

3.4 Impedance Ratio *α*

It is obtained from Part B that the system reaches the lowest resonant frequency when k is 0.5, and Bode diagrams of each transfer function are obtained under the condition that R_f is a fixed value and α is different based on **Eq. 8**, as shown in **Figures 6A–C**.

From **Figures 6A,B**, it can be seen that the LCL filter with the damping inductor has a lower resonance frequency and better high-frequency harmonic filtering effect than that without the damping inductor. However, it also has the disadvantage of large gain at a resonance frequency. **Figures 6A–C** show that the harmonic current gain at the resonance frequency decreases as α increases. Because the harmonics are mainly concentrated in the part above the switching frequency, this disadvantage has little effect on the filtering effect. It can be seen from **Figure 6C** that the introduction of L_f basically does not affect the fundamental wave current flowing into C, and in terms of switching sub-harmonic currents, the introduction of the damping inductor reduces the flow of C. The switching sub-harmonic current is slightly smaller than the switching sub-harmonic current without the damping inductor.

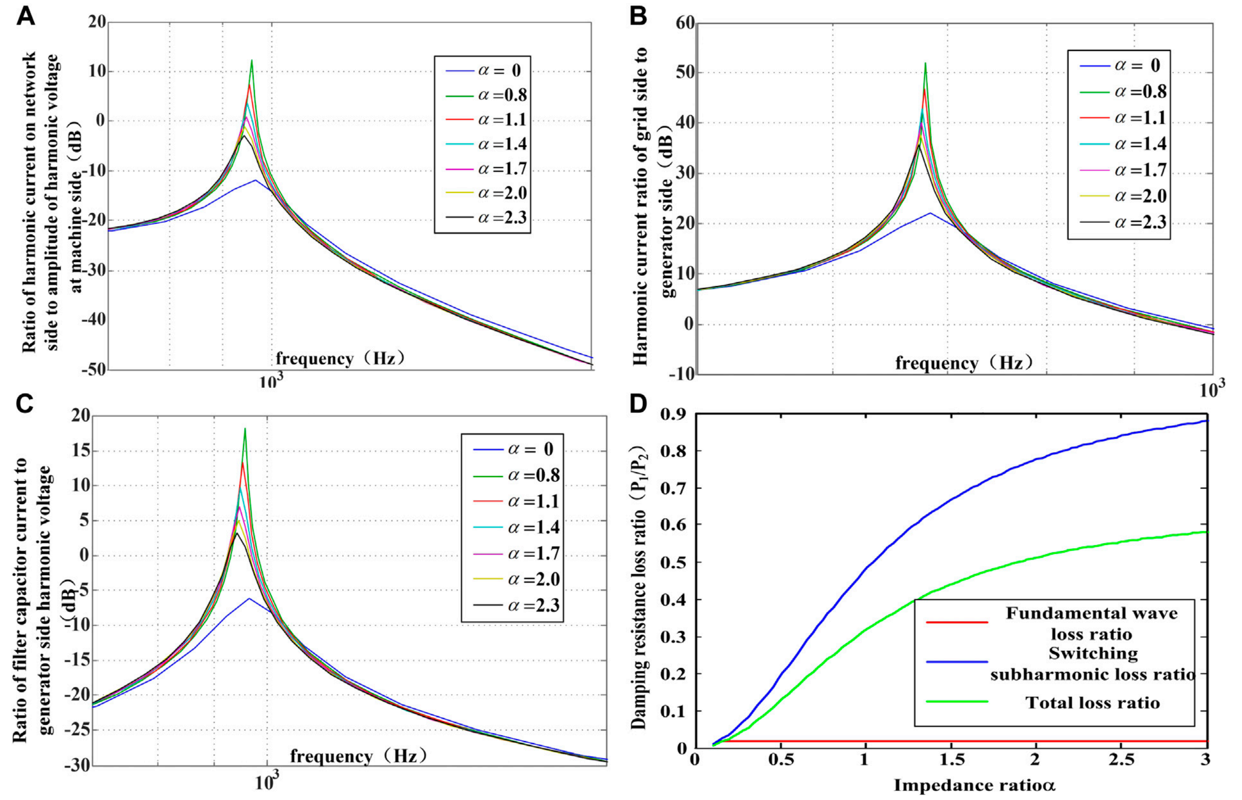

FIGURE 6 | Bode diagrams and damping resistance loss ratio of the LCL filter. **(A)** Ratio of grid-side harmonic current to machine-side amplitude of harmonic voltage. **(B)** Ratio of grid-side harmonic current to machine-side harmonic current. **(C)** Ratio of filter capacitor current to machine-side harmonic voltage. **(D)** Damping resistance loss ratio of LCL filter with damping inductance and without damping inductance.

Figure 6D shows the damping resistance loss ratio of the LCL filter with and without damping inductance. It can be seen from **Figure 6D** that, as α increases, both the fundamental wave loss ratio and the switching harmonic loss increase because L_f has a weak impedance to the fundamental wave, so the fundamental wave current flowing through C basically flows into L_f, and the fundamental wave loss on the damping resistor is small. As α increases, L_f also increases accordingly, which increases the system cost. Therefore, this study chooses $\alpha = 1$. At this time, the loss on the damping resistor of the LCL filter with damping inductor is 1/4–1/3 of that without the damping inductor.

4 DETERMINATION OF FILTER PARAMETERS

Based on the analysis process of Part 3, the design parameters of the LCL filter k and α is set to 0.5 and 1. Under this condition, the resonant system frequency is the lowest and the damping loss is the smallest.

Figure 7 presents the algorithm proposed in this study. The LCL filter is operated as an integrated filter unit instead of separately considering the effects of the grid-connected and the inverter sides. The steps of this design are simple and convenient for adjustment. In addition, this design satisfies the most filter requirements.

The specific operation steps are as follows:

1) Select the basic damping and improved topology.
2) Determine k and α based on Parts 3.1 and 3.4.
3) Design L_T and C in the LCL filter.
4) Determine the R_f range achieved by the maximum attenuation ratio k and α at the resonant angular frequency and the equivalent switching angular frequency.
5) Properly select the inductor value and then solve the actual inductor value on the grid-connected and the inverter sides.
6) Perform a physical design based on harmonic attenuation analysis and THD analysis of the filter.

4.1 Calculating the Total Capacitor *C*

As power factor and efficiency lead to problems in the system, the upper limit of C needs to be considered:

$$C \le \frac{Q_C}{\omega_0 {U_{line}}^2} = \frac{bP_{rated}}{\omega_0 {U_{line}}^2}\ . \tag{13}$$

In **Eq. 13**, Q_c is the fundamental capacitive reactive power allowed by the system, P_{rated} is the total power of the system, b is

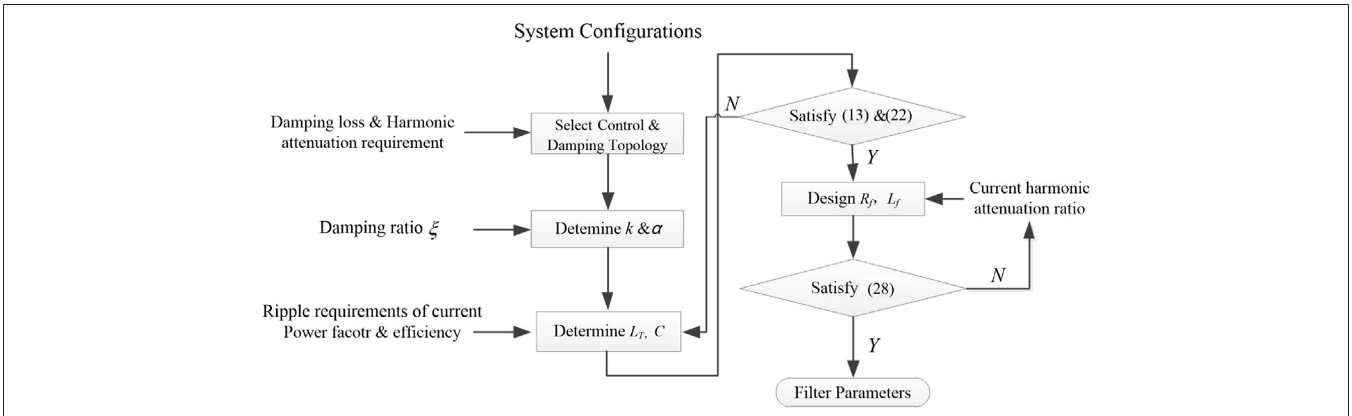

FIGURE 7 | The design process of the LCL filter, where Y and N stand for yes and no, respectively.

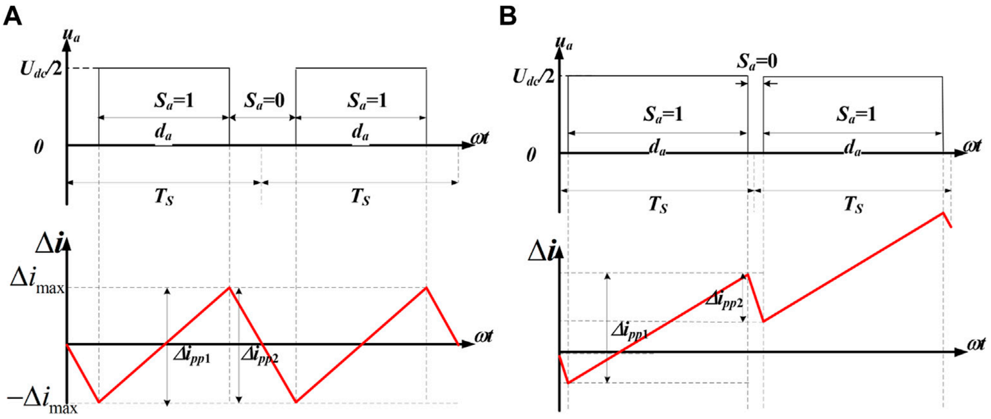

FIGURE 8 | Corresponding situation of phase voltage pulse and phase current ripple (phase *a*). **(A)** $i_a = i_{\max}$. **(B)** $i_{\max} = 0$.

the percentage of capacitive reactive power in the total power, ω_0 is the grid voltage angular frequency, and U_{line} is the grid line voltage valid value.

4.2 Calculating the Total Inductor L_T

The lower limit of L_T is determined by the ripple requirements of the grid-connected current, and its upper limit is determined by dynamic requirements.

4.2.1 Ripple Requirements of Current

Figure 8A shows a diagram of the output phase voltage pulse waveform near the peak of the *a*-phase current of the three-level converter. At this time, the *a*-phase voltage of power grid reaches its maximum E_m (system power factor is 1). According to the basic principle of the circuit, the peak-to-peak values of Δi_{pp1} and Δi_{pp2} during the rise and fall of the inductor current are obtained:

$$\begin{cases} \Delta i_{pp1} = \dfrac{U_{dc}}{6} \cdot \dfrac{(2 - S_{b1} - S_{c1}) - E_m}{L_T} \cdot d_a T_S \\ \Delta i_{pp2} = \dfrac{U_{dc}}{6} \cdot \dfrac{(-S_{b0} - S_{c0}) - E_m}{L_T} \cdot (1 - d_a) T_S \end{cases} . \tag{14}$$

S_{b1}, S_{b0} and S_{c1}, S_{c0} are the switching states of phases *b* and *c* when the switching states of phase *a* are 1 and 0, respectively. In a three-phase symmetric system, it can be known from the circuit theory that when a certain voltage or current reaches its maximum value, the other two phase voltages or currents are −0.5 times the maximum value. The deduction is as follows:

$$S_{xy} = 0 or - 1 \left(x = b, c; y = 0, 1 \right) . \tag{15}$$

In order to maintain the stability of the system, Δi_{pp1} should be equal to $-\Delta i_{pp2}$. Then, based on **Eqs. 14, 15**, the maximum ripple current $\Delta i_{\max}$ of phase *a* can be obtained as follows:

$$\Delta i_{\max} = \frac{2U_{dc}{}^2 + 3U_{dc}E_m - 9E_m{}^2}{18 L_T U_{dc}} T_S . \tag{16}$$

When the maximum ripple required by the system is $I_{rippleM}$, the total inductor L_T needs to meet

$$L_T \geq \frac{2U_{dc}{}^2 + 3U_{dc}E_m - 9E_m{}^2}{18 I_{rippleM} U_{dc}} T_S . \tag{17}$$

4.2.2 Requirements of Current Tracking Rapidity

Figure 8B is the diagram of output phase voltage pulse and the a-phase ripple current near the zero-crossing point of the a-phase current of the three-level converter. According to the basic principle of the circuit, the peak-to-peak value Δi_{pp1} and Δi_{pp2} during the rise and fall of the inductor current are obtained:

$$\begin{cases} \Delta i_{pp1} = \dfrac{U_{dc}}{6} \cdot \dfrac{(2 - S_{b1} - S_{c1})}{L_T} \cdot d_a T_S \\ \Delta i_{pp2} = \dfrac{U_{dc}}{6} \cdot \dfrac{(-S_{b0} - S_{c0})}{L_T} \cdot (1 - d_a) T_S \end{cases} . \tag{18}$$

According to the circuit theory, the voltages of phases b and c are $-\sqrt{3}/2$ and $\sqrt{3}/2$ times the maximum value, respectively, when the current of phase a crosses zero. The derivation is as follows:

$$\begin{cases} S_{by} = 0 or -1 (y = 0, 1) \\ S_{cy} = 0 or 1 (y = 0, 1) \end{cases} . \tag{19}$$

In order to meet the needs of fast current tracking, Δi_{pp1} and Δi_{pp2} need to meet the following relationship:

$$\frac{\Delta i_{pp1} - \Delta i_{pp2}}{T_s} \geq \frac{I_m \sin(\omega T_s)}{T_s} \approx I_m \omega \tag{20}$$

As d_a is approximately equal to 1 at the zero-crossing point of the a-phase current, the total inductor L_T needs to meet

$$L_T \leq \frac{U_{dc}}{6 I_m \omega} . \tag{21}$$

Based on the above analysis, the total inductor of the LCL filter is obtained based on the ripple current and current tracking conditions, as shown in **Eq. 22**. Due to cost and volume, L_T should be as close to its lower limit as possible in practical applications of high-voltage and high-power systems:

$$\frac{2 U_{dc}^2 + 3 U_{dc} E_m - 9 E_m^2}{18 I_{rippleM} U_{dc}} T_S \leq L_T \leq \frac{U_{dc}}{6 I_m \omega} . \tag{22}$$

4.3 Damping Resistor R_f

After the range of C and L_T are determined, R_f is designed according to the correlation degree of the parameters in part 3.

1) The lower limit is designed according to the attenuation effect at the resonant angular frequency from **Eq. 9**, at the value of ω_{res}, and the amplitude ratio of i_g to u_H is obtained as

$$\frac{|i_g|}{|u_o|} = \frac{\sqrt{4\xi^2 + 1}}{2\xi L_f \omega_{res}} = \frac{\sqrt{1/(4\xi^2) + 1}}{L_f \omega_{res}} . \tag{23}$$

If the system requires the maximum attenuation at ω_{res} to be κ ($0 < \kappa < 1$), then

$$\xi = \frac{\omega_{res} R_f C}{2} \geq \frac{1}{2\sqrt{(\kappa L_f \omega_{res})^2 - 1}} . \tag{24}$$

Based on the above derivation, the lower limit value that R_f should meet when $k = 0.5$ is calculated:

$$R_f \geq \frac{1}{\omega_{res} C \sqrt{(\kappa L_f \omega_{res})^2 - 1}} = \frac{1}{\sqrt{16\kappa^2 - 4C/L_f}} \tag{25}$$

2) Determine the upper limit value according to the current harmonic attenuation ratio from **Eq. 9**, at ω_{res}, and the amplitude ratio of i_g to i_i is obtained as

$$\frac{|i_g|}{|u_o|} = \frac{\sqrt{4\xi^2 \omega_{res}^2 \omega_s^2 + \omega_{res}^4}}{\sqrt{4\xi^2 \omega_{res}^2 \omega_s^2 + (\omega_{res}^4 - \omega_s^2/k)}} \tag{26}$$

When $k = 0.5$, $\omega_{res} \geq 2\omega_{res}$, if the system requires the current harmonic attenuation ratio at the equivalent switching frequency ω_s to be the maximum γ ($0 < \gamma < 1$), then

$$R_f \leq \frac{\sqrt{49\gamma^2 - 1}}{2\omega_{res} C \sqrt{1 - \gamma^2}} = \frac{1}{4}\sqrt{\frac{(49\gamma^2 - 1) L_f}{(1 - \gamma^2) C}} \tag{27}$$

Considering the attenuation effect at the resonance frequency and the current harmonic attenuation ratio, the upper and lower limits of R_f is obtained as follows:

$$\frac{1}{\sqrt{16\kappa^2 - 4C/L_f}} \leq R_f \leq \frac{1}{4}\sqrt{\frac{(49\gamma^2 - 1) L_f}{(1 - \gamma^2) C}} . \tag{28}$$

4.4 Design Example

In order to verify the design method proposed above, the minimum resonant frequency and the system loss are considered to design the LCL filter under the parameters as shown in **Table 2**. The overall design steps are as follows.

1) Control grid-side current and obtain the topology of series resistor with small parallel inductor shown in **Figure 3A**, which suppresses the resonant peak and reduces loss of the resistor.
2) Set k and α as 1, according to the principle of the minimum resonant frequency.
3) Determine the range of capacitor and total inductor according to **Eqs. 13**, **22**, and determine the range of added R_f, based on the harmonic attenuation ratio.

5 SIMULATION AND EXPERIMENTAL RESULTS

Based on the previous theoretical analysis, selecting a decimal point in device selection increases the difficulty of industrial design. Therefore, integer parameters are selected and the three-level NPC type SVG simulation and experimental model is established in MATLAB to verify the analysis of this study. The circuit schematic diagram is shown in **Figure 1**, and system parameters and LCL filter element parameters are shown in **Table 2**. L_T = 6 mH, C = 18 uF, R_f = 1Ω, and L_f = 0.08 mH

TABLE 2 | System parameters.

Parameters	Value
DC capacitor C_1, C_2	2000uF
Rated DC voltage U_d	750v
Equivalent switching frequency f_s	3kH$_z$
Equivalent value of grid-side line voltage U_g	380v
Current harmonic attenuation ratio at equivalent switching frequency γ	0.2
Undamped resonant angular frequency attenuation κ	0.707
Impedance ratio of damping inductor to resistor α	1
Rated active power P_{ref}	10kW
Total inductor L_T	5.497m$_H$ ~ 18.517 8 m$_H$
Total capacitor C	6.144 1u$_F$ ~ 22.043 6 u$_F$
Damping resistor R_f	0.353 96Ω ~ 3.947 8Ω
Damping inductor L_f	0.018 778m$_H$ ~ 0.209 44 m$_H$

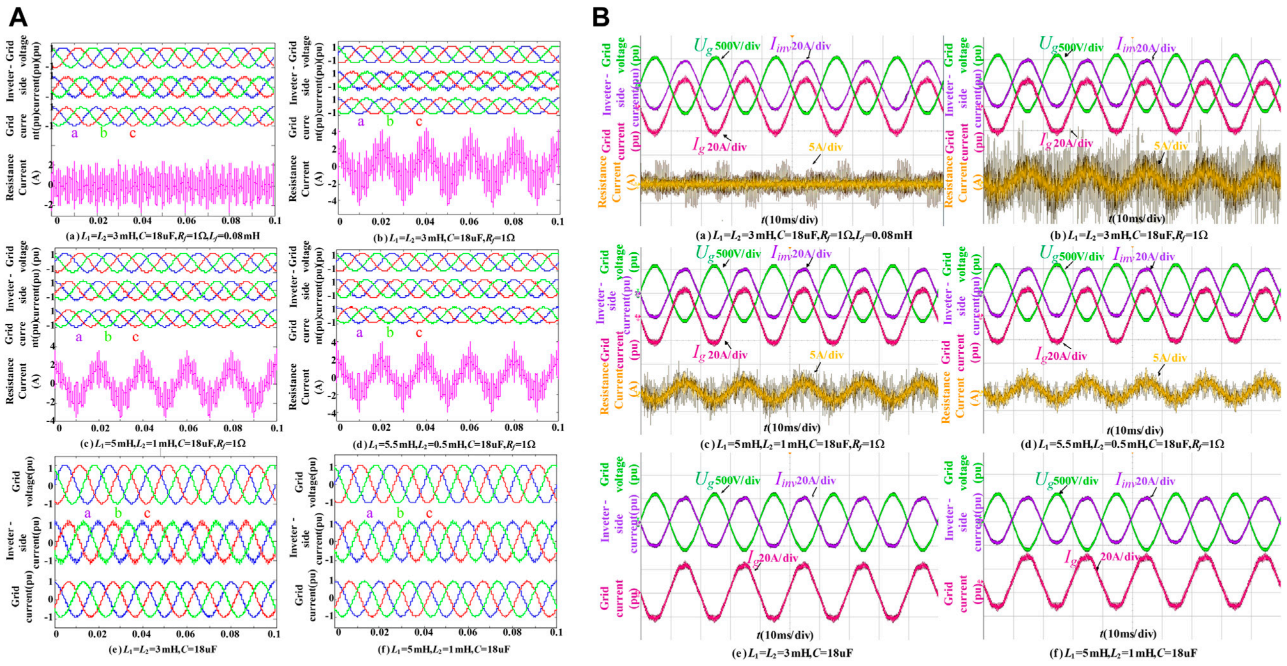

FIGURE 9 | Simulation and experimental results of the LCL filter under different key parameters **(A)** simulation result **(B)** experimental result.

are selected, and the simulation sampling time is 2e–6s. **Figure 9A** shows the simulation waveforms U_a, i_g, i_i, and i_R flowing through R_f during full power operation under different conditions. All the simulation results of different LCL filter parameters of each figure are shown in **Table 3**.

Table 4 is a quantitative comparison of the simulation and experimental results of different filter parameters. It mainly presents three aspects of the filter performance of the system, the total harmonic distortion (THD) of the i_i and that of i_g in the six cases, and $|i_g/i_i|$ and P_{loss}. From the simulation results of the above six different situations, it can be seen that the LCL filter design method based on the optimization of resonance frequency proposed in this study has advantages of small harmonic current into the grid and low damping resistor loss.

TABLE 3 | Comparison of systerm parameters.

Scheme	L_1 (mH)	L_2 (mH)	L_f (mH)	R_f (Ω)	C
A	3	3	0.08	1	18u$_F$
B	3	3	0	1	18u$_F$
C	5	1	0	1	18u$_F$
D	5.5	0.5	0	1	18u$_F$
E	3	3	0	0	18u$_F$
F	5	1	0	0	18u$_F$

Specifically, comparing **Figure 9A** with the relevant content in **Table 4**, it can be found that when the inductor ratio is the same, the existence of the damping resistor reduces the THD of the grid current because it suppresses the occurrence of resonance, and

TABLE 4 | Simulation/experimental results comparison of LCL filter under different key parameters.

Inductor ratio	Damping resistor	Damping inductor	THD_i	THD_g	Harmonic current	P_{loss}
K	R_f	L_f	(%)	(%)	Ratio ($\lvert i_g/i_i \rvert$)	(W)
0.5	1	$0.08m_H$	5.85/6.72	0.91/2.71	0.16/0.40	4.6/8.4
0.5	1	$0m_H$	5.89/7.06	0.94/3.46	0.16/0.49	18.1/34.2
5/6	1	$0m_H$	3.47/5.80	1.04/3.70	0.30/0.64	17.6/30.3
11/12	1	$0m_H$	3.15/5.25	1.68/3.99	0.53/0.76	17.4/29.5
0.5	0	$0m_H$	5.92/7.11	1.02/3.61	0.17/0.51	0/0
5/6	0	$0m_H$	3.47/5.94	1.32/3.89	0.38/0.70	0/0

TABLE 5 | Simulation and experimental values of THD and loss ratio with different methods.

	Simulation	Experiment	Simulation	Experiment
	THD%	*THD%*	$P_{loss}/P_{ref}\%$	$P_{loss}/P_{ref}\%$
This study	0.91	2.71	0.046	0.084
Method 1 Wang et al. (2017)	0.56	2	—	—
Method 2 Jayalath and Hanif (2017)	—	4.27	0.22	0.18
Method 3 Tang et al. (2020)	0.86	1.132	0.2165	0.229

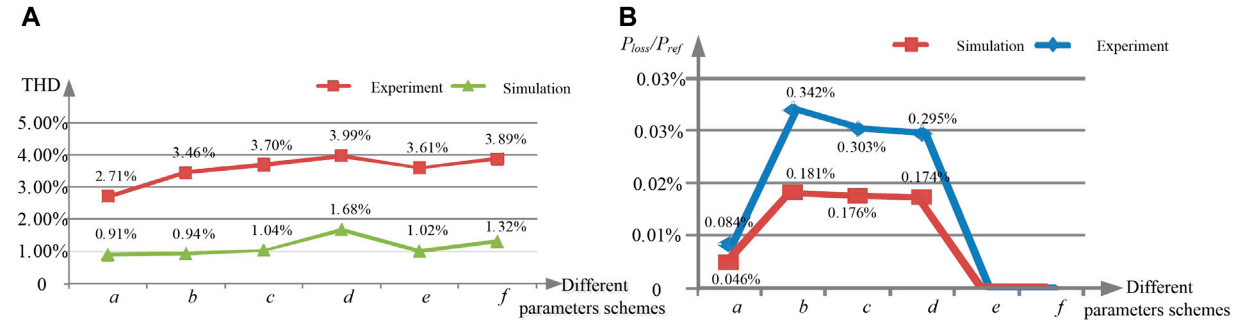

FIGURE 10 | Simulation and experimental results of THD and Ploss/Pref **(A)** THD result **(B)** Ploss/Pref result.

the existence of damping inductor reduces the loss of the damping resistor to about 1/4 of the original value, which is consistent with **Figure 6D**. Comparing the three graphs on the right of **Figure 9B** with **Table 4**, it can be found that when the damping resistor is the same, the closer the inductor ratio is to 0.5, the better the filtering effect is, which is consistent with **Figure 4A** and **Figure 4B**. The larger the inductor ratio is, the greater the harmonic current amplitude ratio is, which is consistent with **Figure 4C**. The larger the inductor ratio is, the smaller the damping resistor loss is, which is consistent with **Figure 6D**.

Figure 9B shows the experimental results of corresponding waveforms of grid voltage U_{ca}, inverter-side current i_{ib}, grid-side current i_{gb}, and current i_{Rb} flowing through the damping resistor when the three-level SVG system under different LCL filter parameters is running at full power. **Table 5** shows the relevant data analysis. Because the actual grid voltage contains about 2% of low-order harmonics, the grid-side current, the inverter-side current THD, and the damping resistor power are all larger than the simulated values. It can be seen from the above analysis that the theoretical analysis and simulation results are similar. **Figures 10A,B** show the gap between the simulation data and the real experimental results. Considering the influence of background harmonics of about 2%, the theory proposed in this study is verified by the above simulation and experimental results.

∗In the case of *e* or *f* in **Figure 10B**, the damping loss is not discussed without adding a damping resistor.

In order to further verify the optimization algorithm, the key parameters of the grid-side current THD and those of damping resistor loss are compared with the methods proposed in the existing literature, as shown in **Table 5**. For the parameter THD, it can be seen that there is little difference from the simulation value of Method 3 (Tang et al., 2020). Nevertheless, due to the high harmonic content of the power grid under laboratory conditions, the experimental value is larger and the THD part of the side current has a certain effect. Compared with Method 3 in terms of THD, it can be found that the method proposed in this study is not much different, which may be due to the simulation parameter setting and measurement error. For resistor loss ratio parameters P_{loss}/P_{ref}, except for Method 1 (Wang et al., 2017) that presents no measurement data, the proposed optimization method is different from the other existing methods. It makes much noticeable improvement in reducing the loss of the damping resistor.

5.1 CONCLUSION

Focusing on the correlation degree of system parameters is important for realizing a high-efficiency LCL filter. This study proposes a bypass inductor type LCL filter parameter optimization for a three-level grid-connected converter. In this design, the inductance ratio k and impedance ratio α are taken as the key variables, and it is found that the optimal undamped resonant frequency is achieved and the system loss is reduced when both κ and α equal 1 in the modified, passive damping topology of parallel inductors. In addition, the design provides a simple parameter design system. Based on the reactive power limit and current ripple, the range of parameters is calculated clearly. The design has great theoretical significance and application value through the simulation and experimental results to verify the validity of the proposed theory, which is especially suitable for large-power and low-switching frequency fields.

DATA AVAILABILITY STATEMENT

The original contributions presented in the study are included in the article/Supplementary Material, further inquiries can be directed to the corresponding author.

AUTHOR CONTRIBUTIONS

LN is responsible for the overall structure and revision. ZS, XZ, and ZA are responsible for writing and the simulation experiment. YZ and LJ are responsible for the evaluation and improvement of the paper.

FUNDING

This work was supported in part by National Natural Science Foundation of China (52177193); Key Research and Development Program of Shaanxi Province (2022GY-182); China Scholarship Council (CSC) State Scholarship Fund International Clean Energy Talent Project (Grant No. (2018) 5046,(2019)157); Open Research Fund of Jiangsu Collaborative Innovation Center for Smart Distribution Network, Nanjing Institute of Technology (XTCX202107).

REFERENCES

Albatran, S., Koran, A., Smadi, I. A., and Ahmad, H. J. (2018). Optimal Design of Passive RC-Damped LCL Filter for Grid-Connected Voltage Source Inverters. *Electr. Eng.* 100, 2499–2508. doi:10.1007/s00202-018-0725-5

Ben Saïd-Romdhane, M., Naouar, M. W., Slama-Belkhodja, I., and Monmasson, E. (2017). Robust Active Damping Methods for LCL Filter-Based Grid-Connected Converters. *IEEE Trans. Power Electro.* 32, 6739–6750. doi:10.1109/TPEL.2016.2626290

Beres, R. N., Wang, X., Liserre, M., Blaabjerg, F., and Bak, C. L. (2016a). A Review of Passive Power Filters for Three-phase Grid-Connected Voltage-Source Converters. *IEEE J. Emerg. Sel Top. Power Electron.* 4 (1), 54–69. doi:10.1109/jestpe.2015.2507203

Beres, R. N., Wang, X., Blaabjerg, F., Liserre, M., and Leth Bak, C. (2016b). Optimal Design of High-Order Passive-Damped Filters for Grid-Connected Applications. *IEEE Trans. Power Electro.* 31, 2083–2098. doi:10.1109/tpel.2015.2441299

Bosch, S., Staiger, J., and Steinhart, H. (2018). Predictive Current Control for an Active Power Filter with LCL-Filter. *IEEE Trans. Ind. Electro.* 65, 4943–4952.doi:10.1109/TIE.2017.2772176

Falkowski, P., and Sikorski, A. (2018). Finite Control Set Model Predictive Control for Grid-Connected AC–DC Converters with LCL Filter. *IEEE Trans. Ind. Electro.* 65 (4), 2844–2852. doi:10.1109/tie.2017.2750627

Guo, X. Q., Wu, W. Y., and Gu, H. R. (2010). Modeling and Simulation of Direct Output Current Control for LCL-Interfaced Grid-Connected Inverters with Parallel Passive Damping. *Simulation Model. Pract. Theor.* 18 (7), 946–956. \\enleadertwodots. doi:10.1016/j.simpat.2010.02.010

Guzman, R., de Vicuña, L. G., Castilla, M., Miret, J., and de la Hoz, J. (2018). Variable Structure Control for Three-phase LCL-Filtered Inverters Using a Reduced Converter Model. *IEEE Trans. Ind. Electro.* 65, 5–15. doi:10.1109/tie.2017.2716881

He, J., Yun, W. L., Xu, D., Liang, X., Liang, B., and Wang, C. (2017). Deadbeat Weighted Average Current Control with Corrective Feed-Forward Compensation for Micro-grid Converters with Nonstandard LCL Filter. *IEEE Trans. Power Electro.* 32 (4), 2661–2674. doi:10.1109/tpel.2016.2580005

Huang, S., Tang, F., Xin, Z., Xiao, Q., and Chiang Loh, P. (2019). Grid-Current Control of a Differential Boost Inverter with Hidden LCL Filters. *IEEE Trans. Power Electro.* 34, 889–903. doi:10.1109/tpel.2018.2817640

Jayalath, S., and Hanif, M. (2017). Generalized LCL-Filter Design Algorithm for Grid-Connected Voltage-Source Inverter. *IEEE Trans. Ind. Electro.* 64 (3), 1905–1915. doi:10.1109/tie.2016.2619660

Kim, Y. J., and Kim, H. (2019). Optimal Design of LCL Filter in Grid-Connected Inverters. *Power Electron. IET* 12 (7), 1774–1782. doi:10.1049/iet-pel.2018.5518

Kouchaki, A., and Nymand, M. (2018). Analytical Design of Passive LCL Filter for Three-phase Two-Level Power Factor Correction Rectifiers. *IEEE Trans. Power Electro.* 33, 3012–3022. \\enleadertwodots. doi:10.1109/tpel.2017.2705288

Kumar, N., Mohamadi, M., and Mazumder, S. K. (2020). Passive Damping Optimization of the Integrated-Magnetics-Based Differential-Mode Ćuk Rectifier. *IEEE Trans. Power Electro.* 35, 10008–10012. doi:10.1109/tpel.2020.2981918

Liserre, M., Blaabjerg, F., and Hansen, S. (2005). Design and Control of an LCL-Filter-Based Three Phase Active Rectifier. *IEEE Trans. onIndustry Appl.* 41 (5), 1281–1290. doi:10.1109/tia.2005.853373

Liu, B., Li, Z., Chen, X., Huang, Y., and Liu, X. (2018). Recognition and Vulnerability Analysis of Key Nodes in Power Grid Based on Complex Network Centrality. *IEEE Trans. Circuits Syst. Express Briefs* 65 (3), 346–350. doi:10.1109/tcsii.2017.2705482

Liu, B., Li, Z., Dong, X., Yu, S. S., Chen, X., Oo, A. M. T., et al. (2021). Impedance Modeling and Controllers Shaping Effect Analysis of PMSG Wind Turbines. *IEEE J. Emerg. Sel. Top. Power Electron.* 9 (2), 1465–1478. doi:10.1109/jestpe.2020.3014412

Su, M., Cheng, B., Sun, Y., Tang, Z., Guo, B., Yang, Y., et al. (2019). Single-Sensor Control of LCL-Filtered Grid-Connected Inverters. *IEEE Acess* 7, 38481–38494. doi:10.1109/access.2019.2906239

Tang, W., Ma, K., and Song, Y. (2020). Critical Damping Ratio to Ensure Design Efficiency and Stability of LCL Filters. *IEEE Trans. Power Electro.* 36, 315–325. doi:10.1109/TPEL.2020.3000897

Wang, X., Blaabjerg, F., and Loh, P. C. (2017). Passivity-Based Stability Analysis and Damping Injection for Multiparalleled VSCs with LCL Filters. *IEEE Trans. Power Electro.* 32, 8922–8935. doi:10.1109/tpel.2017.2651948

Wang, B., Shen, Z., Hong, L., and Jianhui, H. (2018). Linear ADRC Direct Current Control of Grid-Connected Inverter with LCL Filter for Both Active Damping and Grid Voltage Induced Current Distortion Suppression. *IET Power Electro.* 11 (11), 1748–1755. doi:10.1049/iet-pel.2017.0787

Wei, M., and Gao, C. (2017). "Comparison and Analysis of a Novel Passive Damping for LCL Filtered Voltage Source Inverters," in 2017 20th International Conference on Electrical Machines and Systems (ICEMS), Sydney, NSW, 1–5.

Xia, W., and Kang, Js. (2017). Stability Analysis of Static Synchronous Compensator in LCL Distribution Network Considering the Influence of Digital Control Delay. *Trans. China electro Tech. Soc.* 32 (14), 205–216. doi:10.19595/j.cnki.1000-6753.tces.L70752

Xiao, Z., Li, T., Xian, J., Zhang, H., Ma, Z., and Kang, J. (2018). Direct Grid-Side Current Model Predictive Control for Grid-Connected Inverter with LCL Filter. *IET Power Electro.* 11 (15), 2450–2460. doi:10.1049/iet-pel.2018.5338

Xiong, L., Liu, X., Liu, Y., and Zhuo, F. (2020). Modeling and Stability Issues of Voltage-Source Converter Dominated Power Systems: a Review. *CSEE J. Power Energy Syst.*. doi:10.17775/CSEEJPES.2020.03590

Xiong, L., Liu, X., Zhang, D., and Liu, Y. (2021). Rapid Power Compensation Based Frequency Response Strategy for Low Inertia Power Systems. *IEEE J. Emerging Selected Top. Power Electro.* 9 (4), 4500–4513. doi:10.1109/jestpe.2020.3032063

Xiong, L., Liu, X., and Liu, Y. (2021). Decaying DC and Harmonic Components Detection for Absorbing Impact Load Currents in Weak Grids. *IEEE Trans. Power Deliv.* 36 (3), 1907–1910. doi:10.1109/tpwrd.2020.3038077

Yao, W., Yang, Y., Zhang, X., Blaabjerg, F., and Chiang Loh, P. (2017). Design and Analysis of Robust Active Damping for LCL Filters Using Digital Notch Filters. *IEEE Trans. Power Electro.* 32 (3), 2360–2375. \\enleadertwodots. doi:10.1109/tpel.2016.2565598

Young, H. A., Marin, V. A., Pesce, C., and Rodriguez, J. (2020). Simple Finite-Control-Set Model Predictive Control of Grid-Forming Inverters with LCL Filters. *IEEE Access* 8 (8), 1246–1256. \\enleadertwodots. doi:10.1109/access.2020.2991396

Zeng, Z., Xu, S., Ran, L., and Chen, M. (2016). Active Dampers and Control for Resonant Suppression of AC Micro-Grid. *Power Autom. equip.* 36 (03), 15–20. doi:10.16081/j.issn.1006-6047.2016.03.003

Zhang, C., Li, Y., Jia, C., Fu, H., Zhang, X., Zhang, H., et al. (2021). Direct Active Damping Control for Grid-Connected AC/DC Converter with LCL Filter Using Augmented Look-Up Tab. *IET Power Electro.* 14 (6), 1089–1101. doi:10.1049/pel2.12090

Zheng, C., Liu, Y., Li, Q., Liu, S., Zhang, B., Wang, Y., et al. (2019). Integrated Design Method for LCL-type Filter and Current Controller to Improve Inverter Adaptability to Grid Impedance. *IET Power Electro.* 12 (12), 3295–3305. doi:10.1049/iet-pel.2019.0358

Conflict of Interest: The authors declare that the research was conducted in the absence of any commercial or financial relationships that could be construed as a potential conflict of interest.

frontiers in Energy Research

ORIGINAL RESEARCH
published: 17 March 2022
doi: 10.3389/fenrg.2021.828281

The Implementation of Fuzzy PSO-PID Adaptive Controller in Pitch Regulation for Wind Turbines Suppressing Multi-Factor Disturbances

Yixiang Shao, Jian Liu, Junjie Huang, Liping Hu, Liang Guo and Yuan Fang*

NARI Group Corporation, Nanjing, China

The stability of wind turbine output is affected by multi-factor disturbances, which makes traditional proportion-integral-differential (PID) control strategy hardly achieve a satisfactory effect. Hence, a pitch control strategy based on fuzzy adaptive particle-swarm-optimization (PSO)-PID is proposed in this paper. Firstly, the models of wind turbine, pitch regulator, and permanent magnet synchronous generator (PMSG) are built. Then, the influence of various disturbances, such as blade deformation, installation errors, and external wind speed, on the wind wheel speed is analyzed. Furtherly, a wind turbine pitch control strategy is devised in detail, in which the PID parameters are initially optimized by PSO and adaptively adjusted by fuzzy controller. Simulations under gust wind and turbulent wind conditions are carried out, and the results show that compared with fuzzy PID and PID, the fuzzy adaptive PSO-PID could reduce errors of wind wheel speed and wind turbine output power effectively.

Keywords: wind turbine, pitch regulation, fuzzy PSO-PID adaptive controller, disturbances suppression, turbulent wind

Edited by:
Liansong Xiong,
Nanjing Institute of Technology (NJIT), China

Reviewed by:
Xiaokang Liu,
Politecnico di Milano, Italy
Li Rong,
Nanjing Institute of Technology (NJIT), China

****Correspondence:***
Junjie Huang
hjj47634@163.com

Specialty section:
This article was submitted to Process and Energy Systems Engineering, a section of the journal Frontiers in Energy Research

Received: *03 December 2021*
Accepted: *20 December 2021*
Published: *17 March 2022*

Citation:
Shao Y, Liu J, Huang J, Hu L, Guo L and Fang Y (2022) The Implementation of Fuzzy PSO-PID Adaptive Controller in Pitch Regulation for Wind Turbines Suppressing Multi-Factor Disturbances. Front. Energy Res. 9:828281. doi: 10.3389/fenrg.2021.828281

INTRODUCTION

With the aggravation of energy crisis and environmental deterioration of the earth in recent years, the development of renewable energy is more and more urgently demanded. Wind power, an effective mean to deal with the energy crisis, has been widely used in many countries. Its safety and stability are the focuses of attention. The control technology of wind turbines has evolved from a fixed pitch technology to a variable pitch control technology with better efficiency and stability (Mughal and Li, 2015). In a variable pitch control system, the pitch angle changes with the change of wind speed to stabilize wind turbine's output power when the wind speed is stronger than the rated wind speed (Liu et al., 2018). This could not only maintain the high efficiency but also ensure the safe operation of the wind turbine when the wind speed changes (Barahona et al., 2011). **Figure 1** shows the control system of the wind turbine (Xiong et al., 2016), including the pitch control system and the power control system (Xiong et al., 2020 and Xiong et al., 2021).

At present, traditional proportion-integral-differential (PID) control is mostly applied for the pitch regulation in the wind turbine control system. A self-tuning PID control method using reinforcement learning is proposed for the pitch control of large wind turbine generator (Kim et al., 2011). To overcome the shortcomings of conventional PI controller and adapt to nonlinear characteristics of wind turbines, an

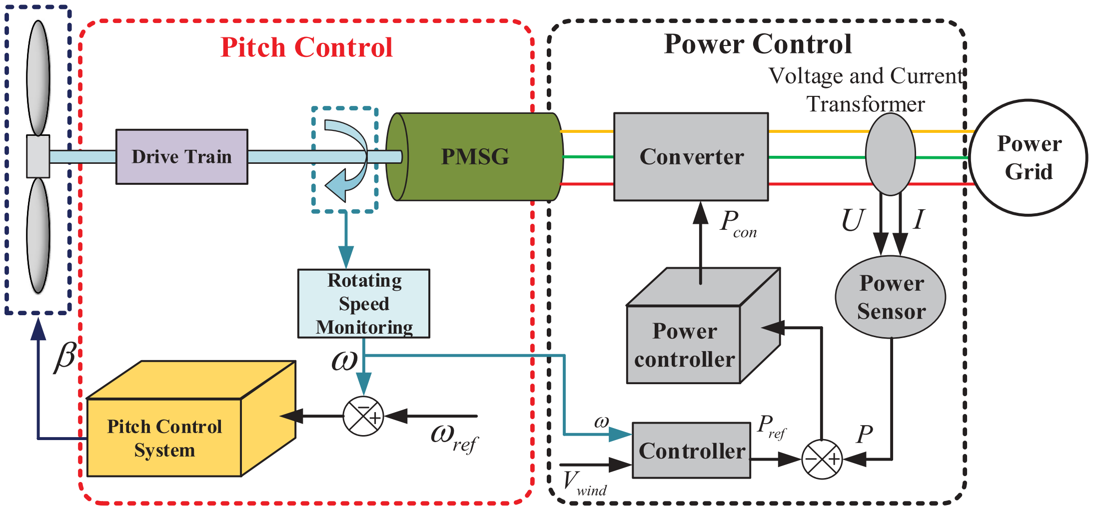

FIGURE 1 | Schematic diagram of the wind turbine control system.

expert PID controller based on a tracking differentiator is proposed in the literature (Anjun et al., 2011). In the literature (Zahra et al., 2017), a PID controller optimized by particle-swarm-optimization (PSO) is designed to capture the maximum power. However, in actual operation, the wind turbine will be affected not only by the instantaneous wind on the wind turbine but also by many other factors, such as initial parameter error, environmental changes, and blade changes. The factors above bring huge challenges for the pitch control strategy design. In severe cases, it may even cause accidents such as the collapse of the wind turbine tower and the burning of the engine room. Therefore, the adaptive pitch control strategy is particularly important for the stable operation of the wind turbine. A nonlinear PID control strategy is designed in the literature (Liu et al., 2017) to ensure the accuracy and stability of the pitch control system, while the response speed is slow. In the literature (Jafarnejadsani et al., 2013), a pitch regulation strategy is proposed based on radial basis function neural network, which enables the wind turbine's output to be smoother under different wind speeds. In the literature (Fdaili et al., 2017), PI controller and fuzzy logic control is used to control the blade pitch angle to limit the output power of the wind turbine at high wind speeds. In order to improve the utilization rate of wind energy, an independent pitch system of proportional resonant controller to ensure the rated power output at high wind speeds is adopted in the literature (Wang et al., 2020).

In this paper, the influence of various disturbances, including external wind speed, blade deformation, environmental changes, and initial parameter errors, on the wind turbine is taken into account. An adaptive pitch control strategy for suppressing multi-factor disturbances is proposed. In the proposed control strategy, the initial parameters of PID are optimized PSO algorithm, and fuzzy rules are designed to adjust its parameters dynamically. Then, simulation analysis is performed under rated conditions to validate the design. The results demonstrate that the control strategy could always maintain the wind wheel speed and the wind turbine's power around rated values and it has higher performance and robustness against disturbance than fuzzy PID control and PID control.

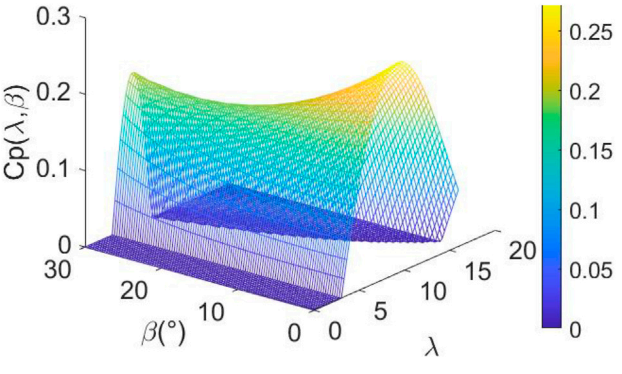

FIGURE 2 | The curve of wind turbine's power coefficients.

AERODYNAMIC CHARACTERISTICS OF WIND TURBINE

The wind power generation system is mainly composed of a mechanical part and an electromechanical conversion part. Combined with the analysis of aerodynamics and Betz theory, the mechanical power captured by the wind turbine from wind energy could be described by (Yin et al., 2017)

$$P_w = \frac{1}{2}\rho\pi R^2 V^3 C_p(\lambda,\beta) \tag{1}$$

where, ρ is the air density, R is the radius of the wind turbine, V is the wind turbine speed, $C_p(\lambda,\beta)$ is the utilization rate of wind energy, β is the pitch angle, and λ is the blade tip speed. The expression of wind energy utilization rate $C_p(\lambda,\beta)$ is shown as

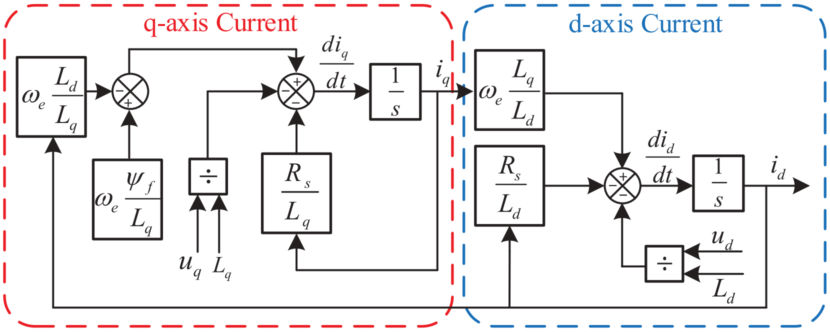

FIGURE 3 | Block diagram of PMSG.

$$C_p(\lambda,\beta) = (0.44 - 0.0167\beta)\sin\left[\frac{\pi(\lambda-3)}{15-0.3\beta}\right] - 0.00184(\lambda-3)\beta \tag{2}$$

The curve of wind turbine's power coefficients is shown in **Figure 2**.

It could be seen from **Figure 2** that there is a maximum value of $C_p(\lambda,\beta)$ for each value of β and the value of λ corresponding to this point is the best blade tip speed. When the external wind speed is stronger than the rated wind speed, β is a fixed value. In order to maintain the maximum wind energy utilization rate, the generator speed should be adjusted according to the wind speed to achieve the best blade tip speed. When the external wind speed is greater than the rated wind speed, the motor torque and the aerodynamic torque cannot be balanced, and the pitch angle should be changed to keep the wind turbine stable.

MODEL OF THE WIND TURBINE PITCH SYSTEM

Modeling of Permanent Magnet Synchronous Generator

Take the permanent magnet rotor pole centerline as the d-axis and the q-axis ahead of the d-axis by 90° in the direction of rotation of the rotor (Yan et al., 2009). The d–q coordinate system rotates synchronously with the rotor(Liu et al., 2021). Get the mathematical model of the generator in the d–q coordinate system as **Eq. 3**, and its block diagram is shown in **Figure 3**.

$$\begin{cases} \dfrac{di_d}{dt} = -\dfrac{R_s}{L_d} i_d + \omega_e \dfrac{L_q}{L_d} i_q - \dfrac{u_d}{L_d} \\ \dfrac{di_q}{dt} = -\dfrac{R_s}{L_q} i_q + \omega_e \left(\dfrac{\psi_f}{L_q} - \dfrac{L_d}{L_q} i_d\right) - \dfrac{u_q}{L_q} \end{cases} \tag{3}$$

where, u and i are the stator voltage and current, respectively. d,q are the d–q axis components after d–q coordinate transformation. ω_e is the electrical angular velocity. R_s is the stator resistance. ψ_f is the permanent magnet flux linkage.

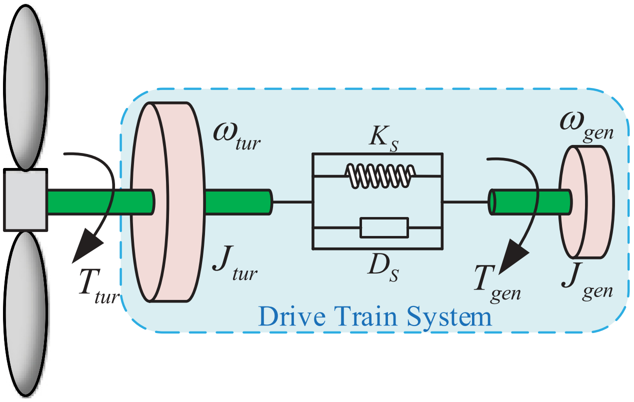

FIGURE 4 | Wind turbine two-mass model.

Modeling of the Transmission System

The two-mass model, shown in **Figure 4**, is often used to model the transmission chain of wind turbines. Particularly, the wind wheel and permanent magnet synchronous generator (PMSG) are, respectively, equivalent to a mass block. Then, a flexible transmission chain connects the two masses. In this way, energy can be converted from mechanical energy to electrical energy.

Using the dynamic model of the spring damping system (Cheng et al., 2019), the model of the drive train system could be expressed as (Mazare et al., 2021)

$$T_{tur} = K_S \int \left(\omega_{tur} - \omega_{gen}\right) dt + D_S\left(\omega_{tur} - \omega_{gen}\right) \tag{4}$$

where, K_S and D_S are the stiffness and damping coefficient of the drive train, respectively. T_{tur} is the mechanical torque output of the wind turbine. T_{tur} is the mechanical torque of the generator. ω_{tur} is the wind turbine speed. ω_{gen} is the mechanical speed of the generator rotor.

The wind turbine runs at a certain angular velocity under the action of aerodynamic torque T_{tur}. The equation of the wind turbine's motion could be expressed as

$$\frac{d\omega_{gen}}{dt} = \frac{T_{tur} - T_e - B\omega_{gen}}{J_{tur}} \tag{5}$$

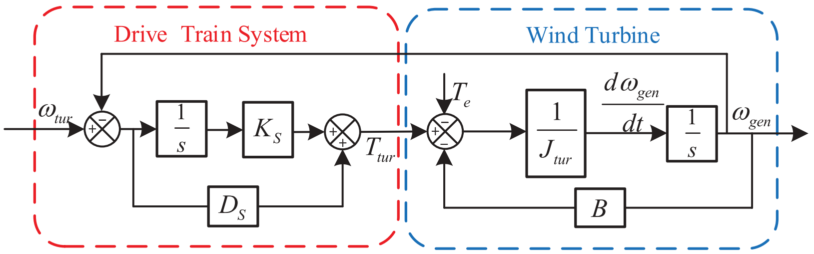

FIGURE 5 | Block diagram of the transmission system.

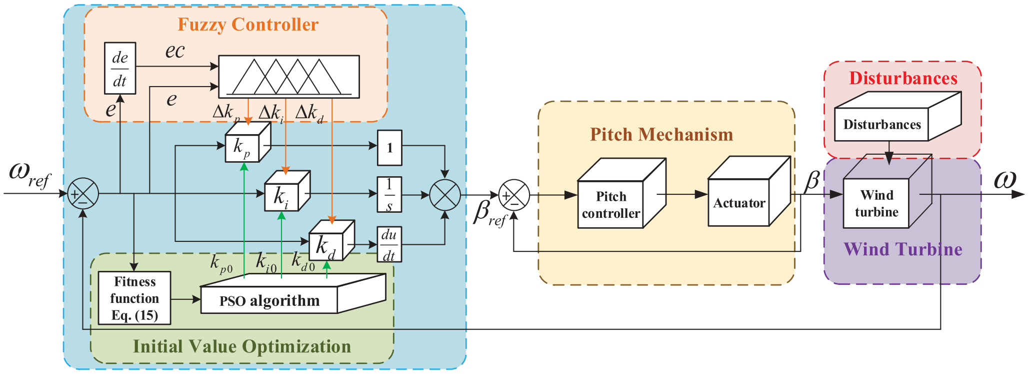

FIGURE 6 | Block diagram of pitch control based on fuzzy PSO-PID control.

where, B is the rotational viscosity coefficient. T_e is the electromagnetic torque. J_{tur} is the equivalent moment of the wind turbine's inertia.

The block diagram of transmission system is shown in **Figure 5**.

Modeling of the Pitch System

In this paper, a first-order inertial link is used to simulate the dynamic characteristics of the pitch actuator (Jia et al., 2021). The expression is usually equivalent to

$$\frac{d\beta}{dt} = \frac{\beta_{ref} - \beta}{T_\beta} \tag{6}$$

where, β is the actual value of the pitch angle. β_{ref} is the given value of the pitch angle. T_β is the time constant of the pitch actuator.

Disturbance Model of Wind Turbine

In actual operation, the wind turbine will be affected by many other disturbance factors, including the blade changes, installation errors, and external wind speed changes.

The blade changes include bending, deformation, and so on. Its disturbance transfer function $D_1(s)$ can be approximated as

$$D_1(s) = \frac{dM}{d\beta} \bullet \frac{\omega_z^2}{s^2 + \varsigma\omega_z s + \omega_z^2} \bullet V(s) \tag{7}$$

where, $V(s)$ is the external wind speed. M is the bending moment of blade flapping. ω_z is the angular frequency corresponding to the blade flapping vibration mode. ς is the aerodynamic damping coefficient of the blade.

The installation errors of the wind turbine include the deviation of the initial pitch angle of each blade and the inclination of the wind turbine tower. Its disturbance transfer function $D_2(s)$ can be approximated as

$$D_2(s) = \frac{k_2 s}{k_1 s + 1} \bullet V(s) \tag{8}$$

where, k_1 and k_2 are the initial errors disturbance coefficients.

The wind speed changes include the influence of other wind turbines in the wind farm on the input wind speed. Its disturbance transfer function $D_3(s)$ can be approximated as

$$D_3(s) = \frac{k_3 s + 1}{k_4 s^2 + k_5 s + 1} \bullet V(s) \tag{9}$$

where, k_3, k_4, and k_5 are the disturbance coefficients of wind speed changes.

In summary, the total disturbance that wind turbines undergo during normal operation is

$$D(s) = D_1(s) + D_2(s) + D_3(s) \tag{10}$$

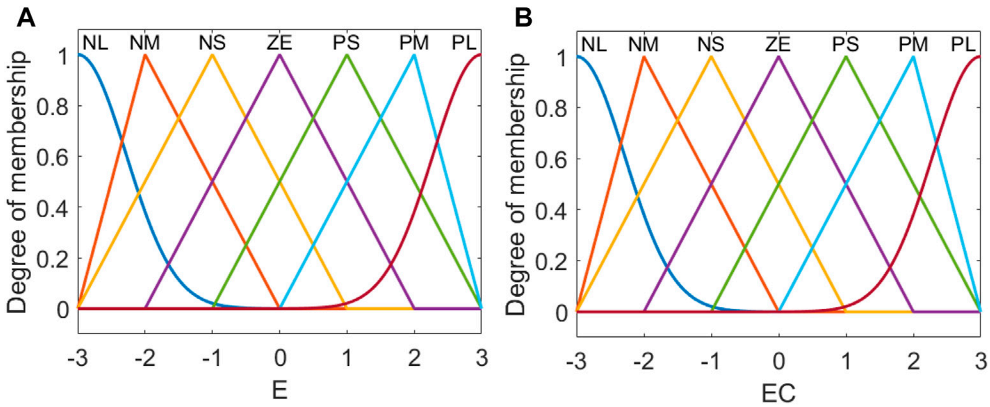

FIGURE 7 | Diagram of fuzzy rules using membership functions. **(A)** is "error E". **(B)** is "error rate of change EC".

TABLE 1 | Rules of fuzzy controller.

E	EC						
	NB	**NM**	**NS**	**ZO**	**PS**	**PM**	**PB**
NB	PB	PB	PM	PM	PS	ZO	ZO
NM	PB	PB	PM	PS	PS	ZO	NS
NS	PM	PM	PM	PS	ZO	NS	NS
ZO	PM	PM	PS	ZO	NS	NM	NM
PS	PS	PS	ZO	NS	NS	NM	NM
PM	PS	ZO	NS	NM	NM	NM	NB
PB	ZO	ZO	NM	NM	NM	NB	NB

THE DESIGN OF CONTROL STRATEGY

To ensure the stability of the wind turbine, fuzzy control is selected because it could be adaptable to complex and nonlinear systems (Qi and Meng, 2012). However, the fuzzy controller is prone to blind zone and dead zone near the control point, and its steady-state performance is low. Therefore, fuzzy control is difficult to meet the control accuracy requirements. PID control is a commonly used control method in the wind turbine pitch system (Pathak and Gaur, 2019). The combination of PID control and fuzzy control could solve these problems. However, if the initial parameters of PID control are selected improperly, it will cause a large overshoot and a long adjustment time for the system, which will cause the wind turbine's power to fluctuate too much. The PSO algorithm could be introduced to optimize the initial parameters. A pitch control strategy based on fuzzy adaptive PSO-PID is designed, and its block diagram is shown in **Figure 6**.

PID Initial Parameters Optimization

The poor PID initial parameters will decrease the system performance, so the PSO algorithm could be introduced to optimize the PID initial parameters. The PSO algorithm is an effective global optimization algorithm. It seeks the optimal value of complex space through information transmission and competition between individuals. The particle swarm searches in an n-dimensional space in particle swarm algorithm. The position of each particle i in space is $x_i = (x_{i1}, x_{i2} \cdots, x_{in})$, and the velocity in space is $v_i = (v_{i1}, v_{i2} \cdots, v_{in})$. The optimal solution is found through continuous iterative correction. During each iteration, the particle updates the velocity and displacement by dynamically tracking the two extremums P_{besti} (personal best) and G_{besti} (global best). The particles change their position and velocity at each iteration according to the following relationships (Iqbal and Singh, 2021)

$$\begin{cases} X_{in}^{k} = X_{in}^{k-1} + V_{in}^{k-1} \\ V_{in}^{k} = wV_{in}^{k} + w_1 r_1 \left(P_{besti} - X_{in}^{k-1}\right) + w_2 r_2 \left(G_{besti} - X_{in}^{k-1}\right) \end{cases} \tag{11}$$

where, w is the inertia weight of the particle's previous step velocity. w_1 and w_2 are the acceleration factors of their own optimal and global optimal, respectively. r_1 and r are two random generated numbers uniformly distributed in the interval [0, 1).

The PSO algorithm needs to select a suitable fitness function to achieve the optimal effect of the control. In this paper, the integral time absolute error (ITAE) is selected. Its expression is

$$fitness\,(t) = \int_0^t \tau |E(\tau)| d\tau \tag{12}$$

where, $E(t)$ is the error between the given value of the rotor speed and the output value of the rotor speed in this paper.

The steps of the PSO algorithm for optimizing PID parameters are as follows:

(1) Initialize the position and velocity of the particles, and take a random value within a certain range to generate the first-generation population.
(2) Calculate the fitness of each particle according to the fitness function.
(3) Record the local optimal solution and the global optimal solution.
(4) Update the velocity and position of the particle to move it closer to the optimal solution.
(5) Until the value of the fitness function is less than the set value or the number of iterations reaches the maximum, the optimal individual is output.

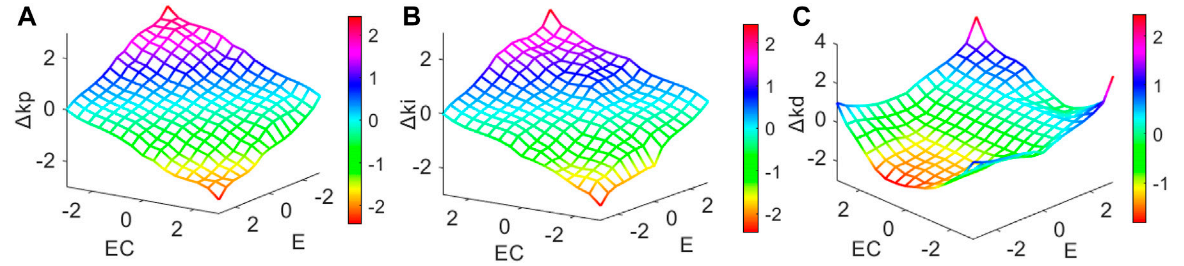

FIGURE 8 | The output curve of fuzzy controller. Part label **(A)** is "the output of Δk_p", part label **(B)** is "the output of Δk_i", part label **(C)** is "the output of Δk_d".

PID Parameters Adaptation

The fuzzy adaptive controller takes the deviation E and the deviation change rate EC (de/dt) as the inputs of the controller, shown in **Figure 6**.

The domain of the input and output of fuzzy control is [−3, 3]. The fuzzy subsets are {NB, NM, NS, ZO, PS, PM, PB}, and the triangle membership function is adopted. The designed fuzzy rules using membership functions are shown in **Figure 7**.

Then, the inputs are transformed into the corresponding fuzzy variable value by the fuzzy controller to realize the fuzzification of the inputs. Fuzzy inference is further performed on the fuzzy inputs according to the formulated fuzzy rules. The fuzzy controller rules are shown in **Table 1**. After defuzzification, the correction value $\triangle k_p$,$\triangle k_i$,$\triangle k_d$ of the variable pitch PID controller is obtained and accumulates them separately in the PID controller.

According to the fuzzy rules, the relationship of inputs (E, EC) and outputs ($\triangle k_p$,$\triangle k_i$,$\triangle k_d$) is shown in **Figure 8**.

SIMULATION AND ANALYSIS

To verify the performance of the proposed strategy, control strategy validation and anti-interference analysis are performed by simulation. All of the simulations are based on a 2 MW wind turbine. Its cut-in, rated, and cut-out wind speeds are 3, 11, and 22 m/s, respectively. The wind wheel diameter is 93.4 m. The wind wheel height is 80 m. The length of the blade is 45 m. The rated turning speed of the wind wheel is 12.1 r/min.

Control Strategy Validation

Control strategy validation of the proposed fuzzy PSO-PID is performed by simulation comparison with PID and fuzzy PID. The simulations are conducted under gust wind and turbulent wind, respectively, in both of the cases. Disturbances of blade changes (D_1), initial parameter error (D_2), and environmental changes (D_3) are considered simultaneously.

In the gust wind case, the gust wind speed curve is shown in **Figure 9**, where the maximum gust wind speed is 14 m/s, and the basic wind speed is 11 m/s. The comparison curves of pitch angle, wind wheel speed, and output power are shown in **Figures 10–12**.

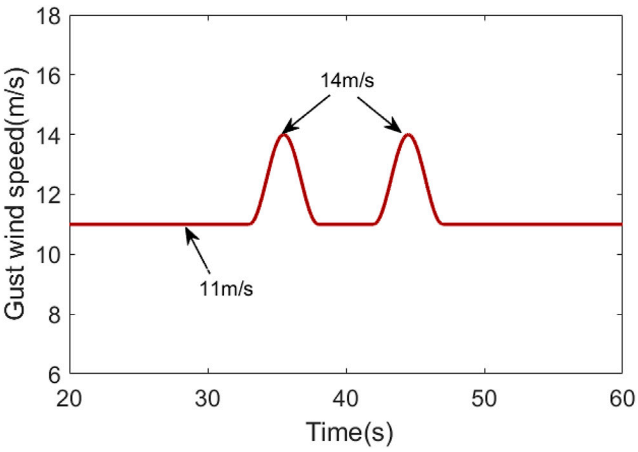

FIGURE 9 | Gust wind speed curve.

It could be seen from **Figure 10** that the maximum value of the pitch angle under fuzzy PSO-PID control is 7.8°. The maximum values of the pitch angle under fuzzy PID control and traditional PID control are 8.2° and 8.3°, respectively. The control method proposed in this paper can reduce the adjustment value of the pitch angle, thereby reducing the loss of the pitch control system.

As can be seen in **Figure 11**, the sudden increase of wind speed causes the pitch angle to increase first and then decrease, so the speed of the wind wheel shows a trend of first decreasing and then increasing. The fluctuation range of the wind wheel speed is the smallest under the fuzzy PSO-PID control, which is only 0.2 r/min. Under fuzzy PID control and traditional PID control, the fluctuation range is 0.4 and 0.9 r/min, respectively. Fuzzy PSO-PID control reduces the fluctuation range by 50% compared with fuzzy PID control.

As can be seen in **Figure 12**, the output power of a wind turbine is positively correlated with the wind wheel speed, so its power conversion trend is consistent with the wind wheel speed. The output power is more stable under fuzzy PSO-PID control, while under the traditional PID control, the output power fluctuates up to 0.14 MW. Therefore, fuzzy PSO-PID control

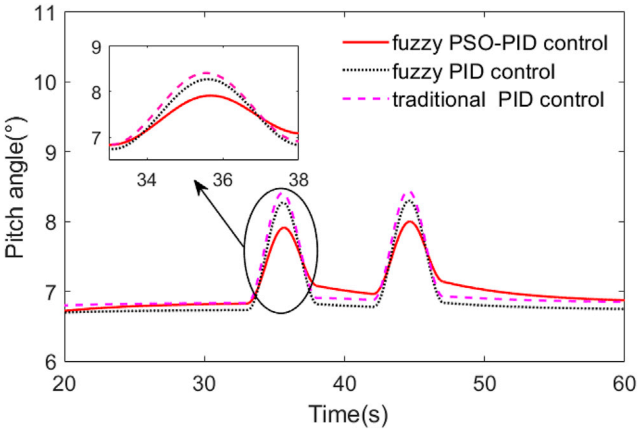

FIGURE 10 | Comparison curves of pitch angle under gust wind.

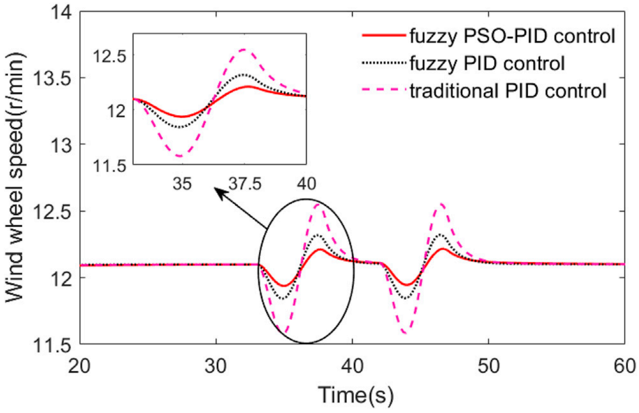

FIGURE 11 | Comparison curves of wind wheel speed under gust wind.

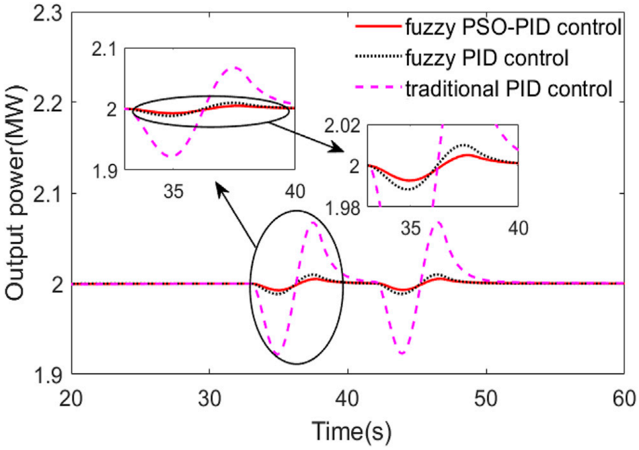

FIGURE 12 | Wind turbine output power curves under gust wind.

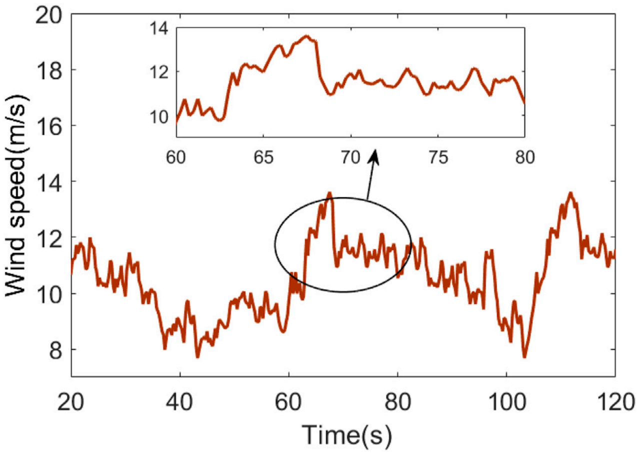

FIGURE 13 | Turbulent wind speed curve.

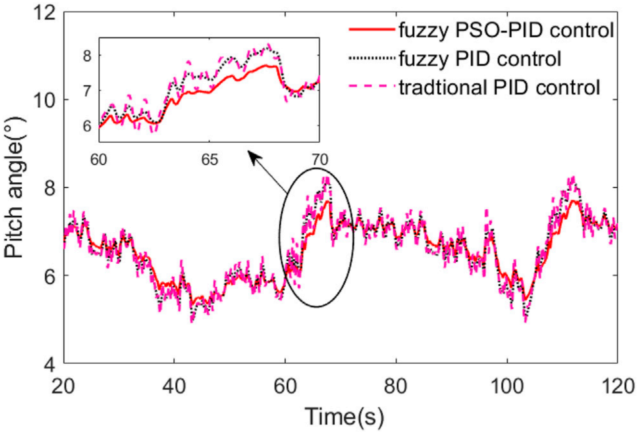

FIGURE 14 | Comparison curves of pitch angle under turbulent wind.

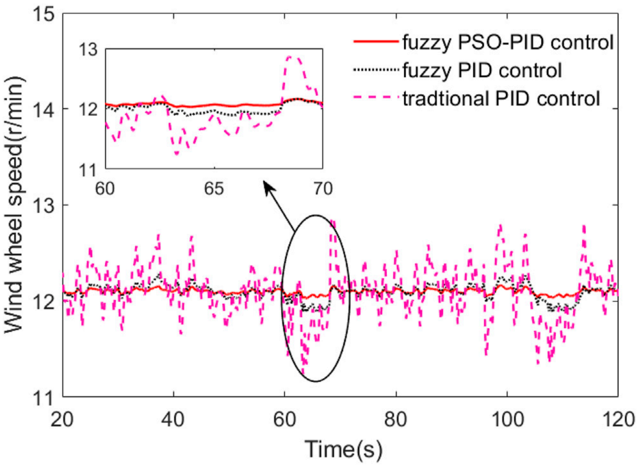

FIGURE 15 | Comparison curves of wind wheel speed under turbulent wind.

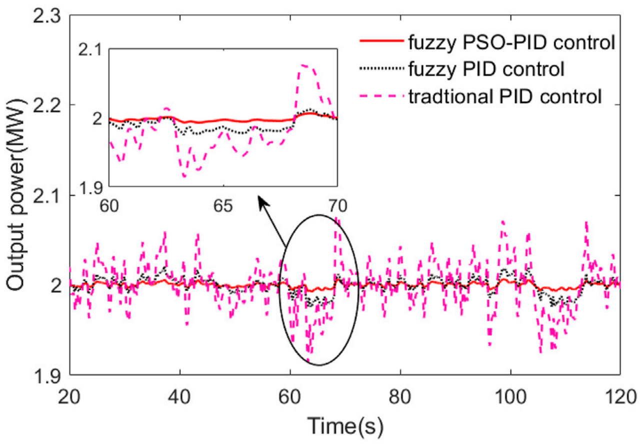

FIGURE 16 | Comparison curves of wind turbine output power under turbulent wind.

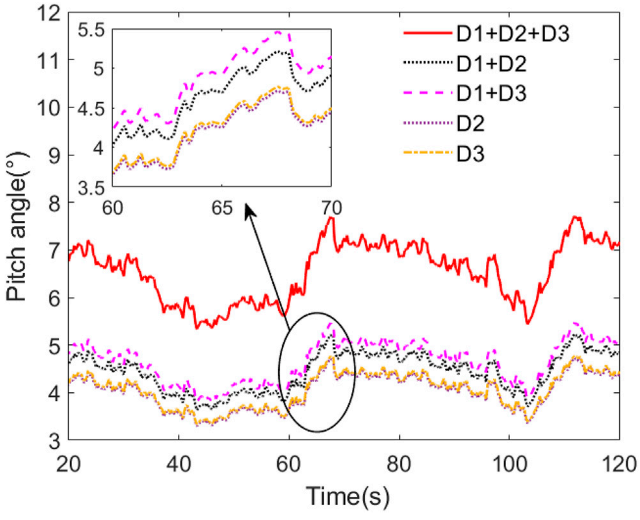

FIGURE 17 | Comparison curves of pitch angle under different disturbances.

has better robustness than fuzzy PID control and traditional PID control.

In the turbulent wind case, the turbulent wind speed is shown in **Figure 13**, where there is a dramatic change in wind speed around 65 s. The comparison curves of pitch angle, wind wheel speed, and output power are shown in **Figures 14–16**.

It could be seen from **Figure 14** that the maximum pitch angle is 7.4° and the minimum pitch angle is 5.9° under fuzzy PSO-PID control between 60 and 70 s where the wind speed changes a lot. The adjustment range of the pitch angle is 2.1° under the fuzzy PID control, and the pitch angle fluctuates sharply and under the traditional PID control. The fuzzy PSO-PID control can reduce the pitch angle adjustment range by about 28.6%.

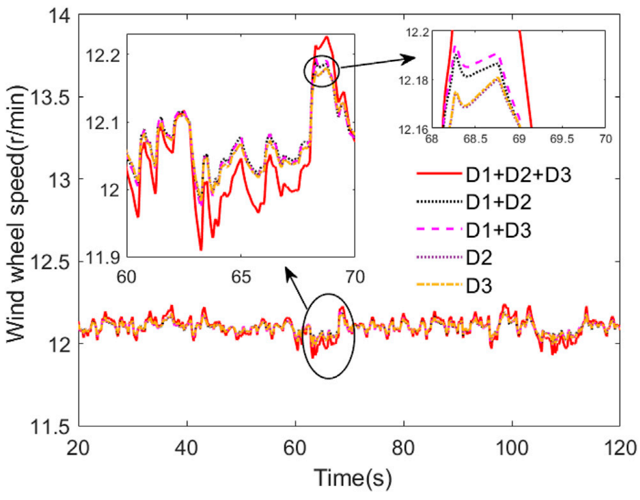

FIGURE 18 | Comparison curves of wind wheel speed under different disturbances.

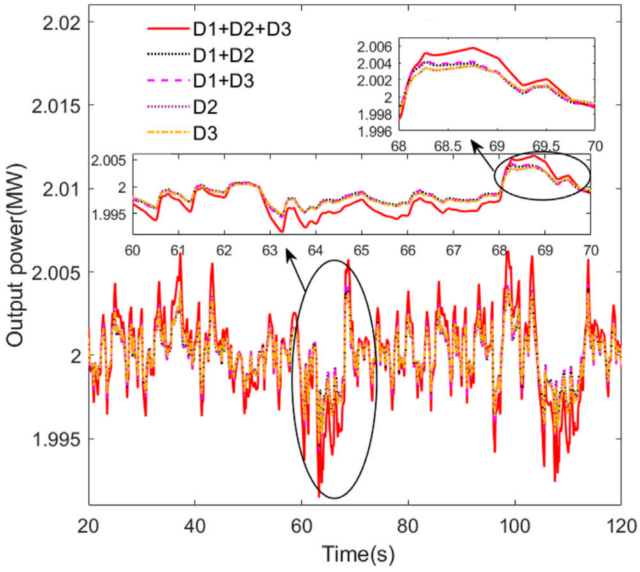

FIGURE 19 | Comparison curves of wind turbine output power under different disturbances.

As can be seen in **Figure 15**, the wind wheel speed fluctuation under traditional PID control is large, the maximum speed reaches 12.8 r/min, and the minimum speed is only 11.2 r/min. The wind wheel speed is not stable enough under fuzzy control compared with fuzzy PSO-PID control. Under the fuzzy PSO-PID control, the wind wheel speed is basically maintained at 12.1 r/min.

As can be seen in **Figure 16**, the output power fluctuation is minimal under fuzzy PSO-PID control compared with PID control and fuzzy PID control. And fuzzy PID control is less robust than fuzzy PSO-PID control.

Anti-Interference Analysis

To verify the anti-interference ability of fuzzy PSO-PID control strategy, five different combinations of disturbances, $D_1 + D_2 + D_3$, $D_1 + D_2$, $D_1 + D_3$, D_2, and D_3, were applied to the wind turbine under turbulent wind conditions. The comparison curves of pitch angle, wind wheel speed, and output power are shown in **Figures 17–19**.

It could be seen from **Figure 17**, since all five cases are using the same control strategies, that the change trend of the pitch angle is basically the same. When three disturbances, two disturbances, and one disturbance are applied to the wind turbine, respectively, the values of the pitch angle are around 7°, 5°, and 3°. The more disturbances applied, the greater the pitch angle of the wind turbine to adjust.

It could be seen from **Figure 18** that the fluctuation range of wind wheel speed is the largest when disturbance combination $D_1 + D_2 + D_3$ is applied to the wind turbine. When only one kind of disturbance is applied to the wind turbine, the fluctuation range of wind wheel speed is minimal, only 0.1 r/min.

It could be seen from **Figure 19** that the output power of the wind turbine under the five combined disturbances is relatively stable. When disturbance combination $D_1 + D_2 + D_3$ is applied to the wind turbine, the output power fluctuates the most, but it is only 0.5% of the rated power. When only one disturbance is applied to the wind turbine, the power fluctuation range is only 0.025% of the rated power.

Through the control strategy validation and anti-interference simulation, it can be found that using fuzzy PSO-PID control can make the wind wheel speed fluctuation smaller when the pitch angle adjustment range is small, and the wind turbine's power remains stable at the rated power. And fuzzy PSO-PID control strategy has a better suppression effect on different combinations of disturbances.

CONCLUSION

In this paper, a fuzzy adaptive PSO-PID is implemented in pitch control for suppressing multi-factor disturbances to improve the stability of wind turbines. In the proposed PID controller, PSO is utilized to optimize its initial parameters, and fuzzy rules are designed to adjust its parameters dynamically. Simulation comparisons with PID control and fuzzy PID control under gust wind and turbulent wind conditions are performed. The results show that in the system with the fuzzy adaptive PSO-PID pitch controller, the pitch angle adjustment range is smaller, and wind wheel speed and output power are smoother. Moreover, the anti-interference capacity of the control is verified by simulations under various combinations of disturbances. Thus, it is demonstrated that the fuzzy adaptive PSO-PID can provide the system with stronger robustness and better performance in suppressing various disturbances.

DATA AVAILABILITY STATEMENT

The original contributions presented in the study are included in the article/supplementary material. Further inquiries can be directed to the corresponding author.

AUTHOR CONTRIBUTIONS

YS contributed to the conception and design of the study. JL and LG organized the database. LH and YF performed the statistical analysis. JH wrote the first draft of the manuscript and wrote sections of the manuscript. All authors contributed to the manuscript revision and read and approved the submitted version.

ACKNOWLEDGMENTS

The authors are grateful for the support by the State Grid Corporation of China Headquarters Management Science and Technology Project (Research on Key Technologies to Improve Wind Turbine Power Generation Efficiency).

REFERENCES

Anjun, X., Hao, X., Shuju, H., and Honghua, X. (2011). "Pitch Control of Large Scale Wind Turbine Based on Expert PID Control," in 2011 International Conference on Electronics, Communications and Control (ICECC), Ningbo, China, 9–11.9.2011 (IEEE), 3836–3839. doi:10.1109/ICECC.2011.6068002

Barahona, B., Sorensen, P., Christensen, L., Sorensen, T., Nielsen, H. K., Larsen, X. G., et al. (2011). Validation of the Standard Method for Assessing Flicker from Wind Turbines. *IEEE Trans. Energ. Convers.* 26 (1), 373–378. doi:10.1109/TEC.2010.2068299

Cheng, J., Li, R., Choobineh, F. F., Hu, Q., and Mei, S. (2019). Dispatchable Generation of a Novel Compressed-Air Assisted Wind Turbine and its Operation Mechanism. *IEEE Trans. Sustain. Energ.* 10 (4), 2201–2210. doi:10.1109/TSTE.2018.2883068

Fdaili, M., Essadki, A., Nadour, M., and Nasser, T. (2017). "Comparative Study of MPPT and Pitch Angle Control Strategies for a Wind Energy Conversion System," in 2017 International Renewable and Sustainable Energy Conference (IRSEC), Tangier, Morocco, 4–7. Dec.2017 (IEEE), 1–6. doi:10.1109/IRSEC.2017.8477291

Iqbal, A., and Singh, G. K. (2021). PSO Based Controlled Six-phase Grid Connected Induction Generator for Wind Energy Generation. *Trans. Electr. Mach. Syst.* 5 (1), 41–49. doi:10.30941/CESTEMS.2021.00006

Jafarnejadsani, H., Pieper, J., and Ehlers, J. (2013). Adaptive Control of a Variable-Speed Variable-Pitch Wind Turbine Using Radial-Basis Function Neural Network. *IEEE Trans. Contr. Syst. Technol.* 21 (6), 2264–2272. doi:10.1109/TCST.2012.2237518

Jia, C., Wang, L., Meng, E., Chen, L., Liu, Y., Jia, W., et al. (2021). Combining LIDAR and LADRC for Intelligent Pitch Control of Wind Turbines. *Renew. Energ.* 169, 1091–1105. (prepublish). doi:10.1016/J.RENENE.2021.01.065

Kim, J.-S., Jeon, J., and Heo, H. (2011). "Design of Adaptive PID for Pitch Control of Large Wind Turbine Generator," in 2011 10th International Conference on Environment and Electrical Engineering (EEEIC), Rome, Italy, 8–11.5.2011 (IEEE), 1–4. doi:10.1109/EEEIC.2011.5874603

Liu, B., Li, Z., Chen, X., Huang, Y., and Liu, X. (2018). Recognition and Vulnerability Analysis of Key Nodes in Power Grid Based on Complex Network Centrality. *IEEE Trans. Circuits Syst.* 65 (3), 346–350. doi:10.1109/TCSII.2017.2705482

Liu, B., Li, Z., Dong, X., Yu, S. S., Chen, X., Oo, A. M. T., et al. (2021). Impedance Modeling and Controllers Shaping Effect Analysis of PMSG Wind Turbines. *IEEE J. Emerg. Sel. Top. Power Electron.* 9 (2), 1465–1478. doi:10.1109/JESTPE.2020.3014412

Liu, X., Yu, W., Yang, L., and Ma, Q. (2017). "Research on Variable-Pitch Control Strategy of Wind Turbine Based on the Nonlinear PID," in 2017 Chinese Automation Congress (CAC), Jinan, China, 20–22.10.2017 (IEEE), 299–303. doi:10.1109/CAC.2017.8242781

Mazare, M., Taghizadeh, M., and Ghaf-Ghanbari, P. (2021). Pitch Actuator Fault-Tolerant Control of Wind Turbines Based on Time Delay Control and Disturbance Observer. *Ocean Eng.* 238, 109724. doi:10.1016/J.OCEANENG.2021.109724

Mughal, M. H., and Li, G. (2015). "Review of Pitch Control for Variable Speed Wind Turbine," in 2015 15th Intl Conf on Scalable Computing and Communications and Its Associated Workshops (UIC-ATC-ScalCom), Beijing, China, 10–14.8.2015 (IEEE), 738–744. doi:10.1109/uic-atc-scalcom-cbdcom-iop.2015.148

Pathak, D., and Gaur, P. (2019). A Fractional Order Fuzzy-Proportional-Integral-Derivative Based Pitch Angle Controller for a Direct-Drive Wind Energy System. *Comput. Electr. Eng.* 78, 420–436. doi:10.1016/j.compeleceng.2019.07.021

Qi, Y., and Meng, Q. (2012). The Application of Fuzzy PID Control in Pitch Wind Turbine. *Energ. Proced.* 16, 1635–1641. doi:10.1016/j.egypro.2012.01.254

Wang, X., Jiang, Z., Lu, H., Wang, X., Meng, Y., and Li, S. (2020). "Independent Pitch Control Strategy and Simulation for Reducing Unbalanced Load of Wind Turbine," in 2020 Chinese Control and Decision Conference (CCDC), Hefei, China, 22–24.8.2020 (IEEE), 5535–5539. doi:10.1109/CCDC49329.2020.9164293

Xiong, L., Liu, X., Liu, Y., and Zhuo, F. (2020). Modeling and Stability Issues of Voltage-Source Converter Dominated Power Systems: a Review. *Csee Jpes*, 1–18. (Early Access). doi:10.17775/CSEEJPES.2020.03590

Xiong, L., Liu, X., Zhang, D., and Liu, Y. (2021). Rapid Power Compensation-Based Frequency Response Strategy for Low-Inertia Power Systems. *IEEE J. Emerg. Sel. Top. Power Electron.* 9 (4), 4500–4513. doi:10.1109/JESTPE.2020.3032063

Xiong, L., Zhuo, F., Wang, F., Liu, X., Chen, Y., Zhu, M., et al. (2016). Static Synchronous Generator Model: A New Perspective to Investigate Dynamic Characteristics and Stability Issues of Grid-Tied PWM Inverter. *IEEE Trans. Power Electron.* 31 (9), 6264–6280. doi:10.1109/TPEL.2015.2498933

Yan, G., Wei, Z., Mu, G., Cui, Y., Chen, W., and Dang, G. (2009). Dynamic Modeling and Control of Directly-Driven Permanent Magnet Synchronous Generator Wind Turbine. *Proceedings of the CSU-EPSA*, 34–39.

Yin, M., Xu, Y., Shen, C., Liu, J., Dong, Z. Y., and Zou, Y. (2017). Turbine Stability-Constrained Available Wind Power of Variable Speed Wind Turbines for Active Power Control. *IEEE Trans. Power Syst.* 32 (3), 2487–2488. doi:10.1109/TPWRS.2016.2605012

Zahra, B., Salhi, H., and Mellit, A. (2017). "Wind Turbine Performance Enhancement by Control of Pitch Angle Using PID Controller and Particle Swarm Optimization," in 2017 5th International Conference on Electrical Engineering - Boumerdes (ICEE-B), Boumerdes, Algeria, 29–31.10.2017 (IEEE), 1–5. doi:10.1109/ICEE-B.2017.8192221

Conflict of Interest: The authors were employed by the NARI Group Corporation.

frontiers
in Energy Research

ORIGINAL RESEARCH
published: 21 March 2022
doi: 10.3389/fenrg.2022.828992

Iterative Linearization Approach for Optimal Scheduling of Multi-Regional Integrated Energy System

Hang Tian, Haoran Zhao, Chunyang Liu and Jian Chen*

Key Laboratory of Power System Intelligent Dispatch and Control of Ministry of Education, Shandong University, Jinan 250061, China

It is challenging to deal with the optimal scheduling problem of the multi-regional integrated energy system (MIES) precisely and efficiently due to its multi-dimensional nonlinear characteristics. This article proposes an iterative linearization approach to solve the complicated and nonlinear MIES optimization problem with a well-balanced trade-off between accuracy and computation efficiency. In particular, the proposed approach is a combination of the modified piecewise linearization (PWL) tactic and the sequential linear programming (SLP) algorithm. The modified PWL method is developed to improve the speed-accuracy trade-off of the linearization, while the SLP algorithm is used to linearize the multi-dimensional nonlinear functions and narrow the approximation error iteratively. In this way, accurate but highly nonlinear formulations such as heat network models in the variable flow and variable temperature (VF-VT) mode can be considered in the optimization and solved efficiently. Finally, the effectiveness of the given approach is validated in a day-ahead optimal scheduling case of a four-region MIES.

Keywords: multi-regional integrated energy system, optimal scheduling, piecewise linearization, sequential linear programming, energy hub

Edited by:
Thomas Alan Adams,
McMaster University, Canada

Reviewed by:
Yunyun Xie,
Nanjing University of Science and Technology, China
Xiao Xu,
University of Electronic Science and Technology of China, China

****Correspondence:***
Haoran Zhao
hzhao@sdu.edu.cn

Specialty section:
This article was submitted to Process and Energy Systems Engineering,
a section of the journal Frontiers in Energy Research

Received: *04 December 2021*
Accepted: *10 February 2022*
Published: *21 March 2022*

Citation:
Tian H, Zhao H, Liu C and Chen J (2022) Iterative Linearization Approach for Optimal Scheduling of Multi-Regional Integrated Energy System. Front. Energy Res. 10:828992. doi: 10.3389/fenrg.2022.828992

1 INTRODUCTION

Integrated energy system (IES) can improve the overall efficiency by cascade utilization and optimized dispatch among all types of energy (Mancarella, 2014). Besides, it is capable of reducing the renewable energy curtailment via its superiority of flexible conversion and various storage (Huang et al., 2020a). Many researchers focus on the optimal scheduling of IES to explore the synergistic benefits of multi-energy utilization. The result of the optimal scheduling can indicate how to maximize system performance, thereby aiding decision-making. The multi-regional integrated energy system (MIES) considers both transregional transmission networks and multiple regional subsystems, whose configurations are usually represented by energy hub (EH) models. Therefore, the formulated optimization problem of MIES is more difficult to calculate than that of a single energy system because of its large-scale, nonlinear, and non-convex features.

When dealing with the aforementioned optimization problems, the existing commercial solvers are usually inefficient and may meet convergence problems. Simplifications of models are usually taken to ensure solvability. Geidl and Andersson (2005) firstly integrates multiple EHs with three energy networks, which simplify the problem by removing transmission constraints. In Shabanpour-Haghighi and Seifi (2015a) and Shabanpour-Haghighi and Seifi (2015b), although a model of the heat network is taken, the hydraulic conditions of pipelines are not considered, which may lead to inaccuracy in the result. Moreover, the energy conversion efficiencies of EHs' devices are kept as constants for simplicity in most EH-related research, which makes the model less accurate (Sheikhi et al., 2015; Zhang et al., 2015b; Moeini-Aghtaie et al., 2013). To sum up, for the optimal scheduling problem of MIES, the precise model usually introduces strong nonlinearity and makes the problem non-solvable or inefficient to calculate; the simplified model makes the calculation affordable but has non-ideal accuracy. Therefore, a trade-off between accuracy and computing efficiency is required, with the goal of maintaining the acceptable performance while removing the unnecessary features.

Linearization and convex relaxation are two mainstream solutions to achieve the aforementioned trade-off. In recent years, convex optimization draws considerable interest because of its global optimality and computation efficiency. Convex relaxation techniques such as second-order cone (SOC) relaxation and semidefinite relaxation are proved to be effective when dealing with the optimization problem of IES (Manshadi and Khodayar, 2018b,a). In particular, the SOC formulation is frequently applied on the branch flow equation in power systems and the Weymouth equation in natural gas networks because of its guaranteed tightness (He et al., 2017; Liu et al., 2018; Wang et al., 2017a). However, currently it is not effective in dealing with the model of heat network or equipment like the gas compressor. The piecewise linearization (PWL) tactic is another classic method to deal with nonlinearity. It is under development earlier and more applicable for different situations. Taylor's expansion based PWL is widely utilized in some literature (Shao et al., 2016). However, it has a non-ideal performance when dealing with the gas flow function, especially when the pipeline is light-loaded (Liu et al., 2020). Besides, Conventional PWL approaches are inefficient when dealing with multi-dimensional nonlinear functions. Taylor's expansion based PWL method combined with the Big M method is usually adopted to tackle this kind of problem (Zhang et al., 2015a). However, this method is proved to be less accurate than other methods (Bao et al., 2019). A three-dimensional linearization method based on the Special Order of Sets (SOS) tactic is proposed in Liu et al. (2020), which introduced numerous continuous and binary variables to formulate the problem. However, the number of piecewise segments need to be limited to keep the computation affordable, which actually harms the accuracy. Moreover, the multi-dimensional modeling process is complicated and time-consuming, which is not efficient to be implemented in a large and complex system. In summary, previous studies on linearization are not sufficient for the MIES with respect to the following aspects. 1) The PWL method carries an additional computation burden due to its stepwise segments. Besides, the performance of several PWL formulations varies. A thorough comparison and analysis of these methods are needed. 2) With the increase of the dimension of nonlinear problems in IES scheduling, the traditional PWL method is inefficient in dealing with multi-dimensional nonlinear functions and needs to be improved. 3) The linearization of the heat network model is always oversimplified, resulting in lower optimization accuracy (Geidl and Andersson, 2005; Shabanpour-Haghighi and Seifi, 2015a,b). Among all the heat network control modes, including constant flow and constant temperature (CF-CT), constant flow and variable temperature (CF-VT), variable flow and constant temperature (VF-CT), and variable flow and variable temperature (VF-VT), the variable flow and variable temperature (VF-VT) mode has greater flexibility and controllability but more severe nonlinearity in its mathematical model. As a result, while previous research presented effective IES scheduling strategies, the majority of them validated the optimal operation of the heat network based on the assumption of constant temperature (CT) (Shao et al., 2017) or constant mass flow rate (CF) (Liu et al., 2019) to avoid the introduction of quadratic terms. The linearized form of the heat network model in the VF-VT mode has not been realized yet.

To bridge the aforementioned gaps, an iterative linearization approach for optimal scheduling of MIES is proposed. The main contributions are summarized as follows:

1. The PWL method is improved with vertical and horizontal modifications. It outperforms other methods in precision and computational efficiency because the same accuracy can be achieved with fewer segments.
2. An iterative linearization approach based on a combination of the modified PWL method and the sequential linear programming (SLP) algorithm is proposed, which can solve the problem with multi-dimensional nonlinear features efficiently.
3. With the aid of this approach, models with strong convexity are considered to improve the overall accuracy and solved within acceptable time, including thermal and hydraulic models of heat network in VF-VT mode and nonlinear EH models.

The remainder of this paper is organized as follows. **Section 2** denotes the formulations of the nonlinear models. **Sections 3** and **4** present the modified PWL method and the iterative approach, respectively. Optimization results are compared and analyzed in **Section 5**. Finally, conclusions are drawn in **Section 6**.

2 MATHEMATICAL MODEL FORMULATION

2.1 Model of Electrical Network

To better fit the power rating of regional energy conversion equipment, the DistFlow model is selected instead of the DC power flow model (Molzahn et al., 2017). The DistFlow model owns better accuracy than the DC power flow model, especially for radial distribution networks. It contains voltages and reactive power, and allows nonzero resistance (Low, 2014). The balance equations of nodal active and reactive power are given as **Eqs 1** and **2**, respectively.

$$P_{ij} = r_{ij} I_{ij} - P_j + \sum_{u:j\rightarrow u} P_{ju} \tag{1}$$

$$Q_{ij} = x_{ij} I_{ij} - Q_j + \sum_{u:j\rightarrow u} Q_{ju} \tag{2}$$

where i, j and u indicate indexes of buses in the electrical network; P_{ij} and Q_{ij} denote the active and reactive power flow (MW, MVar) from bus i to bus j; P_{ju} and Q_{ju} are the active and reactive power flow (MW, MVar) from bus j to bus u; P_j and Q_j are the nodal injection active and reactive power (MW, MVar) of bus j; r_{ij} and x_{ij} are the resistance and reactance (Ω) of transmission line; I_{ij} is the squared value of branch current (kA). The nodal voltage equation, the branch power flow equation and the voltage and current constraints are described in **Eqs 3** and **4** and **Eq. 5**, respectively.

$$V_j = V_i - 2\left(r_{ij}P_{ij} + x_{ij}Q_{ij}\right) + \left(r_{ij}^2 + x_{ij}^2\right)I_{ij} \tag{3}$$

$$I_{ij}V_i = P_{ij}^2 + Q_{ij}^2 \tag{4}$$

$$V_i^{\min} \leqslant V_i \leqslant V_i^{\max},\, I_{ij}^{\min} \leqslant I_{ij} \leqslant I_{ij}^{\max} \tag{5}$$

where V_i and V_j are the squared values of nodal voltage (kV); $V_i^{\min}$ and $V_i^{\max}$ are the lower and upper limits of V_i; $I_{ij}^{\min}$ and $I_{ij}^{\max}$ are the lower and upper bounds of I_{ij}.

2.2 Model of Natural Gas Network

In a general natural gas network, the components usually consist of the gas source (connected with the upper network), transmission pipelines, storage devices, and gas loads. The nodal balance of gas flow is given as **Eq 6**.

$$\boldsymbol{v}_{\mathrm{s}}\boldsymbol{F}_{\mathrm{s}} - \boldsymbol{v}_{\mathrm{l}}\boldsymbol{L} + \boldsymbol{v}_{\mathrm{p}}\boldsymbol{F}_{\mathrm{p}} + \boldsymbol{v}_{\mathrm{c}}\boldsymbol{F}_{\mathrm{com}} + \boldsymbol{v}_{\mathrm{c}}\boldsymbol{F}_{\mathrm{con}} = \boldsymbol{0} \tag{6}$$

where $\boldsymbol{F}_{\mathrm{s}}$, $\boldsymbol{L}$, $\boldsymbol{F}_{\mathrm{p}}$, $\boldsymbol{F}_{\mathrm{com}}$ and $\boldsymbol{F}_{\mathrm{con}}$ indicate the gas flow vectors of source, loads, pipelines, compressors, and the consumption of compressors respectively; $\boldsymbol{v}_{\mathrm{s}}$, $\boldsymbol{v}_{\mathrm{l}}$, $\boldsymbol{v}_{\mathrm{p}}$ and $\boldsymbol{v}_{\mathrm{c}}$ are incidence matrices of gas source, loads, transmission pipelines and compressors for each node. The pressure drop equation, the constraints of nodal pressure and the constraints of gas flow in pipelines are given as **Eqs 7** and **8** and **9**, respectively.

$$\begin{aligned} F_{\mathrm{p},mn} &= \operatorname{sgn}(m,n) C_{mn}\sqrt{\left|\pi_m^2 - \pi_n^2\right|},\ \operatorname{sgn}(m,n) \\ &= \begin{cases} +1, \ (\pi_m - \pi_n) \geqslant 0 \\ -1, \ (\pi_m - \pi_n) < 0 \end{cases} \end{aligned} \tag{7}$$

$$\pi_m^{\min} \leqslant \pi_m \leqslant \pi_m^{\max},\, \pi_n^{\min} \leqslant \pi_n \leqslant \pi_n^{\max} \tag{8}$$

$$F_{\mathrm{s},m}^{\min} \leqslant F_{\mathrm{s},m} \leqslant F_{\mathrm{s},m}^{\max},\, F_{\mathrm{p},mn}^{\min} \leqslant F_{\mathrm{p},mn} \leqslant F_{\mathrm{p},mn}^{\max} \tag{9}$$

where m and n indicate indexes of nodes in the gas network; $F_{\mathrm{p},mn}$ is the gas flow (kcf/h) of pipeline mn; C_{mn} is the coefficient of the pressure drop equation for pipeline mn; π_m and π_n are nodal gas pressures (Psig); $\pi_m^{\min}$, $\pi_n^{\min}$, $\pi_m^{\max}$, $\pi_n^{\max}$ are the lower and upper bounds of nodal pressures (Psig); $F_{\mathrm{s},m}$ is the gas flow (kcf/h) of source at node m; $F_{\mathrm{s},m}^{\min}$ and $F_{\mathrm{s},m}^{\max}$ are the minimum and maximum of $F_{\mathrm{s},m}$; $F_{\mathrm{p},mn}^{\min}$ and $F_{\mathrm{p},mn}^{\max}$ are the lower and upper gas flow limits of pipeline mn. The consumption of the gas compressor powered by gas are given in **Eq. 10**, and **11**. **Equation 12** is derived from substituting **Eq. 10** into **Eq. 11**, eliminating the variable $H_{\mathrm{com},mn}$, which represents the horsepower of compressor. The equation of compression ratio is given as **Eq. 13** and its upper and lower bounds are expressed in **Eq. 14**.

$$F_{\mathrm{com},mn} = \frac{H_{\mathrm{com},mn}}{k_{1,mn}\left[\frac{\pi_n}{\pi_m}\right]^{\alpha_{mn}} - k_{2,mn}} \tag{10}$$

$$F_{\mathrm{con},mn} = a_{\mathrm{con},mn}\left(H_{\mathrm{com},mn}\right)^2 + b_{\mathrm{con},mn}H_{\mathrm{com},mn} + c_{\mathrm{con},mn} \tag{11}$$

$$\begin{aligned} F_{\mathrm{con},mn} &= a_{\mathrm{con},mn}\left(\left(k_{1,mn}\left[\frac{\pi_n}{\pi_m}\right]^{\alpha_{mn}} - k_{2,mn}\right)F_{\mathrm{com},mn}\right)^2 \\ &+ b_{\mathrm{con},mn}\left(\left(k_{1,mn}\left[\frac{\pi_n}{\pi_m}\right]^{\alpha_{mn}} - k_{2,mn}\right)F_{\mathrm{com},mn}\right) + c_{\mathrm{con},mn} \end{aligned} \tag{12}$$

$$R_{\mathrm{com},mn} = \frac{\pi_n}{\pi_m} \tag{13}$$

$$R_{\mathrm{com},mn}^{\min} \leqslant R_{\mathrm{com},mn} \leqslant R_{\mathrm{com},mn}^{\max} \tag{14}$$

where $F_{\mathrm{com},mn}$ is the gas flow (kcf/h) of compressor on pipe mn; $H_{\mathrm{com},mn}$ is the horsepower of compressor; $k_{1,mn}$, $k_{2,mn}$ and α_{mn} are the empirical parameters of compressor; $F_{\mathrm{con},mn}$ is the gas consumption (kcf/h) of compressor on pipeline mn; $a_{\mathrm{con},mn}$, $b_{\mathrm{con},mn}$ and $c_{\mathrm{con},mn}$ are the consumption coefficients of compressor; $R_{\mathrm{com},mn}$ is the compression ratio of compressor, with its lower and upper limits indicated by $R_{\mathrm{com},mn}^{\min}$ and $R_{\mathrm{com},mn}^{\max}$.

2.3 Model of District Heating Network

District heating network is generally composed of supply pipelines and return pipelines (Liu et al., 2016). The continuity of flow equation, the loop pressure equation and the head loss equation are expressed as **Eqs 15**, **16** and **17**, respectively. The loop head loss equation is given as **Eq. 18**, derived by substituting **Eq. 17** into **Eq. 16**. The constraints of mass flow rates and head losses are given in **Eqs 19** and **20**, respectively.

$$\boldsymbol{A}\boldsymbol{m}_{\mathrm{line}} = \boldsymbol{m}_{\mathrm{node}} \tag{15}$$

$$\boldsymbol{B}\boldsymbol{h}_{\mathrm{f}} = \boldsymbol{0} \tag{16}$$

$$\boldsymbol{h}_{\mathrm{f}} = \boldsymbol{K}\boldsymbol{m}_{\mathrm{line}}\left|\boldsymbol{m}_{\mathrm{line}}\right| \tag{17}$$

$$\boldsymbol{B}\boldsymbol{K}\boldsymbol{m}_{\mathrm{line}}\left|\boldsymbol{m}_{\mathrm{line}}\right| = \boldsymbol{0} \tag{18}$$

$$\boldsymbol{m}_{\mathrm{line}}^{\min} \leqslant \boldsymbol{m}_{\mathrm{line}} \leqslant \boldsymbol{m}_{\mathrm{line}}^{\max} \tag{19}$$

$$\boldsymbol{h}_{\mathrm{f}}^{\min} \leqslant \boldsymbol{h}_{\mathrm{f}} \leqslant \boldsymbol{h}_{\mathrm{f}}^{\max} \tag{20}$$

where $\boldsymbol{A}$ denotes the incidence matrix of the heat network, relating the nodes to branches; $\boldsymbol{m}_{\mathrm{line}}$ is the vector of mass flow rates (kg/s) of pipelines, with its lower and upper limits indicated by $\boldsymbol{m}_{\mathrm{line}}^{\min}$ and $\boldsymbol{m}_{\mathrm{line}}^{\max}$; $\boldsymbol{m}_{\mathrm{node}}$ is the vector of mass flow rates (kg/s) through each node, charged from a heat source or discharged to a heat load; $\boldsymbol{B}$ is the incidence matrix of loops, relating the loops to branches; $\boldsymbol{h}_{\mathrm{f}}$ is the vector of head losses (m) of pipelines, with its lower and upper bounds represented by $\boldsymbol{h}_{\mathrm{f}}^{\min}$ and $\boldsymbol{h}_{\mathrm{f}}^{\max}$; $\boldsymbol{K}$ is the vector of resistance coefficients of pipelines. The general heat transfer equation is expressed as **Eq. 21**. The temperature drop equations in the supply network and the return network are given as **Eqs 22** and **23**. The nodal mixture temperature equation is described as **Eq. 24**. The constraints of nodal temperatures in the supply network and the return network are given as **Eqs 25** and **26**.

$$\boldsymbol{\Phi} = C_{\mathrm{p}}\boldsymbol{m}_{\mathrm{node}}\left(\boldsymbol{T}_{\mathrm{s}} - \boldsymbol{T}_{\mathrm{o}}\right) \tag{21}$$

$$T_{q,\mathrm{supply}} = \left(T_{p,\mathrm{supply}} - T_{\mathrm{a}}\right)e^{-\frac{\lambda_{pq}L_{pq}}{C_{\mathrm{p}}m_{\mathrm{line},pq}}} + T_{\mathrm{a}} \tag{22}$$

$$T_{q,\mathrm{return}} = \left(T_{p,\mathrm{return}} - T_{\mathrm{a}}\right)e^{-\frac{\lambda_{pq}L_{pq}}{C_{\mathrm{p}}m_{\mathrm{line},pq}}} + T_{\mathrm{a}} \tag{23}$$

$$\left(\sum \boldsymbol{m}_{\mathrm{out}}\right)\boldsymbol{T}_{\mathrm{out}} = \sum\left(\boldsymbol{m}_{\mathrm{in}}\boldsymbol{T}_{\mathrm{in}}\right) \tag{24}$$

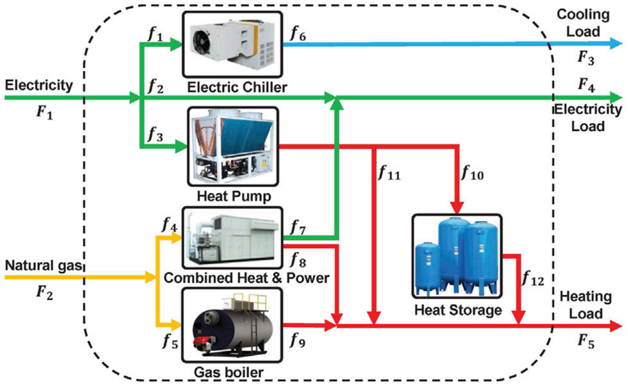

FIGURE 1 | Framework of single EH.

$$T_{p,\text{supply}}^{\min} \leqslant T_{p,\text{supply}} \leqslant T_{p,\text{supply}}^{\max} \tag{25}$$

$$T_{p,\text{return}}^{\min} \leqslant T_{p,\text{return}} \leqslant T_{p,\text{return}}^{\max} \tag{26}$$

where p and q indicate indexes of nodes in the heat network; $\boldsymbol{m}_{\text{node}}$ is the vector of the mass flow rate (kg/s) at each node injected from a source or discharged to a load; $\boldsymbol{\Phi}$ is the vector of heat power (MW) consumed at each node; C_p is the specific heat of water (MJkg^{-1}°C^{-1}) at constant pressure; $\boldsymbol{T}_\text{s}$ and $\boldsymbol{T}_\text{o}$ are vectors of temperatures (°C) of the injected and discharged water flow to each load; In the temperature drop **Eqs 22**, **23**, $T_{p,\text{supply}}$ and $T_{q,\text{supply}}$ are nodal temperatures (°C) of supply networks; $T_{p,\text{return}}$ and $T_{q,\text{return}}$ are nodal temperatures (°C) of return networks; T_a is the ambient temperature (°C); λ_{pq} is the coefficient of heat transfer (MWm^{-1}°C^{-1}) of pipeline pq; L_{pq} is the length (m) of pipeline; The nodal mixture temperature equation is shown in **Eq. 24**, where $\boldsymbol{m}_{\text{out}}$ and $\boldsymbol{m}_{\text{in}}$ are the vectors of mass flow rates (kg/s) of water leaving or coming into each node, with their corresponding temperatures (°C) indicated by $\boldsymbol{T}_{\text{out}}$ and $\boldsymbol{T}_{\text{in}}$ respectively; $T_{p,\text{supply}}^{\min}$ and $T_{p,\text{supply}}^{\max}$ are the minimum and maximum of $T_{p,\text{supply}}$; $T_{p,\text{return}}^{\min}$ and $T_{p,\text{return}}^{\max}$ are the lower and limits of $T_{p,\text{return}}$.

2.4 Model of Energy Hub

To eliminate the nonlinear problem brought by the dispatch factor, auxiliary state variables are introduced to represent each energy flow inside the EH (Wang et al., 2017b). A typical framework of EH is shown in **Figure 1**. The modified coupling equation of EH is given as **Eq. 27**.

$$\begin{bmatrix} F_1 \\ F_2 \\ F_3 \\ F_4 \\ F_5 \\ 0 \\ 0 \\ 0 \\ 0 \\ 0 \\ 0 \end{bmatrix} = \begin{bmatrix} 1 & 1 & 1 & 0 & 0 & 0 & 0 & 0 & 0 & 0 & 0 & 0 & 0 \\ 0 & 0 & 0 & 1 & 1 & 0 & 0 & 0 & 0 & 0 & 0 & 0 & 0 \\ 0 & 0 & 0 & 0 & 0 & 1 & 0 & 0 & 0 & 0 & 0 & 0 & 0 \\ 0 & 1 & 0 & 0 & 0 & 0 & 1 & 0 & 0 & 0 & 0 & 0 & 0 \\ 0 & 0 & 0 & 0 & 0 & 0 & 0 & 1 & 1 & 0 & 1 & 1 & 0 \\ \eta_{\text{ec}}^{\text{c}} & 0 & 0 & 0 & 0 & -1 & 0 & 0 & 0 & 0 & 0 & 0 & 0 \\ 0 & 0 & \eta_{\text{hp}}^{\text{h}} & 0 & 0 & 0 & 0 & 0 & 0 & -1 & -1 & 0 & 0 \\ 0 & 0 & 0 & \eta_{\text{chp}}^{\text{e}} & 0 & 0 & -1 & 0 & 0 & 0 & 0 & 0 & 0 \\ 0 & 0 & 0 & \eta_{\text{chp}}^{\text{h}} & 0 & 0 & 0 & -1 & 0 & 0 & 0 & 0 & 0 \\ 0 & 0 & 0 & 0 & \eta_{\text{gb}}^{\text{h}} & 0 & 0 & 0 & -1 & 0 & 0 & 0 & 0 \\ 0 & 0 & 0 & 0 & 0 & 0 & 0 & 0 & 0 & \eta_{\text{hs}}^{\text{char}} & 0 & \dfrac{-1}{\eta_{\text{hs}}^{\text{dis}}} & -1 \end{bmatrix} * \begin{bmatrix} f_1 \\ f_2 \\ f_3 \\ f_4 \\ f_5 \\ f_6 \\ f_7 \\ f_8 \\ f_9 \\ f_{10} \\ f_{11} \\ f_{12} \\ \Delta E \end{bmatrix} \tag{27}$$

where F_1 to F_5 and f_1 to f_{12} are the outer and inner energy flows (kW h) of the EH; ΔE is the stored energy (kW h) in the heat storage (HS) tank; $\eta_{\text{ec}}^{\text{c}}$, $\eta_{\text{hp}}^{\text{h}}$, $\eta_{\text{chp}}^{\text{e}}$, $\eta_{\text{chp}}^{\text{h}}$, $\eta_{\text{gb}}^{\text{h}}$, $\eta_{\text{hs}}^{\text{char}}$, $\eta_{\text{hs}}^{\text{dis}}$ are the energy conversion efficiencies of electric chiller (EC), heat pump (HP), combined heat and power (CHP) unit (electrical output), CHP unit (heat output), gas boiler (GB), HS (charging) and HS (discharging), respectively. Through this modification, the connection and conversion relationships are integrated into one coupling matrix, which provides considerable flexibility and simplicity to the modeling process without introducing more elements like energy buses and virtual nodes into the modeling process (Liu et al., 2020).

2.5 Objective Function and Problem Formulation

In the system of networked EHs, the heat power of district heat network is supplied by EHs, while EHs are powered by electricity and gas from the upper networks. The objective function can be described as **Eq. (28)**.

$$C_{\text{op}} = \sum_{t=1}^{N_\text{t}} \left(P_{\text{in}} C_{\text{in}} - P_{\text{out}} C_{\text{out}} + M_{\text{gas}} C_{\text{gas}} \right) \tag{28}$$

where t is the index of hour; C_{op} is the total cost (¥) of the whole system during 24 h; N_t denotes the total scheduling time periods, which is set as 24 in this study; P_{in}, P_{out} and M_{gas} are the purchasing electrical power (kW h), selling electrical power (kW h) and gas flow (kcf) at gas source; C_{in}, C_{out} and C_{gas} are the corresponding prices (¥/kW h, ¥/kcf) for P_{in}, P_{out} and M_{gas}.

$$Objective\ function\text{:}\ \ (28),\quad s.t.\ (1)-(27) \tag{29}$$

The formulated problem is a complicated mixed integer nonlinear programming (MINLP) problem, which can hardly be solved by existing commercial solvers. Therefore, a modified PWL method is proposed in the next section to transform part of the MINLP model (one-dimensional nonlinear functions) into the MILP formulation, which can reduce the computation difficulty.

3 LINEARIZATION METHODOLOGY

3.1 Modified Piecewise Linearization Method

In this section, a modified PWL method is proposed, with improved performance of accuracy and computation efficiency (verified in the last subsection) among popular PWL tactics, such as Taylor's expansion based approximation (TEBA) method (Zhang et al., 2015a; Shao et al., 2016), Special Order of Sets (SOS) method (Liu et al., 2020) and binary method (Huang et al., 2020b). The proposed PWL method is based on the binary method with horizontal and vertical modifications, which are introduced in the following subsections.

3.1.1 Binary PWL Method

Through the PWL approximation, the general form of one-dimensional nonlinear function $F(X)$ can be reformulated into the linearized function $L(X)$. The equations of its independent

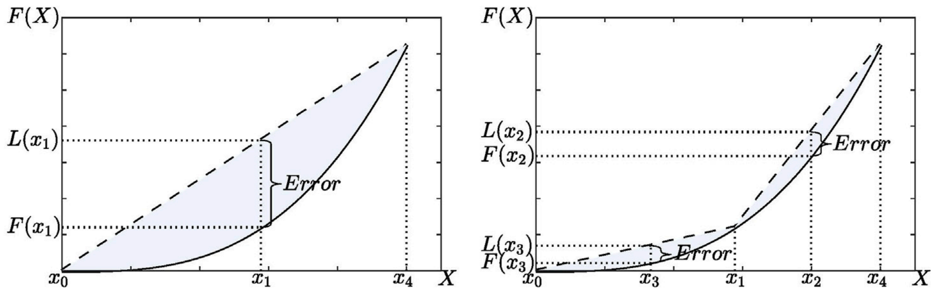

FIGURE 2 | Horizontal Modification for PWL method.

variable, dependent variable, and segment range are described as **Eqs 30**, **31**, and **32**, respectively.

$$X = X_0 + \sum_{k=1}^{N} \sigma_k \tag{30}$$

$$L(X) = F(X_0) + \sum_{k=1}^{N} K_k \sigma_k \tag{31}$$

$$Z_{k+1} \cdot \left(\overline{X_k} - \underline{X_k}\right) \le \sigma_k \le Z_k \cdot \left(\overline{X_k} - \underline{X_k}\right) \tag{32}$$

where k is the index of segment; N is the total number of segments X is a continuous variable; X_0 is the minimum of X; σ_k is the value of the kth segment of X; K_k is the coefficient of the kth segment of $L(X)$; Z_k and Z_{k+1} are binary variables to guarantee the continuity of X and $L(X)$; $\overline{X_k}$ and $\underline{X_k}$ are the upper and lower limit of the kth segment of X.

3.1.2 Horizontal Modification

The accuracy of the PWL approximation depends greatly on the selection of breakpoints. The precision of the approximation can be further improved by adding more piecewise segments. However, the addition of segments leads to a substantial increase in the computational burden. Therefore, the strategy of breakpoint selection is modified here, from the evenly-spaced selection, to the selection at the maximum error of linear approximation. The approximation error is shown as:

$$E = L(X) - F(X) \tag{33}$$

where E is the error of piecewise linearization. The initial breakpoint is determined when the maximum error occurs at $\partial E/\partial X = 0$. The following breakpoints are ranked and selected sequentially according to the maximum errors of their own ranges, as illustrated in **Figure 2**. This process is conducted iteratively until the maximum piecewise segment is reached or the approximation error is less than the predefined tolerance.

3.1.3 Vertical Modification

Based on approximation error value, a vertical modification has been implemented on the PWL approximation, which is denoted in **Eq. 34**.

$$L'(X) = L(X) - \frac{\sum_{k=1}^{N} \int_{x_{k-1}}^{x_k} (L(X) - F(X))dX}{\sum_{k=1}^{N} \sigma_k} \tag{34}$$

where $L'(X)$ is the modified formulation of $L(X)$ after vertical modification; x_{k-1} and x_k are the (k–1)th and kth breakpoint for $L(X)$. This modification can further reduce the approximation error, with its demonstration shown in **Figure 3**.

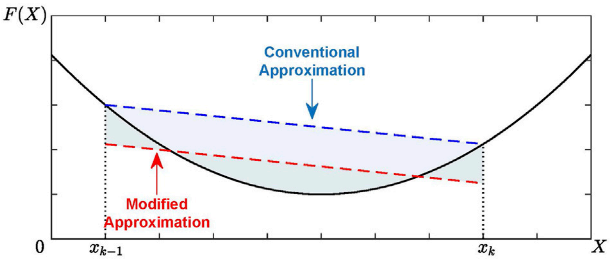

FIGURE 3 | Vertical Modification for PWL method.

3.2 Linearization of Nonlinear Constraints

In this subsection, the above-mentioned modified PWL approach **Eqs (30)–(34)** will be implemented on one-dimensional nonlinear functions.

3.2.1 Modified Model for Gaseous Constraints

Variable substitutions of $\theta_m = \pi_m^2, \theta_n = \pi_n^2, \varphi_{mn} = \theta_m - \theta_n$ are performed to replace the original gas flow function **Eq. 7** by **Eq. 35**. In this way, a dimension reduction is applied to the nonlinear function, which simplifies the linearization process.

$$F_{\mathrm{p},mn} = \mathrm{sgn}(\varphi_{mn}) C_{mn} \sqrt{|\varphi_{mn}|} \tag{35}$$

Besides, the substitution is applied to the variable constraints, which converts **Eq. 8** into **Eq. 36**.

$$\left(\pi_m^{\min}\right)^2 - \left(\pi_n^{\max}\right)^2 \le \varphi_{mn} \le \left(\pi_m^{\max}\right)^2 - \left(\pi_n^{\min}\right)^2 \tag{36}$$

The pressure drop equation is finally reformulated as

$$\varphi_{mn} = \mathrm{sgn}(F_{\mathrm{p},mn}) \frac{F_{\mathrm{p},mn}{}^2}{C_{mn}{}^2} \tag{37}$$

The modified PWL method is then carried out on **Eq. 37**.

3.2.2 Modified Model for Hydraulic Constraints

The hydraulic models, including the equations of pipelines' thermal resistance, friction factor, diameter, Reynolds number, and flow velocity, are given as **Eq. 38**, **39**, **40**, and **41**, respectively.

TABLE 1 | Parameters for devices in **Figure 1**.

Device	Efficiency characteristics: $y = f(x)$	Capacity (kW)
GB	$3x$	900
HP	$0.8x$	400
EC	$-0.000{,}030\ 41x^3 + 0.019\ 01x^2 + 0.259\ 3x$	400
CHP	Electric: $0.000{,}115\ 0x^2 + 0.230\ 5x$	720
	Thermal: $0.0\ 001\ 611x^2 + 0.322\ 8x$	
HS	Charging: $-\ 0.00\ 005x^2 + 0.93x$	800 (3.2 MWh)
	Discharging: $-\ 0.00\ 005x^2 + 0.93x$	

$$K_{pq} = \frac{8L_{pq} f_{pq}}{{D_{pq}}^5 \rho^2 \pi^2 g} \tag{38}$$

$$f_{pq} = \frac{0.3164}{{Re_{pq}}^{0.25}} \tag{39}$$

$$Re_{pq} = \frac{v_{pq} D_{pq}}{\mu} \tag{40}$$

$$v_{pq} = \frac{m_{\text{line},pq}}{\rho \pi D_{pq}^2 / 4} \tag{41}$$

where K_{pq}, f_{pq}, D_{pq}, Re_{pq} and v_{pq} are the resistance coefficient, friction factor, diameter (m), Reynolds number and flow velocity (m/s) of pipeline pq; ρ is water density (kg/m^3); g is the acceleration of gravity (kg·m/s^2); μ is the kinematic viscosity of water (m^2/s). **Eq. 42** is derived from substituting **Eqs. 38–41** into **Eq. (18)**, where $\boldsymbol{W}$ denotes vector of comprehensive coefficients.

$$\boldsymbol{BWm}_{\text{line}} |\boldsymbol{m}_{\text{line}}|^{3/4} = 0 \tag{42}$$

The nonlinear term in **Eq. 42** can be linearized by the proposed PWL approach.

3.2.3 Modified Model for Energy Hubs

The capacities and conversion characteristics of the devices in the EH depicted in **Figure 1** are shown in **Table 1** (Huang et al., 2020b). The modified PWL method is applied to the nonlinear curve of each device.

4 ITERATIVE LINEARIZATION BASED ON SLP ALGORITHM

After the previous PWL section, the remaining multi-dimensional nonlinear functions are handled with the SLP algorithm in this section. The SLP obtains a feasible solution from linearized models and fixes the linearization-related inaccuracies by repeating the steps successively, leading the approximation to reach the solution (Nocedal and Wright, 2006).

4.1 Framework of Linearization and Iteration Process

The framework of the linearization process and iteration approach is illustrated in **Figure 4**. In this framework, the original MINLP model is partially linearized by the proposed PWL method, and the remaining nonlinear functions are going through the iterative linearization process. Several decision variables are predefined to linearize these functions. The variables include the current term I_{ij} in **Eqs 1–5**, the compressor ratio term $R_{\text{com},mn}$ in **Eqs 13**, **14** and the nodal temperature terms $T_{p,\text{supply}}$, $T_{p,\text{return}}$ in **Eqs 21–26**. The decision variables are updated through each iteration, making sure that the error caused by approximation is reduced sequentially. In this way, the model is totally linearized and forms a computational affordable MILP problem.

4.2 Selection of Decision Variables

4.2.1 Decision Variable in Electrical Constraints

As shown in the nonlinear electrical **Equation 4**, the quadratic terms P_{ij}^2 and Q_{ij}^2 bring multi-dimensional nonlinearity into this formulation, which make the model difficult to be linearized. To solve this problem, **Equation 4** is defined as an auxiliary constraint, which does not participate in the optimization directly but is used to update the value of I_{ij} repeatedly in the iteration process. Through this way, the term I_{ij} in **Eqs 1–3** are set as constant, and thus these equations are converted into linear formulations.

4.2.2 Decision Variable in Gaseous Constraints

The three-dimensional nonlinear function **Eq. 12** is difficult to linearize efficiently. In some works, the gas compressor's consumption is replaced by an empirical ratio multiplied with the passing gas flow (Li et al., 2018). To avoid both inaccurate approximation and inefficient linearization, a hybrid method is adopted to calculate the consumption. Firstly, **Equation 13** is defined as an auxiliary constraint, determining the value of compression ratio $\frac{\pi_n}{\pi_m}$ by iterative process, which transform **Equation 12** into a one-dimensional function. Then, the proposed PWL method is applied to this function to remove the nonlinearity of the quadratic term.

4.2.3 Decision Variable in Hydraulic-Thermal Constraints

It is obvious that the thermal **Equations 21–24** contain variable multiplications and exponential term, which introduce nonlinearity and make the hydraulic-thermal model difficult to solve. Also, common NLP and MINLP solvers met convergence problems when trying to optimize this integrated model. Therefore, **Eqs 22–24** are treated as auxiliary constraints, and the nodal temperature values $T_{p,\text{supply}}$ and $T_{p,\text{return}}$ are determined according to the feasible solution of each iteration. In this way, the hydraulic-thermal model is transformed into a MILP format that supports rapid iteration.

4.3 Iteration Procedure

After the previous linearization process, **Eq. 29** is reformulated into MILP form. An iterative approach based on SLP algorithm is carried out to get the final solution. The specific details are provided in **Algorithm 1**.

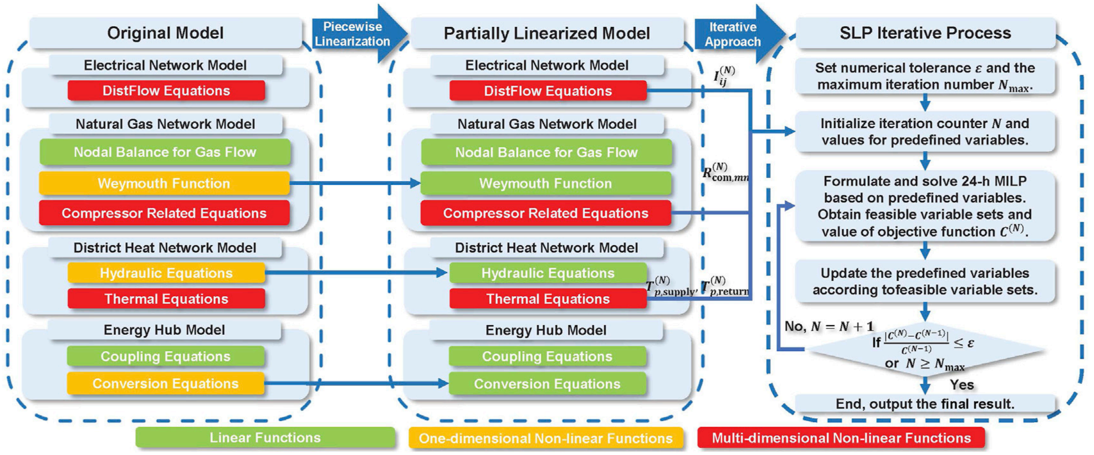

FIGURE 4 | Framework of the linearization process and iteration approach.

Algorithm 1 | Iterative Algorithm Based on Sequential Linear Programming.

Step 1) Set termination conditions: numerical tolerance ε and the maximum iteration number $N_{\max}$.

Step 2) Initialize the parameters: iteration counter $N = 1$, the initial values for the predefined variables $I_{ij}^{(0)} = 0, R_{\text{com},mn}^{(0)} = 1, T_{p,\text{supply}}^{(0)} = 90, T_{p,\text{return}}^{(0)} = 70$.

Step 3) Solve the 24h-horizon MILP formulation of (29), based on the predefined values $I_{ij}^{(N-1)}$, $R_{\text{com},mn}^{(N-1)}$, $T_{p,\text{supply}}^{(N-1)}$, $T_{p,\text{return}}^{(N-1)}$. Get a feasible sets of variables $x^{(N)}$ and the value of objective function $C^{(N)}$.

Step 4) Update $I_{ij}^{(N)}$ by (4), $R_{\text{com},mn}^{(N)}$ by (13) and $T_{p,\text{supply}}^{(N)}$, $T_{p,\text{return}}^{(N)}$ by (22)-(24) according to the feasible variables $x^{(N)}$.

Step 5) Calculate the mismatch of objective function value. If $\left|C^{N} - C^{N-1}\right| / C^{N-1} \le \varepsilon$, the termination condition is satisfied and the iteration is stopped.

Step 6) If $N \ge N_{\max}$, the process will be terminated. Otherwise, return to Step 3, $N = N + 1$.

5 CASE STUDIES

5.1 Accuracy and Efficiency Verification for the Proposed PWL Method

This subsection tests the performance of three mainstream PWL methods and the proposed PWL method in an optimization problem. The three PWL methods include Taylor's expansion based Approximation (TEBA) method (Zhang et al., 2015a; Shao et al., 2016), Special Order of Sets 2 (SOS2) method (Liu et al., 2020), and Binary method (Huang et al., 2020b). The optimization problem is formulated as the day-ahead optimal scheduling of single EH shown in **Figure 1**. The EH contains two devices with linear efficiency curves and three devices with nonlinear efficiency curves, shown in **Table 1**. The optimization result is illustrated and compared in **Figures 5** and **6**.

It is worth noting that when the number of piecewise segments gets large enough, all the methods obtain a relatively precise approximation. However, a large number of segments is impractical since the number of extra binary variables and constraints has a considerable impact on computational efficiency. Therefore, in this comparison, the maximum segment is limited to 20. The benchmark values are derived from directly solving the nonlinear problem by the nonlinear programming (NLP) solver IPOPT.

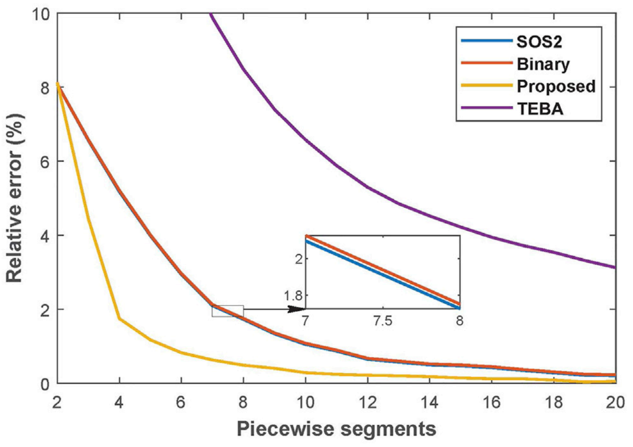

FIGURE 5 | Relative errors of four PWL approaches with increasing segments.

Figures 5 6 compare the approximation accuracy and computation efficiency of these four methods. The results come from the average of 100 calculations. As shown in **Figure 5**, the proposed method's error drops fastest as the

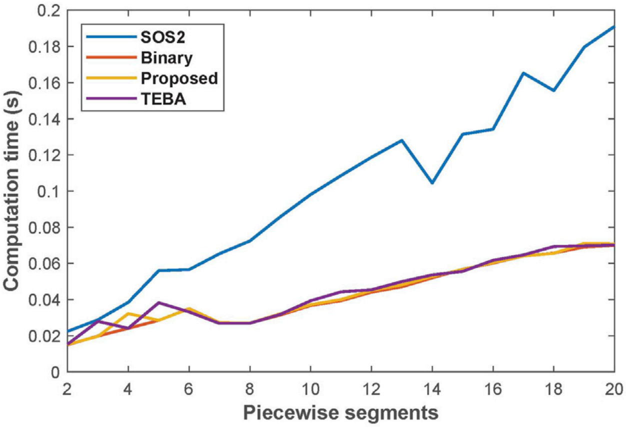

FIGURE 6 | Computation time of four PWL approaches with increasing segments.

number of segments increases. In this case, the proposed method, Binary method, SOS2, and TEBA, require 5, 10, 10, and more than 20 segments, respectively, to achieve an error of less than 1%. It suggests that, given the same number of segments, the proposed method's accuracy is clearly superior to other methods. As can be seen from **Figure 6**, the calculation time of the proposed method, Binary method and TEBA is nearly the same with the increasing segment number, while SOS2 requires a larger computation time. Since the proposed method can reduce the calculation error to an acceptable level with fewer segments, its accuracy advantage can be converted into a boost in computational efficiency.

5.2 Evaluation of Simulation Result

In this subsection, the numerical solution of the optimal scheduling problem is analyzed to confirm the effectiveness of proposed approach of iterative linearization. The demonstration system in **Figure 7** is composed of 4-bus electrical system, 7-node natural gas network, 8-node district heating network (with looped configuration of supply and return pipelines) and four EHs representing different regional IESs, including residential area, commercial area, industrial area and office area with specific layout of equipment and load characteristics.

A set of cases are designed and tested to evaluate the performance of the proposed method. Due to the heavy nonlinearity, the original MINLP model in **Eq. 29** is not solvable for the mainstream solvers like FMINCON and IPOPT (By replacing the binary variables *bin* with constraint $bin\ (1-bin) = 0$, the MINLP problem can be transformed into NLP formulation, which expands the choices of solvers) (Yang et al., 2020). Thus, the solution of the proposed method with high numbers of iterations and piecewise segments is considered accurate and taken as the reference value to compare with other results. Simulation results are obtained from a PC with an Intel Core of i5-7400U 3.00GHz CPU and 16GB RAM; the YALMIP toolbox (Lofberg, 2004) has been used to develop the optimization programs in Matlab R2019a; the solver for nonlinear programming is IPOPT and the MILP problems are solved by GUROBI.

- **Case 1**: The proposed method is carried out with the convergence tolerance of 10^{-5} and the piecewise segment of 30. The result is regarded as the benchmark value for further comparison.
- **Case 2**: The MINLP model in **Eq. 29** is implemented and solved. To make sure that the original nonlinear model is solvable, the conversion efficiencies for devices of EHs are set as constants and the constraints of the heat network are simplified according to (Shabanpour-Haghighi and Seifi, 2015a).
- **Case 3**: The proposed method is performed with the convergence tolerance of 10^{-3} and the piecewise segment of 10.

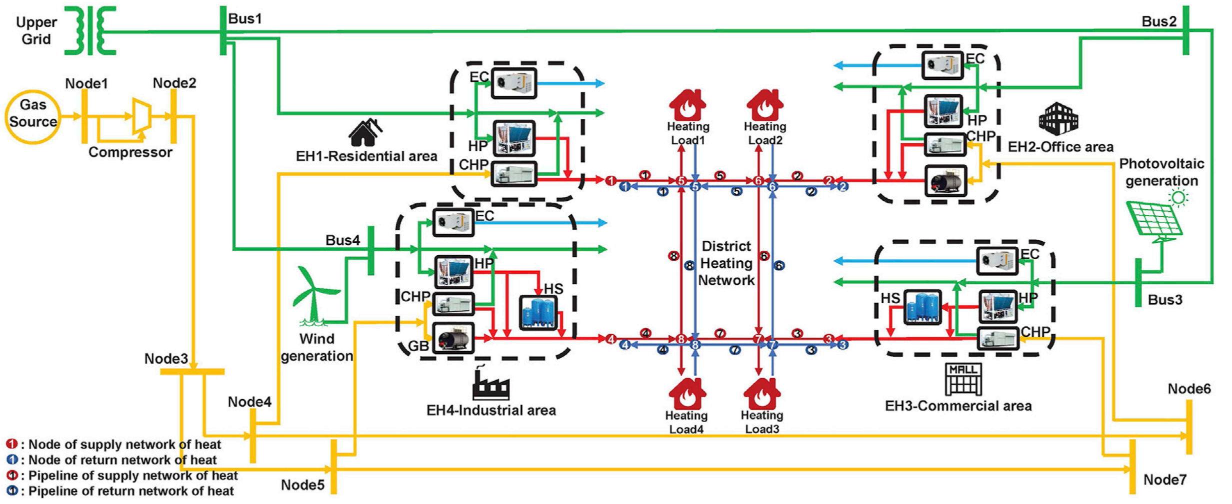

FIGURE 7 | Schematic of the system composed of four networked EHs.

TABLE 2 | Optimization result comparison for different cases.

Case	Iteration	Computation time(s)	Convergence tolerance	Optimal value ($)	Relative error (%)
Case1 (s = 30)	32	92.929	1.00E-05	9,738.09	-
Case2 (NLP)	0	154.220	-	8,595.70	11.694
Case3 (s = 10)	2	3.934	1.00E-03	9,708.62	0.302

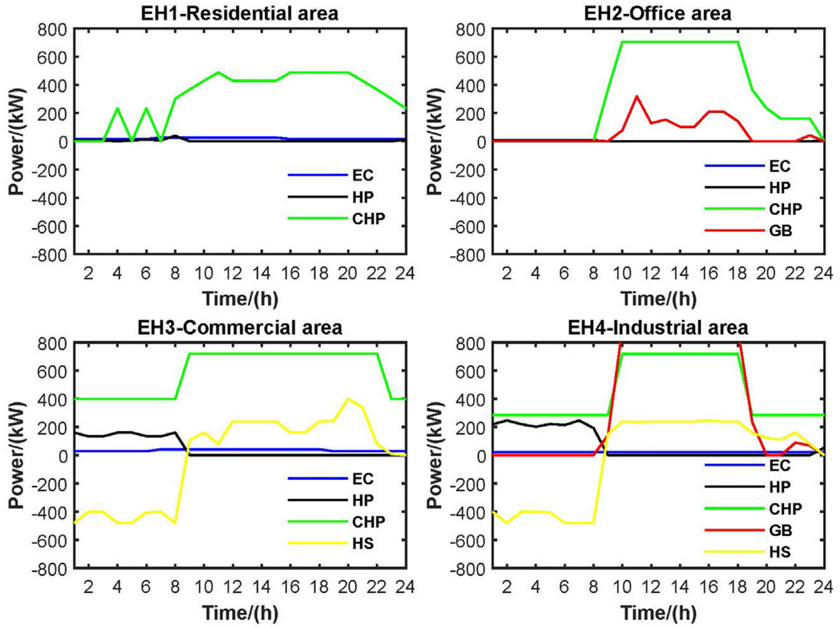

FIGURE 8 | Operation states of energy converters of four regional EHs.

Table 2 presents a comparison of optimization results for three different cases. The table shows that the calculation time and relative error of Case 3 are significantly less than those of Case 2, demonstrating the proposed method's improved accuracy and computation efficiency.

In terms of the calculation time, Case 3 has a clear advantage due to its fast computation (due to its MILP formulation) and fewer iterations. Case 2 is slow due to its MINLP property. In terms of the relative error, Case 3 has good performance since the modified PWL method and iterative approach fix the approximation deviation. Case 2 has a high relative error of 11.694%, mainly because its model is not accurate enough. The electrical and gaseous models are considered accurate because the original nonlinear constraints are taken. The inaccuracy is mainly introduced by simplifying the heating model (neglecting hydraulic constraints and return pipelines) and constant conversion efficiencies adopted for EHs.

Figure 8 shows the operating states of 4 EHs, obtained from the optimization result of Case 3. It is worth noting that the CHP unit in each region is given the highest priority for operation due to its good economic performance. The HS plays a vital role in EH3 and EH4, especially when cooperating with HP. The HP generates heat and stores it in the HS during the peak time of electricity, then the HS release heat during the off-peak time of electricity. However, the HPs are not active in EH1 and EH2 due to the absence of HS. In EH4, the GB is heavily used during the day, while the HP is active at night, since gas is relatively cheaper than electricity in daylight hours.

Since the VF-VT model of heat network is adopted, the mass flow of each pipe and the temperature of each node can be obtained in the optimization, as illustrated in **Figures 9** and **10**.

Unlike the CF-VT mode, which is extensively utilized in China, Russia, and part of Northern European countries, the VF-VT mode can more flexibly manage the flow and thus alter the total quantity of heat given to each node. In the study case, the heat loads in regions one to four are mostly concentrated throughout the daytime, and the peak load of the industrial zone is significantly higher than that of other regions, posing significant challenges to IES collaborative scheduling. As demonstrated in **Figure 10**, each pipeline can vary its flow dramatically with the VF mode to meet a load curve that fluctuates greatly throughout the day. Among all the pipelines, pipeline 4 has the highest flow and changes the most during the day since it is mostly utilized to supply the heat load in the industrial area.

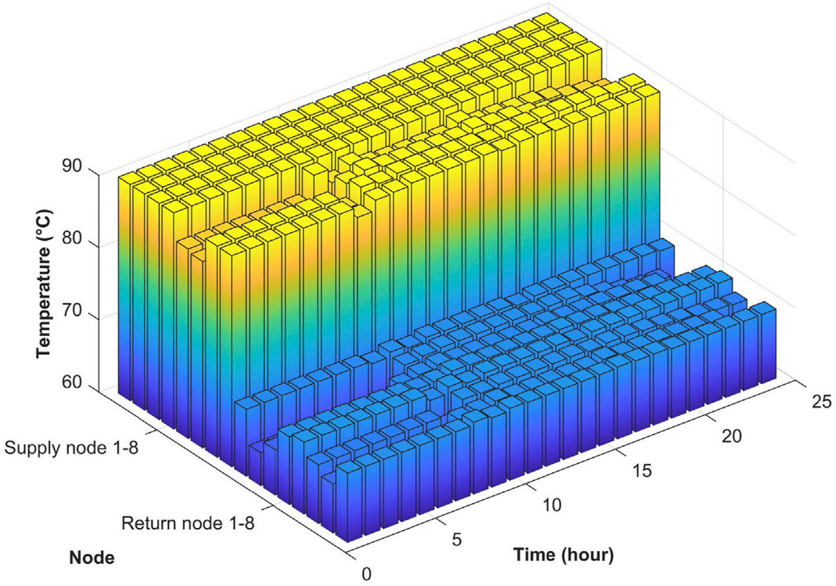

FIGURE 9 | Temperatures for each node in the heat network.

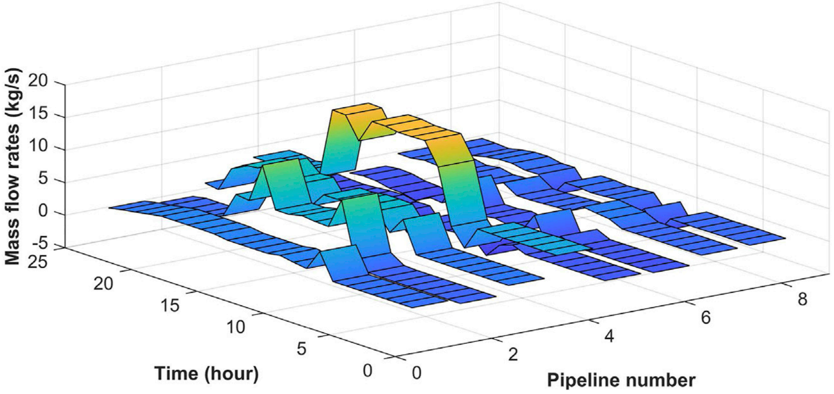

FIGURE 10 | Mass flow rate for each pipe in the heat network.

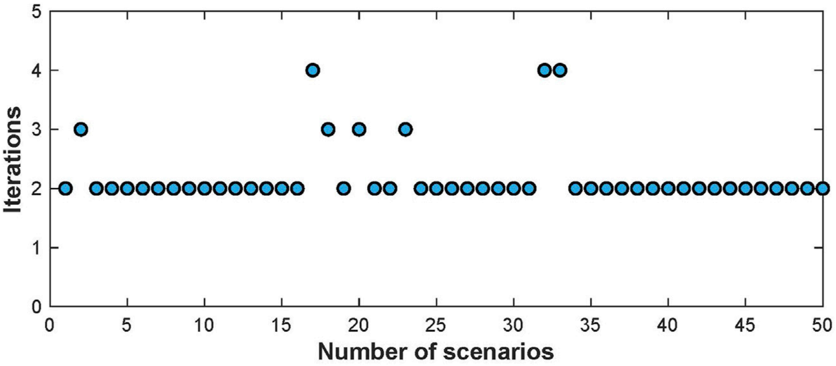

FIGURE 11 | Iterations of the proposed method in scenarios of fluctuating loads.

5.3 Adaptability Analysis

Assume that loads of electricity, heat, and gas differ uniformly with a proportion of 10% compared to the initial load values. The Monte Carlo simulation method is adopted to produce 50 scenarios with fluctuating loading conditions.

Figure 11 demonstrates the variations of the solutions under multiple scenarios. It is demonstrated that most scenarios converge within two iterations. Only a few of them require one or two more iterations, validating the convergence and adaptability of the proposed approach.

6 CONCLUSION

This paper proposes a modified piecewise linearization (PWL) method to improve the linearization performance and combines it with the sequential linear programming (SLP) algorithm to deal with the multi-dimensional nonlinear problem. The formulated mixed integer linear programming (MILP) problem is tested in a multi-regional integrated energy system (MIES) including electrical, heat, and gas networks as well as four energy hubs (EH) representing residential, commercial, industrial, and office regions, respectively. The results demonstrate that the iterative linearization method can solve the optimal scheduling problem of a multi-region integrated energy system accurately and efficiently while keeping a modest number of segments and iterations. In addition, the findings from this study make several contributions to the current literature:

1. The method presented in this paper helps solve two kinds of problems that are difficult to deal with by traditional PWL methods. The first problem is the slowdown in computation speed caused by the introduction of integer variables. In this study, the PWL method is improved to accomplish the same effect with fewer segments, minimizing the calculation time increased by the additional integer variables. The other problem is that dealing with multivariable nonlinear equations is challenging using the traditional PWL method. In this work, the PWL method is combined with the SLP algorithm to transform a complex mixed integer nonlinear programming (MINLP) problem into a MILP problem that can be solved efficiently with the powerful state-of-the-art MILP solvers.
2. The proposed method can achieve a more desirable trade-off between accuracy and computational efficiency when solving MILP problems, which is especially suitable for complex and nonlinear multi-regional integrated energy system scheduling problems. Compared with the original nonlinear model, the newly formulated MILP model is computationally cheaper with only a slight loss in accuracy. The results of the case study show that the two factors that may slow down the computational efficiency, namely segments and iterations, can be kept within a tolerable range and hence have a minimal effect on calculation performance.

Although the proposed algorithm has successfully demonstrated its effectiveness in solving MINLP problems, it lacks certain considerations in terms of time-scale interaction mechanisms between multiple energy systems, as well as the time delay and energy storage effect of gas/heating pipelines. Taking these considerations into account, the proposed algorithm has not been proven to be effective, which means it will be investigated further in our future work.

DATA AVAILABILITY STATEMENT

The original contributions presented in the study are included in the article/Supplementary Material, further inquiries can be directed to the corresponding author.

AUTHOR CONTRIBUTIONS

HT: Conceptualization, Methodology, Software, Validation, Formal analysis, Investigation, Writing-original draft, Visualization, Resources. HZ: Methodology, Software, Validation, Writing-review editing, Supervision, Project administration, Funding acquisition. CL: Methodology, Validation, Writing-review editing, Project administration. JC: Methodology, Writing-review editing, Project administration.

FUNDING

This work was supported by National Key R&D Program of China under grant 2018YFA0702200.

REFERENCES

Bao, Y.-Q., Wu, M., Zhou, X., and Tang, X. (2019). Piecewise Linear Approximation of Gas Flow Function for the Optimization of Integrated Electricity and Natural Gas System. *IEEE access* 7, 91819–91826. doi:10.1109/ACCESS.2019.2927103

Geidl, M., and Andersson, G. (2005). “A Modeling and Optimization Approach for Multiple Energy Carrier Power Flow,” in *2005 IEEE Russia Power Tech* (IEEE), 1–7. doi:10.1109/PTC.2005.4524640

He, Y., Shahidehpour, M., Li, Z., Guo, C., and Zhu, B. (2018). Robust Constrained Operation of Integrated Electricity-Natural Gas System Considering Distributed Natural Gas Storage. *IEEE Trans. Sustain. Energ.* 9, 1061–1071. doi:10.1109/TSTE.2017.2764004

Huang, W., Zhang, N., Cheng, Y., Yang, J., Wang, Y., and Kang, C. (2020a). Multienergy Networks Analytics: Standardized Modeling, Optimization, and Low Carbon Analysis. *Proc. IEEE* 108, 1411–1436. doi:10.1109/JPROC.2020.2993787

Huang, W., Zhang, N., Wang, Y., Capuder, T., Kuzle, I., and Kang, C. (2020b). Matrix Modeling of Energy Hub with Variable Energy Efficiencies. *Int. J. Electr. Power Energ. Syst.* 119, 105876. doi:10.1016/j.ijepes.2020.105876

Li, Y., Li, Z., Wen, F., and Shahidehpour, M. (2019). Privacy-preserving Optimal Dispatch for an Integrated Power Distribution and Natural Gas System in Networked Energy Hubs. *IEEE Trans. Sustain. Energ.* 10, 2028–2038. doi:10.1109/TSTE.2018.2877586

Liu, B., Meng, K., Dong, Z. Y., and Wei, W. (2019). Optimal Dispatch of Coupled Electricity and Heat System with Independent thermal Energy Storage. *IEEE Trans. Power Syst.* 34, 3250–3263. doi:10.1109/TPWRS.2019.2901254

Liu, F., Bie, Z., and Wang, X. (2019). Day-ahead Dispatch of Integrated Electricity and Natural Gas System Considering reserve Scheduling and Renewable Uncertainties. *IEEE Trans. Sustain. Energ.* 10, 646–658. doi:10.1109/TSTE.2018.2843121

Liu, T., Zhang, D., and Wu, T. (2020). Standardised Modelling and Optimisation of a System of Interconnected Energy Hubs Considering Multiple Energies-Electricity, Gas, Heating, and Cooling. *Energ. Convers. Manag.* 205, 112410. doi:10.1016/j.enconman.2019.112410

Liu, X., Wu, J., Jenkins, N., and Bagdanavicius, A. (2016). Combined Analysis of Electricity and Heat Networks. *Appl. Energ.* 162, 1238–1250. doi:10.1016/j.egypro.2014.11.92810.1016/j.apenergy.2015.01.102

Lofberg, J. (2004). "Yalmip: A Toolbox for Modeling and Optimization in Matlab," in 2004 IEEE international conference on robotics and automation (IEEE Cat. No. 04CH37508) (IEEE), 284–289.

Low, S. H. (2014). Convex Relaxation of Optimal Power Flow-Part I: Formulations and Equivalence. *IEEE Trans. Control. Netw. Syst.* 1, 15–27. doi:10.1109/TCNS.2014.2309732

Mancarella, P. (2014). Mes (Multi-energy Systems): An Overview of Concepts and Evaluation Models. *Energy* 65, 1–17. doi:10.1016/j.energy.2013.10.041

Manshadi, S. D., and Khodayar, M. E. (2018b). A Tight Convex Relaxation for the Natural Gas Operation Problem. *IEEE Trans. Smart Grid* 9, 5467–5469. doi:10.1109/TSG.2018.2817069

Manshadi, S., and Khodayar, M. (2020a). Coordinated Operation of Electricity and Natural Gas Systems: A Convex Relaxation Approach. *IEEE Trans. Smart Grid* 10, 3342–3354. doi:10.1109/PESGM41954.2020.9281784

Moeini-Aghtaie, M., Abbaspour, A., Fotuhi-Firuzabad, M., and Hajipour, E. (2014). A Decomposed Solution to Multiple-Energy Carriers Optimal Power Flow. *IEEE Trans. Power Syst.* 29, 707–716. doi:10.1109/TPWRS.2013.2283259

Molzahn, D. K., Dörfler, F., Sandberg, H., Low, S. H., Chakrabarti, S., Baldick, R., et al. (2017). A Survey of Distributed Optimization and Control Algorithms for Electric Power Systems. *IEEE Trans. Smart Grid* 8, 2941–2962. doi:10.1109/TSG.2017.2720471

Nocedal, J., and Wright, S. (2006). *Numerical Optimization*. Springer Science & Business Media.

Shabanpour-Haghighi, A., and Seifi, A. R. (2015a). Energy Flow Optimization in Multicarrier Systems. *IEEE Trans. Ind. Inf.* 11, 1067–1077. doi:10.1109/TII.2015.2462316

Shabanpour-Haghighi, A., and Seifi, A. R. (2015b). Multi-objective Operation Management of a Multi-Carrier Energy System. *Energy* 88, 430–442. doi:10.1016/j.energy.2015.05.063

Shao, C., Ding, Y., Wang, J., and Song, Y. (2018). Modeling and Integration of Flexible Demand in Heat and Electricity Integrated Energy System. *IEEE Trans. Sustain. Energ.* 9, 361–370. doi:10.1109/TSTE.2017.2731786

Shao, C., Wang, X., Shahidehpour, M., Wang, X., and Wang, B. (2017). An Milp-Based Optimal Power Flow in Multicarrier Energy Systems. *IEEE Trans. Sustain. Energ.* 8, 239–248. doi:10.1109/TSTE.2016.2595486

Sheikhi, A., Bahrami, S., and Ranjbar, A. M. (2015). An Autonomous Demand Response Program for Electricity and Natural Gas Networks in Smart Energy Hubs. *Energy* 89, 490–499. doi:10.1016/j.energy.2015.05.109

Wang, C., Wei, W., Wang, J., Bai, L., Liang, Y., and Bi, T. (2018a). Convex Optimization Based Distributed Optimal Gas-Power Flow Calculation. *IEEE Trans. Sustain. Energ.* 9, 1145–1156. doi:10.1109/TSTE.2017.2771954

Wang, Y., Zhang, N., Kang, C., Kirschen, D. S., Yang, J., and Xia, Q. (2019b). Standardized Matrix Modeling of Multiple Energy Systems. *IEEE Trans. Smart Grid* 10, 257–270. doi:10.1109/TSG.2017.2737662

Yang, L., Zhao, X., and Xu, Y. (2020). A Convex Optimization and Iterative Solution Based Method for Optimal Power-Gas Flow Considering Power and Gas Losses. *Int. J. Electr. Power Energ. Syst.* 121, 106023. doi:10.1016/j.ijepes.2020.106023

Zhang, X., Shahidehpour, M., Alabdulwahab, A., and Abusorrah, A. (2016a). Hourly Electricity Demand Response in the Stochastic Day-Ahead Scheduling of Coordinated Electricity and Natural Gas Networks. *IEEE Trans. Power Syst.* 31, 592–601. doi:10.1109/TPWRS.2015.2390632

Zhang, X., Shahidehpour, M., Alabdulwahab, A., and Abusorrah, A. (2015b). Optimal Expansion Planning of Energy Hub with Multiple Energy Infrastructures. *IEEE Trans. Smart Grid* 6, 2302–2311. doi:10.1109/TSG.2015.2390640

Conflict of Interest: The authors declare that the research was conducted in the absence of any commercial or financial relationships that could be construed as a potential conflict of interest.

frontiers
in Energy Research

ORIGINAL RESEARCH
published: 28 March 2022
doi: 10.3389/fenrg.2022.863292

Energy Optimal Dispatch of the Data Center Microgrid Based on Stochastic Model Predictive Control

Yixin Zhu, Jingyun Wang, Kaitao Bi, Qingzhu Sun, Yu Zong and Chenxi Zong*

School of Internet of Things Engineering, Jiangnan University, Wuxi, China

Renewable energy outputs such as wind turbines and photovoltaics, as well as data center workloads are both random and uncertain. In order to enhance the stability and economy of the data center in actual operation effectively, a multi-time scale optimal dispatch method for the data center microgrid based on stochastic model predictive control is proposed in this paper. In the day-ahead scheduling stage, the characteristic of the data center that batch workloads are allowed to be served delayed is considered. And the scenario analysis method is applied to describe the uncertainty of loads and renewable energy outputs, based on which an economic optimization scheduling model is established to minimize the system operating cost. The intra-day scheduling utilizes the rolling optimization and feedback correction of model predictive control to correct the deviation of loads and renewable energy outputs and adjust the day-ahead dispatch plan in real time, which ensures the effectiveness of day-ahead plan and the stability of system operating. Through the simulation results of a typical data center microgrid, the effectiveness of the proposed method is verified.

Keywords: data center, stochastic model predictive control, scenarios analysis method, batch workload, energy optimal dispatch

Edited by:
Liansong Xiong,
Nanjing Institute of Technology (NJIT), China

Reviewed by:
Tianhua Zhu,
Aalborg University, Denmark
Xuanlyu Wu,
Northwestern Polytechnical University, China
Shi Hongtao,
North Minzu University, China

****Correspondence:***
Jingyun Wang
wangjingyun1107@163.com

Specialty section:
This article was submitted to Process and Energy Systems Engineering, a section of the journal Frontiers in Energy Research

Received: *27 January 2022*
Accepted: *01 March 2022*
Published: *28 March 2022*

Citation:
Zhu Y, Wang J, Bi K, Sun Q, Zong Y and Zong C (2022) Energy Optimal Dispatch of the Data Center Microgrid Based on Stochastic Model Predictive Control. Front. Energy Res. 10:863292. doi: 10.3389/fenrg.2022.863292

1 INTRODUCTION

With the rapid development of big data and cloud computing technology in recent years, the quantity and scale of data centers have been expanding. At the same time, the electricity consumption is also growing tremendously. It is estimated that about 2% of the world's total electricity consumption is related to data centers, and the power demand of this sector is increasing at an annual rate of 15%–20% (Ebrahimi et al., 2015). The electricity bills that some data centers pay to the electricity market is as high as tens of millions. In order to reduce the electricity consumption costs, more and more data centers choose to connect lower-cost renewable energy generators such as wind turbines (WT) and photovoltaics (PV) to their power supply system (Liu B et al., 2021). Futhermore, data centers belong to the category of first-class loads; hence, power supply cannot be interrupted. It is necessary for data centers to equip with alternative power sources to ensure the sustainable and reliable power supply (Wang et al., 2020). Thus, data center construction areas always integrate energy storage systems (ESS), conventional power generators, and renewable energy generators, which constitute a typical microgrid system (Li and Qi, 2018; Yu et al., 2018). On the other hand, batch workloads in data centers are allowed to be served delayed and migrated and can be flexibly allocated according to the peak–valley difference of the electricity price. With the technology of the energy management and optimal dispatch, the power consumption and operating cost of data centers can be reduced effectively.

Recently, the research on energy management in data centers has been increasing. In the study by Chen et al. (2016a), the data center is considered as a microgrid, where renewable energy outputs and ESS are optimized, but the scheduling of data center workloads was ignored. The classification of data center workloads was studied by Ding et al. (2019), wherein by allocating the batch workloads and utilizing renewable energy, the energy consumption of the data center was reduced effectively. The impact on the main grid caused by data center workload migration is considered in a study by Wang et al. (2016), and the interaction between the main grid and data center is modeled as a two-stage programing problem. In a study by Wen and Liu (2019), an optimal scheduling model of the hybrid wind–solar–hydro power generation system with data center workloads was studied. The demand side and power supply side-joint scheduling was adopted, which improved the economy of the system. In a study by Wang et al. (2017), a day-ahead resource dispatch problem considering conventional generator fuel and carbon emission costs was proposed, and a mixed integer linear programming (MILP) model was formulated to solve it.

Although many progresses have been made in the research on energy management of the data center, most research mainly studied the energy management of the data center operating in a certain scenario. In fact, the renewable energy and data center workloads are quiet random and uncertain. The randomness of renewable outputs and workloads distribution, as well as the change of electricity price, are considered in Ding et al. (2018), and a day-ahead stochastic planning scheme for the data center microgrid (DCMG) was proposed. A stochastic programming based on the MILP model for the data center energy management was proposed in Xu et al. (2019), which can deal with the influence of uncertainty effectively. The aforementioned studies consider the influence of uncertain factors in the data center, but the optimal dispatch was only in the day-ahead stage. In actual operation, real-time variety of workloads and renewable energy outputs will still affect the security and economy of the data center, and the stability of the main grid will be affected at the same time (Liu et al., 2018; Xiong et al., 2020).

Model predictive control (MPC) is an advanced method for process control, which has been widely used in a variety of complex dynamic systems (Camacho and Bordons, 2004). Recently, it also has drawn much attention of the energy management studies. In the study by Chen et al. (2013), a MPC-based appliance scheduling method for a smart home was proposed with the consideration of dynamic prices and appliance usage patterns. In the study by Zhang et al. (2015), a closed-loop scheduling model for microgrid energy management was established based on MPC. Through the closed-loop feedback, model prediction, and iterative update strategy of MPC, the economy of the system was improved. However, the aforementioned scheduling models lack the guidance of day-ahead plans, and the optimization results do not have the global optimality.

The contributions of this article are listed as follows:

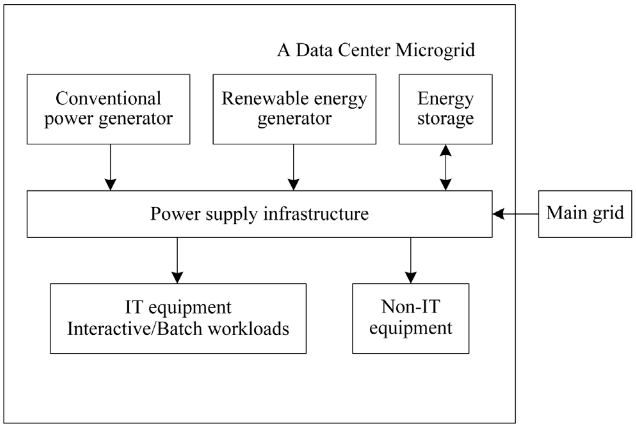

FIGURE 1 | The structure of a DCMG.

(1) Considering the unique characteristics of data center workloads and describing stochastic factors with the scenario analysis method, a multi-time scale optimal dispatch model combining day-ahead and intra-day rolling correction of DCMG was constructed based on stochastic model predictive control (SMPC).
2) The case study of a typical DCMG scenario was conducted to verify the effectiveness and feasibility of the proposed multi-time scale model.

2 THE DATA CENTER MICROGRID SYSTEM

The structure of the DCMG is shown in **Figure 1**. A DCMG usually consists of conventional generators, distributed renewable generators, ESS, and data center loads. In most cases, it needs to purchase electricity power from the main grid. The main difference between the DCMG and general microgrids is the unique power consumption characteristic. The workload of the data center refers to the information and data that need to be processed, which depends on the user's behavior of using the network, and has greater randomness and uncertainty. The workload also determines the total power consumption of the data center, which is the basis for the flexible adjustment of the data center's electrical load.

According to the differences in user's computing requirements, the data center workload can be divided into two categories: the interactive and batch workloads. The interactive workload must be served immediately (usually a few seconds) when the users submit requests for computing services, such as opening a web page, entering passwords, and sending voice messages. The batch workload can be processed more flexibly before the deadline. The service time can be delayed by several hours or even 1 day. The batch job normally includes scientific computing, data backup, image processing, and other data-intensive tasks (Chen et al., 2016b). Therefore, dispatching the batch workload according to the peak-to-valley electricity price can reduce the operating cost of the data center.

The total power consumption of the data center includes the consumption of IT equipments and non-IT equipments (such as refrigeration system, lighting system, etc.). power usage effectiveness (PUE) is an important indicator to measure the energy efficiency of a data center (Jaureguialzo, 2011). It is defined as the ratio of the total power consumption of the data center to the power consumption of IT equipments. The PUE value is always greater than 1, and the lower the PUE value, the more energy-efficient the data center. According to the PUE value and the power consumed by IT equipment, the total power consumption of the data center can be calculated.

3 ENERGY OPTIMAL DISPATCH MODEL OF THE DCMG BASED ON SMPC

3.1 Day-Ahead Optimization Scheduling

3.1.1 The Objective Function

The objective of the day-ahead optimization scheduling is to minimize the total operating cost of the data center. In this article, power demand and renewable energy output forecasts are considered as stochastic parameters owing to their randomness and uncertainty. The scenario analysis method is based on the probability theory; the research object of uncertainty information is described by scenarios, and each scenario constructed corresponds to a certain probability. The key of the method is to fully reflect the uncertainty information with limited scenarios. In this article, it is used to transform the uncertainty of the DCMG into multiple deterministic scenarios. The objective function is shown as follows:

$$\min C = \sum_{s=1}^{S}\sum_{t=1}^{T} Pr_s \cdot F_s^t \tag{1}$$

$$F_s^t = \sum_{i=1}^{N_{\mathrm{DG}}} \left(C_{\mathrm{f}}\left(P_{Gi}^{s,t}\right) + C_{\mathrm{OM}}\left(P_{Gi}^{s,t}\right) + C_{\mathrm{eav}}\left(P_{Gi}^{s,t}\right)\right) + C_{\mathrm{pp}}\left(P_{\mathrm{Grid}}^{s,t}\right) \tag{2}$$

where C indicates the total operating cost of the data center; S indicates the number of total scenarios, which is the combination of the sample sets of each part; Pr_s indicates the probability of the scenario s, which is the product of sample probabilities of each part; T indicates the total time periods of day-ahead optimization scheduling, which is 24 h; $F\ t\ s$ indicates the operating cost in the t-th period and the s-th scenario; and N_{DG} indicates the number of distributed generators. $C_{\mathrm{f}}(\cdot)$, $C_{\mathrm{OM}}(\cdot)$, and $C_{\mathrm{eav}}(\cdot)$ indicate the fuel consumption cost, maintenance cost, and pollution emission cost of distributed generators, respectively; $P\ s,t$ Gi indicates the output of the ith distributed generator in the t-th period; $P\ s,t$ Grid indicates the electricity purchase power from the main grid in the t-th period; and $C_{\mathrm{pp}}(\cdot)$ indicate the cost of the purchasing electricity from the main grid.

3.1.2 The Constraint Conditions

Based on the structure of the DCMG shown in **Figure 1**, the constraints including power consumption of the data center, distributed generators, ESS, and interaction with the main grid need to be considered in the day-ahead dispatch model. In addition, the DCMG system must satisfy the power balance between supply and demand, which is the premise for the data center to realize stable and economic operation.

(1) Data Center Workload Constraint

Suppose that there are M servers with the same structure in the data center, and the loads distribution of each server is equal, limited by the computing power of CPU, there is an upper limit on the workloads that can be processed in each time period that can be calculated as follows:

$$L^t \le L_C, \forall t \tag{3}$$

where L^t indicates total workloads processed by the CPU in the t-th period, and L_{C} indicates the upper limit of the workloads processed by the CPU of the data center, and

$$L^t = L_{\mathrm{ds}}^t + L_{\mathrm{dt}}^t - \sigma_{\mathrm{load}}^t, \forall t \tag{4}$$

where L_{ds}^t and L_{dt}^t indicate the interactive and batch workloads of the data center in the t-th period, and σ_{load}^t indicates the workloads that is being processed in the t-th period.

The process of the flexible scheduling of batch workloads can be expressed as follows (Wang et al., 2017):

$$Q_{\mathrm{dt}}^t = Q_{\mathrm{dt}}^{t-1} + L_{\mathrm{dt}}^t - \sigma_{\mathrm{load}}^t, \forall t \le \tag{5}$$

$$Q_{\mathrm{dt}}^T = 0 \tag{6}$$

where $Q\ {}^t_{dt}$ indicates the batch workloads that have not been processed by the data center until the t-th period.

The power consumed by IT equipments is related to the quantities of workloads processed by the CPU. According to the concept of PUE, the total power consumption of the data center can be calculated. The total power of the data center in the t-th period can be expressed as shown in (Yu et al., 2014):

$$P_{\mathrm{Load}}^t = M\left(\delta + \mu L_t\right), \forall t \tag{7}$$

$$\delta \triangleq P_{\mathrm{idle}} + (PUE - 1)P_{\mathrm{peak}} \tag{8}$$

$$\mu \triangleq P_{\mathrm{peak}} - P_{\mathrm{idle}} \tag{9}$$

where $P\ {}^t_{Load}$ indicates the total power of the data center in the t-th period; M is the quantity of servers in the data center; δ and μ are the intermediate variables for calculation; P_{idle} and P_{peak} respectively indicate the power consumption when the server is in the idle and busy states.

(2) System Power Balance Constraint

$$\sum_{i=1}^{N_{\mathrm{DG}}} P_{Gi}^{s,t} + P_{\mathrm{Grid}}^{s,t} = P_{\mathrm{Load}}^{s,t} + P_{\mathrm{ESS}}^{s,t} \tag{10}$$

where $P\ s,t$ ESS indicates the charging and discharging power of ESS in the tth period, the positive value represents ESS charging, and the negative value represents ESS discharging.

(3) Interaction Power with the Main Grid Constraint

$$P_{\mathrm{Grid}}^{\min} \le P_{\mathrm{Grid}}^{s,t} \le P_{\mathrm{Grid}}^{\max} \tag{11}$$

where *P*min Grid and *P*max Grid respectively indicate the upper and lower limits of the interaction power between the DCMG and the main grid.

(4) Distributed Generators Operating Constrain

$$P_{Gi}^{\min} \le P_{Gi}^{s,t} \le P_{Gi}^{\max} \tag{12}$$

$$\Delta P_{Gi}^{\min} \le P_{Gi}^{s,t} - P_{Gi}^{s,t-1} \le \Delta P_{Gi}^{\max} \tag{13}$$

Eq. 12 is the output power constraint of distributed generators, where *P*min G*i* and *P*max G*i* respectively indicate the maximum and minimum output power of the *i*th distributed generator. **Eq. 13** is the climb power constraint of operating distributed generators, where Δ*P*max G*i* and Δ*P*min G*i* respectively indicate the upper and lower limits of the climbing power of the *i*th distributed generator.

(5) ESS Constraint

The constraints during the operation of ESS mainly include the upper and lower limits of charging and discharging power and the state of charge (SOC) constraint.

$$-P_{\text{ESS}}^{\max} \le P_{\text{ESS}}^{s,t} \le P_{\text{ESS}}^{\max} \tag{14}$$

where *P s,t* ESS indicates the maximum of charging and discharging power of ESS.

The SOC of ESS in the *t*-th period can be expressed by the formulas in following:

$$S_{\text{ESS}}^{s,t} = S_{\text{ESS}}^{s,t-1}(1-\sigma) + \eta \frac{P_{\text{ESS}}^{s,t}\Delta t}{E_{\text{ESS}}} \tag{15}$$

where *S s,t* ESS indicates the SOC of ESS in the *t*-th period; σ indicates the self-consumption rate of ESS; η indicates the charging and discharging efficiency of ESS; E_{ESS} indicates the total capacity of ESS; and Δt indicates the time interval.

The SOC constraint of ESS is expressed as follows:

$$S_{\text{ESS}}^{\min} \le S_{\text{ESS}}^{s,t} \le S_{\text{ESS}}^{\max} \tag{16}$$

$$S_{\text{ESS}}^{s,t=0} = S_{\text{ESS}}^{s,t=T} \tag{17}$$

where *S*max ESS and *S*min ESS respectively indicate the upper and lower limits of the SOC. In addition, the SOC should be consistent at the beginning and the end of the dispatch cycle.

3.2 Intra-Day Rolling Optimization Scheduling

The MPC is a kind of a model-based closed-loop optimization control strategy. The core of MPC is to continuously perform rolling optimization in a finite-time domain based on the mathematical model of the controlled object. The strategy mainly includes the following steps:

(1) At the current time step k and the current state $\boldsymbol{x}(k)$, MPC predicts the future state of the system based on the prediction model. Considering the current and future constraints, obtain the control command sequences at the future time steps k+1, k+2, . . . , $k + M$ by solving the optimization problem.
(2) Apply the control command of the first time step to the system.
(3) At the time step k+1, update the state $x(k+1)$ and repeat the aforementioned steps.

Taking a typical grid-connected DCMG as an example, it consists of WT, PV, a micro gas turbine (MT), a fuel cell generator (FC), ESS, and data center loads. The state variable at the time step k is

$$\boldsymbol{x}(k) = [P_{\text{MT}}(k), P_{\text{FC}}(k), P_{\text{ESS}}(k), S_{\text{ESS}}(k), P_{\text{Grid}}(k)]^{\text{T}}$$

The control variable is

$$\boldsymbol{u}(k) = [\Delta P_{\text{MT}}(k), \Delta P_{\text{FC}}(k), \Delta P_{\text{ESS}}(k)]^{T}$$

The disturbance variable is

$$\boldsymbol{r}(k) = [\Delta P_{Load}(k), \Delta P_{WT}(k), \Delta P_{PV}(k)]^{T}$$

The output variable is

$$\boldsymbol{y}(k) = [P_{Grid}(k), S_{\text{ESS}}(k)]^{T}$$

The multi-input and multi-output state space model can be established as follows:

$$\boldsymbol{x}(k+\Delta t) = \begin{bmatrix} P_{\text{MT}}(k+\Delta t) \\ P_{\text{FC}}(k+\Delta t) \\ P_{\text{ESS}}(k+\Delta t) \\ S_{\text{ESS}}(k+\Delta t) \\ P_{\text{Grid}}(k+\Delta t) \end{bmatrix} = \begin{bmatrix} 1 & 0 & 0 & 0 & 0 \\ 0 & 1 & 0 & 0 & 0 \\ 0 & 0 & 1 & 0 & 0 \\ 0 & 0 & -\eta\dfrac{\Delta t}{E_{\text{ESS}}} & 1-\sigma & 0 \\ 0 & 0 & 0 & 0 & 1 \end{bmatrix} \begin{bmatrix} P_{\text{MT}}(k) \\ P_{\text{FC}}(k) \\ P_{\text{ESS}}(k) \\ S_{\text{ESS}}(k) \\ P_{\text{Grid}}(k) \end{bmatrix} + \begin{bmatrix} 1 & 0 & 0 \\ 0 & 1 & 0 \\ 0 & 0 & 1 \\ 0 & 0 & -\eta\dfrac{\Delta t}{E_{\text{ESS}}} \\ -1 & -1 & -1 \end{bmatrix} \begin{bmatrix} \Delta P_{\text{MT}}(k) \\ \Delta P_{\text{FC}}(k) \\ \Delta P_{\text{ESS}}(k) \end{bmatrix} + \begin{bmatrix} 0 & 0 & 0 \\ 0 & 0 & 0 \\ 0 & 0 & 0 \\ 0 & 0 & 0 \\ 1 & -1 & -1 \end{bmatrix} \begin{bmatrix} \Delta P_{\text{Load}}(k) \\ \Delta P_{\text{WT}}(k) \\ \Delta P_{\text{PV}}(k) \end{bmatrix} \tag{18}$$

$$\boldsymbol{y}(k) = \begin{bmatrix} P_{\text{Grid}}(k) \\ S_{\text{ESS}}(k) \end{bmatrix} = \begin{bmatrix} 0 & 0 & 0 & 0 & 1 \\ 0 & 0 & 0 & 1 & 0 \end{bmatrix} \cdot \begin{bmatrix} P_{\text{MT}}(k) & P_{\text{FC}}(k) & P_{\text{ESS}}(k) & S_{\text{ESS}}(k) & P_{\text{Grid}}(k) \end{bmatrix}^{T} \tag{19}$$

The objective of the intra-day optimization dispatch is to minimize the error between the prediction output value of the output variable and the day-ahead plan value and ensure that the adjustment value of each controllable device in the system is as small as possible. The intra-day rolling optimization dispatch model can be expressed as follows:

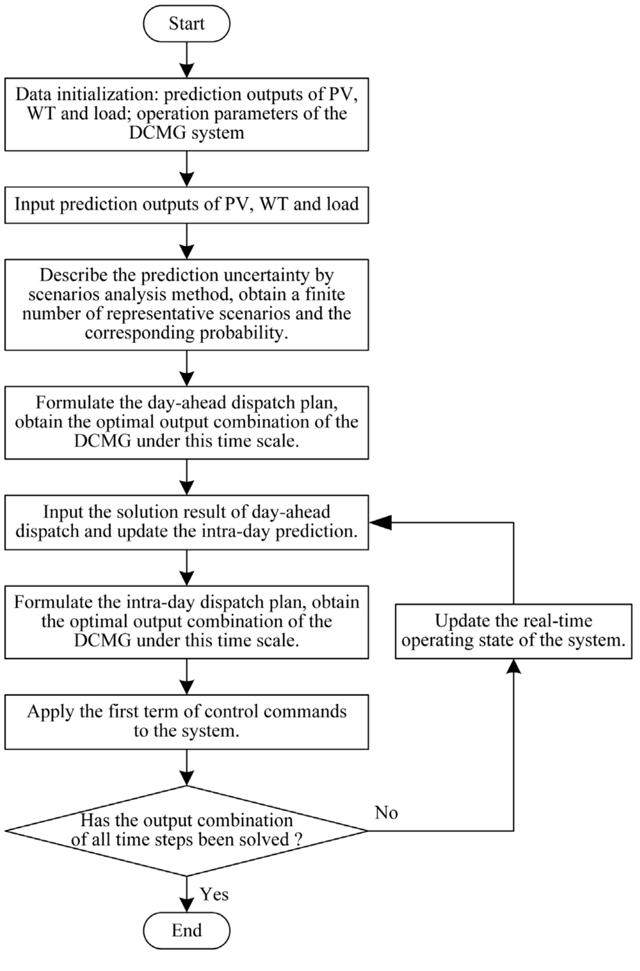

FIGURE 2 | Flow chart of the energy optimal dispatch.

$$\min J = (\boldsymbol{R}_{\mathrm{DA}} - \boldsymbol{Y}_{\mathrm{f}})^T \boldsymbol{W}_{\mathrm{err}} (\boldsymbol{R}_{\mathrm{DA}} - \boldsymbol{Y}_{\mathrm{f}}) + \boldsymbol{U}^{\mathrm{T}} \boldsymbol{Q}_{\mathrm{u}} \boldsymbol{U}$$
$$s.t. \begin{cases} \Delta P_{\mathrm{MT}}^{\min} \le \Delta P_{\mathrm{MT}}^{t} \le \Delta P_{\mathrm{MT}}^{\max} \\ P_{\mathrm{MT}}^{\min} \le P_{\mathrm{MT}}^{t} \le P_{\mathrm{MT}}^{\max} \\ \Delta P_{\mathrm{FC}}^{\min} \le \Delta P_{\mathrm{FC}}^{t} \le \Delta P_{\mathrm{FC}}^{\max} \\ P_{\mathrm{FC}}^{\min} \le P_{\mathrm{FC}}^{t} \le P_{\mathrm{FC}}^{\max} \\ \Delta P_{\mathrm{ESS}}^{\min} \le \Delta P_{\mathrm{ESS}}^{t} \le \Delta P_{\mathrm{ESS}}^{\max} \\ P_{\mathrm{ESS}}^{\min} \le P_{\mathrm{ESS}}^{t} \le P_{\mathrm{ESS}}^{\max} \\ S_{\mathrm{ESS}}^{\min} \le S_{\mathrm{ESS}}^{t} \le S_{\mathrm{ESS}}^{\max} \end{cases} \tag{20}$$

where $\boldsymbol{R}_{\mathrm{DA}}$ and $\boldsymbol{Y}_{\mathrm{f}}$ respectively indicate the day-ahead plan value and the intra-day prediction output value of the output variable; $\boldsymbol{W}_{\mathrm{err}}$ and $\boldsymbol{Q}_{\mathrm{u}}$ are the weight coefficient matrices.

By solving the above model, the optimal control command sequences of output adjustment for each device in the control time domain was obtained. At the current time step, only the first control command was executed. At the next time step, the aforementioned rolling optimization process is repeated. In addition, the real-time operating state of the system is used for feedback correction during each rolling optimization, which ensures better stability and robustness of the rolling optimization strategy.

TABLE 1 | Parameter values of the DCMG system.

Equipment	Parameter	Value
WT	Rated power	400 kW
	Operation and maintenance Cost	0.0296 ￥/kWh
PV	Rated power	300 kW
	Operation and maintenance Cost	0.0096 ￥/kWh
MT	Rated power	800 kW
	Climbing power	160
	Operation and maintenance Cost	0.0352 ￥/kWh
FC	Rated power	400 kW
	Climbing power	80 kW
	Operation and maintenance Cost	0.0293 ￥/kWh
ESS	Total capacity	2,400 kWh
	Rated charge and discharge power	240 kW
	Initial value of SOC	0.2
	Range of SOC	0.1–0.9
	Charge and discharge efficiency	95%
	Self-consumption rate	0.01
The main grid	Maximum of the interaction power	2000 kW

TABLE 2 | Electricity price of the main grid parameter values.

Time period	Time interval	Price(￥/kWh)
Valley period	0:00–7:00 23:00–24:00	0.291
Normal period	7:00–10:00 15:00–18:00 21:00–23:00	0.633
Peak period	10:00–15:00 18:00–21:00	1.005

3.3 Energy Optimal Dispatch Strategy Based on SMPC

In this article, the energy optimal dispatch of the DCMG was divided into two stages: day-ahead optimization scheduling and intra-day rolling optimization scheduling, constituting a multi-time scale optimal model. The flow chart of the specific optimal model solution process is shown in **Figure 2**.

In the aforementioned solving process, the SMPC-based energy optimal dispatch strategy of the DCMG constitutes the MILP problem. Based on MATLAB software, this article uses=d the CPLEX solver and the YALMIP toolbox to solve the aforementioned MILP problem.

4 CASE STUDY

4.1 Setting

A typical DCMG system was taken as an example. The system structure is consistent with the aforementioned DCMG system. In addition, the data center can purchase electricity from the main grid. The main basic parameters of the system are shown in **Table 1**. The time-of-use electricity price of the main grid is shown in **Table 2** (Xiao et al., 2014).

Since it is currently difficult to obtain the detailed statistical information of data center workloads, some studies assume that

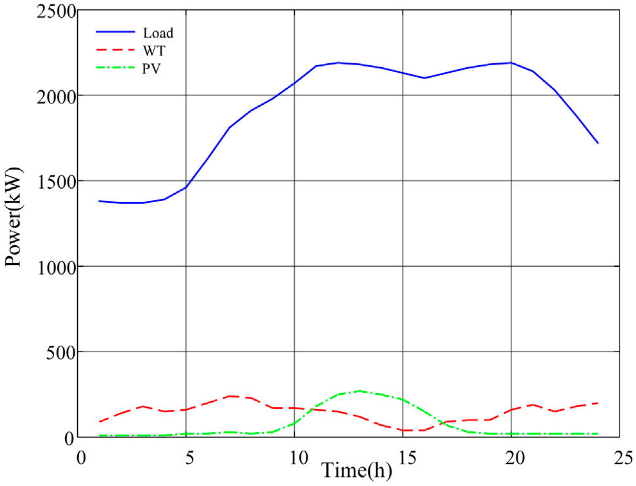

FIGURE 3 | Prediction power of WT, PV, and load of the data center.

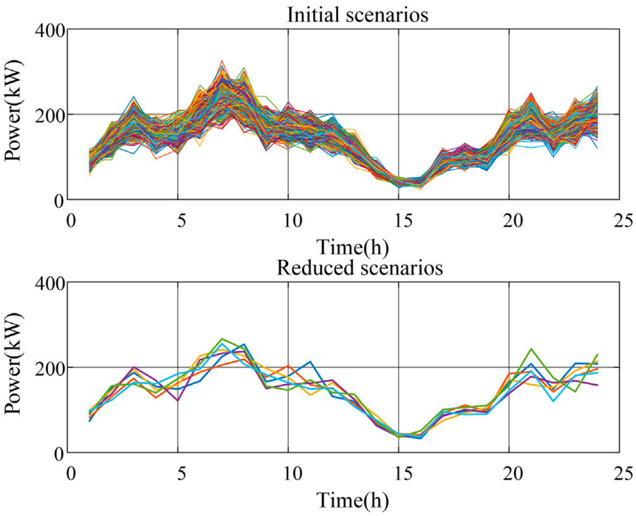

FIGURE 4 | Scenario generation and reduction results of WT.

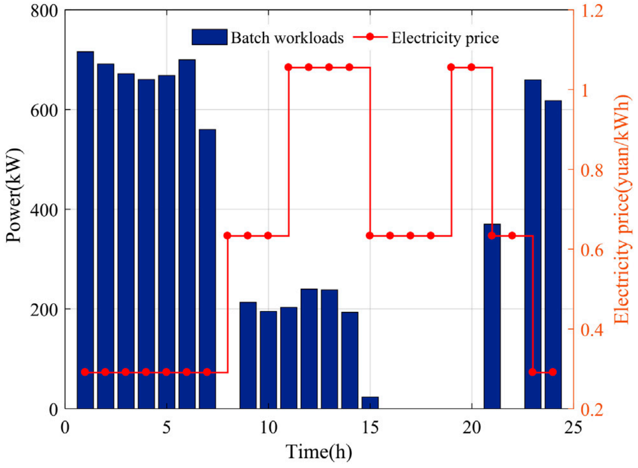

FIGURE 5 | The allocation of data center batch workloads.

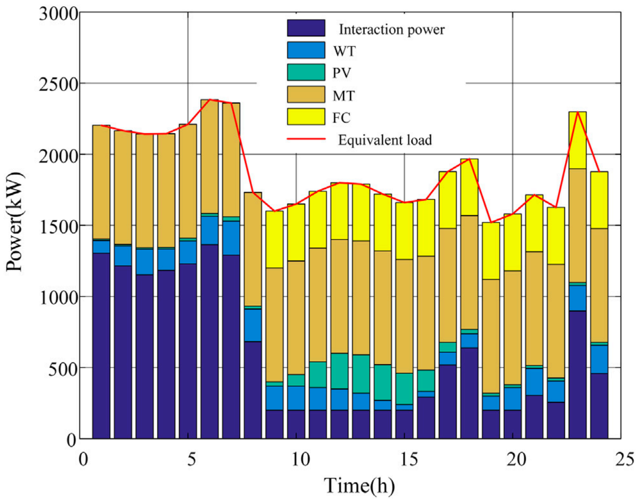

FIGURE 6 | Day-ahead Optimization results.

there is a certain proportion relationship between the interactive and batch workloads (Luo et al., 2014; Li and Qi, 2018). In this article, it was set that the ratio of interactive and batch workloads were 4:1. In the actual situation, the ratio depends on the users of the data center. The parameters of the data center are set based on the data in the stdy by Yu et al. (2014). The PUE value is set to 1.2 based on the description of the study by Dou et al. (2017).

4.2 Result Analysis

4.2.1 Day-Ahead Optimization Results

The prediction power curves of WT, PV outputs, and total loads of the data center are shown in **Figure 3**. Considering that all the prediction errors of them obey the normal distribution, first, a large number of initial power scenarios were generated by Latin hypercube sampling (LHS). Then, based on the similarity of each scenario, the initial scenarios were reduced by employing the backward reduction algorithm (Wang et al., 2015). Finally, a set of loads and renewable energy output scenarios was obtained, as well as corresponding probabilities. Considering that the outputs of WT changes more dramatically (Liu J et al., 2021), the number of WT output scenarios after the reduction was 6, and the number of PV output and load scenarios was 5, with a total of 150 scenarios. **Figure 4** shows the results of scenario generation and the reduction of the WT output.

Figure 5 shows the allocation result of the batch workloads of the DCMG system. The interactive workloads in each period need to be served immediately, while the batch workloads allows flexible scheduling. It can be seen that the batch workloads are allocated to the period with the lowest electricity price (23:00-7:00) as far as possible.

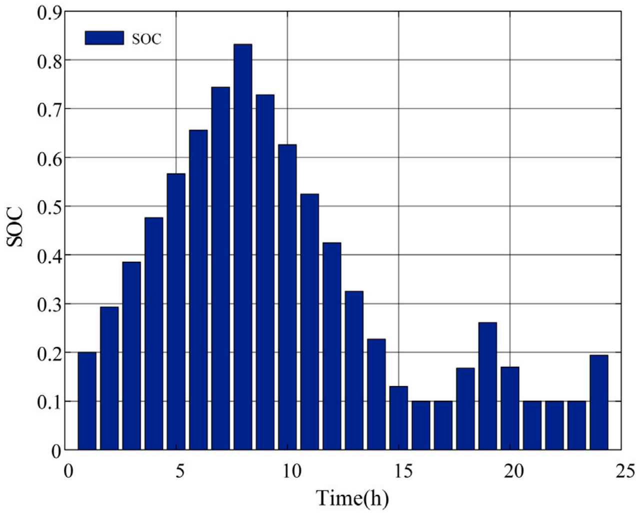

FIGURE 7 | SOC of ESS.

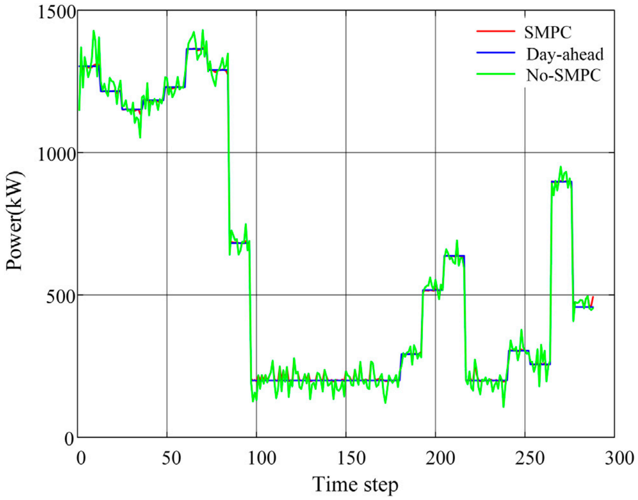

FIGURE 9 | Comparison of interaction power with the main grid.

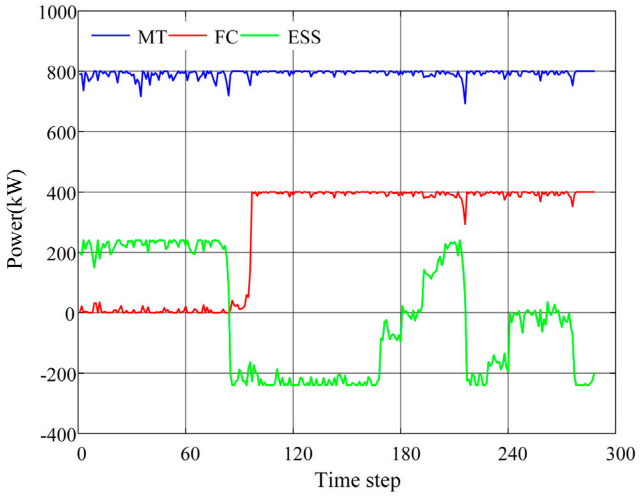

FIGURE 8 | Intra-day rolling optimization results.

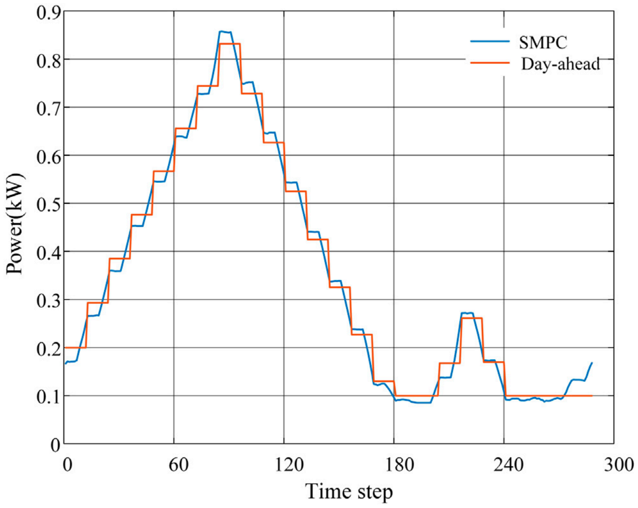

FIGURE 10 | Comparison of SOC.

The day-ahead optimization dispatch plan of each device in the DCMG system is shown in **Figure 6**. For the convenience of analysis, the concept of “equivalent load” in the figure was derived from **Eq. 10**. The equivalent load is equal to the sum of the load and the charging and discharging power of ESS. It can be seen from **Figure 6** that the output of each unit in the DCMG system satisfies the power balance constraint. Because the output power of WT and PV is limited by the installed capacity, it only accounts for a small part of the load demand. When the electricity price is at the peak, MT and FC are the main power supply sources. In the valley period of electricity price, since some batch workloads allocated to these periods are to be served and ESS works in the charging state, the proportion of electricity purchased from the main grid increased obviously.

The SOC of ESS is shown in **Figure 7**. The variation of SOC is maintained within the set range of 0.1–0.9, and SOC satisfies the balance at the beginning and end of the dispatch cycle. It can be seen that ESS is arranged to charge in the valley period and discharge in the peak period, which achieves the “peak-to-valley arbitrage” and improves the economy of system operation.

4.2.2 Intra-day Rolling Optimization Results

The intra-day rolling optimization period is 1 h, and the time step is 5 min. The number of rolling optimization in 1 day is 288. After the intra-day rolling optimization and adjustment, the actual outputs of MT, FC, and ESS are shown in **Figure 8**. In order to ensure that the interaction power between the DCMG and the main grid can effectively track the day-ahead plan value, the

TABLE 3 | Comparison of operating costs.

Comparison items	Total cost/ ¥
Day-ahead	22,794
No-SMPC	21,873
SMPC	19,764

intra-day optimization scheduling revises the day-ahead outputs of controllable devices to a certain extent.

Figure 9 shows the results of the interactive power with the main grid in different cases. In actual operation, if the rolling optimization is not applied, the power fluctuations caused by the prediction error of uncertain factors are all compensated by the main grid. It can be seen from **Figure 9** that the interaction power curve without rolling optimization fluctuates sharply near the planned value, resulting in poor stability and security when the DCMG is connected to the main grid. However, the interaction power curve after SMPC-based optimization is basically consistent with the day-ahead planned curve.

The comparison results of the SOC value between the actual value and the day-ahead plan value are shown in **Figure 10**. It can be seen that ESS can track the SOC curve of day-ahead plan well during the intra-day actual operation. According to **Figures 9**, **10**, the SMPC-based optimization method proposed in this article can deal with the influence of uncertain factors and ensure the stability and security of the data center in actual operation.

Table 3 compares the total operating costs of the DCMG system under different scheduling strategies. It can be seen that the cost of the SMPC-based dispatch decreases more than the no-SMPC dispatch, which shows that the SMPC-based optimal dispatch strategy considering the batch workloads can reduce the operation cost and improve the economy of the DCMG system.

5 CONCLUSION

In order to futher improve the operating economy of the data center and reduce the adverse effects casued by the uncertainty of renewable energy outputs and data center workloads, this artilce puts forward a SMPC-based energy optimal dispatch strategy of the DCMG system. The scenario analysis method is used to describe the uncertainty by transforming it into multiple deterministic scenarios. Based on the SMPC method, the DCMG system was optimized from day-ahead and intra-day time scales. In the day-ahead scheduling stage, the optimization dispatch model is established with the objective of preparing the lowest operating cost, which achieves flexible allocation of batch workloads and obtains the optimal output plan for each device. In the intra-day rolling optimization scheduling stage, the actual outputs of controllable devices were adjusted, and the interactive power with the main grid and SOC value of ESS tracked the day-ahead planned value. The results of case analysis show that the rolling optimization and feedback correction mechanism of SMPC can cope with the negative influence of uncertain factors and guarantee the stability and economy of the DCMG system in actual operating.

DATA AVAILABILITY STATEMENT

The original contributions presented in the study are included in the article/Supplementary Material, further inquiries can be directed to the corresponding author.

AUTHOR CONTRIBUTIONS

YZ and JW contributed to conception and design of the study and wrote the original draft. KB contributed to the study methodology and data analysis. QS contributed to data investigation and software analysis. YZ and CZ contributed to supervision and writing-review and editing. All authors have read and agreed to the published version of the manuscript.

FUNDING

This work was supported by the National Natural Science Foundation of China (NSFC) (51807079).

REFERENCES

Camacho, E. F., and Bordons, C. (2004). *Model Predictive Control*. second ed. New York, USA: Springer-Verlag.

Chen, C., Wang, J., Heo, Y., and Kishore, S. (2013). MPC-based Appliance Scheduling for Residential Building Energy Management Controller. *IEEE Trans. Smart Grid* 4 (3), 1401–1410. doi:10.1109/TSG.2013.2265239

Chen, T., Wang, X., and Giannakis, G. B. (2016b). Cooling-Aware Energy and Workload Management in Data Centers via Stochastic Optimization. *IEEE J. Sel. Top. Signal. Process.* 10 (2), 402–415. doi:10.1109/JSTSP.2015.2500189

Chen, T., Zhang, Y., Wang, X., and Giannakis, G. B. (2016a). Robust Workload and Energy Management for Sustainable Data Centers. *IEEE J. Select. Areas Commun.* 34 (3), 651–664. doi:10.1109/JSAC.2016.2525618

Ding, Z., Cao, Y., Xie, L., Lu, Y., and Wang, P. (2019). Integrated Stochastic Energy Management for Data Center Microgrid Considering Waste Heat Recovery. *IEEE Trans. Ind. Applicat.* 55 (3), 2198–2207. doi:10.1109/TIA.2018.2890789

Ding, Z., Xie, L., Lu, Y., Wang, P., and Xia, S. (2018). Emission-Aware Stochastic Resource Planning Scheme for Data Center Microgrid Considering Batch Workload Scheduling and Risk Management. *IEEE Trans. Ind. Applicat.* 54 (6), 5599–5608. doi:10.1109/TIA.2018.2851516

Dou, H., Qi, Y., Wei, W., and Song, H. (2017). Carbon-Aware Electricity Cost Minimization for Sustainable Data Centers. *IEEE Trans. Sustain. Comput.* 2 (2), 211–223. doi:10.1109/TSUSC.2017.2711925

Ebrahimi, K., Jones, G. F., and Fleischer, A. S. (2015). Thermo-economic Analysis of Steady State Waste Heat Recovery in Data Centers Using Absorption Refrigeration. *Appl. Energ.* 139, 384–397. doi:10.1016/j.apenergy.2014.10.067

Jaureguialzo, E. (2011). “PUE: The Green Grid metric for evaluating the energy efficiency in DC (Data Center). Measurement method using the power demand,” in 2011 IEEE 33rd International Telecommunications Energy Conference (INTELEC), 1–8. doi:10.1109/INTLEC.2011.6099718

Li, J., and Qi, W. (2018). Toward Optimal Operation of Internet Data Center Microgrid. *IEEE Trans. Smart Grid* 9 (2), 971–979. doi:10.1109/TSG.2016.2572402

Liu, B., Li, Z., Chen, X., Huang, Y., and Liu, X. (2018). Recognition and Vulnerability Analysis of Key Nodes in Power Grid Based on Complex Network Centrality. *IEEE Trans. Circuits Syst.* 65 (3), 346–350. doi:10.1109/TCSII.2017.2705482

Liu, B., Li, Z., Dong, X., Yu, S. S., Chen, X., Oo, M. T., et al. (2021). Impedance Modeling and Controllers Shaping Effect Analysis of PMSG Wind Turbines. *IEEE J. Emerging Selected Top. Power Electron.* 9 (2), 1465–1478. doi:10.1109/JESTPE.2020.3014412

Liu, J., Miura, Y., Bevrani, H., and Ise, T. (2021). A Unified Modeling Method of Virtual Synchronous Generator for Multi-Operation-Mode Analyses. *IEEE J. Emerg. Sel. Top. Power Electron.* 9 (2), 2394–2409. doi:10.1109/JESTPE.2020.2970025

Luo, J., Rao, L., and Liu, X. (2014). Temporal Load Balancing with Service Delay Guarantees for Data Center Energy Cost Optimization. *IEEE Trans. Parallel Distributed Syst.* 25 (3), 775–784. doi:10.1109/TPDS.2013.69

Wang, H., Huang, J., Lin, X., and Mohsenian-Rad, H. (2016). Proactive Demand Response for Data Centers: A Win-Win Solution. *IEEE Trans. Smart Grid* 7 (3), 1584–1596. doi:10.1109/TSG.2015.2501808

Wang, P., Cao, Y., Ding, Z., Tang, H., Wang, X., and Cheng, M. (2020). Stochastic Programming on Cost Optimization in Geographically Distributed Internet Data Centers. *Csee Jpes*, 1–14. doi:10.17775/CSEEJPES.2020.02930

Wang, P., Xie, L., Lu, Y., and Ding, Z. (2017). "Day-ahead Emission-Aware Resource Planning for Data center Considering Energy Storage and Batch Workloads," in IEEE Conference on Energy Internet and Energy System Integration (EI2), Beijing, China, 26-28 Nov. 2017 (IEEE), 1–6. doi:10.1109/EI2.2017.8245657

Wang, Y., Wu, W., and Zhang, B. (2015). Robust Voltage Control Model for Active Distribution Network Considering Load and Photovoltaic Uncertaintie. *Automation Electric Power Syst.* 39 (09), 138–144. doi:10.7500/AEPS20141130008

Wen, Z., and Liu, J. (2019). An Optimal Scheduling Method for Hybrid Wind-Solar-Hydor Power Generation System with Data Center in Demad Side. *Power Syst. Technol.* 43 (07), 2449–2460. doi:10.13335/j.1000-3673.pst.2018.1142

Xiao, H., Pei, W., Kong, L., Qi, Z., OuYang, H., and Mu, L. (2014). Decision Analysis and Economic Benefit Evaluation of Microgrid Power Output Considering Surplus Photovoltaic Power Selling to Grid. *Automation Electric Power Syst.* 38 (10), 10–16. doi:10.7500/AEPS20130531009

Xiong, L., Liu, X., Liu, Y., and Zhuo, F. (2020). Modeling and Stability Issues of Voltage-Source Converter Dominated Power Systems: A Review. *Csee Jpes*. (Early Access), 1–18. doi:10.17775/CSEEJPES.2020.03590

Xu, T., Zhang, H., Yang, H., Zhang, M., and Liu, L. (2019). Research on Stochastic Optimization Model of Energy Management for Data Center Microgrids. *J. Electric Meas. Instrumentation* 33 (08), 101–107. doi:10.13382/j.jemi.B1902158

Yu, L., Jiang, T., Cao, Y., and Zhang, Q. (2014). Risk-Constrained Operation for Internet Data Centers in Deregulated Electricity Markets. *IEEE Trans. Parallel Distributed Syst.* 25 (5), 1306–1316. doi:10.1109/TPDS.2013.2297095

Yu, L., Jiang, T., and Zou, Y. (2018). Distributed Real-Time Energy Management in Data Center Microgrids. *IEEE Trans. Smart Grid* 9 (4), 3748–3762. doi:10.1109/TSG.2016.2640453

Zhang, Y., Zhang, T., Liu, Y., and Guo, B. (2015). Optimal Energy Management of a Residential Local Energy Network Based on Model Predictive Control. *Proc. CSEE* 35 (14), 3656–3666. doi:10.13334/j.0258-8013.pcsee.2015.14.021

Conflict of Interest: The authors declare that the research was conducted in the absence of any commercial or financial relationships that could be construed as a potential conflict of interest.

frontiers | Frontiers in Energy Research

ORIGINAL RESEARCH
published: 04 April 2022
doi: 10.3389/fenrg.2022.864914

Integrated Optimal Planning of Distribution Network With Geographical-Zone-Restricted Renewable Energy Sources

Ke Qing[1], **Qi Huang**[1,2] **and Yuefang Du**[1]*

[1]Sichuan Provincial Key Lab Science and Technology of China, University of Electronic Science and Technology of China, Chengdu, China, [2]College of Nuclear Technology and Automation Engineering, Chengdu University of Technology, Chengdu, China

Recently, a lot of renewable energy sources have been integrated into the distribution network. In consideration of economy and construction feasibility, some renewable energy sources are required to be installed in specific areas. In this paper, a bi-layer distribution network planning optimization model that considers the geographical restrictions of the installation locations of the substation, pumped storage plant, photovoltaic (PV) and wind power, as well as the impact of operation on planning, is proposed. In the planning optimization layer, the optimal distribution network topology with minimal total cost is obtained. The locations of the renewable energy sources and the substation are determined by the particle swarm optimization (PSO), and then all the components are interconnected using the dynamic minimum spanning tree (DMST) method. In the operation optimization layer, the economic operation strategy of the hybrid energy system with uncertainty is obtained by the scenario-based stochastic optimal power flow (OPF). The forecast error of the uncertain variable is represented by the probability distribution function, and the roulette wheel mechanism (RWM) is used to generate the stochastic scenarios. A modified 103-bus system is used to test the effectiveness of the proposed method, and the simulation results show that the proposed method can effectively reduce the total cost of the distribution network.

Keywords: distribution network planning, renewable energy, particle swarm optimization, dynamic minimum spanning tree, net present value, geographical constraints

Edited by:
Sheila Samsatli,
University of Bath, United Kingdom

Reviewed by:
Jiakun Fang,
Huazhong University of Science and Technology, China
Qi Zhu,
Xi'an Shiyou University, China

Correspondence:
Yuefang Du
yuefangdu@hotmail.com

Specialty section:
This article was submitted to Process and Energy Systems Engineering,
a section of the journal Frontiers in Energy Research

Received: *29 January 2022*
Accepted: *11 March 2022*
Published: *04 April 2022*

Citation:
Qing K, Huang Q and Du Y (2022) Integrated Optimal Planning of Distribution Network With Geographical-Zone-Restricted Renewable Energy Sources. Front. Energy Res. 10:864914. doi: 10.3389/fenrg.2022.864914

1 INTRODUCTION

With the shortage of fossil energy and the increasingly serious environmental pollution problems, renewable energy sources such as photovoltaic (PV) and wind power have been developed rapidly in recent years (Chen et al., 2021; Hu et al., 2021; Mohandes et al., 2021). The installation location of the renewable energy is affected by geographical conditions. In order to achieve maximum economic benefits, PV power stations are usually installed in areas with high illumination intensity, and wind farms are built in places with sufficient wind energy (Hou et al., 2016; Li et al., 2020; Marcochi de Melo et al., 2021). To easily obtain water sources and build upstream reservoirs, pumped storage plants are generally built near rivers in mountainous areas. However, there lacks effective methods to handle such cases at present. It is necessary to find a cost-effective approach for distribution network planning that takes into account geographical constraints.

The optimization of distribution network planning and operation is an intensively studied topic in power engineering (Baringo et al., 2020; MohammadiFathabad et al., 2020; Ugranlı, 2020). The traditional distribution network contains transmission, substation, distribution and power equipment (Khator and Leung, 1997). In reference (Carrano et al., 2006), there is only traditional power equipment and no distributed generation devices in the distribution network. The planning of this distribution system is to optimize the connection of cables with the highest economic benefits and system reliability. With the integration of a large number of distributed energy equipment such as wind power, PV, energy storage equipment, new planning approaches need to be explored for the modern distribution network to improve the economic efficiency and determine the scheduling of newly connected renewable power generation equipment (Ding et al., 2012; (Wang et al., 2014). With the knowledge of the pumped storage capacity and wind speed, the generating/pumping power of the pumped storage and output power of wind farm are optimized in (Ding et al., 2012) to minimize the operation cost of distribution network. In the work of (Wang et al., 2014), a robust optimization problem is formulated to optimize the location and the size of the distribution generation to minimize microgrid costs.

Traditionally, the planning optimization and operation optimization of the distribution network are independently executed, and the operation optimization is carried out after the planning optimization. When renewable energy sources or energy storage equipment are connected to the distribution network, the operation mode of these equipment will affect the transmission losses of the grid and operation mode of the equipment (Ashoornezhad et al., 2021; Koutsoukis and Georgilakis, 2022; Mejia et al., 2022). Therefore, the traditional separated planning method cannot guarantee optimal results. It is imperative to combine the planning optimization and operation optimization together for better performance (Carpinelli et al., 2013; Sedghi et al., 2016; Tang and Low, 2017; Celli et al., 2018; Lazzeroni and Repetto, 2019). In (Lazzeroni and Repetto, 2019), the size and location of the battery are optimized to reduce the power loss. A battery planning optimization framework to improve wind power penetration, in which the optimal placement and daily scheduling of energy storage strategies are optimized, is proposed in (Ghofrani et al., 2013). To improve the voltage profile, reliability and economic benefits of the distribution network, a comprehensive strategic model is proposed to plan the location and size of photovoltaic, battery storage and distributed static compensator (Roy Ghatak et al., 2018). The authors in (Arasteh et al., 2016) presented a bi-level optimization model for distribution network. This model considered the distribution network reconfiguration and the demand response. However, the location and capacity of distributed devices are not optimized in this article. In (Zhang et al., 2013), the optimal pumped storage capacity is found by a multi-scenario approach aiming to reduce the operation cost of the distribution network and wind power curtailments. However, the network loss is not considered. There are also many researches on the expansion planning of distribution networks (Ouyang et al., 2010; Ganguly et al., 2013; Ziari et al., 2013; Koutsoukis et al., 20142014; Muñoz-Delgado et al., 2016), including the planning of new cables, substations, distributed generation equipment and energy storage equipment, etc. In (Tarôco et al., 2016), the allocation of the substations, distributed generation units, and the topology of distribution network are formulated as a multi-objective optimization to reduce the cost and improve the system reliability. A multi-stage expansion planning problem considering the load growth is formulated in (Sedghi et al., 2013), and is solved by a modified particle swarm optimization (PSO) algorithm. This expansion planning problem is divided into four stages. At each stage, new substations, main and reserve feeders, energy storage units and distribution generators will be installed into the existing distribution network. However, the geographical constraints of storage units and distributed generation equipment are not considered, i.e., those components can be installed on any existing node. The work in (Xing et al., 2016) presented an expansion planning model of the distribution network considering the allocation of the new cable, substation and distributed generator. The optimization model is formulated as a mixed integer non-linear programming problem, which is solve by a second-order cone programming method. However, the locations of the substation and distributed generation are limited to a few pre-selected nodes.

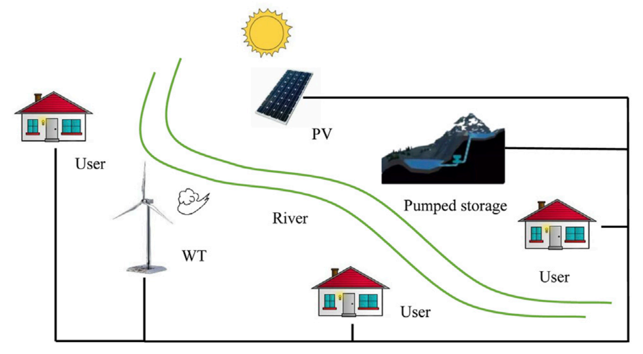

FIGURE 1 | Diagram of distribution network integrated planning problem.

This paper proposes a bi-layer integrated planning approach for the distribution network. Geographical location constraints are considered in the distribution network optimization model. The proposed optimization model combines the planning and operation optimization of distribution network to reduce the total cost of the distribution network. The uncertainty of the load, illumination intensity, wind speed and electricity price is modeled by the probability distribution function, and the roulette wheel mechanism (RWM) is adopted to generate the stochastic scenarios. In the planning layer, an effective PSO-based method is adopted to determine the locations of the substation, pumped storage plant, PV and WT, then a DMST method is used to connect all the components with minimal cable cost. In the operation layer, the optimal operation strategy is obtained based on the topology determined in the planning layer.

The rest of this paper is organized as follows. The problem formulation is presented in **Section 2**. The solution approach of the optimization problem is given in **Section 3**. The case study and conclusions are presented in **Section 4** and **Section 5**, respectively.

2 PROBLEM FORMULATION

A diagram of a modern distribution network with renewable energy sources, such as wind turbine (WT), PV and pumped storage plant, is shown in **Figure 1**. Unlike traditional power generation equipment, these renewable energy sources are environmentally friendly, but they have strict requirements on the location of the construction.

In this study, an integrated optimal planning model of distribution network with geographical location constraints is formulated. The objective of distribution network planning optimization is to find the most cost-effective layout and dispatch strategy of the distribution network. The optimization problem is divided into two layers, i.e., integrated planning optimization and embedded operation optimization layer. In the integrated planning optimization layer, the locations of substation, pumped storage plant, PV, WT, pumped storage plant and the connection layout of all components are optimized to obtain the optimal distribution network topology. The embedded operation optimization is to schedule the pumped storage plant power to minimize the operation cost of the distribution system under the topology obtained from the integrated planning optimization layer.

2.1 Integrated planning optimization layer: minimize the total cost of the distribution network

The net present value (NPV) (Huang et al., 2020) of the total cost of distribution network operators in the planning years, that is, the sum of the cable cost and the distribution network operation cost, is taken as the objective function:

$$F\left(L_{xy}\right) = min\left(NPV_{CC} + NPV_{OC}\right) \tag{1}$$

where

$$L_{xy} = \left(L_x, L_y\right) \in A \tag{2}$$

Here F represents the objective function value. NPV_{CC} is the total NPV of the cable cost. NPV_{OC} is the total NPV of the distribution network operation cost. L_{xy} is a vector which represents the locations of the substation, pumped storage plant, PV and WT. L_x and L_y represent the abscissa and ordinate coordinates of L_{xy}, respectively. A represents a restriction zone where components can be installed. In this study, two types of restriction zones are considered, i.e., rectangle and parallelogram. Based on the actual situation, the construction locations of the substation, PV and WT are set as a rectangular area. According to the shape of the river, the construction location of the pumped storage is set as a parallelogram area. For rectangular areas, the construction locations can be expressed as the limitations of x coordinate and y coordinate, respectively. The geographical constraints for rectangular areas are presented as

$$L_x^{min} \le L_x \le L_x^{max} \tag{3}$$

$$L_y^{min} \le L_y \le L_y^{max} \tag{4}$$

where L_x^{min} and L_x^{max} indicate the lower and upper limits of the L_x, respectively. L_y^{min} and L_y^{max} indicate the lower and upper limits of the L_y, respectively. For parallelogram areas, the construction locations can be expressed as the limitations of x coordinate and y coordinate, respectively, and a limitation between the x coordinate and the y coordinate. It can be presented as a combination of **Eqs 3**, **4**, **5**.

$$k_1 L_x - b_1 \le L_y \le k_2 L_x - b_2 \tag{5}$$

where k_1, b_1, k_2, b_2 are the parameters of the parallelogram areas.

The cost of the cable includes the initial investment cost, maintenance cost and replacement cost. It depends on the length and type of the cable, so it is closely related to the connection layout of the distribution network. Different installation locations of the components will correspond to different distribution network connection layouts. The NPV of the cable cost within the planning years is expressed as

$$NPV_{CC} = \sum_{y=1}^{N_{Plan}} C_{CCost,y} * (1 + r)^{-y} \tag{6}$$

where

$$C_{CCost,y} = \sum_{l=1}^{N_l}\left(L_l * C_{I,m,y} + L_l * C_{R,m,y} + L_l * C_{M,m,y}\right) \tag{7}$$

where $C_{CCost,y}$ is the total cost of the cable at year y. N_{Plan} is the planning horizon. $C_{I,m,y}$, $C_{R,m,y}$ and $C_{M,m,y}$ represent the unit initial investment cost, replacement cost and maintenance cost of type m cable at year y, respectively. L_l is the length of cable l. N_l is the total number of cables.

2.2 Embedded operation optimization layer: minimize the operation cost of the distribution network.

The locations of the substation, pumped storage plant, PV and WT will affect the connection layout of cables. Meanwhile, the locations of these equipment and the connection mode of the cables will affect the operation mode of the distribution network, especially the power losses. In order to improve the economic benefits of distribution network operator, the objective function of operation optimization is to minimize the NPV of the distribution network operation cost in the planning years. It is expressed as

$$NPV_{OC}\left(P_{PS}\right) = \min \sum_{y=1}^{N_{Plan}} C_{OC,y} * (1 + r)^{-y} \tag{8}$$

where

$$C_{OC,y} = \sum_{t=1}^{T_y} P_{PG}(t) * C_P(t) \tag{9}$$

Here $C_{OC,y}$ is the operation cost of the distribution network at year y. r is the interest rate. $P_{PG}(t)$ is the active power purchased from the power grid at time t. $C_P(t)$ is the electricity price at time t. T_y is the number of simulation hours per year. P_{PS} is the control variables in the embedded optimization layer, which represents the operating power of pumped storage plant. The positive value represents that the pumped storage plant absorbs electricity from the power grid for water storage, while the negative value represents that the pumped storage plant generates electricity and delivers electricity to the distribution network.

The main constraints of the optimization including the power flow constraints and pumped storage plant constraints. The power flow constraints are described as

$$P_{PV,i} + P_{WT,i} - P_{Load,i} - P_{PS,i} = V_i \sum_{j=1}^{N_{Bus}} V_j \left(G_{i,j} \cos\theta_{i,j} + B_{i,j} \sin\theta_{i,j} \right) \tag{10}$$

$$Q_{Load,i} = -V_i \sum_{j=1}^{N_{Bus}} V_j \left(G_{i,j} \sin\theta_{i,j} - B_{i,j} \cos\theta_{i,j} \right) \tag{11}$$

$$V_i^{min} \le V_i(t) \le V_i^{max} \tag{12}$$

$$I_{i,j}(t) \le I_{i,j}^{max} \tag{13}$$

where $P_{\text{PV},i}$ is active power generated by PV. $P_{\text{Load},i}$ and $Q_{\text{Load},i}$ are the active power and reactive power of load, respectively. V_i and V_j are the voltage of node i and j, respectively. V_i^{min} and V_i^{max} are the minimum and maximum allowable voltage of the node i, respectively. $G_{i,j}$ and $B_{i,j}$ are the real and imaginary elements of the admittance matrix. $\theta_{i,j}$ is the phase angle difference between node i to node j. N_{Bus} is the total number of buses in the distribution network. $I_{i,j}(t)$ is the current from bus i to bus j at time t. $I_{i,j}^{\max}$ is the upper limit of current from bus i to bus j.

Pumped storage plants have two operation modes: pumping and generating electricity (Ma et al., 2015). The generating mode and pumping mode are described as **Eqs 14**, **15**, respectively.

$$P_{PS}(t) = e_T \rho g h q_g(t) \tag{14}$$

$$P_{PS}(t) = \frac{\rho g h q_p(t)}{e_p} \tag{15}$$

where e_T and e_p are the efficiency of the turbine generator and pump motor, respectively. ρ is the density of water. g is the acceleration of gravity. h is the elevating head. $q_g(t)$ and $q_p(t)$ are the water volumetric flow rate of the turbine generator and pump motor at time, respectively.

The amount of water in the upper reservoir is calculated by

$$Q_{UR}(t+1) = Q_{UR}(t) + \int_t^{t+1} q_p(t)dt - \int_t^{t+1} q_g(t)dt \tag{16}$$

where $Q_{UR}(t)$ is the water quantity in the upper reservoir at time t.

In order to represent the storage state of a pumped storage plant, the state of charge (SOC) is introduced. The SOC of a pumped storage plant is expressed as

$$SOC_{PS}(t) = \frac{Q_{UR}(t)}{Q_{UR}^{max}} \tag{17}$$

where Q_{UR}^{max} is the maximum limit of upper reservoir water quantity. $SOC_{PS}(t)$ is the SOC of the pumped storage plant at time t.

The amount of the water in the upper reservoir should be between the maximum allowable reservoir capacity and the minimum allowable reservoir capacity. It also requires that the amount of water in the upstream reservoir remain unchanged for 1 day. These constraints of the pumped storage plant are presented as follows.

$$Q_{UR}^{min} \le Q_{UR}(t) \le Q_{UR}^{max} \tag{18}$$

$$SOC_{PS}(T_{Start}) = SOC_{PS}(T_{End}) \tag{19}$$

where Q_{UR}^{min} is the minimum limit of upper reservoir water quantity. T_{Start} and T_{End} are the start and end time of the day, respectively.

3 Solution Approach

From the previous section, it can be seen that the formulated distributed network planning optimization model is a non-linear problem. There are many methods to solve such problem, such as dynamic programming (Ganguly et al., 2013), differential algorithm (Zhang et al., 2016), and genetic algorithm (Ghofrani et al., 2013), (Awad et al., 2014). Considering the complexity of this optimization model, a method based on the particle swarm optimization and dynamic minimum spanning tree (PSO-DMST) is proposed to solve the corresponding bi-layer planning problem. The details of the problem solving are given below.

3.1 Particle Swarm Optimization-Dynamic Minimum Spanning Tree Method in Planning Optimization Layer

The locations of the PV, WT, substation and pumped storage plant are determined by the PSO method (Kennedy and Eberhart, 1995). Each particle represents a potential coordinate (x, y) of the component. The update formulas of the particles are as follows.

$$v_{id}^{k+1} = \omega v_{id}^k + r_1 c_1 \left(p_{id}^k - x_{id}^k \right) + r_2 c_2 \left(g_{id}^k - x_{id}^k \right) \tag{20}$$

$$x_{id}^{k+1} = x_{id}^k + v_{id}^{k+1} \tag{21}$$

where v_{id}^k and x_{id}^k denote the position and velocity of the particle in the k th iteration, respectively. p_{id}^k and g_{id}^k denote the personal best and the global best of k th iteration of dimension d, respectively. ω is the inertia weight. c_1 and c_2 are learning coefficients. r_1 and r_2 are two random numbers in the range [0,1]. In order to improve the performance of the algorithm, the linearly decreasing inertia weight is used in this study (Fei and He, 2015), which is presented as

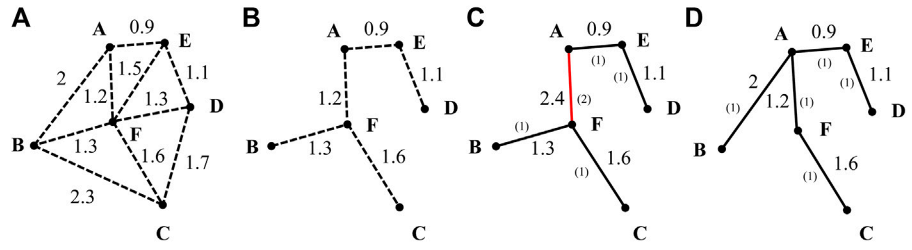

FIGURE 2 | Layout by MST and DMST **(A)** Undirected graph **(B)** MST before cable selection **(C)** MST after cable selection **(D)** DMST.

$$\omega = \omega_{\max} - (\omega_{\max} - \omega_{\min})\frac{k}{k_{\max}} \tag{22}$$

where ω_{max} and ω_{min} are the maximum and minimum inertia weights, respectively. k and k_{max} are the iteration number and maximum number of iterations, respectively.

Once the locations of the PV, WT, substation and pumped storage plant are determined, it is necessary to find an effective way to connect all the components in the distribution network. This problem is similar to the minimum spanning tree (MST) problem in graph theory (Bondy and Murty, 1976). In MST, each PV, WT, substation and pumped storage plant and load corresponds to a vertex in the graph, and these vertices are connected with minimum total weight. In the traditional MST, the weight is the distance between two vertices, that is, the cable length between two components. This method can finally connect all components with the shortest cable. After the distribution network topology is determined, the cable type is selected according to the peak load, and then the total cable cost can be calculated according to the length and type of the cable. However, MST can only guarantee that the length of the cable is the shortest but does not guarantee that the cost of the cable is the smallest.

Since one of the optimization goals is to minimize the cost of the cable, on the basis of the MST, the DMST that takes into account the influence of the load size on the cable selection is adopted for the cable connection. In DMST, the weight of two vertices is the cost of the cable that connecting two vertices. Thus, the minimum cost of cable can be guaranteed over the planning horizon. **Figure 2** is presented as an example to show the difference between the MST and DMST for cable connection. **Figure 2A** is the undirected graph that gives all possible connecting cables and the corresponding length of each cable. **Figure 2B** and **Figure 2C** show the cable connection result obtained by MST method. **Figure 2D** is the cable connection result obtained by DMST. Here, two types of cables distinguished by color and the number in parentheses are adopted. The numbers in parentheses indicate the type of the cable. When the number of connected loads is less than or equal to 2, a cable with a smaller capacity (black solid line, type 1) can be selected, and when the number of connected loads exceeds 2, a cable with a larger capacity (red solid line, type 2) should be selected. And it assumes that the unit cost of black cable is 1 and that of red cable is 2. It can be seen that the cable cost of MST is 7.3, and that the cable cost of DMST is 6.8. Therefore, it demonstrated that the DMST method can obtain lower cable cost than the MST method.

3.2 Scenario-Based Stochastic Optimal Power Flow in Operation Optimization Layer

In the distribution network, there are many uncertain variables, such as load, renewable energy generation and electricity price. Taking into account these uncertainties, a scenario-based stochastic model is adopted to optimize the operation of distribution network.

The process of the scenario-based stochastic modeling is mainly divided into three steps: scenario generation, scenario reduction and scenario aggregation. Firstly, the RWM is used to generate the original scenarios based on the probability density function of the forecast error. In this paper, it is considered that the forecast errors of load, PV output, wind power generation and electricity price obey normal distribution. Secondly, similar scenarios and the scenarios with low probability are omitted. Thirdly, the optimization problem is solved under the remaining scenarios in a deterministic model, and the expected solution results are obtained by the scenario aggregation. More details on the modeling of the required scenarios can be found in reference (Mohammadi et al., 2014).

The final value of the uncertain variable can be calculated by

$$P^{s}_{n,m,t} = P^{\text{forecast}}_{n,m,t} + \Delta P^{s}_{n,m,t} \tag{23}$$

where n is the index of the uncertain variables, i.e., PV output, WT output, load, and electricity price. m is the number of uncertain variables with index n. $P^{\text{forecast}}_{n,m,t}$ is the initial forecast value and $\Delta P^{s}_{n,m,t}$ is the estimated forecast error.

The length of each scenario is equal to the number of uncertain variables multiplied by the time dimension. The structure of each scenario can be expressed as follows.

$$\Big[P^{s}_{PV,1},\ldots,P^{s}_{PV,t},\ldots,P^{s}_{PV,T},P^{s}_{WT,1},\ldots,P^{s}_{WT,t},\ldots,$$
$$P^{s}_{WT,T},P^{s}_{L,1},\ldots,P^{s}_{L,t},\ldots,P^{s}_{L,T},C^{s}_{P,1},\ldots,C^{s}_{P,t},\ldots,C^{s}_{P,T}\Big] \tag{24}$$

where $P^{s}_{PV,t}$ is the PV output at hour t in the s th scenario. $P^{s}_{WT,t}$ is the WT generation at hour t in the s th scenario. $P^{s}_{L,t}$ is the value of the load at hour t in the s th scenario. $C^{s}_{P,t}$ is the electricity price at hour t in the s th scenario. N_L is the total number of the loads. T is the scheduling horizon of 1 day.

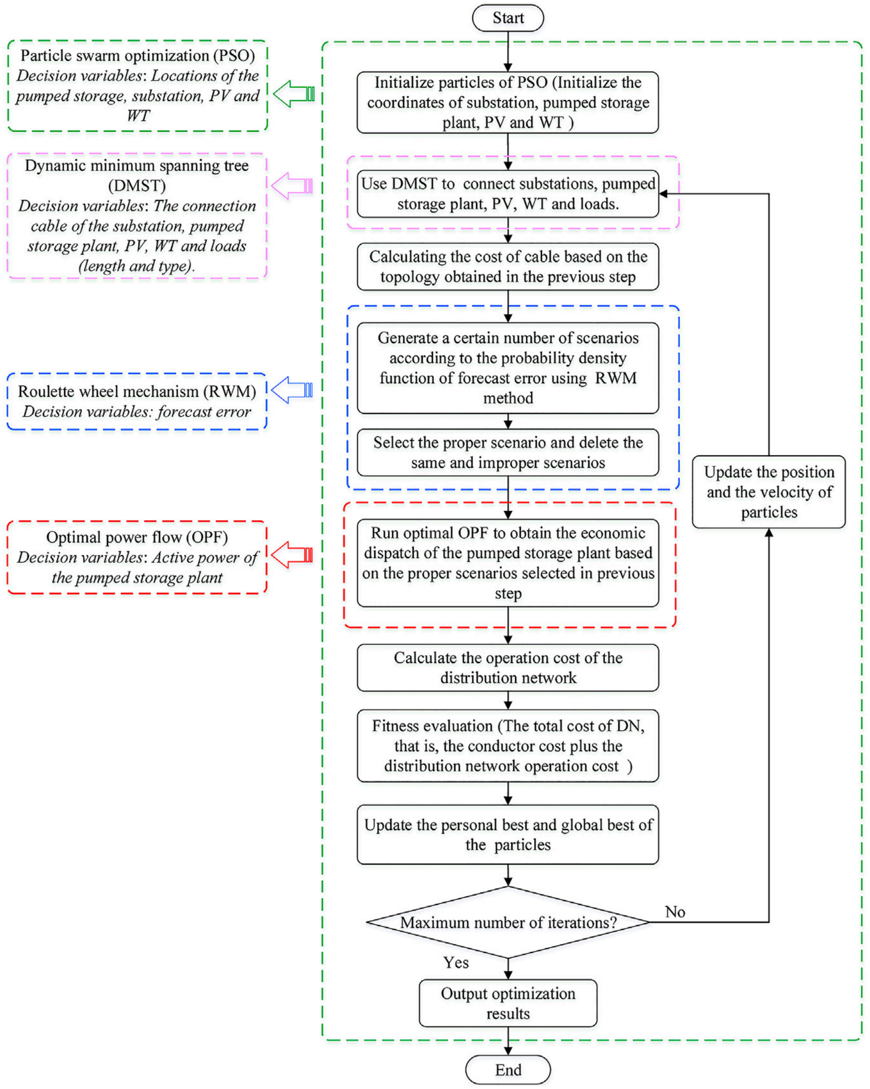

FIGURE 3 | Flowchart of the proposed bi-layer planning model.

Based on the generated scenarios, the optimal power flow is carried out in MATPOWER 6.0 toolbox (Zimmerman et al., 2011) to find the optimal operation strategy of the distribution network, check the power flow constraints, and calculate the operation cost of the distribution network.

3.3 Proposed Optimization Framework

Combining the two optimization layers, the whole flow chart of the optimization problem is shown in **Figure 3**. The main steps are presented as follows.

Step 1. : Initialize the position and velocity of PSO particles, that is, the potential construction location of substation, pumped storage plant, PV and WT.

Step 2. : Use the DMST to connect the substation, pumped storage plant, PV, WT and loads.

Step 3. : Calculate the cost of cables based on the topology obtained in the previous step.

Step 4. : Generate a certain number of scenarios based on the probability density function of the forecast error using the roulette wheel mechanism.

Step 5. : Select the proper scenarios and delete the same and improper scenarios.

Step 6. : According to the cable connection mode obtained in the previous step, run OPF of the selected scenario to find the optimal

TABLE 1 | Geographical constraints of each component.

Component	*x*-axis (km)	*y*-axis (km)	Relationship between x-axis and *y*-axis (km)
Substation	[−0.5,12]	[−2,−1]	/
Pumped storage plant	[11.25,12.75]	[4.5,12]	$15\,L_x - 179.25 \le L_y \le 15L_x - 164.25$
PV	[1.5,3.5]	[12.5,14.5]	/
WT	[8.5,11.5]	[13.5,16]	/

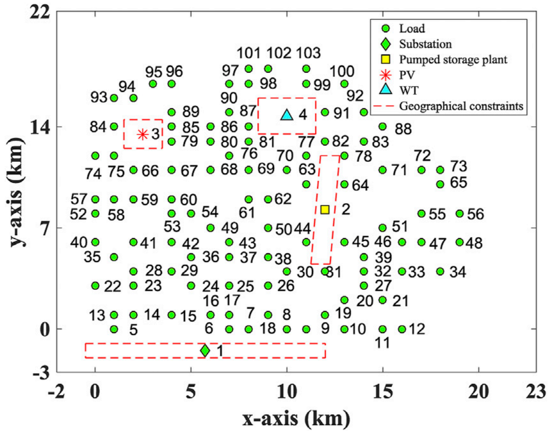

FIGURE 4 | 103-bus distribution network under study.

operation strategy that minimizes the operation cost of the distribution network.

Step 7. : Calculate the total operating cost of the distribution network based on the operation mode of the pumped storage plant obtained in the previous step.

Step 8. : Fitness evaluation, that is, calculate the total cost of the distribution network (cable cost plus operation cost).

Step 9. : According to fitness value, update the personal best and the global best of the particles.

Step 10. : Determine whether the maximum number of iterations has been reached. If it is achieved, terminate the algorithm and output the result; if not, update the position and velocity of the particle and go to step 2.

4 CASE STUDY

4.1 System Description

The proposed distribution planning method is tested on a modified 103-bus distribution system with a base voltage of 34.5 kV. The original coordinates of the loads are referred to (Carrano et al., 2005), and some modifications were made to them for this study. In the modified 103-bus distribution system, there are 99 loads with fixed position coordinates, as well as one substation, one pumped storage plant, one PV and one WT whose position coordinates need to be optimized. It is assumed that the distribution network is connected to the transmission network at coordinates (10, −5) km. Geographical constraints are expressed in **Table 1**. The modified system with the geographical location limitations is shown in **Figure 4**. Seven types of cables are selected to connect all components. Details of each cable are shown in **Table 2** (Carrano et al., 2005).

The load, photovoltaic power generation, wind power and electricity price data are obtained from Denmark power grid. The base load values for each load are obtained from (Carrano et al., 2005). The rated active power of the photovoltaic is 1 MW. The maximum water quantity of the upper reservoir is 50,000 m^3. The total efficiency of pumped storage is 0.75, and the maximum generating power is 1 MW. In this study, the pumping head is 60 m high. It is assumed that the total planning period is 15 years. The total number of particle swarm is 25 and the maximum iteration number is 100. The learning coefficients of PSO are 2. The minimum and maximum values of inertia weight are 0.4 and 0.9, respectively.

TABLE 2 | Cable parameters.

Type	Resistance (Ω/km)	Reactance (Ω/km)	Nominal power (kW)	Line installation cost ($/km)	Maintenance cost ($/km)
1	1.6118	0.4853	2,817	32,126.23	1733.54
2	1.0145	0.4679	3,776	32,321.31	1733.54
3	0.6375	0.4505	5,115	32,653.55	1733.54
4	0.5205	0.4428	5,975	32,780.81	1733.54
5	0.4019	0.4331	6,860	33,378.78	1733.54
6	0.3184	0.4237	7,983	33,752.81	1733.54
7	0.2006	0.4026	10,828	34,100.00	1733.54

TABLE 3 | Case description.

case	Locations of the substation, pumped storage plant, PV and WT	Planning procedure and operation procedure
1	At the random locations of the constrained zone	Separated
2	At the left of the constrained zone	Separated
3	To be optimized by proposed method	Separated
4	To be optimized by proposed method	Simultaneously

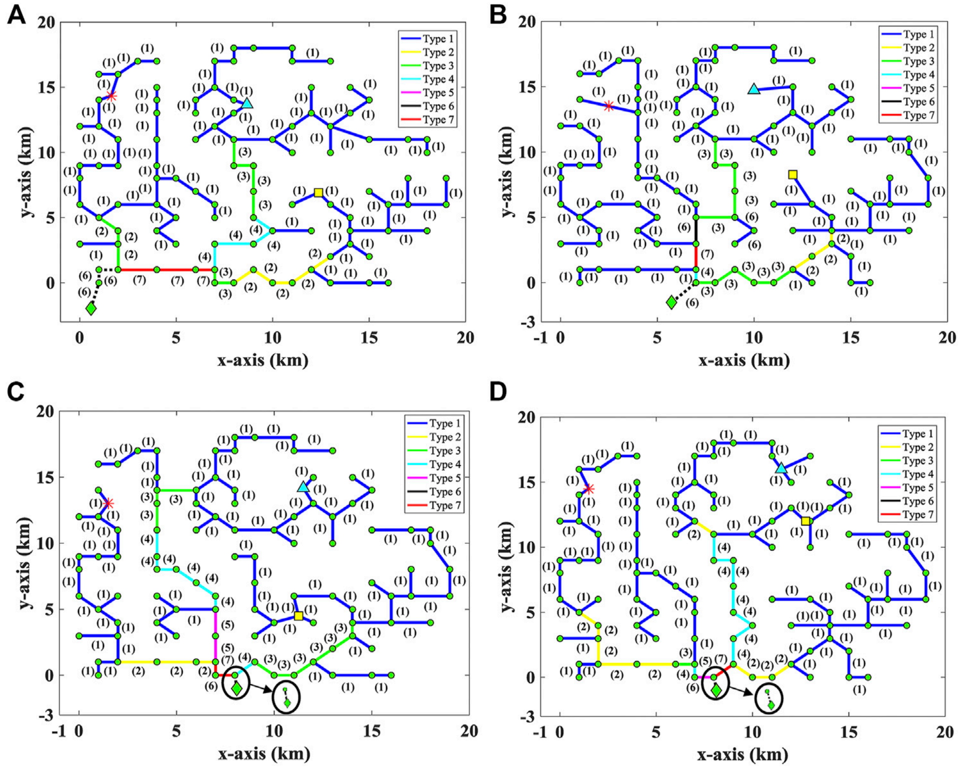

FIGURE 5 | Distribution network topology **(A)** Case 1 **(B)** Case 2 **(C)** Case 3 **(D)** Case 4.

TABLE 4 | The Coordinates of the 103-bus distribution network in four cases.

case	Substation (km)	Pumped storage plant (km)	PV (km)	WT (km)
1	0.58, –1.96;	12.38, 6.93;	1.63, 14.35;	8.66, 13.67;
2	5.75,–1.5;	12, 8.25;	2.5,13.5;	10,14.75;
3	8.08,–1;	11.25,4.5;	1.5,13;	11.5,14.16;
4	8.13,–1;	12.75,12;	1.5,14.5;	11.5,16;

TABLE 5 | The results of the 103-bus distribution network in four cases.

case	NPV of cable cost ($)	NPV of operation cost ($)	NPV of total cost ($)
1	8.419×10^6	1.7300×10^7	2.5719×10^7
2	8.277×10^6	1.7187×10^7	2.5464×10^7
3	7.847×10^6	1.7178×10^7	2.5025×10^7
4	7.849×10^6	1.7166×10^7	2.5015×10^7

According to the geographical constraints and optimization procedure, the studies are categorized into 4 cases, as shown in **Table 3**. Case 1 is the base case, in which the locations of the components are random selected in the constrained zone, and the planning and operation procedure are separated. In case 2, the locations of the components are determined by experience of the staff, i.e., the center of the constrained zone. In case 3 and case 4, the locations of the components are determined by the proposed method. The difference between case 3 and case 4 is the sequence of planning optimization and operation optimization.

4.2 Experimental Results

The topologies of the distribution network planning problem in four cases are shown in **Figure 5**. In **Figures 5A,B,C,D** are the topologies

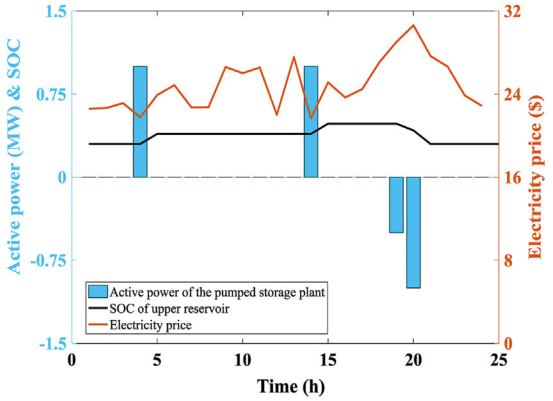

FIGURE 6 | Active power of the pumped storage plant.

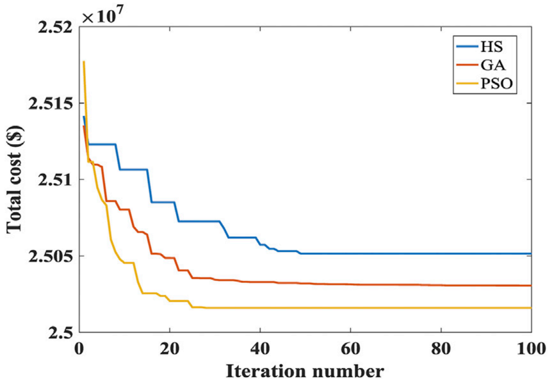

FIGURE 7 | Convergence process.

of the distribution network in case 1, case 2, case 3 and case 4, respectively. The coordinates of the substation, pumped storage plant, PV and WT in the four cases are shown in **Table 4**. In these figures, the solid line represents one cable, and the dotted line represents two cables of the same type. Different types of cables are distinguished by color and the number in parentheses is the type of the cable.

From these topologies, it can be seen that all the loads, substation, pumped storage plant, PV and WT in the studied distribution network are connected without crossover. Meanwhile, the locations of the substation, pumped storage plant, PV and WT are also in the constrained zones. Details of the optimization results, including the NPV of cable cost, the NPV of operation cost and the NPV of total cost, are presented in **Table 5**.

Comparing the NPV of cable cost in the four cases, it can be seen that the values of case 3 and case 4 are smaller than those of case 1 and case 2. The results of case 3 and case 4 are similar. It demonstrated that, compared with experience oriented or random selected locations, the proposed method helps to reduce the total cost of the cable. Comparing the NPV of operation cost in four cases, the lowest operation cost is obtained by case 4. This indicates that the location and connection mode of the components have an important influence on the operation of the distribution network. It can be found that although the cable cost of case 4 is higher than case 3, the operating cost of case 4 is much smaller than case 3, so the minimum total cost is obtained from case 4. This shows that when the topology optimization and operation optimization of the distribution network are separated, although the distribution network topology with smaller equipment investment cost can be obtained, the corresponding operating cost may not be minimal. Because the operation cost accounts for a large proportion of the total cost, the result of combining topology optimization and operation optimization is better than that of separating them. In order to improve the economic benefits, it is necessary to combine the planning optimization and operation optimization of the distribution network.

To prove the effectiveness of the proposed method, the economic dispatch of pumped storage plant in a selected scenario is presented in **Figure 6**. From **Figure 6**, it can be seen that pumped storage pumps water when the electricity price is low, and generates electricity when the electricity price is high, which can increase the profit of the distribution network operator.

To further verify the effectiveness of the proposed PSO-based method, the performance of the PSO-based method is compared with genetic algorithm (GA) and harmony search (HS) in case 4. The comparison results are shown in **Figure 7**. It shows that the PSO-based method converges quickly and its optimization result is better than two other methods under the same experimental environment.

5 CONCLUSION

In this paper, an integrated planning optimization model for the distribution network with geographical restrictions is established. The integrated planning optimization model is divided into two layers. In the planning optimization layer, the PSO method is used to optimize the locations of the substation, pumped storage plant, PV and WT, and then the DMST method is used to connect all the components without crossover. In the embedded operation optimization layer, considering the uncertainty of load, illumination intensity, wind speed and electricity price, a scenario-based stochastic OPF is carried out and the dispatch of the pumped storage plant is determined. The dispatch results show that the operating state of the pumped storage is closely related to the electricity price. It charges when the electricity price is low and discharges when the electricity price is high. By using the proposed method, both the total cost of the cable and the operation cost of the distribution network are reduced. In addition, the PSO-based optimization method is compared with the GA and the HS. The comparison results show that the PSO-based method converges faster and obtains better experimental results than the other two methods. In summary, the proposed method can provide cost-effective guidance for the planning and operation of distribution network with the consideration of geographical constraints.

DATA AVAILABILITY STATEMENT

The original contributions presented in the study are included in the article/Supplementary Material, further inquiries can be directed to the corresponding author.

AUTHOR CONTRIBUTIONS

KQ contributed to the conception and design of the proposed strategy. All authors wrote and edited the manuscript.

FUNDING

This work was supported by the National Natural Science Foundation of China under Grant 52107073.

REFERENCES

Arasteh, H., Sepasian, M. S., and Vahidinasab, V. (2016). An Aggregated Model for Coordinated Planning and Reconfiguration of Electric Distribution Networks. *Energy* 94, 786–798. doi:10.1016/j.energy.2015.11.053

Ashoornezhad, A., Falaghi, H., Hajizadeh, A., and Ramezani, M. (2021). A Two-Stage Multi-Period Distribution Network Expansion Planning Considering the Integration of Private Investors. *Int. Trans. Electr. Energ. Syst.* 31 (12), e13226. doi:10.1002/2050-7038.13226

Awad, A. S. A., el-Fouly, T. H. M., and Salama, M. M. A. (2014). Optimal ESS Allocation and Load Shedding for Improving Distribution System Reliability. *IEEE Trans. Smart Grid* 5 (5), 2339–2349. doi:10.1109/tsg.2014.2316197

Baringo, L., Boffino, L., and Oggioni, G. (2020). Robust Expansion Planning of a Distribution System with Electric Vehicles, Storage and Renewable Units. *Appl. Energ.* 265, 114679. doi:10.1016/j.apenergy.2020.114679

Bondy, J. A., and Murty, U. S. R. (1976). *Graph Theory with Applications*. London: The Macmillan Press Ltd.

Carpinelli, G., Celli, G., Mocci, S., Mottola, F., Pilo, F., and Proto, D. (2013). Optimal Integration of Distributed Energy Storage Devices in Smart Grids. *IEEE Trans. Smart Grid* 4 (2), 985–995. doi:10.1109/tsg.2012.2231100

Carrano, E. G., Soares, L. A. E., Takahashi, R. H. C., Saldanha, R. R., and Neto, O. M. (2006). Electric Distribution Network Multiobjective Design Using a Problem-specific Genetic Algorithm. *IEEE Trans. Power Deliv.* 21 (2), 995–1005. doi:10.1109/tpwrd.2005.858779

Carrano, E. G., Takahashi, R. H. C., Cardoso, E. P., Neto, O. M., and Saldanha, R. R. (2005). *Multiobjective Genetic Algorithm in the Design of Electric Distribution Networks: Simulation Data*. Orlando, FL: Tech. Rep. Univ. Fed. Minas Gerais, available at: http://www.mat.ufmg.br/~taka/techrep/agnet01.pdf.

Celli, G., Pilo, F., Pisano, G., and Soma, G. G. (2018). Distribution Energy Storage Investment Prioritization with a Real Coded Multi-Objective Genetic Algorithm. *Electric Power Syst. Res.* 163, 154–163. doi:10.1016/j.epsr.2018.06.008

Chen, H., Gao, L., and Zhang, Z. (2021). Multi-objective Optimal Scheduling of a Microgrid with Uncertainties of Renewable Power Generation Considering User Satisfaction. *Int. J. Electr. Power Energ. Syst.* 131, 107142. doi:10.1016/j.ijepes.2021.107142

Ding, H., Hu, Z., and Song, Y. (2012). Stochastic Optimization of the Daily Operation of Wind Farm and Pumped-Hydro-Storage Plant. *Renew. Energ.* 48, 571–578. doi:10.1016/j.renene.2012.06.008

Fei, S.-w., and He, Y. (2015). A Multiple-Kernel Relevance Vector Machine with Nonlinear Decreasing Inertia Weight PSO for State Prediction of Bearing. *Shock and Vibration* 2015, 1–6. doi:10.1155/2015/685979

Ganguly, S., Sahoo, N. C., and Das, D. (2013). Multi-objective Planning of Electrical Distribution Systems Using Dynamic Programming. *Int. J. Electr. Power Energ. Syst.* 46, 65–78. doi:10.1016/j.ijepes.2012.10.030

Ghofrani, M., Arabali, A., Etezadi-Amoli, M., and Fadali, M. S. (2013). A Framework for Optimal Placement of Energy Storage Units within a Power System with High Wind Penetration. *IEEE Trans. Sustain. Energ.* 4 (2), 434–442. doi:10.1109/tste.2012.2227343

Hou, P., Hu, W., Chen, C., and Chen, Z. (2016). Optimisation of Offshore Wind Farm cable Connection Layout Considering Levelised Production Cost Using Dynamic Minimum Spanning Tree Algorithm. *IET Renew. Power Generation* 10 (2), 175–183. doi:10.1049/iet-rpg.2015.0052

Hu, J., Liu, X., Shahidehpour, M., and Xia, S. (2021). Optimal Operation of Energy Hubs with Large-Scale Distributed Energy Resources for Distribution Network Congestion Management. *IEEE Trans. Sustain. Energ.* 12 (3), 1755–1765. doi:10.1109/tste.2021.3064375

Huang, C., Hou, H., Yu, G., Zhang, L., and Hu, E. (2020). Energy Solutions for Producing Shale Oil: Characteristics of Energy Demand and Economic Analysis of Energy Supply Options. *Energy* 192, 116603. doi:10.1016/j.energy.2019.116603

Kennedy, J., and Eberhart, R. (1995). Particle Swarm Optimization." in Proceedings of ICNN'95 - International Conference on Neural Networks. Perth, WA, Australia, 1942–1948.

Khator, S. K., and Leung, L. C. (1997). Power Distribution Planning: A Review of Models and Issues. *IEEE Trans. Power Syst.* 12 (3), 1151–1159. doi:10.1109/59.630455

Koutsoukis, N. C., and Georgilakis, P. S. (2022). A Multistage Distribution Network Planning Method Considering Distributed Generation Active Management and Demand Response. *IET Renew. Power Gen* 16 (1), 65–76. doi:10.1049/rpg2.12325

Koutsoukis, N. C., Georgilakis, P. S., and Hatziargyriou, N. D. (2014). *A Tabu Search Method for Distribution Network Planning Considering Distributed Generation and UncertaintiesInternational Conference on Probabilistic Methods Applied to Power Systems*. Durham: PMAPS, 1–6.

Lazzeroni, P., and Repetto, M. (2019). Optimal Planning of Battery Systems for Power Losses Reduction in Distribution Grids. *Electric Power Syst. Res.* 167, 94–112. doi:10.1016/j.epsr.2018.10.027

Li, J., Hu, W., Wu, X., Huang, Q., Liu, Z., Chen, C., et al. (2020). Cable Connection Optimization for Onshore Wind Farms Considering Restricted Area and Topography. *IEEE Syst. J.* 14 (3), 3082–3092. doi:10.1109/jsyst.2020.2982843

Ma, T., Yang, H., Lu, L., and Peng, J. (2015). Pumped Storage-Based Standalone Photovoltaic Power Generation System: Modeling and Techno-Economic Optimization. *Appl. Energ.* 137, 649–659. doi:10.1016/j.apenergy.2014.06.005

Marcochi de Melo, D., Lopes, E. C., Motta, J. G., Asano, R., Valverde, M., Suyama, R., et al. (2021). Integrated Intelligent Geoprocessing Tool for Screening Candidate Locations Suitable for Distributed Generation Deployment. *Renew. Energ.* 177, 797–806. doi:10.1016/j.renene.2021.05.100

Mejia, M. A., Macedo, L. H., Muñoz-Delgado, G., Contreras, J., and Padilha-Feltrin, A. (2022). Medium-term Planning of Active Distribution Systems Considering Voltage-dependent Loads, Network Reconfiguration, and CO2 Emissions. *Int. J. Electr. Power Energ. Syst.* 135, 107541. doi:10.1016/j.ijepes.2021.107541

Mohammadi Fathabad, A., Cheng, J., Pan, K., and Qiu, F. (2020). Data-driven Planning for Renewable Distributed Generation in Distribution Systems. *IEEE Trans. Power Syst.* (99), 1

Mohammadi, S., Soleymani, S., and Mozafari, B. (2014). Scenario-Based Stochastic Operation Management of Microgrid Including Wind, Photovoltaic, Micro-turbine, Fuel Cell and Energy Storage Devices. *Int. J. Electr. Power Energ. Syst.* 54, 525–535. doi:10.1016/j.ijepes.2013.08.004

Mohandes, B., Wahbah, M., Moursi, M. S. E., and El-Fouly, T. H. M. (2021). Renewable Energy Management System: Optimum Design and Hourly Dispatch. *IEEE Trans. Sustain. Energ.* 12 (3), 1615–1628. doi:10.1109/tste.2021.3058252

Muñoz-Delgado, G., Contreras, J., and Arroyo, J. M. (2016). Multistage Generation and Network Expansion Planning in Distribution Systems Considering Uncertainty and Reliability. *IEEE Trans. Power Syst.* 31 (5), 3715–3728. doi:10.1109/TPWRS.2015.2503604

Ouyang, W., Cheng, H., Zhang, X., and Yao, L. (2010). Distribution Network Planning Method Considering Distributed Generation for Peak Cutting. *Energ. Convers. Manag.* 51 (12), 2394–2401. doi:10.1016/j.enconman.2010.05.003

Roy Ghatak, S., Sannigrahi, S., and Acharjee, P. (2018). Optimised Planning of Distribution Network with Photovoltaic System, Battery Storage, and DSTATCOM. *IET Renew. Power Generation* 12 (15), 1823–1832. doi:10.1049/iet-rpg.2018.5088

Sedghi, M., Ahmadian, A., and Aliakbar-Golkar, M. (2016). Optimal Storage Planning in Active Distribution Network Considering Uncertainty of Wind Power Distributed Generation. *IEEE Trans. Power Syst.* 31 (1), 304–316. doi:10.1109/tpwrs.2015.2404533

Sedghi, M., Aliakbar-Golkar, M., and Haghifam, M.-R. (2013). Distribution Network Expansion Considering Distributed Generation and Storage Units

Using Modified PSO Algorithm. *Int. J. Electr. Power Energ. Syst.* 52, 221–230. doi:10.1016/j.ijepes.2013.03.041

Tang, Y., and Low, S. H. (2017). Optimal Placement of Energy Storage in Distribution Networks. *IEEE Trans. Smart Grid* 8 (6), 3094–3103. doi:10.1109/tsg.2017.2711921

Tarôco, C. G., Takahashi, R. H. C., and Carrano, E. G. (2016). Multiobjective Planning of Power Distribution Networks with Facility Location for Distributed Generation. *Elect. Power Syst. Res.* 141, 562

Ugranlı, F. (2020). Probabilistic Distribution Planning: Including the Interactions between Chance Constraints and Renewable Energy. *Sustain. Energ. Grids Netw.* 23, 100372.

Wang, Z., Chen, B., Wang, J., Kim, J., and Begovic, M. M. (2014). Robust Optimization Based Optimal DG Placement in Microgrids. *IEEE Trans. Smart Grid* 5 (5), 2173–2182. doi:10.1109/tsg.2014.2321748

Xing, H., Cheng, H., Zhang, Y., and Zeng, P. (2016). Active Distribution Network Expansion Planning Integrating Dispersed Energy Storage Systems. *IET Generation, Transm. Distribution* 10 (3), 638–644. doi:10.1049/iet-gtd.2015.0411

Zhang, N., Kang, C., Kirschen, D. S., Xia, Q., Xi, W., Huang, J., et al. (2013). Planning Pumped Storage Capacity for Wind Power Integration. *IEEE Trans. Sustain. Energ.* 4 (2), 393–401. doi:10.1109/tste.2012.2226067

Zhang, Y., Dong, Z. Y., Luo, F., Zheng, Y., Meng, K., and Wong, K. P. (2016). Optimal Allocation of Battery Energy Storage Systems in Distribution Networks with High Wind Power Penetration. *IET Renew. Power Generation* 10 (8), 1105–1113. doi:10.1049/iet-rpg.2015.0542

Ziari, I., Ledwich, G., Ghosh, A., and Platt, G. (2013). Optimal Distribution Network Reinforcement Considering Load Growth, Line Loss, and Reliability. *IEEE Trans. Power Syst.* 28 (2), 587–597. doi:10.1109/tpwrs.2012.2211626

Zimmerman, R. D., Murillo-Sánchez, C. E., and Thomas, R. J. (2011). MATPOWER: Steady-State Operations, Planning and Analysis Tools for Power Systems Research and Education. *IEEE Trans. Power Syst.* 26, 12.

Conflict of Interest: The authors declare that the research was conducted in the absence of any commercial or financial relationships that could be construed as a potential conflict of interest.

frontiers | Frontiers in Energy Research

ORIGINAL RESEARCH
published: 07 April 2022
doi: 10.3389/fenrg.2022.856635

Anomaly Detection of Hydropower Units Based on Recurrent Neural Network

Lei Xiong[1], **Jiajun Liu**[1]*, **Feng Yang**[1], **Gang Zhang**[1] **and Jian Dang**[1,2]

[1]School of Electrical Engineering, Xi'an University of Technology, Xi'an, China, [2]Xi'an Key Laboratory of Intelligent Energy, Xi'an University of Technology, Xi'an, China

Anomaly detection for hydraulic turbine unit has an important role in hydropower system. In hydropower systems, different components will produce n-dimensional heterogeneous time series with different characteristics at all times. Due to the characteristic evolution and time dependence, vibration-based anomaly detection for hydraulic turbine unit is extremely challenging. In this paper, we propose a conditional quantile regression based recurrent neural network (QRNN), which models the time dependence and probability distribution between random variables. The proposed method aims to extract the actual representation patterns from the fitted models and it can effectively detect anomalies in the non-uniform time series of feature evolution. The experimental results show that the proposed method has better accuracy in anomaly detection (error reduction by 34%) than the traditional method, and saves at least 25.6% of execution time.

Keywords: anomaly detection, hydropower system, n-dimensional heterogeneous time series, quantile regression based recurrent neural network (QRNN), characteristic evolution

OPEN ACCESS

Edited by:
Liansong Xiong,
Nanjing Institute of Technology (NJIT),
China

Reviewed by:
Yu Zhou,
Taiyuan University of Technology,
China
Rize Jin,
Tianjin Polytechnic University, China
Yingjie Wang,
University of Liverpool,
United Kingdom

****Correspondence:***
Jiajun Liu
xautljj@163.com

Specialty section:
This article was submitted to
Process and Energy Systems
Engineering,
a section of the journal
Frontiers in Energy Research

***Received:** 17 January 2022*
***Accepted:** 24 February 2022*
***Published:** 07 April 2022*

Citation:
Xiong L, Liu J, Yang F, Zhang G and
Dang J (2022) Anomaly Detection of
Hydropower Units Based on Recurrent
Neural Network.
Front. Energy Res. 10:856635.
doi: 10.3389/fenrg.2022.856635

1 INTRODUCTION

In order to control the stability and security, data analysis and detection methods play an important role in power systems (Liu et al., 2017; Xiong et al., 2019; Xiong et al., 2021). Different from the wind power system (Liu et al., 2020), the operation process of a hydropower unit is complex. According to the statistics, the vibration signal of the unit can reflect more than 80% of the fault characteristics. Therefore, we propose to detect the fault of hydropower turbine unit based on mining the vibration signal data in this paper. Due to highly nonlinear, instability and time-varying characteristics of the vibration signal data of the hydraulic turbine unit, it is difficult to be modeled precisely. At present, the non-stationary vibration signal processing methods include short-time Fourier transform, Mode Decomposition and so on. In order to solve the problems of empirical mode decomposition on mathematical theory, Konstantin et al. (Iyer et al., 2016) proposed variational mode decomposition method. Assuming that the signal is composed of modal functions with different center frequencies, it is decomposed by self-adaptive and quasi-orthogonal methods in the variational framework. Breiman et al. (Breiman, 2001) proposed the random forest theory. Based on decision tree, this method generates several decision trees by randomly feature selection and samples. After each decision tree is trained separately, the final sample category is voted on. However, they are not suitable for processing the multivariate vibration time series data of hydraulic turbine unit.

Extreme value theory (EVT) (Xu et al., 2018), Peak over-threshold (POT) (Hundman et al., 2018), and distance-based (Dragomiretskiy and Zosso, 2013) can be used for time series anomaly detection (Wu et al., 2014). All these methods may involve a large number of distribution assumptions, parameter adjustments, and heavy calculations in the conversion process. This may increase the calculation cost. Although there are many studies on anomaly detection (Mehrotra et al., 2017), they either focus on deterministic methods (Filonov et al., 2016) or random methods (Dasgupta and Osogami, 2017; Lai et al., 2018), and ignore time dependence of the time series (Guha et al., 2016). In (Manzoor et al., 2018), the goal is to identify independent anomalous objects rather than identifying anomalous time series patterns based on their time dependence. In time series modeling, historical observations are very important for understanding current data. Therefore, it is better to use a sequence of observations: X_(t-T), X_(t-T+1), . . ., X_t rather than X_t to calculate the anomaly score in time series.

Vector auto regression (VAR) and support vector regression (SVR) can be applied to multivariate time series (Lai et al., 2018). However, many of these models are difficult to scale up and include exogenous variables (Liu et al., 2020). Supervised methods (Laptev et al., 2015; Shipmon et al., 2017) require labeled data for model training, and can only identify known types of anomalies. The unsupervised method does not need to label the data, which can be divided into two categories: the deterministic model and random model. For deterministic model. In order to capture both the long-term dynamics and short-term effects simultaneously, the non-linear dynamics modeling, long short term memory (LSTM) methods (Hochreiter and Schmidhuber, 1997; Gers et al., 2000; Borovykh et al., 2017; Grob et al., 2018) have been proposed for forecasting events based on sequence models. For deterministic model, (Filonov et al., 2016) proposed a LSTM-based predictive models to detect spacecraft anomalies. Although LSTMs are deterministic and have no random variables, they can handle the time dependence of heterogeneous time series. For random model, recurrent neural network (Dasgupta and Osogami, 2017; Lai et al., 2018) is used for time series anomaly detection. Auto-encoder-based methods are used for time series anomaly detection in (Boudiaf et al., 2016; Xu et al., 2018). Variants of convolution and recurrent neural networks are used for modeling temporal patterns (Calvo-Bascones et al., 2021). Deep convolutional neural networks (Kim, 2014; Yang et al., 2015) have been used for time series human activity recognition. Memory guided normality for anomaly detection is proposed in (Park et al., 2020). Deep learning based anomaly detection methods for video and industrial control system are proposed in Wang et al. (2020) and Nayak et al. (2021), respectively. The deep neural network (Sen et al., 2019), (Salinas et al., 2017) has been proposed to high dimensional time series forecasting, however, it is limited to training on entire time series and then perform multi-step ahead forecast which is practically computational resource demanding in feature evolving heterogeneous time series. Recently, (Pang et al., 2021) give a survey of deep learning methods for anomaly detection. However, in the hydraulic turbine system, different subsystems and parts will produce n-dimensional heterogeneous time series with different characteristics at all times. This will form a heterogeneous time series of feature evolution.

In this paper, we propose a quantile regression (Geraci and Bottai, 2007) based recurrent neural network (QRNN) for anomaly detection of hydropower units. The proposed method can explicitly model the temporal dependence among stochastic variables with properly estimated probability distributions. Considering the feature evolution of heterogeneous time series, the most difficult part in this method is still how to detect anomalies. The most intuitive way to verify the reliability of the detection model is to find the correct estimated distribution probability. The higher the probability, the higher the confidence. But this does not mean higher accuracy. The proposed method aims to extract the actual representational patterns from the fitted models, thereby studying their reconstruction error probability distribution by using a conditional quantile regression method to limit mistakes when it is forced to make decision on normality by guidance of principled uncertainty estimates. Inspired by the distribution assumptions-free QR (Koenker and Bassett Jr, 1978; Koenker and Machado, 1999; Koenker and Hallock, 2001) build on asymmetric laplace distribution (Kotz et al., 2001), we proposed QRNN to model the conditional distribution $P(\widehat{y}_t|X_{t-T}, X_{t-T+1}, \ldots, X_t)$, where $\widehat{y}_t$ is the predicted value. The contributions of this paper can be summarized as follows:

- According to the characteristics of hydraulic turbine data, we propose a quantile regression based recurrent neural network for anomaly detection, which can model temporal dependencies and stochasticity explicitly in vibration time series data. And it can study the reconstruction error probability distribution by using a conditional quantile regression method.
- We propose an incremental online method to update the co-evolving heterogeneous for multiple streaming data.
- We propose to apply stochastic methods to detect anomalies in heterogeneous time series with feature evolution, which is proved robust and powerful in the experiment.

The rest of this paper is organized as follows. In **Section 2**, we introduce the problem and the related model used in this paper. In **Section 3**, we describe the proposed method in detail. In **Section 4**, we conduct several experiments to evaluate the advantage of the proposed method. At the end, we conclude the paper in **Section 5**.

2 PROBLEM AND MODEL

2.1 Formal Description of the Problem

Formalize the anomaly detection problem in the feature evolution time series, $[T_0, T)$ represents the observation window of the observed event. In general, it can be assumed that $T_0 = 0$. Each feature F uses a continuous time stamp sequence $T_u = t_1, \ldots, t_n$. $X_{t-T:t} \in R^{M\times(T+1)}$ represents the observation sequence X_{t-T}, X_{t-T+1}, . . ., X_t. $\hat{y}$ and y represents the predicted value and the true value. L represents the loss function. In the problem of time series anomaly detection, past historical observations are very important for understanding and capturing the dynamic patterns in the current data stream. We use the observation sequence $X_{t-T:t}$ to calculate the anomaly score of X_t. Given $X = x_1, \ldots, x_N$, where N is the length of the vector x. The observation x_t is the N-dimensional vector $x_t = [x_t^1, \ldots, x_t^N]$ and $X \in R^{M\times N}$ at time

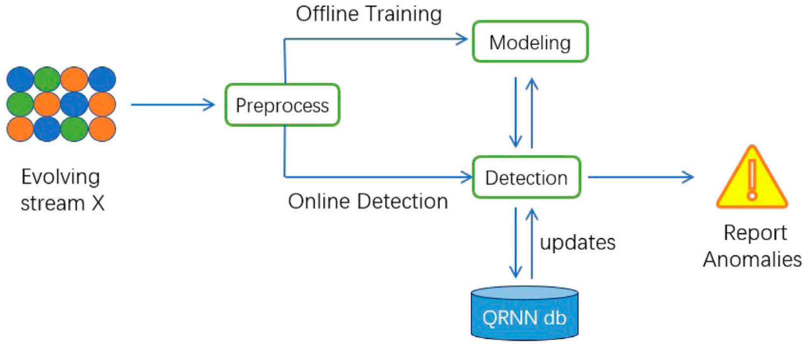

FIGURE 1 | The proposed neural network model with LSTM encoder and predictor-detector network.

$t(t \leq N)$. According to the past historical observation data $X_{t-T:t}$, the problem of anomaly detection in vibration time series data of hydraulic turbine unit is formally defined as follows.

Problem: Given the historical observation sequence represented by the time series in the order given as $X_{t-T:t}$, where t is the current time point, report an anomaly score for a given current data point X_t instantly at any time.

2.2 Long Short-Term Memory

LSTM is a kind of deep recurrent neural network. It is widely used in time series. LSTM realizes the memory function in time through the opening and closing of the door. It can effectively solve the problem of gradient disappearance and gradient explosion in general situations. The key is to introduce a gating unit system. The system stores historical information through the internal memory unit-cell state unit. Different gates can make the network know when to forget historical information, when to update cells status dynamically. Cells are cyclically connected to each other, instead of hidden units in the general cyclic network. If the input gate sigmoid allows new information input, its value can be added to the state. The state unit has linear self-circulation. Its weight is controlled by the forget gate. The output of the cell can be closed by the output gate. The status unit can also be used as an additional input for the gating unit.

$$f_t = \sigma\left(w_f * [C_{t-1}, Z_t, h_{t-1}] + b_f\right) \tag{1}$$

$$i_t = \sigma\left(w_i * [C_{t-1}, Z_t, h_{t-1}] + b_i\right) \tag{2}$$

$$C_t = f_t * C_{t-1} + i_t * RELU\left(w_c * [Z_t, h_{t-1}] + b_c\right) \tag{3}$$

$$o_t = \sigma\left(w_o * [C_t, Z_t, h_{t-1}] + b_o\right) \tag{4}$$

$$h_t = o_t * RELU\left(C_t\right) \tag{5}$$

Here f, i, o, h, C, c, w, Z, b, $\sigma()$ respectively represents forget gate, input gate, output gate, hidden state vector, unit state vector, weight matrix, feature vector, bias vector and sigmoid function. In this paper, we select to use LSTM due to the following features: *1*) it is able to support end to end modeling; *2*) it is easy to incorporate exogenous; *3*) it is powerful in feature extraction for vibration time series data of hydraulic turbine unit.

3 THE PROPOSED METHOD

3.1 The Architecture of QRNN

This paper propose to combine LSTM and conditional quantile regression to model explicitly temporal dependencies and stochasticity in vibration time series data of hydraulic turbine unit. The overall structure of QRNN consists of two parts: *1*) offline training *2*) online anomaly detection. As shown in **Figure 2**, the proposed neural network is composed of two recurrent neural networks, such as the LSTM encoder and predictor-detector network. It can be considered as $f = pd(e(h_t, (x,y)_t))$ where f is the predicted scores, x_t and y_t are the input variables, h_t is the encoder state, $e(.)$ is an encoder and $pd(.)$ is the predictor-detector network. The LSTM encoder is trained to extract useful temporal and non-linear patterns contained in vibration time series data, which can be used to guide the predictor-detector network of anomaly detection. If exogenous variables are available, they can get concatenated with extracted feature vectors from the LSTM encoder and used as input to the predictor-detector network. The predictor-detector network consists of an LSTM and dense layers for output prediction. The training process can be carried out daily training according to business needs, such as once a week or once a month. The offline part is composed of preprocessing sub-module (shared by online and offline modules) and start-up sub-module. The online part consists of real-time detection and update sub-modules. The data is preprocessed in the preprocessing module. The data is divided into sequences through a sliding window of length T. The startup module builds the model and deploys it to memory after training, testing, and verification. The fitted model can now perform real-time anomaly detection. In streaming or online settings, new observations after preprocessing (such as X_t at time t) can be sent to the detection module and provide anomaly scores. If the abnormal score of X_t is lower or higher than the abnormal threshold, X_t is marked as abnormal. The update of sub-module will update the parameters of each operation in QRNN db. The overall structure is shown in **Figure 1**.

QRNN is composed of LSTM encoder and prediction-detector network. The network can essentially be regarded as a large neural network, expressed as $f = pd(e(h_t, (x,y)_t))$, where f is the

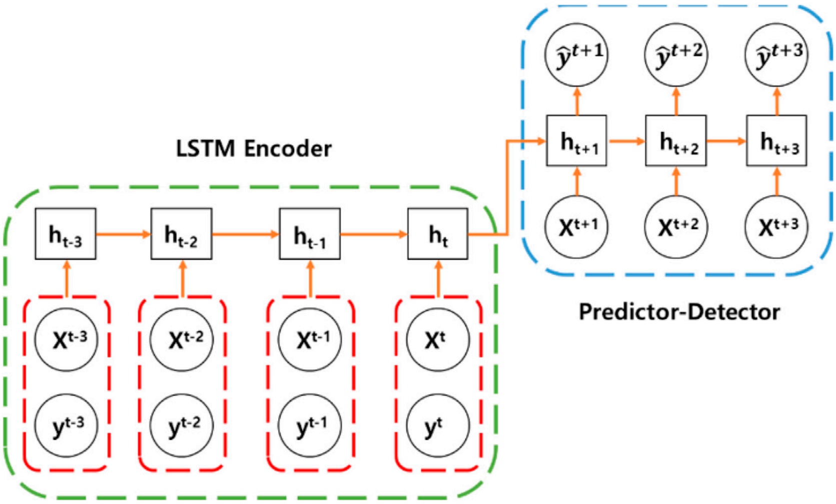

FIGURE 2 | The overall structure of QRNN.

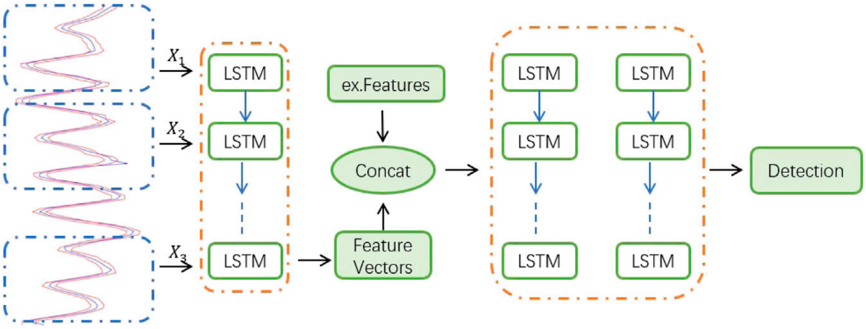

FIGURE 3 | QRNN architecture diagram.

prediction score, x_t and y_t are input variables, h_t is the state of the encoder, $e(.)$ is the ana encoder, and $pd(.)$ is the prediction-detection network. The trained LSTM encoder can extract useful time and nonlinear dynamic patterns contained in the heterogeneous time series of feature evolution. These patterns can be used to guide the prediction-detection network to perform anomaly detection.

If exogenous variables are available, they can be connected with the feature vector extracted from the LSTM encoder and used as input to the predictor-detector network. This is because in reality, it is not necessary to observe all the content needed to predict the output through the input. After the LSTM encoder network is trained, the output from the last cell state is sent to the prediction-detection network. This is also the training prediction score evolution data stream $\hat{y}_{t+M:\,t} = pd\left(h_{t-T}, X_{t+M:\,t}\right)$, where $h(.)$ is the hidden coding state, as shown in **Figure 3**. The proposed QRNN prediction-detection network consists of an LSTM layer and a fully connected output prediction layer. The last dense layer is modeled as three outputs and three loss functions. One for the desired fitting model. The other two are used to guide the upper and lower bounds of forecast uncertainty estimates. It is worth noting that the total loss is calculated as the sum of individual quantile losses. And the output is all quantile predictions of different quantile values defined by $\tau \in [0, 1]$.

3.2 Fault Detection and Loss Function

QRNN is an anomaly detector based on prediction. The anomaly detection depends on the quality of the predicted value. When predicting normal data, the probability distribution of the error can be calculated, and then used to find the maximum posterior probability estimate of the normal behavior of the test data. In order to predict more accurately, it is necessary to set thresholds for the upper and lower bounds. Beyond this threshold, data points can be marked as abnormal, as shown in **Figure 4**. In the deep learning regression task setting, the mean square error function is the most commonly used loss function.

$$\xi_t = y_t - \hat{y}_t \tag{6}$$

Intuitively speaking, taking the negative power of the mean square error function approximates the Gaussian process whose

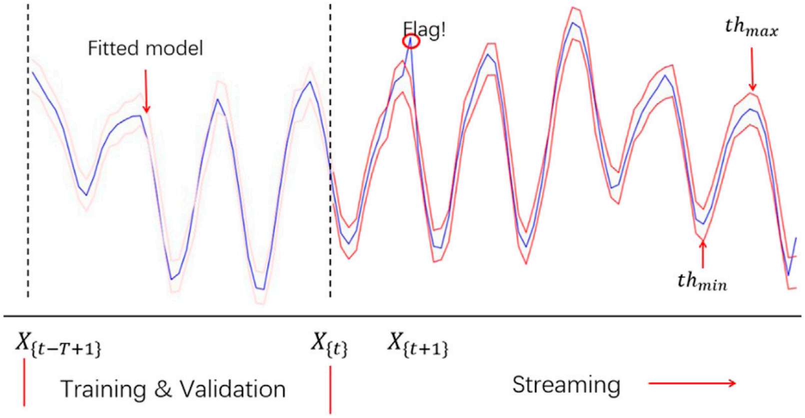

FIGURE 4 | Schematic diagram of anomaly detection.

mode corresponds to the mean parameter. Non-parametric distributions like conditional quantiles are very useful in quantifying uncertainty estimation in decision-making and minimizing risk.

The goal of Quantile regression (QR) is to estimate the conditional median or any other quantile of the distribution. It can be done by solving the following formula.

$$\min_{\xi \in R} \sum \rho_r (y_i - \xi) \tag{7}$$

Where the function $\rho_r(.)$ is the tilted absolute value function that yields the τth sample quantiles. To obtain an estimate of the conditional median function, we replace the scalar ξ by the parametric function $\xi(x_i, \beta)$, which can be formulated as a linear function of parameters.

$$\min_{\beta \in R} \sum \rho_r (y_i - \xi(x_i, \beta)) \tag{8}$$

Quantile regression learns to predict the conditional quantiles $\hat{y}_{\tau_{t+1:M}} | (X_{t-T:t}, \tau)$ for the given target distribution *via* formula **(9)**, in which $\hat{y}_\tau(.)$ is the predicted value at the given quantile.

$$P\left(\hat{y}_{t+1:M} \le \hat{y}_{\tau_{t+1:M}}\right) = \tau \tag{9}$$

We focus on putting weights to the distances between points on the distribution function and the fitted regression line based on the selected quantile. We select to use QR due to it has the following key features: *1*) It does not make any distribution assumption on the error; *2*) QR can describe the outcome variable of the entire conditional distribution; *3*) QR is more robust to outliers and setting errors of the error distribution; *4*) QR can expand the flexibility of parametric and non-parametric regression methods.

We set $\tau \in [0, 1]$ to generate the predicted value $y_{t+1:M}$ with the smallest reconstruction error ξ, as shown in the formula **(6)** in the predictive detector network. And calculate the quantile loss of a single data point by formula **(10)**. Because we needed a complete conditional distribution rather than a point estimate of uncertainty estimation, the average loss function $L(.)$ on a given data distribution can be defined by formula **(11)**, where $f^W(x_t)$ is the fitting model under the given quantile τ, y_t and x_t are true values.

$$L(\xi_t|\tau) = \begin{cases} \tau\xi_t & if\ \xi_t \ge 0 \\ (\tau - 1)\xi_t & if\ \xi_t < 0 \end{cases} \tag{10}$$

$$L(y_t, f^W(x_t)\tau) = \frac{1}{L}\sum_{t=1}^{L} L(y_t, f^W(x_t)|\tau) \tag{11}$$

In the case of a loss function, the prediction-detector network is modeled as three outputs and three loss functions, with the lower quantile, the median (fitting model) and the upper quantile. At $\tau = 0.5$, the loss function will estimate the median value instead of the average value. With the upper quantile and the lower quantile, a reliable uncertainty estimate can be provided for forecasting.

3.3 Time Series Evolution

It needs to be considered that during the operation of the turbine, the data update of each subsystem arrives in the form of a stream over time. This may include updates to existing features, or new features, as shown in **Figure 1**. Generally, a time series may have endogenous variables (for example, the output is a function of the previous output), or may not have exogenous variables that are not affected by other variables in the system. But the output depends on it. Most work ignores exogenous variables. But in order to improve quality and improve anomaly detection, this article introduces exogenous variables. When performing anomaly detection on the time series of various hydraulic turbines, sometimes there may be patterns that were not previously available. It deviates greatly from the training model. This may be a training data set observed in a specific mode. In general, it requires that each time a new data set is reached, the entire process of training the model must start from the beginning. For hydraulic turbine time series fault detection models, training the entire model requires a large amount of data sets and a large amount of time. In actual situations, it is impractical to keep training the model with the arrival of new

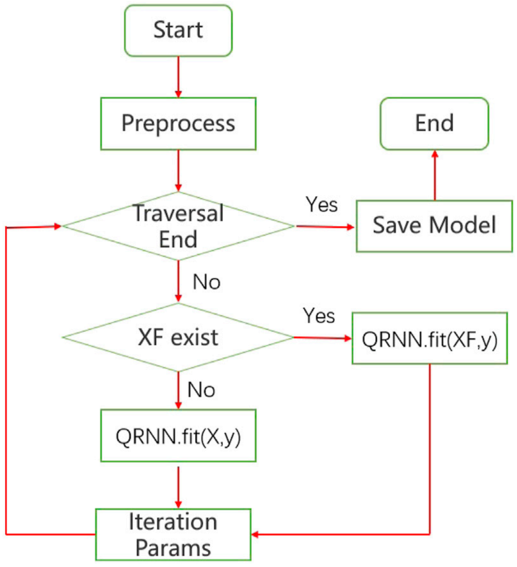

FIGURE 5 | The overall algorithm of QRNN.

TABLE 1 | Data set attributes.

Loads	Rotating speed (rpm)	Sequence length
0HP	1,797	2,43,938
1HP	1,772	4,83,903
2HP	1,750	4,83,903
3HP	1,730	4,83,903

TABLE 2 | Mean square error of trend prediction of QRNN, CNN, GRU, and BiLSTM methods on data sets under different loads.

	CNN	GRU	BiLSTM	QRNN
0HP	1.261×10^{-4}	1.326×10^{-4}	2.082×10^{-4}	1.122×10^{-4}
1HP	1.217×10^{-4}	1.345×10^{-4}	$2.139, \times, 10^{-4}$	1.056×10^{-4}
2HP	1.155×10^{-4}	1.272×10^{-4}	1.947×10^{-4}	1.021×10^{-4}
3HP	1.268×10^{-4}	1.333×10^{-4}	1.445×10^{-4}	0.909×10^{-4}

data. In order to solve this problem, an online incremental update scheme is needed to provide threshold and model updates. QRNN can receive previously unavailable characteristics or evolved data points for learning, without starting from scratch, so as to mark abnormal data points and update model parameters in real time, as shown in formula **(12)** and **(13)**, where th_{up} and th_{lo} are the upper and lower thresholds of the abnormal score calculated by the selected quantile, $\alpha1$ and $\alpha2$ are the higher and lower bounds, respectively, and $\hat{f}(.)$ is the fitted model at the corresponding quantile ($\tau = 0.5$ corresponds to the median).

$$th_{up} = \hat{f}(x_t)_{\tau=\alpha2} \tag{12}$$

$$th_{lo} = \hat{f}(x_t)_{\tau=\alpha1} \tag{13}$$

Based on the conditional quantile regression, with the emergence of a new data set, the confidence of the model parameter distribution will be automatically updated. The threshold value will be incrementally updated, as described in the loss function above. With this setting, QRNN can perform anomaly detection in vibration time series data of hydraulic turbine unit.

Figure 5 shows the overall algorithm of QRNN. For preprocessing, offline training, evaluation, testing and detection is performed. The fitted model $\hat{f}(.)$ is loaded into memory ready for anomaly detection which is performed in formula **(12)** and **(13)**. After the traversal is completed, the fitted model is saved to QRNNdb. QRNN is design to operate with multiple settings depending on whether exogenous features are present. During fitting, different processing needs to be performed according to whether the exogenous feature (XF) is existed. During this procedure, LSTM encoder can be used as feature extractor. Upon the arrival of vibration time series data of hydraulic turbine unit, the proposed QRNN will predict its value and seamlessly flag its anomaly score. At the same time, the model parameters will be updated. The prediction, model updates and abnormal scoring can be completed in a single pass at O(1) time complexity.

4 EVALUATION

In order to verify the efficiency of the proposed method, we adopted the hydraulic turbine working simulation data set provided by Case Western Reserve University (CWRU) to perform the experiment and evaluation. The test bench consists of a two-horsepower motor, a torque sensor/encoder, and an electronic device for power measurement and control. The vibration data is collected by an accelerometer. The accelerometer is placed at the 12 o'clock position of the drive end and the fan end of the motor housing, which using a 16-channel DAT recorder (Smith and Randall, 2015). Experimental data of the drive end is collected at 12,000 sampling points per second and 48,000 sampling points per second. The fan data is collected at 12,000 sample per second (Boudiaf et al., 2016). The detailed attributes of the data set used in the experiment are shown in **Table 1**. We use python and Keras framework to build neural network. The experimental setting is CPU 2.30 GHz, 8G DDR4 3200 MHZ, and GeForce GTX 1050Ti GPU.

Adam optimizer is used in this method, which is an extension of SGD. In this algorithm, an adaptive gradient algorithm is introduced to adjust the learning rate. The errors of different methods on different load data sets are shown in **Table 2**. "1HP" in the table represents that there is a load in the device. In the QRNN method, the ability of anomaly detection largely depends on trend prediction, so the accuracy of trend prediction is very important. It can be seen from the table that the QRNN method has a greater improvement in the accuracy of trend prediction compared to other methods. Compared with the errors of CNN, GRU and BiLSTM, the QRNN method has reduced 41, 44, and 65% respectively.

One-dimensional CNN can be well applied to the time series analysis of sensor data (Roska and Chua, 1993) (such as

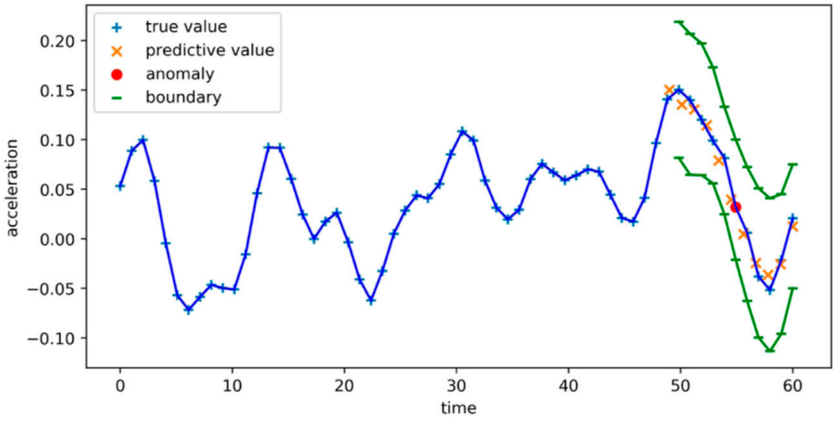

FIGURE 6 | CNN for anomaly detection.

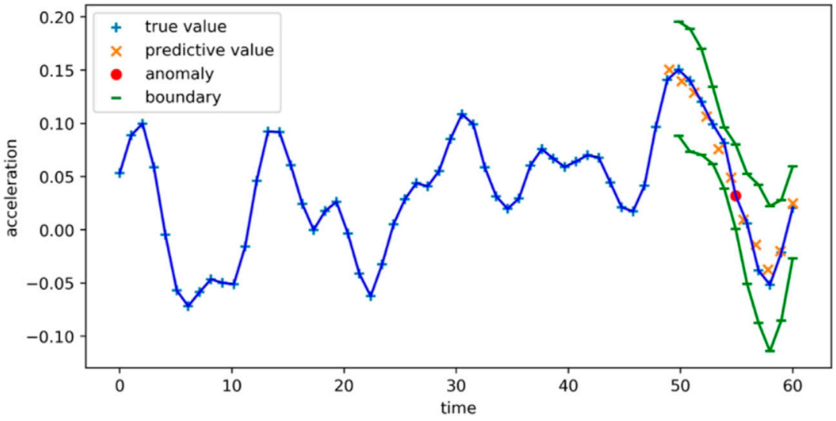

FIGURE 7 | GRU for anomaly detection.

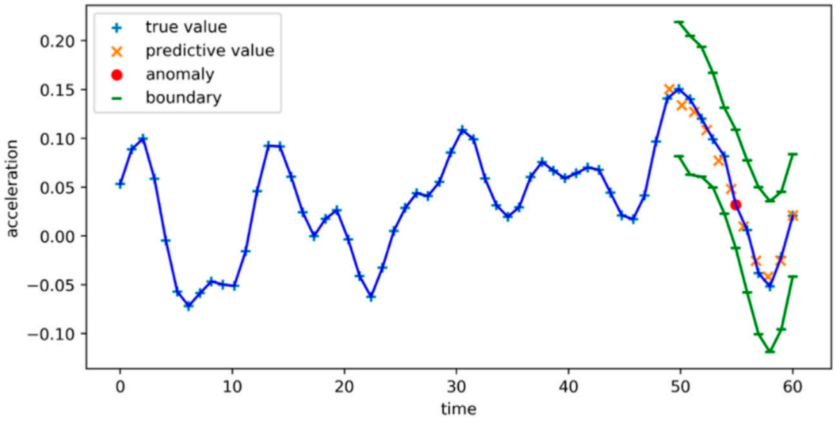

FIGURE 8 | BiLSTM for anomaly detection.

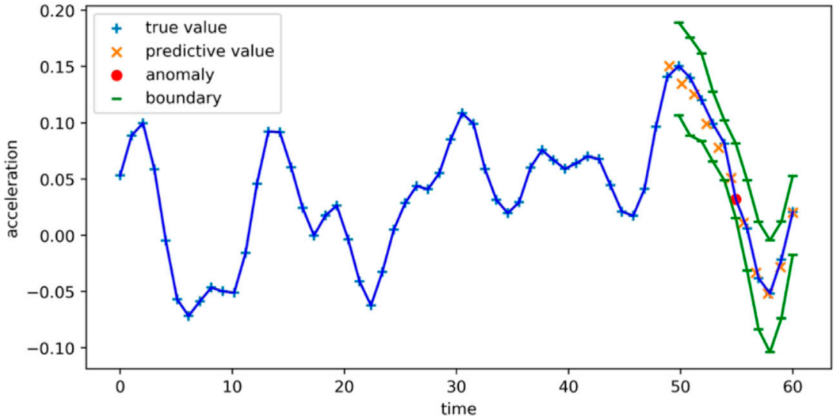

FIGURE 9 | QRNN for anomaly detection.

TABLE 3 | TP, FP, FN, TN value, precision, recall and running time of each method.

	TP	FP	FN	TN	Precision (%)	Recall (%)	Time (ms)
CNN	323	53	102	9,522	85.9	76.0	154.7
GRU	367	37	58	9,538	90.8	86.4	164.3
BiLSTM	379	27	46	9,548	93.3	89.2	159.4
QRNN	398	17	27	9,558	95.9	93.6	125.3

gyroscope or accelerometer data). It can also be used to analyze signal data with a fixed length period (such as audio signals). It can well identify simple patterns in the data, and then use these patterns to generate more complex patterns in higher-level layers. It is generally feasible to use one-dimensional convolution to process time series. The results of CNN are shown in **Figure 6**.

Long short-term memory network (LSTM) was born to solve the problem of long-term dependence. As a variant of LSTM, GRU combines the forget gate and input gate into a single update gate. It mixes the cell state and the hidden state, and adds some other changes. The final model is simpler than the standard LSTM model. BiLSTM is also a variant of LSTM, which takes context into account. The results of GRU and BiLSTM are shown in **Figures 7**, **8**, respectively.

The main body of the QRNN framework is composed of LSTM encoders. LSTM network is used to solve the vanishing gradient problem. It supports end-to-end modeling and nonlinear feature extraction. In the process of training the neural network, the error margin has a direct impact on the accuracy of the model, especially the time. This is a hyper parameter and needs to be specified before training. The basis for the formulation is the convergence speed of the model and the learning accuracy of the sample. When it is too large, neither the training accuracy nor the test accuracy is high enough to meet actual needs. If it is too small, although the learning effect is more ideal, it takes a lot of time. The parameter is set between 10^{-4} 10^{-2} generally. When the training error is lower than this value, the training is considered sufficient, and the training should be stopped. The results of the QRNN are shown in **Figure 9**.

We count TP (True Positive), FP (False Positive), FN (False Negative), and TN (True Negative) based on the experimental data. TP represents the number of abnormal points marked by the neural network that are correctly marked. FP means that it is actually a normal point but is marked as an abnormal point. FN represents the number of normal points marked as abnormal points. TN represents the number of normal points that are marked correctly. We calculate the precision and recall rate of each method based on TP, FP, FN, and TN. The precision rate ($\frac{TP}{TP+FP}$) is used to measure the degree to which the method finds the right way, and the recall rate ($\frac{TP}{TP+FN}$) measures the degree to which the method is found to be complete. As shown in **Table 3**, it can be seen that the QRNN has the highest accuracy and recall rates (95.9%, 94.3%). In addition, although the structure of QRNN is relatively complex and the training time is longer than CNN and GRU, the overall running time (125.3 MS) is significantly shorter than them.

5 CONCLUSION

Anomaly detection of evolution time series is important for hydraulic turbine systems. This paper introduces a vibration-based anomaly detection method. It can deal with time-dependent and non-linear complex dynamic sequences. As a window-based anomaly detection method, it has scalability, high-efficiency stream processing efficiency and can effectively deal with the heterogeneity and randomness in the constantly changing data stream. After experimental evaluation based on real data sets, it indicates that the proposed method is fast, robust and accurate compared to the traditional anomaly detection methods.

DATA AVAILABILITY STATEMENT

The data underlying this article are available in the article and in its online Supplementary Material.

AUTHOR CONTRIBUTIONS

LX wrote the first draft of the paper, JL directed the paper writing and provided project support for the paper, and FY, GZ and the JD put forward many valuable amendments in the paper writing.

FUNDING

This research was funded by National Natural Science Foundation of China (52009106); Natural Science Basic Research Plan of Shaanxi Province (2019JQ-130).

REFERENCES

Borovykh, A., Bohte, S., and Oosterlee, C. W. (2017). “Conditional Time Series Forecasting with Convolutional Neural Networks,” in *Proceedings of the International Conference on Artificial Neural Networks*. United States: arXiv.

Boudiaf, A., Moussaoui, A., Dahane, A., and Atoui, I. (2016). A Comparative Study of Various Methods of Bearing Faults Diagnosis Using the Case Western reserve university Data. *J. Fail. Anal. Preven.* 16, 271–284. doi:10.1007/s11668-016-0080-7

Breiman, L. (2001). Random Forests. *Machine Learn.* 45, 5–32. doi:10.1023/a:1010933404324

Calvo-Bascones, P., Sanz-Bobi, M. A., and Welte, T. M. (2021). Anomaly Detection Method Based on the Deep Knowledge behind Behavior Patterns in Industrial Components. Application to a Hydropower Plant. *Comput. Industry* 125, 103376. doi:10.1016/j.compind.2020.103376

Dasgupta, S., and Osogami, T. (2017). “Nonlinear Dynamic Boltzmann Machines for Time-Series Prediction,” in *The AAAI Conference on Artificial Intelligence*. San Francisco, United States: AAAI Press, 31.

Dragomiretskiy, K., and Zosso, D. (2013). Variational Mode Decomposition. *IEEE Transactions Signal. Processing* 62, 531–544. doi:10.1109/TSP.2013.2288675

Filonov, P., Lavrentyev, A., and Vorontsov, A. (2016). Multivariate Industrial Time Series with Cyber-Attack Simulation: Fault Detection Using an Lstm-Based Predictive Data Model. NIPS.

Geraci, M., and Bottai, M. (2007). Quantile Regression for Longitudinal Data Using the Asymmetric Laplace Distribution. *Biostatistics* 8, 140–154. doi:10.1093/biostatistics/kxj039

Gers, F. A., Schmidhuber, J., and Cummins, F. (2000). Learning to Forget: Continual Prediction with Lstm. *Neural Comput.* 12, 2451–2471. doi:10.1162/089976600300015015

Grob, G. L., Cardoso, Â., Liu, C., Little, D. A., and Chamberlain, B. P. (2018). “A Recurrent Neural Network Survival Model: Predicting Web User Return Time,” in *Joint European Conference on Machine Learning and Knowledge Discovery in Databases* (United States: Springer), 152–168.

Guha, S., Mishra, N., Roy, G., and Schrijvers, O. (2016). “Robust Random Cut forest Based Anomaly Detection on Streams,” in *International Conference on Machine Learning* (Canada: ACM), 2712–2721.

Hochreiter, S., and Schmidhuber, J. (1997). Long Short-Term Memory. *Neural Comput.* 9, 1735–1780. doi:10.1162/neco.1997.9.8.1735

Hundman, K., Constantinou, V., Laporte, C., Colwell, I., and Soderstrom, T. (2018). “Detecting Spacecraft Anomalies Using Lstms and Nonparametric Dynamic Thresholding,” in *The 24th ACM SIGKDD International Conference*. New York, United States: ACM, 387–395. doi:10.1145/3219819.3219845

Iyer, A. P., Li, L. E., Das, T., and Stoica, I. (2016). “Time-evolving Graph Processing at Scale,” in *The Fourth International Workshop on Graph Data Management Experiences and Systems*. New York, United States: ACM, 1–6. doi:10.1145/2960414.2960419

Kim, Y. (2014). “Convolutional Neural Networks for Sentence Classification,” in *Proceedings of the 2014 Conference on Empirical Methods in Natural Language Processing*, 1746–1751. doi:10.3115/v1/d14-1181

Koenker, R., and Bassett, G., Jr (1978). Regression Quantiles. *Econometrica*, 33–50. doi:10.2307/1913643

Koenker, R., and Hallock, K. F. (2001). Quantile Regression. *J. Econ. Perspect.* 15, 143–156. doi:10.1257/jep.15.4.143

Koenker, R., and Machado, J. A. F. (1999). Goodness of Fit and Related Inference Processes for Quantile Regression. *J. Am. Stat. Assoc.* 94, 1296–1310. doi:10.1080/01621459.1999.10473882

Kotz, S., Kozubowski, T., and Podgórski, K. (2001). *The Laplace Distribution and Generalizations: A Revisit with Applications to Communications, Economics, Engineering, and Finance*, 183. Basel: Birkhauser.

Lai, G., Chang, W.-C., Yang, Y., and Liu, H. (2018). “Modeling Long-And Short-Term Temporal Patterns with Deep Neural Networks,” in *The 41st International ACM SIGIR Conference*. United States: ACM, 95–104. doi:10.1145/3209978.3210006

Laptev, N., Amizadeh, S., and Flint, I. (2015). “Generic and Scalable Framework for Automated Time-Series Anomaly Detection,” in *The 21th ACM SIGKDD International Conference*. New York, United States: ACM, 1939–1947. doi:10.1145/2783258.2788611

Liu, B., Li, Z., Chen, X., Huang, Y., and Liu, X. (2017). Recognition and Vulnerability Analysis of Key Nodes in Power Grid Based on Complex Network Centrality. *IEEE Trans. Circuits Syst. Express Briefs* 65, 346–350. doi:10.1109/tcsii.2017.2705482

Liu, B., Li, Z., Dong, X., Samson, S. Y., Chen, X., Oo, A. M., et al. (2020). Impedance Modeling and Controllers Shaping Effect Analysis of Pmsg Wind Turbines. *IEEE J. Emerging Selected Top. Power Electro.* 9, 1465–1478. doi:10.1109/jestpe.2020.3014412

Manzoor, E., Lamba, H., and Akoglu, L. (2018). “Xstream: Outlier Detection in Feature-Evolving Data Streams,” in *The 24th ACM SIGKDD International Conference*. New York, United States: ACM, 1963–1972.

Mehrotra, K. G., Mohan, C. K., and Huang, H. (2017). *Anomaly Detection Principles and Algorithms*. USA: Springer.

Nayak, R., Pati, U. C., and Das, S. K. (2021). “A Comprehensive Review on Deep Learning-Based Methods for Video Anomaly Detection,” in *Image and Vision Computing*. Holland: ELSEVIER, 106. doi:10.1016/j.imavis.2020.104078

Pang, G., Shen, C., Cao, L., and Hengel, A. V. D. (2021). Deep Learning for Anomaly Detection. *ACM Comput. Surv.* 54, 1–38. doi:10.1145/3439950

Park, H., Noh, J., and Ham, B. (2020). “Learning Memory-Guided Normality for Anomaly Detection,” in *Proceedings of the IEEE/CVF Conference on Computer Vision and Pattern Recognition*. United States: IEEE, 14372–14381. doi:10.1109/cvpr42600.2020.01438

Roska, T., and Chua, L. O. (1993). The Cnn Universal Machine: an Analogic Array Computer. *IEEE Trans. Circuits Syst.* 40, 163–173. doi:10.1109/82.222815

Salinas, D., Flunkert, V., Gasthaus, J., and Deep, A. (2017). Probabilistic Forecasting with Autoregressive Recurrent Networks (NIPS).

Sen, R., Yu, H.-F., and Dhillon, I. S. (2019). Think Globally, Act Locally: A Deep Neural Network Approach to High-Dimensional Time Series Forecasting. *Proc. Neural Inf. Process. Syst. Conf. (Nips)* 32, 4837–4846. https://arxiv.org/abs/1905.03806.

Shipmon, D. T., Gurevitch, J. M., Piselli, P. M., and Edwards, S. T. (2017). *Time Series Anomaly Detection; Detection of Anomalous Drops with Limited Features and Sparse Examples in Noisy Highly Periodic Data*. Preprint Repository Name [arXiv]. Available at: https://arxiv.org/abs/1708.03665.

Smith, W. A., and Randall, R. B. (2015). Rolling Element Bearing Diagnostics Using the Case Western reserve university Data: A Benchmark Study. *Mech. Syst. signal Process.* 64-65, 100–131. doi:10.1016/j.ymssp.2015.04.021

Wang, C., Wang, B., Liu, H., and Qu, H. (2020). "Anomaly Detection for Industrial Control System Based on Autoencoder Neural Network," in *Wireless Communications and Mobile Computing*. United Kingdom: Hindawi. doi:10.1155/2020/8897926

Wu, K., Zhang, K., Fan, W., Edwards, A., and Philip, S. Y. (2014). "Rs-forest: A Rapid Density Estimator for Streaming Anomaly Detection," in *ICDM* (United States: IEEE) 600–609. doi:10.1109/icdm.2014.45

Xiong, L., Liu, X., Liu, L., and Liu, Y. (2021). Amplitude-phase Detection for Power Converters Tied to Unbalanced Grids with Large X/r Ratios. *IEEE Trans. Power Electro.* 37, 2100–2112. doi:10.1109/tpel.2021.3104591

Xiong, L., Liu, X., Zhao, C., and Zhuo, F. (2019). A Fast and Robust Real-Time Detection Algorithm of Decaying Dc Transient and Harmonic Components in Three-phase Systems. *IEEE Trans. Power Electro.* 35, 3332–3336. doi:10.1109/tpel.2019.2940891

Xu, H., Chen, W., Zhao, N., Li, Z., Bu, J., Li, Z., et al. (2018). "Unsupervised Anomaly Detection via Variational Auto-Encoder for Seasonal Kpis in Web Applications," in *The 2018 World Wide Web Conference*. Switzerland: ACM, 187–196. doi:10.1145/3178876.3185996

Yang, J., Nguyen, M. N., San, P. P., Li, X. L., and Krishnaswamy, S. (2015). "Deep Convolutional Neural Networks on Multichannel Time Series for Human Activity Recognition," in *Deep Convolutional Neural Networks on Multichannel Time Series for Human Activity Recognition* (Buenos Aires, Argentina: IJCAI Press).

Conflict of Interest: The authors declare that the research was conducted in the absence of any commercial or financial relationships that could be construed as a potential conflict of interest.

frontiers | Frontiers in Energy Research

ORIGINAL RESEARCH
published: 11 April 2022
doi: 10.3389/fenrg.2022.864122

Research on the Amplitude–Phase Motion Equation for the Modeling of Wind Power System

Qunying Liu[1]*, Maojie Cai[1], Yazhou Jiang[2], Deqing Zhu[1], Runsheng Zheng[1], Shuheng Chen[1] and Changhua Zhang[1]

[1]University of Electronic Science and Technology of China, Chengdu, China, [2]Clarkson University, Potsdam, NY, United States

The increasing penetration of wind power together with its high volatility could significantly impact the transient stability of the power grid. To quickly evaluate this impact, current engineering practice is primarily relying on time-domain simulation, which is computationally expensive despite that the results are more accurate. To solve this computational complexity issue, the amplitude–phase motion method is proposed to establish the electromechanical transient simulation model of the double-fed induction generator (DFIG) for wind energy. However, the traditional amplitude–phase motion equation (APME) suffers from the instability control from the abrupt change of terminal voltage induced by the system changes or flickers. To improve the transient stability of DFIG, this study firstly incorporates the q-axis current together with the amplitude change of terminal voltage into the phase error of the phase-locked loop (PLL). Then, the output phase of the terminal voltage of DFIG is highly combined with the q-axis current and the amplitude of terminal voltage to improve the internal control effect of the typical APME. The simulation results in the four-machine two-area power system with one wind farm demonstrate that the proposed method is able to maintain a stable operation of the wind farm and the power grid when experiencing a sharp disturbance of wind speed.

Keywords: wind farm, amplitude–phase motion equation, stability and robustness, dynamics, power-electronic interface

Edited by:
Liansong Xiong,
Nanjing Institute of Technology (NJIT),
China

Reviewed by:
Lixiong Xu,
Sichuan University, China
Fengkai Hu,
General Electric, United States

Correspondence:
Qunying Liu
lqy1206@126.com

Specialty section:
This article was submitted to Process and Energy Systems Engineering, a section of the journal Frontiers in Energy Research

Received: *28 January 2022*
Accepted: *03 March 2022*
Published: *11 April 2022*

Citation:
Liu Q, Cai M, Jiang Y, Zhu D, Zheng R, Chen S and Zhang C (2022) Research on the Amplitude–Phase Motion Equation for the Modeling of Wind Power System.
Front. Energy Res. 10:864122.
doi: 10.3389/fenrg.2022.864122

1 INTRODUCTION

To achieve a sustainable energy system of the future, it is imperative to integrate more variable renewable energy, such as wind and solar, and other new energy sources into the power grid. High wind power permeability is the development trend under the requirement of emission reduction and green energy. The installed wind power capacity was 330 million kW in China in 2021 (Yan et al., 2021). The wind turbines are connected to the grid through power-electronic converters, which results in the low inertia compared to the traditional power system with dominantly fossil fuel–driven generators. Therefore, the power system experiences much more extended swing under contingencies, which degrades the stability margin. Another significant issue resulting from the power-electronics–based power system is harmonic oscillation (Ebrahimzadeh et al., 2019). Compared to the PSS and AVR for traditional synchronous generators with a time constant of seconds, power converters for wind and solar are modulated in ns, which provides much faster dynamics and causes multiple time-scale control problems in the power system (Yuan et al., 2017). Therefore, the traditional modeling method of power system stability analysis may not be able to capture these emerging issues from power-electronic dominant power grids with renewables. It is in an urgent need to study the operational characteristics of power-electronic grid–connected renewables and provide theoretical support to maintain a stable operation of the power system with high penetration of new energy.

For the transient stability of the power system under high wind power penetration, it is important to establish a low-order, accurate, and open model (Zhang et al., 2017). The modeling analysis methods can be divided into three categories generally: the eigenvalue analysis method based on the state space theory, the impedance analysis method, and the amplitude–phase motion equation method. The eigenvalue analysis is a time-domain analysis method based on the state space, which is used to analyze the small signal stability in traditional power systems (Wang and Blaabjerg, 2019). The results are accurate while imposing a high computational complexity in simulation (Zong et al., 2020; Liu et al., 2021; Wu et al., 2021). The impedance method regards each device in the power system as an impedance, which can be characterized by its voltage and current. In this method, the grid and the generator are regarded as the combination of ideal source and impedance, respectively. Usually, the Nyquist criterion is used to determine the stability of power systems (Wen et al., 2016; Yan et al., 2016; Gao et al., 2018; Duan and Sheng, 2019). These models are simple in principle and easy to implement for analysis (Arabi et al., 2000). However, the impedance must be recalculated under different operation conditions. Moreover, the generator side cannot be regarded as a current source model if the output impedance of the generator is not large enough (Sun, 2011). It lacks the connection among key physical states in the dynamic process, so it is difficult to be applied to analyze dynamic problems at multiple time scales for large-scale power systems (Yuan et al., 2016).

How to keep the clear description of system characteristics without sacrificing the computation speed has always been the pursued goal. When the dynamic process of the power system suffers a disturbance, the power on each component will be changed to achieve a new balance by regulating the amplitude and phase of voltage as well. By the amplitude–phase motion equation method, the clear description between power imbalance and system states can be constructed (Yang et al., 2020), by simplifying the external characteristics into the amplitude and phase changes of voltage (Huang et al., 2019). In nature, by changing the voltage amplitude and phase, the amplitude and phase motion equation reproduces the system characteristics from the view of power balance between the input and the output of the whole system, which is explicit in the physical meaning and is simpler in modeling.

The modeling of DFIG has been realized in many research studies. Both the impendence method and the amplitude–phase method have analyzed the small signal dynamical behavior of power systems focusing on the different input–output relation. Through analysis, He et al. (2019) have concluded that the amplitude and phase motion equation of a single-machine infinite-bus system is similar to the classical second-order swing equation for a synchronous generator connected to an infinite bus, which supports the application of amplitude and phase motion equation in a dynamic process. This method applies to a wide range of scenarios, such as multi-input multi-output models and new perspective of equivalent system. The multi-input multi-output model is regarded as a single-input single-output equivalent model on the current time scale, and its voltage amplitude and phase dynamics are analyzed, respectively, in the study of Li et al. (2019). In the study of Zhao et al. (2018), the rotation of the rotor and the voltage of the capacitor are regarded as a real dynamical system, and the relationship between power balance and voltage change has been analyzed from the perspective of the component voltage vector. The vector controls have been proposed to solve the multiple time-scale problems of the electronic power system. In the study of Zhang et al. (2018), a frequency modulation method based on the phase motion equation has been proposed, and a typical phase-locked loop (PLL) synchronous vector control has been used to solve the problem of islanding. The time-scale problems of DC voltage control of the power system with the voltage source converter (VSC) connected to the grid have been studied by Yuan and Yuan (2018). The vector controls, including the DC voltage control, the phase-locked loop control, and the terminal voltage control, have been introduced to effectively replace the detection of VSC terminal voltage with the output power.

The angle stability has been realized to be a crucial factor that affects the stability of the power system. A typical APME model for the DFIG is proposed by Zhang et al. (2017), based on which the phase information has been added into the current-limiting control module by a feedback control loop. However, considering that the decrease of the voltage amplitude or the flicker of terminal phase affects the phase in the PLL and changes the dynamics of phase in the terminal voltage, a terminal voltage feedback control is further introduced into the DFIG model, which will make the change of terminal voltage phase closer to the real scenarios. Then, an improved APME model is established, and three cases are analyzed, including the steady-state process, the load changes, and the wind changes. The results show that the improved APME model does not change sharply with the change of wind speed.

2 OPERATION CHARACTERISTIC OF DFIG

A typical DFIG model is shown in **Figure 1A**. The stator side is directly connected to the grid through a transformer, while the rotor side is connected to the grid through an alternative current (AC)–direct current (DC)–alternative current (AC) converter. The control of DFIG mainly depends on the rotor side controller and the grid side controller. In general, the active power and reactive power of DFIG are mainly controlled to maximize the utilization of wind energy at the rotor side. The controller on the grid side keeps the DC voltage constant by changing the modulation coefficient, which also keeps the input power and the current in the sinusoidal waveform.

Figure 1B is the GSC/RSC controller of the typical DFIG model. The active and reactive power is calculated by the terminal voltage and its current. The PLL controller samples phase information from terminal voltage, and this

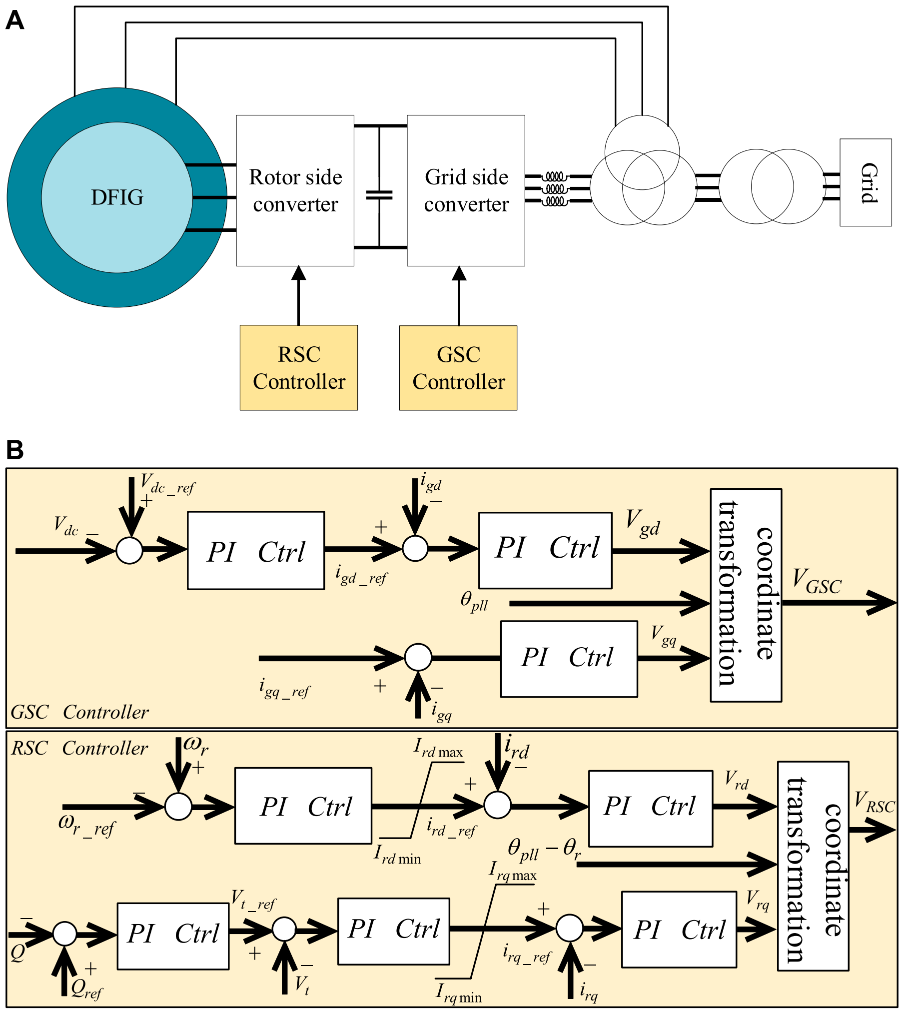

FIGURE 1 | (A) Typical DFIG model. **(B)** Control module of the typical DFIG model.

phase information combining with frequency obtained by the PLL controller is the basis for establishing the dq coordinate. The system is decoupled in the dq coordinate. The power system after decoupling can be more convenient for analysis and control. The active power can be controlled independently by adjusting the q-axis current of rotor, while the reactive power can be controlled independently by the d-axis current of rotor. **Figure 1B** shows a method to decouple the system. In the GSC controller module, the DC voltage V_{dc} between two converters, grid side current i_{gd}, and phase of PLL θ_{pll} are used to control the voltage of grid side converter V_{GSC}. In the RSC controller module, the reactive power Q, terminal voltage V_t, rotor speed ω_r, rotor current i_{rd}/i_{rq}, and the error between the phase of PLL and the phase of rotor θ_{pll} -θ_r are used to control the voltage of rotor side converter V_{RSC}.

The DFIG is a strongly coupled system because of the flux between stator windings and rotor windings. There exists a rotor magnetic field while three-phase AC is acting on the rotor windings. This field cuts the stator windings to produce the induced three-phase current. In return, the field produced by AC on stator windings also influences the current on rotor windings by changing its magnitude and phase. Thus, there are mutual constraints among stator current, rotor current, and stator voltage. The electromagnetic torque equation, active power equation, and reactive power equation are listed as the following equation, in which both components on the dq-axis have effects on power and torque:

$$\begin{cases} P_s = \frac{3}{2}\mathrm{Re}\left(\vec{u}_{sdq}\,\vec{i}^{*}_{sdq}\right) = \frac{3}{2}\left(u_{sd}i_{sd} + u_{sq}i_{sq}\right), \\ Q_s = \frac{3}{2}\mathrm{Im}\left(\vec{u}_{sdq}\,\vec{i}^{*}_{sdq}\right) = \frac{3}{2}\left(u_{sq}i_{sd} - u_{sd}i_{sq}\right), \\ T_e = \frac{3}{2}n_p\left(\Psi_{sd}i_{sq} - \Psi_{sq}i_{sd}\right) = \frac{3}{2}n_p\left(\Psi_{rq}i_{rd} - \Psi_{rd}i_{rq}\right) \\ \quad = \frac{3}{2}n_p L_m\left(i_{sq}i_{rd} - i_{sd}i_{rq}\right), \end{cases} \tag{1}$$

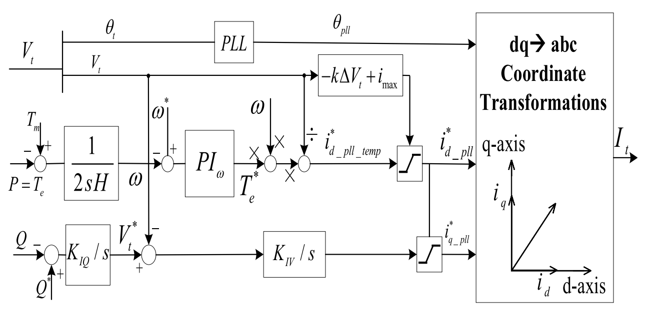

FIGURE 2 | Control block of the GE model.

where P_s is the active power; Q_s is the reactive power; s is the electromagnetic torque; u_{sdq} is the stator dq-axis voltage; i_{sdq} is the stator dq-axis current; Ψ_{sd} represents the component of flux on the d-axis; Ψ_{sq} represents the component of flux on the q-axis; n_p is the number of pole-pairs; and L_m is the mutual inductance between the stator and the rotor.

The vector control (VC) method is the core control method of DFIG, which can decouple their relationship and make the control of DFIG simpler. In the VC method, the stator current is transformed into dq-axis current on dq coordination. If the stator flux linkage is chosen as the d-axis, the components of stator flux can be written as **Eq. 2** and the voltages on the dq-axis are shown as **Eq. 3**:

$$\begin{cases} \Psi_{sd} = \left|\Psi_{sdq}\right| = \Psi_s, \\ \Psi_{sq} = 0, \end{cases} \tag{2}$$

$$u_{sd} = 0, u_{sq} = U_s = \omega_1 \Psi_s, \tag{3}$$

where Ψ_s is the magnitude of stator flux; Ψ_{sdq} is the vector of stator flux space; and ω_1 is the velocity of synchronous angular.

The electromagnetic torque equation can be simplified as **Eq. 4**, in which the magnitude of torque is only determined by the stator flux on the d-axis and rotor current on the q-axis. The stator flux on the d-axis is almost a constant here, so the rotor current on the q-axis can dominate the magnitude of electromagnetic torque. The active and reactive power can be simplified as **Eq. 5**. **Equation 5** is further simplified as **Eq. 7** by **Eq. 6**. Under the condition that the stator flux remains unchanged, the active power is only determined by the rotor current on the q-axis and the reactive power is mainly determined by the rotor current on the d-axis:

$$T_e = \frac{3}{2} n_p \left(\Psi_{sd} i_{sq} - \Psi_{sq} i_{sd}\right) = -\frac{3}{2} n_p \frac{L_m}{L_s} \Psi_s i_{rq}, \tag{4}$$

$$\begin{cases} P_s = \frac{3}{2} u_{sq} i_{sq} = \frac{3}{2} U_s i_{sq}, \\ Q_s = \frac{3}{2} u_{sq} i_{sd} = \frac{3}{2} U_s i_{sd}, \end{cases} \tag{5}$$

$$\begin{cases} i_{sd} = \frac{L_m}{L_s} \left(i_{ms} - i_{rd}\right), \\ i_{sq} = -\frac{L_m}{L_s} i_{rq}, \end{cases} \tag{6}$$

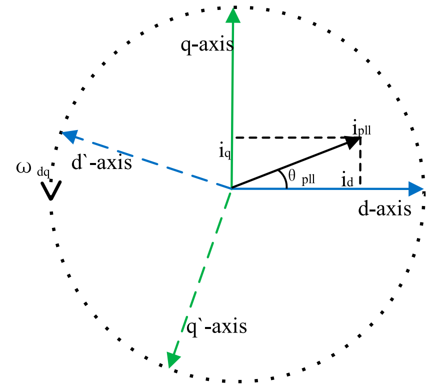

FIGURE 3 | dq-axis spatial relationship.

$$\begin{cases} P_s = -\frac{3}{2} \omega_1 \Psi_s \frac{L_m}{L_s} i_{rq}, \\ Q_s = \frac{3}{2} \omega_1 \Psi_s \frac{L_m}{L_s} \left(i_{ms} - i_{sd}\right), \end{cases} \tag{7}$$

where L_s represents the inductance of stator windings and i_{ms} is the field current of stator.

The time scale of the AC current control loop and the DC voltage control loop is quite faster than that of the electromechanical characteristics, so they have often been ignored in the conventional control. The GE model, ignoring the AC current control loop and the DC voltage control loop, uses the main characteristics to describe the system (Clark et al., 2010). Under the premise that the main characteristics of DFIG can be reflected in the electromechanical time scale, this model is simple and the results are accurate, while its order is lower. Therefore, the GE model has been widely used in power system simulation. Hence, the GE model is taken as an example to analyze the structure and the control mode of the wind turbine. The control block of the GE model is shown in **Figure 2**.

The rotating speed is calculated according to the electromagnetic torque and mechanical torque. Then, the reference value of the electromagnetic torque is calculated by the reference speed. The active current is given by the electromagnetic torque, speed, and the terminal voltage. The difference of reactive power is used to calculate the voltage reference. In the transient process, when the terminal voltage amplitude decreases, the active component of current will decrease due to the inertia, while the PI control will damp the collapse and increase the voltage by increasing the reactive current. Of course, the amplitude change of the terminal voltage will directly affect the active current, and the following equation gives its mathematical expression:

$$i^*_{d-pll} = \begin{cases} i_{\max}, & \Delta V_t < 0 \\ i_{\max} - k_v \Delta V_t, & 0 \le \Delta V_t \le 0.4 \\ 0, & 0.4 \le \Delta V_t \end{cases} \tag{8}$$

where $i_{\max}$ is the maximum transient current of DFIG, whose value is set to 1.2 p.u. The control parameter k_v is set to 3.05 by default, and i_{d-pll}^* is the expected output of active current on the d-axis.

Considering that the voltage drop ΔV_t is within [0, 0.4 p.u.], and the voltage drop is 0.1 p.u., the following equation can be obtained:

$$\Delta V_t = 0.9 - V_t. \tag{9}$$

The spatial relationship on the dq-axis is shown in **Figure 3**.

The transient current i_{pll} of any phase and magnitude can be expressed by a combination of the dq-axis current amplitude and the phase output θ_{pll} of PLL. The transient current i_{pll} is also a spatial vector, which can be expressed in the form of magnitude and phase. The dq-axis will rotate with the change of the frequency and phase of the terminal voltage, which can be obtained from the PLL block connected to the terminal of DFIG. After decomposing current i_{pll} into two vertical components, the active and reactive power of DFIG can be controlled, respectively, through i_q and i_d. Then, the spatial vector i_{pll} is decomposed on the dq-axis for analysis and control:

$$\begin{cases} i_d^2 + i_q^2 = i_{\mathrm{pll}}^2, \\ \theta_{pll} = \arctan \dfrac{i_q}{i_d}. \end{cases} \tag{10}$$

3 DFIG MODEL CONSTRUCTION BASED ON AMPLITUDE–PHASE MOTION EQUATION

The idea of amplitude–phase motion equation is to construct its physical relationship through the change of the external input to the output. Physically, the object studied can be regarded as a black box. When the input power of the system is not balanced with the actual output power, the voltage of each component in the system will change in amplitude and phase, in order to achieve a new balance. Therefore, the model can reflect the dynamics of the external voltage amplitude and phase. Its physical nature is that the unbalanced power between the expected output and the actual output of the power system is embodied by the change of voltage amplitude and phase. Both the expected active power and reactive power are the reference values calculated by the control part.

Due to a large inertia of turbine, the electromechanical time scale with a time constant of 1 s is slow compared to the electromagnetic phenomenon (wind converter control is in ns). As the current time scale and voltage time scale are usually 0.01 and 0.1 s, respectively, it is assumed that the change and control of both the active power and the reactive power are instantaneous in the electromechanical time scale.

Since the actual output power of DFIG is the terminal voltage multiplied by the conjugate current, combined with **Eqs 8–10**, the actual outputs of active power and reactive power are calculated as follows:

$$\begin{aligned} P + jQ = \vec{V}_t * \overline{\vec{I}}_{pll} &= V_t e^{j\theta_t}\left(i_d^* - j i_q^*\right) e^{-j\theta_{pll}} \\ &= V_t\left(i_d^* \cos\theta_{err} + i_q^* \sin\theta_{err} - j * i_q^* \cos\theta_{err} \right. \\ &\qquad \left. + j * i_d^* \sin\theta_{err}\right), \end{aligned} \tag{11}$$

where $\theta_{err} = \theta_t - \theta_{pll}$; $\overline{\vec{I}}_{pll}$ represents the conjugation of the current phasor vector; $\vec{V}_t$ represents the phasor of the voltage vector; i_d^* is the expected output of active current on the d-axis; i_q^* is the expected output of reactive current on the q-axis; θ_t is the terminal voltage phase; θ_{pll} is the output phase of the PLL; and θ_{err} is the phase error of the PLL. In this expression, the parameters θ_{err}, which have direct influences on the phase error of PLL, are determined by the terminal voltage phase and the output phase of the PLL. In the actual transient process, both the decrease of voltage amplitude and the flicker of voltage phase will affect the phase dynamics of DFIG. Hence, it is desired to improve the above expression for the improved transient performance by making θ_{err} directly respond to the change of terminal voltage amplitude. Meanwhile, phase dynamics also correlated with the variation of reactive current i_q. In this study, the expected reactive current on the q-axis is also deduced to construct the relationship with θ_{err}, which is expressed as

$$\begin{aligned} P + jQ = \vec{V}_t * \overline{\vec{I}}_{pll} &= V_t e^{j\theta_t}\left(i_d^* - j i_q^*\right) e^{-j\theta_{pll}} \\ &= V_t e^{j\theta_t}\left(i_d^* - j i_q^*\right) e^{j\theta_{pll}} e^{-2j\theta_{pll}} \\ &= V_t e^{j\theta_t}\left(i_d^* - j i_q^*\right) e^{j\theta_{pll}} e^{-2j \arctan \frac{i_q^*}{i_d^*}}, \end{aligned} \tag{12}$$

$$\theta_{err} = \theta_t + \theta_{pll} - 2\arctan \frac{i_q^*}{i_d^*}. \tag{13}$$

The active and reactive power can be obtained as

$$P + jQ = V_t\left(i_d^* - j i_q^*\right) e^{j\theta_{err}}. \tag{14}$$

Furthermore, Euler's formula $e^{ix} = \cos x + i * \sin x$ is used to expand **Eq. 14** in order to observe the active and reactive power, respectively. The following results can be obtained:

$$\begin{aligned} P + jQ &= V_t\left(i_d^* - j i_q^*\right)\left(\cos\theta_{err} + j * \sin\theta_{err}\right) \\ &= V_t\left(i_d^* \cos\theta_{err} + i_q^* \sin\theta_{err} - j * i_q^* \cos\theta_{err} + j * i_d^* \sin\theta_{err}\right). \end{aligned} \tag{15}$$

Now, the unification of the right and left sides of the equation has been achieved. Both sides of the equation are complex numbers composed of real and imaginary parts. They can be further expressed as

$$\begin{pmatrix} P \\ Q \end{pmatrix} = V_t \begin{bmatrix} \cos\theta_{err} & \sin\theta_{err} \\ \sin\theta_{err} & -\cos\theta_{err} \end{bmatrix} \begin{bmatrix} i_d^* \\ i_q^* \end{bmatrix}. \tag{16}$$

It can be seen from **Eq. 13** that the phase error θ_{err} of PLL is jointly determined by the actual terminal voltage phase, the phase on the phase-locked loop, and the expected current reference on the dq-axis. In the expression of θ_{err}, the terminal

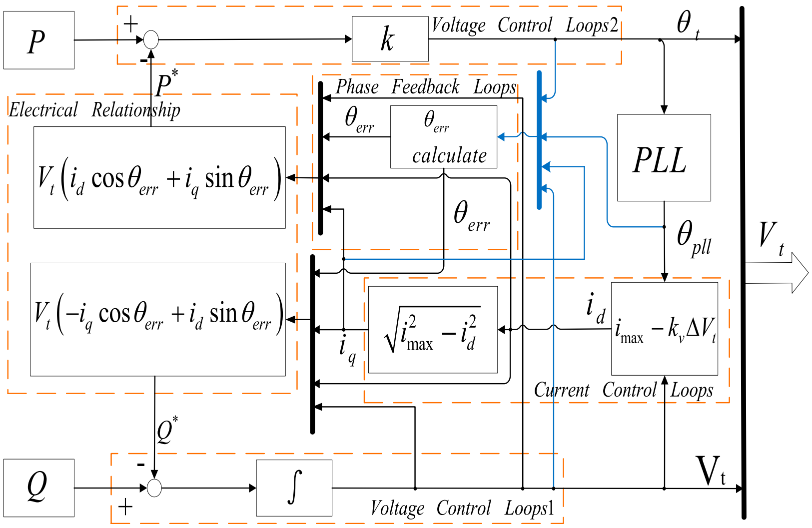

FIGURE 4 | Improved amplitude–phase motion equation model.

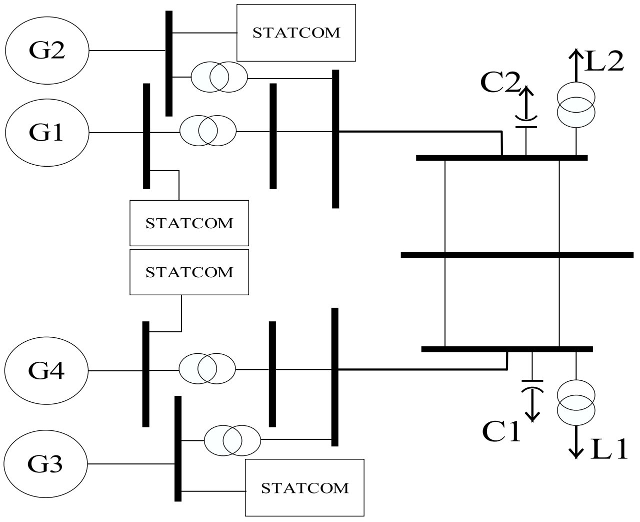

FIGURE 5 | Four-machine two-area wind power system.

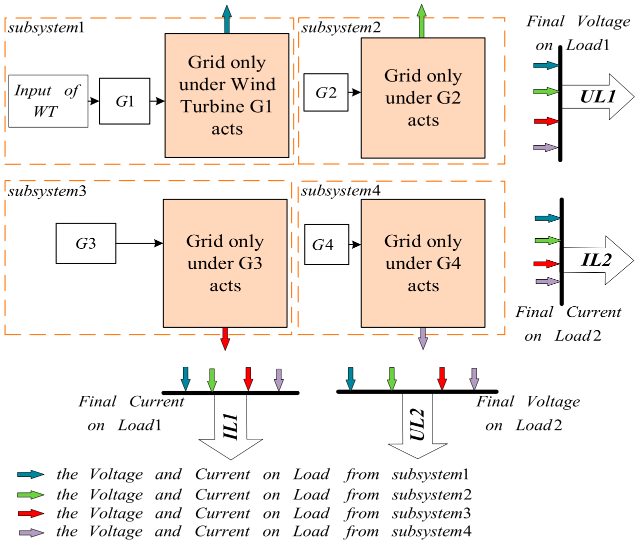

FIGURE 6 | Block diagram of the four-machine two-area power system.

voltage cannot be reflected directly. By using **Eq. 15** and **Eq. 16**, d-axis current i_d^* is deduced from the voltage amplitude. Furthermore, i_d^* in **Eq. 13** is replaced, and the terminal voltage amplitude is introduced into θ_{err}, as shown in the following equation:

$$i_d^* = i_{\max} - k_v \Delta V_t = i_{\max} - k_v (0.9 - V_t). \tag{17}$$

Then, θ_{err} is changed as

$$\theta_{err} = \theta_t + \theta_{pll} - 2\arctan \frac{i_q^*}{i_{\max} - k_v (0.9 - V_t)}, \tag{18}$$

where the amplitude of terminal voltage V_t and the current i_q are coupled into the phase error θ_{err} of PLL. From the perspective of control, the changes of terminal voltage amplitude and the q-axis current are fed to the phase dynamics of DFIG, by adding a feedback control to the typical model.

Figure 4 shows the derived amplitude–phase motion equation model based on the typical model of DFIG. The left side of the block diagram is the actual outputs of the active and reactive power of DFIG. The right end is the terminal voltage, and the middle is the control module based on the derivation equation above, in which there are the voltage control loops, the current control loops, and the phase deviation feedback loops from left to right.

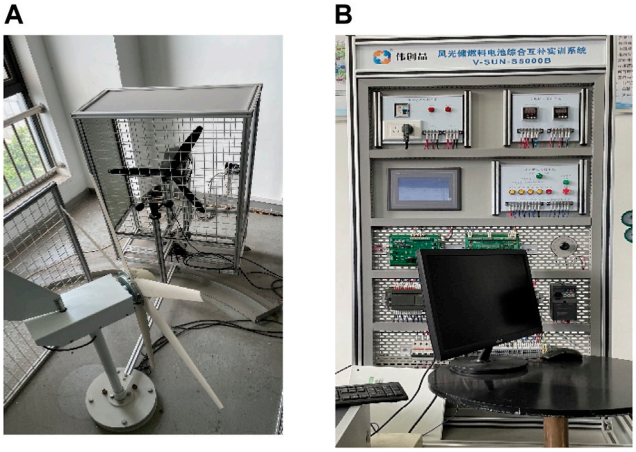

FIGURE 7 | (A) Impeller of DFIG. **(B)** Wind turbine system.

4 CASE STUDY

In order to verify the proposed optimization model, a typical IEEE benchmark case of a four-machine two-area power system with one wind farm has been established according to the schematic diagram in **Figure 5**, which has been analyzed and calculated by comparing the typical amplitude–phase motion equation model and the improved amplitude–phase motion equation model.

Figure 5 is further transformed to the block diagram of the four-machine two-area power system model (shown in **Figure 6**) for simulation. It consists of an improved amplitude–phase motion equation model of DFIG proposed in this paper and three traditional thermal generators. The generator G1 of the first subsystem is the optimization model based on the amplitude–phase motion equation, and the generator G3 of the third subsystem is the PV bus composed of the synchronous generator set. Generators G2 and G4 in the other two subsystems are PQ buses composed of the synchronous generators. The four generators in the power system are separated into four subsystems. In this part, the impedance modeling method is used to model the transmission network. According to the voltage and current relationship, each component is equivalent to a complex impedance model. The main components involved include the transmission lines, transformers, loads, and compensation capacitors. The general transmission line is equivalent to the complex impedance model, which is the combination of the resistance and reactance, while the long-distance transmission line is equivalent to the parallel form of the complex impedance and the capacitance admittance between the line and the ground. The transformer is equivalent to three complex impedances by a $\prod$ equivalent model. The compensation capacitor is equivalent to admittance $G + jB$. The loads, L1 and L2, are expressed as constant impedance models and are represented by the complex impedance.

The simulation platform is shown in **Figure 7**. The four-machine two-area power system with the improved amplitude–phase motion equation is embedded in **Figure 7B**. In **Figure 7A**, an impeller and a blade that simulates the change of wind speed are used as the source of variable wind speed for the case study. The details are discussed in **Section 4.2**. In **Figure 7B**, the wind turbine control system includes the auxiliary power supply control, output display, and wind simulation unit. The terminal voltage and the current signals needed by the amplitude–phase motion equation model come from the output unit.

TABLE 1 | Values of parameters.

Parameters	Values (p.u.)
P_1, Q_1	1, −0.2
P_2, Q_2, V_{t2}	1, 0.2, 1
U_3	1
P_4, Q_4, V_{t4}	1, 0.2, 1
$R_{L1}+jX_{L1}$, $R_{L2}+jX_{L2}$	$1.02+j1.02$
Y_{L1}, Y_{L2}	$0.4902-j0.4902$

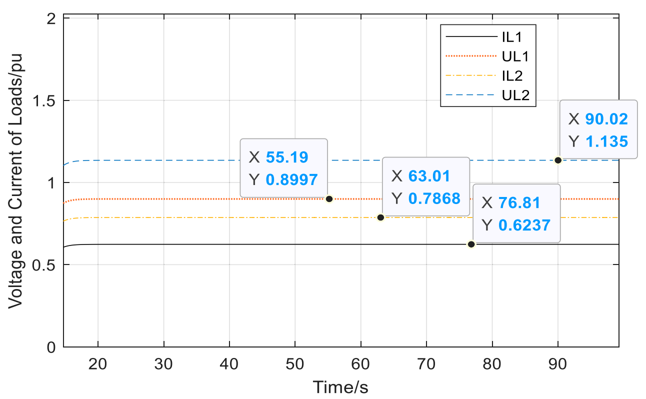

FIGURE 8 | Voltage and current curves on load under operation condition I of the improved APME model.

Under the different operation conditions and with the different network structure parameters, the improved amplitude–phase motion equation is studied in the four-machine two-area power system model established here. At the same time, the performance of the four-machine two-area power system, with a typical amplitude–phase motion equation model, is given for comparison with the improved one under the same operation condition. And the advantages of the improved APME model are analyzed in this section.

4.1 Operation Condition I: Steady-State Process Simulation

The operating conditions are set as follows: the parameters of G1 are P_1 and Q_1, the parameters of two constant impedance loads in the system are $R_{L1} + jX_{L1}$ and $R_{L2} + jX_{L2}$, while Y_{L1} and Y_{L2} are the admittance of loads. The parameters of G2 are V_{t2}, P_2, and Q_2. The parameter of G3 is U_3, and the parameters of G4 are V_{t4}, P_4, and Q_4. In the steady-state simulation, there is no fault set. The values of each parameter are set as shown in **Table 1**.

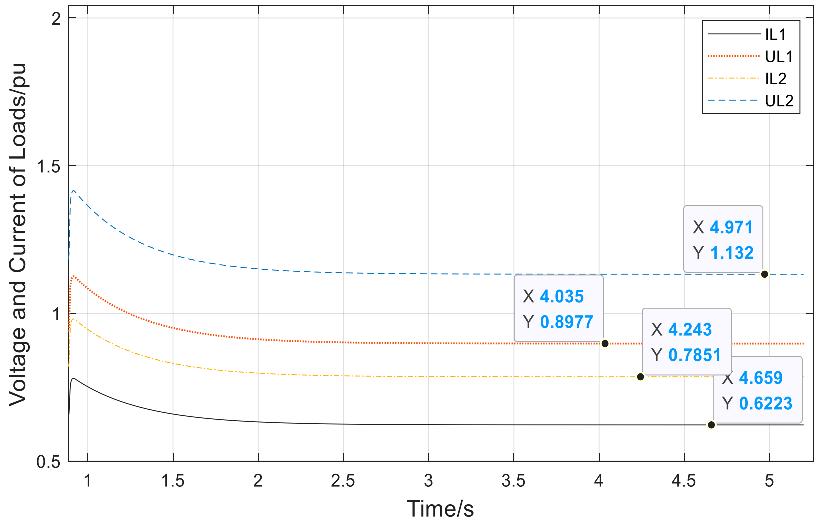

FIGURE 9 | Voltage and current curves on load under operation condition I of the typical APME model.

TABLE 2 | Voltage and current details on loads under operation condition I.

	Improved APME	Typical APME	Difference (%)
IL1	0.6237	0.6223	0.225
UL1	0.8997	0.8977	0.223
IL2	0.7868	0.7851	0.217
UL2	1.135	1.132	0.265

Figure 8 is the voltage and current curve of the load in the power system with the improved APME model of DFIG, where IL1 represents the current passing through L1 and UL1 represents the voltage of L1. IL2 represents the current passing through L2, and UL2 represents the voltage of L2. It can be seen from **Figure 8** that when the four-machine two-area power system has been started, the improved APME model has been regulated to reach a stable state very soon. The voltage and current in stabilization are within the reasonable range. The simulation result of the model is in line with the theoretical analysis of the power grid.

Figure 9 displays the voltage and current curves of the load in the power system with a typical DFIG model. By comparing **Figures 8**, **9**, it can be seen that the voltage and current curves of loads in the system reach a stable state quickly in both the improved and the typical model with a similar trend. The static parameters of loads are shown in **Table 2**. The difference of voltage and current before and after the DFIG model is improved is calculated.

The simulation results of the typical model are used as a reference to analyze the parameter difference of the two models, and the difference of current on $L1$ can be derived as

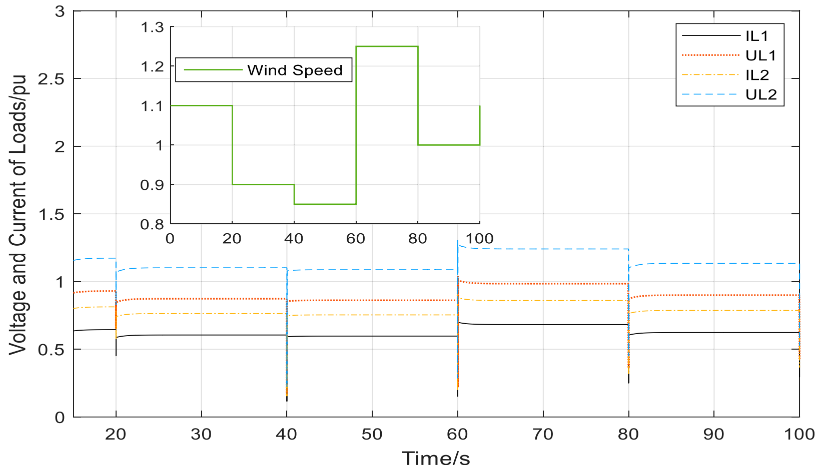

FIGURE 10 | Voltage and current curves on load with wind speed change of the improved APME model.

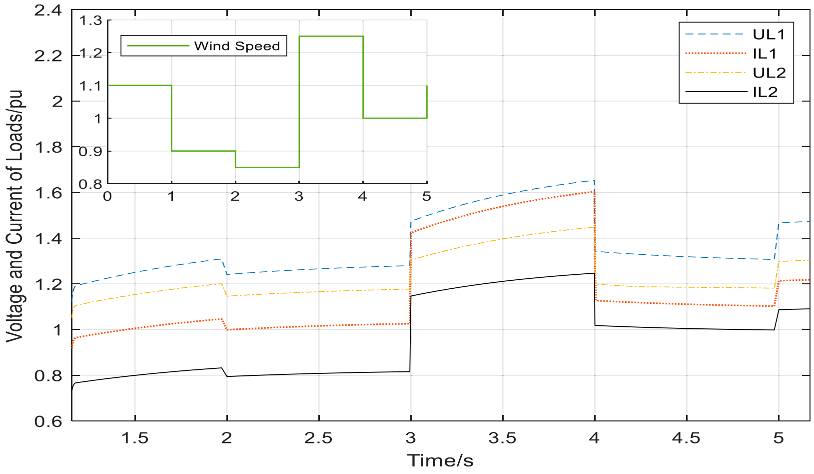

FIGURE 11 | Voltage and current curves on load with wind speed change of the typical APME model.

TABLE 3 | Values of parameters.

Parameters	Values (p.u.)
P_1, Q_1	0.125, -0.2
P_2, Q_2, V_{t2}	1, 0.2, 1
U_3	1
P_4, Q_4, V_{t4}	1, 0.2, 1

$$IL1_{diff} = \left| \frac{IL1_{After} - IL1_{Before}}{IL1_{Before}} \right| \times 100\%. \tag{19}$$

The differences of the four parameters are all lower than 0.3%, which means that the steady-state process demonstrated by the two models under this set of parameters is basically the same. The improved APME model runs in line with the typical model under the same parameter setting. Its simulation performs the same as typical ones, without any fluctuation in the steady state, which verifies that the improved APME model is available under this group of parameter setting.

4.2 Operation Condition II: Impact of Wind Speed

Due to its randomness, the wind speed changes constantly with the change of temperature and air pressure, and gust wind may occur occasionally, which leads to shape changes of the speed. To simulate this change, the wind speed in a day is roughly divided into five periods: 2 m/s from 6 to 9 a.m., 4 m/s from 9 a.m. to 13 p.m., 6 m/s from 13 to 17 p.m., 8 m/s from 17 to 19 p.m., and

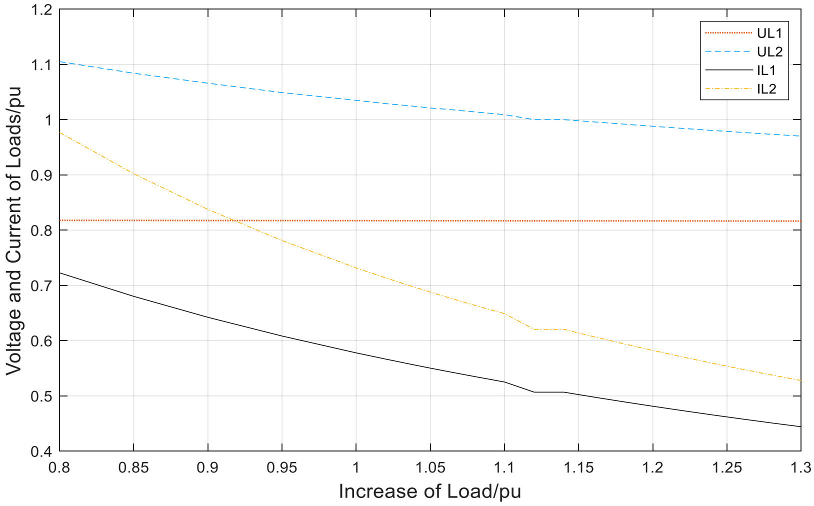

FIGURE 12 | Voltage and current curves on load with the increase of load of the improved APME model.

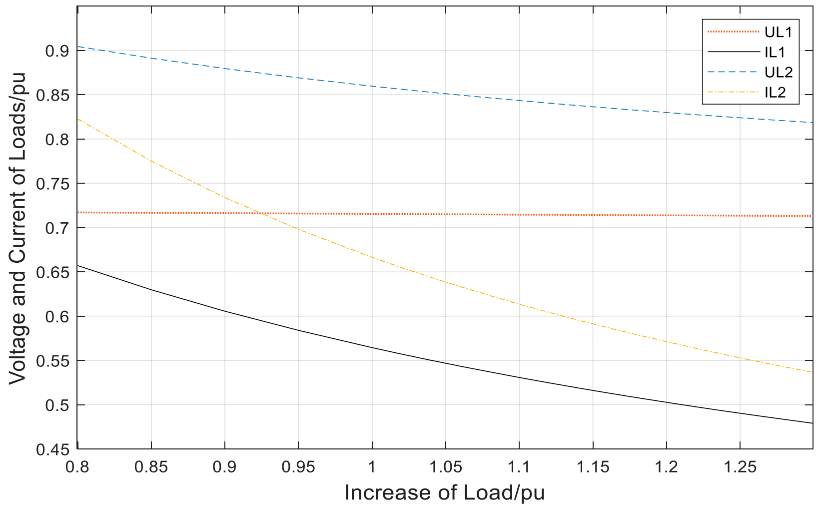

FIGURE 13 | Voltage and current curves on load with the increase of load of the typical APME model.

10 m/s after 19 p.m. All parameters are set to be the same as those in operation condition I, except the power injection from the DFIG.

Figure 10 shows the variation of voltage and current of the loads in the four-machine two-area power system, when wind speed changes with time mentioned above. As shown in **Figure 10**, the change of wind speed directly causes the output power change of DFIG, thus affecting the voltage and current of the load in the grid. When the wind speed changes suddenly, the voltage amplitude of loads does not change sharply, which indicates that the optimization model proposed in this paper has strong robustness and anti-interference ability.

In order to verify the model proposed in this paper, it is necessary to simulate the typical amplitude–phase motion equation of DFIG model under the same conditions. **Figure 11** is the result of a typical model, without optimization control mentioned in this paper, in which the voltage and the current of the loads with the change of wind speed can be observed. The key parameters of simulation are set as follows: the variation of wind speed is divided into five sections, 1.1, 0.9, 0.85, 1.25, and 1 successively. The output power of the conventional generator G2 is $P_2 = 1, Q_2 = -0.2$. The output voltage of G3 is 1 p.u., and the output power of the conventional generator G4 is $P_4 = 1, Q_4 = 0.2$. The value of two constant impedances in the power system is $Y_{L1} = Y_{L2} = 0.4902 - j0.4902$.

The results show that the output voltage of DFIG follows the change of wind speed. Compared with the improved APME model, it is more sensitive to the change of wind speed. As such, it is concluded that its robustness is not as strong as the improved model. Actually, the output of DFIG is not allowed to change significantly with the change of wind speed. Otherwise, DFIG is a great fluctuation to the power system, which will cause the instability of the whole system. In addition, it can be seen from the results that the voltage and current of the loads in the system are slightly higher when wind speed changes suddenly. The model proposed here can keep the voltage and current fluctuating within a small range.

4.3 Operation Condition III: Impact of Loads

The loads have a great influence on power system stability, and the capacity to contain load variation within a certain range is also an index to be considered. The variation of the load voltage in the four-machine two-area model at different load rates is studied. In a general power system, the voltage may lose stability when the wind power exceeds 4% of the total power generated in the system. In order to ensure a better operating state of the model, the voltage and current with the increase of load are calculated

TABLE 4 | Voltage and current details of Load 2 before and after improvement (per unit).

RL1/RL2	UL2 (B-O)	UL2 (A-O)	IL2 (B-O)	IL2 (A-O)
0.80	0.9044	1.105	0.8226	0.9767
0.85	0.8912	1.084	0.7750	0.902
0.90	0.8795	1.066	0.7338	0.8374
0.95	0.8690	1.049	0.6980	0.7811
1.00	0.8596	1.0350	0.6664	0.7316
1.02	0.8561	1.0290	0.6548	0.7134
1.04	0.8527	1.0240	0.6438	0.6961
1.05	0.8511	1.0210	0.6385	0.6878
1.06	0.8495	1.0190	0.6333	0.6796
1.08	0.8464	1.0140	0.6232	0.6638
1.10	0.8434	1.0090	0.6135	0.6487
1.12	0.8405	1.0000	0.6043	0.6204
1.14	0.8377	1.0000	0.5955	0.6204
1.16	0.8350	0.9960	0.5871	0.6072
1.18	0.8324	0.9920	0.5790	0.5944
1.20	0.8299	0.9880	0.5712	0.5822
1.22	0.8274	0.9842	0.5637	0.5704
1.24	0.8251	0.9805	0.5565	0.5591
1.26	0.8228	0.9770	0.5495	0.5483
1.28	0.8206	0.9735	0.5428	0.5378
1.30	0.8185	0.9702	0.5364	0.5277

under the output power of the wind turbine to account for 4% of the total generating capacity of all generators. As a result, the parameters of four generators are set as shown in **Table 3**, while the load parameter changes gradually from $Y_{L1} = Y_{L2} = 0.6250 - j0.6250$ p.u. to $0.3846 - j0.3846$ p.u.

Figure 12 demonstrates the overall trend of the voltage and the current when loads decrease with an increased load impedance in the improved APME model. The amplitude of current change is larger than that of voltage, and the changes of voltage and current amplitudes of L2 are larger than those of L1. The amplitude of current change is larger than that of voltage when the power of loads changes. It means that this model tries to keep the voltage stable. Obviously, when keeping the parameters of generator unchanged, the increase of the loads causes the reallocation of the power of the power system, and the voltage at the load bus will decrease, which is consistent with the actual operation situation.

The increased load in a typical APME model is studied too (shown in **Figure 13**). The changes and trends of the voltage and the current are the same with the improved model proposed in this paper. **Table 4** shows the voltage and current of L2 before and after being improved in the DFIG model, in the same scenario of the increased load, which once again proves the following conclusion: this model keeps the voltage stable, and both the improved and typical models have the same dynamic trends when loads increase.

5 CONCLUSION

An improved APME model for transient analysis based on the amplitude–phase motion equation has been proposed in this paper. In the actual transient process, the decrease of voltage amplitude or the flicker of voltage phase will affect the phase dynamics of DFIG. Based on the typical amplitude–phase motion equation model of DFIG, the phase dynamics of DFIG is improved, and a different expression of θ_{err} is derived, which is equivalent to adding a feedback control to the control loops of DFIG. The amplitude of the terminal voltage and the q-axis current are introduced to influence the phase error of the PLL. That is, the output current of the current control unit and the terminal voltage amplitude are introduced into the phase control loop of the terminal voltage, so that the phase output of the terminal voltage can directly reflect the terminal voltage amplitude. As a result, the control loop inside the DFIG is improved, and the coupling model becomes stronger, which makes the operation characteristics closer to the real scenarios. When the wind speed changes sharply, the proposed model in this paper has better robustness and smooth operation ability than the typical one.

DATA AVAILABILITY STATEMENT

The original contributions presented in the study are included in the article/Supplementary Material, and further inquiries can be directed to the corresponding author.

AUTHOR CONTRIBUTIONS

QL was responsible for modeling and writing. MC was responsible for the simulation. YJ was responsible for reviewing and modification. DZ and RZ were responsible for data calculation. SC and CZ were responsible for feasibility verification.

FUNDING

This study was supported by the NSFC under Grant No. 51677020.

REFERENCES

Arabi, S., Kundur, P., Hassink, P., and Matthews, D. (2000). “Small Signal Stability of a Large Power System as Affected by New Generation Additions[C],” in 2000 Power Engineering Society. Summer Meeting (Cat. No.00CH37134), 16-20 July 2000, Seattle, WA, USA (IEEE), 2, 812–816.

Clark, K., Miller, N., and Sanchez-Gasca, J. (2010). *Modeling of GE Wind Turbine-Generators for Grid Studies(version 4.5) [R]*. New York: General Electric International,Inc.

Duan, Q., and Sheng, W. (2019). Stability Analysis of Power Routers Connected to Power Electronic Distribution Grid[J]. *Power Syst. Technol.* 43 (01), 227–235. doi:10.13335/j.1000-3673.pst.2018.0753

Ebrahimzadeh, E., Blaabjerg, F., Wang, X., and Bak, C. L. (2019). Optimum Design of Power Converter Current Controllers in Large-Scale Power Electronics Based Power Systems. *IEEE Trans. Ind. Applicat.* 55 (3), 2792–2799. doi:10.1109/tia.2018.2886190

Gao, J., Zhao, J., Qu, K., and Li, F. (2018). “Reconstruction of Impedance-Based Stability Criterion in Weak Grid[J],” in 2018 3rd International Conference on Intelligent Green Building and Smart Grid (IGBSG), Yilan, Taiwan, 22-25 April 2018 (IEEE), 1–4. doi:10.1109/IGBSG.2018.8393572

He, M., He, W., Hu, J., Yuan, X., and Zhan, M. (2019). Nonlinear Analysis of a Simple Amplitude-phase Motion Equation for Power-Electronics-Based Power System. *Nonlinear Dyn.* 95 (3), 1965–1976. doi:10.1007/s11071-018-4671-6

Huang, H., Ju, P., Pan, X., Jin, Y., Yuan, X., and Gao, Y. (2019). Phase-amplitude Model for Doubly Fed Induction Generators. *J. Mod. Power Syst. Clean. Energ.* 7 (2), 369–379. doi:10.1007/s40565-018-0450-0

Li, S., Yan, Y., and Yuan, X. (2019). SISO Equivalent of MIMO VSC-Dominated Power Systems for Voltage Amplitude and Phase Dynamic Analyses in Current Control Timescale. *IEEE Trans. Energ. Convers.* 34 (3), 1454–1465. doi:10.1109/tec.2019.2908222

Liu, J., Miura, Y., Bevrani, H., and Ise, T. (2021). A Unified Modeling Method of Virtual Synchronous Generator for Multi-Operation-Mode Analyses[J]. *IEEE J. Emerging Selected Top. Power Elect.* 9 (2), 2394–2409. doi:10.1109/JESTPE.2020.2970025

Sun, J. (2011). Impedance-Based Stability Criterion for Grid-Connected Inverters. *IEEE Trans. Power Electron.* 26 (11), 3075–3078. doi:10.1109/tpel.2011.2136439

Wang, X., and Blaabjerg, F. (2019). Harmonic Stability in Power Electronic-Based Power Systems: Concept, Modeling, and Analysis. *IEEE Trans. Smart Grid* 10 (3), 2858–2870. doi:10.1109/tsg.2018.2812712

Wen, B., Boroyevich, D., Burgos, R., Mattavelli, P., and Shen, Z. (2016). Analysis of D-Q Small-Signal Impedance of Grid-Tied Inverters. *IEEE Trans. Power Electron.* 31 (1), 675–687. doi:10.1109/tpel.2015.2398192

Wu, T., Xie, X., and Jiang, Q. (2021). Three-port Admittance Modeling of Grid-Connected Converters Considering Frequency-Coupling and AC/DC Coupling Effects[J]. *Proc. CSEE* 42 (1), 248–259. doi:10.13334/j.0258-8013.pcsee.210330

Yan, X., Cui, S., Sun, X., and Sun, Y. (2021). Transient Modeling of Doubly-Fed Induction Generator Based Wind Turbine on Full Operation and Rapid Starting Condition[J]. *Power Syst. Technol.* 45 (04), 1250–1260. doi:10.1049/rpg2.12090

Yan, Y., Yuan, X., and Hu, J. (2016). "Interaction Analysis of Multi VSCs Integrated into Weak Grid in Current Control time-Scale[C]," in 2016 IEEE Power an. Energy Society General Meeting (PESGM), Boston, MA, USA, 17-21 July 2016 (IEEE), 1–6. doi:10.1109/PESGM.2016.7741677

Yang, Z., Mei, C., Cheng, S., and Zhan, M. (2020). Comparison of Impedance Model and Amplitude-phase Model for Power- Electronics-Based Power System. *IEEE J. Emerg. Sel. Top. Power Electron.* 8 (3), 2546–2558. doi:10.1109/jestpe.2019.2927109

Yuan, H., and Yuan, X. (2018). Modeling and Characteristic Analysis of Grid-Connected VSCs Based on Amplitude-phase Motion Equation Method for Power System Transient Process Study in DC-Link Voltage Control Timescale [J]. *Proc. CSEE* 38 (23), 6882–6892+7122. doi:10.13334/j.0258-8013.pcsee.180103

Yuan, X., Cheng, S., and Hu, J. (2016). Multi-time Scale Voltage and Power Angle Dynamics inPower Electronics Dominated Large Power Systems[J]. *Proc. CSEE* 36 (19), 5145–5154+5395. doi:10.13334/j.0258-8013.pcsee.161247

Yuan, X., Hu, J., and Cheng, S. (2017). Multi-time Scale Dynamics in Power Electronics-Dominated Power Systems. *Front. Mech. Eng.* 12 (3), 303–311. doi:10.1007/s11465-017-0428-z

Zhang, D., Ying, J., and Yuan, X. (2017). Modelling and Optimization of Wind Turbine Electromechanical Transient Characteristics Using Magnitude Phase Motion Equation[J]. *Proc. CSEE* 37 (14), 4044–4051+4283. doi:10.13334/j.0258-8013.pcsee.170597

Zhang, M., Yuan, X., and Hu, J. (2018). Inertia and Primary Frequency Provisions of PLL-Synchronized VSC HVDC when Attached to Islanded AC System. *IEEE Trans. Power Syst.* 33 (4), 4179–4188. doi:10.1109/tpwrs.2017.2780104

Zhao, M., Yuan, X., and Hu, J. (2018). Modeling of DFIG Wind Turbine Based on Internal Voltage Motion Equation in Power Systems Phase-Amplitude Dynamics Analysis. *IEEE Trans. Power Syst.* 33 (2), 1484–1495. doi:10.1109/tpwrs.2017.2728598

Zong, H., Zhang, C., Lyu, J., Cai, X., Molinas, M., and Rao, F. (2020). Generalized MIMO Sequence Impedance Modeling and Stability Analysis of MMC-HVDC with Wind Farm Considering Frequency Couplings. *IEEE Access* 8, 55602–55618. doi:10.1109/access.2020.2981177

Conflict of Interest: The authors declare that the research was conducted in the absence of any commercial or financial relationships that could be construed as a potential conflict of interest.

frontiers | Frontiers in Energy Research

ORIGINAL RESEARCH
published: 12 April 2022
doi: 10.3389/fenrg.2022.845637

Optimal Capacity Planning of Power to Hydrogen in Integrated Electricity–Hydrogen–Gas Energy Systems Considering Flexibility and Hydrogen Injection

Jinpeng Wang[1,2], *Pingliang Zeng*[1]*, *Yalou Li*[3] *and Jia Liu*[1]

[1]*Department of Automation, Hangzhou Dianzi University, Hangzhou, China,* [2]*School of Electrical and Control Engineering, Henan University of Urban Construction, Pingdingshan, China,* [3]*Electric Power Research Institute, Beijing, China*

OPEN ACCESS

Edited by:
Weihao Hu,
University of Electronic Science and Technology of China, China

Reviewed by:
Yanfei Li,
Hunan University of Technology and Business, China
Nikolaos Koltsaklis,
Czech Technical University in Prague, Czechia
Shutang You,
The University of Tennessee, Knoxville, United States

Correspondence:
Pingliang Zeng
plzeng@hotmail.com

Specialty section:
This article was submitted to Process and Energy Systems Engineering, a section of the journal Frontiers in Energy Research

Received: *30 December 2021*
Accepted: *10 March 2022*
Published: *12 April 2022*

Citation:
Wang J, Zeng P, Li Y and Liu J (2022) Optimal Capacity Planning of Power to Hydrogen in Integrated Electricity–Hydrogen–Gas Energy Systems Considering Flexibility and Hydrogen Injection.
Front. Energy Res. 10:845637.
doi: 10.3389/fenrg.2022.845637

With increasing penetration of renewable energy, it is important to source adequate system flexibility to maintain security of supply and minimize renewable generation curtailment. Power to hydrogen (P2H) plays an important role in the low-carbon renewable dominated energy systems. By blending green hydrogen produced from renewable power into the natural gas pipelines, it is possible to help integrate large-scale intermittent generation and smooth the variability of renewable power output through the interconnection of the natural gas network, hydrogen energy network, and electric network. A two-stage stochastic mixed-integer nonlinear planning framework for P2H sizing and siting is proposed in this paper, considering system flexibility requirements. The problem is then reduced to a mixed-integer second-order cone (MISOC) model through convex transformation techniques in order to reduce the computation burden. Then, a distributed algorithm based on Bender's decomposition is applied to obtain the optimal solution. A modified hybrid IEEE 33-node and Gas 20-node system is then used for simulation tests. The results showed that investment of P2H can significantly reduce the total capital and operational costs with lower renewable generation curtailment and electricity demand shedding. Numerical tests demonstrated to demonstrate the validity of the proposed MISOC model.

Keywords: power to hydrogen (P2H), hydrogen injections, system flexibility, low carbon, benders decomposition

1 INTRODUCTION

Over the recent years, various renewable energies, such as solar power and wind power, have seen rapid development. However, the connection of large-scale renewable energy to the electric network has dramatically changed the characteristics and increased the uncertainty of power flow, posing significant challenges to system operations in terms of power balancing and load following. Flexible resources, such as demand-side response, large-scale energy storage, power to hydrogen, etc., are the key to integrating large-scale renewable generation.

For environmental reasons, coal-fired generations are gradually being phased out, leading to a scarcity of flexible resources. As a result, energy storages, such as pumped storage, compressed air energy storage, chemical battery storage, etc., have developed by leaps and bounds in recent years. However, the development of large-scale pumped storage and compressed air storage is constrained by geographic and geological conditions. Chemical battery storage is not limited by geography, but their discharge time is

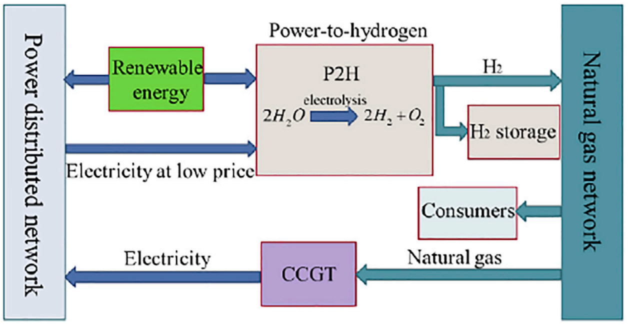

FIGURE 1 | Basic structure diagram of a hybrid renewable energy system.

1 min–8 h (Mongird et al., 2019) and is suitable for medium- or short-term (Zablocki, 2019) use. As hydrogen has the appealing characteristics of being stored for the longer term and on a large scale, hydrogen energy storage has the prospects of being used as a long-term or seasonal energy storage. With the high penetration of renewable energy, the green hydrogen produced by P2H using surplus renewable energy can be stored on a large scale or used as an industrial raw material.

As a result, over the past few years, the development of green hydrogen has attracted the increasing attention of researchers and governments due to its characteristics of a high energy density and the ability to store it in large quantities. The total abandoned renewable energy has decreased from 312.523 to 66.797 MWH with the presence of power to hydrogen (Heris et al., 2020). To reduce CO_2 emissions, the cost-optimal design and operation of power to gas in Germany are studied in depth (Welder et al., 2018). In addition, the value of hydrogen storage in pipes and salt caverns has been analyzed (Welder, 2018).

In addition, Ref. Dolci et al. (2019) and Hu et al. (2020) present the power-to-hydrogen pathways, and the technical advances and barriers to green hydro development are also given. The green hydrogen-based power-to-gas facility is investigated in Germany and Texas in Glenk and Reichelstein (2019), which shows that green hydrogen production is already cost-competitive in niche applications. With ultra-high penetration of renewable energy, an optimal planning model (Pan, 2020) for electricity–hydrogen integrated energy systems considering power to hydrogen and seasonal storage is constructed in Pan et al., (2020). Li et al. (2019) have developed operation optimization modeling of power to hydrogen in active distribution networks coordinated with the district heating network (Li et al., 2019). Gils et al. (2019) have investigated the transition pathway toward a climate-neural energy system in Germany and concluded that hydrogen plays a critical role in the seasonal balance of power supply and demand but cannot completely replace other coupling options (Gils et al., 2021).

Hydrogen is an important industrial raw material, and it is only economically beneficial to convert hydrogen into methane when subsidies are provided (Robinius et al., 2017). Liu et al. (2020) indicate that both power to hydrogen (P2H) and power to methane (P2M) help to reduce operational costs and decrease CO_2 emissions. From the perspective of energy system operation, the impact of P2H on the system flexibility is analyzed (Cloete and Hirth, 1922) in Cloete et al. (2020) and Ge et al. (2020) . With the increasing penetration level of renewable energy, the traditional grid is evolving into a new energy system with widespread participation of variable generation and flexible demand (Gea-Bermúdez et al., 2021). The large-scale, long-duration energy storage devices will be one of the key enablers in the low-carbon renewable-dominated energy systems. To improve the management efficiency and deal with the stochastic nature of renewable energy, this paper aims to investigate the site selection and optimal capacity determination approach of large-scale energy storage technologies, also known as P2H, and their role in enhancing system flexibility.

The contributions and innovations of this article are as follows: first, a two-stage stochastic mixed-integer planning framework for P2H sizing and siting is proposed, considering the uncertainty of the

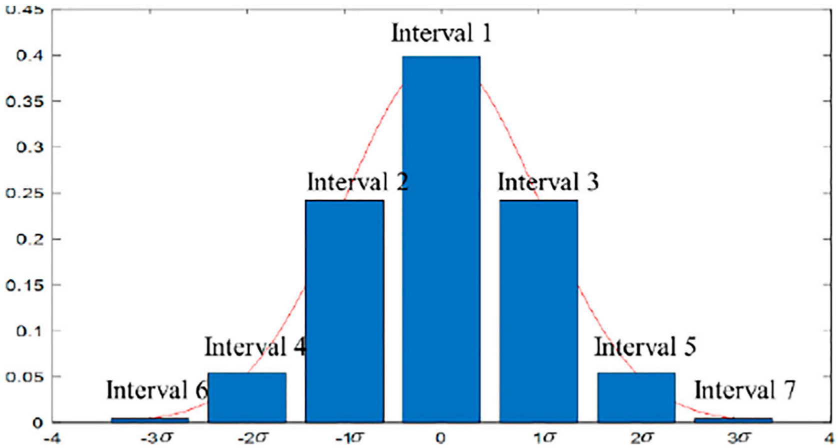

FIGURE 2 | Wind out power/load forecast error.

renewable energy output and the investment cost of the P2H equipment. The model's objective was to minimize the investment cost, operation cost, renewable output curtailment cost, and electricity demand shedding cost. Second, by blending permissible green hydrogen produced from surplus renewable energy into the natural gas pipelines, the effects of the injected hydrogen concentration on the gas pipeline transmission coefficient, that is, gas specific gravity, net calorific value, gas compressibility factor, etc., were investigated. Third, based on the system flexibility supply–demand balance mechanism, we quantified the enhanced effect of P2H on hourly system flexibility.

The rest of this article is organized as follows: the low-carbon-emission hybrid renewable energy system structure is proposed in **Section 2**, and the modeling of renewable energy and load demand uncertainties are also described. In **Section 3**, a two-stage stochastic planning model of P2H has been constructed, considering system flexibility and hydrogen injections. The nonlinear nonconvex terms are simplified to obtain a mixed-integer second-order cone (MISOC) programming model in **Section 4**. In **Section 5**, a distributed algorithm for the model is designed based on Bender's decomposition and cut plane. Simulations are carried out to verify the effectiveness of the proposed MISOC model and solution algorithm in **Section 6**. The conclusion is illustrated in **Section 7**.

2 INTEGRATED ELECTRICITY–HYDROGEN-GAS SYSTEM

2.1 System Description

The integrated electricity–hydrogen-gas energy system is illustrated in **Figure 1**. It consists of the power system, natural gas distribution system, and carbon-free hydrogen system. The interaction between the power system and the natural gas system is realized mainly through a combined cycle gas turbine (CCGT). The CCGT generation unit with a fast-responding, high efficiency uses natural gas from the distribution gas system to generate electricity. The connection of large-scale renewable energy to the distribution network makes it possible to produce hydrogen by electrolyzing water with renewable energy. It is worth noting that hydrogen is more accessible to store for long periods than electricity. Therefore, hydrogen storage technology can be used as a medium- or long-term energy storage option for excess renewable energy. In this article, green hydrogen produced by surplus renewable energy sources plays a vital role in the integrated electricity distribution system, natural gas system, and hydrogen energy system. Power-to-hydrogen devices make full use of surplus renewable energy, and it is then blended and injected into the existing gas distribution pipeline with a maximal volumetric limit proportion of 15% hydrogen.

In future high-renewable energy penetration scenarios, the uncertainty and intermittence of renewable energy output will significantly impact supply power reliability. To deal with these problems, the system's flexibility needs to be enhanced urgently. Based on the characteristics of flexible resources in the distribution network, we have developed a system flexibility supply and demand balance model. In addition, considering the direct injection of hydrogen produced by P2H into the natural gas pipelines, the hydrogen concentration on the gas specific gravity, the calorific value, and the compressibility factor have been investigated. Finally, a two-stage stochastic planning model is constructed with the objective of minimizing the investment and operation costs during the planning horizon. In the proposed hybrid energy system, we consider several renewable energy generation units, such as wind turbines and photovoltaics, equipped in the system. To promote renewable energy consumption and enhance the system's flexibility, the investment cost of P2H and the renewable energy curtailment cost are included as one of the optimization objectives. Scenario generation and reduction methods have been utilized to address renewable energy sources and load uncertainty.

2.2 Uncertainty Modeling and Scenario Generation

A scenario-based approach is adopted to deal with the uncertainty and stochastic characteristics of renewable output and electrical load demand (Dagoumas and Koltsaklis, 2019). For the sake of simplicity, renewable generation output and load can be modeled as follows:

$$
\begin{aligned}
P_{load,t} &= P^{\text{fore}}_{load,t} + \Delta P_{load,t} \quad t = 1, \ldots, 24 \\
P_{wind,t} &= P^{\text{fore}}_{wind,t} + \Delta P_{wind,t} \quad t = 1, \ldots, 24
\end{aligned}
\tag{1}
$$

The forecast errors, $\Delta P_{wind,t}, and\, \Delta P_{load,t}$, are assumed to be Gaussian distribution. The probability density functions of normally distributed random variables are discretized in **Figure 2**

$$
\begin{aligned}
\Delta P^{load}_{i,t} &= \alpha^{load}_{i,t}\ \text{i} \in \text{interval}\,1, \cdots \text{interval}\,7 \\
\Delta P^{wind}_{j,t} &= \beta^{wind}_{j,t}\text{j} \in \text{interval}\,1, \cdots \text{interval}\,7
\end{aligned}
\tag{2}
$$

where $\Delta P^{load}_{i}, and\, \Delta P^{wind}_{j}$ are the probabilities of intervals 1–7 at time t related to prediction errors, and their specific values are $\alpha^{load}_{i,t}, and\, \beta^{wind}_{j,t}$.

Then, the corresponding cumulative distribution functions (CDFs) are calculated separately using the probability density functions for the discrete intervals described above. Based on Monte Carlo simulations, two random variables, $\eta \in [0, 1]$ and $\lambda \in [0, 1]$, are generated. The randomly generated variables η and λ are compared with the cumulative probability distribution functions values above, respectively, to determine in which interval η and λ lie in. If $CDF(interval\ 1) \le \eta < CDF(interval\ 2)$, then, the binary variable $B^{Load}_{2,t,s}$ equals to 1, and the other binary variables $B^{Load}_{(1,t,s)}, \ldots, B^{Load}_{(7,t,s)}$ related to load prediction errors equal to 0; the same applies to λ

$$
\begin{aligned}
&\text{scenario (s)} = \left[B^{Load}_{(1,t,s)}, \ldots, B^{Load}_{(7,t,s)}, B^{Wind}_{(1,t,s)}, \ldots, B^{Wind}_{(7,t,s)}\right]_{t=1,\ldots,24} \\
&\sum_{interval=1}^{7} B^{Load}_{(interval,t,s)} = 1\ \forall \text{t}, \forall \text{s} \\
&\sum_{interval=1}^{7} B^{Wind}_{(interval,t,s)} = 1\ \forall \text{t}, \forall \text{s}
\end{aligned}
\tag{3}
$$

The probabilities of the generated scenarios are listed as follows, and the sum of the probabilities of all scenarios equals to 1

$$\pi_s = \frac{\prod_{24}^{t=1}\left(\sum_{7}^{i=1}\left(B_{i,t,s}^{Load} \times \alpha_{i,t}^{load}\right) \times \sum_{7}^{j=1} B_{j,t,s}^{Wind} \times \beta_{j,t}^{wind}\right)}{\sum_{N_s}^{s=1}\left(\prod_{7}^{t=1}\left(B_{i,t,s}^{Load} \times \alpha_{i,t}^{load}\right) \times \sum_{7}^{j=1}\left(B_{j,t,s}^{Wind} \times \beta_{j,t}^{wind}\right)\right)} \tag{4}$$

$$\sum_{s=1}^{N_s} \pi_s = 1$$

Due to a large number of scenarios, it will lead to the burden of computation. It is generally essential to balance the solving tractability and the modeling accuracy. Therefore, the scenario reduction techniques using the fast forward algorithm (Hajiabbas and Mohammadi-Ivatloo, 2020) are listed as follows:

$$\begin{gathered} P_s = \sum_{t=1}^{24} P_{t,s}^{load} + \sum_{t=1}^{24} P_{t,s}^{wind}\ \forall \mathrm{s} \\ v(s, s') = |P_s - P_{s'}| \quad \forall \mathrm{s} \end{gathered} \tag{5}$$

where $P_{t,s}^{load}$ and $P_{t,s}^{wind}$ are the load demand and renewable energy output at time t under the typical scenario s, respectively. $v(s, s')$ is a matrix of N_s multiplied by N_s , which is the distance between P_s

$$\begin{gathered} s_1 = \arg\left\{ \begin{matrix} \min \\ s' \in \Omega \end{matrix} \sum_{s\in\Omega} \pi_s v\left(s, s''\right) \right\} \\ \Omega_S = \Omega_S \cup \{s_1\} \\ \Omega_J = \Omega \backslash \{s_1\} \end{gathered} \tag{6}$$

.

After obtaining the first selected scenarios through the above steps, the distance between the chosen and nonselected scenarios is calculated, and the set of scenes chosen is updated

$$\begin{gathered} s_i = \arg\left\{ \begin{matrix} \min \\ S' \in \Omega \end{matrix} \begin{matrix} \Sigma \\ s \in \Omega_J\backslash\{s''\} \end{matrix} \pi_s \begin{matrix} \min \\ ss'' \in \Omega_S \cup \{s\} \end{matrix} v(s, s'') \right\} \\ \Omega_S = \Omega_S \cup \{s_i\} \\ \Omega_J = \Omega_J \backslash \{s_i\} \end{gathered} \tag{7}$$

.

Finally, the probabilities of the reduced scenarios are calculated. The probability of a nonselected scenario is added to the probability of a selected scenario that is close to it. The specific calculation is as follows:

$$\pi_s^* = \pi_s + \begin{matrix} \Sigma \\ s' \in J(s) \end{matrix} \pi_{s'} S \in \Omega_s\ S' \in \Omega_J \tag{8}$$

3 OPTIMAL P2H PLANNING CONSIDERING FLEXIBILITY REQUIREMENTS IN AN INTEGRATED MULTI-VECTOR ENERGY SYSTEM

In this section, a two-stage stochastic dynamic mixed-integer nonlinear programming model is constructed for optimal P2H planning to minimize the investment and annual operation costs (Bramstoft et al., 2020) of integrated multi-vector energy systems.

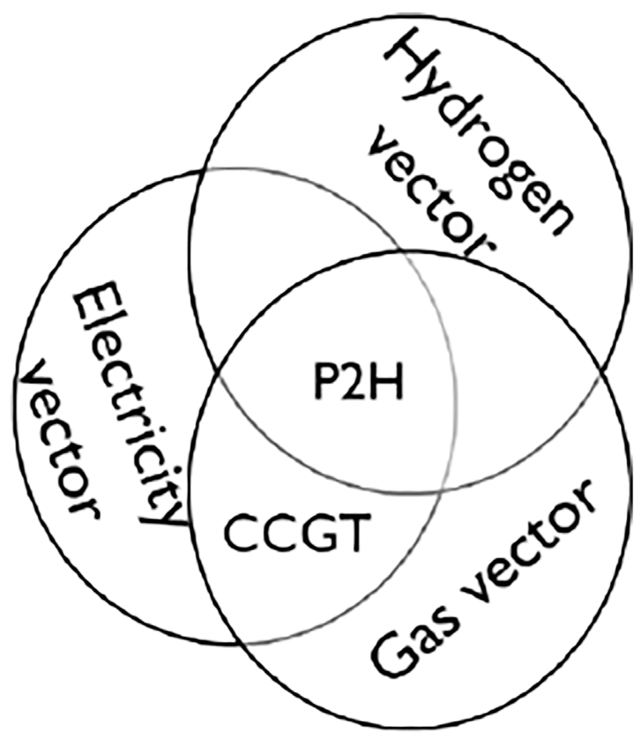

FIGURE 3 | Schematic of the coupling relation between electricity–gas–hydrogen energy networks.

3.1 The Objective Function

The optimal P2H planning problem considering the system flexibility requirement can be formulated as the following stochastic model:

$$\min \quad f = C_{inv} + C_{ope} \tag{9}$$

$$C_{inv} = \sum_{i\in\Omega_{p2h}} \frac{r(1+r)^{\tau_{i,\xi}}}{(1+r)^{\tau_{i,\xi}} - 1} I_i P_i^{\max} c_i \tag{10}$$

$$\begin{aligned} C_{ope} = D \sum_{s=1}^{N_s} \pi(S) \sum_{t=1}^{T} \Bigg[& \sum_{i\in\Omega_{ele}} e_i^{ele} P_{i,t,s}^{ele} + \\ & \sum_{n\in\Omega_{saurce}} g_n^{saurce} P_{n,t,s}^{saurce} + \sum_{j\in\Omega_{renew}} c_j^{renew} \Delta P_{j,t,s}^{renew} \\ & + \sum_{k\in\Omega_{load}} c_k^{load} \Delta P_{k,t,s}^{load} + \sum_{m\in\Omega_{gas}} c_m^{gas} \Delta P_{m,t,s}^{gas} \Bigg] \end{aligned} \tag{11}$$

subject to

$$0 \le P_i^{\max} \le \bar{P}_i^{\max}\ \forall \mathrm{i} \tag{12}$$

$$I_i \in \{0, 1\}\ \forall \mathrm{i} \in \Omega_{p2h} \tag{13}$$

$$0 \le \sum_{i\in\Omega_{p2h}} I_i \le N^{\max} \tag{14}$$

$$\sum_{i\in\Omega_{p2h}} I_i P_i^{\max} \le P^{\max} \tag{15}$$

$$P_{i,t,s}^{ele}, P_{n,t,s}^{saurce}, \Delta P_{j,t,s}^{renew}, \Delta P_{k,t,s}^{load}, \Delta P_{m,t,s}^{gas} \in \Omega_o\ \forall \mathrm{t}, \forall \mathrm{s} \tag{16}$$

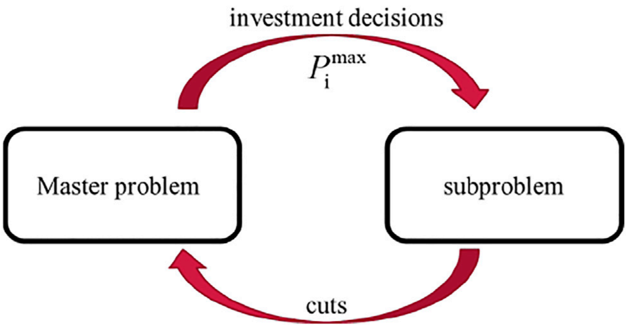

FIGURE 4 | Structure of the distributed algorithm.

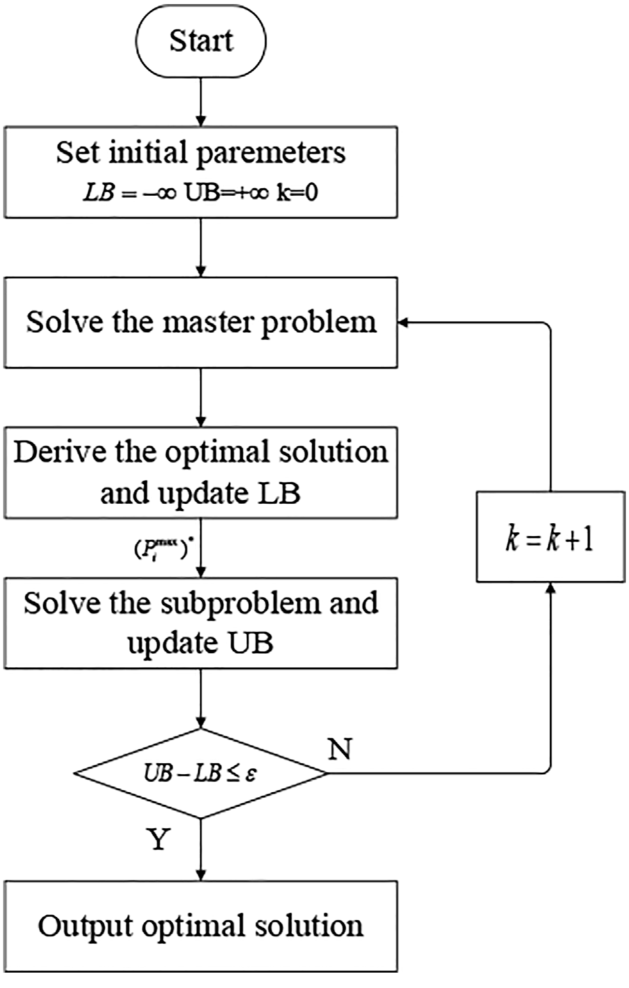

FIGURE 5 | Flowchart of the distributed algorithm.

The objective function (9) comprises two terms: P2H investment cost C_{inv} and operation cost C_{ope}. C_{ope} includes the costs of purchasing electricity and gas, the renewable energy curtailment cost, and the electricity and gas load shedding cost. It is worth noting that the generation cost of CCGT is not included in the operation cost as it is already calculated in the output costs of the gas sources. **Equation 12** sets the maximum capacity investment of each P2H. **Equations 14**, **15** limit the number of installed P2H devices and the total investment cost. The binary variable I_i is a decision variable on whether a prospective P2H device is constructed at node i or not. $D, e_i^{ele}, c_j^{renew}, c_k^{load}$ in **Eq. 12** are the number of days in the year, the time-of-use electricity price, the cost of abandoned renewable energy, and the load (Liu et al., 2020), respectively.

3.2 Operation Constraints

3.2.1 Power Distribution Network

The power flow equations of the radial distribution network can be presented by the DistFlow model, which can be seen as follows (Li et al., 2020):

$$P_{ij}+P_j^g-r_{ij}i_{ij}=\sum_{k\epsilon\pi(j)}P_{jk}+P_j^d\ \forall t,\forall s \tag{17}$$

$$Q_{ij}+Q_j^g-x_{ij}i_{ij}=\sum_{k\epsilon\pi(j)}Q_{jk}+Q_j^d\ \forall t,\forall s \tag{18}$$

$$U_j=U_i-2\left(r_{ij}P_{ij}+x_{ij}Q_{ij}\right)+\left(z_{ij}\right)^2 i_{ij}\ \forall t,\forall s \tag{19}$$

$$i_{ij}U_i=P_{ij}^2+Q_{ij}^2\ \forall t,\forall s \tag{20}$$

Eq. 17 above can be modified with high penetration renewable energy connection as follows:

$$\begin{aligned}P_{ij}+P_j^g-r_{ij}i_{ij}+P_j^{renew}-\Delta P_j^{renew}+P_j^{CCGT}\\=\sum_{k\epsilon\pi(j)}P_{jk}+P_j^d-\Delta P_j^{load}+P_j^{p2h}\end{aligned} \tag{21}$$

where P_{ij}, Q_{ij} are the active and reactive powers through line $l(ij)$, respectively. Definitions of the several optimization variables $U_i, r_{ij}, i_{ij}, x_{ij}, z_{ij}, P_j^d, Q_j^g, Q_j^d$ are in Ref. Heris et al., 2020.

We can depict the boundary constraints in the power distribution network as follows:

$$0\leq P_{j,t,s}^{CCGT}\leq P_j^{CCGT,MAX}\ \forall j,\forall t,\forall s \tag{22}$$

$$0\leq P_{j,t,s}^{renew}\leq P_{j,t,s}^{renew,\max}\ \forall j,\forall t,\forall s \tag{23}$$

$$0\leq P_{j,t,s}^{ele}\leq {}_{j,t,s}^{ele,\max}\ \forall \mathrm{j},\forall \mathrm{t},\forall \mathrm{s} \tag{24}$$

$$0\leq \Delta P_{j,t,s}^{load}\leq P_j^d\ \forall \mathrm{j},\forall \mathrm{t},\forall \mathrm{s} \tag{25}$$

$$0\leq P_{j,t,s}^{p2h}\leq P_j^{\max}\ \forall j,\forall t,\forall s \tag{26}$$

$$P_{ij}^{\min}\leq P_{ij,t,s}\leq \bar{P}_{ij}^{\max}\ \forall t,\forall s \tag{27}$$

$$Q_{ij}^{\min}\leq Q_{ij,t,s}\leq \bar{Q}_{ij}^{\max}\ \forall t,\forall s \tag{28}$$

$$U_j^{\min}\leq U_{j,t,s}\leq U_j^{\max}\quad \mathrm{U}_{ref}=V_{ref}^2 \tag{29}$$

Equation 21 constrains the power balance at node j, considering the curtailment of renewable energy and shedding load. **Equations 22**, **23** enforce limits on the output of the CCGT generation unit and each renewable energy source. **Equation 24** depicts the boundary of the amount of electricity purchased. **Equations 25–29** give the lower and upper bounds on the variables $\Delta P_{j,t,s}^{load}, P_{j,t,s}^{p2h}, P_{ij,t,s}, Q_{ij,t,s}, U_{j,t,s}$.

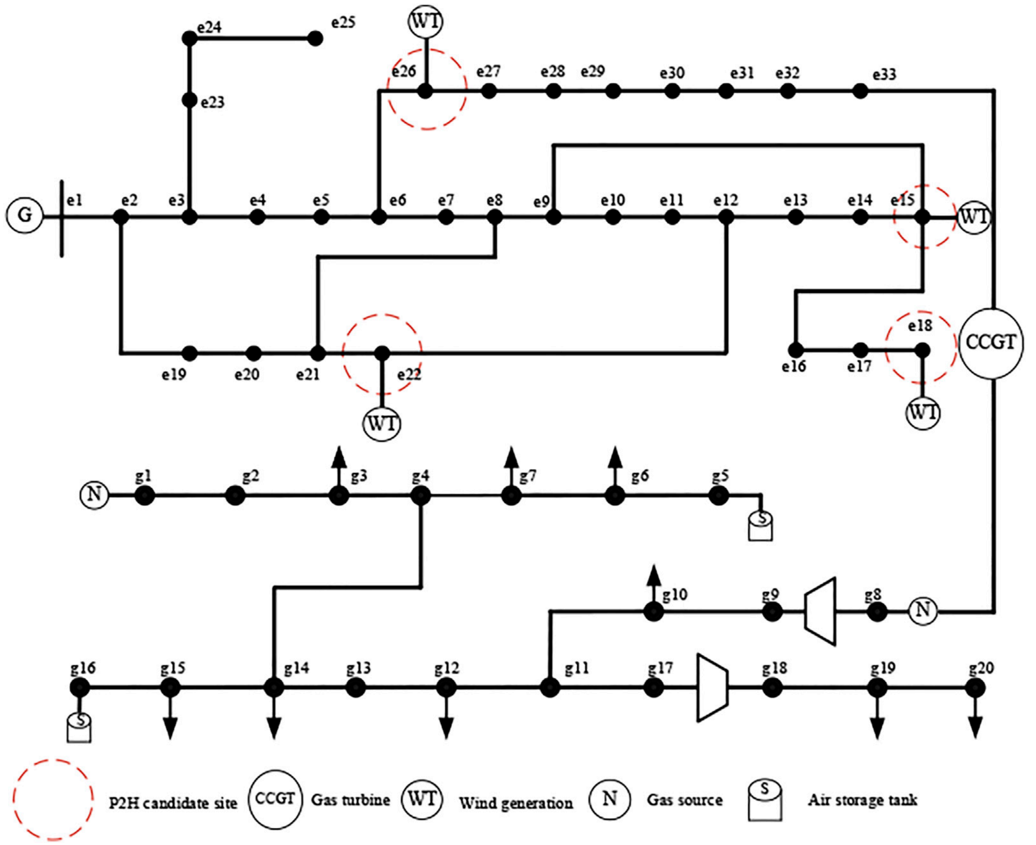

FIGURE 6 | Configuration of the hybrid renewable energy system.

3.2.2 Natural Gas Distribution Network

The steady-state flow equation **Eq. 20** related to the pressure of gas and the flow rate in the distributed gas network is depicted as follows:

$$Q_{ij} = 1.1494 \times 10^{-3} \left(\frac{T_b}{P_b}\right) \left[\frac{\left(\left|P_i^2 - P_j^2\right|\right)}{GT_f LZf}\right]^{0.5} D^{2.5} \tag{30}$$

where G, T_f, L, Z, f indicate the gas specific gravity, the average flowing temperature of the gas, the pipe length (km), the gas compressibility factor, and the friction factor, respectively. Terms T_b, P_b are the base temperature and pressure, respectively.

It is important to note that the gas thermal–physical properties change with its composition (Deymi-Dashtebayaz et al., 2019). When green hydrogen produced from renewable energy sources is injected into a natural gas pipeline, the gas thermo-physical properties vary with the hydrogen concentration, which can be described below:

$$Z_i = a \cdot v_i + b \text{ i} \in \Omega_{saurce} \tag{31}$$

$$\text{LHV}_i^{gas} = c \cdot v_i + d \text{ i} \in \Omega_{saurce} \tag{32}$$

$$G_i = e \cdot v_i + f \text{ i} \in \Omega_{saurce} \tag{33}$$

.

$$0 \le v_i \le 15\% \text{ i} \in \Omega_{saurce} \tag{34}$$

where LHV_i^{gas} is the net calorific value of gas mixtures at node i and v_i is the hydrogen concentration by volume injected into the pipeline. In addition, a, b, c, d, e, f are constants. From **Eqs 31–33** above, we can also see that Z_i, LHV_i^{gas}, G_i are each approximately linearly related to the hydrogen concentration v_i at gas node i (Dolci, 2019). **Equation 34** enforces the upper and lower bounds on the concentration of hydrogen in a natural gas pipeline. No additional investment in gas distribution pipelines and end-use appliances is needed within this concentration range.

In addition to the above constraints, certain boundary constraints need to be considered

$$P_{i,t,s}^{\min} \le P_{i,t,s} \le P_{i,t,s}^{\max} \ \forall \text{i}, \forall \text{t}, \forall \text{s} \tag{35}$$

$$Q_{l,t,s}^{\min} \le Q_{l,t,s} \le Q_{l,t,s}^{\max} \ \forall l(ij), \forall \text{t}, \forall \text{s} \tag{36}$$

$$0 \le P_{n,t,s}^{saurce} \le P^{saurce,\max} \text{ n} \in \Omega_{saurce}, \forall t, \forall s \tag{37}$$

$$0 \le \Delta P_{m,t,s}^{gas} \le P_{m,t,s}^{gas,load} \text{ m} \in \Omega_{gas}, \forall t, \forall s \tag{38}$$

.

$$P_{j,t,s} = \beta_{ij} \cdot P_{i,t,s} \ \forall \text{t}, \forall \text{s} \tag{39}$$

Equations 35, 36 enforce limits on the pressure of the gas node and the flow rate in each pipeline. **Equations 37, 38** indicate the upper and lower bounds for natural gas source output and shedding gas load.

Pressure drops occur during the transmission of natural gas. Therefore, a compressor is placed in the natural gas pipeline to

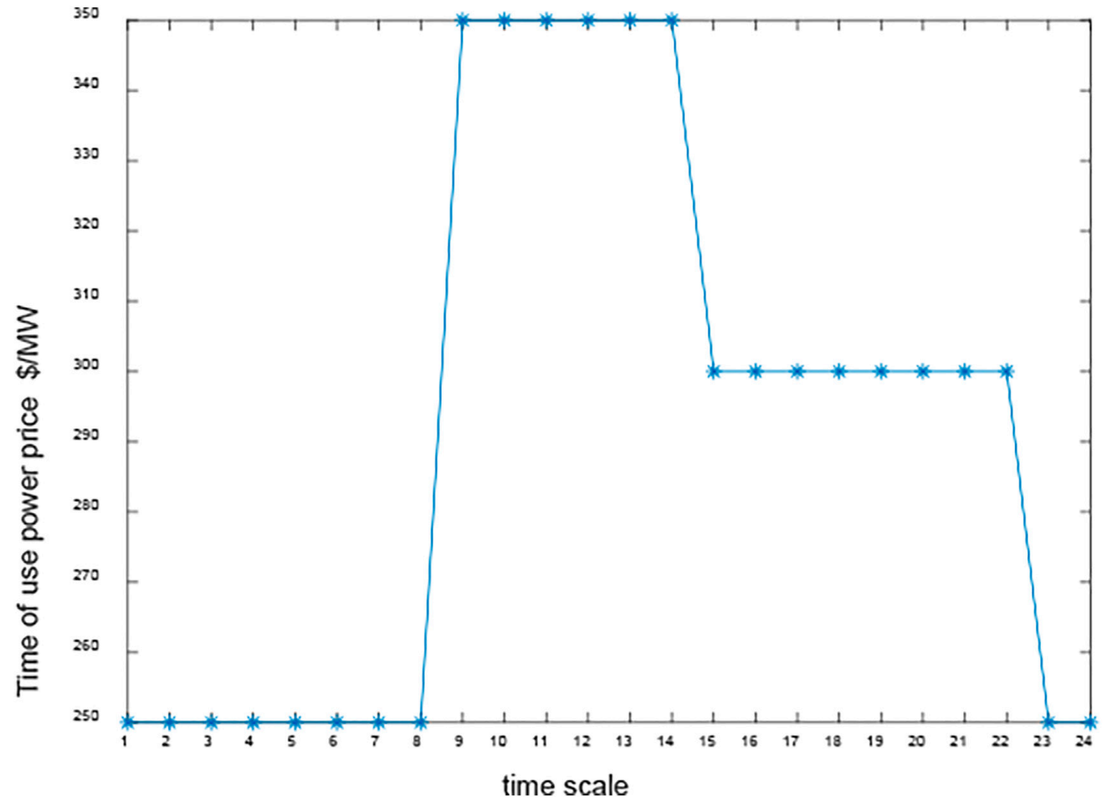

FIGURE 7 | Time-of-use electricity price.

maintain the nodal pressure at the required level. **Equation 39** indicates the gas pressure relationship at nodes i and j. β_{ij} is the ratio of the compressor inlet pressure to the outlet pressure.

Considering the effect of hydrogen injection, the energy balance equation for each natural gas distribution network node is formulated as follows:

$$P^{saurce}_{j,t,s} + (1/\alpha)P^{h2\_saurce}_{j,t,s} + \sum_{i\in\Omega s} Q_{ij,t,s} = \sum_{k\in\Omega r} Q_{jk,t,s} + \sum_{GT\in\Omega_{cg}} P^{gas}_{GT,t,s} + P^{gas,load}_{j,t,s} - \Delta P^{gas}_{j,t,s}, \forall t, \forall s \tag{40}$$

$$\alpha = \frac{LHV^{CH_4}}{LHV^{H_2}} \tag{41}$$

.
$$P^{h2\_saurce}_{i,t,s} = C_{ij} \cdot P^{h2}_{j,t,s} \tag{42}$$

where LHV^{CH_4}, LHV^{H_2} are the net calorific values of natural gas and hydrogen, respectively, while α is their ratio. **Equation 40** enforces the nodal gas balance for the gas distribution network. In this equation, the shedding gas load and hydrogen injection are considered. Due to the decrease in the Wobbe index of the gas mixture, it is worth considering the differential properties of the calorific value of natural gas and hydrogen. **Equation 42** indicates that the green hydrogen produced by P2H is coupled to the gas source and then blended with natural gas at a specific concentration.

3.2.3 Flexibility Supply and Demand Balance

When renewable energy's share is relatively low, the volatility and uncertainty have less impact on the energy system. At this stage of the planning process, the flexibility supply and demand balance in the system is usually not considered for the time being. However, with a high proportion of renewable energy, insufficient flexibility supply can lead to a large number of renewable energy curtailments, which prevents the system from operating correctly (Koltsaklis and Dagoumas, 2018). Therefore, the system's flexibility is quantified in the process of optimizing the size of P2H.

Flexibility in the integrated energy system is characterized by multiple time scales, locations, and directions (Agbonaye et al., 2021). From the prospect of time scale, system flexibility can be categorized into very short-term ramp (≤ 15 min), short-term ramp (15 min – $4h$), and peak shaving ($24h$) (Lu et al., 2018). This article focuses on the supply–demand of system flexibility at an hourly scale.

Flexibility resources such as P2H, CCGT, etc., are introduced to supply flexibility. Of these, P2H, CCGT, and system power purchase can provide both upward and downward flexibility, while wind abandonment can only provide downward flexibility, and shedding load can only supply upward flexibility. The detailed formulae are shown below:

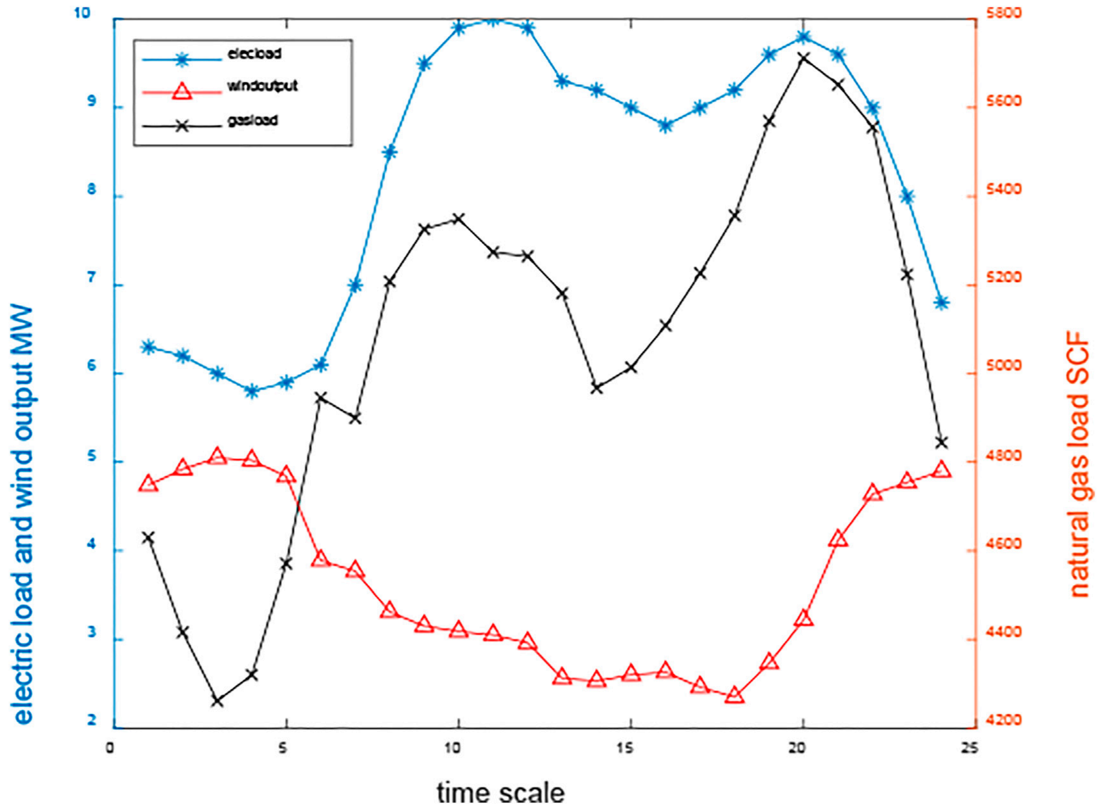

FIGURE 8 | Predicted values of electrical load, wind output, and the gas load.

$$F^{s-up}_{p2h,t,s} = \sum_{p2h\in\Omega_{p2h}} \min\left(R^{down}_{p2h}\tau, P^{p2h}_{p2h,t,s} - P^{\min}_{p2h,t,s}\right)\forall t, \forall s \tag{43}$$

$$F^{s-down}_{p2h,t,s} = \sum_{p2h\in\Omega_{p2h}} \min\left(R^{up}_{p2h}\tau, P^{\max}_{p2h} - P^{p2h}_{p2h,t,s}\right)\forall t, \forall s \tag{44}$$

$$F^{s-up}_{GT,t,s} = \sum_{GT\in\Omega gt} \min\left(R^{up}_{GT}\tau, P^{CCGT-MAX}_{GT} - P^{CCGT}_{GT,t,s}\right)\forall t, \forall s \tag{45}$$

$$F^{s-down}_{GT,t,s} = \sum_{GT\in\Omega gt} \min\left(R^{down}_{GT}\tau, P^{CCGT}_{GT,t,s} - P^{CCGT-MIN}_{GT}\right)\forall t, \forall s \tag{46}$$

$$F^{s-up}_{buy,t,s} = \sum_{buy\in\Omega_{ele}} \min\left(R^{up}_{buy}\tau, P^{ele,\max}_{buy,t,s} - P^{ele}_{buy,t,s}\right) \forall t, \forall s \tag{47}$$

$$F^{s-down}_{buy,t,s} = \sum_{buy\in\Omega_{ele}} \min\left(R^{down}_{buy}\tau, P^{ele}_{buy,t,s} - P^{ele,\min}_{buy,t,s}\right) \forall t, \forall s \tag{48}$$

$$F^{s-up}_{k,t,s} = \sum_{k\in\Omega_{load}} \Delta P^{load}_{k,t,s} \ \forall t, \forall s \tag{49}$$

$$F^{s-down}_{j,t,s} = \sum_{j\in\Omega_{renwe}} \Delta P^{renew}_{j,t,s} \ \forall t, \forall s \tag{50}$$

$$F^{s-up}_{sum,t,s} = F^{s-up}_{p2h,t,s} + F^{s-up}_{GT,t,s} + F^{s-up}_{buy,t,s} + F^{s-up}_{k,t,s} \ \forall t, \forall s \tag{51}$$

$$F^{s-down}_{sum,t,s} = F^{s-down}_{p2h,t,s} + F^{s-down}_{GT,t,s} + F^{s-down}_{buy,t,s} + F^{s-down}_{j,t,s} \ \forall t, \forall s \tag{52}$$

where $R^{up}_{p2h}, R^{up}_{GT}, R^{up}_{buy}$ represent the upward ramp rates of P2H, CCGT, and the power purchase, respectively, and $R^{down}_{p2h}, R^{down}_{GT}, R^{down}_{buy}$ are the downward ramp rates of P2H, CCGT, and the power purchase, respectively. $F^{s-up}_{sum,t,s}, F^{s-down}_{sum,t,s}$ denote the total upward and downward flexibility capacities provided by the various flexibility resources, respectively.

Equations 43, **45**, **47**, **49** define the upward flexibility capacity, and **Eqs 44**, **46**, **48**, **50** explain the downward flexibility capacity. It is also observed that **Eqs 51**, **52** give the total flexibility supply capacity.

The flexibility demand arises mainly from fluctuations in the net load. Therefore, the proposed hybrid system's upward and downward flexibility demand can be described by the following equations:

$$P^{net}_{t,s} = \sum_{k\in\Omega_{load}} P^{d}_{k,t,s} - \sum_{j\in\Omega_{renew}} P^{renew}_{j,t,s} \ \forall t, \forall s \tag{53}$$

$$F^{D-up}_{t,s} = F^{net}_{t+1,s} - F^{net}_{t,s} \left(F^{net}_{t+1,s} \ge F^{net}_{t,s}\right) \tag{54}$$

$$F^{D-down}_{t,s} = F^{net}_{t,s} - F^{net}_{t+1,s} \left(F^{net}_{t+1,s} \le F^{net}_{t,s}\right) \tag{55}$$

The system flexibility supply–demand equilibrium equation is as follows:

$$F^{up}_{t,s} = F^{s-up}_{sum,t,s} - F^{D-up}_{t,s} \ge 0 \ \forall t, \forall s \tag{56}$$

$$F^{down}_{t,s} = F^{s-down}_{sum,t,s} - F^{D-down}_{t,s} \ge 0 \ \forall t, \forall s \tag{57}$$

Equations 56, **57** emphasize that the system's ability to supply flexibility is greater than the demand for flexibility.

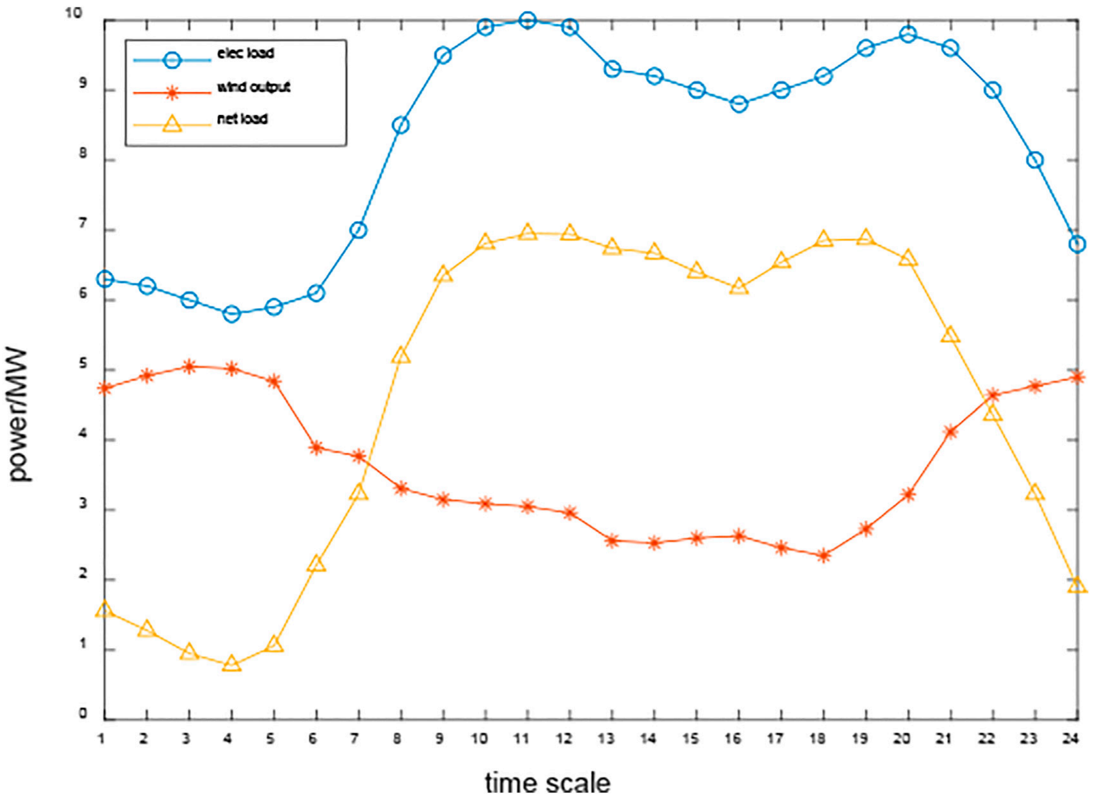

FIGURE 9 | Power demand load, wind power, and the net load of the system.

TABLE 1 | Other parameters used in the simulation.

Parameter	r	c_i \$/kW	g^{saurce} \$/SCF	c^{renew} \$/MW	c^{load} \$/MW	c^{gas}
Value	0.08	1300	0.0746	200	900	0.4

TABLE 2 | Comparison of planning and operation costs.

Cost term	Total cost M\$	Annualized investment cost/M\$	Electricity purchase cost/M\$	Gas purchase cost/M\$	Renewable output curtailment cost/M\$	Electricity demand shedding cost/M\$	Gas demand shedding cost/M\$
Case 1	22.648	0	11.81	9.9691	0.6524	0.21681	0
Case 2	21.854	0.28313	11.992	9.551	0.027705	0	0

TABLE 3 | Case 2 results.

Equipment	Node	Capacity/kW	Investment cost/M\$
P2h1	15	469.7	0.61061
P2h2	18	802.7	1.0435
P2h3	22	0	0
P2h4	26	188.9	0.24557
Total		1461.3	1.8997

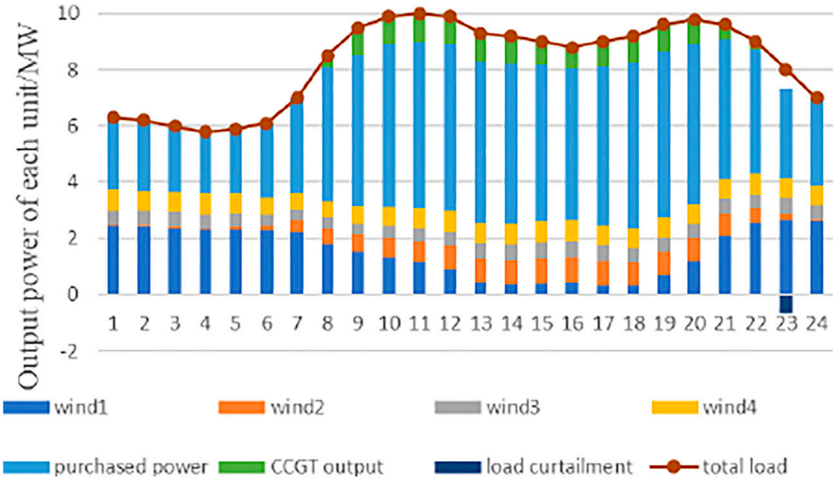

FIGURE 10 | Optimal generator outputs of case 1.

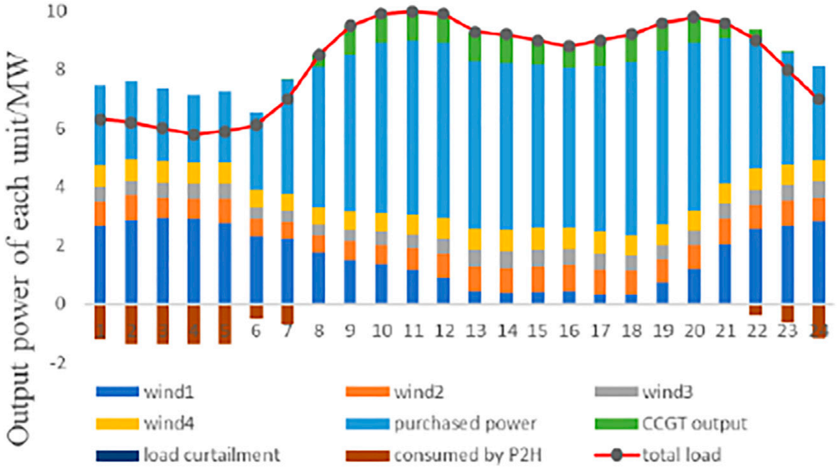

FIGURE 11 | Optimal generator outputs of case 2.

3.2.4 Modeling of Energy Coupling Devices

A schematic of the coupling relation between electricity–gas-hydrogen energy networks is illustrated in **Figure 3**. P2H plays a crucial role in coupling multi-energy networks, and CCGT links the gas networks and power grid effectively.

The simplified P2H and CCGT models are given in the following equations:

$$P_{j,t,s}^{CCGT} = \eta_{GT} \cdot P_{GT,t,s}^{gas} \; \mathrm{GT} \in \Omega_{cg}, j \in \Omega_{gt}, \forall t, \forall s \tag{58}$$

$$P_{j,t,s}^{h2} = \gamma_j \cdot P_{j,t,s}^{p2h} \; j \in \Omega_{p2h}, \forall t, \forall s \tag{59}$$

where η_{GT}, γ_j are the energy conversion efficiencies of CCGT and P2H, respectively.

4 MODEL SIMPLICATIONS

The model constructed above is a mixed-integer nonlinear nonconvex programming model, which is difficult to solve quickly and efficiently. It is therefore essential to simplify the model to reduce the computational burden.

The nonlinear terms $I_i P_i^{\max}$, $i_{ij} U_i$ and terms of form $\min(X, Y)$ are dealt with in **Appendix A**.

There are quadratic terms in **Eq. 30**, so **Eq. 30** is nonlinear and nonconvex. The results tend to fall into the local optimum, and it is not easy to obtain the global optimum exactly. Here, **Eq. 30** can be reformulated as follows:

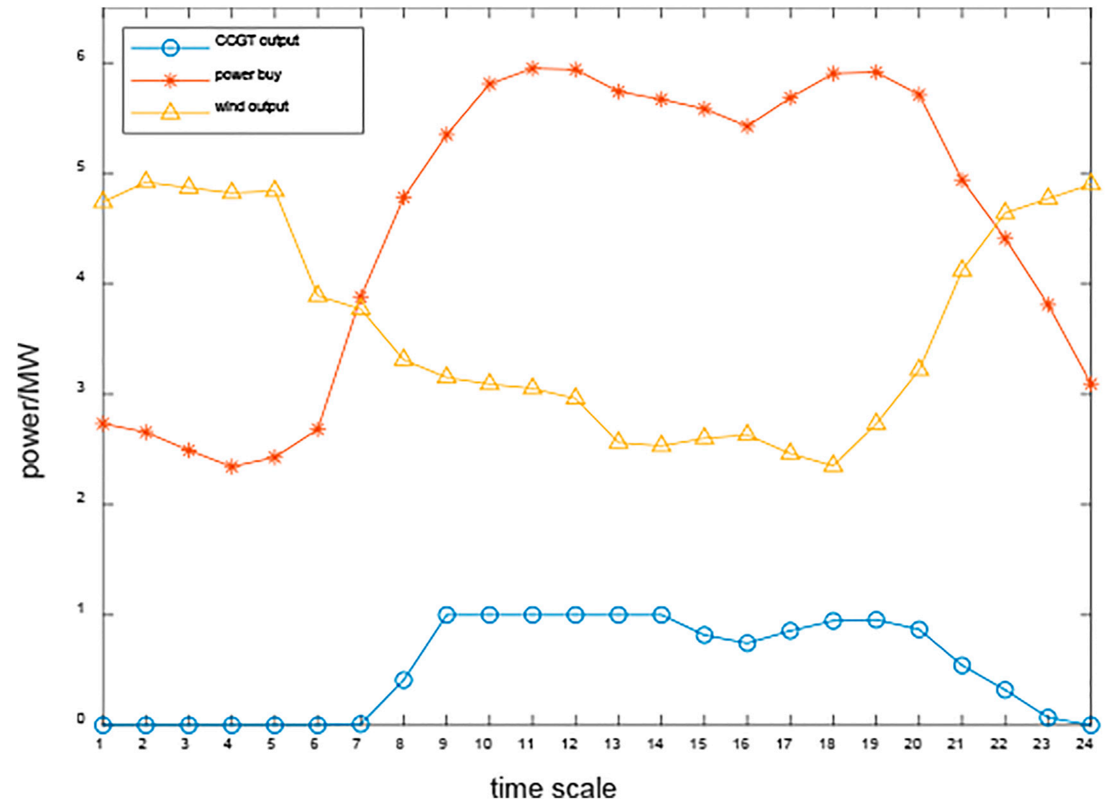

FIGURE 12 | Power output of each unit of case 2.

$$\rho \cdot Q_{ij}^2 = \xi \cdot \left(P_i^2 - P_j^2\right) \tag{60}$$

$$\xi = \begin{cases} 1 \ \mathrm{P}_i \ge \mathrm{P}_j \\ -1 \ \mathrm{P}_i < \mathrm{P}_j \end{cases} \tag{61}$$

$$\rho = \frac{\left(GT_f LZ f P_b\right)^2}{T_b^2 D^5 \left(1.1494 \times 10^{-3}\right)^2} \tag{62}$$

.

Let $\pi_i = P_i^2$, $\pi_j = P_j^2$. Then, **Eq. 62** can be rewritten as follows:

$$\rho \cdot Q_{ij}^2 = \xi \cdot \left(\pi_i - \pi_j\right) \tag{63}$$

Let x_l be the gas flow direction. When $x_l = 1$, it means $Q_{ij} \ge 0$. When $x_l = 0$, it denotes $Q_{ij} < 0$. Therefore, the transmission characteristic constraint and capacity constraint denoted by **Eq. 65** can be equivalently expressed as follows:

$$(2x_l - 1)\pi_i + (1 - 2x_l)\pi_j = \rho \cdot Q_{ij}^2 \tag{64}$$

$$-Q_{ij}^{\max}(1 - x_l) \le Q_{ij} \le x_l \tag{65}$$

.

Equation 66 can be further relaxed to

$$(2x_l - 1)\pi_i + (1 - 2x_l)\pi_j \ge \rho \cdot Q_{ij}^2 \tag{66}$$

.

For the line $l = (i, j)$, new variables $z_{li} = x_l \pi_i$ and $z_{lj} = x_l \pi_j$ are introduced due to the product of variables x_l and π. Constraint **Eq. 68** is further replaced with equations in Singh and Kekatos, 2020. The nonlinear, nonconvex terms are converted into mixed-integer second-order cone constraints with the above transformation

$$x_l \underline{\pi}_i \le z_{li} \le x_l \bar{\pi}_i \tag{67}$$

$$\pi_i + (x_l - 1)\bar{\pi}_i \le z_{li} \le \pi_i + (x_l - 1)\underline{\pi}_i \tag{68}$$

$$x_l \underline{\pi}_j \le z_{lj} \le x_l \bar{\pi}_j \tag{69}$$

$$\pi_j + (x_l - 1)\bar{\pi}_j \le z_{lj} \le \pi_j + (x_l - 1)\underline{\pi}_j \tag{70}$$

$$2z_{li} - 2z_{lj} + \pi_j - \pi_i \ge \rho \cdot Q_{ij}^2 \tag{71}$$

$$-Q_{ij}^{\max}(1 - x_l) \le Q_{ij} \le x_l Q_{ij}^{\max} \tag{72}$$

.

5 DISTRIBUTED ALGORITHMS BASED ON BENDER'S DECOMPOSITION AND CUT PLANE

Since large-scale mixed-integer programming models are difficult to solve in an efficient and quick manner, this section develops a distributed algorithm based on Bender's decomposition (Gharaei et al., 2019). The basic idea of the distributed algorithm is to group the constraints and variables of a complex problem into more minor and easily tractable master problems and subproblems, which is shown in **Figure 4**.

The section below details the master problem and the subproblem based on Bender's decomposition and cut plane.

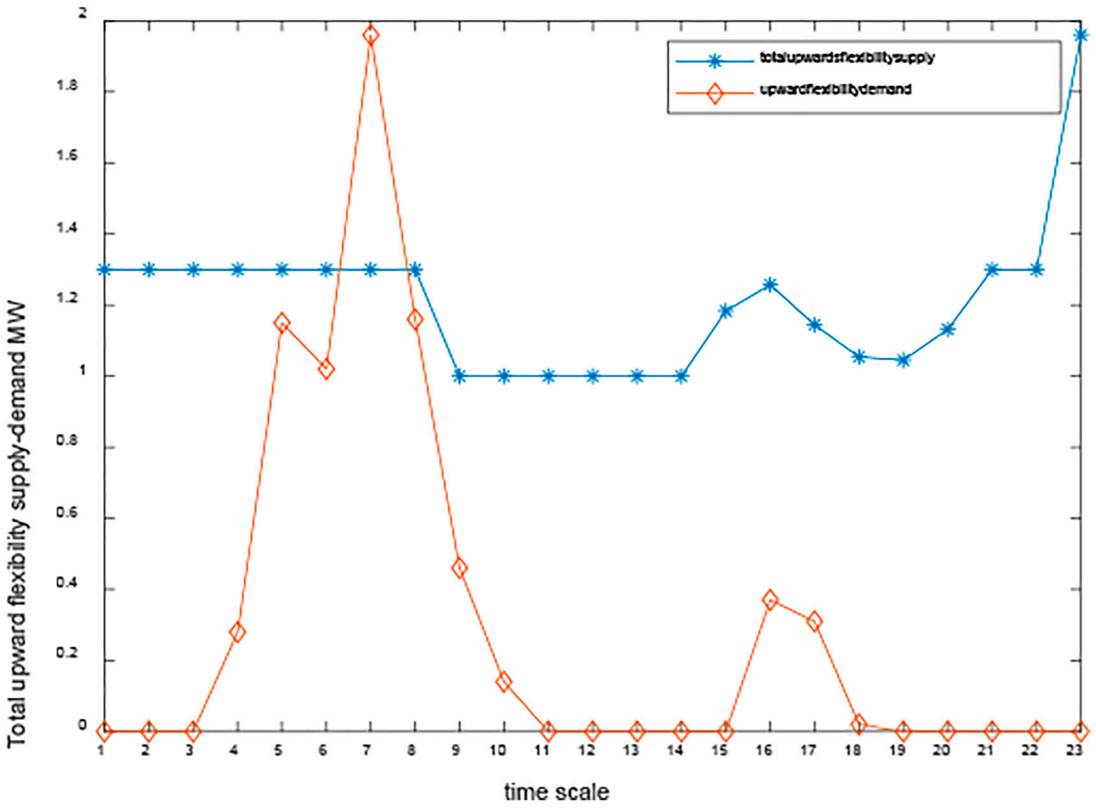

FIGURE 13 | Total upward flexibility supply–demand of case 1.

The master problem with respect to the problem **Eq. 9** is formulated as follows (Conejo et al., 2006):

$$\min \sum_{i\in\Omega_{p2h}} \frac{r(1+r)^{\tau_{i,\xi}}}{(1+r)^{\tau_{i,\xi}}-1} Z_i c_i + \eta \tag{73}$$

.

$$C_{ope} + \sum \lambda_i^{(k)}\left(P_i^{\max} - P_i^{\max(k)}\right) \le \eta \tag{74}$$

This is subject to constraints **Eq. 12–Eq. 15**, **Eq. A3**, and **Eq. 74**. The subproblem related to **Eq. 9** is depicted below:

$$\min \quad C_{ope} \tag{75}$$

.

$$P_i^{\max} = P_i^{\max(k)}: \lambda_i \tag{76}$$

The dual variables$\lambda_i$with respect to equation constraint (79) are given following a colon. The subproblem is subject to constraints **Eqs 18**, **19**, **Eqs 21–29**, **Eqs 31–42**, **Eqs 43–59**, **Eqs 67–72**, **Eq. 76**, and **Eqs A1**, **A2**.

The detailed interactions between the master problem and the subproblem are presented below.

Step 1. Initialization. Set $LB = -\infty, UB = +\infty, k = 0$.

Step 2. Solve the aforementioned master problem **Eq. 76** to obtain the optimal values Z_i^*, η^* and update lower bound $LB = \sum_{i\in\Omega_{p2h}} \frac{r(1+r)^{\tau_{i,\xi}}}{(1+r)^{\tau_{i,\xi}}-1} (Z_i^*)^k c_i + (\eta^*)^k$.

Step 3. Call the commercial solver Gurobi to solve the subproblem in (78) and update the upper bound $\min\left(UB, \sum_{i\in\Omega_{p2h}} \frac{r(1+r)^{\tau_{i,\xi}}}{(1+r)^{\tau_{i,\xi}}-1} (Z_i^*)^k c_i + (C_{ope}^*)^k\right)$.

Step 4. If $UB - LB \le \varepsilon$, the optimal values are obtained and the algorithm terminates. Otherwise, update the iteration counter $k = k + 1$, and go to Step 2.

It is noted that if $k = 0$, then the constraint **Eq. 75** is not incorporated in the master problem. The flowchart of the distributed optimization algorithm to solve the two-stage stochastic dynamic MISOC program is shown in **Figure 5**.

6 CASE STUDY AND DISCUSSION

6.1 Description of Test Systems

In this section, simulations are carried out to verify the effectiveness of the proposed MISOC model and solution algorithm. The configuration of the simulation test systems is presented in **Figure 6**, which is composed of a modified IEEE 33-bus distributed network and a Belgian 20-node gas network comprising two gas compressors, four gas sources, and 1 CCGT. The wind turbine capacity installed at bus 15 is 3 MW, and the other three 1 MW wind units are located at buses e18, e22, and e26. The installed capacity of the CCGT

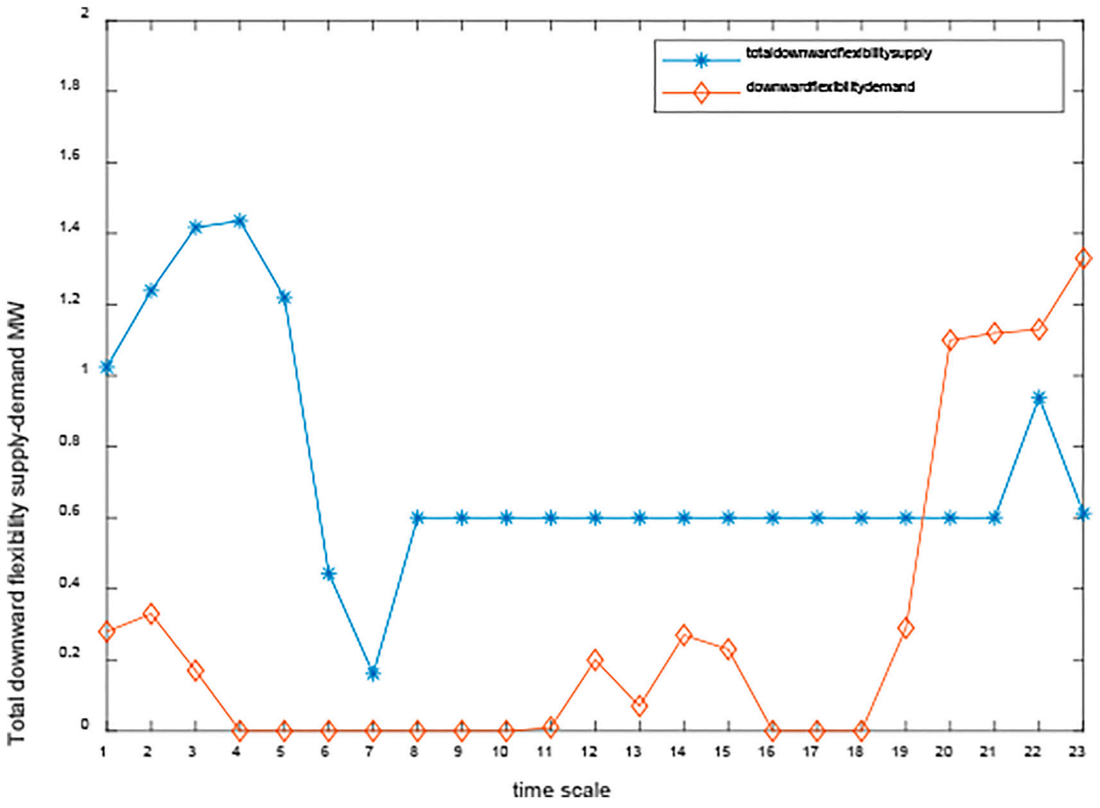

FIGURE 14 | Total downward flexibility supply–demand of case 1.

unit at bus e33 is 1 MW, which obtains its gas supply from node g8. In addition, two gas compressors are employed in the distribution gas network to manage the gas pressures in the gas network. The CCGT unit is the coupling device between the electricity and gas system. It is worth noting that the variables ρ of pipelines are considered constants, calculated in terms of a permissible hydrogen concentration of 10 vol%.

The time-of-use electricity price is illustrated in **Figure 7**. The predicated electrical load, the wind output power, and the gas load of the hybrid renewable energy system are shown in **Figure 8**. Based on Monte Carlo simulation and scenario reduction techniques, these data were used to generate the 10 operation scenarios for the study. The system net load is depicted in **Figure 9**. With high penetration renewable energy connection, it can be seen that the peak-valley difference of the demand becomes greater. At the same time, the net load profile varies more steeply. Therefore, it is urgent to enhance the system's flexibility and promote the consumption of renewable energy.

The other parameters used in the simulation are depicted in **Table 1**, and some of them can be found in Ref. Menon, 2005.

6.2 Simulation Results

In order to verify the performance and effectiveness of the two-stage MISOC model and the distributed solution algorithm proposed in this article, two cases are designed for comparative analysis. The simulations are carried out on a laptop with Intel i7-9750H CPU and 16 GB memory.

Case 1. Basic scenario, optimal operation of the hybrid renewable energy system without P2H. The case mainly analyzes the total operation costs without P2H.

Case 2. Comprehensive scenario, coordinated operation, and planning of the hybrid renewable energy system with P2H, the flexibility, and hydrogen injections are also taken into account. The case primarily discusses the total investment and operation costs of the system, and it also focuses on the impact of P2H on the system flexibility.

6.2.1 Planning and Operation Result Analysis

The annual total costs of the two cases are provided in **Table 2**, including investment costs, purchased electricity costs, purchased gas costs, renewable energy curtailment costs, the electricity load-shedding cost, and the gas load-shedding cost. A comparison of the data in the sixth and seventh columns of **Table 2** shows that after the construction of P2H, the renewable output curtailment cost drops from M$ (million dollars) 0.6524 to M$0.027705, and the electricity demand shedding cost decreases from M$0.21681 to M$0. It can also be seen that the annual total cost of case 2 is reduced by M$0.794 compared to case 1 by reducing the renewable energy

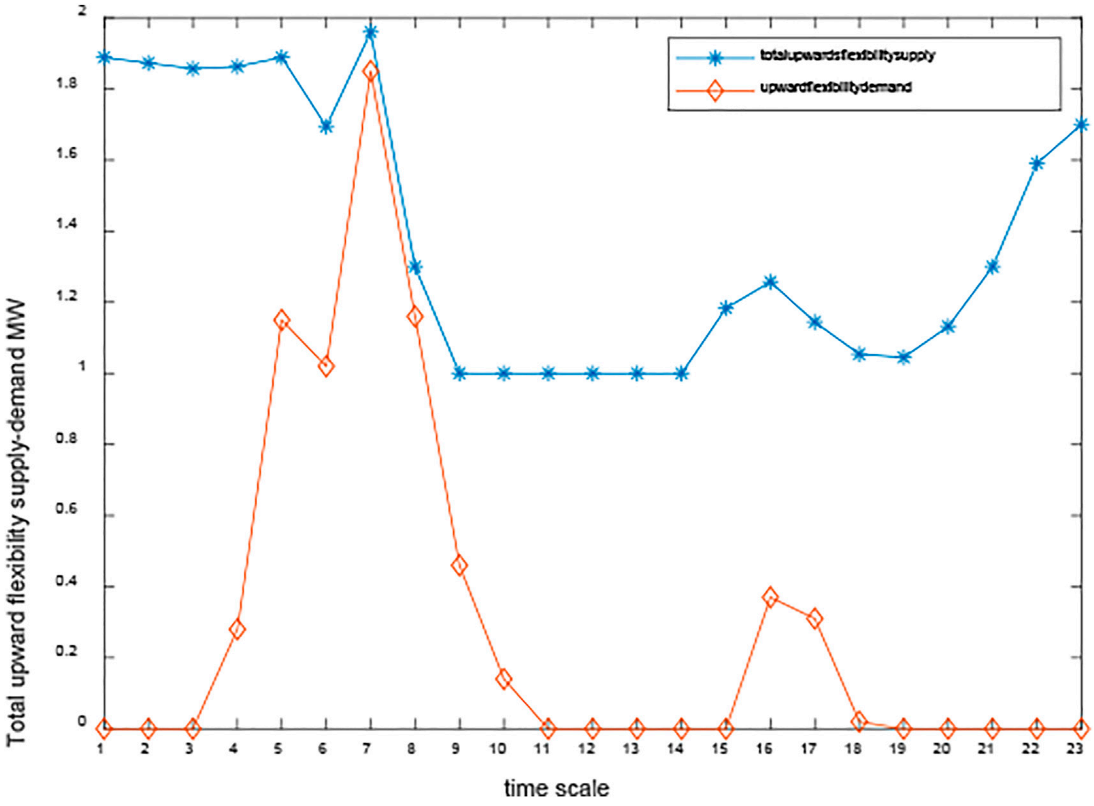

FIGURE 15 | Total upward flexibility supply–demand of case 2.

curtailment costs and the load-shedding costs. Although the capital costs of P2H exist in Case 2, the annual total cost is still lower than that of case 1. In the meantime, we conclude that the abandoned wind power reaches 0.1814 and 0.1981 MW in Case 2, which occurs at wind turbines 1 and 2 at 3 a.m. 4 a.m., respectively. This phenomenon occurs largely because the wind speed is higher, and wind turbines produce more power when the electrical load is lower.

The planning results of P2H in Case 2 are shown in **Table 3**. It is shown that the installed capacity of P2H at buses 15, 18, and 26 is 469.7, 803, and 189 kW, respectively. The total investment cost of P2H is M$1.8998. The life cycle of P2H is assumed to be 10 years. Therefore, the annual investment cost is M$0.28313, considering the interest rate. It is worth noting that the capacity of the wind generator equipped at bus 15 is 3 MW, which is larger than the other three. Meanwhile, the electricity demand in this area is high, and the wind power output is mainly supplied to the electrical consumers. Thus, the capacity of P2H installed at bus 15 is lower than that of bus 18.

Take scenario 5 as an example. The optimal generator outputs of two cases in the hybrid renewable energy system are shown in **Figures 10**, **11**. In this scenario, the renewable energy penetration level is 40%. As demonstrated from **Figures 4**, **10**, wind generators, the distribution system operator, and the CCGT unit supply the electrical load demand to the end users, and the electrical load shedding mainly occurs at 11 p.m. P2H participates in the operation of the system as a flexible unit in Case 2. As shown in **Figure 11**, in Case 2, four wind generators, one CCGT unit, and the distributed system operator serve as the source to supply electricity to the consumers and P2H. The higher wind speeds from 1 to 7 a.m. make the wind turbine generators output more power. However, the power demand of end users is low during this time. P2H produces hydrogen using surplus wind power to reduce renewable curtailment. At 8 in the morning, the electrical load demand increases sharply, and the output of the wind turbines decreases, at which point the CCGT unit starts to supply the electrical load. The electrical load peaks at 10 a.m. and 11 a.m. When the CCGT unit output reaches its maximum power, P2H does not consume power. The electricity price is high at this stage, so the electricity purchase is less. With the gradual reduction of power load demand, the output power of the CCGT unit decreases. From 10 to 12 p.m., the electricity load gradually decreases. On the contrary, the wind generators' output increases. The P2H units consume surplus renewable energy to produce hydrogen during this period, and the CCGT generator does not supply electricity to consumers.

As can be seen from **Figure 11**, case 2 yields smaller load-shedding and renewable energy curtailment than case 1. P2H plays a vital role in promoting the consumption of renewable energy.

The power output of the CCGT unit, the power purchased from the grid, and the four wind generators of case 2 are shown in **Figure 12**.

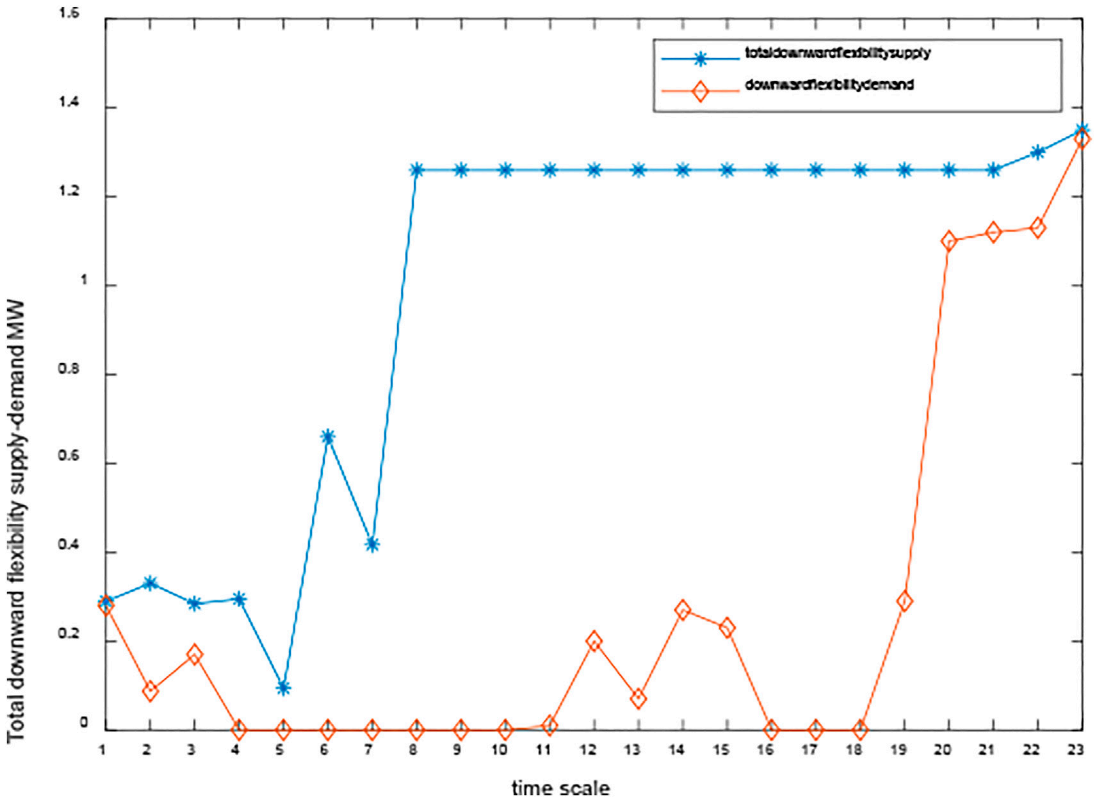

FIGURE 16 | Total downward flexibility supply–demand of case 2.

6.2.2 System Flexibility Analysis

This part investigates the hybrid renewable energy system's flexible supply and demand balance. The effect and role of P2H in system flexibility supply are evaluated by comparing the results of the two cases.

The total upward/downward flexibility supply and demand of case 1 are comparatively studied in **Figures 13**, **14**. As shown in **Figure 13**, the blue line represents the total upward flexibility supply, and the orange line indicates the upward flexibility demand. We can also learn from **Figure 13** that the demand for upward flexibility is greater at 6, 7, and 8 a.m. and reaches its maximum at 7 a.m. At 7 in the morning, the upward flexibility adequacy is less than 0, which indicates that upward flexibility supply is less than upward flexibility demand. **Figure 14** illustrates the total downward flexibility supply and demand of case 1. We can learn from the following figure that there is a greater need for downward flexibility from 8 to 11 p.m. During this period, the supply of downward flexibility has not been able to meet the demand for downward flexibility, and there has been a shortage of downward flexibility.

The total upward/downward flexibility supply and demand of case 2 are shown in **Figures 15**, **16**, respectively. It is shown in **Figure 15** that there is a greater need for upward flexibility during the period from 6 to 8 a.m. However, after the construction of P2H, the lack of upward flexibility no longer exists with the coordinated optimization of flexibility resources. As can be seen in **Figure 15**, the same phenomenon is present in downward flexibility. By comparing **Figure 13** with **Figure 15** and **Figure 14** with **Figure 16**, we can conclude that the system flexibility can be effectively enhanced after the construction of P2H, which helps promote the consumption of renewable energy.

7 CONCLUSION

This article proposes a low-carbon-emission hybrid renewable energy system to utilize power, hydrogen, and natural gas in an integrated mode. The P2H element serves as a key multi-energy coupling device connecting the distributed power network and gas and hydrogen networks.

In order to cope with the uncertainty of power load and renewable energy output, multiple operating scenarios are generated based on Monte Carlo simulations and the fast forward algorithm. Then, a two-stage stochastic planning model is constructed to consider the hybrid energy system flexibility and hydrogen injections. The nonlinear, nonconvex terms in the model are simplified, and a MISOC programming model is constructed to reduce the computation burden and further improve the solving efficiency. The results obtained by solving the above MISOC model using the distributed algorithm validate the effect of the construction of P2H.

Simulation results show that P2H can effectively reduce renewable energy curtailment, thus promoting the renewable energy consumption. On one hand, the upward/downward flexibility of the system has been enhanced by coordinating P2H and other flexibility resources. On the other hand, by injecting the hydrogen produced by P2H into the gas-distributed pipeline, the cost of hydrogen is effectively decreased, while reducing the system's CO_2 emissions.

Due to fluctuations in renewable energy output, the operational efficiency of electrolysis equipment is challenging to achieve in practice, and the actual available capacity of the equipment is reduced.

DATA AVAILABILITY STATEMENT

The original contributions presented in the study are included in the article/Supplementary Material, further inquiries can be directed to the corresponding author.

AUTHOR CONTRIBUTIONS

JW, writing the original draft, conceptualization, formal analysis, methodology and writing programs; PZ, writing, review and editing, conceptualization and investigation; YL, funding acquisition, project administration, supervision; JL, conceptualization, writing, review and editing.

FUNDING

This work was supported by funds provided via the National Key Research and Development Program of China (Grant No. 2018YFE0208400). The authors are also grateful for the support from the Science and Technology Project of State Grid Corporation of China (Key Technologies of Novel Integrated Energy System Considering Cross-border Interconnection).

REFERENCES

Agbonaye, O., Keatley, P., Huang, Y., Ademulegun, O. O., and Hewitt, N. (2021). Mapping Demand Flexibility: A Spatio-Temporal Assessment of Flexibility Needs, Opportunities and Response Potential. *Appl. Energ.* 295, 117015. doi:10.1016/j.apenergy.2021.117015

Bobo, L., Venzke, A., and Chatzivasileiadis, S. (2021). Second-order Cone Relaxations of the Optimal Power Flow for Active Distribution Grids: Comparison of Methods. *Int. J. Electr. Power Energ. Syst.* 127, 106625. doi:10.1016/j.ijepes.2020.106625

Bramstoft, R., Pizarro-Alonso, A., Jensen, I. G., Ravn, H., and Münster, M. (2020). Modelling of Renewable Gas and Renewable Liquid Fuels in Future Integrated Energy Systems. *Appl. Energ.* 268, 114869. doi:10.1016/j.apenergy.2020.114869

Cloete, S., and Hirth, L. (1922). Flexible Power and Hydrogen Production: Finding Synergy between CCS and Variable Renewables. *Energy* 192, 116671. doi:10.1016/j.energy.2019.116671

Conejo, A. J., Baringo Morales, L., Kazempour, S. J., and Siddiqui, A. S. (2016). Investment in Electricity Generation and Transmission. *Springer Nat.* doi:10.1007/978-3-319-29501-5

Conejo, A. J., Castillo, E., Minguez, R., and Garcia-Bertrand, R. (2006). *Decomposition Techniques in Mathematical Programming:Engineering and Science Applications*. Springer, 558.

Dagoumas, A. S., and Koltsaklis, N. E. (2019). Review of Models for Integrating Renewable Energy in the Generation Expansion Planning. *Appl. Energ.* 242, 1573–1587. doi:10.1016/j.apenergy.2019.03.194

Deymi-Dashtebayaz, M., Ebrahimi-Moghadam, A., Pishbin, S. I., and Pourramezan, M. (2019). Investigating the Effect of Hydrogen Injection on Natural Gas Thermo-Physical Properties with Various Compositions. *Energy* 167, 235–245. doi:10.1016/j.energy.2018.10.186

Dolci, F., Thomas, D., Hilliard, S., Guerra, C. F., Hancke, R., Ito, H., et al. (2019). Incentives and Legal Barriers for Power-To-Hydrogen Pathways: An International Snapshot. *Int. J. Hydrogen Energ.* 44, 11394–11401. doi:10.1016/j.ijhydene.2019.03.045

Ge, P., Hu, Q., Wu, Q., Dou, X., Wu, Z., and Ding, Y. (2020). Increasing Operational Flexibility of Integrated Energy Systems by Introducing Power to Hydrogen. *IET Renew. Power Generation* 14, 372–380. doi:10.1049/iet-rpg.2019.0663

Gea-Bermúdez, J., Jensen, I. G., Münster, M., Koivisto, M., Kirkerud, J. G., Chen, Y.-k., et al. (2021). The Role of Sector Coupling in the green Transition: A Least-Cost Energy System Development in Northern-central Europe towards 2050. *Appl. Energ.* 289, 116685. doi:10.1016/j.apenergy.2021.116685

Gharaei, A., Karimi, M., and Hoseini Shekarabi, S. A. (2019). Joint Economic Lot-Sizing in Multi-Product Multi-Level Integrated Supply Chains: Generalized Benders Decomposition. *Int. J. Syst. Sci. Operations Logistics* 7, 309–325. doi:10.1080/23302674.2019.1585595

Gils, H. C., Gardian, H., and Schmugge, J. (2021). Interaction of Hydrogen Infrastructures with Other Sector Coupling Options towards a Zero-Emission Energy System in Germany. *Renew. Energ.* 180, 140–156. doi:10.1016/j.renene.2021.08.016

Glenk, G., and Reichelstein, S. (2019). Economics of Converting Renewable Power to Hydrogen. *Nat. Energ.* 4, 216–222. doi:10.1038/s41560-019-0326-1

Hajiabbas, M. P., and Mohammadi-Ivatloo, B. (2020). Optimization of Power System Problems _Methods, Algorithms and MATLAB Codes. *Springer* 262. doi:10.1007/978-3-030-34050-6

Heris, M.-N., Mirzaei, M. A., Asadi, S., Mohammadi-Ivatloo, B., Zare, K., Jebelli, H., et al. (2020). Evaluation of Hydrogen Storage Technology in Risk-Constrained Stochastic Scheduling of Multi-Carrier Energy Systems Considering Power, Gas and Heating Network Constraints. *Int. J. Hydrogen Energ.* 45, 30129–30141. doi:10.1016/j.ijhydene.2020.08.090

Hu, G., Chen, C., Lu, H. T., Wu, Y., Liu, C., Tao, L., et al. (2020). A Review of Technical Advances, Barriers, and Solutions in the Power to Hydrogen (P2H) Roadmap. *Engineering* 6, 1364–1380. doi:10.1016/j.eng.2020.04.016

Koltsaklis, N. E., and Dagoumas, A. S. (2018). State-of-the-art Generation Expansion Planning: A Review. *Appl. Energ.* 230, 563–589. doi:10.1016/j.apenergy.2018.08.087

Li, J., Lin, J., Song, Y., Xing, X., and Fu, C. (2019). Operation Optimization of Power to Hydrogen and Heat (P2HH) in ADN Coordinated with the District Heating Network. *IEEE Trans. Sustain. Energ.* 10, 1672–1683. doi:10.1109/tste.2018.2868827

Li, R., Chen, L., Yuan, T., and Li, C. (2020). Optimal Dispatch of Zero-Carbon-Emission Micro Energy Internet Integrated with Non-supplementary Fired Compressed Air Energy Storage System. *J. Mod. Power Syst. Clean Energ.* 4, 566–580. doi:10.1007/s40565-016-0241-4(2016).20Menon

Liu, J., Zeng, P. P., Xing, H., Li, Y., and Wu, Q. (2020). Hierarchical Duality-Based Planning of Transmission Networks Coordinating Active Distribution Network Operation. *Energy* 213, 118488. doi:10.1016/j.energy.2020.118488

Lu, Z., Li, H., and Qiao, Y. (2018). Probabilistic Flexibility Evaluation for Power System Planning Considering its Association with Renewable Power Curtailment. *IEEE Trans. Power Syst.* 33, 3285–3295. doi:10.1109/tpwrs.2018.2810091

Menon, E. S. (2005), *Gas Pipeline Hydraulics R1. Continuing Education and Development, Inc.*, 21.

Mongird, K., Fotedar, V., Viswanathan, V., and Koritarov, V. (2019). *Energy Storage Technology and Cost Characterization Report*.

Pan, G., Gu, W., Lu, Y., Qiu, H., Lu, S., and Yao, S. (2020). Optimal Planning for Electricity-Hydrogen Integrated Energy System Considering Power to Hydrogen and Heat and Seasonal Storage. *IEEE Trans. Sustain. Energ.* 11, 2662–2676. doi:10.1109/tste.2020.2970078

Robinius, M., Welder, L., and Ryberg, D. S. (2017). "Power-to-hydrogen and Hydrogen-To-X:Which markets?Which Economic potential?Answers from the Literature," in 14th International Conference on the European Energy Market (EEM).

Singh, M. K., and Kekatos, V. (2020). Natural Gas Flow Solvers Using Convex Relaxation. *IEEE Trans. Control. Netw. Syst.* 7, 1283–1295. doi:10.1109/tcns.2020.2972593

Welder, L., Ryberg, D. S., Kotzur, L., Grube, T., Robinius, M., and Stolten, D. (2018). Spatio-temporal Optimization of a Future Energy System for Power-To-Hydrogen Applications in Germany. *Energy* 158, 1130–1149. doi:10.1016/j.energy.2018.05.059

Zablocki, A. (2019). *Fact Sheet Energy Storage*. Washington, DC: Environmental and Energy Study Institute.

Conflict of Interest: The authors declare that the research was conducted in the absence of any commercial or financial relationships that could be construed as a potential conflict of interest.

APPENDIX AMODEL SIMPLIFICATIONS

Term $i_{ij}U_i$ in **Eq. 20** can be relaxed to the following second-order cone programming constraints (Bobo et al., 2021):

$$\left\| \begin{matrix} 2P_{ij,t,s} \\ 2Q_{ij,t,s} \\ i_{ij,t,s} - U_{i,t,s} \end{matrix} \right\| \leq i_{ij,t,s} + U_{i,t,s} \; \forall t, \forall s \tag{A1}$$

Equations 43–48 are of the form $Z = \min(X, Y)$, which can be dealt with the big M method

$$\begin{array}{l} Y - X \leq M\omega \\ X - Y \leq M(1-\omega) \\ Z \geq Y - M\omega \\ Z \leq X + M\omega \\ Z \geq X - M(1-\omega) \\ Z \leq Y + M(1-\omega) \end{array} \tag{A2}$$

.

where ω is the binary variable, and $\omega = 1$ indicates that $X \leq Y$.

The nonlinear term $I_i P_i^{\max}$ in the objective function (10) is the product of variables I_i and $P_i^{\max}$, which can be equivalently replaced with the following constraints (Conejo et al., 2016):

$$\begin{array}{l} Z_i \leq I_i \cdot \bar{P}_i^{\max} \\ Z_i \geq I_i \cdot \underline{P}_i^{\max} \\ Z_i \leq P_i^{\max} + \underline{P}_i^{\max} \cdot (1 - I_i) \\ Z_i \geq P_i^{\max} - \bar{P}_i^{\max} \cdot (1 - I_i) \end{array} \tag{A3}$$

where Z_i is an auxiliary variable used to substitute for $I_i P_i^{\max}$. $\bar{P}_i^{\max}$, and $\underline{P}_i^{\max}$ are the upper and lower bound values of $P_i^{\max}$, respectively. It can be observed that when the binary variable I_i equals to 0, $Z_i = 0$, and when $I_i = 1$, $Z_i = P_i^{\max}$.

NOMENCLATURE

Binary Variable

$\mathbf{I}$ The P2H device is built or not (1:'built', 0:'not')

$\mathbf{x}$ Gas flow direction, (1:'the gas flow rate is positive' and 0: 'otherwise')

Sets

Ω The initial set of all generated scenarios

Ω_{cg} A set of gas nodes connecting CCGT

Ω_s A set of selected scenarios

Ω_J A set of remaining scenarios after the selected scenarios are removed

Ω_{p2h} A set of candidate locations for P2H devices

Ω_{ele} A set of nodes that purchase electricity

Ω_{renew} A set of nodes equipped with renewable energy sources

Ω_{source} A set of nodes equipped with natural gas supply units

Ω_o A set of feasible solutions to the operation optimization problem

Ω_{load} A set of electric demand nodes

Ω_{gas} A set of gas demand nodes

Ω_{gt} A set of electric nodes equipped with gas turbines

Continuous variables

$P_{load,t}$ $P_{wind,t}$ Actual electric demand and renewable energy output at time t

$P_{wind,t}^{fore}$ $P_{load,t}^{fore}$ The predicted output of renewable energy/demand at time t

$\Delta P_{wind,t}$ $\Delta P_{load,t}$ The prediction errors about renewable energy output and electric demand at time t

$P_{t,s}^{net}$, $F_{t,s}^{D-up}$ $F_{t,s}^{D-down}$ The net load and the total upward/downward flexibility demand capacity at time t for the scenario s

$P_i^{\max}$ Capacity of candidate P2H(MW)

P_j^{p2h} The consumed electricity by P2H

$\Delta P_{k,t,s}^{load}$ The shedding electric load (MW)

$\Delta P_{m,t,s}^{gas}$ The shedding gas load (m^3)

$P_{i,t,s}^{ele}$ The power purchased from TSO

$P_{n,t,s}^{saurce}$ The output of the gas source n

$P_{j,t,s}^{gas,load}$ The gas load at node j , at time t, for scenario s

$\Delta P_{j,t,s}^{renew}$ The curtailment of renewable energy

P_j^{renew}, P_j^{CCGT}, P_j^g The renewable energy output, the CCGT output, and the power purchase at node j

$P_{GT,t,s}^{gas}$ The gas consumed by CCGT

Q_{ij} Gas flow rate through the pipeline l_{ij}

$P_{i,t,s}$ The pressure of gas node i at time t under the scenario s

$P_{j,t,s}^{h2}$, $P_{i,t,s}^{h2-saurce}$ The output of hydrogen produced by P2H and the hydrogen coupled to the gas source

$F_{p2h,t,s}^{s-up}$, $F_{GT,t,s}^{s-up}$ $F_{buy,t,s}^{s-up}$, $F_{k,t,s}^{s-up}$ The upward flexibility capacity provided by P2H, CCGT, power purchase, and the shedding load

$F_{p2h,t,s}^{s\_down}$, $F_{GT,t,s}^{s\_down}$ $F_{buy,t,s}^{s\_down}$, $F_{j,t,s}^{s\_down}$ The downward flexibility capacity provided by P2H, CCGT, power purchase, and the renewable curtailment

$F_{t,s}^{up}$, $F_{t,s}^{down}$ The system upward and downward flexibility adequacy

Parameters

r, $\tau_{i,\varepsilon}$ The discount rate/life cycle of the device ε at node i

c_i unit investment cost of candidate device ε (\$/MWh)

π_s The probability of each scenario

N_s The total number of all scenes

C_{ij} The incident matrix related to the sites of P2H and gas sources

frontiers | Frontiers in Energy Research

ORIGINAL RESEARCH
published: 14 April 2022
doi: 10.3389/fenrg.2022.876299

Economic Boundary Analysis of Echelon Utilization of Retired Power Battery Considering Replacement Cost

Yali Wang[1], **Ze Ye**[1], **Wen Wei**[1,2]*, **Yongfei Wu**[1], **Aijun Liu**[1] **and Shuangfeng Dai**[1]

[1]College of Economics and Management, Changsha University of Science and Technology, Changsha, China, [2]College of Economics and Management, Hunan University of Science and Technology, Yueyang, China

As a large number of new energy electric vehicles are retired, the sequential utilization of retired power batteries has become one of the important means to improve the economic benefits of batteries, but there is a problem of disunity between available capacity and cycle life. Therefore, a peak-load power distribution method based on the principle of equal life of retired power batteries was proposed, which could effectively avoid the life difference caused by the battery difference and reduce the replacement cost. At the same time, in order to give reasonable investment suggestions for the stepwise utilization of retired power batteries, three economic boundary value models, including the payback period, peak–valley price difference, and investment cost, were constructed based on the leveling cost. Through the simulation of a 60 MW/160 MWh lithium iron phosphate decommissioned battery storage power station with 50% available capacity, it can be seen that when the cycle number is 2000 and the peak–valley price difference is above 0.8 yuan/kWh, it has investment value.

Keywords: decommissioning power battery, echelon utilization, peak cutting and valley filling, power distribution, economic boundary

OPEN ACCESS

Edited by:
Liansong Xiong,
Nanjing Institute of Technology (NJIT), China

Reviewed by:
Ning Li,
Xi'an University of Technology, China
Zhang Lei,
Capital Normal University, China
Donghai Zhu,
Huazhong University of Science and Technology, China

***Correspondence:**
Wen Wei
weiwenhn@163.com

Specialty section:
This article was submitted to Process and Energy Systems Engineering, a section of the journal Frontiers in Energy Research

Received: *15 February 2022*
Accepted: *21 March 2022*
Published: *14 April 2022*

Citation:
Wang Y, Ye Z, Wei W, Wu Y, Liu A and Dai S (2022) Economic Boundary Analysis of Echelon Utilization of Retired Power Battery Considering Replacement Cost.
Front. Energy Res. 10:876299.
doi: 10.3389/fenrg.2022.876299

INTRODUCTION

The state attaches great importance to the development of the new energy electric vehicle industry and actively arranges it as a national strategic emerging industry. During the 14th Five-Year Plan period, the total scale of new energy electric vehicle production and sales will reach tens of millions of vehicles. However, when the EV battery's available capacity falls below 70–80%, it must be decommissioned (Zhao et al., 2021a; Li Y Q et al., 2021; Xie et al., 2020). At that time, the capacity of the decommissioned battery in China will be as high as 25 GWh (Zhang et al., 2021). Direct scrapping will not only increase the processing cost but also cause a waste of resources (Tian et al., 2020; Yan et al., 2019). To explicitly encourage the cascade utilization of power batteries, the five departments issued management measures for the cascade utilization of power batteries of new energy vehicles in September 2021 (Li J L et al., 2022). At the same time, the majority of academics turned their attention to retired power battery echelon utilization (Lai et al., 2021; Xu et al., 2019; Zhang H et al., 2020).

When the power battery is decommissioned, the available capacity is about 70%. If it is selected and reorganized to participate in power grid service, it can not only reduce the battery recovery pressure but also provide greater economic benefits (Jiang et al., 2021; Yu and Zhou, 2020; Gao et al., 2022; Sathrea et al., 2015; Sedighizadeh et al., 2019). According to Dipti et al. (2020), cascade lithium-ion batteries exhibit better environmental benefits than new batteries in some application scenarios, demonstrating the social value of cascade utilization of retired power batteries. Ma et al. (2021) applied decommissioned power batteries to wind power smoothing scenarios and then reduced the amount of abandoned air and improved the economic benefits of decommissioned power batteries by constructing the objective function of maximum daily returns. By establishing the cascade utilization model, Fan et al. (2021) improved the prediction accuracy of new energy and the revenue of retired batteries. The moving average method was used by Cui et al. (2020) to separate the predicted power fluctuation components of wind power, and then, retired power batteries were used to reduce wind power fluctuation and improve wind power consumption. From a demand-side management perspective, Fazelpour et al. (2014) and Finn et al. (2012) proposed that charging step utilization battery devices during off-peak load periods can reduce charging costs and studied the charging and discharging strategies of step utilization battery according to peak and valley pricing. Sun et al. (2021) proposed that the project exhibits investment value when the recovery price of step utilization battery is lower than 0.4 yuan/Wh. The normalization method is used to construct the economic boundary analysis model, according to Li and Li (2021). When the number of cycles is more than 2000 and the peak–valley price difference is 0.8 yuan/kWh, profits can be achieved.

From the above research, it is not difficult to find that it is feasible to use retired power batteries to participate in the peak load adjustment and fluctuation suppression of power grid from the perspective of economy and technology, but the available capacity and cycle life of retired batteries are not uniform (Zhang J et al., 2020), and how to construct the "peak–valley price difference" boundary value model in electricity market transactions has become a research focus (Cai and Li, 2021; Cao et al., 2021). Therefore, this paper proposes a retired power battery cascade utilization economic model and investment economic boundary model taking into account replacement cost. Compared with existing studies, this paper has the following contributions:

1) This paper proposes a peak-load power distribution method based on the principle of equal life of retired batteries to reduce the replacement cost increased by the difference in cycle life, thus improving the economy of the system.

2) This paper constructs three economic boundary models based on leveling cost, including the payback period, peak–valley price difference, and investment cost, which can provide reasonable suggestions for the investment of retired power battery's echelon utilization.

ECONOMIC OPTIMIZATION MODEL OF RETIRED POWER BATTERY CASCADE UTILIZATION

Step Utilization Cost Model of Retired Power Battery

The step utilization cost of power battery mainly includes battery recovery cost, equipment cost (power converter and management system cost), integration cost, replacement cost, operation and maintenance cost, and scrap cost.

Cost Recovery (C_1)

$$C_1 = C_B \cdot E_N, \tag{1}$$

where C_B is the unit price of the recovered battery, yuan/Wh, and E_N is the recovery rated capacity, Wh.

Equipment Cost (C_2)

$$C_2 = C_P \cdot P_N + C_M \cdot E_N, \tag{2}$$

where C_p is the unit price of the power converter, yuan/W; C_M is the unit price of the management system, yuan/Wh; and P_N is the recovery rated power, W.

Integration Cost (C_3)

Due to individual differences, charging and discharging efficiency, available capacity, rated power, etc., decommissioned power batteries need to be screened, classified, and assembled, thus increasing the cost:

$$C_3 = C_S \cdot E_N, \tag{3}$$

where C_S is the unit battery integration cost, yuan/Wh.

Replacement Cost (C_4)

Based on the individual differences of retired batteries, the service life termination time is not uniform during operation, and the battery body needs to be replaced constantly (Li et al., 2022; Lu et al., 2021). In the meantime, the battery access port management system cannot be reused and must be replaced at the same time. As a result, the cost of replacement includes both the battery body and the management system:

$$C_4 = n \cdot (C_B + C_M) \cdot E, \tag{4}$$

where n is the number of replacement times expressed as

$$n = \frac{N \cdot (T \cdot m)}{k}, \tag{5}$$

where N is the project cycle, k is the number of remaining cycles of the power battery, T is the number of operating days per year, and m is the number of cycles per day.

Operation and Maintenance Cost (C_5)

$$C_5 = C_{\mathrm{W}} \cdot E_{\mathrm{N}}, \tag{6}$$

where C_W is the annual operation and maintenance unit price, yuan/Wh/year.

Scrap Cost (C_6)

After the service life of power battery, the cost of residual body treatment is generally calculated by the residual value rate:

$$C_6 = -(C_1 + C_2 + C_3 + C_4 + C_5) \cdot \beta, \tag{7}$$

where β is the salvage rate.

Therefore, the power battery cost (C) can be expressed as follows:

$$C = C_1 + C_2 + C_3 + C_4 + C_5 + C_6. \tag{8}$$

Retired Power Battery Step Utilization Income Model

At present, the power market is not perfect, and the incomes of energy storage mainly include the following: first, direct incomes of low storage and high generation to earn power price difference and peak adjustment compensation (Chen et al., 2022; Wang et al., 2020) and, second, indirect incomes of reducing thermal power generation through energy storage to save environmental costs (Li et al., 2020).

Peak Cutting and Valley Filling

$$B_1 = (\eta P_D - P_C) \Delta t P_{price,} \tag{9}$$

where B_1 is the income from peak cutting and valley filling, η is the charge–discharge efficiency, P_{price} is the real-time peak–valley price difference of power grid, $\triangle$t is each charge and discharge time, P_C is the charging power, and P_D is the discharge quantity.

Peak Adjustment Compensation

$$B_2 = e \sum_{\mathrm{t}=1}^{T} \eta P_D, \tag{10}$$

where B_2 is the annual peak regulation compensation income and e is the contract price.

Environmental Income

$$B_3 = \sum_{\mathrm{h}=1}^{H} \eta P_D \theta_h \Delta t P_{price,h,} \tag{11}$$

where B_3 is the environmental benefit, H is the total number of pollutants, θ_{h} is the emission density of the hth pollutant, and $P_{\mathrm{price,h}}$ is the unit emission cost of the hth pollutant.

Therefore, the power battery income (B) can be expressed as follows:

$$B = B_1 + B_2 + B_3. \tag{12}$$

In summary, the net present value of successive utilization of retired power batteries can be expressed as follows:

$$NPV = \sum_{i=1}^{N} (B - C), \tag{13}$$

where N is the project cycle.

POWER DISTRIBUTION METHOD OF RETIRED POWER BATTERY STEP UTILIZATION

Due to the difference in rated capacity loss and available power consumption (as shown in **Figure 1**) (Fan et al., 2021), the charging and discharging efficiency and depth of decommissioned power batteries are different. As a result, the available capacities of retired power batteries vary (Klein et al., 2016; Zhao et al., 2021b). If the even distribution principle is followed when participating in peak-load cutting and valley filling, it may result in insufficient energy supply for some batteries and redundancy for some batteries. At the same time, if the battery is charged and discharged sequentially according to the size of available capacity, it may increase the battery imbalance damage (that is, the battery charge and discharge frequency is not uniform) and then increase the replacement cost. As a result, based on the principle of decommissioned power battery life span, this paper proposes a method to allocate charging and discharging power based on battery capacity, thereby avoiding the problem of increasing replacement cost caused by inconsistent charging and discharging. The specific implementation process is as follows:

Step 1: Determine the required charge–discharge efficiency of the system ($\triangle P$).

Step 2: Initialize the total available capacity of the current retired power battery ($\triangle P_{\mathrm{D}}$):

$$\Delta \mathrm{P}_D = \sum_{k=1}^{K} \Delta P_k, \tag{14}$$

where $\triangle \mathrm{P}_k$ is the available capacities of retired power batteries in group K and K is the total number of groups.

Step 3: Determine the ratio coefficient of charge and discharge by the processing method of normalization (g):

$$g = \begin{cases} \dfrac{\Delta P}{\boldsymbol{\Delta P_D}}, \Delta P \leq \Delta P_D \\ 1, \quad \Delta P \geq \Delta P_D. \end{cases} \tag{15}$$

Step 4: Determine the charge and discharge amount of each group:

$$\Delta P_{\mathrm{k\_1}} = \Delta P_{\mathrm{k}} \cdot g. \tag{16}$$

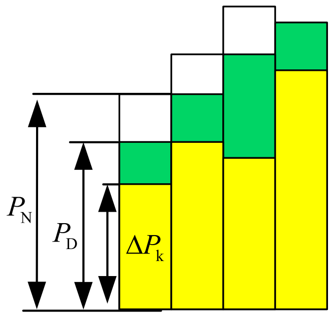

FIGURE 1 | Schematic diagram of available capacity of different retired power batteries.

ECONOMIC BOUNDARY MODEL BASED ON LEVELING COST

Payback Period Boundary Model

The levelized cost of energy (LCOE) is widely used at home and abroad to evaluate the economy of power generation projects (Li and Li, 2021). The boundary of the investment payback period refers to the time required for power generation projects from investment to full investment recovery. The longer the project investment payback period, the higher the investment risk:

$$\begin{cases} \sum_{i=0}^{n} NPV = 0, \\ \sum_{i=1}^{n} \frac{R_i}{(1+r)^i} = \sum_{i=1}^{n} \frac{C_i}{(1+r)^i}, \end{cases} \tag{17}$$

where R_i is the income in the ith year, C_i is the input cost in the ith year, n is the boundary life of the payback period, and r is the discount rate.

The power battery ladder utilization gains can be expressed by the sum of discounted values multiplied by the LCOE and the current year's power production E_n, and then, **Eq. 14** can be further expressed as follows:

$$\sum_{i=1}^{n} \frac{LCOE \times E_n}{(1+r)^i} = \sum_{i=1}^{n} \frac{C_i}{(1+r)^i}, \tag{18}$$

$$E_n = \eta \times DOD \times E_N, \tag{19}$$

where η is the charge–discharge efficiency and the depth of discharge (DOD) is the charge–discharge depth.

Investing in the LCOE Boundary Model

The investment LCOE boundary value refers to the LCOE required to recover the investment in the whole life cycle, according to **formula (15)**:

$$LCOE = \frac{\sum_{i=1}^{N} \frac{C_i}{(1+r)^i}}{\sum_{i=1}^{N} \frac{E_n}{(1+r)^i}} \tag{20}$$

Investment Cost Boundary Model

The boundary value of investment cost refers to the maximum acceptable recovery cost value of investment recovery within the whole life cycle according to the current LCOE value (about 0.7 yuan/kWh) (Fan et al., 2021):

$$C_B = \left(LCOE \times \sum_{i=1}^{N} \frac{E_n}{(1+r)^i} - \sum_{i=1}^{N} \frac{(C_4 + C_5)}{(1+r)^i} - C_2 - C_3 - C_6 \right) \Big/ E_N \tag{21}$$

ANTI-TRUTH ANALYSIS

Simulation Parameters

Taking 60 MW/160 MWh as an example, the usable capacity of the energy storage system is 50%, the specific parameters are shown in **Table 1** (Li and Li, 2021), the peak-to-valley time-of-use electricity price of non-residential users is shown in **Table 2**, the capacity decay rate is calculated according to 5%/100 times (Sun et al., 2021), and the environmental cost parameters are shown in **Table 3**.

Economic Benefit Analysis

The decommissioned power battery model is solved by a genetic algorithm (Chen, 2016; Hlal et al., 2019; Saini and Gidwani, 2022; Jiang et al., 2019), in which the original load (Wei et al., 2021) and peak adjusted curve are shown in **Figure 2**, and the output curve after peak shaving of the decommissioned power battery is shown in **Figure 3**. Assuming that the decommissioned power battery's service life and project life are both 5 years, no need exists for replacement costs at this time, and the annual investment cost and income of the decommissioned power battery are shown in **Table 4**.

According to **Figure 2**, finding that energy storage demonstrates a good effect of "peak shaving and valley filling" is not difficult, effectively assisting the power grid to participate in peak regulation. Simultaneously, according to **Table 4**, it can be seen that the decommissioned power battery demonstrates certain economic benefits in participating in peak shaving, and the investment payback period is 4.2 years, which can recover the cost during the life cycle and exhibits investable value.

Profit Margin Analysis

Analysis of Economically Sensitive Parameters

According to **formula (17)**, the current LCOE = 0.86 (yuan/kWh); however, the current peak-to-valley electricity price difference is 0.6 yuan/kWh, indicating that the decommissioned power battery ladder uses only the peak–valley electricity price difference income that relies on peak-to-valley filling, and it does not exhibit profitability. When combined with the cost of the decommissioned power battery in **Table 4** and the parameters in **Table 1**, it is clear that the price of the recovery price, the number of cycles, and the technical cost (including equipment cost and integration cost) of the single battery result in a significant impact on the economic

TABLE 1 | Parameters of echelon energy storage.

Parameter	Numerical value	Parameter	Numerical value
C_B (yuan/Wh)	0.5	T (days)	330
C_P (yuan/W)	0.5	N (years)	10
C_M (yuan/Wh)	0.15	η	0.85
C_S (yuan/Wh)	0.3	r	5%
C_W (yuan/kWh/year)	0.05	k (number of cycles)	2,500
e (yuan/kWh)	0.5	m	2
β	5%		

TABLE 2 | Time-of-use (TOU) power price.

Species	Peak		Flat section		Trough		Peak–valley price difference
	Period	Price	Period	Price	Period	Price	
Residents	8:00–12:00 17:00–21:00	1.0	12:00–17:00 21:00–4:00	0.6	04:00–8:00	0.3	0.7
Industrial	8:00–12:00 17:00–21:00	1.3	12:00–17:00 21:00–4:00	0.8	04:00–8:00	0.4	0.9

TABLE 3 | Type and cost of emissions.

Gas species	Displacement (kg/MWh)	Cost (yuan/kg)
Dust	0.5	2.92
SO_2	0.5	6.24
NO_x	0.75	8.03
CO_2	0.3	0.03
CO	0.05	1.01

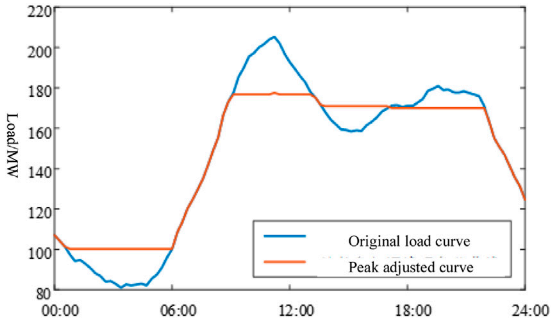

FIGURE 2 | Comparison diagram of post-peak load involving original load and energy storage.

utilization of the decommissioned power battery ladder. Therefore, this section analyzes the relationship between battery recovery unit price, technical cost, and LCOE sensitive parameters in the case of 1,500 cycles, 2,000 cycles, and 2,500 cycles, respectively, as shown in **Figures 4–6**, respectively.

In **Figure 4**, when the number of cycles k = 1,500 times, the battery cost boundary is about 0.4 yuan/kWh, and the technical cost boundary is 0.25 yuan/kWh, or the sum of the two is about 0.65 yuan/kWh. In **Figure 5**, when k = 2,000 times, the battery cost boundary is about 0.5 yuan/kWh, and the technical cost boundary is 0.35 yuan/kWh, or the sum of the two is about 0.85 yuan/kWh. In **Figure 6**, when k = 2,500 times, the battery cost boundary is about 0.52 yuan/kWh, and the technical cost boundary is 0.35 yuan/kWh, or the sum of the two is about 0.87 yuan/kWh. However, when the number of cycles exceeds 2,000, the boundary cost change is not obvious because the charging and discharging power, depth, and usable capacity of decommissioned batteries are essentially identical, with the only difference being the difference in life.

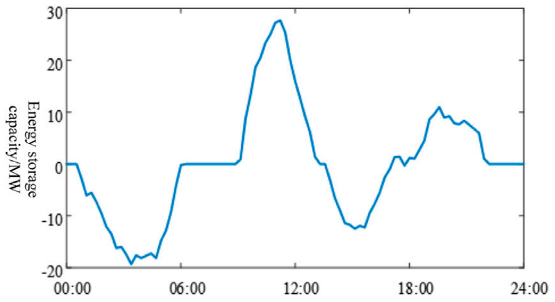

FIGURE 3 | Output curve of the decommissioned power battery.

It is not hard to see from **Figures 4–6** that, under the same battery recycling unit price and technical cost, the LCOE continues to decline as the number of cycles increases. At present, the maximum peak-to-valley price difference of the electricity price of Jiangsu residents is 0.8154 yuan/kWh, while the peak-to-valley price difference of 35 kV industrial users can reach 0.89 yuan/kWh, and the peak-to-valley price difference of 1–10 kV industrial and commercial users in Beijing can reach 1.14 yuan/kWh. When the number of cycles exceeds 2,000 times, making a profit is a possibility. At the same time, the National Development and Reform Commission issued the "Notice on

TABLE 4 | Annual investment costs and benefits of decommissioning power batteries.

Cost and benefit items and composition		Amount of money
Fixed investment cost (ten thousand yuan)	Battery investment cost	8,000
	Equipment investment cost	3,900
	Integration cost	1800
Average annual investment cost (ten thousand yuan)	Operation and maintenance cost	80
	Scrap cost	-17.2
Average annual income (ten thousand yuan)	Direct income	3,293.3
	Environmental income	35.1
NPV (ten thousand yuan)		525.6

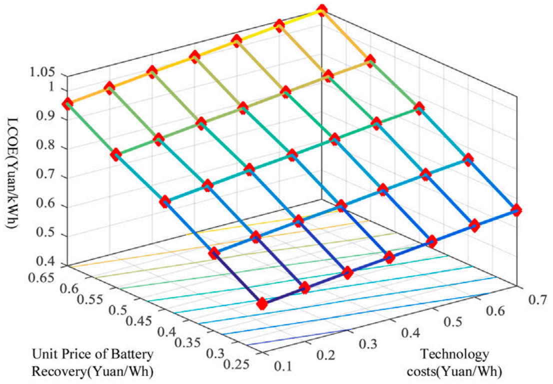

FIGURE 4 | K = 1,500 times sensitive cost parameter relationship.

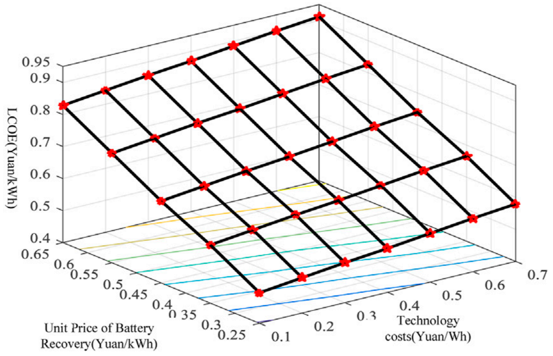

FIGURE 5 | K = 2,000 times sensitive cost parameter relationship.

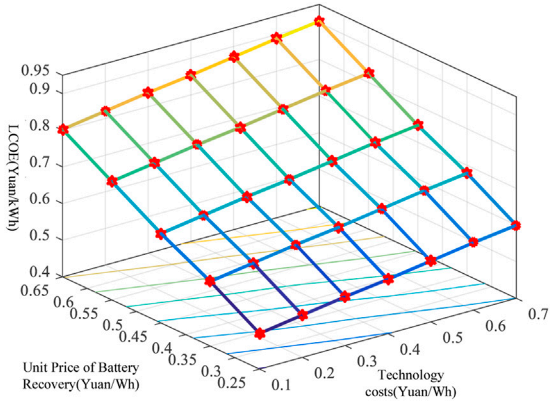

FIGURE 6 | K = 2,500 times sensitive cost parameter relationship.

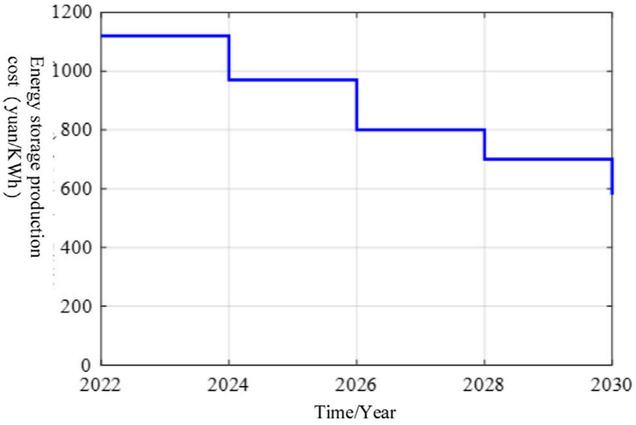

FIGURE 7 | Change trend of investment cost of the retired power battery.

Further Improving the Time-Sharing Electricity Price Mechanism" (National Development and Reform Commission, 2021), which stipulates that the peak-to-valley electricity price difference reaches 4:1, further providing usable space for energy storage investment.

Economic Boundary Value Analysis

In recent years, the price of lithium iron phosphate batteries and the cost of energy storage technology have both declined, further improving the profit margins of power battery cascade utilization. As a result, this section investigates the payback period boundary value, LCOE boundary value, and investment cost (battery recovery and technical cost) boundary value based on the aforementioned economic model of cascade utilization of power batteries. For the study of the payback period boundary value, assuming that the whole life cycle of the decommissioned power battery is 8 years, the number of cycles is 2,000 times, the current LCOE is 0.7 (yuan/kWh) (Li and Li, 2021), and the investment cost changes are shown in **Figure 7**. Then, the

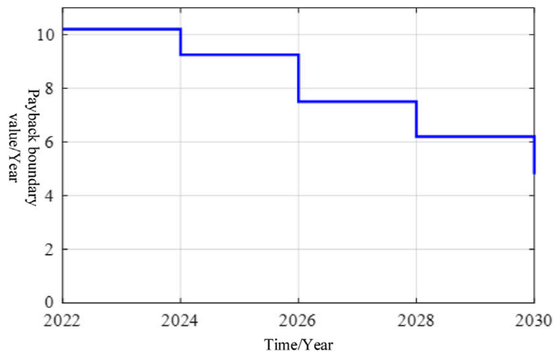

FIGURE 8 | Payback boundary value.

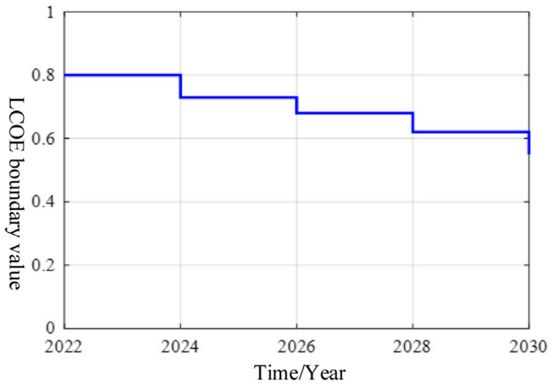

FIGURE 9 | LCOE boundary value.

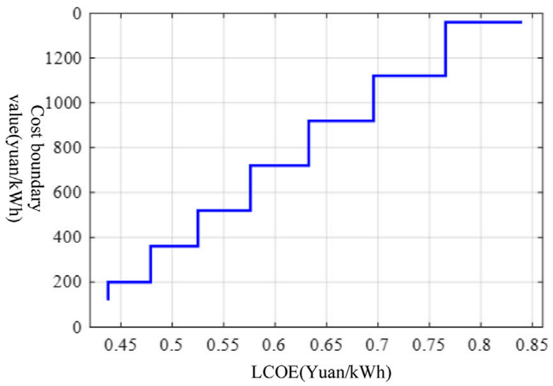

FIGURE 10 | Cost boundary value.

relationship between the payback period boundary value and the evolution trend of energy storage cost is shown in **Figure 8**.

According to **Figure 8**, as energy storage costs are reduced, the payback period boundary value continues to shrink. For example, in 2026, when the energy storage cost is reduced to 0.8 yuan/kWh, the payback period boundary value is approximately 7.8 years, allowing the investment cost to be recovered over the life cycle. The payback period is reduced to 4.8 years when the cost of energy storage falls to 0.58 yuan/kWh in 2030.

In the study of LCOE boundary values, according to **Eq. 20**, it can be seen that the current LCOE = 0.86 (yuan/kWh), making the profit difficult. **Figure 9** depicts the relationship between the LCOE boundary value and the cost evolution trend of the decommissioned power battery when the total life cycle of the decommissioned power battery is 8 years and the number of cycles is 2,000.

From **Figure 9**, it is not difficult to find that, with the continuous reduction of costs, the LCOE boundary value continues to decrease, which indicates that the profit space is getting larger and larger, and when it is 2028, the LCOE is reduced to 0.6 yuan/kWh, meeting the current peak-to-valley price difference in most domestic provinces. A better chance of achieving profitability before 2028 occurs if the National Development and Reform Commission is constantly formulating and releasing the peak–valley electricity price spread policy.

When the decommissioned power battery life cycle is 8 years and the number of cycles is 2000, the decommissioned power battery cost boundary study refers to the corresponding investment cost value when the LCOE boundary value changes. **Figure 10** depicts the relationship between the two.

From **Figure 10**, finding that the cost boundary value of decommissioned power batteries is directly proportional to LCOE is not difficult. Peak and trough electricity price spread in Jiangsu, Zhejiang, Hubei, and Shandong provinces will reach 0.7486 yuan/kWh, 0.503 yuan/kWh, 0.6116 yuan/kWh, and 0.568 yuan/kWh, respectively, under the new regulations. At this point, the national peak-to-valley electricity price difference is roughly 0.6 yuan/kWh, and if one only relies on “peak shaving and valley filling” to earn the peak-to-valley price difference income, the cost must be reduced to less than 0.8 yuan/kWh to achieve the decommissioning power battery cascade utilization profit. Combined with the cost change forecast of **Figure 7**, the investment recovery period needs to wait until 2026.

CONCLUSION

In this paper, an economic model of “peak-load cutting and valley filling” for retired batteries was established, as well as an economic boundary model based on leveling cost, to address the step utilization problem of a large number of retired power batteries. Through the simulation analysis of an actual decommissioned battery storage power station, the following can be concluded:

1) The decommissioned battery storage power station exhibits a good effect of “peak cutting and valley filling,” and it can effectively assist the power grid to participate in peak regulation. At the same time, it results in certain economic benefits, and the investment payback period is 4.2 years, which can recover the cost in the life cycle and exhibits investable value.

2) Battery recovery costs, technical costs, and cycle times all demonstrate an impact on the investment benefit and decision to decommission a battery storage power station. The retired battery

cascade utilization demonstrates an investment value when the cycle number is 2,000 and the peak–valley price difference is greater than 0.8 yuan/kWh.

3) With the continuous introduction of peak–valley price difference policy and the continuous development of energy storage technology, a large space of investment value exists for the cascade utilization of retired power batteries. This paper's analysis of an economic boundary model based on leveling costs provides a theoretical foundation for investors to make investment decisions.

In summary, the echelon utilization of decommissioned power batteries is affected by factors such as investment costs, peak-to-valley price differences, and cycle times. Therefore, when making investment decisions, investors need to make reasonable arrangements according to the actual working model.

DATA AVAILABILITY STATEMENT

The original contributions presented in the study are included in the article/Supplementary Material, further inquiries can be directed to the corresponding author.

AUTHOR CONTRIBUTIONS

ZY proposed the research direction and guided the project. YW, WW and SD were the primary writers of the manuscript. YW and AL revised the article language. All authors discussed the results and provided feedback on the manuscript.

REFERENCES

Cai, S., and Li, Y. (2021). Incentive Policy for Battery Energy Storage Systems Based on Economic Evaluation Considering Flexibility and Reliability Benefits. *Front. Energ. Res.* 9, 634912. doi:10.3389/fenrg.2021.634912

Cao, S., Zhang, H., Cao, K., Chen, M., Wu, Y., and Zhou, S. (2021). Day-Ahead Economic Optimal Dispatch of Microgrid Cluster Considering Shared Energy Storage System and P2P Transaction. *Front. Energ. Res.* 9, 645017. doi:10.3389/fenrg.2021.645017

Chen, C. Q. (2016). *Secure and Economic Dispatching on Grid-Connected Microgrid Considering Integrated of Wind energy[D]*. Changsha: Hunan university.

Chen, C., Li, X., and Huang, J. (2022). Meter and Wind FM Peaceful Wave Suppression of Topology Structure Dynamic storage[J/OL]. *Therm. Power generation* 51 (04), 55–61. doi:10.19666/j.r.LFD.202108152

Cui, C. S., Xie, L. R., Bao, H. Y., and Zhang, H. (2020). Capacity Configuration of Retired Battery Energy Storage System for Smoothing Wind Power Fluctuations [J]. *Chin. J. Power Sourc.* 44 (8), 1185–1190. doi:10.3969/j.issn.1002-087X.2020.08.028

Fan, G. Q., Lyu, P., Fan, G. W., Huang, J., Chen, H., Wang, H., et al. (2021). Effect of Second-Use of Retired Batteries on New Energy Consumption [J]. *Zhejiang Electric Power* 40 (3), 121–126. doi:10.19585/j.zjdl.202103018

Fazelpour, F., Vafaeipour, M., Rahbari, O., and Rosen, M. A. (2014). Intelligent Optimization to Integrate a Plug-In Hybrid Electric Vehicle Smart Parking Lot with Renewable Energy Resources and Enhance Grid Characteristics. *Energ. Convers. Manage.* 77, 250–261. doi:10.1016/j.enconman.2013.09.006

Finn, P., Fitzpatrick, C., and Connolly, D. (2012). Demand Side Management of Electric Car Charging: Benefits for Consumer and Grid. *Energy* 42, 358–363. doi:10.1016/j.energy.2012.03.042

Gao, Y., Cai, Y., and Liu, C. (2022). Annual Operating Characteristics Analysis of Photovoltaic-Energy Storage Microgrid Based on Retired Lithium Iron Phosphate Batteries. *J. Energ. Storage* 45, 103769. doi:10.1016/j.est.2021.103769

Hlal, M. I., Ramachandaramurthy, V. K., Sarhan, A., Pouryekta, A., and Subramaniam, U. (2019). Optimum Battery Depth of Discharge for Off-Grid Solar PV/battery System. *J. Energ. Storage* 26, 100999. doi:10.1016/j.est.2019.100999

Jiang, F., Peng, X., Tu, C., Guo, Q., Deng, J., and Dai, F. (2021). An Improved Hybrid Parallel Compensator for Enhancing PV Power Transfer Capability. *IEEE Trans. Ind. Electron.*, 1. doi:10.1109/TIE.2021.3121694

Jiang, F., Tu, C., Guo, Q., Shuai, Z., He, X., and He, J. (2019). Dual-Functional Dynamic Voltage Restorer to Limit Fault Current. *IEEE Trans. Ind. Electron.* 66 (7), 5300–5309. doi:10.1109/tie.2018.2868254

Kamath, D., Arsenault, R., Kim, H. C., and Anctil, A. (2020). Economic and Environmental Feasibility of Second-Life Lithium-Ion Batteries as Fast-Charging Energy Storage. *Environ. Sci. Technol.* 54 (11), 6878–6887. doi:10.1021/acs.est.9b05883

Klein, M., Tong, S., and Park, J. W. (2016). In-plane Nonuniform Temperature Effects on the Performance of a Large-Format Lithium-Ion Pouch Cell. *Appl. Energ.* 165, 639–647. doi:10.1016/j.apenergy.2015.11.090

Lai, X., Huang, Y., Deng, C., Gu, H., Han, X., Zheng, Y., et al. (2021). Sorting, Regrouping, and Echelon Utilization of the Large-Scale Retired Lithium Batteries: A Critical Review. *Renew. Sustain. Energ. Rev.* 146 (2), 111162. doi:10.1016/j.rser.2021.111162

Li, J. L., Li, Y. X., Lü, C., Zhou, W., Wu, Y. W., and Ma, S. L. (2022). Research on Key Technologies of Screening and Clustering Retired Batteries under the Target of Carbon Neutrality [J/OL]. *Power Syst. Technol.* 46 (02), 429–441. doi:10.13335/j.1000-3673.pst.2021.0655

Li, P., Liu, J., Deng, Z., Yang, Y., Lin, X., Jonathan, C., et al. (2022). Increasing Energy Utilization of Battery Energy Storage via Active Multivariable Fusion-Driven Balancing[J]. *Energy* 243, 122772. doi:10.1016/j.energy.2021.122772

Li, X., and Li, P. Q. (2021). Analysis on the Economics and Economic Boundaries of Largescale Application of Power Batteries in cascade utilization[J/OL]. *Energ. Storage Sci. Technol.* 11 (02), 717–725. doi:10.19799/j.cnki.2095-4239.2021.0487

Li, X. Q., Yu, H. F., Li, X. R., Zhang, D., Jiang, X., Zhu, S. R., et al. (2020). Planning Method for Multi-Functional Application Demand Considering Dynamic Life Cycle Characteristics of Energy Storage[J]. *Electric Power Construction* 41 (01), 45–54. doi:10.3969/j.issn.1000-7229.2020.01.006

Li, Y. Q., Peng, P., and Liu, B. J. (2021). Research on the Integration and Control Strategy of Echelon Use Battery Energy Storage System [J]. *Power Elect.* 55 (3), 13–16. doi:10.3969/j.issn.1000-100X.2021.03.004

Lu, L., Chen, S., Zhang, X., Pang, T., and Huang, C. X. (2021). Secondary Frequency Modulation Control Strategy for Power System Considering SOC Consistency of Large-Scale Battery Storage[J]. *Therm. Power Generation* 50 (07), 108–117. doi:10.19666/j.rlfd.202012296

Ma, L., Wei, C. W., Xie, L. R., and Wang, K. F. (2021). Coordinated Control Strategy for Wind Storage Active Power of Decommissioned Power Battery [J]. *Acta Energiae Solaris Sinica* 42 (10), 437–443. doi:10.19912/j.0254-0096.tynxb.2019fgc-0007

National Development and Reform Commission (2021). Notice of National Development and Reform Commission on Further Improving tOU Pricing Mechanism. https://www.ndrc.gov.cn/xxgk/zcfb/tz/202107/t20210729_1292067.html?code=&state=123.

Saini, P., and Gidwani, L. (2022). An Investigation for Battery Energy Storage System Installation with Renewable Energy Resources in Distribution System by Considering Residential, Commercial and Industrial Load Models. *J. Energ. Storage* 45, 103493. doi:10.1016/j.est.2021.103493

Sathre, R., Scown, C. D., Kavvada, O., and Hendrickson, T. P. (2015). Energy and Climate Effects of Second-Life Use of Electric Vehicle Batteries in California through 2050. *J. Power Sourc.* 288 (1), 82–91. doi:10.1016/j.jpowsour.2015.04.097

Sedighizadeh, M., Mohammadpour, A. H., and Alavi, S. M. M. (2019). A Two-Stage Optimal Energy Management by Using ADP and HBB-BC Algorithms for Microgrids with Renewable Energy Sources and Storages. *J. Energ. Storage* 21, 460–480. doi:10.1016/j.est.2018.12.010

Sun, Z., Tian, H., Wang, W. X., Pan, M. Y., and Zhang, L. (2021). Research on Economy of Echelon Utilization Battery Energy Storage System for User-

Side Peak Load Shifting [J]. *Acta Energiae Solaris Sinica* 42 (4), 95–100. doi:10.19912/j.0254-0096.tynxb.2017-0369

Tian, J., Wang, Y., Liu, C., and Chen, Z. (2020). Consistency Evaluation and Cluster Analysis for Lithium-Ion Battery Pack in Electric Vehicles. *Energy* 194, 116944–116955. doi:10.1016/j.energy.2020.116944

Wang, J., Liu, W. X., Li, S. Q., Liu, Z. Q., Yang, M. Y., and Guo, H. M. (2020). A Method to Evaluate Economic Benefits of Power Side Battery Energy Storage Frequency/Peak Regulation Considering the Benefits of Reducing Thermal Power Unit Losses[J]. *Power Syst. Technol.* 44 (11), 4236–4245. doi:10.13335/j.1000-3673.pst.2020.0149

Wei, W., Wang, Y., Dai, S. F., Chen, C. Q., and Chen, L. (2021). Energy Storage Economic Optimization Scheduling Method for Multi-Scene Demand of Peak and Frequency Modulation[J]. *Energies*, 14. 8605. doi:10.3390/en14248605

Xie, B. J., Lou, W. M., Luo, Y. F., Wang, H. X., and Li, K. (2020). SOC Estimation of Decommissioned Lithium-Ion Batteries Based on H∞ Unscented Kalman Filter [J]. *Zhejiang Electric Power* 39 (8), 53–60. doi:10.19585/j.zjdl.202008009

Xu, X., Mi, J., Fan, M., Yang, K., Wang, H., Liu, J., et al. (2019). Study on the Performance Evaluation and Echelon Utilization of Retired LiFePO4 Power Battery for Smart Grid. *J. Clean. Prod.* 213, 1080–1086. doi:10.1016/j.jclepro.2018.12.262

Yan, X., Deng, H., Guo, Q., and Qu, W. (2019). Study on the State of Health Detection of Power Batteries Based on Adaptive Unscented Kalman Filters and the Battery Echelon Utilization[J]. *Trans. China Electrotechnical Soc.* 34 (18), 3937–3948. doi:10.19595/j.cnki.1000-6753.tces.171452

Yu, Y., and Zhou, D. W. (2020). Reheat Pressure Optimization of Secondary Reheat Unit with Cascade Cycle[J]. *Therm. Power generation* 49 (07), 142–146. doi:10.19666/j.rlfd.202001013

Zhang, C. L., Zhao, S. S., and Zhang, B. (2021). A Fast Classification Method Based on Factor Analysis and K-Means Clustering for Retired Electric Vehicle Batteries [J]. *Power Syst. Prot. Control.* 49 (12), 16–24. doi:10.19783/j.cnki.pspc.201413

Zhang, H., Huang, J., Hu, R., Zhou, D., Khan, H. u. R., and Ma, C. (2020). Echelon Utilization of Waste Power Batteries in New Energy Vehicles: Review of Chinese Policies. *Energy* 206, 118178. doi:10.1016/j.energy.2020.118178

Zhang, J., Guerra, O. J., Eichman, J., and Pellow, M. A. (2020). Benefit Analysis of Long-Duration Energy Storage in Power Systems with High Renewable Energy Shares. *Front. Energ. Res.* 8, 527910. doi:10.3389/fenrg.2020.527910

Zhao, W., Min, J., Li, Z. Y., Sun, R., and Jiang, Y. (2021b). Energy Utilization Efficiency Estimation Method for Second-Use Lithium-Ion Battery Packs Based on a Battery Consistency Model[J]. *Trans. China Electrotechnical Soc.* 36 (10), 2190–2198. doi:10.19595/j.cnki.1000-6753.tces.200243

Zhao, W., Yuan, X. L., Zhou, Y. X., Li, P. Q., and Lei, E. T. (2021a). Capacity Configuration Method of a Second-Use Battery Energy Storage System Considering Economic Optimization within Service Life [J]. *Power Syst. Prot. Control.* 49 (12), 16–24. doi:10.19783/j.cnki.pspc.201233

Conflict of Interest: The authors declare that the research was conducted in the absence of any commercial or financial relationships that could be construed as a potential conflict of interest.

frontiers | Frontiers in Energy Research

ORIGINAL RESEARCH
published: 26 April 2022
doi: 10.3389/fenrg.2022.846006

Distributed Collaborative Optimization of a Multi-Region Integrated Energy System Based on Edge Computing Unit

Mengxue Wang[1], *Haoran Zhao*[1]*, *Hang Tian*[1] *and Qiuwei Wu*[2]

[1]Key Laboratory of Power System Intelligent Dispatch and Control of Ministry of Education, Shandong University, Jinan, China, [2]Department of Electrical Engineering, Technical University of Denmark, Lyngby, Denmark

The coordinated optimization scheduling of the integrated energy systems is vital in multi-energy complementarity and hierarchical utilization. However, the centralized optimization is inferior to the distributed optimization of the large-scale multiregion integrated energy system (MRIES) in data processing capacity and information security. This study proposes a distributed computing architecture based on the edge computing unit (ECU), which takes the energy hub as the main body and sets the partitioning principle and method of MRIES. The ECU can finally realize the whole-system collaborative optimization of MRIES, which contains electrical, natural gas, and district heating networks through internal autonomous optimization and boundary information interaction with the cloud computing center. At the same time, an improved nested algorithm based on the consensus-alternating direction method of multipliers is proposed, which ensures the convergence of the mixed-integer linear program and effectively improves the convergence speed. Combining the advantages of the model and algorithm provides a theoretical and algorithmic support for the optimization research of the MRIES.

Keywords: edge computing unit, multiregional integrated energy system, distributed collaborative optimization, energy hub, energy conservation

Edited by:
Athanasios I. Papadopoulos,
Centre for Research and Technology Hellas (CERTH), Greece

Reviewed by:
Yue Xia,
China Agricultural University, China
Hua Ye,
Chinese Academy of Sciences (CAS), China

***Correspondence:**
Haoran Zhao
hzhao@mail.sdu.edu.cn

Specialty section:
This article was submitted to Process and Energy Systems Engineering, a section of the journal Frontiers in Energy Research

Received: *30 December 2021*
Accepted: *1 April 2022*
Published: *26 April 2022*

Citation:
Wang M, Zhao H, Tian H and Wu Q (2022) Distributed Collaborative Optimization of a Multi-Region Integrated Energy System Based on Edge Computing Unit. Front. Energy Res. 10:846006. doi: 10.3389/fenrg.2022.846006

1 INTRODUCTION

Carbon peak and carbon neutrality targets put forward higher requirements for accelerating energy transformation in China. Therefore, the optimization of energy structure, energy conservation, and improvement of energy efficiency has become the most basic direction of energy development (Yunzhou et al., 2021). The construction of the IES is conducive to promoting the integration of source, network, load and storage, and multi-energy complementarity, which can realize the sustainable development for optimizing energy structure and improving energy efficiency. As the crucial part of IES research, RIES (Na et al., 2020) is mostly modeled in the form of EH. With EH as the main body, the RIES can be divided into functional units such as industrial areas, commercial areas, and residential areas. Based on the advantages of the geographical range, the RIES can conveniently realize the flexible optimization and scheduling decisions, which cannot be achieved without the assistance of multi-energy collaborative management, direct monitoring, and analysis of the operational data. Therefore, the RIES is an effective control and computing unit of IES intelligent evolution at present.

The IES distributed optimization has unique advantages over the centralized optimization in data acquisition cost, processing difficulty, application scale, information privacy, and security. A reasonable partition method of the IES and a suitable distributed algorithm are the fundamental problems of the IES distributed optimization. Haozhong et al. (2019) and Jianzhu Chen et al. (2019) used the different improved ADMM to conduct the distributed optimization of the IES based on the energy network decoupled. Jianzhu Chen et al. (2019) took CHP as the central part of the model and optimized the RIES in the distributed double layer, which took the delay of the bottom thermal ring network into account. In the study by Zhang et al., (2018), ADMM was adopted to optimize the pricing strategy of the multi-EH system with the underlying heating network. In the studies by Chen et al. (2018) and Chen et al. (2021), the static and dynamic characteristics of the EHs were taken into consideration and optimized, respectively. Zhang et al. (2018) proposed a multi-agent bargaining learning method, which optimized the large-scale IES in a distributed way, while the EH worked as the agent. Based on C-ADMM, Xu et al. (2019) improved the algorithm and analyzed the MRIES consisting of electrical, gas, and thermal three-ring networks with the four EHs. In comparison, Wen et al. (2017) used an improved method based on the C-ADMM dealing with the distributed optimization of a large-scale electric-gas system. ADMM was used for the distributed optimization of the multi-agent IES in the study by Haitao et al. (2021). Wu et al. (2020) used a hierarchical optimization method to carry out the distributed optimization of the electric–thermal system.

At present, the distributed collaborative optimization of the MRIES still has shortcomings:

(1) The role of MRIES in energy management and allocation is weakened by the decoupling method based on the different energy networks, which will be more complicated with the increase of the number and types of coupling devices.
(2) The distributed optimization with the EH as the main body does not consider the upper and lower energy network constraints. As a result, the global optimal solution cannot be obtained directly through the data interaction between the EHs.
(3) There is lack of a suitable distributed algorithm considering the EH off-design performance to support the expansion of the MRIES.

Therefore, this study proposes a distributed computing architecture based on an ECU and develops an IES partitioning method corresponding to it. And then, this study puts forward an improved algorithm adapted to the distributed characteristics of the model, forming a complete set of distributed computing methods based on ECU.

With the EH as the main body, the ECU is equivalent to RIES in geographical scope and structural level. The global optimal scheduling scheme is finally obtained through optimization within the unit and information interaction with the cloud. This architecture not only protects the information privacy and security of the RIES but also dramatically reduces the pressure of data transmission, storage, and processing in the cloud through edge computing, which reduces the difficulty of processing complex data of the IES. In addition, this study proposes a set of IES partitioning methods according to the connected positions of the EHs to reasonably partition ECU regions and provide a model basis for algorithm improvement. Based on the detailed RIES model, the improved C-ADMM nested algorithm fits the ECU model well, which can solve the nonconvergence problem caused by MISOCP and guarantee the optimization results with fewer iterations. They complement each other and provide a theoretical and methodological support for the MRIES distributed cooperative optimization.

In this article, the concept of the proposed ECU, modeling method, and improved algorithm are introduced in detail, and an example of the MRIES is used to verify the scalability and effectiveness of them.

2 EDGE COMPUTING UNIT FRAMEWORK FOR IES DISTRIBUTED OPTIMIZATION SCHEDULING

Internet of things, cloud computing, edge computing, and other technologies have played an important role in smart home management (Albataineh et al., 2020), power market (Chen S. et al., 2019), smart grid (Liu et al., 2021), (Cao et al., 2019), and other fields, but they have not fully emerged in the IES. Therefore, the ECU model proposed in this article will serve as a new energy management framework and provide a new idea for the unified management and coordinated scheduling of the IES multiple energy sources.

2.1 Framework of Edge Computing Unit

Corresponding to the cloud computing center in the IES, the ECU proposed in this article is the local energy data management unit, which can reduce cloud computing burden by finishing a part of the computing tasks at the local (Weisong et al., 2017). The structure of the ECU model presented in this article is shown in **Figure 1**.

EC, HP, CHP, and GB, as the coupling equipment convert power and natural gas into cold, heating, and power. Cooling and power are directly supplied to the local load, while the heating is transmitted to the HS or the DHN to jointly support the heating demand of the local load.

The modeling method of the upper radiant heat network is similar to that of the power grid and natural gas network. Therefore, the ring heating network is only established at the lower layer in this study for heat circulation. The ring network has high security and reliability (Wang et al., 2016), and the computing method for the ring network also meets the requirements of the radial heating network.

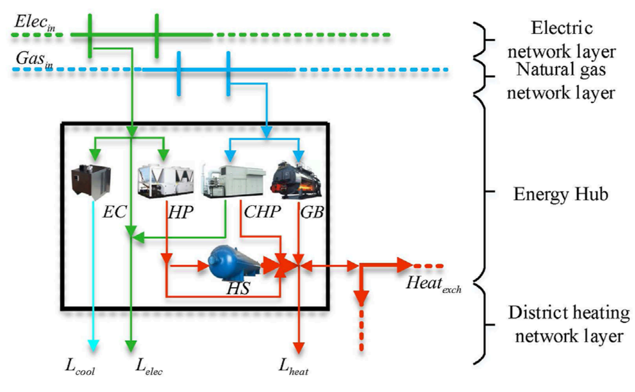

FIGURE 1 | Structure diagram of ECU.

The ECU supports the multizone expansion, where the units are connected to each other through a power grid, natural gas network, and DHN, becoming the main body of the MRIES.

2.2 Data Exchange Process of Optimization Scheduling in Multiregion Integrated Energy System

The ECU obtains the data of the devices and nodes through the local awareness layer and submits the boundary information to the cloud after internal optimization. Then, the cloud feeds back the consensus information obtained from the centralized computing to each ECU. After that, the ECU adjusts the internal operation according to the consensus information. The MRIES achieves global optimization through several iterations.

The centralized optimization needs to submit all the device data to the cloud, which results in vast costs of communication facility construction, data transmission, storage, and processing. It deviates from the energy development idea of energy conservation and emission reduction. Meanwhile, the information security and privacy cannot be guaranteed, as shown in **Figure 2A**.

Figure 2B shows the distributed optimization based on the energy system decoupled. Each computing unit needs to process the data of the whole system, which is the mainstream distributed computing method at present. Although the amount of cloud workload is reduced by two to three times, it is still affected by the wide geographical range of the MRIES. Meanwhile, the cost of the communication facility construction is still relatively high. In addition, this method deconstructs the EH model, resulting in the separate operation of each coupling device. As the number and types of the coupling devices increase, the computational complexity of this method will increase and the cost of data transmission and storage will also increase significantly.

The decoupled method based on the ECU is shown in **Figure 2A**, where the data are transmitted within the RIES and only submits the boundary information at the coupling point between the ECUs to the cloud. This decoupled method dramatically reduces the cost of communication facility construction, data transmission, storage, and processing, while ensuring the security and privacy of the data. Furthermore, the ECU collects the data of three types of energy and processes them in a centralized manner, which can better play a synergistic role in optimization. In addition, this method lays a foundation for future research work of the unified energy management.

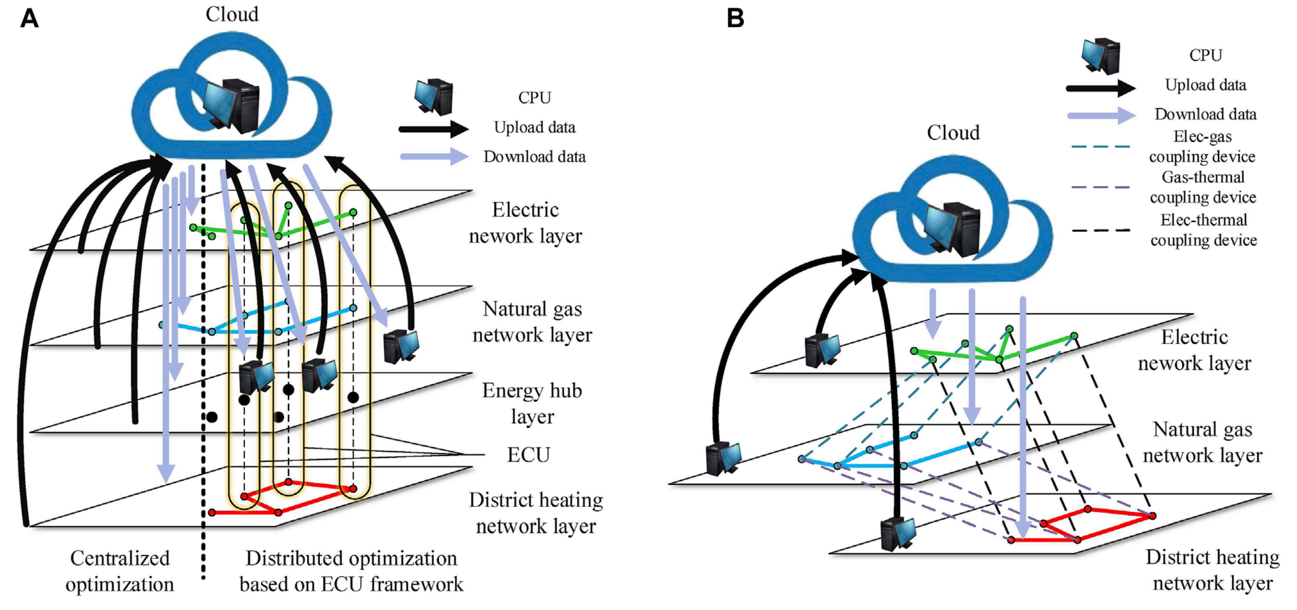

FIGURE 2 | Data flow of different optimization methods in IES. **(A)** Data flow of the centralized optimization and the ECU architecture distributed optimization. **(B)** Data flow of the distributed optimization decoupled according to energy networks.

3 MODELING OF THE EDGE COMPUTING UNIT

3.1 IES Decoupled Principle Based on Edge Computing Unit

As previously mentioned, EH is the main body and the energy management unit of the RIES. Therefore, the EH serves as the main body of the ECU to decouple the energy system. The partition principle should be based on the whole system's lowest communication cost. The communication cost is proportional to the physical distance between the nodes. Therefore, we decouple the energy networks separately according to the adaptive method of P-median problem as shown in **Eq. 1**.

$$\begin{aligned}&\min\sum_{r\in\mathbf{R}}\sum_{f\in\mathbf{F}} l_{rf}y_{rf}\\&\text{s.t.}\sum_{r\in\mathbf{R}} y_{rf}=1,\quad \forall f\in\mathbf{F}\\&y_{rf}\in\{0,1\},\quad \forall r\in\mathbf{R},\forall f\in\mathbf{F}.\end{aligned}\tag{1}$$

The objective function minimizes the information transmission distance within the network partitions, while the constraints ensure that the nodes are completely partitioned without repetition and omission. The IES model contains an electrical network, natural gas network, and DHN in the study. Therefore, the objective function should be applied in the three networks. After that, we can get the indices of the nodes in each unit of every network, but we need to further determine the boundaries between the units to provide the boundary data for cloud computing. As a result, **section 3.2** provides a decoupled method to distinguish the boundaries between the units under different EH connection conditions.

3.2 IES Decoupled Method Based on the Edge Computing Unit

As previously mentioned, the units contain different nodes but are connected by an energy transmission line. The transmission line also falls within the scope of unit internal optimization, so the virtual node needs to be inserted into the transmission line to establish clear boundaries between the units and serve as a data collection point of the connecting transmission line.

This study proposed a decoupled method, where the EH serves as the core in each ECU. Based on the connected position of the EH to the energy network, the whole system is decoupled by the partition method as given below. In **Figure 3**, the source represents the source of the energy network, which is the generator in the electrical network and the compressor in the natural gas network. EH represents a real hub. The virtual node is located in the middle of the transmission line, and the node data are the energy data in the middle of the transmission line. The virtual transmission line is lossless, aiming to reduce the coupling degree between the nodes.

3.2.1 Tandem Type

This type refers to the nodes of the EHs that are series nodes in the network. It contains three subtypes, such as the head subtype, concatenation subtype, and end subtype.

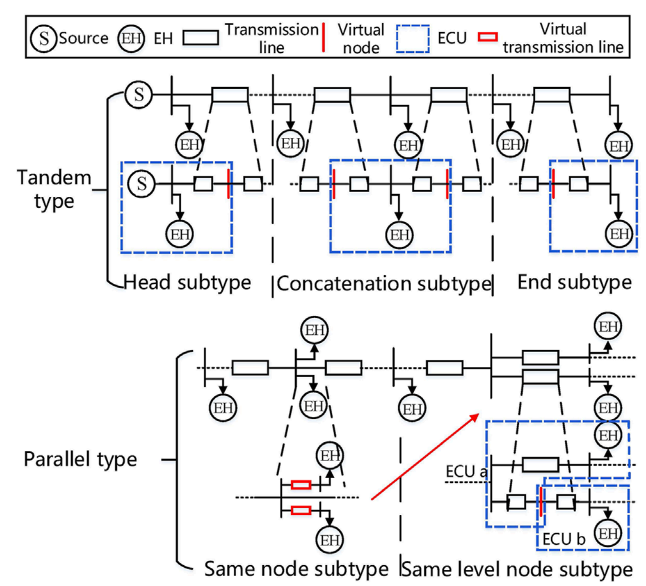

FIGURE 3 | Network partition method.

The concatenation subtype refers to the condition where the node of the EH is neither the end nor the head in the network. In this condition, the energy transmission line should be split in the middle and inserted with a virtual node on each side of the EH. The virtual node is included by the ECUs on both sides, and the insertion position of the virtual node is the boundary between the units. The data of the virtual node during the local optimization within the ECU are the boundary information submitted to the cloud.

The head/end subtype refers to the condition where the node of the EH is the head/end in the network. In this case, a virtual node should be inserted into the middle of the transmission line on only one side.

3.2.2 Parallel Type

This type contains two subtypes: same node subtype and same level node subtype, which, respectively, mean the EHs connected to the same nodes and the same level nodes in the network, as shown in **Figure 3**. When dealing with the same level node, a virtual node is inserted in the middle of one transmission line to transform it to the end subtype. As for the same node subtype, these node data for the EHs couple tightly, so a section of virtual transmission line should be added before each EH, which is transformed into the same level node subtype.

The energy networks are decoupled based on the abovementioned methods. The total energy consumption of a single ECU is the amount of the difference between the inflow and outflow.

3.3 Electrical Network Model in the Edge Computing Unit

In this study, the Distflow model is used to simulate the power flow of the distribution network in the ECU (Baran and

Wu 1989), and the SOCP is used to deal with the nonlinear model. The power balance of the node described in **Eqs 2–4** is the voltage loss equation, and **Eq. 5** represents the relationship between the branch current, node voltage, and power.

$$P_{j,t}^{\mathrm{in}} = -\sum_{g\in\mathbf{\Pi}}(j)\,P_{g,t}^{\mathrm{G}} - \sum_{pv\in\mathbf{\Pi}}(j)\,P_{pv,t}^{\mathrm{PV}} - \sum_{wt\in\mathbf{\Pi}}(j)\,P_{wt,t}^{\mathrm{WT}} - \left(P_{ij,t} - \hat{I}_{ij,t}R_{ij}\right) + \sum_{o\in\mathbf{\Omega}}(j)\,P_{jo,t} + \sum_{d\in\mathbf{\Pi}}(j)\,P_{d,t}^{\mathrm{LD}} + P_{j,t}^{\mathrm{EH}}. \tag{2}$$

$$Q_{j,t}^{\mathrm{in}} = -\left(Q_{ij,t} - \hat{I}_{ij,t}X_{ij}\right) + \sum_{o\in\mathbf{\Omega}}(j)\,Q_{jo,t} + \sum_{d\in\mathbf{\Pi}}(j)\,Q_{d,t}^{\mathrm{LD}}. \tag{3}$$

$$\hat{V}_{j,t} = \hat{V}_{i,t} - 2\left(P_{ij,t}R_{ij} + Q_{ij,t}X_{ij}\right) + \hat{I}_{ij,t}\left(R_{ij}^2 + X_{ij}^2\right). \tag{4}$$

$$\left(2P_{ij,t}\right)^2 + \left(2Q_{ij,t}\right)^2 + \left(\hat{I}_{ij,t} - \hat{V}_{i,t}\right)^2 \le \left(\hat{I}_{ij,t} + \hat{V}_{i,t}\right)^2. \tag{5}$$

The capacity limitation of the transmission line is shown as **Eq. 6**.

$$\begin{cases} \hat{I}_{ij,t}^{\min} \le \hat{I}_{ij,t} \le \hat{I}_{ij}^{\max} \\ \hat{V}_{i}^{\min} \le \hat{V}_{i,t} \le \hat{V}_{i}^{\max} \end{cases}. \tag{6}$$

Power consumption of the ECU is shown as **Eq. 7**.

$$P_{n,t}^{\mathrm{ECU}} = \sum_{i\in\mathbf{I}_n^{\mathrm{upper}}} P_{i,t}^{\mathrm{in}} - \sum_{j\in\mathbf{J}_n^{\mathrm{under}}} P_{j,t}^{\mathrm{in}}. \tag{7}$$

3.4 Natural Gas Network Model in the Edge Computing Unit

The natural gas network model in the ECU is similar to the electrical network, including the node energy balance constraint and pipeline transport constraint. **Eq. 8** represents the balance between the inflow and outflow of node *b*.

$$G_{b,t}^{\mathrm{in}} = -G_{ab,t} + \sum_{\omega\in\mathbf{\Lambda}}(b)\,G_{b\omega,t} + \sum_{d\in\mathbf{\Upsilon}}(b)\,G_{d,t}^{\mathrm{LD}} + G_{b,t}^{\mathrm{EH}}. \tag{8}$$

The natural gas network in this article is a medium–low pressure network without considering the compressor model (Hu et al., 2020). The second-order cone programming is used to relax the Weymouth equation of the natural gas network, as shown in **Eq. 9** (Liu et al., 2020). **Eqs 10,11** are the upper and lower limits of the gas transmission volume and natural gas pressure of the pipeline, respectively.

$$\left(G_{ab,t}\right)^2 + \left(K_{ab}\pi_{b,t}\right)^2 \le \left(K_{ab}\pi_{a,t}\right)^2. \tag{9}$$

$$0 \le G_{ab,t} \le G_{ab}^{\max}. \tag{10}$$

$$\pi_a^{\min} \le \pi_{a,t} \le \pi_a^{\max}. \tag{11}$$

The natural gas consumption of the ECU is shown as **Eq. 12**.

$$G_{n,t}^{\mathrm{ECU}} = \sum_{a\in\mathbf{A}_n^{\mathrm{upper}}} G_{a,t}^{\mathrm{in}} - \sum_{b\in\mathbf{B}_n^{\mathrm{under}}} G_{b,t}^{\mathrm{in}}. \tag{12}$$

3.5 DHN Model in the Edge Computing Unit

This study uses the available heating H^{av} to describe the thermal flow in a pipe. Two strong-coupled variables, temperature *T* and mass flow *q* in the DHN model are decoupled to form the thermal flow network model and the basic flow-temperature equation.

The linearized heat loss equation shows as **Eq. 14**, and Wei et al., (2017) prove that it has good accuracy when the initial temperature is 88 ~92°C. Section 4.2 will introduce the improved distributed algorithm based on linear heat loss.

$$H^{\mathrm{av}} = \mu q\left(T - T^{\mathrm{rw}}\right) \tag{13}$$

$$\Delta H_{uv}^{\mathrm{av}} = 2pi\frac{T^{\mathrm{sw}} - T^{\mathrm{e}}}{\sum R}l_{uv}. \tag{14}$$

The setup of the reference direction of heating medium flow in the DHN is shown in **Figure 4**. The EH_n represented the *n*th EH. The thermal flow network model is shown as **Eq. 15**.

$$\begin{cases} H_{n,u,t}^{\mathrm{EH}} + \sum_{m\in\mathbf{\Psi}(u)} H_{um,t}^{\mathrm{av}} = 0 \\ H_{um,t}^{\mathrm{av}} = -\left(H_{mu,t}^{\mathrm{av}} - \Delta H_{mu}^{\mathrm{av}}\right),\ \text{if}\ H_{mu,t}^{\mathrm{av}} > 0 \\ H_{um}^{\mathrm{av,min}} \le H_{um,t}^{\mathrm{av}} \le H_{um}^{\mathrm{av,max}},\ \text{if}\ H_{um,t}^{\mathrm{av}} > 0 \end{cases}. \tag{15}$$

A mixed-integer model of the thermal flow network is established based on the abovementioned equation to obtain the available heating distribution. Combined with the basic flow-temperature equation below, we can calculate the transmission temperature and thermal flow in the pipe.

$$\begin{cases} H_{u,t}^{\mathrm{EH}} = kq_{u,t}^{\mathrm{EH}}\left(T_{u,t}^{\mathrm{EH}} - T^{\mathrm{rw}}\right) \\ H_{uv,t}^{\mathrm{av}} = kq_{uv,t}\left(T_{uv,t} - T^{\mathrm{rw}}\right) \\ T_{u,t}^{\mathrm{EH}} = T_{u,t},\ \text{if}\ H_{u,t}^{\mathrm{EH}} > 0 \\ T_{u,t}^{\mathrm{EH}} = T^{\mathrm{sw}},\ \text{if}\ H_{u,t}^{\mathrm{EH}} < 0 \\ T_{uv,t} = T_{u,t},\ \text{if}\ H_{uv,t}^{\mathrm{av}} > 0 \\ q_{u,t}^{\mathrm{EH}} + \sum_{m\in\mathbf{\Psi}(u)} q_{um,t} = 0 \\ q_{uv,t} + q_{vu,t} = 0 \end{cases}. \tag{16}$$

The DHN operation cost is caused by the operation cost of circulating water pumps in the network. Therefore, the EHR is introduced to describe the cost of the circulating water pumps. **Eq. 17** represents the heat network operation cost of the *n*th ECU.

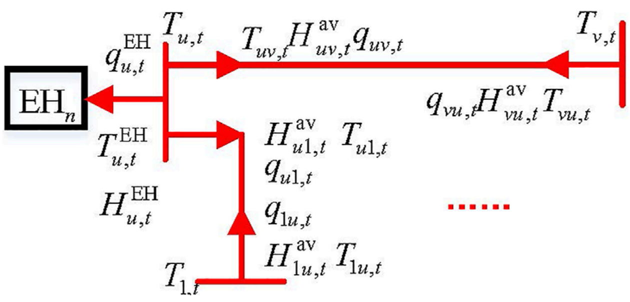

FIGURE 4 | Direction of heating medium flow in the DHN.

Each pipe is configured with a circulating water pump in this study.

$$C_n^{\text{heat}} = \sum_t \sum_{p=1}^{W} \left(\text{EHR}_p c_{e,t} \left| H_{p,t} \right| \right). \tag{17}$$

3.6 EH Model Considering Off-Design Performance

The EH is the energy conversion main body of the ECU. In this article, the standard matrix model is adopted for the EH model (Wang et al., 2017), and the piecewise linearization method is used to improve the accuracy of the EH model (Huang et al., 2019).

The energy flow direction of the coupling equipment is shown in **Figure 5**. **Eqs 18–20** describe the standard model of the EH. The heating output from the EH and the heating obtained from the DHN jointly support the heat load in this region.

$$V = \left[P_{\text{in}}^{\text{Grid}} \; P_{\text{in}}^{\text{EC}} \, P_{\text{in}}^{\text{HP}} \, P_{\text{in}}^{\text{CHP}} \, P_{\text{in}}^{\text{GB}} \, P_{\text{out}}^{\text{EC}} \; P_{\text{out}}^{\text{HP}} \; P_{\text{out, e}}^{\text{CHP}} \; P_{\text{out, h}}^{\text{CHP}} \; P_{\text{out}}^{\text{GB}} \, P_{\text{in}}^{\text{HS}} \; P_{\text{out}}^{\text{HS}} \right]^T. \tag{18}$$

$$V1 = \left[P^{\text{EH}} \quad G^{\text{EH}} \quad L_{\text{cool}} \quad L_{\text{elec}} \quad \left(L_{\text{heat}} - H^{\text{EH}} \right) \quad 0 \quad 0 \right]^T \tag{19}$$

$$Z \times V = V1. \tag{20}$$

To simplify the nonlinearity of the coupling equipment efficiency, this study uses the piecewise linearization method as shown in **Eqs 21–23** dealing with the nonlinear efficiency function of the coupling devices instead of the constant efficiency.

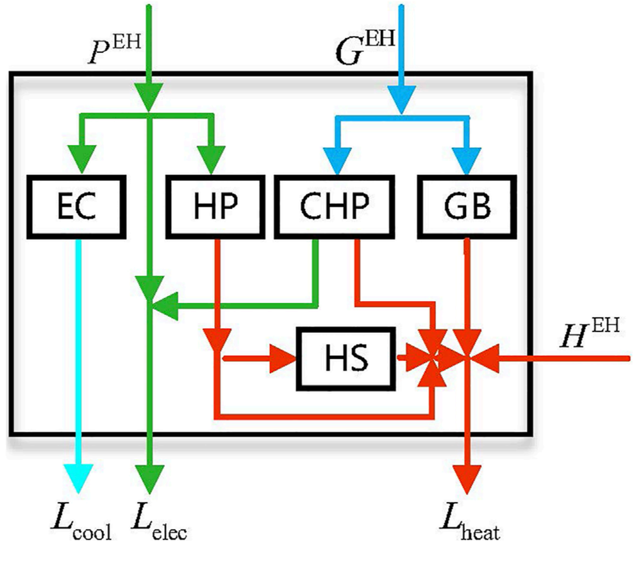

FIGURE 5 | Energy flows inside the EH.

$$X = X_0 + \sum_{\gamma \in \Gamma} \sigma_\gamma. \tag{21}$$

$$F_{\text{L}}(X) = F(X_0) + \sum_{\gamma \in \Gamma} \eta_\gamma \sigma_\gamma. \tag{22}$$

$$I_{\gamma+1}\left(\overline{X\gamma} - \underline{X\_\gamma} \right) \le \sigma_\gamma \le I_\gamma \left(\overline{X\gamma} - \underline{X\_\gamma} \right). \tag{23}$$

3.7 Objective Function of the Edge Computing Unit

The model of the ECU has been completed. The internal power grid and the natural gas network build up the SOCP, while the DHN and EH build up the MILP problem. This study takes the minimum economic cost as the optimization objective, and the objective function and the constraints of each ECU are shown in **Eq 24**.

$$\min \sum_t \left[\left(c_{e,t} P_{n,t}^{\text{ECU}} + c_{g,t} G_{n,t}^{\text{ECU}} \right) + \sum_{p=1}^{W} \left(\text{EHR}_p c_{e,t} \left| H_{p,t} \right| \right) \right]. \tag{24}$$
$$s.t. (2) - (16), (18) - (23)$$

4 NESTED ALGORITHM BASED ON C-ADMM

The ADMM algorithm performs well in the distributed optimization and has many improved forms. The multiregion expansion form of the standard ADMM, which guarantees convergence, is complex and does not conform to the calculation form of the ECU proposed in this article (Wang et al., 2013). The GS-ADMM cannot guarantee the convergence of multiregion expansion when $n \ge 3$, which is in the form of a serial computation (Ma et al., 2016). The C-ADMM supports the multizone expansion and is a parallel computing form, so it is used as the improved basis of the distributed algorithm in this study.

It is the key to coordinate the consensus information for the C-ADMM. The ECUs connect with each other through the power line, natural gas pipeline, and heat pipe as shown in **Figure 6**. The coupled information includes P, Q, I, U of the power line, G, π of the natural gas pipeline, and H of the heat pipe, which has an equality relationship with the consensus parameters at the virtual node as shown in **Eq. 25**.

$$x_{\alpha\beta,\alpha,t} = z_{\alpha\beta,t} = x_{\alpha\beta,\beta,t} \tag{25}$$

According to **Eq. 24**, the Lagrange expansion of the C-ADMM is shown in **Eq. 26**. **Eq. 27** is used to update the consensus variables and penalty factor.

$$L_n = \sum_{t=1}^{T} \left\{ \left(c_{e,t} P_{n,t}^{\text{ECU}} + c_{g,t} G_{n,t}^{\text{ECU}} \right) + \sum_{p=1}^{W} \left(\text{EHR}_p c_{e,t} \left| H_{p,t} \right| \right) + \sum_{\alpha \in \Theta_n} \left[\lambda_{\alpha\beta,\alpha,t} \left(x_{\alpha\beta,\alpha,t} - z_{\alpha\beta,t} \right) + \frac{\rho}{2} \left\| x_{\alpha\beta,\alpha,t} - z_{\alpha\beta,t} \right\|_2^2 \right] \right\}. \tag{26}$$

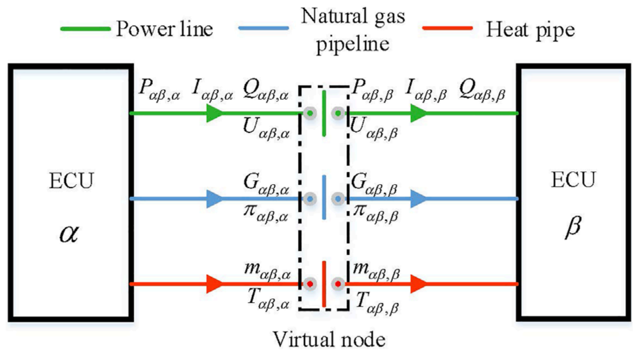

FIGURE 6 | Consensus variables between the ECUs.

$$\begin{cases} z_{\alpha\beta,t}^{k+1} = \frac{1}{2}\left[x_{\alpha\beta,\alpha,t}^{k+1} + x_{\alpha\beta,\rho,t}^{k+1} + \frac{1}{\rho}\left(\lambda_{\alpha\beta,\alpha,t}^{k} + \lambda_{\alpha\beta,\beta,t}^{k}\right)\right] \\ \lambda_{\alpha\beta,\alpha,t}^{k+1} = \lambda_{\alpha\beta,\alpha,t}^{k} + \rho\left(x_{\alpha\beta,\alpha,t}^{k+1} - z_{\alpha\beta,t}^{k+1}\right) \end{cases}. \tag{27}$$

In order to ensure the convergence of the optimization problems with discrete variables, previous work improved the C-ADMM algorithm, such as solving the MISOCP nonconvergence caused by the ring natural gas network through the nested computation of the discrete variables relaxation (Wen et al., 2017). The nonconvergence problem was solved by embedding the NC-ADMM method into the subproblem (Chen et al., 2020).

In order to ensure the convergence of the MISOCP constituent, a nested subalgorithm was added to the C-ADNN algorithm in this article, as shown in **Eq. 28**. The additional increment term describes that all the ECUs support transmission loss of the DHN which can constrain the direction of each iteration and improve the convergence speed, while the loss linearization of the heat network is the premise of this improvement. The algorithm flow chart is shown in **Figure 7**.

$$L_n = (25) + \lambda_{\text{loss}}^{\text{H}}\left(\sum_{n=1}^{N} H_{n,t}^{\text{EH}} - \sum_{p=1}^{W} \Delta H_p^{\text{av}}\right) + \frac{\rho}{2}\left\|\sum_{n=1}^{N} H_{n,t}^{\text{EH}} - \sum_{p=1}^{W} \Delta H_p^{\text{av}}\right\|_2^2. \tag{28}$$

The nested subalgorithm is introduced as given below.

Step 1. Initializing the discrete variables B, k, and θ. Setting the error tolerance δ.

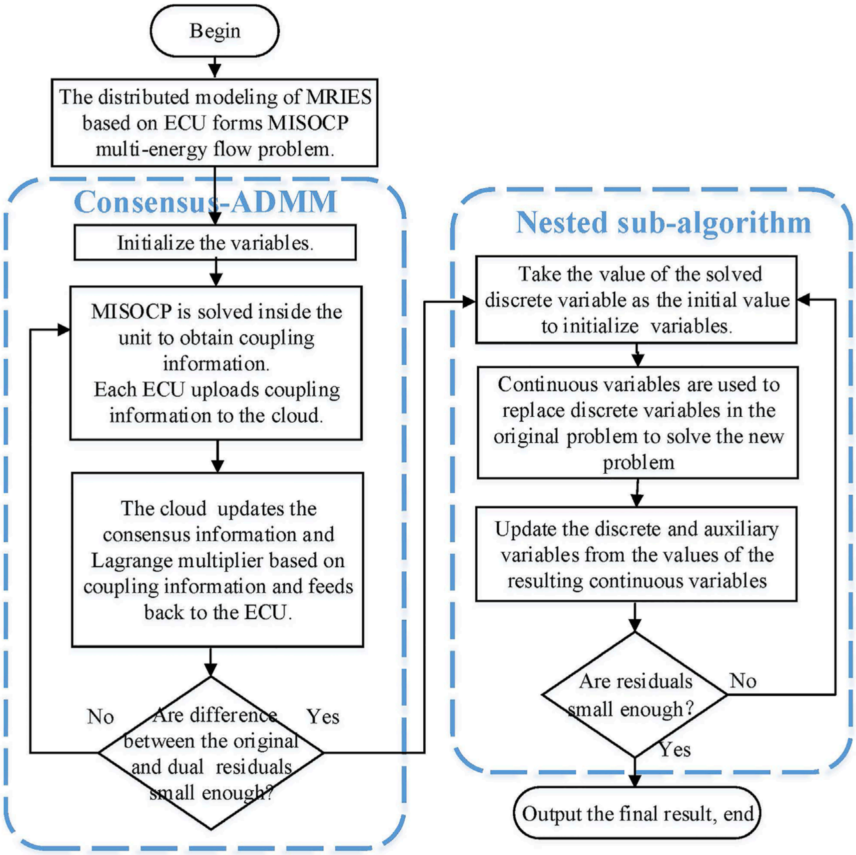

FIGURE 7 | Algorithm flow chart of the improved C-ADMM.

Step 2. Combining **Eqs 2–16** and **Eqs 18–23** to solve **Eq. 29** and then obtaining the value of C_B, before which the unknown variable C_B takes place of the discrete variable B.

$$C_{B,s}^{k+1} = \underset{C\_B\leftarrow B}{\arg\min}\left[(27) + \sum_{s=1}^{S}\frac{\theta}{2}\left\|B_s^k - C_{B,s}^k + z_{B,s}^k\right\|_2^2\right]. \tag{29}$$

Step 3. Updating the discrete variables B and auxiliary variables z_B as shown in **Eq. (30)**.

$$\begin{cases} B_s^{k+1} = \underset{B}{\arg\min}\sum_{s=1}^{S}\left\|B_s^k - C_{B,s}^k + z_{B,s}^k\right\|_2^2 \\ z_{B,s}^{k+1} = z_{B,s}^k + \left(B_s^k - C_{B,s}^k\right) \end{cases}. \tag{30}$$

Step 4. Comparing the error obtained by **Eq. 29** with δ. If the error is little enough, the iterative process will be broken, and if on the contrary, steps two to four will be repeated.

The addition of the nested subalgorithm makes the solution approach the feasible region infinitely. When the difference between the original and the dual errors of the original problem is small enough, the convergence process can be sped up significantly.

5 CASE STUDY

5.1 System Description

According to the partition method, the insertion of virtual nodes into the energy networks and partitioning them is based on the principle stated in **section 3.1**. The ECUs can completely contain all the nodes without repeat, as shown in **Figure 8A**. The partition details are shown in **Figure 8B**.

This article uses the improved C-ADMM algorithm to complete the distributed optimization of the MRIES in two scenarios.

Scenario A: Optimizing the MRIES containing electrical, gas, and heating networks based on the ECUs.

Scenario B: Optimizing the MRIES containing the electrical and natural gas networks based on the ECUs.

In both the scenarios, the MRIES have the same loads. Nevertheless, in Scenario B, the coupling equipment produces the heating to meet the heating demands.

Conversion efficiency functions of the coupling devices are shown in **Table 1**. The types of coupling devices in the MRIES are shown in **Table 2**. The energy prices and loads of each EH are shown in **Figure 9**.

The codes were written in MATLAB 9.4.0.813654 (R2018a), and all the experiments were conducted on a desktop with 3.00 GHz Intel Core i5 and 16.0 GB RAM.

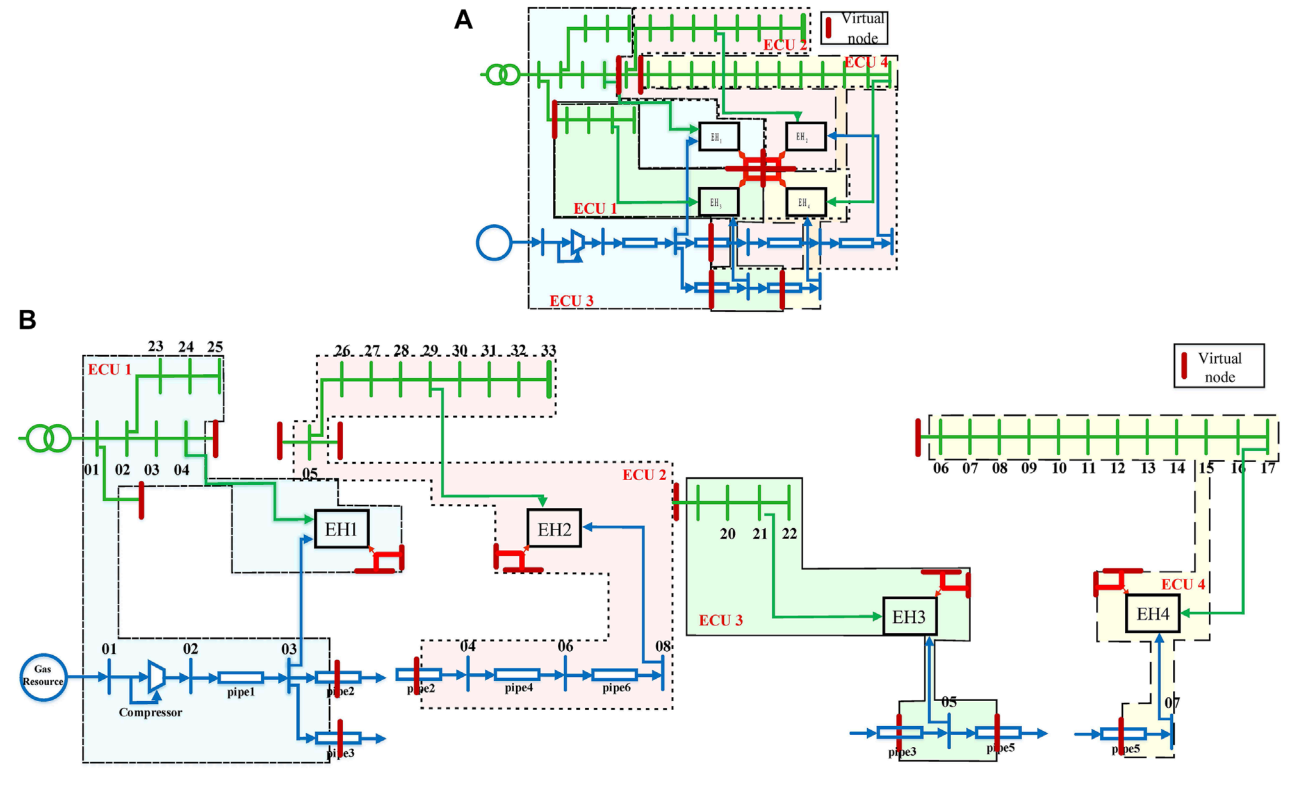

FIGURE 8 | MRIES partition based on ECU. **(A)** Overall partition of MRIES. **(B)** Partition details of MRIES.

TABLE 1 | Parameters of the energy coupling equipment.

Coupling Device	Capacity (kW)	Efficiency Function
EC	400	Out = −0.00003041*In3+0.01901*In2+0.2593*In
HP	400	Out = 3*In
CHP	e:300	Out = 0.0001150*In2+0.2305*In
	h:420	Out = 0.0001611*In2+0.3228*In
GB	900	Out = 0.8*In
HS	800	h = −0.00005*In+0.93
	(3.2 MWh)	g = −0.00005*Out+0.93

TABLE 2 | Region type and the configuration of EHs.

	Region Types	Equipment				
		EC	HP	CHP	GB	HS
EH1	Residential area	✓	✓	✓		
EH2	Office area	✓	✓	✓	✓	
EH3	Business area	✓	✓	✓		✓
EH4	Industrial area	✓	✓	✓		✓

5.2 Analysis of Optimization Results

The improved algorithm proposed is used to optimize this MRIES in this article. The energy inputs to the equipment of the four ECUs in the different scenarios are shown in **Figure 10**.

As shown in **Figure 10A**, to support the heating load concentrated in midday, the HP is constantly working during low loading time of energy consumption when the power is cheaper. The heating is stored in the HS at night, which releases when the electricity price is high. In addition to this, the GB supports the remaining heating demand. Since there is no GB in EH3, it can only generate heat through the CHP. Furthermore, EH3 has the largest electric load at midday. As a result, the CHP runs at full capacity at all the time. In addition, the CHPs in EH2 and EH4 also run at full capacity at midday when the electric and heating load is large. On the other hand, the electric and heating load is relatively small in EH1. Therefore, the CHP is mainly used for power and heating supply in the peak load period, and the HP will start up for heat supplement during the flat power demand period.

As shown in **Figure 10B**, EH4 uses HP and GB with a high cost to supply heat due to the lack of DHN for heat exchange in scenario B. EH3 no longer needs to provide the heating to the DHN, which produced significant heating in scenario A. As a result, the utilization rate of HP and HS becomes lower. The overall energy cost response of the MRIES weakened in scenario B.

The heating generated by the EH, which is beyond the local heating load, is transmitted to the DHN. As shown in **Figure 11**, the energy represented by the blue block is equal to the energy of other color blocks higher than the heat load line (except the purple block that indicates heating storage). It should be noted that for the intuitive description, the load curves in **Figure 11** are superimposed of electricity, gas, and heating load curves.

Because the coupling of the ECU in the electric network and natural gas network is only reflected in energy transmission, the energy interaction of each ECU in the DHN is mainly analyzed. The energy outputs of each EH device and the energy interaction with the DHN are integrated into **Figures 11A–D**. Evidently, the DHN realizes the heating interaction between the ECUs and dramatically increases the flexibility of energy utilization of the system. In scenario A, the EH1 internal equipment composition is relatively simple, which mainly

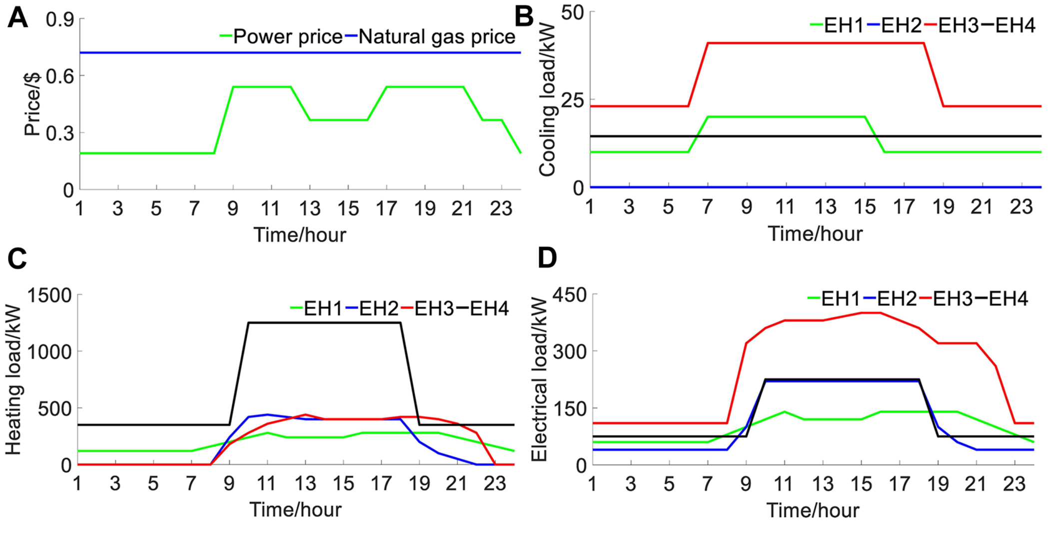

FIGURE 9 | Model data of MRIES. **(A)** Energy price of system. **(B)** Daily cooling load of each EH. **(C)** Daily heat load of each EH. **(D)** Daily electrical load of each EH.

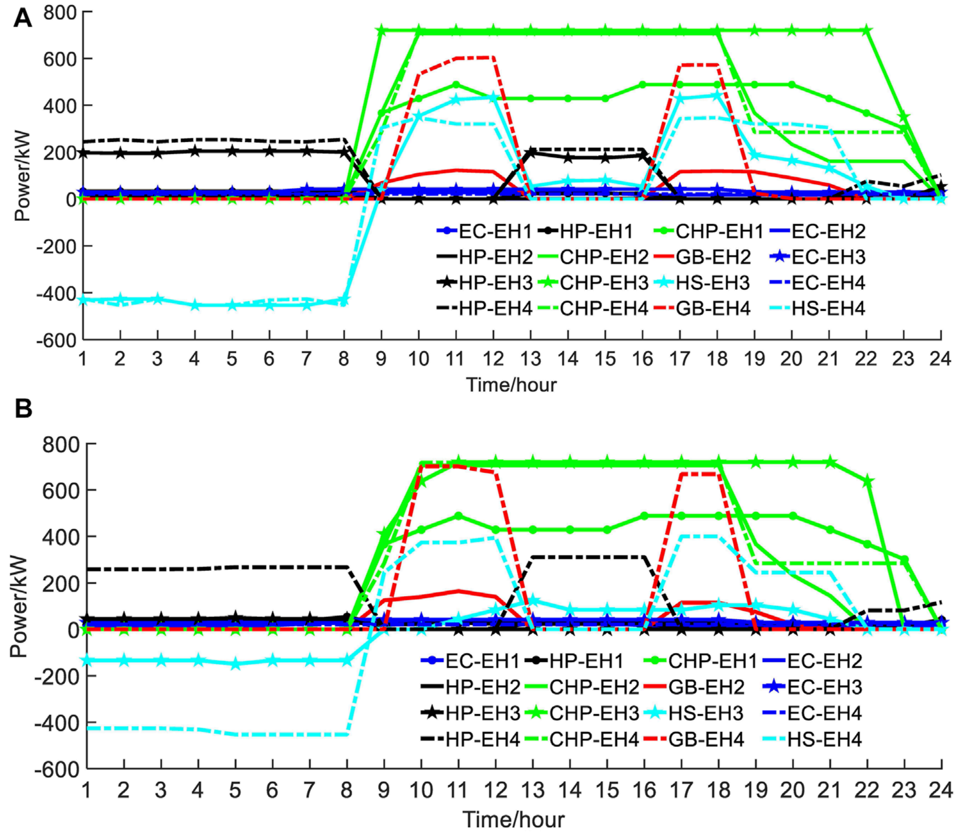

FIGURE 10 | Energy input of each equipment. **(A)** Energy input of each equipment in scenario A. **(B)** Energy input of each equipment in scenario B.

absorbs the heat from the DHN. Although EH4 has many types of internal heat generation equipment, it still mainly absorbs the heat from the DHN due to its large heating load.

From **Figure 11E–H**, we can see that the heating support of EH3 is significantly reduced in scenario B. EH1, EH2, and EH4 have to convert energy through the coupling equipment in their units to meet the local loads, confirming the previous analysis conclusion. The total energy cost of scenario A is 12,281.24 dollars while that of scenario B is 15,234.56 dollars. For now, we can get the importance of the multi-energy cooperative scheduling.

5.3 Comparison of Algorithm Performance

The accuracy and convergence performance of the algorithm proposed are improved in this article. As analyzed previously, the improved algorithm can realize the MRIES global optimization through the unit internal optimization and information interaction between the units. The distributed optimization is not based on the whole system data; it can only approach the result of the centralized algorithm infinitely but cannot be better than that, and the insufficient iteration of the MISOCP will aggravate this error. The centralized algorithm which optimizes based on the whole system data can provide a precision reference for the improved distributed algorithm. The improved C-ADMM algorithm in this article adds the nested subalgorithm, which can not only overcome the nonconvergence problem caused by the MISOCP but can also approach the feasible region more closely than the C-ADMM algorithm, making the results more accurate. The results of the centralized algorithm, C-ADMM algorithm, and improved C-ADMM algorithm are shown as **Table 3**. The total energy cost error of the improved C-ADMM algorithm is about 0.1%. In contrast, the error of the C-ADMM algorithm is about 1.3%. In addition, the electricity and gas cost error are also relatively less. This shows that the improved algorithm proposed in this article achieves better optimization results than the original C-ADMM.

By comparing the convergence performance of the improved algorithm proposed in this article with that of the C-ADMM, the improved algorithm meets the accuracy requirement after 40 iterations. In comparison, the original algorithm needs 90 iterations under the same parameters as shown in **Figure 12**. In this article, the unit internal optimization and the information interaction between the units with the cloud are integrated and simulated on a computer. According to the simulation statistics, the C-ADMM algorithm takes 79.71 s, while the improved

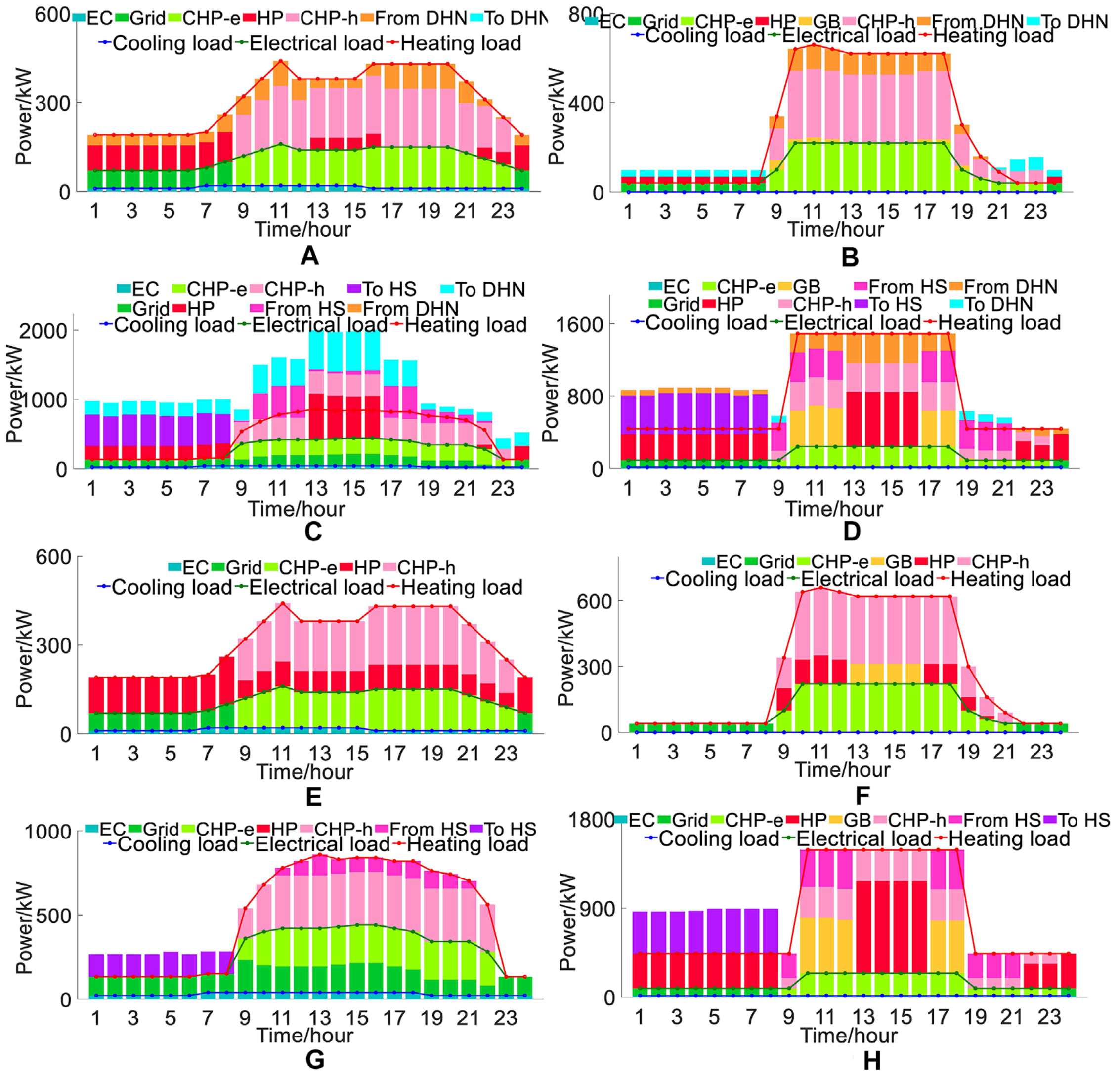

FIGURE 11 | Energy components of the EHs in scenario A and B. **(A)** Energy components of EH1 in scenario A. **(B)** Energy components of EH2 in scenario A. **(C)** Energy components of EH3 in scenario A. **(D)** Energy components of EH4 in scenario A. **(E)** Energy components of EH1 in scenario B. **(F)** Energy components of EH2 in scenario B. **(G)** Energy components of EH3 in scenario B. **(H)** Energy components of EH4 in scenario B.

C-ADMM algorithm takes 40.76 s. Therefore, the convergence performance of the improved algorithm is better than that of the original algorithm.

The rationality of the distributed optimization with the ECU as a subsystem was verified by the improved algorithm. At the same time, the improved algorithm is proven to be superior to the original algorithm. The ECU provides a standard unit form for the improved consensus-ADMM algorithm, and their strengths are closely combined to achieve good optimization results.

TABLE 3 | Comparison of the algorithm error.

Algorithm	Total cost		Power cost		Natural gas cost	
	data/$	error	data/$	error	data/$	error
Centralized optimization	12,281.24	0	5,950.02	0	6,343.91	0
C-ADMM	12,436.12	1.3%	5,694.48	4.3%	6,741.64	6.3%
Improved C-ADMM	12,293.95	0.1%	5,715.71	3.9%	6,578.99	3.7%

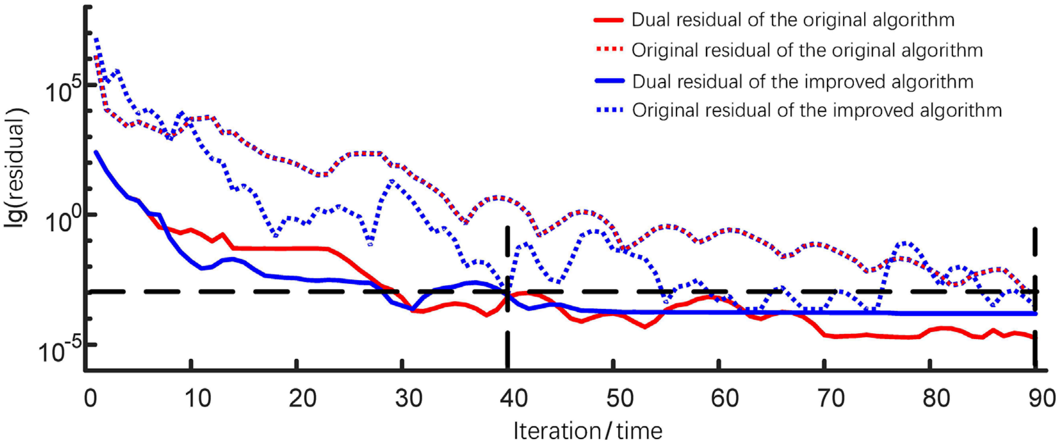

FIGURE 12 | Comparison of the residual convergence in the distributed algorithms.

6 CONCLUSION AND PROSPECTS

From the perspective of the data interaction architecture, this study compares the differences, advantages, and disadvantages of the centralized optimization and distributed optimization, where the IES is decoupled according to the energy networks and the distributed optimization based on the proposed ECU framework. In addition, a unified network partition method is proposed, and the ECU model is introduced in detail.

This study improved the C-ADMM method to adapt to the ECU model. A study case verifies the improved convergence performance of the improved algorithm, and the algorithm was proven to assist the ECU model in completing the distributed optimization of the MRIES well.

In conclusion, the ECU model proposed in this article can fully play the advantages of energy utilization and data management of the RIES and serve as a distributed unit connected to the upper energy network and the lower load layer. Moreover, it breaks through the limitation that the IES distributed optimization with EH as the main body failed to consider the constraints of networks. In addition, the ECU framework can be used as the unit of the MRIES for further research, such as model predictive control and study for the uncertainty involved by wind power and photovoltaic. In addition, the future work will consider carbon emission in the optimization objective for the carbon peak and carbon neutrality targets.

DATA AVAILABILITY STATEMENT

The raw data supporting the conclusions of this article will be made available by the authors, without undue reservation.

AUTHOR CONTRIBUTIONS

MW: conceptualization, methodology, software, validation, formal analysis, investigation, writing—original draft, visualization, and resources. HZ: methodology, software, validation, writing—review and editing, supervision, project administration, and funding acquisition. HT: methodology, writing—review and editing, and project administration. QW: methodology, validation, writing—review and editing, and project administration.

FUNDING

This work was supported by the National Key R&D Program of, China under Grant No. 2018YFA0702200.

REFERENCES

Albataineh, H., Nijim, M., and Bollampall, D. (2020). “The Design of a Novel Smart home Control System Using Smart Grid Based on Edge and Cloud Computing,” in *2020 IEEE 8th International Conference on Smart Energy Grid Engineering (SEGE)*, 88–91. doi:10.1109/SEGE49949.2020.9181961

Baran, M. E., and Wu, F. F. (1989). Network Reconfiguration in Distribution Systems for Loss Reduction and Load Balancing. *IEEE Trans. Power Deliv.* 4, 1401–1407. doi:10.1109/61.25627

Cao, K., Zhou, J., Xu, G., Wei, T., and Hu, S. (2019). “Exploring Renewable-Adaptive Computation Offloading for Hierarchical Qos Optimization in Fog Computing,” in *IEEE Transactions on Computer-Aided Design of Integrated Circuits and Systems*, 1. doi:10.1109/TCAD.2019.2957374

Chen, F., Deng, H., and Shao, Z. (2020). “Distributed Robust Synergistic Scheduling of Electricity, Natural Gas, Heating and Cooling Systems via Admm,” in *International Journal of Energy Research*. doi:10.1002/er.6379

Chen, J., Zhang, W., Lin, D., Zhihao, L. I., Song, G., and Yifeng, G. U. (2019). “Distributed Optimal Dispatch of Integrated Electricity-Gas-Heating System

Based on Improved Alternative Direction Multiplier Method," in *Automation of Electric Power Systems*. doi:10.7500/AEPS20180720004

Chen, Q., Xia, M., Chen, M., and Hu, H. (2018). "Distributed Energy Management for Integrated Energy System Considering Multiple Independent Operators," in *2018 IEEE Power Energy Society General Meeting (PESGM)*, 1–5. doi:10.1109/pesgm.2018.8586052

Chen, S., Bai, Y., Zhang, Y., Liu, X., Zhang, J., Gao, T., et al. (2019). "A Framework of Decentralized Electricity Market Based on the Collaborative Mechanism of Blockchain and Edge Computing," in *2019 IEEE International Conference on Service Operations and Logistics, and Informatics (SOLI)*, 219–223. doi:10.1109/SOLI48380.2019.8955023

Chen, W., Mu, Y., Hongjie, J., Wei, W., and Wei, H. (2021). "Operation Optimization Method for Regional Integrated Energy System that Considers Part-Load Performances of Devices," in *Power System Technology*. doi:10.13335/j.1000-3673.pst.2020.1149

Haitao, H., Zha, J., Xi, C., and Jian, L. (2021). *Research on Distributed Cooperative Optimization of Multi-Agent Integrated Energy System Based on Admm Algorithm*. Harbin, Heilongjiang Province: Electrical Measurement & Instrumentation, 1–9. Available at: http://kns.cnki.net/kcms/detail/23.1202.TH.20210506.1312.006.html (Accessed April 10, 2022).

Haozhong, C., Xiao, H., Li, W., Yuquan, L., and Qi, Y. (2019). "Review on Research of Regional Integrated Energy System Planning," in *Automation of Electric Power Systems*, 43, 12. doi:10.7500/AEPS20180416006

Hu, X., Shang, C., Cheng, H., Wang, L., Chen, D., and Yong, L. (2020). "Review and prospect of Calculation Method for Energy Flow in Integrated Energy System," in *Automation of Electric Power Systems*, 44, 13. doi:10.7500/AEPS20191113001

Huang, W., Zhang, N., Wang, Y., Capuder, T., and Kang, C. (2019). "Matrix Modeling of Energy Hub with Variable Energy Efficiencies," in *International Journal of Electrical Power and Energy Systems*. doi:10.1016/j.ijepes.2020.105876

Liu, D., Zeng, X., and Wang, Y. (2021). "Control Strategy of Virtual Power Station in Distribution Transformer Area under Edge Computing Architecture," in *Transactions of China Electrotechnical Society*, 52–56. doi:10.19595/j.cnki.1000-6753.tces.l90517

Liu, T., Zhang, D., and Wu, T. (2020). Standardised Modelling and Optimisation of a System of Interconnected Energy Hubs Considering Multiple Energies-Electricity, Gas, Heating, and Cooling. *Energ. Convers. Manage.* 205, 112410. doi:10.1016/j.enconman.2019.112410

Ma, M., Fan, L., and Miao, Z. (2016). "Consensus Admm and Proximal Admm for Economic Dispatch and Ac Opf with Socp Relaxation," in *North American Power Symposium*. doi:10.1109/naps.2016.7747961

Na, L., Xichao, Z., Bing, W., Lin, C., Tai, J., and Chongchao, P. (2020). "Research on Optimization Models of Integrated Energy System," in *Shanghai Energy Conservation*, 6. doi:10.13770/j.cnki.issn2095-705x.2020.06.007

Wang, J., Gu, W., Lu, S., and Zhang, C. (2016). "Coordinated Planning of Multi-District Integrated Energy System Combining Heating Network Model," in *Automation of Electric Power Systems*, 40, 8. doi:10.7500/AEPS20160426010

Wang, X., Hong, M., Ma, S., and Luo, Z. Q. (2013). "Solving Multiple-Block Separable Convex Minimization Problems Using Two-Block Alternating Direction Method of Multipliers," in *Pacific Journal of Optimization*, 11. doi:10.48550/arXiv.1308.5294

Wang, Y., Zhang, N., Kang, C., Kirschen, D. S., Yang, J., and Xia, Q. (2017). "Standardized Matrix Modeling of Multiple Energy Systems," in *IEEE Transactions on Smart Grid*. doi:10.1109/TSG.2017.2737662

Wei, G., Lu, S., Wang, J., Yin, X., and Wang, Z. (2017). "Modeling of the Heating Network for Multi-District Integrated Energy System and its Operation Optimization," in *Proceedings of the Chinese Society of Electrical Engineering*, 3737. doi:10.13334/j.0258-8013.pcsee.160991

Weisong, S., Hui, S., Jie, C., Zhang, Q., and Liu, W. (2017). Edge Computing–An Emerging Computing Model for the Internet of Everything Era. *Comput. Res. Develop.* 54, 18. doi:10.7544/issn1000-1239.2017.20160941

Wen, Y., Qu, X., Li, W., Liu, X., and Ye, X. (2017). "Synergistic Operation of Electricity and Natural Gas Networks via Admm," in *IEEE Transactions on Smart Grid*, 1. doi:10.1109/TSG.2017.2663380

Wu, M., Wan, C., Wang, L., Wang, K., and Jiang, Y. (2020). "Hierarchical Autonomous Cooperative Operation of District Integrated Heating and Power System," in *2020 IEEE/IAS Industrial and Commercial Power System Asia (I&CPS Asia)*. doi:10.1109/icpsasia48933.2020.9208372

Xu, D., Wu, Q., Zhou, B., Li, C., and Huang, S. (2019). "Distributed Multi-Energy Operation of Coupled Electricity, Heating and Natural Gas Networks," in *IEEE Transactions on Sustainable Energy*, 1. doi:10.1109/TSTE.2019.2961432

Yunzhou, Z., Hongcai, D., Xiaoyu, W., Rui, C., and Ning, Z. (2021). Development Trends and Key Issue of china's Integrated Energy Services. *Electric Power* 2, 1–10. doi:10.11930/j.issn.1004-9649.202012040

Zhang, X., Yu, T., Zhang, Z., and Tang, J. (2018). Multi-agent Bargaining Learning for Distributed Energy Hub Economic Dispatch. *IEEE Access* 6, 39564–39573. doi:10.1109/access.2018.2853263

Conflict of Interest: The authors declare that the research was conducted in the absence of any commercial or financial relationships that could be construed as a potential conflict of interest.

NOMENCLATURE

Abbreviations

ADMM	Alternating direction multiplier method
C-ADMM	Consensus-alternating direction multiplier method
CHP	Combined heat and power
DHN	District Heating Network
ECU	Edge computing unit
EC	Electrical chiller
EHR	Electricity consumption to transferred heating quantity ratio
EH	Energy hub
GB	Gas boiler
GS-ADMM	Gauss–Seidel alternating direction multiplier method
HP	Heat pump
HS	Heat storage
IES	Integrated energy system
MILP	Mixed-integer linear programming
MISOCP	Mixed-integer second-order cone programming
MRIES	Multiregion integrated energy system
NC-ADMM	Nonconvex alternating direction multiplier method
RIES	Regional integrated energy system
SOCP	Second-order core programing

Indices

a, b, ω	Index of natural gas network nodes
d	Index of loads in energy networks
g, pv, wt	Indices of electrical generating units, photovoltaic power plants, and wind turbines
i, j, o	Index of electrical network nodes
k	Index of iteration numbers
p	Index of heating network pipelines
r, f	Indices of unpartitioned nodes and EH nodes in energy networks
s	Index of binary variables
t	Index of time intervals
u, v, m	Index of heating network nodes

Parameters

μ	Proportionality constant
ρ	Penalty factor in the C-ADMM algorithm
ΣR	Total thermal resistance between the heat medium and surrounding medium per kilometer of pipe
θ	Penalty factor in the subalgorithm
$c_{e,t}, c_{g,t}$	Electricity price and natural gas price at t
K_{ab}	Weymouth characteristic parameter of the pipeline ab
l_{uv}	Length of the pipe uv
N	Number of EHs
pi	Circular constant
S	Number of binary variables
W	Number of pipes in the DHN

Sets

$\gamma \in \Gamma$	Set of segments in piecewise linearization
$\Lambda(b), \Upsilon(b)$	Set of loads and downstream nodes connected to node j in the natural gas network
$\Phi(u)$	Set of downstream nodes connected to node u in the DHN
$\Pi(j), \Omega(j)$	Set of devices and downstream nodes connected to node j in the power system
Θ_n	Set of energy transmission lines between the nth ECU with others
A_n^{upper}, B_n^{under}	Set of upstream and downstream virtual nodes of the ECU n in the natural gas network
I_n^{upper}, J_n^{under}	Set of upstream and downstream virtual nodes of the ECU n in the power system

Variables

ΔH_p^{av}	Available heating loss of the pth pipe
$\Delta H_{uv}^{av}, \Delta H_{mu}^{av}$	Available heating loss of pipe uv and pipe mu
$\hat{I}_{ij,t}$	Square value of branch ij current at t
$\hat{I}_{ij}^{max}, \hat{I}_{ij}^{min}$	Lower/upper bounds of square value of branch ij current
$\hat{V}_{(\cdot),t}$	Square value of the node voltage at t
$\hat{V}_i^{max}, \hat{V}_i^{min}$	Lower/upper bounds of square value of node i voltage
$\mathbb{I}_\gamma, \mathbb{I}_{\gamma+1}$	Binary variables to guarantee the continuity of X and $F_L(X)$
$\overline{X\gamma}, X_\gamma$	Lower/upper bounds of the γ-th segment of X
$\pi_{(\cdot),t}$	Gas pressure of node at t
π_a^{min}, π_a^{max}	Lower/upper bounds of gas pressure of node a
$\sigma_\gamma, \eta_\gamma$	Value of the γ-th segment of X and coefficient of the γ-th segment of $F_L(X)$
EHR_p	The EHR of the water pump p
$C_B, z_{B,B}$	Continuous variable, auxiliary variable, and binary variable,$C_B \in [0,1]$
C_n^{heat}	Cost of the DHN connected to EH n
$F(X), F_L(X)$	Nonlinear function and its linearized function
$G_{(\cdot\cdot),t}$	Natural gas in pipeline at t
$G_{(\cdot),t}^{in}$	Natural gas injected into the node at t
G_{ab}^{max}	Upper bounds of natural gas in the pipeline ab
$G_{b,t}^{EH}$	Natural gas injected to the EH connected to node b at t
$G_{d,t}^{LD}$	Natural gas injected to load d at t
$G_{n,t}^{ECU}$	Natural gas consumption of the ECU n at t
H^{EH}	Heating input of EH from the DHN
H^{av}	Available heating

$H_{p,t}$	Heating transferred in pipe p
$H_{u,t}^{EH}$	Heating injected into the EH connected to the node u at t
$H_{um,t}^{av,min}, H_{um,t}^{av,max}$	Lower/upper bounds of available heating from node u to node m
$H_{um,t}^{av}, H_{mu,t}^{av}$	Available heating from node u to node m and node m to node u at t
$H_{uv,t}^{av}, H_{vu,t}^{av}$	Available heating from node u to node v and node v to node u at t
$L_{cool}, L_{elec}, L_{heat}$	Cooling, electricity, and heating loads of the EH
P^{EH}, G^{EH}	Power and natural gas input of the EH
$P_{(\cdot\cdot),t}, Q_{(\cdot\cdot),t}$	Active power and reactive power on branch at t
$P_{(\cdot),t}^{in}, Q_{(\cdot),t}^{in}$	Active power and reactive power injected to node at t
$P_{in}^{CHP}, P_{out,e}^{CHP}, P_{out,h}^{CHP}$	Input and output energy of the CHP
$P_{in}^{EC}, P_{out}^{EC}$	Input and output energy of the EC
$P_{in}^{GB}, P_{out}^{GB}$	Input and output energy of the GB
P_{in}^{Grid}	Input energy from the grid
$P_{in}^{HP}, P_{out}^{HP}$	Input and output energy of the HP
$P_{in}^{HS}, P_{out}^{HS}$	Input and output energy of the HS
$P_{d,t}^{LD}, Q_{d,t}^{LD}$	Active power and reactive power injected to load d at t
$P_{g,t}^{G}$	Active power generated from the generator g at t
$P_{j,t}^{EH}$	Active power injected to the EH connected to node j at t
$P_{n,t}^{ECU}$	Power consumption of the ECU n at t
$P_{pv,t}^{PV}$	Active power generated from photovoltaic power plants pv at t
$P_{wt,t}^{WT}$	Active power generated from wind turbine wt at t
q	Mass flow
$q_{u,t}^{EH}$	Mass flow injected into the EH of node u at t
$q_{uv,t}, q_{vu,t}$	Mass flow from node u to node v and node v to node u at t
R_{ij}, X_{ij}	Resistance and reactance of branch ij
T, T^{e}	Real temperature and ambient temperature
T^{rw}, T^{sw}	Return water temperature and supply water temperature
$T_{(\cdot),t}$	Node temperature at t
$T_{u,t}^{EH}$	Temperature of heat medium injected into the EH connected to node u at t
$T_{uv,t}, T_{vu,t}$	Temperature of heat medium from node u to node v and node v to node u at t
V	Matrix of coupling equipment's input and output energy
$V1$	Matrix of the EH's input resources and loads
X, X_0	Continuous variable and its initial value
$x_{\alpha\beta,\alpha,t}, x_{\alpha\beta,\beta,t}$	Coupling variables on both sides of the virtual node at t
y_{rf}	Binary variable of node r partition to region f
Z	Standard matrix of the EH
$z_{\alpha\beta,t}$	Consensus variable of the virtual node at t
$\lambda_{\alpha\beta,\alpha,t}, \lambda_{\alpha\beta,\beta,t}$	Lagrange multipliers of the ECUs on both sides of the virtual node at t
λ_{loss}^{H}	Lagrange multiplier in terms of the transmission loss in the DHN at t
B_s^k, B_s^{k+1}	The sth binary variables in the kth and the $(k+1)$-th iteration
$C_{B,s}^k, C_{B,s}^{k+1}$	The sth continuous variables in the kth and the $(k+1)$-th iteration
$z_{B,s}^k, z_{B,s}^{k+1}$	The sth auxiliary variables in the kth and the $(k+1)$-th iteration

Advantages of publishing in Frontiers

OPEN ACCESS
Articles are free to read
for greatest visibility
and readership

FAST PUBLICATION
Around 90 days
from submission
to decision

HIGH QUALITY PEER-REVIEW
Rigorous, collaborative,
and constructive
peer-review

TRANSPARENT PEER-REVIEW
Editors and reviewers
acknowledged by name
on published articles

Frontiers
Avenue du Tribunal-Fédéral 34
1005 Lausanne | Switzerland

Visit us: www.frontiersin.org
Contact us: frontiersin.org/about/contact

REPRODUCIBILITY OF RESEARCH
Support open data
and methods to enhance
research reproducibility

DIGITAL PUBLISHING
Articles designed
for optimal readership
across devices

FOLLOW US
@frontiersin

IMPACT METRICS
Advanced article metrics
track visibility across
digital media

EXTENSIVE PROMOTION
Marketing
and promotion
of impactful research

LOOP RESEARCH NETWORK
Our network
increases your
article's readership